

AJNR

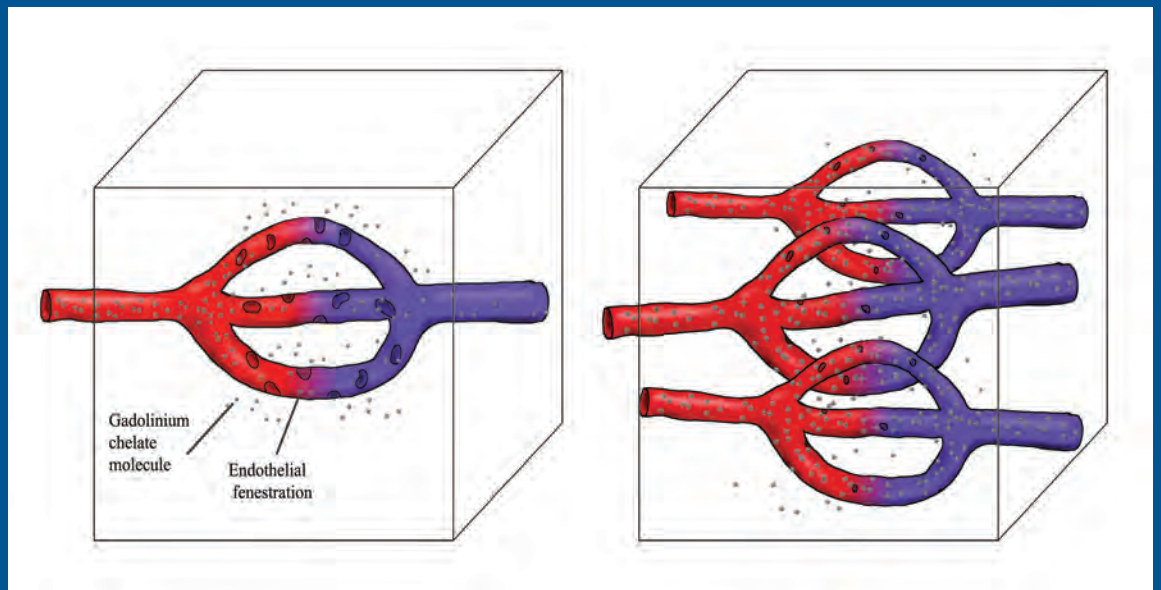
AMERICAN JOURNAL OF NEURORADIOLOGY

MAY 2015
VOLUME 36
NUMBER 5
WWW.AJNR.ORG

THE JOURNAL OF DIAGNOSTIC AND
INTERVENTIONAL NEURORADIOLOGY

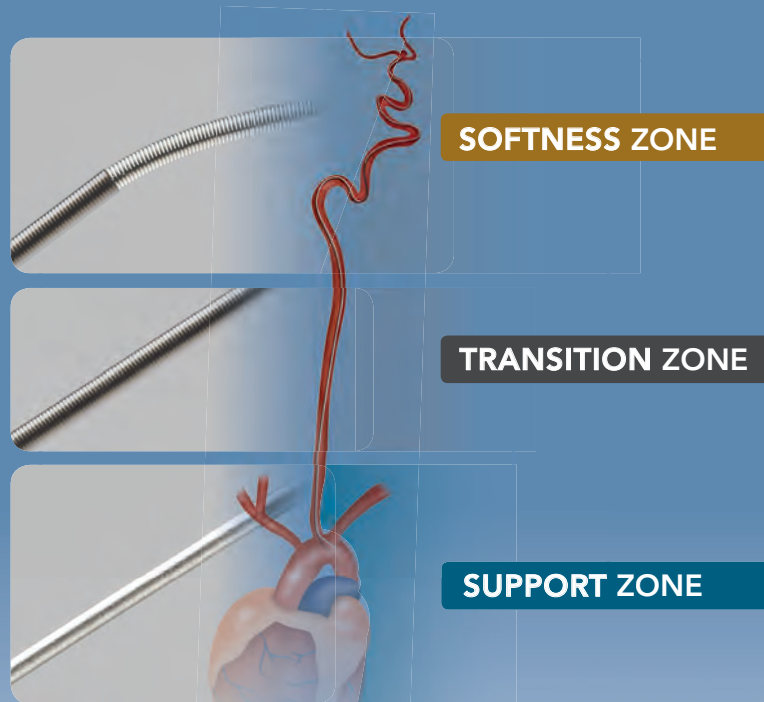
Spinal cord ischemia
Biomarkers in ischemic stroke
Dual-energy CT in SAH

Official Journal ASNR • ASFNR • ASHNR • ASPNR • ASSR



Advanced

by MicroVention



ENHANCED CONTROL TO MAXIMIZE COIL PERFORMANCE

The **V-Trak[®] Advanced Coil System**, the next generation to power the performance of our most technically advanced line of coils. Offering the optimal combination of support and flexibility.

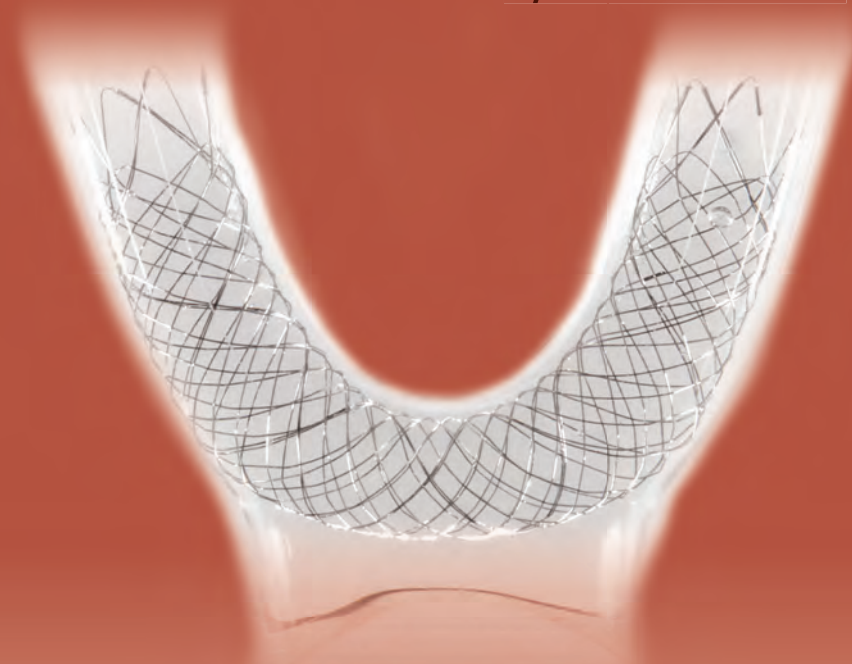
microvention.com

MICROVENTION, V-Trak, LVIS and Headway are registered trademarks of MicroVention, Inc. Scientific and clinical data related to this document are on file at MicroVention, Inc. Refer to Instructions for Use, contraindications and warnings for additional information. Federal (USA) law restricts this device for sale by or on the order of a physician. © 2015 MicroVention, Inc. 1/15

CE
0297

Support

by MicroVention



LOW-PROFILE VISUALIZED INTRALUMINAL SUPPORT

The **LVIS®** and **LVIS® Jr. devices** are the next generation technology for optimal intraluminal support and coverage for stent-assist coil procedures.

Used with  **Headway**
Microcatheter

RX only.

Humanitarian Device:

Authorized by Federal Law for use with bare platinum embolic coils for the treatment of unruptured, wide neck (neck \geq 4 mm or dome to neck ratio $<$ 2), intracranial, saccular aneurysms arising from a parent vessel with a diameter \geq 2.5 mm and \leq 4.5 mm. The effectiveness of this device for this use has not been demonstrated.

For more information or a product demonstration,
contact your local MicroVention representative:



MicroVention, Inc.

Worldwide Headquarters

1311 Valencia Avenue

Tustin, CA 92780 USA

MicroVention UK Limited

MicroVention Europe, S.A.R.L.

MicroVention Deutschland GmbH

PH +1.714.247.8000

PH +44 (0) 191 258 6777

PH +33 (1) 39 21 77 46

PH +49 211 210 798-0

COILING OPTIMIZED



NOW AVAILABLE

**BARRICADE COMPLEX
FINISHING COIL**

- ◆ Extremely soft profile of The Barricade Finishing coil now in a complex shape
- ◆ Excellent microcatheter stability for confident coil placement
- ◆ Available in a size range of 1mm-5mm

BARRICADE™ COIL SYSTEM



MADE IN AMERICA

The Barricade Coil System is intended for the endovascular embolization of intracranial aneurysms and other neurovascular abnormalities such as arteriovenous malformations and arteriovenous fistulae. The System is also intended for vascular occlusion of blood vessels within the neurovascular system to permanently obstruct blood flow to an aneurysm or other vascular malformation and for arterial and venous embolizations in the peripheral vasculature. Refer to the instructions for use for complete product information.

18 TECHNOLOGY DRIVE #169, IRVINE CA 92618

p: 949.788.1443 | f: 949.788.1444

WWW.BLOCKADEMEDICAL.COM

MKTG-031 Rev. A



BLOCKADE
M E D I C A L

AJNR

AMERICAN JOURNAL OF NEURORADIOLOGY

MAY 2015
VOLUME 36
NUMBER 5
WWW.AJNR.ORG

Publication Preview at www.ajnr.org features articles released in advance of print. Visit www.ajnrblog.org to comment on AJNR content and chat with colleagues and AJNR's News Digest at <http://ajnrdigest.org> to read the stories behind the latest research in neuroimaging.

EDITORIALS

PERSPECTIVES

- 817 **Coffee Houses and Reading Rooms** *M. Castillo*

EDITORIALS

- 819 **Teaching Lessons by MR CLEAN** *L. Pierot, V. Mendes Pereira, C. Cognard, and R. von Kummer*
- 821 **Comeback Victory** *V. Mendes Pereira and T. Krings*

REVIEW ARTICLES

- 825 **Spinal Cord Ischemia: Practical Imaging Tips, Pearls, and Pitfalls**
M.I. Vargas, J. Gariani, R. Sztajzel, I. Barнауre-Nachbar, B.M. Delattre, K.O. Lovblad, and J.-L. Dietemann
- 831 **CSF Flow in the Brain in the Context of Normal Pressure Hydrocephalus**
W.G. Bradley Jr

RESEARCH PERSPECTIVES

- 839 **Imaging Biomarkers in Acute Ischemic Stroke Trials: A Systematic Review**
G.W.J. Harston, N. Rane, G. Shaya, S. Thandeswaran, M. Cellnerini, F. Sheerin, and J. Kennedy

COMMENTARY

- 844 **Imaging Biomarkers in Ischemic Stroke Clinical Trials: An Opportunity for Rigor** *R.G. González*

FUNCTIONAL VIGNETTE

- 846 **Memory Part 2: The Role of the Medial Temporal Lobe** *F.D. Raslau, I.T. Mark, A.P. Klein, J.L. Ulmer, V. Mathews, and L.P. Mark*

BRAIN

- 850 **Evaluating Blood-Brain Barrier Permeability in Delayed Cerebral Infarction after Aneurysmal Subarachnoid Hemorrhage** *J. Ivanidze, K. Kesavabhotla, O.N. Kallas, D. Mir, H. Baradaran, A. Gupta, A.Z. Segal, J. Claassen, and P.C. Sanelli*
- 855 **Evaluation of Virtual Noncontrast Images Obtained from Dual-Energy CTA for Diagnosing Subarachnoid Hemorrhage** *X.Y. Jiang, S.H. Zhang, Q.Z. Xie, Z.J. Yin, Q.Y. Liu, M.D. Zhao, X.L. Li, and X.J. Mao*

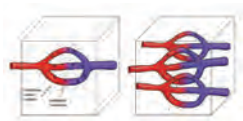
COMMENTARY

- 861 **Dual-Energy CTA to Diagnose Subarachnoid Hemorrhage: Ready for Prime Time?** *J.L. Brisman*



- 863 **Neurovascular Manifestations in Hereditary Hemorrhagic Telangiectasia: Imaging Features and Genotype-Phenotype Correlations** *T. Krings, H. Kim, S. Power, J. Nelson, M.E. Faughnan, W.L. Young, K.G. terBrugge, and the Brain Vascular Malformation Consortium HHT Investigator Group*

- Indicates Editor's Choices selection
- Indicates Fellows' Journal Club selection
- Indicates open access to non-subscribers at www.ajnr.org
- Indicates article with supplemental on-line table
- Indicates article with supplemental on-line photo
- Indicates article with supplemental on-line video
- Indicates Evidence-Based Medicine Level 1
- Indicates Evidence-Based Medicine Level 2



Similar K^{trans} is seen for low permeability/high area and high permeability/low area.



Trevo[®] XP

PROVUE RETRIEVER

Take Control. Capture More.

The newly designed Trevo[®] XP ProVue Retriever takes proven Trevo Retriever performance to new levels for **easy delivery**, **easy placement**, and **easy visualization**.

When you're in control, it's amazing what you can capture.

stryker[®]
Neurovascular

- 871 **Pixel-by-Pixel Comparison of Volume Transfer Constant and Estimates of Cerebral Blood Volume from Dynamic Contrast-Enhanced and Dynamic Susceptibility Contrast-Enhanced MR Imaging in High-Grade Gliomas**
P. Alcaide-Leon, D. Pareto, E. Martinez-Saez, C. Auger, A. Bharatha, and A. Rovira
-   877 **Diffusion and Perfusion MRI to Differentiate Treatment-Related Changes Including Pseudoprogession from Recurrent Tumors in High-Grade Gliomas with Histopathologic Evidence** *A.J. Prager, N. Martinez, K. Beal, A. Omuro, Z. Zhang, and R.J. Young*
-  886 **Discrimination of Tumorous Intracerebral Hemorrhage from Benign Causes Using CT Densitometry** *Y.S. Choi, T.H. Rim, S.S. Ahn, and S.-K. Lee*
- 893 **Dilated Perivascular Spaces in the Basal Ganglia Are a Biomarker of Small-Vessel Disease in a Very Elderly Population with Dementia**
T.P. Hansen, J. Cain, O. Thomas, and A. Jackson
-   899 **Increased Number of White Matter Lesions in Patients with Familial Cerebral Cavernous Malformations** *M.J. Golden, L.A. Morrison, H. Kim, and B.L. Hart*
-   904 **Pituitary-Targeted Dynamic Contrast-Enhanced Multisection CT for Detecting MR Imaging–Occult Functional Pituitary Microadenoma**
M. Kinoshita, H. Tanaka, H. Arita, Y. Goto, S. Oshino, Y. Watanabe, T. Yoshimine, and Y. Saitoh
-   909 **Clinical Utility of Arterial Spin-Labeling as a Confirmatory Test for Suspected Brain Death** *K.M. Kang, T.J. Yun, B.-W. Yoon, B.S. Jeon, S.H. Choi, J.-h. Kim, J.E. Kim, C.-H. Sohn, and M.H. Han*

FUNCTIONAL

- 915 **Disrupted Resting-State Functional Connectivity in Progressive Supranuclear Palsy** *M.C. Piattella, F. Tona, M. Bologna, E. Sbardella, A. Formica, N. Petsas, N. Filippini, A. Berardelli, and P. Pantano*

INTERVENTIONAL *Published in collaboration with Interventional Neuroradiology*

- 922 **WEB Treatment of Intracranial Aneurysms: Feasibility, Complications, and 1-Month Safety Results with the WEB DL and WEB SL/SLS in the French Observatory** *L. Pierot, J. Moret, F. Turjman, D. Herbreteau, H. Raoult, X. Barreau, S. Velasco, H. Desal, A.-C. Januel, P. Courtheoux, J.-Y. Gaurvit, C. Cognard, S. Soize, A. Molyneux, and L. Spelle*
- COMMENTARY
- 928 **Challenges of the WEB Device for Intracranial Aneurysms: How to Widen the Spectrum and Compare Favorably** *G.A. Schubert*
-  930 **Uncertainty and Agreement Regarding the Role of Flow Diversion in the Management of Difficult Aneurysms** *T.E. Darsaut, J.-C. Gentric, C.M. McDougall, G. Gevry, D. Roy, A. Weill, and J. Raymond*
- 937 **Anterior Choroidal Artery Patency and Clinical Follow-Up after Coverage with the Pipeline Embolization Device** *E. Raz, M. Shapiro, T. Becske, D.W. Zumofen, O. Tanweer, M.B. Potts, H.A. Riina, and P.K. Nelson*
- 943 **Prospective Study of Early MRI Appearances following Flow-Diverting Stent Placement for Intracranial Aneurysms** *BJ. McGuinness, S. Memon, and J.K. Hope*
-  949 **Association between Venous Angioarchitectural Features of Sporadic Brain Arteriovenous Malformations and Intracranial Hemorrhage**
M.D. Alexander, D.L. Cooke, J. Nelson, D.E. Guo, C.F. Dowd, R.T. Higashida, V.V. Halbach, M.T. Lawton, H. Kim, and S.W. Hetts
-   953 **Quantifying Intracranial Aneurysm Wall Permeability for Risk Assessment Using Dynamic Contrast-Enhanced MRI: A Pilot Study** *P. Vakil, S.A. Ansari, C.G. Cantrell, C.S. Eddleman, F.H. Dehkordi, J. Vranic, M.C. Hurley, H.H. Batjer, B.R. Bendok, and T.J. Carroll*



**ASNR 2016 – 54th Annual Meeting &
The Foundation of the ASNR Symposium 2016**

May 21–26 • Washington Marriott Wardman Park • Washington, DC

**ASNR 2017 – 55th Annual Meeting &
The Foundation of the ASNR Symposium 2017**

April 22-27 • Long Beach Convention & Entertainment Center • Long Beach, California

**ASNR 2018 – 56th Annual Meeting &
The Foundation of the ASNR Symposium 2018**

June 2-7 • Vancouver Convention Centre • Vancouver, B.C., Canada

**ASNR 2019 – 57th Annual Meeting &
The Foundation of the ASNR Symposium 2019**

May 18–23 • Hynes Convention Center • Boston, Massachusetts

**Request Programming and Registration Materials
for the ASNR 54th Annual Meeting, Contact:**

ASNR 54th Annual Meeting
c/o American Society of Neuroradiology
800 Enterprise Drive, Suite 205
Oak Brook, Illinois 60523-4216

Phone: 630-574-0220
Fax: 630-574-0661
Email: meetings@asnr.org
Website: www.asnr.org/2016

**Scan now
to visit our
website**



960 **Exploring the Value of Using Color-Coded Quantitative DSA Evaluation on Bilateral Common Carotid Arteries in Predicting the Reliability of Intra-Ascending Aorta Flat Detector CT–CBV Maps** Q. Zhang, R. Xu, Q. Sun, H. Zhang, J. Mao, T. Shan, W. Pan, Y. Deuerling-Zheng, M. Kowarschik, and J. Beilner

 967 **Assessing Blood Flow in an Intracranial Stent: A Feasibility Study of MR Angiography Using a Silent Scan after Stent-Assisted Coil Embolization for Anterior Circulation Aneurysms** R. Irie, M. Suzuki, M. Yamamoto, N. Takano, Y. Suga, M. Hori, K. Kamagata, M. Takayama, M. Yoshida, S. Sato, N. Hamasaki, H. Oishi, and S. Aoki

971 **The Curved MCA: Influence of Vessel Anatomy on Recanalization Results of Mechanical Thrombectomy after Acute Ischemic Stroke** B.J. Schwaiger, A.S. Gersing, C. Zimmer, and S. Prothmann

977 **Dual-Lumen Balloon Catheters May Improve Liquid Embolization of Vascular Malformations: An Experimental Study in Swine** J.C. Gentric, J. Raymond, A. Batista, I. Salazkin, G. Gevry, and T.E. Darsaut

HEAD & NECK

982 **CT Findings in the External Auditory Canal after Transcanal Surgery** V. Mingkwansook, H.D. Curtin, and H.R. Kelly

987 **Predictors of Multigland Disease in Primary Hyperparathyroidism: A Scoring System with 4D-CT Imaging and Biochemical Markers** A.R. Sepahdari, M. Bahl, A. Harari, H.J. Kim, M.W. Yeh, and J.K. Hoang

SPINE

  993 **Postoperative Intraspinal Subdural Collections after Pediatric Posterior Fossa Tumor Resection: Incidence, Imaging, and Clinical Features** J.H. Harreld, N. Mohammed, G. Goldsberry, X. Li, Y. Li, F. Boop, and Z. Patay

 1000 **Incidence of Inadvertent Intravascular Injection during CT Fluoroscopy–Guided Epidural Steroid Injections** P.G. Kranz, T.J. Amrhein, and L. Gray

  1008 **Validation of Multisociety Combined Task Force Definitions of Abnormal Disk Morphology** C.H. Cho, L. Hsu, M.L. Ferrone, D.A. Leonard, M.B. Harris, A.A. Zamani, and C.M. Bono

ONLINE FEATURES (www.ajnr.org)

LETTERS

E33 **Panhypopituitarism with Ectopic Posterior Pituitary Lobe, Heterotopia, Polymicrogyria, Corpus Callosum Dysgenesis, and Optic Chiasm/Nerve Hypoplasia: Is That an Undefined Neuronal Migration Syndrome?** N.C. Ören, E. Cagiltay, F. Akay, and S. Toyran

E36 **Head Circumference: A Key Sign in Dating Abusive Head Trauma** C. Adamsbaum and C. Rey-Salmon

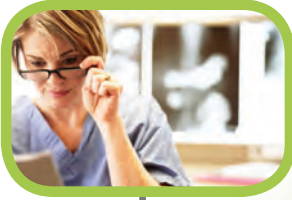
E37 **Reply** D. Wittschieber, B. Karger, T. Niederstadt, H. Pfeiffer, and M.L. Hahnemann

E38 **We Know Now: Mavridis Atrophy Is Associated with Cognitive Impairment in Parkinson Disease** I.N. Mavridis

E39 **ERRATUM**

BOOK REVIEWS R.M. Quencer, Section Editor

Please visit www.ajnrblog.org to read and comment on Book Reviews.



Simplify the MOC Process



Manage your CME Credits Online

CMEgateway.org

Available to Members of Participating Societies

American Board of Radiology (ABR)
American College of Radiology (ACR)
American Roentgen Ray Society (ARRS)
American Society of Neuroradiology (ASNR)
Commission on Accreditation of Medical
Physics Educational Programs, Inc. (CAMPEP)
Radiological Society of North America (RSNA)
Society of Interventional Radiology (SIR)
SNM
The Society for Pediatric Radiology (SPR)

It's Easy and Free!

Log on to CME Gateway to:

- View or print reports of your CME credits from multiple societies from a single access point.
- Print an aggregated report or certificate from each participating organization.
- Link to SAMs and other tools to help with maintenance of certification.

American Board of Radiology (ABR) participation!

By activating ABR in your organizational profile, your MOC-fulfilling CME and SAM credits can be transferred to your own personalized database on the ABR Web site.

Sign Up Today!

go to CMEgateway.org

Official Journal:

American Society of Neuroradiology
 American Society of Functional Neuroradiology
 American Society of Head and Neck Radiology
 American Society of Pediatric Neuroradiology
 American Society of Spine Radiology

EDITOR-IN-CHIEF

Mauricio Castillo, MD

Professor of Radiology and Chief, Division of Neuroradiology, University of North Carolina, School of Medicine, Chapel Hill, North Carolina

SENIOR EDITORS

Harry J. Cloft, MD, PhD

Professor of Radiology and Neurosurgery, Department of Radiology, Mayo Clinic College of Medicine, Rochester, Minnesota

Nancy J. Fischbein, MD

Professor of Radiology, Otolaryngology-Head and Neck Surgery, Neurology, and Neurosurgery and Chief, Head and Neck Radiology, Department of Radiology, Stanford University Medical Center, Stanford, California

Jeffrey S. Ross, MD

Staff Neuroradiologist, Barrow Neurological Institute, St. Joseph's Hospital, Phoenix, Arizona

Pamela W. Schaefer, MD

Clinical Director of MRI and Associate Director of Neuroradiology, Massachusetts General Hospital, Boston, Massachusetts, and Associate Professor, Radiology, Harvard Medical School, Cambridge, Massachusetts

Charles M. Strother, MD

Professor of Radiology, Emeritus, University of Wisconsin, Madison, Wisconsin

Jody Tanabe, MD

Professor of Radiology and Psychiatry, Chief of Neuroradiology, University of Colorado, Denver, Colorado

EDITORIAL BOARD

Ashley H. Aiken, *Atlanta, Georgia*
 A. James Barkovich, *San Francisco, California*
 Walter S. Bartynski, *Charleston, South Carolina*
 Barton F. Branstetter IV, *Pittsburgh, Pennsylvania*
 Jonathan L. Brisman, *Lake Success, New York*
 Julie Bykowski, *San Diego, California*
 Donald W. Chakeres, *Columbus, Ohio*
 Alessandro Cianfoni, *Lugano, Switzerland*
 Colin Derdeyn, *St. Louis, Missouri*
 Rahul S. Desikan, *San Diego, California*
 Richard du Mesnil de Rochemont, *Frankfurt, Germany*
 Clifford J. Eskey, *Hanover, New Hampshire*
 Massimo Filippi, *Milan, Italy*
 David Fiorella, *Cleveland, Ohio*
 Allan J. Fox, *Toronto, Ontario, Canada*
 Christine M. Glastonbury, *San Francisco, California*

John L. Go, *Los Angeles, California*
 Wan-Yuo Guo, *Taipei, Taiwan*
 Rakesh K. Gupta, *Lucknow, India*
 Lotfi Hacein-Bey, *Sacramento, California*
 David B. Hackney, *Boston, Massachusetts*
 Christopher P. Hess, *San Francisco, California*
 Andrei Holodny, *New York, New York*
 Benjamin Huang, *Chapel Hill, North Carolina*
 Thierry A.G.M. Huisman, *Baltimore, Maryland*
 George J. Hunter, *Boston, Massachusetts*
 Mahesh V. Jayaraman, *Providence, Rhode Island*
 Valerie Jewells, *Chapel Hill, North Carolina*
 Timothy J. Kaufmann, *Rochester, Minnesota*
 Kenneth F. Layton, *Dallas, Texas*
 Ting-Yim Lee, *London, Ontario, Canada*
 Michael M. Lehl, *Erlangen, Germany*
 Michael Lev, *Boston, Massachusetts*
 Karl-Olof Lovblad, *Geneva, Switzerland*
 Franklin A. Marden, *Chicago, Illinois*
 M. Gisele Matheus, *Charleston, South Carolina*
 Joseph C. McGowan, *Merion Station, Pennsylvania*
 Kevin R. Moore, *Salt Lake City, Utah*
 Christopher J. Moran, *St. Louis, Missouri*
 Takahisa Mori, *Kamakura City, Japan*

Suresh Mukherji, *Ann Arbor, Michigan*
 Amanda Murphy, *Toronto, Ontario, Canada*
 Alexander J. Nemeth, *Chicago, Illinois*
 Laurent Pierot, *Reims, France*
 Jay J. Pillai, *Baltimore, Maryland*
 Whitney B. Pope, *Los Angeles, California*
 M. Judith Donovan Post, *Miami, Florida*
 Tina Young Poussaint, *Boston, Massachusetts*
 Joana Ramalho, *Lisbon, Portugal*
 Otto Rapalino, *Boston, Massachusetts*
 Álex Rovira-Cañellas, *Barcelona, Spain*
 Paul M. Ruggieri, *Cleveland, Ohio*
 Zoran Rumboldt, *Rijeka, Croatia*
 Amit M. Saindane, *Atlanta, Georgia*
 Erin Simon Schwartz, *Philadelphia, Pennsylvania*
 Aseem Sharma, *St. Louis, Missouri*
 J. Keith Smith, *Chapel Hill, North Carolina*
 Maria Vittoria Spampinato, *Charleston, South Carolina*
 Gordon K. Sze, *New Haven, Connecticut*
 Krishnamoorthy Thamburaj, *Hershey, Pennsylvania*
 Kent R. Thielen, *Rochester, Minnesota*
 Cheng Hong Toh, *Taipei, Taiwan*
 Thomas A. Tomsick, *Cincinnati, Ohio*
 Aquilla S. Turk, *Charleston, South Carolina*
 Willem Jan van Rooij, *Tilburg, Netherlands*
 Arastoo Vossough, *Philadelphia, Pennsylvania*
 Elysa Widjaja, *Toronto, Ontario, Canada*
 Max Wintermark, *Charlottesville, Virginia*
 Ronald L. Wolf, *Philadelphia, Pennsylvania*
 Kei Yamada, *Kyoto, Japan*

EDITORIAL FELLOW

Asim F. Choudhri, *Memphis, Tennessee*

YOUNG PROFESSIONALS ADVISORY COMMITTEE

Asim K. Bag, *Birmingham, Alabama*
 Anna E. Nidecker, *Sacramento, California*
 Peter Yi Shen, *Sacramento, California*

HEALTH CARE AND SOCIOECONOMICS EDITOR

Pina C. Sanelli, *New York, New York*

Founding Editor

Juan M. Taveras

Editors Emeriti

Robert I. Grossman, Michael S. Huckman,
 Robert M. Quencer

Special Consultants to the Editor

Sandy Cheng-Yu Chen, Juan Pablo Cruz,
 Girish Fatterpekar, Ryan Fitzgerald,
 Katherine Freeman, Yvonne Lui,
 Sapna Rawal, Greg Zaharchuk

INR Liaisons

Timo Krings, Karel terBrugge

Managing Editor

Karen Halm

Electronic Publications Manager

Jason Gantenberg

Executive Director, ASNR

James B. Gantenberg

Director of Communications, ASNR

Angelo Artemakis

AJNR (Am J Neuroradiol) ISSN 0195–6108 is a journal published monthly, owned and published by the American Society of Neuroradiology (ASNR), 800 Enterprise Drive, Suite 205, Oak Brook, IL 60523. Annual dues for the ASNR include \$170.00 for journal subscription. The journal is printed by Cadmus Journal Services, 5457 Twin Knolls Road, Suite 200, Columbia, MD 21045; Periodicals postage paid at Oak Brook, IL and additional mailing offices. Printed in the U.S.A. POSTMASTER: Please send address changes to American Journal of Neuroradiology, P.O. Box 3000, Denville, NJ 07834, U.S.A. Subscription rates: nonmember \$380 (\$450 foreign) print and online, \$305 online only; institutions \$440 (\$510 foreign) print and basic online, \$875 (\$940 foreign) print and extended online, \$365 online only (basic), extended online \$790; single copies are \$35 each (\$40 foreign). Indexed by PubMed/Medline, BIOSIS Previews, Current Contents (Clinical Medicine and Life Sciences), EMBASE, Google Scholar, HighWire Press, Q-Sensei, RefSeek, Science Citation Index, and SCI Expanded. Copyright © American Society of Neuroradiology.



Go Green!

AJNR urges American Society of Neuroradiology members to reduce their environmental footprint by voluntarily suspending their print subscription.

The savings in paper, printing, transportation, and postage not only help members cut down on clutter, but go to fund new electronic enhancements and expanded content.

The digital edition of *AJNR* presents the print version in its entirety, along with extra features including:

- Publication Preview
- Case of the Week
- Podcasts
- Special Collections
- The *AJNR* Blog
- Weekly Poll

It also **reaches subscribers much faster than print**. An **electronic table of contents** will be sent directly to your mailbox to notify you as soon as it publishes.

Readers can **search, reference, and bookmark** current and archived content 24 hours a day on www.ajnr.org, rather than thumb through stacks of accumulated paper issues for articles and images they need.



<http://www.ajnr.org/cgi/feedback>

ASNR members who wish to opt out of print can do so by using the Feedback form on the *AJNR* Website (<http://www.ajnr.org/cgi/feedback>). Just type "Go Green" in the subject line to stop print and spare our ecosystem.

Coffee Houses and Reading Rooms

 M. Castillo, *Editor-in-Chief*

The famous Austrian writer Stephan Zweig is again very popular thanks to the reprinting of many of his books. Just a few days before committing suicide (together with his wife) in Rio de Janeiro (1942), he finished *The World of Yesterday*.^{*} A little over a year later, Viking Press published it in English. In it, Zweig extolls the role that cafés played in Vienna before, during, and just after the First World War. In this book, cafés are said to have been places of culture and the exchange of ideas. For the price of a cup of coffee, one could read an unlimited number of newspapers and journals, engage in conversation with others (no matter how famous, thus the “democratic” feel of these places), write, listen to literary readings, and, overall, learn about what was going on and express one’s own ideas and points of view.

Because I live in a small university town with many cafés, it is quite obvious to me that this has changed dramatically. Although the “gaining information” part is still probably true, most individuals in cafés sit by themselves, with their computers and other electronic personal devices in front of them, and do not talk to anyone: Silence reigns. Folks are actually afraid to talk in these places and even order in whispers! When there, I know that I feel as if I just entered a library and not a café. In many, the price of a cup of coffee will buy only a limited time to be on-line, which, once reached, results in customers leaving for the next café for another hour of Internet, solitude, and silence. One can safely assume that this occurs all over the United States and that except for information being exchanged on-line, cafés have become fairly isolating places. A few years ago, while in Buenos Aires, I found myself in café where people were talking, arguing, playing chess, and smoking. What a miracle that was, and how unfortunate that our dysfunctional coffee house model has now extended to other parts of our lives.

Isn’t this what has also happened to our radiology reading rooms? Before the PACS, referring physicians would come to the reading room, often carrying articles, journals, or books to show and share with us and to talk about patients. They would get the benefit of listening to us while we obtained information that helped us interpret the findings, making us better radiologists. Ideas for many new projects arose from these interactions. Nowadays, our referring physicians almost never come to the reading room, and they look at the images themselves. When they disagree with our reports, they tend to ignore them and place their own thoughts in the patient’s record.

RedRICK Technologies is a company that prides itself in creating the “reading room of the future.”¹ One look at their work-

zone solutions reveals large rooms partitioned into smaller spaces by all sorts of acoustic treatments effectively isolating radiologists from their surroundings, which probably makes consultations with clinical teams impossible. In these spaces, noise abatement is imperative so that voice recognition systems will function optimally. In a 12-page white paper entitled “Designing the Perfect Reading Room for Digital Mammography,” not one mention is made of space for interaction with referring physicians, but a lot of content is dedicated to eliminating noise, the correct ambient lighting, soothing wall colors, interpreting a large number of studies per year, low time per study, and fast turnaround times.² Placing reading rooms away from heavy foot traffic is advised, but again, it results in remoteness that makes it inconvenient for referring physicians. Conversely, another article states that because information can be moved anywhere, having our reading rooms close to where patient care is occurring enables our involvement with specialists and patients and promotes collaboration and communication.³ This article also recommends a minimum of 125 square feet per reading station, which is larger than that found in traditional reading rooms and makes for better and more pleasant consultations. Their design plans even have spaces for bookshelves! Architects know that sound control is more difficult in small partitioned spaces than in larger ones. Partitions in parallel arrangements also make noise more difficult to control.

Both articles here cited are older than 10 years. Fast forward to 2012, and the ideas expressed in them seem not to have changed as seen in an article “Building a New Radiology Reading Room: Lessons Learned” published in *Diagnostic Imaging*.⁴ The “reading room of the future” strives to be a “low stress” environment. When asked, radiologists perceive extraneous noise as one of the most stressful issues in reading rooms. When adding acoustic insulating paneling is not enough, some have tried noise-cancellation technology (similar to that used in some newer cars to block the noise produced by engines and tire-road contact). In reading rooms, these systems emit a noise that is related to the frequency of background human voices to help diminish them and help voice-recognition work optimally. Music apparently also helps improve the radiologist’s working environment. In one small experiment, radiologists listened to Baroque music via the Pandora music streaming service (<http://www.pandora.com/>). Five of 8 indicated that music made them more relaxed, 3 said it improved concentration, 2 noticed increased productivity and greater diagnostic accuracy, and half felt that overall it improved work satisfaction.⁵

In the past, our reading rooms needed to be dark, but as our displays got brighter, many current reading rooms now have windows. Nicely lit rooms are inviting to our colleagues. Plans for future reading rooms include intelligent ambient lighting that changes in color and intensity throughout the day (similar to that found in the new commercial airplanes such as the Boeing 787). Having lots of glass around the radiologists may help bring in light, and this concept was taken to the extreme when the Univer-

^{*}The (great) movie, *The Grand Budapest Hotel*, written and directed by Wes Anderson, pays homage to this book by Zweig.

<http://dx.doi.org/10.3174/ajnr.A4182>

sity of Pennsylvania had plans to place its radiologists in what was called the “fishbowl.” In it, patients would have been able to see them work, but the plan was eventually dropped as patients apparently were not interested in watching radiologists work (pretty boring to watch if you ask me).⁶ As the luminosity of our monitors improves, background lighting of higher intensity is sometimes allowed. Ambient lighting, particularly of the fluorescent type, results in fatigue, so it must be carefully used.⁷ Conversely, higher luminosity screens result in less fatigue. Ambient light color should match the images displayed on the screens so that interpretation of studies becomes easier. Bones are easier to examine with yellow background light; gray-scale images, with blue light; colored renderings of blood flow, with red light; and so forth.⁸ Overall, 90% of the light should come from indirect fixtures, while 10% should arise from direct sources. Reflection on screens is basically negligible for flat panel monitors, but radiologists still seem to prefer dark spaces with only task lighting when needed.

There are 2 tendencies with respect to reading room designs: to consolidate into 1 or 2 large “ballrooms” or to split these larger rooms into smaller enclosures. Obviously, consolidation is cheaper, the help of others may expedite interpretations, and hopefully, there will be some cross-pollination of ideas. These larger rooms can be furnished in 2 ways: peripheral or central spine approaches.⁷ In the latter, a long central axis of reading stations is placed in the middle of a room, while in the former, the PACS stations are located on the periphery of the room, a disposition that most radiologists prefer as do administrators because more radiologists can be crammed into 1 room. In my own reading room, we opted for both arrangements (luckily we have a lot of space; to view a similar idea, watch “UCLA—Designing Radiology Reading Rooms for the Next Millennium” on YouTube). One side has the usual peripheral arrangement, and the other side has a round carrel housing 3 reading stations (wires come into its central portion through the ceiling, resulting in a cleaner, organized look). On the square side, there is space to seat about 20 individuals, and with the help of a large-screen television on the wall, we have most of our conferences and consultations with referring physicians there. This sort of mixed arrangement leaves space for 1 view box (remember them?) on 1 wall.

Because the need for view boxes has nearly gone away, reading rooms with hybrid (electronic and conventional) arrangements are few. Some institutions have remodeled their ballrooms into smaller, individualized spaces. This is typically the case in some private practices or when radiologists interpret studies from home. The compromise is to create medium-sized reading rooms that house 3–4 radiologists, hopefully all with similar interests and expertise. By locating these reading rooms in the central part of an older ballroom, the periphery is free and can be used for collaborations and consultations. While most of us still interpret sitting, others like to stand when working. Most radiologists prefer their electronic medical record (or clinical information system) display to the right of the imaging monitors. Some years ago, we had a fellow who had carpal tunnel syndrome, and though I will not discuss ergonomics of equipment and furniture here, we got him a gaming mouse that exasperated me with its ridiculous high sensitivity but helped ease his pain. We do not have cup

holders in our reading room, but I agree that they prevent spills and accidents and help keep work surfaces cleaner.

In 2007, at the Radiological Society of North America annual meeting, Philips Healthcare exhibited what they called “Reading Room 2020.” One continuous acoustic wall surrounded the radiologist, and its flattest portion served as a huge screen. Its PACS was keyboard- and mouseless with all of these interfaces projected onto the flat surface of the working table, and all of this was complemented by ambient color-changing lighting. You can still watch a video of it on YouTube. Watching it reminds me of the command deck on the Enterprise on one of the more recent *Star Trek* movies, and though conceptually it was a beautiful idea, today it seems impractical and too expensive. A few years before (2004), GE Healthcare also showed its version of its reading room of the future, which now looks like a cross between an inexpensive spaceship and one of those portable self-cleaning toilets found in the streets of Paris.

The best place for our reading rooms of the future is where patients will be cared for. One recent article describes an initial experience with integrating a reading room with a clinic. A radiologist was present in the area for a 3-hour shift each day, and not surprising, the referring physicians stated that more than 90% of consultations benefited patient care and most affected management.⁹ The radiologist’s presence was critical when reviewing external images brought in by patients. The authors of that article clearly stated, “As radiologists go from high volume interpretations to adding value by guiding and counseling clinicians, a shift to the integrated radiology reading room makes sense.” This type of arrangement would bring back the “café” spirit to our reading rooms by making us work closer, talk more, and exchange ideas with our referring physicians and allow us to work while they are not present. It would also expose our trainees to the patients and their immediate problems.

At home, with my family, we often talk about how much better everything is today compared with the past, but once a week, I like going into the past. Every Thursday, a friend of mine and I get together at a local watering hole that we like because it has no televisions, no Internet, just music coming out of an old Bose system (<http://www.bose.com>) with a tube amplifier, and other people doing nothing but talking, exchanging ideas, and maintaining their friendships over coffee and drinks.

REFERENCES

1. RedRICK Technologies. Reading room environments that redefine space and time. <http://www.redricktechnologies.com/About.aspx>. Accessed October 10, 2014
2. Xthona A. Designing the perfect reading room for digital mammography. White paper. Barco, September 5, 2003, November 11, 2010. http://www.barco.com/barcoview/downloads/The_perfect_mammography_reading_room_2011_-_White_paper.pdf. Accessed October 28, 2014
3. Stein MA. Reading room design scenarios. *IE Imaging Economics*. July 9, 2000. <http://www.imagingeconomics.com/2000/07/reading-room-design-scenarios>. Accessed October 28, 2014
4. Howell WL. Building a new radiology reading room: lessons learned. *Diagnostic Imaging*. <http://www.diagnosticimaging.com/pacs-and-informatics/building-new-radiology-reading-room-lessons-learned>. Accessed October 28, 2014
5. Ridley EL. Wii remote, Baroque music can lighten the load in reading rooms. *AuntMinnie*. April 28, 2009. http://www.auntminnie.com/index.aspx?sec=sup_n&sub=pac&pag=dis&ItemID=85578. Accessed October 10, 2014

6. Ridley EL. Flexibility helps in reading room design. *AuntMinnie*. June 28, 2011. http://www.auntminnie.com/index.aspx?sec=sup_n&sub=pac&pag=dis&ItemID=95707. Accessed October 10, 2014
7. Siegel E, Reiner B. Radiology reading room design: the next generation. *Applied Radiology Online*. April 4, 2002. <http://www.arch4rad.com/Articles-10-07-AppliedRadiology-ReadingRoom-NextGeneration.htm>. Accessed October 10, 2014
8. Fratt L. Redesigning the reading room. *HealthImaging*. April 1, 2005. <http://www.healthimaging.com/topics/imaging-informatics/redesigning-reading-room?page=0%2C0>. Accessed October 10, 2014
9. Rosenkrantz AB, Lepor H, Taneja SS, et al. **Adoption of an integrated radiology reading room within a urologic clinic: initial experience in facilitating clinician consultations.** *J Am Coll Radiol* 2014;11:496–500

EDITORIAL

Teaching Lessons by MR CLEAN

L. Pierot, V. Mendes Pereira, C. Cognard, and R. von Kummer

After centuries of therapeutic nihilism for patients with ischemic stroke and 2 decades of systemic thrombolytic therapy with modest effects, there is hope that increasing arterial recanalization rates with endovascular treatment (EVT) can improve clinical and functional outcomes. Given that data from 3 previous randomized trials (SYNTHESIS Expansion, Interventional Management of Stroke III [IMS III], and Mechanical Retrieval and Recanalization of Stroke Clots Using Embolectomy [MR-RESCUE]) failed to demonstrate a beneficial clinical effect, the positive outcomes from the Multicenter Randomized Clinical trial of Endovascular treatment for Acute ischemic stroke in the Netherlands (MR CLEAN) have renewed the enthusiasm and hope among physicians treating stroke.^{1–4} Initial data from additional trials (Endovascular Treatment for Small Core and Proximal Occlusion Ischemic Stroke [ESCAPE], Extending the Time for Thrombolysis in Emergency Neurological Deficits-Intra-Arterial [EXTEND-IA], and Solitaire FR With the Intention For Thrombectomy as Primary Endovascular Treatment for Acute Ischemic Stroke [SWIFT PRIME]) provide further evidence supporting the MR CLEAN results.^{5,6} It appears that the new-generation interventional devices could enable highly effective stroke treatment in a time window broader than before, making restrictions of IV therapy alone either clinically irrelevant or applying to a very defined patient population.

Why Is the MR CLEAN Outcome Positive?

MR CLEAN was designed to compare EVT plus usual stroke care (intervention) versus usual stroke care alone (control) in 500 patients with proved occlusions of proximal major arteries of the anterior cerebral circulation. Usual stroke care included treatment with IV-rtPA in 90.6% of the control patients and 87.1% in intervention patients. All primary and secondary end point results statistically favored EVT, especially in a population in which poor prognosis is seen with usual stroke care alone. On the basis of the imaging data, the absence of arterial occlusion at the target site on

24-hour CTA was significantly higher with EVT compared with usual stroke care alone (75.4% versus 32.9%; OR, 6.27). Compared with another large prospective EVT/stent retriever series such as the Solitaire Thrombectomy for Acute Revascularization (STAR) (79.2%), the successful reperfusion rate on DSA (TICI 2b or 3) was lower in MR CLEAN (58.7%).⁷ In both trials, TICI was independently evaluated by a core laboratory, but as mentioned by the MR CLEAN authors, the differentiation between 2a and 2b was not always easy, particularly in the absence of a lateral DSA view. In such cases, a conservative approach was taken and recanalization was graded as TICI 2a. In addition, center experience may be an important factor to consider. STAR was conducted in highly experienced neurointerventional centers, whereas MR CLEAN was conducted in 16 Dutch centers with at least 1 member of the intervention team having completed at least 5 procedures with a particular type of device.

Most important, MR CLEAN results demonstrated an increased rate of functional independence in the EVT group (32.6%) compared with the usual care group (19.1%), with an absolute difference of 13.5%. Compared with previous randomized trials, the percentage of patients with favorable clinical outcomes in MR CLEAN is relatively low (40.8% in IMS III and 42.0% in SYNTHESIS) and even lower than that in the placebo group in the European Cooperative Acute Stroke Study (ECASS III) (45%).⁸ It can be presumed that some patients who were enrolled into previous trials such as ECASS-III, IMS-III, and SYNTHESIS had spontaneous good clinical outcomes because they did not require confirmation of large-vessel occlusion (LVO) with baseline imaging. However, compared with EVT/stent-retriever studies requiring baseline vessel imaging, the rate of functional independence reported in MR CLEAN is low (SWIFT, 37%; STAR, 57.9%; Thrombectomy Revascularization of Large Vessel Occlusions in Acute Ischemic Stroke 2 [TREVO 2], 40%; North American Solitaire Stent-Retriever Acute Stroke Registry [NASA Registry], 42%).^{7,9–11}

The MR CLEAN patient population primarily comprised patients who had failed IV-rtPA (ie, IV-rtPA-treated patients without clinical improvement after receiving only the full dose administered during 1 hour). Most of the centers initiated rtPA after plain CT and subsequently performed CTA only when it had been determined that the patient was not clinically improving. Given that close to 90% of patients in both arms received IV-rtPA, the treatment response of this particular patient population can per se explain the poor outcome of the usual treatment arm. The MR CLEAN population is different in comparison with those in previous and upcoming trials. In terms of workflow metrics, there was a long delay between symptom onset and groin puncture in MR CLEAN (260 minutes compared with 208 minutes in IMS III and 225 minutes in SYNTHESIS). Initiation of IV treatment was not delayed in MR CLEAN (87 minutes) compared with IMS III (121 minutes) and SYNTHESIS (165 minutes).

Another contributing factor is the screening of consecutive eligible patients into the MR CLEAN trial. The Dutch health system allowed EVT for ischemic stroke only inside the MR CLEAN trial. This factor enabled high recruitment rates and avoided the “cherry picking” of presumably easy-to-treat patients. MR CLEAN was thus a “real life” study in a small country with short

<http://dx.doi.org/10.3174/ajnr.A4316>

distances, including all centers irrespective of their experience with ischemic stroke treatment.

The MR CLEAN investigators did not put their patients at additional risk. Safety results demonstrated that new ischemic strokes in different vascular territories occurred in the EVT treatment group; however, mortality did not increase, while functional outcome at 3 months improved.

In summary, data from the MR CLEAN trial significantly favored the EVT treatment arm in achieving a significant decrease of the median modified Rankin Scale score from 4 (severe disability) to 3 (moderate disability) due to several factors: 1) the inclusion of patients who failed IV-rtPA treatment, 2) excellent trial execution without allowing EVT outside the trial setting, and 3) safe implementation of EVT by the participating centers. MR CLEAN probably gives us a more realistic picture of clinical outcome after medical treatment in patients with large-vessel occlusion and failed IV treatment.

Role of the EVT Technique in MR CLEAN

Since the implementation of EVT in ischemic stroke by Zeumer et al,¹² several techniques have been developed, from intra-arterial (IA) administration of thrombolytics to mechanical thrombectomy with stent retrievers and aspiration devices.¹³ Data from previous randomized studies demonstrate that stent retrievers are superior to other clot-retriever devices (eg, Merci retriever; Concentric Medical, Mountain View, California) in terms of recanalization, mortality, and clinical outcome.^{9,10} IMS III, MR-RESCUE, and SYNTHESIS included heterogeneous EVT techniques that significantly impacted procedure times and revascularization results.^{14,15} MR CLEAN allowed only devices that had received US Food and Drug Administration approval or a Conformité Européenne marking. In contrast to the IMS III, MR RESCUE, and SYNTHESIS trials, 190 of the 196 (96.9%) patients who actually received EVT were treated with stent retrievers. Twenty-four percent received IA thrombolytics in addition. Additional information on procedural techniques such as the use of distal access catheters or guide catheters with balloon occlusion of the internal carotid artery was not reported. In contrast to other trial protocols, patients with internal carotid artery occlusion were included and treated with cervical carotid stent placement ($n = 30$, 12.9%). The results suggest that the use of stent retrievers was the main component of the success of the trial. MR CLEAN, however, was not a trial testing the efficacy of stent retrievers in the treatment of ischemic stroke, but of EVT in general. The therapeutic impact of other components (anesthesia, proximal-versus-distal access, aspiration, IA thrombolytics before or after EVT) needs to be assessed.

What Can We Learn from Subgroup Analyses?

Several subgroup analyses have been presented in the initial publication of the MR CLEAN results. Data suggest that endovascular treatment with stent retrievers has a relatively similar efficacy regardless of initial NIHSS values, suggesting that the severity of acute ischemic stroke need not be taken into account when considering EVT. However, it is not logical to perform EVT in patients with initial low NIHSS scores and spontaneous good prognosis. Indeed, the median NIHSS score was 17 in the interventional arm of MR CLEAN and 18 in the

medical arm, making it unlikely that many patients with low NIHSS scores were included. A detailed analysis of the outcomes from patients with very low baseline NIHSS scores and extended ischemic lesions on brain imaging is required and would be interesting.

The question of revascularization in patients older than 80 years is still controversial. Subgroup analysis in the NASA registry showed that being older than 80 years of age is predictive of poor clinical outcomes (mRS 0–2 in 27.3%) and greater mortality (43.9%) compared with younger patients (mRS 0–2, 45.4%; mortality, 27.3%).¹⁶ In MR CLEAN, the patient age range was 23–96 years, and 81/500 patients were older than 80 years (16.2%). In this subgroup of elderly patients, there is clearly a great benefit of EVT (odds ratio, 3.24 versus 1.60 in patients younger than 80).

As previously demonstrated, there is a very limited benefit of EVT in patients with a low ASPECTS (OR, 1.09 in patients with ASPECTS 0–4, but 1.97 and 1.61 with ASPECTS 5–7 and 8–10, respectively); this criterion should probably be a contraindication to EVT.¹⁷

The data also reveal a benefit of EVT when there is an associated extracranial ICA occlusion (OR, 1.43 versus 1.85 when absent). A precise analysis of the strategy of treatment in tandem lesions is important to determine the best approach. Finally, the data also established a high benefit of EVT in case of ICA terminus occlusion (OR, 2.43 versus 1.61 when absent).

How to Improve the EVT Results?

Numerous analyses have shown that reducing the delay for recanalization is essential if we want to improve the clinical outcome of patients with ischemic stroke.¹⁸ In MR CLEAN, the median time from stroke onset to groin puncture (not to recanalization) was relatively long, exceeding the 260-minute time window for which IV-rtPA is approved. This suggests that ischemic stroke can be effectively treated beyond 3 or 4.5 hours; a subgroup analysis on the impact of time to intervention on clinical outcomes would be of value. Intervention with EVT should be based on clinical examination and brain and vessel imaging. Every management step has to be carefully analyzed to reduce the time from stroke onset to EVT. Delaying endovascular intervention until IV thrombolysis fails does not make sense and should not be part of the decision-making process; further studies should clarify whether IV-rtPA improves the efficacy of EVT. Several technical questions concerning the use of EVT also need to be answered, including how to reduce the rate of procedural complications (11.2% in MR CLEAN), such as embolization to new territories (8.6%) and vessel dissection or perforation (2.6%); determining the type of anesthesia (general anesthesia or conscious sedation) to be used; the systemic use of balloon-guide catheters; distal clot aspiration; and so forth.¹⁹ Finally, considerations to modify the design of the stent retrievers to reduce the risk of arterial dissection or rupture should also be evaluated.

Continuous work is also needed to improve the selection of patients to be treated with mechanical thrombectomy. A precise analysis should be conducted to determine the severity of the stroke to be treated. Should patients with mild or moderate symp-

toms be treated? On the contrary, is mechanical thrombectomy indicated in patients with severe stroke? It will also be important to determine whether mechanical thrombectomy is indicated regardless of the patient's age (see above). The role of imaging in patient selection will have also to be carefully evaluated.

Will MR CLEAN Results Affect the Management of Patients with Ischemic Stroke?

A single trial with a positive outcome is certainly not sufficient to claim that EVT is now the first-line treatment for ischemic stroke. Positive data from 3 additional trials (ESCAPE, EXTEND-IA, and SWIFT PRIME) are now available. On the basis of this evidence, it is likely that EVT will rapidly become the first-line treatment in patients with ischemic stroke with LVO. This will tremendously impact the health care system, because it will be necessary to offer this demanding treatment by well-trained interventional neuroradiologists to all patients without delay.²⁰ This means early identification of patients with ischemic stroke who will benefit from EVT, the establishment of stroke centers offering this service 24 hours/7 days, and enabling training in the EVT of cerebral arteries.

MR CLEAN has shown the value of EVT initiated within 6 hours of ischemic stroke onset caused by LVO of the anterior circulation. According to the clinical severity of ischemic stroke of the posterior circulation and recent data from a registry showing high recanalization rates in patients with basilar artery occlusion, continued evaluation in this group of patients seems important.²¹ Indeed further trials will be necessary to precisely define the arterial occlusion type, brain pathology, and finally the time window in which EVT is indicated for patients with anterior or posterior circulation stroke and the management of patients with wake-up stroke.

Disclosures: Laurent Pierot—RELATED: Consulting Fee or Honorarium: Codman, Covidien/ev3, and MicroVention; UNRELATED: Consultancy: Sequent. Vitor Mendes Pereira—RELATED: Consulting Fee or Honorarium: Covidien, Comments: Principal Investigator for the STAR trial, co-Principal Investigator for the SWIFT PRIME trial, Steering Committee of the Trevo and Medical Management versus Medical Management Alone in Wake Up and Late Presenting Strokes trial. Christophe Cognard—UNRELATED: Consultancy: Codman, Covidien/ev3, MicroVention, Sequent, and Stryker. Rüdiger von Kummer—RELATED: Consulting Fee or Honorarium: Lundbeck, Covidien, Penumbra, and Boehringer Ingelheim; Support for Travel to Meetings for the Study or Other Purposes: Lundbeck, Covidien, Penumbra, and Boehringer Ingelheim; Fees for Participation in Review Activities (such as data monitoring boards, statistical analysis, end point committees, and the like): Lundbeck; UNRELATED: Board Membership: Lundbeck, Covidien, Penumbra, and Boehringer Ingelheim; Payment for Lectures (including service on Speakers Bureaus): Lundbeck, Penumbra.

REFERENCES

1. Broderick JP, Palesch YY, Demchuk AM, et al; Interventional Management of Stroke (IMS) III Investigators. **Endovascular treatment after intravenous t-PA versus t-PA alone for stroke.** *N Engl J Med* 2013;368:893–903
2. Ciccone A, Valassori L, Nichelatti M, et al; SYNTHESIS Expansion Investigators. **Endovascular treatment for acute ischemic stroke.** *N Engl J Med* 2013;368:904–13
3. Kidwell CS, Jahan R, Gornbein J, et al; MR RESCUE Investigators. **A trial of imaging selection and endovascular treatment for ischemic stroke.** *N Engl J Med* 2013;368:914–23
4. Berkhemer OA, Fransen PSS, Beumer D, et al; MR CLEAN Investigators. **A randomized trial for intraarterial treatment for acute ischemic stroke.** *N Engl J Med* 2015;372:11–20
5. Goyal M, Demchuk AM, Menon BK, et al; ESCAPE Trial Investigators. **Randomized assessment of rapid endovascular treatment of ischemic stroke.** *N Engl J Med* 2015;372:1019–30
6. Campbell BC, Mitchell PJ, Kleinig TJ, et al; EXTEND-IA Investigators. **Endovascular therapy for ischemic stroke with perfusion-imaging selection.** *N Engl J Med* 2015;372:1009–18
7. Pereira VM, Gralla J, Davalos A, et al. **Prospective, multicenter, single-arm study of mechanical thrombectomy using Solitaire flow restoration in acute ischemic stroke.** *Stroke* 2013;44:2802–07
8. Hacke W, Kaste M, Bluhmki E, et al; ECASS Investigators. **Efficacy and safety of alteplase for acute ischemic stroke in a 3- to 4.5-hour time window: results of ECASS III.** *N Engl J Med* 2008;359:1317–29
9. Nogueira RG, Lutsep HL, Gupta R, et al; TREVO 2 Trialists. **Trevo versus Merci retrievers for thrombectomy revascularisation of large vessel occlusions in acute ischaemic stroke (TREVO 2): a randomised trial.** *Lancet* 2012;380:1231–40
10. Saver JL, Jahan R, Levy EI, et al; SWIFT Trialists. **Solitaire flow restoration device versus Merci retriever in patients with acute ischaemic stroke (SWIFT): a randomized, parallel-group, non-inferiority trial.** *Lancet* 2012;380:1241–49
11. Zaidat OO, Castonguay AC, Gupta R, et al. **North American Solitaire Stent Retriever Acute Stroke registry: post-marketing revascularization and clinical outcome results.** *J Neurointerv Surg* 2014;6:584–88
12. Zeumer H, Hacke W, Kolmann HL, et al. **Local fibrinolysis in basilar artery thrombosis [in German].** *Dtsch Med Wochenschr* 1982;107:728–31
13. Pierot L, Soize S, Benaissa A, et al. **Techniques for endovascular treatment of acute ischemic stroke: from intra-arterial fibrinolytics to stent-retrievers.** *Stroke* 2015;46:909–14
14. Pierot L, Gralla J, Cognard C, et al. **Mechanical thrombectomy after IMS III, SYNTHESIS, and MR-RESCUE.** *AJNR Am J Neuroradiol* 2013;34:1671–73
15. Pierot L, Söderman M, Bendszus M, et al. **Statement of ESMINT and ESNR regarding recent trials evaluating the endovascular treatment at the acute stage of ischemic stroke.** *Neuroradiology* 2013;55:1313–18
16. Castonguay AC, Zaidat OO, Novakovic R, et al. **Influence of age on clinical and revascularization outcomes in the North American Solitaire Stent-Retriever Acute Stroke Registry.** *Stroke* 2014;45:3631–36
17. Soize S, Barbe C, Kadziolka K, et al. **Predictive factors of outcome and hemorrhage after acute ischemic stroke treated by mechanical thrombectomy with a stent-retriever.** *Neuroradiology* 2013;55:977–87
18. Khatri P, Yeatts SD, Mazighi M, et al; IMS III Trialists. **Time to angiographic reperfusion and clinical outcome after acute ischaemic stroke: an analysis of data from the Interventional Management of Stroke (IMS III) phase 3 trial.** *Lancet Neurol* 2014;13:567–74
19. Soize S, Kadziolka K, Estrade L, et al. **Mechanical thrombectomy in acute stroke: prospective pilot trial of the Solitaire FR device while under conscious sedation.** *AJNR Am J Neuroradiol* 2013;34:360–65
20. Flodmark O, Grisold W, Richling B, et al. **Training of future interventional neuroradiologists: the European approach.** *Stroke* 2012;43:2810–13
21. Singer OC, Berkefeld J, Nolte CH, et al; ENDOSTROKE Study Group. **Mechanical recanalization in basilar artery occlusion: the ENDOSTROKE study.** *Ann Neurol* 2015;77:415–24

EDITORIAL

Comeback Victory

V. Mendes Pereira and T. Krings

The International Stroke Conference (ISC) 2015, in Nashville, Tennessee, was a memorable meeting. During a crowded plenary session, we witnessed the presentation of 4 randomized con-

<http://dx.doi.org/10.3174/ajnr.A4342>

trolled trials (RCTs) that will change acute ischemic stroke (AIS) treatment, favoring an endovascular approach: Multicenter Randomized Clinical trial of Endovascular treatment for Acute ischemic stroke in the Netherlands (MR CLEAN), Endovascular Treatment for Small Core and Proximal Occlusion Ischemic Stroke (ESCAPE), Extending the Time for Thrombolysis in Emergency Neurological Deficits–Intra-Arterial (EXTEND-IA), and Solitaire FR With the Intention For Thrombectomy as Primary Endovascular Treatment for Acute Ischemic Stroke (SWIFT PRIME).¹⁻⁴ It was maybe even more memorable, given that only 2 years ago, in a similarly crowded session at the same conference, the presentation and simultaneous publication of 3 other RCTs, Interventional Management of Stroke III (IMS III),⁵ SYNTHESIS,⁶ and Mechanical Retrieval and Recanalization of Stroke Clots Using Embolectomy (MR RESCUE),⁷ led to completely different results, despite handling seemingly the same problem: whether the addition of intra-arterial therapies to the established intravenous treatment leads to improved patient outcome. Two years ago, these 3 studies were a serious blow at a time of huge excitement in the interventional/endovascular community because we had started to experience the beneficial effects of the new-generation devices, the stent retrievers, and were finally able to move away from the kitchen sink approach to stroke treatment.

However at the ISC 2013, in Honolulu, Hawaii, there was also a silver lining: the Solitaire FR Thrombectomy for Acute Revascularization (STAR) trial, which was subsequently published in *Stroke*, demonstrated positive results for mechanical thrombectomy.⁸ That study pooled data from high-volume stroke centers that had documented experience with stent retrievers. Moreover, this study focused on patient selection (including documentation of the vascular occlusion), procedure standardization, and revascularization results (successful recanalization reported in the modified TICI score). In this study, good clinical outcomes at 3 months (mRS 0–2) were obtained in 57.9%, final revascularization rates were 88.1% (modified TICI 2b or 3), mortality was 6.9%, and the symptomatic hemorrhagic rate was 1.5%. Some critiques remarked that these results were “too good to be true,” though 2 previous studies, Solitaire FR With the Intention for Thrombectomy (SWIFT)⁹ and Thrombectomy Revascularization of Large Vessel Occlusions in Acute Ischemic Stroke (TREVO 2),¹⁰ had demonstrated that stent retrievers do represent a breakthrough in the endovascular treatment of AIS. For most interventionalists, these studies showed the potential of this new generation of mechanical thrombectomy, which was the technology used in the recently presented RCTs.

Despite the negative results of the 2013 RCTs, it took only little more than 2 years to overcome the skepticism around the endovascular treatment of AIS. This change was made possible due to the personal effort of leaders in the field of stroke; organized effort of professional societies; trial designs, execution, and center and patient selection; and standardized outcome measures. The lessons learned from previous trials with negative results were understood, and effort was made not to replicate them. Patient inclusion was based on well-defined parenchymal and angiographic imaging criteria and was consecutive rather than sporadic. In addition, center/team/operator selection was based on experience

and workflow capacity, and the use of next-generation technology was a common criterion among all those new trials. Some of them, targeted to select the best possible potential population for an AIS study, used advanced mismatch perfusion imaging. However, their results presented some variances, and they should be analyzed from different perspectives to get the right message from each one.

The first of the 4 published trials was the MR CLEAN study,² a Dutch trial that, despite all uncertainty from the stroke community, demonstrated that intra-arterial treatment for AIS caused by an anterior circulation occlusion up to 6 hours after stroke onset is safe and clinically effective. They enrolled 500 patients in 2 randomized and controlled arms: intervention and control. The release of the MR CLEAN results generated an “on hold” response in all other trials as recommended by their leadership or data and safety monitoring boards until an unplanned interim analysis was conducted on their own populations. MR CLEAN had a major impact not only because it was the first study with positive findings but also because the authors had wisely chosen the best population for the question at hand and answered it in a “real world” scenario. In the favor of the trial, they had a structured health system, confined geography, and committed centers and health policy makers (allowing reimbursement only under the auspices of the trial). Thus, they enrolled patients fast, including patients with salvageable brain (median ASPECTS scores of 9 in both arms) with a proved arterial occlusion. Additionally, they used stent retrievers in 97% of patients. However, their final recanalization results (58.7%) were not that impressive, and neither were the clinical outcomes in both arms (32.6%, interventional; 19.1%, control). They also reported 9% of emboli to new territories on DSA following stent thrombectomy, a rate not reported in any previous study using these new devices, to our knowledge.

The endovascular results suggest that a learning curve effect might have been present because the study started in 2010, at the beginning of the use of stent retrievers in Europe.¹¹ The advantage of this study becomes apparent when looking at the trial execution: When MR CLEAN was designed and executed, the consensus was not to consider a patient a potential candidate for endovascular treatment of AIS without full IV rtPA treatment. Thus, patients included in this trial were the “failed IV rtPA” population, with a proximal occlusion detected after intravenous treatment. This explains the rather poor clinical outcomes in the control arm along with the fact that they had long needle-to-puncture times in the interventional arm as well. This workflow is reflected on the reported times of the study: The authors were extremely fast at initiating the IV rtPA (85–87 minutes from stroke onset) but performed randomization only at a median time of 111–119 minutes after IV therapy started. This aspect does not disparage the study; it just explains why the outcome results are different (at a superficial sight) compared with other trials. For future meta-analyses and subset studies, note that this patient population was different from the ones evaluated in IMS III, SYNTHESIS, ESCAPE, or SWIFT PRIME.

The second recently published trial, ESCAPE,¹ was a well-designed and executed trial focused on sequential (or consecutive) patient randomization, stringent imaging-selection criteria (ASPECTS score, leptomeningeal collateral evaluation, and site

occlusion imaging), quick workflow with targeted times after stroke onset, and next-generation technology. The authors randomized 316 patients in 2 arms (endovascular intervention versus standard of care control) in a therapeutic window of 12 hours. The trial was stopped following interim analysis because of the overwhelming benefit of endovascular treatment. Due to the optimized workflow, the mean time between CT and the onset of endovascular treatment was 51 minutes and the mean time from CT to recanalization was 84 minutes. Reperfusion (TICI 2b or 3) was achieved in 72.4%. Good clinical outcomes (mRS 0–2) were achieved in 53% of patients treated by endovascular means compared with 29.6% in the control arm. Absolute reduction in mortality was 8.6 ($R = 0.4$), and the number of treated patients needed to achieve independence was 4. Despite inclusion being permitted for up to 12 hours, >75.3% of included patients were IV-rtPA candidates (also <4.5 hours).

SWIFT PRIME was the third trial (in order of the number of patients reported) and was also put on hold for unplanned interim analysis on release of the MR CLEAN results and was subsequently stopped. This study included 196 patients in 2 arms: IV rtPA alone versus IV rtPA associated with the Solitaire stent retriever (Covidien, Irvine, California). The focus of this trial was workflow performance targets and patient selection based on imaging. The latter was initially based on perfusion mismatch criteria, but after one-third of patients were included, the steering committee decided to change to parenchymal and site occlusion imaging criteria. Good clinical outcomes (mRS 0–2) were achieved in 60.2% of patients treated in the interventional arm compared with 35.5% in the control arm. In the endovascular arm, successful reperfusion rates were 88%, with a substantial amount being TICI 3 (68.7%). This outcome probably reflects the experience of the selected centers and a standard endovascular protocol at all participating sites. The symptomatic hemorrhagic rate was 1%, and mortality was 9.2% (intra-arterial) versus 12.4% (controls). The STAR trial, which had very similar patient and center inclusion criteria, arrived at very similar results for intra-arterial treatment.⁸

The Australian/New Zealand EXTEND-IA trial³ included 70 patients until October 2014. The authors selected candidate patients by using mismatch perfusion imaging randomized into medical therapy alone versus a combined intravenous/intra-arterial approach with mechanical thrombectomy using a stent retriever. They reported reperfusion (TICI 2b/3) rates of 86% in the intra-arterial treatment arm that were associated with a good clinical outcome in 72%, compared with good clinical outcome rates of 39% in the control arm. Despite the small number of selected patients, this difference was statistically significant and justified stopping the trial. Mortality and symptomatic hemorrhagic rates were 3% and 0% in the interventional arm compared with 7% and 2% in the control arm.

These trials have the following in common: efficient trial execution, patient selection based on imaging, and results that overwhelmingly favored intra-arterial treatment, which led to the early end of the trials with <50% of the initially planned patients included. The higher estimated number of patients stems presumably from pessimism about endovascular treatment for AIS that prevailed during the design of these studies following the

2013 initial results, leading to more conservative expectations. With increasing imaging complexity (from ESCAPE to SWIFT PRIME and EXTEND-IA) and thus more granular patient selection, the rate of good clinical outcomes increased. This result may suggest the value of selection criteria based on advanced imaging for patients with AIS. However, the more we “cherry pick” our patients in a real-world scenario, the fewer patients overall will be treated by endovascular means and more patients with potentially treatable strokes may remain untreated. Future studies and guidelines will determine how to innovate for imaging to determine acute stroke treatment.

Determination of imaging criteria is only one of the unanswered questions related to the extent of the investigation: Is there an age limit? How far can we stretch the time limit? How do we treat associated vascular lesions (such as carotid stenosis)? In addition to the pure procedural questions, we must answer system-wide questions: How can we ensure standards of training? How do we change prehospital care guidelines concerning patient transfer? What is the cost per quality-adjusted life year or treatment that society can pay? Should this treatment become “more available” to the detriment of quality? Obviously a number of discussions are needed.

Regarding the latter question, one can envision 2 antithetical scenarios: first, with a nonstroke clinician seeing the patient and a general nonspecialized radiologist reading a basic head CT, thus making treatment decisions performed by a non-neurointerventionally trained team. In the other, the stroke-specialized neurology team and the diagnostic neuroradiology team make a decision based on advanced imaging for a neurointerventionally trained group in an institution prepared to welcome patients with AIS and offer each patient the workflow, revascularization rates, clinical outcomes, and safety targets described by the most recent RCTs. The questions to ask ourselves, our professional societies, the policy makers, and our health system are related to these 2 scenarios: What are the minimum requirements we are willing to accept? How many centers do we need? What are the available resources, and how can we best reach our goal of offering the best care to as many patients as possible?

Disclosures: V. Mendes Pereira—RELATED: Principal Investigator for the STAR trial and Co-Principal Investigator for SWIFT PRIME, sponsored trials by Covidien.

REFERENCES

1. Goyal M, Demchuk AM, Menon BK, et al; ESCAPE Trial Investigators. **Randomized assessment of rapid endovascular treatment of ischemic stroke.** *N Engl J Med* 2015;372:1019–30
2. Berkhemer OA, Fransen PS, Beumer D, et al; MR CLEAN Investigators. **A randomized trial of intraarterial treatment for acute ischemic stroke.** *N Engl J Med* 2015;372:11–20
3. Campbell BC, Mitchell PJ, Kleinig TJ, et al; EXTEND-IA Investigators. **Endovascular therapy for ischemic stroke with perfusion-imaging selection.** *N Engl J Med* 2015;372:1009–18
4. Saver JL, Goyal M, Bonafe A, et al; SWIFT PRIME Investigators. **Solitaire with the Intention for Thrombectomy as Primary Endovascular Treatment for Acute Ischemic Stroke (SWIFT PRIME) trial: protocol for a randomized, controlled, multicenter study comparing the Solitaire revascularization device with IV tPA with IV tPA alone in acute ischemic stroke.** *Int J Stroke* 2015;10:439–38
5. Broderick JP, Palesch YY, Demchuk AM, et al; Interventional Management of Stroke (IMS) III Investigators. **Endovascular therapy af-**

- ter intravenous t-PA versus t-PA alone for stroke.** *N Engl J Med* 2013;368:893–903
6. Ciccone A, Valvassori L, Nichelatti M, et al; SYNTHESIS Expansion Investigators. **Endovascular treatment for acute ischemic stroke.** *N Engl J Med* 2013;368:904–13
 7. Kidwell CS, Jahan R, Gornbein J, et al; MR RESCUE Investigators. **A trial of imaging selection and endovascular treatment for ischemic stroke.** *N Engl J Med* 2013;368:914–23
 8. Pereira VM, Gralla J, Davalos A, et al. **Prospective, multicenter, single-arm study of mechanical thrombectomy using Solitaire flow restoration in acute ischemic stroke.** *Stroke* 2013;44:2802–07
 9. Saver JL, Jahan R, Levy EI, et al; SWIFT Trialists. **Solitaire flow restoration device versus the Merci retriever in patients with acute ischaemic stroke (SWIFT): a randomised, parallel-group, non-inferiority trial.** *Lancet* 2012;380:1241–49
 10. Nogueira RG, Lutsep HL, Gupta R, et al; TREVO 2 Trialists. **Trevo versus Merci retrievers for thrombectomy revascularisation of large vessel occlusions in acute ischaemic stroke (TREVO 2): a randomised trial.** *Lancet* 2012;380:1231–40
 11. Dávalos A, Pereira VM, Chapot R, et al; Solitaire Group. **Retrospective multicenter study of Solitaire FR for revascularization in the treatment of acute ischemic stroke.** *Stroke* 2012;43:2699–705

Spinal Cord Ischemia: Practical Imaging Tips, Pearls, and Pitfalls

M.I. Vargas, J. Gariani, R. Sztajzel, I. Barnaure-Nachbar, B.M. Delattre, K.O. Lovblad, and J.-L. Dietemann



ABSTRACT

SUMMARY: Ischemia of the spinal cord is a rare entity with a poor prognosis. Brain ischemia is no longer a diagnostic challenge; on the contrary, ischemia of the spinal cord remains difficult, particularly in children. In this article, we illustrate the principal causes in children and adults, clinical presentation, different techniques for the diagnosis by MR imaging (diffusion, spinal MR angiography, and 1.5 versus 3T), pathophysiology, and differential diagnosis. We will discuss current knowledge, perspectives, and pitfalls.

Ischemia of the spinal cord is rare, its prevalence is not well-known, and it has a poor prognosis. It accounts for approximately 6% of all acute myelopathies and approximately 1%–2% of all vascular neurologic pathologies.¹

Several causes are implicated in ischemia of the spinal cord, which differ in the pediatric and adult populations. In children, the most common causes are cardiac malformations and trauma. In adults, atheromatosis is one of the principal causes, but thoraco-abdominal aneurysms, aortic surgery,² embolic disease, dissection, systemic hypotension, spinal arteriovenous malformations, diving,³ coagulopathies, cocaine,⁴ sickle cell disease,⁵ and idiopathic causes are also implicated.

In the past decade, new methods such as diffusion imaging of the spinal cord^{6,7} allow a better analysis in the acute setting.

In this article, we describe the technical protocols, differential diagnosis, pitfalls, and solutions.

Clinical Presentation

Clinical presentation depends mainly on the location and extent of the infarction. As with cerebral infarction, the onset of spinal cord infarction is typically abrupt. Most patients develop symptoms quickly, with a maximal symptomatology reached within 12 hours for >50% of patients and within 72 hours for most patients.⁸ The neurologic presentation of spinal cord infarction is largely defined by the vascular territory involved. The severity of the impairments can

vary widely, from paraplegia to minor weakness. The involved cord level can be anywhere along the length of the cord. Back pain often accompanies spinal cord ischemia and has been reported in as many as 70% of patients, typically at the level of the lesion.⁸

Different Clinical Manifestations

Anterior Spinal Artery Syndrome. The most common clinical presentation of a spinal cord infarction is anterior spinal artery syndrome. Anterior spinal artery infarct typically presents as a bilateral loss of motor function and pain/temperature sensation, with relative sparing of proprioception and vibratory senses below the level of the lesion. The acute stages are characterized by flaccidity and loss of deep tendon reflexes; spasticity and hyper-reflexia develop during ensuing days and weeks. Autonomic dysfunction may be present and can manifest as hypotension (either orthostatic or frank hypotension), sexual dysfunction, and/or bowel and bladder dysfunction. If the lesion is in the rostral cervical cord, respiration is compromised.

Incomplete Syndrome of the Spinal Artery Syndrome. Ischemia may be localized at the level of the anterior horns; in this case, clinical presentations may be the following:

- 1) Acute paraplegia (pseudopolyomyelitic form) without sensory abnormalities and without sphincter dysfunction
- 2) Painful bilateral brachial diplegia in the case of a cervical lesion (the man-in-the-barrel syndrome)⁹
- 3) Progressive distal amyotrophy due to chronic lesions of the anterior horns; this form may be misdiagnosed as lateral amyotrophic sclerosis.

Posterior Spinal Artery Syndrome. Posterior spinal artery infarction produces loss of proprioception and vibratory senses below the level of the injury and total anesthesia at the level of the injury.

From the Divisions of Neuroradiology (M.I.V., I.B.-N., K.O.L.), Radiology (J.G., B.M.D.), and Neurology (R.S.), Geneva University Hospitals, Geneva, Switzerland; and Division of Radiology (J.-L.D.), Strasbourg University Hospitals, Strasbourg, France.

Please address correspondence to Maria Isabel Vargas, MD, Geneva University Hospitals, Division of Neuroradiology, DISIM, Rue Gabrielle-Perret-Gentil 4, 1211 Genève 14, Switzerland; e-mail: Maria.I.Vargas@hcuge.ch

Indicates open access to non-subscribers at www.ajnr.org

<http://dx.doi.org/10.3174/ajnr.A4118>

Weakness has been described but is typically mild and transient. Unilateral involvement is more common, but bilateral presentations have also been described.⁸

Other Less Typical Presentations.

- 1) Sulcocommissural syndrome presents as a partial Brown-Sequard syndrome clinical picture with sparing of postural sen-



FIG 1. Localization of the artery of Adamkiewicz in a patient with aortic thrombus. MR angiography shows the thrombus in the abdominal aorta below the renal arteries (arrows, A). No ischemia is visible in the conus medullaris (B). The artery of Adamkiewicz is permeable (arrows, C).

sibility. The syndrome consists of hemiparesis with a contralateral spinothalamic sensory deficit.

- 2) Infarction at the level of conus medullaris may be misdiagnosed as a cauda equina syndrome.
- 3) Central spinal infarct occurs after cardiac arrest or prolonged hypotension; its clinical presentation includes bilateral spinothalamic sensory deficit with sparing of the posterior columns. Motor deficit and sphincter dysfunction are usually absent.
- 4) Transverse medullary infarction (full transverse lesions) presents with sudden and severe inability to walk due to paraplegia or paraparesis or, in cases of higher cord lesions, tetraplegia or tetraparesis. There may be complete sensory loss involving all modalities. Pain is reported as tightness radiating circumferentially. Sphincter dysfunction is present with loss of bladder and bowel control. It is often of embolic origin.

Spinal Transient Ischemic Attacks. Transient symptoms lasting a few minutes to several hours, so-called spinal transient ischemic attacks, have also been described in a variety of clinical settings, but these are unusual.⁸

Vascularization of the Spinal Cord

The vascularization of the spinal cord is supplied principally by the anterior spinal artery, 0.2–0.8 mm; posterolateral spinal artery, 0.1–0.4 mm; and arteria radicularis magna or artery of Adamkiewicz, 0.5–1.2 mm.

The anterior spinal artery supplies the anterior two-thirds of the spinal cord, situated in the pia mater along the anterior median fissure and descending vertically. It is formed by 2 small branches arising from the fourth segment of the vertebral arteries with fusion at the level of the foramen magnum and branches arising from the vertebral artery, the ascending cervical artery, the inferior thyroid artery, the intercostal arteries, the lumbar artery,



FIG 2. Ischemia provoked by an atheroma. Note the important atheromatosis of the abdominal aorta nicely shown by the volume-rendering reconstruction of CT angiography (A). Ischemia of the conus medullaris shown by MR imaging is hyperintense on T2 with a restriction of diffusion (arrows, B–E).



FIG 3. Evolution of ischemia. The first MR image shows the subtle signal anomaly on T2 and diffusion sequences (arrows, A–C). Follow-up 48 hours later shows an important tumefaction and high signal on T2WI associated with a restriction of diffusion of the cervical spinal cord at the C4–C7 levels (arrows, D–G).

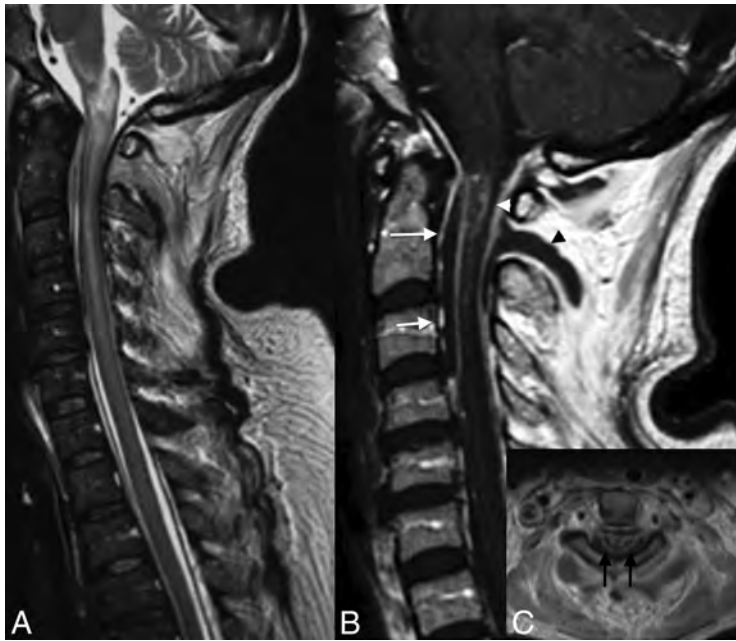


FIG 4. Venous infarction in a patient with epidural and paraspinal abscesses. Note large intramedullary high signal on T2 of the cervical spinal cord (A). T1WI with contrast medium demonstrates an intramedullary enhancement (B and C), the anterior (arrows, B) and posterior epidural (white arrowhead, B), and paraspinal abscesses (black arrowhead, B). Note enhancement on axial T1 of both sides of the median line, reflecting venous ischemia.

the iliolumbar artery and lateral sacral arteries, and principally by the artery of Adamkiewicz.

The artery of Adamkiewicz or the arteria radicularis magna has a particular “hairpin turn” form and must be differentiated from the anterior radiculomedullary vein, which has the same form but is larger and more tortuous.¹⁰ It arises on the left side of the aorta between the T8 and L1 segments, to anastomose with the anterior spinal artery and supply the lower two-thirds of the spinal cord (conus medullaris). Lesions of this artery

produce motor deficits of the legs and fecal and urinary incontinence.

The 2 posterolateral spinal arteries arise from the posteroinferior cerebellar arteries and supply the posterior third (posterior columns, posterior roots, and dorsal horns) of the spinal cord.

Venous System of the Spinal Cord

The venous system is divided into intrinsic and extrinsic systems. The intrinsic veins are divided into sulcal and radial veins, and the extrinsic veins are composed of the anterior and posterior spinal veins. The anterior median spinal vein¹¹ runs with the anterior spinal artery and continues to the filum terminale vein. One posterior median, the greatest spinal vein, is accompanied by 2 posterolateral veins.

The extrinsic system is in contact with the spinal pia mater and includes the pial venous network, the longitudinal collectors, and the radicular veins. This configuration produces large lateral and dorsoventral anastomotic systems.¹²

Spinal veins drain into the anterior and posterior radiculomedullary veins, which in turn drain into the paravertebral and intervertebral plexuses.¹³ These venous plexuses drain into the segmental veins, draining into the ascending lumbar veins, azygos system, and pelvic venous plexuses.

The radiculomedullary veins communicate with the epidural venous system. There are 3 levels of intercommunicating veins¹⁴:

- 1) The internal vertebral venous plexus, formed by intradural and epidural veins, communicating with the intracranial



FIG 5. Cervical spinal canal stenosis and venous infarction. Note the cervical spinal canal stenosis from C4 to C6 due to cervical spondylosis (asterisks, A) and the intramedullary high signal on T2WI (arrow, B) at the same level with the “snake eye” appearance on axial T2WI (arrows, C).

venous system and draining into the external vertebral veins

- 2) The external vertebral venous plexus, located around the vertebra
- 3) The basivertebral veins, within the vertebra.

Pathophysiologic Mechanisms

The origin of ischemia in adults is primarily an embolus (Fig 1) or plaque (Fig 2) that leads to the occlusion of an artery. When systemic hypotension is the cause, the mechanism is the same as that in ischemia resulting from an overdose of β blockers (Fig 3), with the lesion appearing in the watershed areas.

Other sources are also implicated such as the following:

- Cardiac surgery and minimally invasive procedures
- Compression of the radicular artery by a disk^{15,16}
- Cervical degenerative canal associated with minor trauma.

Venous origin is also involved in cases of the following:

- 1) Arteriovenous fistulas leading to an increased venous pressure with, first, a vasogenic edema appearing as a hyperintensity on T2, which may enhance. This persistence can lead to ischemia if the malformation is not treated and can mimic a subacute arterial ischemic lesion
- 2) Coagulopathies
- 3) Epidural infection leading to epidural venous thrombosis with secondary spinal cord infarction (Fig 4)
- 4) Myelopathy related to cervical stenosis, in most cases, related to chronic venous infarction responsible for the classic “snake-eye” sign (Fig 5).

Last, anatomy can play an important role in the origin of ischemia as illustrated by Gailloud et al.¹⁷ Their article shows proxi-

Table 1: Technical MR imaging parameters of the spinal cord protocol at 3T

Sequences	TR (ms)	TE (ms)	Section	
			Thickness (mm)	B0
SE T1	670	10	3	
SE T2	4000	128	3	
STIR	5860	108	3	
Axial GE T2	450	17	3	
Axial SE T2	4000	124	3	
Diffusion	2600	68	3	$b=500-700$
DTI	2600	73	2	$b=500-800$, 20–25 directions

Note:—SE indicates spin-echo; GE, gradient-echo.

Table 2: Technical MR imaging parameters of the spinal cord protocol at 1.5T

Sequences	TR (ms)	TE (ms)	Section	
			Thickness (mm)	B0
SE T1	590	10	3	
SE T2	3270	71	3	
STIR	3000	38	3	
Axial GE T2	590	24	3	
Axial SE T2	4640	79	3	
Diffusion	6000	67	3	$b=500-700$
DTI	3200	67	3	$b=500-800$, 20–25 directions

Note:—SE indicates spin-echo; GE, gradient-echo.

mal non-ostial intersegmental artery stenosis at the upper thoracic level, resulting from the leftward deviation of the descending aorta and the existence of a fixed point along the course of the intersegmental arteries.

In children, minor trauma is a cause of ischemia related to fibrocartilage emboli¹⁸ and also spasm. Other origins include complications of cardiac surgery or traction for scoliosis after orthopedic surgery,¹⁹ sickle cell anemia, and umbilical artery catheter in the neonate. Few series in the literature exist concerning ischemia in children.^{20,21} Stettler et al²⁰ found that the most affected territory is the spinal anterior artery. The differential diagnosis includes idiopathic myelopathy and infectious and inflammatory myelitis.

Imaging

Diffusion revolutionized the diagnosis of brain ischemia in the early 90s; however, it has only been used for the spine in the past decade^{6,22} and remains a technical challenge because of the need for strong gradients, the size of the spinal cord, flow artifacts, and so forth. A few series in the literature concern the use of this technique in ischemia.^{22,23} CT and conventional angiography are not useful for the diagnosis; however in older patients, the visualization of atheromatosis or vascular lesions (aorta, lumbar arteries) after surgery can orient the diagnosis.

MR imaging is the examination of choice for the diagnosis of ischemia and for the differential diagnosis; the following technical protocol is recommended at 1.5T and 3T (see Tables 1 and 2 for details of parameters): sagittal spin-echo T2 or T2 STIR, sagittal spin-echo T1, axial gradient-echo T2 at the cervical and dorsal levels, spin-echo T2 at the medullary conus, and diffusion-weighted images in the sagittal or axial planes. The advantage of the sagittal plane is the larger coverage with a shorter acquisition time. However, the axial plane is useful to

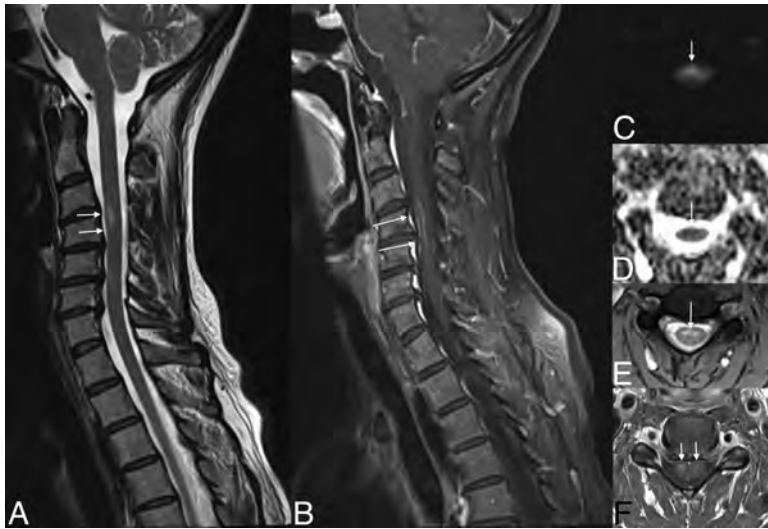


FIG 6. Subacute ischemia. Note the slight hypersignal of the spinal anterior territory at the level of C4–C6 on T2WI (arrows, A and E), associated with a restriction of diffusion (arrows, C and D) and enhancement (arrows, D).

visualize hypersignal on both sides of the median line in cases of ischemia of the spinal anterior artery.^{23,24} This axial plane can be useful to differentiate ischemia from other entities. DTI is primarily used in research, and a few centers use it in clinical practice. Its contribution in this disease is minor.

Contrast media can aid in the diagnosis in the acute stage (Fig 3) because enhancement is absent at this stage and can differentiate it from inflammatory, tumoral, or infectious diseases. The choice of 1.5T and 3T is controversial for the visualization of ischemia. Imaging of the cervical spine is of higher quality at 3T; however, artifacts remain at the thoracic level.²⁵ In clinical routine, an adaptation of the FOV and resolution of MR images in children by age is recommended.

In case of suspicion of a thrombus in the abdominal aorta, the visualization of the artery of Adamkiewicz by MR angiography can help in the diagnosis.

Patterns of Ischemia of the Spinal Cord

In the acute stage, ischemia presents as a restriction in diffusion-weighted imaging of the spinal cord, hyperintense signal on T2 and STIR, and isointense on T1 and may be associated with a slight enlargement of the cord, without enhancement, which appears in the subacute phase (Figs 3 and 6).

Depending on the affected artery, the territory touching the white or gray matter will vary and the shape will be different.

Kumral et al²⁶ and Novy et al⁸ illustrated the different patterns of spinal cord ischemia; the anterior spinal artery territory is limited to the anterior horns bilaterally or unilaterally and the adjacent white matter. The posterior spinal artery infarct is limited to the posterior columns alone or to the surrounding white matter and can be unilateral or bilateral. In the chronic stages, localized atrophy is possible.

In adults, infarction of the vertebral body has been associated with spinal cord ischemia^{8,27,28} associated with high signal and enhancement of the adjacent disk,²⁹ which can be explained by the common vascularization of the vertebral

body, disk, and spinal cord. Hemorrhagic transformation may occur.

Key Points

Diffusion imaging is recommended in all acute myelopathies of the spinal cord. The analysis of vessels, such as the aorta and lumbar arteries, can guide the diagnosis. In the acute stage, there is no enhancement in ischemia, which is generally present in inflammatory, tumoral, and infectious pathologies. Major involvement (hyperintensity on T2) of the spinal cord in an acute epidural infection can be related to venous infarcts.

Disclosures: Bénédicte M. Delattre—UNRELATED: Employment: Philips Healthcare.* Comments: My institution receives part of my salary from Philips Healthcare; Other: Philips Healthcare, Comments: employee of Philips Healthcare from April 2012 to October 2013. *Money paid to the institution.

REFERENCES

- Sandson TA, Friedman JH. Spinal cord infarction: report of 8 cases and review of the literature. *Medicine* 1989;68:282–92
- Piffaretti G, Bonardelli S, Bellosta R, et al. Spinal cord ischemia after simultaneous and sequential treatment of multilevel aortic disease. *J Thorac Cardiovasc Surg* 2014;148:1435–42.e1
- Kamtchum Tatuene J, Pignel R, Pollak P, et al. Neuroimaging of diving-related decompression illness: current knowledge and perspectives. *AJNR Am J Neuroradiol* 2014;35:2039–44
- Gorelik N, Tampieri D. Cocaine-induced vasospasm causing spinal cord transient ischemia. *Neuroradiol J* 2012;25:364–67
- Márquez JC, Granados AM, Castillo M. MRI of cervical spinal cord infarction in a patient with sickle cell disease. *Clin Imaging* 2012;36:595–98
- Vargas MI, Delavelle J, Jlassi H, et al. Clinical applications of diffusion tensor tractography of the spinal cord. *Neuroradiology* 2008;50:25–29
- Nogueira RG, Ferreira R, Grant PE, et al. Restricted diffusion in spinal cord infarction demonstrated by magnetic resonance line scan diffusion imaging. *Stroke* 2012;43:532–35
- Novy J, Carruzzo A, Maeder P, et al. Spinal cord ischemia: clinical and imaging patterns, pathogenesis, and outcomes in 27 patients. *Arch Neurol* 2006;63:1113–20
- Berg D, Mullges W, Koltzenburg M, et al. Man-in-the-barrel syndrome caused by cervical spinal cord infarction. *Acta Neurol Scand* 1998;97:417–19
- Bowen BC, DePrima S, Pattany PM, et al. MR angiography of normal intradural vessels of the thoracolumbar spine. *AJNR Am J Neuroradiol* 1996;17:483–94
- Thron AK. Vascular anatomy of the spine and spinal cord. In: Hurst RW, Rosenwasser RH, eds. *Interventional Neuroradiology*. New York: Informa Healthcare; 2008:39–55
- Moes P, Maillot C. Superficial veins of the human spinal cord: an attempt at classification [in French]. *Arch Anat Histol Embryol* 1981;64:5–110
- Lasjaunias PL. Functional vascular anatomy of the brain, spinal cord and spine. In: Lasjaunias PL, ed. *Surgical Neuroangiography*. Vol. 3. New York: Springer-Verlag; 1990
- Groen RJ, du Toit DF, Phillips FM, et al. Anatomical and pathological considerations in percutaneous vertebroplasty and kyphoplasty: a reappraisal of the vertebral venous system. *Spine* 2004;29:1465–71

15. Hirsch E, Vautravers P, Dietemann JL, et al. **Acute lumbar spinal cord disease caused by lumbar disk hernia** [in French]. *Presse Med* 1986;15:843–44
16. Pau A, Cossu M, Turtas S, et al. **Spinal cord dysfunction from lumbar disk herniation**. *Acta Neurol (Napoli)* 1989;11:439–43
17. Gailloud P, Ponti A, Gregg L, et al. **Focal compression of the upper left thoracic intersegmental arteries as a potential cause of spinal cord ischemia**. *AJNR Am J Neuroradiol* 2014;35:1226–31
18. Reisner A, Gary MF, Chern JJ, et al. **Spinal cord infarction following minor trauma in children: fibrocartilaginous embolism as a putative cause**. *J Neurosurg Pediatr* 2013;11:445–50
19. Lewis SJ, Gray R, Holmes LM, et al. **Neurophysiological changes in deformity correction of adolescent idiopathic scoliosis with intraoperative skull-femoral traction**. *Spine* 2011;36:1627–38
20. Stettler S, El-Koussy M, Ritter B, et al. **Non-traumatic spinal cord ischaemia in childhood: clinical manifestation, neuroimaging and outcome**. *Eur J Paediatr Neurol* 2013;17:176–84
21. Blennow G, Starck L. **Anterior spinal artery syndrome: report of seven cases in childhood**. *Pediatr Neurosci* 1987;13:32–37
22. Thurnher MM, Bammer R. **Diffusion-weighted MR imaging (DWI) in spinal cord ischemia**. *Neuroradiology* 2006;48:795–801
23. Loher TJ, Bassetti CL, Lovblad KO, et al. **Diffusion-weighted MRI in acute spinal cord ischaemia**. *Neuroradiology* 2003;45:557–61
24. Stepper F, Lovblad KO. **Anterior spinal artery stroke demonstrated by echo-planar DWI**. *Eur Radiol* 2001;11:2607–10
25. Vargas MI, Delavelle J, Kohler R, et al. **Brain and spine MRI artifacts at 3 Tesla**. *J Neuroradiol* 2009;36:74–81
26. Kumral E, Polat F, Gulluoglu H, et al. **Spinal ischaemic stroke: clinical and radiological findings and short-term outcome**. *Eur J Neurol* 2011;18:232–39
27. Yuh WT, Marsh EE 3rd, Wang AK, et al. **MR imaging of spinal cord and vertebral body infarction**. *AJNR Am J Neuroradiol* 1992;13:145–54
28. Faig J, Busse O, Salbeck R. **Vertebral body infarction as a confirmatory sign of spinal cord ischemic stroke: report of three cases and review of the literature**. *Stroke* 1998;29:239–43
29. Amoiridis G, Ameridou I, Mavridis M. **Intervertebral disk and vertebral body infarction as a confirmatory sign of spinal cord ischemia**. *Neurology* 2004;63:1755

CSF Flow in the Brain in the Context of Normal Pressure Hydrocephalus

W.G. Bradley Jr



ABSTRACT

SUMMARY: CSF normally flows back and forth through the aqueduct during the cardiac cycle. During systole, the brain and intracranial vasculature expand and compress the lateral and third ventricles, forcing CSF craniocaudad. During diastole, they contract and flow through the aqueduct reverses. Hyperdynamic CSF flow through the aqueduct is seen when there is ventricular enlargement without cerebral atrophy. Therefore, patients presenting with clinical normal pressure hydrocephalus who have hyperdynamic CSF flow have been found to respond better to ventriculoperitoneal shunting than those with normal or decreased CSF flow. Patients with normal pressure hydrocephalus have also been found to have larger intracranial volumes than sex-matched controls, suggesting that they may have had benign external hydrocephalus as infants. While their arachnoidal granulations clearly have decreased CSF resorptive capacity, it now appears that this is fixed and that the arachnoidal granulations are not merely immature. Such patients appear to develop a parallel pathway for CSF to exit the ventricles through the extracellular space of the brain and the venous side of the lymphatic system. This pathway remains functional until late adulthood when the patient develops deep white matter ischemia, which is characterized histologically by myelin pallor (ie, loss of lipid). The attraction between the bare myelin protein and the CSF increases resistance to the extracellular outflow of CSF, causing it to back up, resulting in hydrocephalus. Thus idiopathic normal pressure hydrocephalus appears to be a “2 hit” disease: benign external hydrocephalus in infancy followed by deep white matter ischemia in late adulthood.

ABBREVIATIONS: ACSV = aqueductal CSF stroke volume; DESH = disproportionately enlarged subarachnoid space hydrocephalus; DWMI = deep white matter ischemia; ISP = interstitial space; NPH = normal pressure hydrocephalus; PC = phase-contrast; SAS = subarachnoid space

The classic teaching is that cerebrospinal fluid is formed primarily in the choroid plexus within the ventricles at a rate of 500 mL/day. It flows primarily out of the ventricular system via the foramina of Lushka and Magendie into the subarachnoid space (SAS). Once in the SAS, the CSF flows either down around the spinal cord or up over the cerebral convexities, eventually being primarily absorbed by the arachnoid granulations (macroscopic) and arachnoidal villi (microscopic) on either side of the superior sagittal sinus. This CSF resorption pattern was based on tracer studies performed many years ago by using large molecules.

Recently, a microscopic flow of CSF has been described that functions like the lymphatic system in other parts of the body.¹ It has been shown, by using gadolinium and small fluorescent tracers in mice,

that CSF enters the perivascular Virchow-Robin spaces surrounding the arteries from the SAS.² Lining these arteries and arterioles are continuous astrocytic endfeet—the glia limitans—which have high concentrations of aquaporin-4 water channels, which transport CSF from the Virchow-Robin spaces into the interstitial space (ISP) of the brain. This microscopic CSF flux picks up waste products, (eg, solutes and β amyloid) and exits the ISP via the aquaporin-4 channels lining the Virchow-Robin spaces surrounding the exiting veins. Given the lymphatic-like function and involvement of the astroglia, this fluid flow has been dubbed the “glymphatic system.”

The movement of CSF into the brain via the Virchow-Robin spaces is powered by arterial pulsations.³ Given that these are reduced in some elderly patients, the glymphatic flux is decreased; this decrease may lead to the accumulation of β amyloid and potentially contribute to Alzheimer disease. Water moves freely into the ISP from the SAS but not from the ventricular compartment into the ISP, unless there is increased intraventricular pressure. From there, the CSF can drain via the aquaporin-4 channels into any venous structure, (eg, the vein of Galen, straight sinus, or superficial cortical veins; ie, not necessarily the arachnoidal villi).

From the Department of Radiology, University of California, San Diego, San Diego, California.

Please address correspondence to William G. Bradley Jr, MD, Department of Radiology, University of California, San Diego, 200 Arbor Dr, MC 8224, San Diego, CA 92103; e-mail: wgbradley@ucsd.edu

Indicates open access to non-subscribers at www.ajnr.org

<http://dx.doi.org/10.3174/ajnr.A4124>

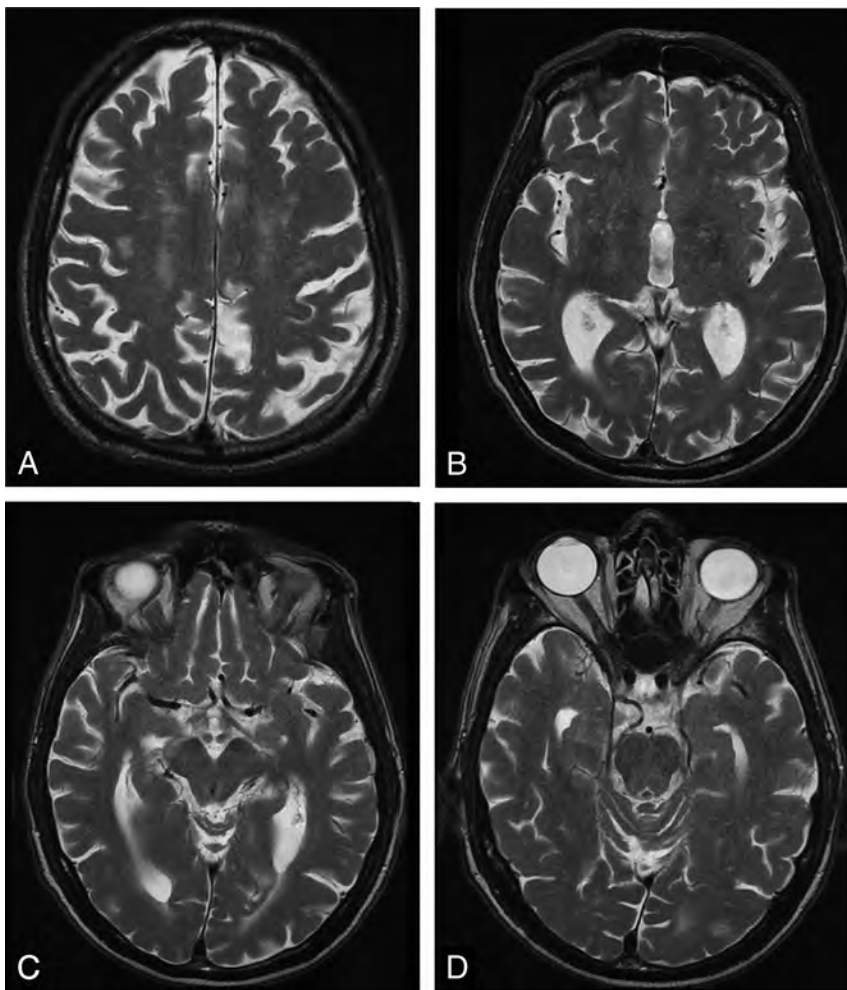


FIG 1. NPH on T2-weighted fast spin-echo, axial images. *A*, A section through the centrum semiovale demonstrates deep white matter ischemia. *B*, A section through third ventricle shows loss of the waist due to slight enlargement with minimal CSF flow void. *C* and *D*, Sections through the aqueduct and upper fourth ventricle show CSF flow void. Although less conspicuous than in the past by using conventional spin-echo, the CSF flow void sign is now more specific for hyperdynamic flow, albeit less sensitive.

Normal Macroscopic CSF Flow

Superimposed on the slow egress of CSF from the ventricles to the SAS is a more prominent pulsatile motion due to the beating of the heart. During systole, blood flows into the brain causing it to expand inward, compressing the ventricles, and outward, compressing the cortical veins and SAS. The inward expansion leads to pulsatile outflow of CSF through the aqueduct and the rest of the ventricular system. This outflow results in a normal MR imaging CSF flow void in the aqueduct.⁴ The systolic expansion forces CSF and venous blood out of the fixed volume of the skull by the Monro-Kellie hypothesis.⁵ This process results in the systolic outflow of CSF for the foramen magnum and from there down the SAS of the spinal canal. During diastole, the volume of the brain decreases and CSF flows in a reverse direction through the aqueduct and the foramen magnum.

While most CSF is produced by the choroid plexus, recent evidence suggests that a portion of the CSF is made by the capillaries in the brain parenchyma. Similarly, it has been estimated that up to 20% of the CSF uptake occurs in the brain parenchyma or via the lymphatics near the cribriform plate or covering the

cranial nerves in the basal cisterns. Regardless of the exact percentage of CSF produced by the brain versus the choroid plexus, the bulk flow of CSF is out of the lateral ventricles via the foramen of Monro through the third ventricle and aqueduct and then through the fourth ventricle.

Obstruction of the outflow of CSF proximal to the outlet foramina of the fourth ventricle was termed “obstructive hydrocephalus,” while obstruction distal to the foramina of Lushka and Magendie was termed “communicating hydrocephalus” by Dandy >100 years ago. Most obstructive hydrocephalus in adults is due to tumors obstructing the outflow of CSF upstream of the outlet foramina of the fourth ventricle. Most cases of communicating hydrocephalus are due to subarachnoid hemorrhage or meningitis, the former obstructing the arachnoid villi and the latter often obstructing more proximally at the level of basal cisterns, particularly with viscous fungal, tubercular, or other granulomatous meningitides. A subset of communicating hydrocephalus seen in the elderly is termed “normal pressure hydrocephalus” (NPH) (Fig 1) and is defined by the clinical triad of gait disturbance, dementia, and incontinence.

A subset of communicating hydrocephalus seen in infants 6–12 months of age is termed “benign external hydrocephalus”⁶ or “benign enlargement of the subarachnoid spaces of infancy,”⁷ supposedly due to decreased uptake of CSF

by “immature” arachnoid granulations (Fig 2). Because their sutures are still open, such children present with a percentile head circumference growing at a faster rate than the percentile of body weight or body length and are referred for imaging to exclude a brain tumor. CSF accumulates over the frontal convexities as the head enlarges; this accumulation leads to a characteristic imaging appearance (Fig 2). Because this condition has been considered the result of immature arachnoid granulations, which will eventually catch up to the production of CSF, these children do not need to be shunted—though recent findings suggest that this condition may not be as benign as previously thought (see below).

MR imaging is generally considered the best technique to evaluate hydrocephalus, partly because of its ability to image directly in the midsagittal plane and partly due to the various pulse sequences available. The best MR imaging technique to evaluate hydrocephalus is FLAIR, which is sensitive to the presence of interstitial edema (Fig 3). Immediately following obstruction, CSF production continues unabated and the amount of interstitial edema surrounding the lateral ventricles is at its greatest. While

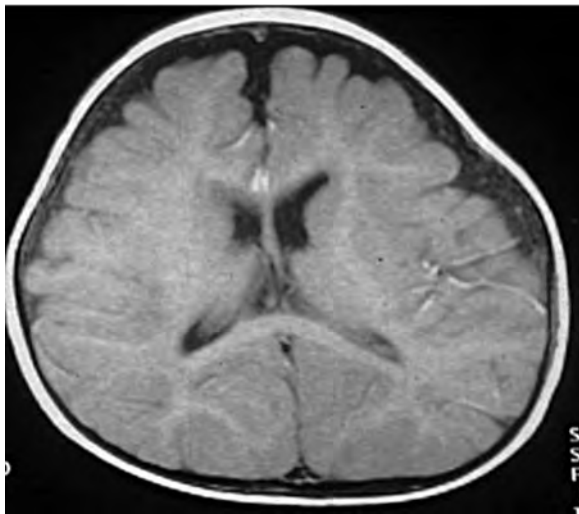


FIG 2. Benign external hydrocephalus in a 7-month-old infant with mild ventriculomegaly and increased CSF in the frontal subarachnoid space.

this feature is usually thought to be due to the pressure gradient across the ventricular wall forcing the CSF out transependymally, interstitial edema may also be due to CSF produced by the brain, which cannot get into the higher pressure ventricles. With time, the ventricles will enlarge to accommodate the increased intraventricular pressure and the pressure gradient will decrease, decreasing the amount of interstitial edema. Eventually the lateral ventricles will enlarge to the point at which the mean intraventricular pressure is normal and the interstitial edema resolves. At this point, the hydrocephalus is said to be “compensated” or “arrested.” While the mean intraventricular pressure may be normal, the pulse pressure is often 6–8 times normal and is referred to as a “waterhammer pulse.” The pounding of the lateral ventricles on the paracentral fibers of the corticospinal tracts, which supply the legs, may contribute to the gait disturbance in NPH.

NPH

Normal pressure hydrocephalus was first described by Hakim and Adams⁸ and Adams et al⁹ in 1965. At that time, the cause was not known—that is, the disease was considered “idiopathic.” Since that time, patients with known causes of chronic communicating hydrocephalus have also been included as NPH. These known patients tend to be younger and respond better to shunting than those with the idiopathic variety, possibly because of poor historical selection criteria for the idiopathic form.

To be diagnosed with NPH, patients must first have enlarged ventricles and at least a portion of the clinical triad. The gait disturbance is usually the first symptom to appear, followed by dementia and last by urinary incontinence. The best response to shunting occurs earlier in the disease when gait is the primary symptom. In the first decade following the description of NPH in the literature, some patients who had only dementia were shunted, with obvious poor results, which led some to question the very existence of NPH. Today, up to 10%¹⁰ of patients with dementia may have NPH and therefore may be treatable by shunting. Of course such patients will also have a gait disturbance.

When an elderly patient presents with a gait disturbance sug-

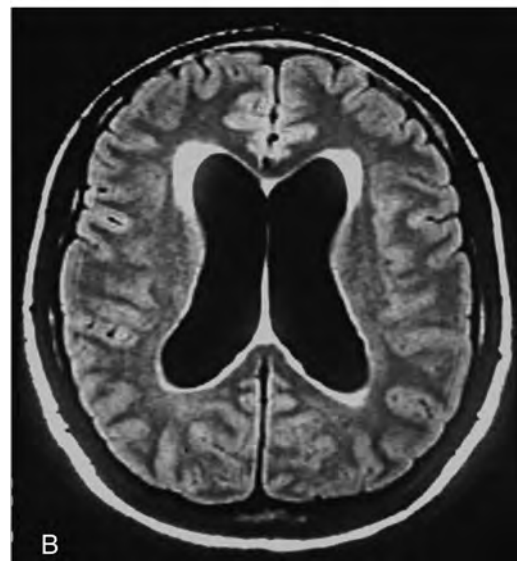
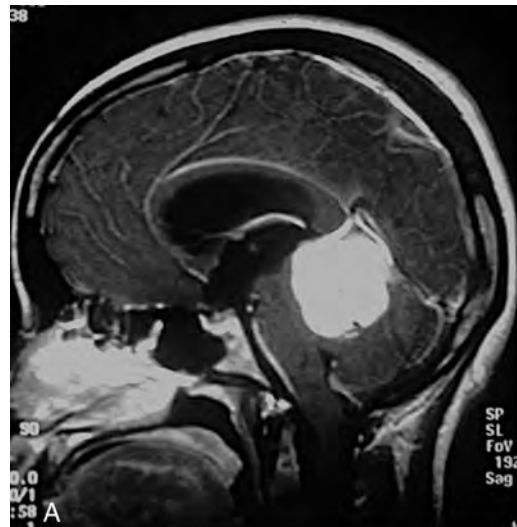


FIG 3. Interstitial edema shown on an axial FLAIR image from an obstructing juvenile pilocytic astrocytoma.

gestive of NPH, the first diagnostic test is usually MR imaging looking for ventricular dilation out of proportion to any sulcal enlargement (ie, the pattern of communicating hydrocephalus rather than atrophy). The amount of interstitial edema surrounding the lateral ventricles should be minimal to absent (which goes along with the normal mean intraventricular pressure). There is frequently associated evidence of deep white matter ischemia also known as small-vessel ischemia or leukoaraiosis (Fig 1A).¹¹ The third ventricle walls, which generally bow inward (producing a waist), become parallel or even bowed out and may have a prominent CSF flow void that extends down through the aqueduct to the obex of the fourth ventricle (Fig 1).

The CSF flow void is indicative of hyperdynamic CSF flow similar to the flow voids seen in arteries on MR imaging. The extent of the CSF flow void on conventional spin-echo images in the past was found to correlate with a successful response to ventriculoperitoneal shunting.¹² Unfortunately, the more modern MR imaging techniques such as fast/turbo spin-echo are much more intrinsically flow-compensated and do not have the same

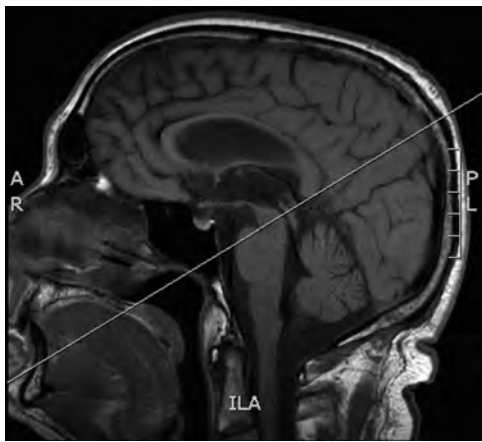


FIG 4. Slice positioning perpendicular to the midaqueduct for a phase-contrast CSF flow study.

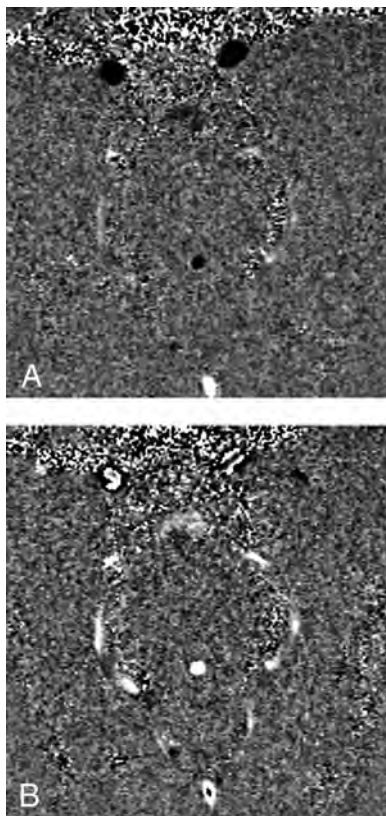
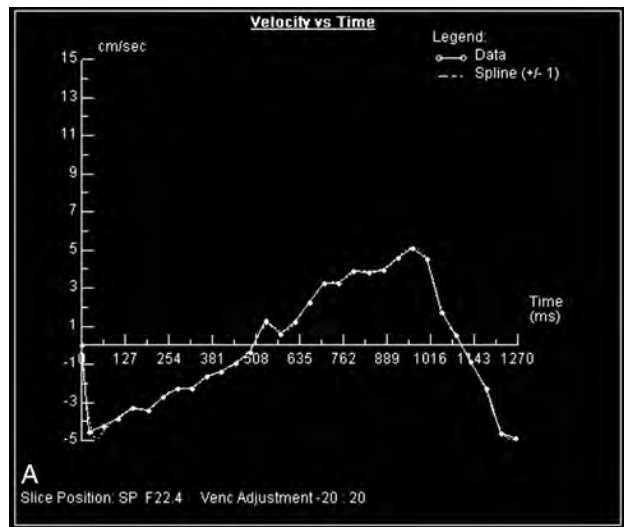


FIG 5. Phase-contrast images showing aqueductal flow up during diastole (black) and down during systole (white).

flow void as seen in the early days of MR imaging. These features led to the development of more sophisticated phase-contrast (PC) MR imaging techniques to evaluate CSF flow for the selection of appropriately symptomatic patients for possible ventriculoperitoneal shunting for NPH.¹³

With PC-MR imaging, the slice is positioned in an angled axial plane so that it is perpendicular to the aqueduct (Fig 4). Higher resolution is better because the aqueduct is such a small structure. We use a 512×512 matrix over a 16-cm FOV, achieving a spatial resolution of $312 \mu\text{m}$ (0.312 mm) (Fig 5), though some use lower spatial resolution to save time. Like phase-contrast MR angiogra-



Slice Position: SP F22.4	Region: 1
Range,ms: 0 to 1263	Venc Adjustment: -20 cm/sec 20 cm/sec
Body Surface Area (BSA):	---- m ²
Velocity	
Peak Velocity:	15.14 cm/sec
Average Velocity:	-0.004 cm/sec
Flow	
Average Flow Over Range:	-0.001 ml/sec
Average Flow Per Minute:	---- l/min
Forward Volume:	0.255 ml
Reverse Volume:	0.255 ml
Net Forward Volume:	-0.001 ml
Net Forward Volume / BSA:	---- ml/m ²
Area	
Average Area:	0.150 cm ²
Minimum Area:	0.150 cm ²
Maximum Area:	0.150 cm ²

B

FIG 6. Volumetric, almost sinusoidal, CSF flow through the aqueduct during 1 cardiac cycle. Integrating the areas under and over the horizontal zero flow line yields the volumes of CSF going caudad in systole and cephalad in diastole, respectively, as shown in the chart. These should be within 5%, and their average is the CSF stroke volume.

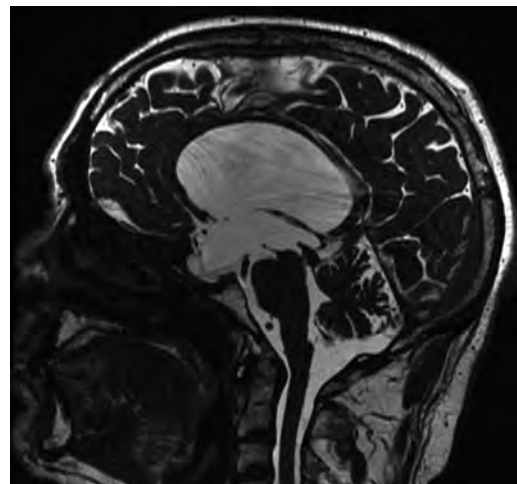


FIG 7. Midsagittal FIESTA image showing a web in the distal aqueduct.

phy, the encoding velocity needs to be specified before the study being performed or aliasing will occur. Because most of these studies are performed by the MR imaging technologists without physician supervision, we use encoding velocities of 10, 20, and 30 cm/s to balance aliasing versus sensitivity. We also use retrospective cardiac gating with either chest (electrocardiogram) leads or finger plethysmography. Most MR imaging systems today have automated software that calculates the volume of CSF flowing craniocaudal during systole and caudocranial during diastole. Because the flow down and the flow up are within 5% of each other (with a small net forward motion), we take the average and call it the “aqueductal CSF stroke volume” (ACSV). While our early phase-contrast CSF flow studies took 14 minutes to perform,¹⁴ modern techniques that have multiple views per TR (eg,

NOVA; VasSol, River Forest, Illinois) take 1–2 minutes for each encoding velocity.

We have found that patients who respond to shunting for NPH have at least twice the ACSV of healthy elderly patients. This is because they have enlarged ventricles and minimal, if any, atrophy. As noted above, when the brain expands during systole in healthy elderly patients, it expands outward toward the SAS and inward toward the ventricles. In patients with early NPH, the brain is already expanded out against the inner table of the calvarium, so all systolic expansion is directed inward against the enlarged ventricles. This larger drumhead of the enlarged ventricles leads to hyperdynamic CSF flow through the aqueduct, which we measure as an elevated ACSV. If these patients are not shunted, they will eventually develop atrophy and the amount of systolic expansion and the ACSV will be reduced. Thus, hyperdynamic CSF flow indicates that atrophy has not yet taken place.

While different investigators have used different values for the ACSV appropriate for shunting, it is highly machine- and technique-dependent. Therefore, it is recommended that anyone wishing to use PC-MR imaging to diagnose shunt-responsive NPH first perform CSF flow studies on a number of healthy elderly patients without dilated ventricles to determine what is normal on that scanner. Then when a patient with suspected NPH is evaluated, an ACSV at least twice that value should be sought before recommending shunting.

While this last sentence suggests that a single number might be used to recommend shunting, this is obviously never the case in medicine. First the quality of the PC CSF flow technique must be evaluated. Lower encoding velocities tend to be more accurate but are more susceptible to velocity aliasing, while higher encoding velocities are less sensitive to aliasing but are noisier. The sinusoi-

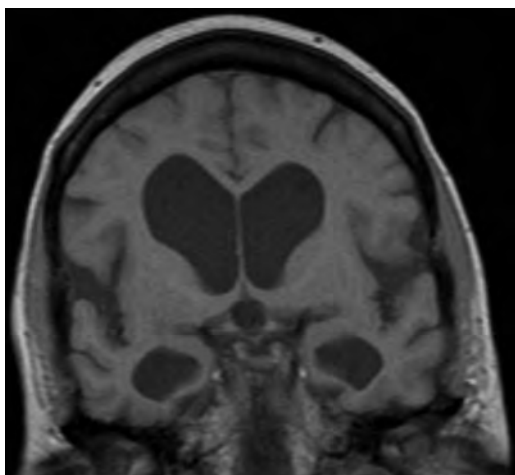


FIG 8. DESH pattern of NPH with ventriculomegaly, prominent Sylvian cisterns, and tight superior convexities.

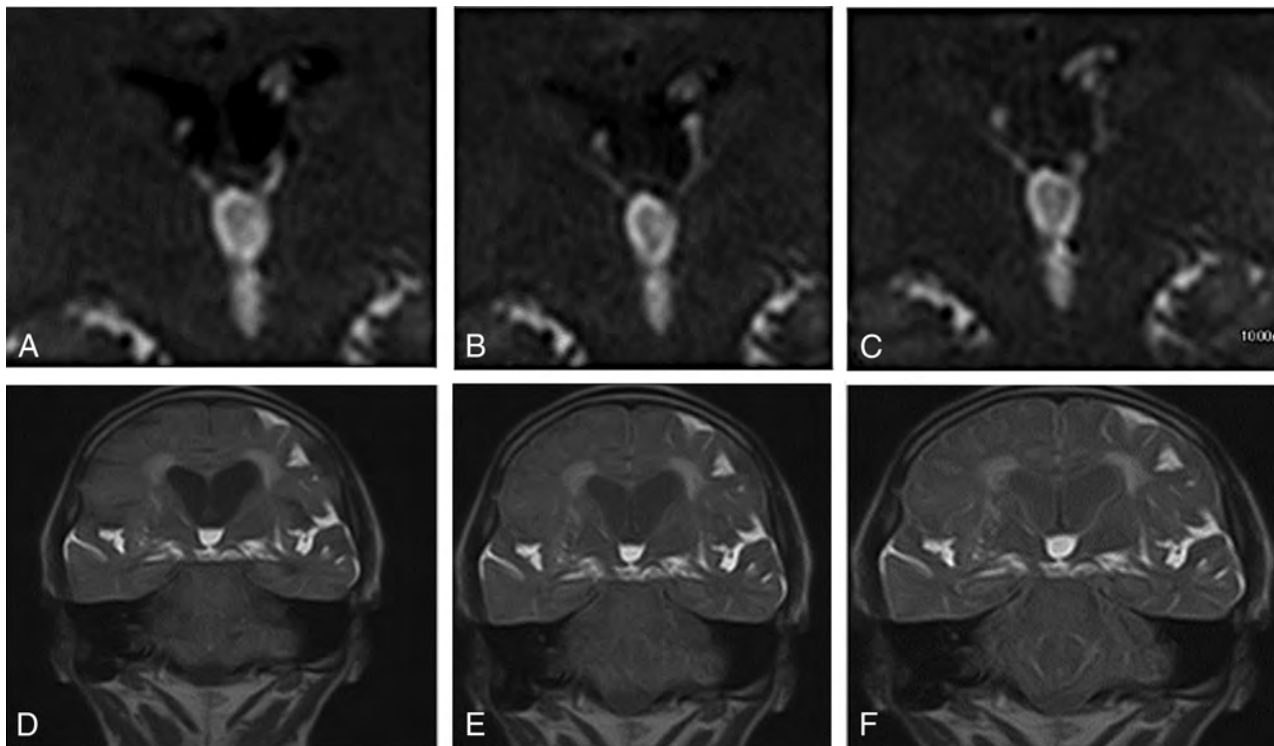


FIG 9. Time-SLIP in a healthy individual (A–C) with lateral ventricular reflux and in a patient with NPH (D–F) without reflux. Images courtesy of Shinya Yamada, MD.

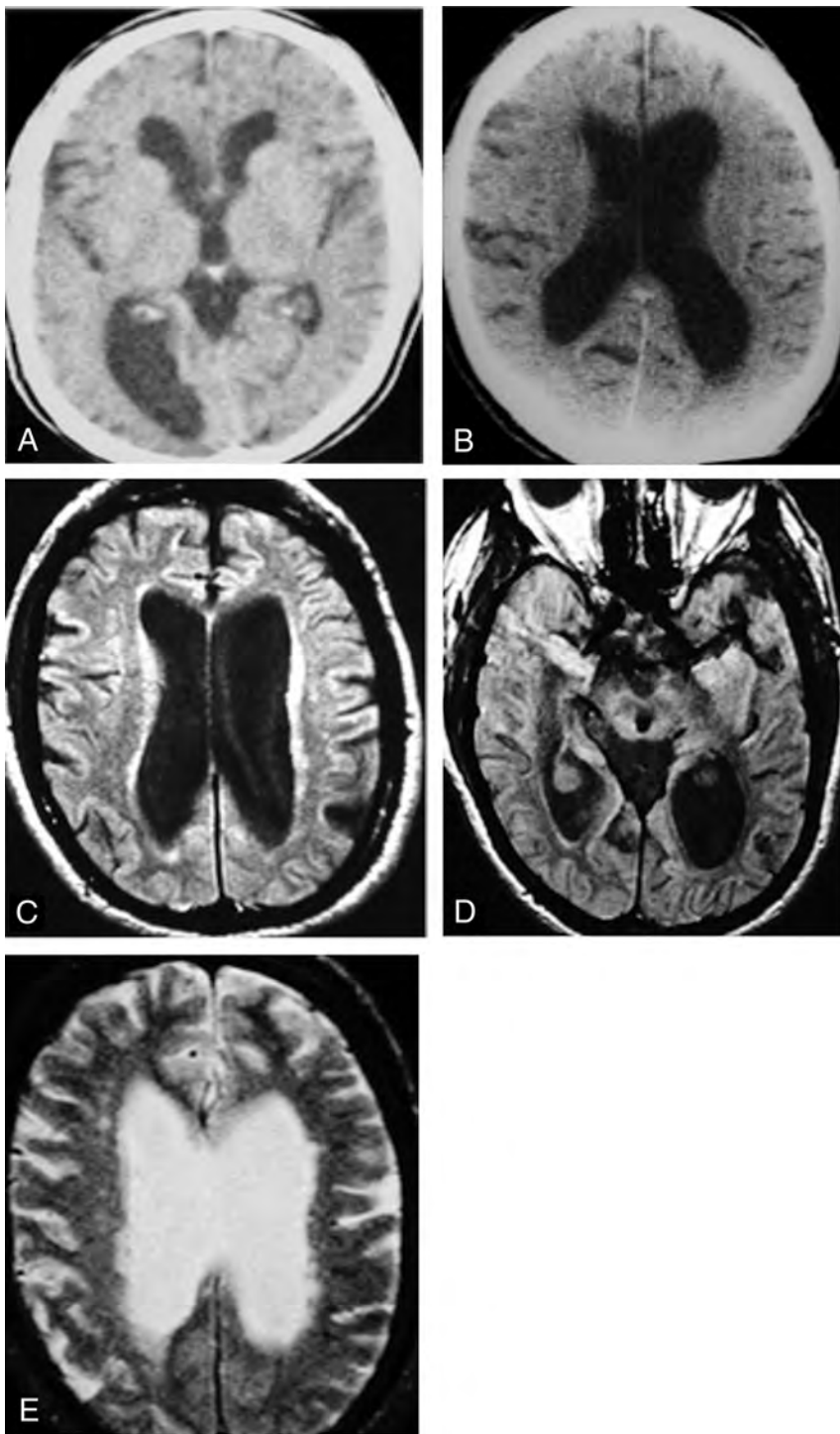


FIG 10. Future patient with NPH with 19 years of earlier imaging showing ventriculomegaly before symptoms of NPH. A, CT scan from 19 years earlier obtained for suspected giant cell arteritis shows mild ventriculomegaly. He was 67 years of age at this point and was walking 20 miles per day. B, At age 70, he clearly has ventriculomegaly but no symptoms of NPH. C–E, Now at 76 years of age, MR imaging shows ventriculomegaly, DWMI, and an aqueductal CSF flow void. He will not develop symptoms of NPH for another 10 years. Reprinted with permission from Bradley et al.²⁰ Copyright 2006 Wiley-Liss, Inc.

dal volumetric CSF flow curve (Fig 6) should be evaluated for aliasing and to be certain that the area under the curve above the zero flow line (diastole) equals the area below the line (systole). If systolic flow is greater than diastolic flow, it is possible that the retrospective cardiac gating is not adequately sampling diastole.

If the ACSV is not twice normal in a patient with symptomatic

NPH, it is most likely that the patient has already developed atrophy and will be less likely (but not impossible) to improve with a shunt. It has been shown that patients very early in their disease may not have developed hyperdynamic CSF flow yet and may benefit from a repeat study in 6 months.¹⁵

When we perform MR imaging for possible NPH, we perform routine MR imaging of the brain, a PC-MR imaging CSF flow study, and bright CSF, thin-section sagittal imaging to evaluate possible aqueductal stenosis. Depending on the MR imaging vendor, this could be FIESTA (GE Healthcare, Milwaukee, Wisconsin) (Fig 7), TrueFISP (Siemens, Erlangen, Germany), or balanced fast-field echo (Philips Healthcare, Best, the Netherlands), but it is important to get a section thickness of <1 mm. Because aqueductal stenosis presents with the same clinical triad as NPH, plus chronic headaches, these patients are often referred for imaging to exclude NPH. As part of the routine MR imaging, we also perform a midcoronal sequence (either T1- or T2-weighted) looking for the disproportionately enlarged subarachnoid space hydrocephalus (DESH) pattern,¹⁶ which is qualitatively large Sylvian cisterns and a tight superior convexity SAS (Fig 8), though we have not found this sign to be as useful as the ACSV in predicting shunt-responsive NPH.

In the United States, PC-MR imaging is often combined with a high-volume CSF tap test or the more invasive external lumbar drainage to evaluate a suitably symptomatic patient with NPH for ventriculoperitoneal shunting. In Europe, saline infusion is commonly used. In Japan, it has been reported that the tap test does not add any diagnostic value if there is a DESH pattern.¹⁷

While most experience demonstrating hyperdynamic CSF flow in NPH was with PC-MR imaging, there is a new technique called time-spatial labeling inversion pulse (Time-SLIP), which clearly has some utility.¹⁸ Time-SLIP is a CSF tagging technique similar to arterial spin-labeling,

which can show increased CSF displacement through the aqueduct in NPH or no displacement in aqueductal stenosis. When it is applied in the coronal plane through the foramen of Monro, CSF regurgitation into the lateral ventricles can be seen in healthy patients during diastole (Fig 9, A–C); however, there is very little regurgitant flow in NPH (Fig 9, D–F).

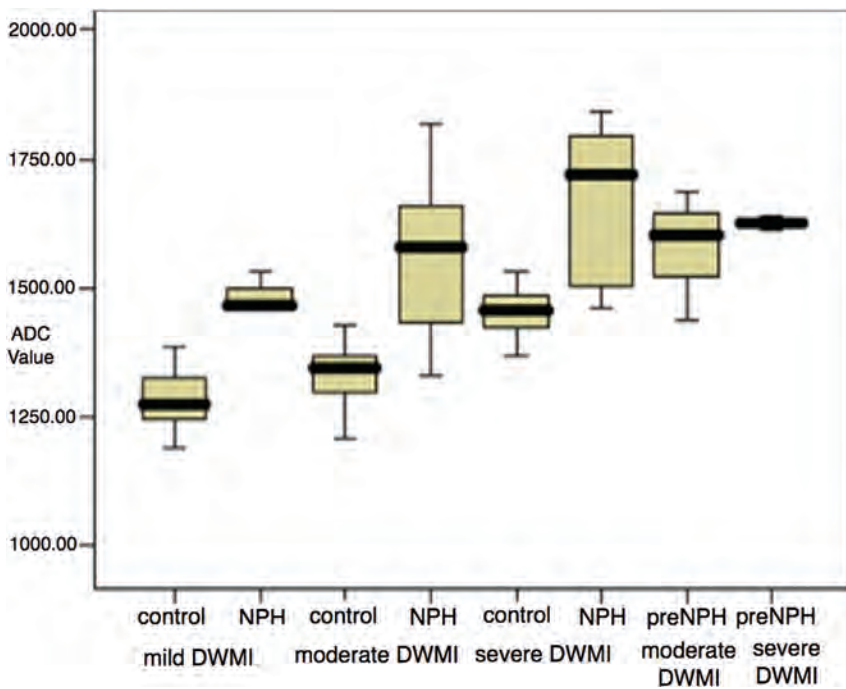


FIG 11. Apparent diffusion coefficient versus the degree of DWMI in NPH and age-matched controls, showing significantly higher ADC (indicating higher water content) in patients with NPH versus controls for a given degree of DWMI. Reprinted with permission from Bradley et al.²⁰ Copyright 2006 Wiley-Liss, Inc.

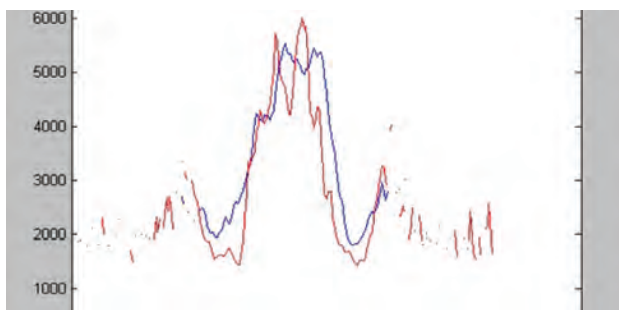


FIG 12. ADC profile in the mid-coronal plane in healthy individuals (red) and patients with NPH (blue). The central double peak is the lateral ventricles. Note the higher water content in the extracellular space next to the ventricles in the NPH group, possibly due to impaired centrifugal flow from DWMI. Reprinted with permission from Bradley et al.²⁰ Copyright 2006 Wiley-Liss, Inc.

Possible Etiology of Idiopathic NPH

Because I have used various MR imaging indicators of hyperdynamic CSF flow for >30 years now, it is tempting to speculate on the etiology of “idiopathic” NPH. We know that patients with shunt-responsive NPH have both hyperdynamic CSF flow and deep white matter ischemia (DWMI) (Fig 1). We also know that patients with NPH have significantly ($P < .003$) larger intracranial volumes than age- and sex-matched controls and have had dilated ventricles for years before becoming symptomatic (Fig 10).¹⁹ The increased intracranial volume raises the possibility that perhaps these patients had benign external hydrocephalus as infants.²⁰

With decreased uptake of CSF by the arachnoidal granulations after passing through the usual pathway (ie, the fourth ventricle outlet foramina), such patients might have developed a parallel pathway for CSF resorption, similar to a parallel electrical circuit

with a fixed voltage drop that can now conduct twice as much current. A potential parallel pathway for CSF resorption would be the extracellular space of the brain. Thus CSF would cross the ependyma into the ISP and be transported out the venous Virchow-Robin spaces via the aquaporin-4 water channels. These patients would continue with this dual pattern of CSF resorption, with some of the CSF gliding over the myelin lipid, until their elderly years when they develop DWMI, which might be considered the second “hit” in this disease.²⁰

The histopathologic hallmark of DWMI is myelin pallor.²¹ With less lipid, there is more water and high signal on T2-weighted and FLAIR images (Fig 1). The outward-flowing CSF in the ISP of the brain is no longer gliding over the myelin lipid but is now attracted to the myelin protein. This attraction between the polar water molecules of the CSF and the charged side groups of the myelin protein increases the resistance to CSF outflow via the extracellular or interstitial space of the

brain. The outflowing CSF is essentially dammed up by the DWMI and backs up; this process leads to hydrocephalus. According to Hakim’s hypothesis,^{8,9} the tangential shearing forces near the ventricles lead to gait disturbance and the subsequent radial shearing forces compress the cortex against the inner table of the calvarium leads to dementia.

In support of the above hypothesis is the finding that there is more water in the extracellular space of the brain in patients with NPH than in age-matched controls.²⁰ This finding is because the apparent diffusion coefficient from diffusion-weighted imaging is elevated compared with that in healthy individuals. While DWMI has a higher water content than normal brain as noted above, the ADC is statistically higher for a given degree of DWMI in patients with NPH than in healthy elderly patients (Fig 11). It is also highest in the periventricular region, supporting the concept that the DWMI is damming up the outflowing CSF (Fig 12).

Note that the right-hand columns in Fig 11 are labeled “preNPH.” These patients were considered healthy elderly controls without symptoms of NPH. They may fall into the same category as the patient illustrated in Fig 10, who had enlarged ventricles 19 years before he developed symptoms of NPH. The Japanese call this AVIM (asymptomatic ventriculomegaly with features of idiopathic NPH on MR imaging). It is important to observe these patients for the potential development of a future gait disturbance.

ACKNOWLEDGMENTS

I thank Abdulrahman A. Almutairi, MD, for assistance with the images.

REFERENCES

1. Iliff JJ, Wang M, Liao Y, et al. **A paravascular pathway facilitates CSF flow through the brain parenchyma and the clearance of interstitial solutes, including amyloid β .** *Sci Transl Med* 2012;4:147ra111
2. Iliff JJ, Lee H, Yu M. **Brain-wide pathway for waste clearance captured by contrast-enhanced MRI.** *J Clin Invest* 2013;123:1299–309
3. Iliff JJ, Wang M, Zeppenfeld DM, et al. **Cerebral arterial pulsation drives paravascular CSF-interstitial fluid exchange in the murine brain.** *J Neurosci* 2013;33:18190–99
4. Bradley WG Jr, Kortman KE, Burgoyne B. **Flowing cerebrospinal fluid in normal and hydrocephalic states: appearance on MR images.** *Radiology* 1986;159:611–16
5. Mokri B. **The Monro-Kellie hypothesis: applications in CSF volume depletion.** *Neurology* 2001;56:1746–48
6. Zahl SM, Egge A, Helseth E, et al. **Benign external hydrocephalus: a review, with emphasis on management.** *Neurosurg Rev* 2011;34:417–32
7. Nickel RE, Gallenstein JS. **Developmental prognosis for infants with benign enlargement of the subarachnoid spaces.** *Dev Med Child Neurol* 1987;29:181–86
8. Hakim S, Adams RD. **The special clinical problem of symptomatic hydrocephalus with normal cerebrospinal fluid: observations on cerebrospinal fluid hydrodynamics.** *J Neurol Sci* 1965;2:307–27
9. Adams RD, Fisher CM, Hakim S, et al. **Symptomatic occult hydrocephalus with “normal” cerebrospinal fluid pressure: a treatable syndrome.** *N Engl J Med* 1965;273:117–26
10. Spetzler RF. **Normal pressure hydrocephalus.** *Barrow Quarterly* 2003;19:1
11. Bradley WG Jr, Whittemore AR, Watanabe AS, et al. **Association of deep white matter infarction with chronic communicating hydrocephalus: implications regarding the possible origin of normal pressure hydrocephalus.** *AJNR Am J Neuroradiol* 1991;12:31–39
12. Bradley WG Jr, Whittemore AR, Kortman KE, et al. **Marked CSF flow void: an indicator of successful shunting in patients with suspected normal pressure hydrocephalus.** *Radiology* 1991;178:459–66
13. Nitz WR, Bradley WG Jr, Watanabe AS, et al. **Flow dynamics of cerebrospinal fluid: assessment with phase-contrast velocity MR imaging performed with retrospective cardiac gating.** *Radiology* 1992;183:395–405
14. Bradley WG Jr, Scalzo D, Queralto J, et al. **Normal-pressure hydrocephalus: evaluation with cerebrospinal fluid flow measurements at MR imaging.** *Radiology* 1996;198:523–29
15. Scollato A, Tenenbaum R, Bahl G, et al. **Changes in aqueductal CSF stroke volume and progression of symptoms in patients with unshunted idiopathic normal pressure hydrocephalus.** *AJNR Am J Neuroradiol* 2008;29:192–97
16. Hashimoto M, Ishikawa M, Mori E, et al. **Study of INPH on neurological improvement (SINPHOND): diagnosis of idiopathic normal pressure hydrocephalus is supported by MRI-based scheme: a prospective cohort study.** *Cerebrospinal Fluid Res* 2010;7:18
17. Ishikawa M, Hashimoto M, Mori E, et al. **The value of the cerebrospinal fluid tap test for predicting shunt effectiveness in idiopathic normal pressure hydrocephalus.** *Fluids Barriers CNS* 2012;9:1
18. Yamada S, Miyazaki M, Kanazawa H, et al. **Visualization of cerebrospinal fluid movement with spin labeling at MR imaging: preliminary results in normal and pathophysiologic conditions.** *Radiology* 2008;249:644–52
19. Bradley WG, Safar FG, Furtado C, et al. **Increased intracranial volume in normal pressure hydrocephalus: a clue to the etiology of “idiopathic” NPH?** *AJNR Am J Neuroradiol* 2004;25:1479–84
20. Bradley WG Jr, Bahl G, Alksne JE, et al. **Idiopathic normal pressure hydrocephalus may be a “two hit” disease: benign external hydrocephalus in infancy followed by deep white matter ischemia in late adulthood.** *J Magn Reson Imaging* 2006;24:747–55
21. Marshall VG, Bradley WG Jr, Marshall CE, et al. **Deep white matter infarction: correlation of MR imaging and histopathologic findings.** *Radiology* 1988;167:517–22

Imaging Biomarkers in Acute Ischemic Stroke Trials: A Systematic Review

G.W.J. Harston, N. Rane, G. Shaya, S. Thandeswaran, M. Cellerini, F. Sheerin, and J. Kennedy



ABSTRACT

BACKGROUND AND PURPOSE: Imaging biomarkers are increasingly used to provide a better understanding of the pathophysiology of acute ischemic stroke. However, this approach of routinely using imaging biomarkers to inform treatment decisions has yet to be translated into successful randomized trials. The aim of this study was to systematically review the use of imaging biomarkers in randomized controlled trials in patients with acute ischemic stroke, exploring the purposes for which the imaging biomarkers were used.

MATERIALS AND METHODS: We performed a systematic review of imaging biomarkers used in randomized controlled trials of acute ischemic stroke, in which a therapeutic intervention was trialed within 48 hours of symptom onset. Data bases searched included MEDLINE, EMBASE, strokecenter.org, and the Virtual International Stroke Trials Archive (1995–2014).

RESULTS: Eighty-four studies met the criteria, of which 49 used imaging to select patients; 31, for subgroup analysis; and 49, as an outcome measure. Imaging biomarkers were broadly used for 8 purposes. There was marked heterogeneity in the definitions and uses of imaging biomarkers and significant publication bias among post hoc analyses.

CONCLUSIONS: Imaging biomarkers offer the opportunity to refine the trial cohort by minimizing participant variation, to decrease sample size, and to personalize treatment approaches for those who stand to benefit most. However, within imaging modalities, there has been little consistency between stroke trials. Greater effort to prospectively use consistent imaging biomarkers should help improve the development of novel treatment strategies in acute stroke and improve comparison between studies.

ABBREVIATIONS: RCT = randomized controlled trial; TCD = transcranial Doppler

Treatment options for patients with acute ischemic stroke are limited. Despite attempts to develop novel neuroprotectants and strategies for reperfusion, very few have made it into routine practice. This failure of progress is multifactorial in origin but includes failure to properly account for patient heterogeneity and a lack of proved surrogate outcomes.¹

Imaging has been widely embraced, both in clinical practice and

research studies, to achieve various aims, including the following: reducing the heterogeneity of participants in a trial; stratifying patients into those who may or may not benefit from treatments; and assessing intervention efficacy and/or safety.^{2,3} The Acute Stroke Imaging Research Roadmap II was developed on the background of recent null acute stroke trials incorporating selection by using penumbral imaging.² It reinforced the need for a rigorous definition of regions of interest, defined a framework for using imaging biomarkers in imaging studies (with the specific example of revascularization), and called for coordinated imaging data collection.

The aim of this study was to systematically review randomized intervention trials in patients with acute ischemic stroke, using the groupings developed in the Acute Stroke Imaging Research Roadmap II and detailing the purposes for which they were used.

Please address correspondence to George Harston, AVIC, University of Oxford, Level 2, John Radcliffe Hospital, Headington, Oxford, OX3 9DU, UK; e-mail: george.harston@rdm.ox.ac.uk; @AMICStroke

 Indicates open access to non-subscribers at www.ajnr.org

 Indicates article with supplemental on-line appendix and tables.

<http://dx.doi.org/10.3174/ajnr.A4208>

Received August 4, 2014; accepted after revision October 24.

From the Radcliffe Department of Medicine (G.W.J.H., G.S., S.T., J.K.), University of Oxford, Oxford, United Kingdom; Department of Neuroradiology (N.R., M.C., F.S.), Oxford University Hospitals NHS Trust, Oxford, United Kingdom; and Neurointervention Service (N.R.), Royal Melbourne Hospital, Melbourne Health, Victoria, Australia.

This work was supported by the National Institute for Health Research Oxford Biomedical Research Centre Programme, the Dunhill Medical Trust (grant number OSRP1/1006), and the Centre of Excellence for Personalized Healthcare funded by the Wellcome Trust and Engineering and Physical Sciences Research Council (grant number WT 088877/Z/09/Z).

Preliminary analysis of some of these data previously presented in poster form at: European Stroke Conference, May 28–31, 2013; London, UK; and World Federation of Interventional and Therapeutic Neuroradiology, November 9–13, 2013; Buenos Aires, Argentina.

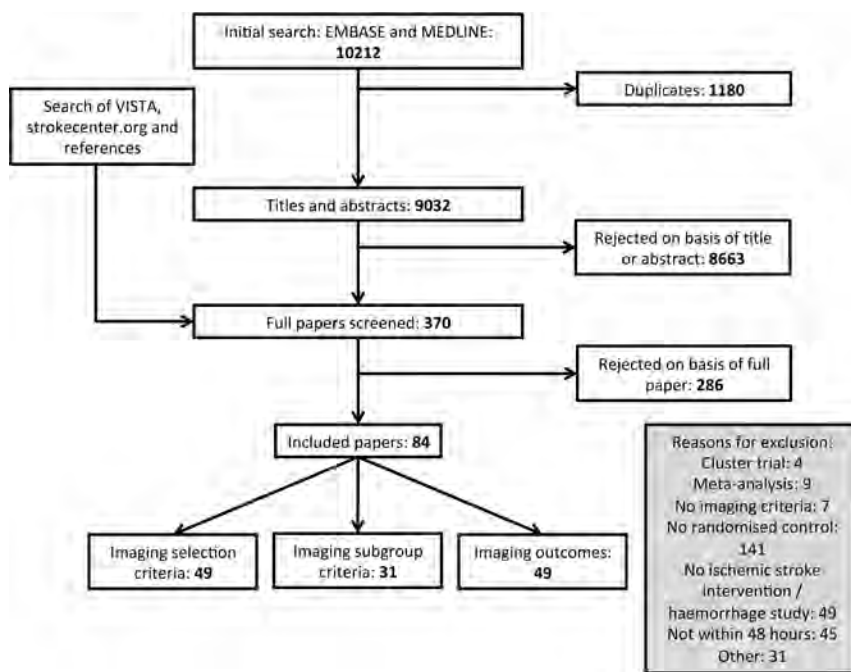


FIG 1. Schema of systematic review.

Table 1: Use of imaging in stroke trials

	Trial Eligibility	Outcome Measure	Subgroup Analysis
Infarct volume	29	62	34
Edema	5	NA	0
Diagnosis/territory of infarction	9	NA	5
Vessel status	16	17	23
Ischemic penumbra	10	7	22
Perfusion status only	2	27	1
Collaterals	0	0	2
Composite/other	0	4	2

Note:—NA indicates not applicable.

MATERIALS AND METHODS

Eligibility Criteria

This systematic review selected studies analyzing data from randomized controlled trials (RCTs) of acute ischemic stroke therapies (eg, intravenous thrombolysis, glycemic control, and hypothermia). Subject enrollment was required within 48 hours of symptom onset, and imaging biomarkers were used to select patients, measure outcome, or define subgroups (preplanned or post hoc). Any form of imaging including CT, MRI, SPECT, or transcranial Doppler (TCD) was allowed. Studies that used imaging solely to exclude patients with intracranial hemorrhage at trial enrollment were not included in the analysis. Other exclusion criteria were the following: studies of hemorrhagic stroke or transient ischemic attack, cluster trials, studies in children, those not comparing treatment and control groups, and those using historical controls. When ≥ 2 articles described the same populations, both studies were included, provided different imaging biomarkers were used in each.

Search Strategy

MEDLINE and EMBASE (1995 to March 2014) were searched by using a combination of terms, their derivatives, and related terms: RCTs, acute stroke, and imaging (On-line Appendix). Searches

were limited to English language articles with adult human subjects. Additional searches were made of strokecenter.org and the Virtual International Stroke Trials Archive (www.vista.gla.ac.uk). Two of the 3 reviewers screened each title and abstract independently (G.W.J.H., N.R., G.S.). The same reviewers independently reviewed the full texts of all potentially relevant studies, and those included were accepted by consensus (Fig 1).

Data Extraction

Data extracted included year, number of patients enrolled, details of the imaging biomarker, and the results of the trial. The imaging biomarkers were classified into the groups identified in the Acute Stroke Imaging Research Roadmap II with particular attention to Treatment-Relevant Acute Imaging Targets.² The purpose for which each group was used (trial eligibility, outcome measure, or subgroup analyses [preplanned or post hoc]) was recorded.

RESULTS

Search Results

The electronic search yielded 10,212 titles, of which 1180 were duplicates. Screening of the remaining studies and additional manual searching produced 370 to be appraised. Two hundred eighty-six were excluded following review of the article, leaving 84 to be included in the final analysis (Fig 1, On-line References). We identified 8 groups of imaging biomarkers: infarct volume, edema, diagnosis/territory of infarction, vessel status, ischemic penumbra, perfusion status, collaterals, and composite/other (Table 1).² Forty-nine studies used imaging for trial eligibility, 49 studies used ≥ 1 imaging outcome (eg, infarct volume or recanalization), and 31 studies used imaging criteria to define ≥ 1 subgroup (eg, stratification by infarct volume). Eighty-five different imaging-defined subgroups were identified in these 31 studies, 17 of which were preplanned and the remaining 68 subgroups were defined post hoc.

Imaging Biomarkers

Infarct volume was extensively used as an exclusion criterion from trial recruitment and subgroup eligibility assessment (Table 1). The most consistent definition used was an infarct volume on noncontrast CT of greater than one-third of the MCA territory (16/29 studies) (On-line Table 1). Other definitions used ranged from any evidence of ischemia on noncontrast CT to greater than two-thirds of the MCA territory demonstrating restricted diffusion on DWI. One trial of hemicraniectomy for malignant MCA syndrome excluded patients with an infarct volume of less than a predefined level (145 mL on DWI).⁴

Imaging was used in a variety of other ways to establish trial

Table 2: Proportion of analyses showing a positive outcome using imaging biomarkers for inclusion/exclusion or outcome assessment

	Preplanned	Post Hoc	P Value
Inclusion/exclusion			
Subgroup studies	3/17	28/68	
RCTs	10/49		
Total	13/66	28/68	.009 ^a
Outcome	13/84	19/42	.0005 ^a

^a Fisher exact test.

eligibility: DWI to confirm the diagnosis before enrollment, the presence of edema on CT to exclude patients, and location of infarction within a specific vascular territory for either inclusion or exclusion (On-line Table 1).

Vessel occlusion by using angiography (CTA, MRA, or DSA) and TCD was commonly identified before enrollment in a trial. Of the 16 trials that selected according to vessel-occlusion status, 12 used imaging to identify a target for the intervention and the remaining 4 excluded patients with carotid occlusions on the basis of the futility of the intervention (On-line Table 1).

Perfusion deficit alone was used in only 2 studies to select patients for inclusion (Table 1), whereas 13 studies used reperfusion as an outcome criterion in 27 different efficacy analyses. There was considerable heterogeneity in the timing of the assessment of reperfusion (4 hours to 3 months), which was made using a variety of modalities (MRI perfusion, CTP, SPECT) (On-line Table 2).

Identification of the ischemic penumbra, as a means of either patient selection or outcome assessment, was common (Table 1). On-line Table 3 demonstrates the variety of ways in which penumbra has been defined. All except 1 study defined penumbra using MRI perfusion measures, such as mean transit time or time-to-maximum, to identify hypoperfused tissue that extended beyond the DWI lesion, and most used a threshold of 20% mismatch to define ischemic penumbra to select patients. No trial using MRI perfusion resulted in a positive outcome. However, this threshold (20% mismatch to define the ischemic penumbra) was used with success in an evaluation of tenecteplase by using CTP (On-line Table 3).⁵ In addition to trials of reperfusion therapies, several neuroprotective trials also used penumbral imaging for inclusion.

Subgroup Analyses

The comparison of the results of studies with preplanned imaging-defined subgroups or imaging-based outcomes compared with post hoc analyses can be seen in Table 2. There are significantly more positive results in studies using post hoc analyses. For instance, no preplanned subgroup analysis of mismatch eligibility criteria has demonstrated a positive effect of what otherwise had been a null trial by primary analysis, whereas 2 post hoc–defined subgroup analyses have demonstrated a positive effect (On-line Table 3): those patients with very large perfusion deficits and small DWI lesions⁶; and patients with a 20% mismatch profile only once images were properly coregistered.⁷ More generally, the definitions used for subgroup selection were less consistent than those used for trial eligibility criteria (On-line Table 4). Using the example of quantification of cerebral infarction, we found that

definitions ranged from strata of absolute volumes to scoring systems such as the Alberta Stroke Programme Early CT Score.⁸

DISCUSSION

This review reinforces the framework outlined in the Acute Stroke Imaging Research Roadmap II.² It identifies groupings of imaging biomarkers that have been used across RCTs, reflecting the individual needs of those trials. However, there is marked heterogeneity in the definition of these imaging biomarkers among trials, with a large number of post hoc subgroup analyses exploring further imaging biomarker definitions.

In general terms, the use of imaging biomarkers is intended to produce a more homogeneous population within a trial, with the hope of limiting patient selection to those for whom the intervention is most likely to be of benefit. This should allow smaller trials to be conducted over shorter periods. We identified 8 groupings of imaging biomarkers used in acute stroke trials: infarct volume, edema, diagnosis/territory of infarction, vessel status, ischemic penumbra, perfusion status, collaterals, and composite/other. All were used to evaluate trial eligibility or outcome assessment, or for subgroup analysis.

This review highlights the variability of imaging biomarker definitions and acquisitions in RCTs. Taking infarct volume as an example, one-third of the MCA territory as a threshold on non-contrast CT was the most consistent imaging biomarker used for trial eligibility. Less consistency was seen when infarct volume was used to assess outcome. Timing of measurements, technique used, and measurement technique were all highly variable among trials (On-line Table 2). When an imaging biomarker becomes more complex, the epitome being ischemic penumbra, even more heterogeneity exists (On-line Table 3).

The impact of the inconsistent measurement of imaging biomarkers is important. For example, if infarct volume is used as an outcome assessment, edema and atrophy can affect the infarct volume at different times.⁹ Within the same patients the blinded adjudication of FLAIR and T2 images by neuroradiologists results in different infarct volume estimates and discrepant interrater agreements.¹⁰ The reliability and repeatability of a biomarker in defining a pathologic process will be affected by the contrast-to-noise ratio afforded by the imaging technique.¹¹ For example, DWI has a greater contrast-to-noise ratio than T2-weighted MR imaging, CT, and CTP, allowing a clearer definition of the extent of a lesion,^{11,12} thus reducing measurement error and improving interrater agreement.¹³ Even when there is excellent interrater agreement among neuroradiologists, substantial measurement errors can still exist that affect sample-size calculation for a RCT, particularly when the infarct volumes are small or moderate.¹⁴ Automated approaches to volume measurement offer the prospect of limiting human measurement error but introduce challenges of their own in the accommodation of thresholds that vary among individuals and that are also influenced by timing from stroke onset.¹⁴

The relationship between patients, imaging biomarkers, treatments, and eventual clinical outcomes is complex. Failure to accurately understand these relationships and, thus, selecting an inappropriate biomarker have contributed to the criticisms of recent RCTs. Defining a treatment-responsive group by using an

imaging biomarker is an entirely different task to selecting those who are destined to do well, independent of treatment, as was seen in the Mechanical Retrieval and Recanalization of Stroke Clots Using Embolectomy study.^{15,16} The only positive RCT of intravenous thrombolysis used within 3 hours of stroke onset is not included in this review because patients were not excluded by infarct volume criterion.¹⁷ Of note, post hoc analysis demonstrated that infarct volume was not a treatment modifier within 3 hours.¹⁸ The optimal threshold of infarct volume used to exclude patients from trial enrollment remains unclear.^{6,19}

Several prospective observational studies have explored alternate definitions of the ischemic core using DWI to select patients for endovascular therapy (Diffusion and Perfusion Imaging Evaluation for Understanding Stroke Evolution Study 2 used a threshold of >70 mL on DWI to exclude patients).¹⁹⁻²² These data suggest that patients selected by using lower infarct volume thresholds than used previously have a greater capacity to benefit from endovascular treatment. This promising approach from observational studies now needs to be translated into RCTs.

Expected treatment effects on a biomarker used as an imaging outcome and its relationship with clinical outcomes also need to be understood when designing a RCT. For example, the recanalization rate with intravenous tPA in the Interventional Management of Stroke III trial was twice what was predicted, and the highly significant increase in revascularization was not associated with improvement in clinical outcomes.²³

The Acute Stroke Imaging Research Roadmap II outlines a framework for use within a RCT, advocating the use of a consistent Treatment-Relevant Acute Imaging Target within all arms. This would allow secondary analyses to address the additional value of imaging while the primary focus remains on the therapeutic intervention. This area deserves further methodologic consideration; this review highlights the large number of subgroup analyses, typically post hoc, performed using data from the RCTs. We found an excess of positive post hoc subgroup analyses, suggesting that any apparently useful subgroups should be viewed with caution, given the risk of publication bias.^{1,24} This may give a false sense of promise from apparently successful post hoc attempts to stratify patients (Table 2), meaning that these positive results should be used only for hypothesis generation and validation in separate patient research cohorts, and before widespread clinical adoption.²⁵

Successful meta-analyses of pooled data of RCTs of intravenous thrombolysis and hemicraniectomy have contributed to their wide adoption into national stroke clinical guidelines and practice.^{15,16} The inconsistent use of imaging biomarkers highlighted in this review markedly hampers such meta-analyses. For instance, it would be inappropriate to combine cohorts in whom mismatch was defined using different modalities and thresholds. It is equally challenging to interpret results from individual studies in which different imaging modalities are used to define enrollment criteria: for instance, the Mechanical Retrieval and Recanalization of Stroke Clots Using Embolectomy study used either MRI or CT to assess the favorability of the penumbra pattern.¹⁵ The advantage of this approach is to maximize the number of sites that may take part in a RCT, hopefully reducing study duration and broadening the generalizability of the results. How-

ever, unless the equivalence of the biomarkers is robustly established, the reliability of data interpretation is potentially compromised. The Acute Stroke Imaging Research Roadmap II begins to address these difficulties with the example of the clarification of revascularization status and associated concepts.^{2,26}

There remains an unmet need for a robust pathway for stroke imaging biomarker development from the preclinical studies through translational and observational studies ready for use in RCTs and clinical settings. This pathway needs to accommodate the possibility that the imaging that drives scientific discovery may or may not be available for clinical use in acute stroke. For example, diffusion MRI is a widely used and validated method for identifying core infarct in animal model studies and has been used in several RCTs. On the other hand, perfusion CT has almost no preclinical validation but is commonly used in RCTs. The relationship between how and whether different imaging modalities measure the same pathophysiology must be established. Existing initiatives developed from expert consensus may expedite this process and ensure a more homogeneous use of biomarkers in RCTs.^{27,28}

CONCLUSIONS

Imaging biomarkers offer the opportunity to refine the trial cohort by minimizing participant variation, to decrease sample size, and to personalize treatment approaches for those who stand to benefit most. However, within imaging modalities, there has been little consistency among stroke trials. Greater effort to prospectively use consistent imaging biomarkers should help improve the development of novel treatment strategies in acute stroke and improve comparison between studies.

ACKNOWLEDGMENTS

We wish to acknowledge the facilities provided by the Oxford Acute Vascular Imaging Centre.

Disclosures: George W.J. Harston—*RELATED: Grant:* research grants via the University of Oxford.* *Comments:* Dunhill Medical Trust, National Institute for Health Research Oxford Biomedical Research Centre, Centre of Excellence for Personalized Healthcare, funded by the Wellcome Trust and Engineering and Physical Sciences Research Council. Neil Rane—*UNRELATED: Travel/Accommodations/Meeting Expenses Unrelated to Activities Listed:* received travel grants and participated in funded meetings from Codman Neurovascular, Microvention, Stryker, Covidien; *Other:* current fellowship position partly funded by Codman Neurovascular, not institutionally organized by the author; received scholarship funding for current position from HCA International Foundation, United Kingdom (private hospital group). Please also see departmental disclosures of the first author. Sivarajan Thandeswaran—*RELATED: Grant:* National Institute for Health Research Oxford Biomedical Research Centre,* Dunhill Medical Trust,* Centre of Excellence for personalized health care funded by the Wellcome Trust and the Engineering and Physical Sciences Research Council.* Fintan Sheerin—*RELATED: Grant:* See lead author's disclosures for funding/grant details*; *UNRELATED: Expert Testimony:* second opinion on clinical scans provided for a patient challenging a decision by their health insurance company. I do not currently do medicolegal work; *Payment for Lectures (Including service on Speakers Bureaus):* Oxford MRI and Oxford Neuroradiology courses, *Comments:* honorarium for educational lectures; *Travel/Accommodations/Meeting Expenses Unrelated to Activities Listed:* study expenses: Oxford University Hospitals study funds paid for British Society of Neuroradiologists conference fee 2013. *Money paid to the institution.

REFERENCES

1. Wardlaw JM. Surrogate outcomes: a cautionary note. *Stroke* 2009; 40:1029-31

2. Wintermark M, Albers GW, Broderick JP, et al. **Acute Stroke Imaging Research Roadmap II.** *Stroke* 2013;44:2628–39
3. Wintermark M, Sanelli PC, Albers GW, et al. **Imaging recommendations for acute stroke and transient ischemic attack patients: a joint statement by the American Society of Neuroradiology, the American College of Radiology, and the Society of NeuroInterventional Surgery.** *AJNR Am J Neuroradiol* 2013;34:E117–27
4. Vahedi K, Vicaut E, Mateo J, et al. **Sequential-design, multicenter, randomized, controlled trial of early decompressive craniectomy in malignant middle cerebral artery infarction (DECIMAL Trial).** *Stroke* 2007;38:2506–17
5. Parsons M, Spratt N, Bivard A, et al. **A randomized trial of tenecteplase versus alteplase for acute ischemic stroke.** *N Engl J Med* 2012;366:1099–107
6. Parsons MW, Christensen S, McElduff P, et al. **Pretreatment diffusion- and perfusion-MR lesion volumes have a crucial influence on clinical response to stroke thrombolysis.** *J Cereb Blood Flow Metab* 2010;30:1214–25
7. Nagakane Y, Christensen S, Brekenfeld C, et al. **EPITHET: positive result after reanalysis using baseline diffusion-weighted imaging/perfusion-weighted imaging co-registration.** *Stroke* 2011;42:59–64
8. Barber PA, Demchuk AM, Zhang J, et al. **Validity and reliability of a quantitative computed tomography score in predicting outcome of hyperacute stroke before thrombolytic therapy: ASPECTS Study Group—Alberta Stroke Programme Early CT Score.** *Lancet* 2000;355:1670–74
9. Inoue M, Mlynash M, Christensen S, et al. **Early diffusion-weighted imaging reversal after endovascular reperfusion is typically transient in patients imaged 3 to 6 hours after onset.** *Stroke* 2014;45:1024–28
10. Neumann AB, Jonsdottir KY, Mouridsen K, et al. **Interrater agreement for final infarct MRI lesion delineation.** *Stroke* 2009;40:3768–71
11. González RG, Schaefer PW, Buonanno FS, et al. **Diffusion-weighted MR imaging: diagnostic accuracy in patients imaged within 6 hours of stroke symptom onset.** *Radiology* 1999;210:155–62
12. González RG. **Low signal, high noise and large uncertainty make CT perfusion unsuitable for acute ischemic stroke patient selection for endovascular therapy.** *J Neurointerv Surg* 2012;4:242–45
13. Campbell BC, Tu HT, Christensen S, et al. **Assessing response to stroke thrombolysis: validation of 24-hour multimodal magnetic resonance imaging.** *Arch Neurol* 2012;69:46–50
14. Ay H, Arsava EM, Vangel M, et al. **Interexaminer difference in infarct volume measurements on MRI: a source of variance in stroke research.** *Stroke* 2008;39:1171–76
15. Kidwell CS, Jahan R, Gornbein J, et al. **A trial of imaging selection and endovascular treatment for ischemic stroke.** *N Engl J Med* 2013;368:914–23
16. Powers WJ. **Intravenous thrombolysis of basilar artery thrombosis.** *Ann Neurol* 2014;75:456–57
17. National Institute of Neurological Disorders and Stroke rt-PA Stroke Study Group. **Tissue plasminogen activator for acute ischemic stroke.** *N Engl J Med* 1995;333:1581–87
18. Patel SC, Levine SR, Tilley BC, et al. **Lack of clinical significance of early ischemic changes on computed tomography in acute stroke.** *JAMA* 2001;286:2830–38
19. Lansberg MG, Straka M, Kemp S, et al. **MRI profile and response to endovascular reperfusion after stroke (DEFUSE 2): a prospective cohort study.** *Lancet Neurol* 2012;11:860–67
20. Simonsen CZ, Sørensen LH, Karabegovic S, et al. **MRI before intra-arterial therapy in ischemic stroke: feasibility, impact, and safety.** *J Cereb Blood Flow Metab* 2014;34:1076–81
21. Wisco D, Uchino K, Saqqur M, et al. **Addition of hyperacute MRI aids in patient selection, decreasing the use of endovascular stroke therapy.** *Stroke* 2014;45:467–72
22. Yoo AJ, Verduzco LA, Schaefer PW, et al. **MRI-based selection for intra-arterial stroke therapy: value of pretreatment diffusion-weighted imaging lesion volume in selecting patients with acute stroke who will benefit from early recanalization.** *Stroke* 2009;40:2046–54
23. Broderick JP, Palesch YY, Demchuk AM, et al. **Endovascular therapy after intravenous t-PA versus t-PA alone for stroke.** *N Engl J Med* 2013;368:893–903
24. Tzoulaki I, Siontis KC, Evangelou E, et al. **Bias in associations of emerging biomarkers with cardiovascular disease.** *JAMA Intern Med* 2013;173:664–71
25. Rothwell PM. **Treating individuals 2: subgroup analysis in randomised controlled trials: importance, indications, and interpretation.** *Lancet* 2005;365:176–86
26. Tomsick T. **TIMI, TIBI, TICI: I came, I saw, I got confused.** *AJNR Am J Neuroradiol* 2007;28:382–84
27. European Society of Radiology. **White paper on imaging biomarkers.** *Insights Imaging* 2010;1:42–45
28. Kessler LG, Barnhart HX, Buckler AJ, et al. **The emerging science of quantitative imaging biomarkers terminology and definitions for scientific studies and regulatory submissions.** *Stat Methods Med Res* 2015;24:9–26

Imaging Biomarkers in Ischemic Stroke Clinical Trials: An Opportunity for Rigor

The effective treatment of major strokes due to major cerebral artery occlusion is a great opportunity for diagnostic and interventional neuroradiology. These represent approximately one-third of all strokes and result in the most deaths and poor outcomes. The relevant physiology (occlusion site, infarct core, and penumbra) is revealed by neuroimaging, and many patients, perhaps most, are effectively and safely treatable by neurointerventional methods. After an early success, there were many clinical trial failures. However, there are indications of a major breakthrough with the positive results reported by the completed A Randomized Trial of Intraarterial Treatment for Acute Ischemic Stroke¹ and in early interim analyses of other trials. While highly encouraging, the good outcome rate of <33% suggests that there are opportunities for improvement. The role of imaging biomarkers in enhancing this opportunity looms large. However, optimal patient outcomes will only be achieved if the neuroradiology community uses rigor in the application of stroke imaging biomarkers.

There are several possible reasons for prior clinical trial failures. One factor was poorly effective devices for vessel recanalization. Recently introduced devices appear to have largely resolved this problem. The remaining major obstacle is patient selection. In a review published in this issue of the *American Journal of Neuroradiology*, Harston et al² provide a timely and valuable service by documenting the problem of heterogeneity in the types of imaging biomarkers heretofore used in stroke trials. They suggested that this is an important reason for the failure of many of these trials. They further suggest that more homogeneity in the use of imaging biomarkers would be better. While the article covers much important ground, it does not fully explore why such heterogeneity has resulted in repeated, though not uniform, failures in clinical trials.

There are at least 3 reasons why imaging biomarkers fail:

- 1) The wrong measurement has been chosen
- 2) The measurement criterion is mistaken
- 3) There are significant errors in making the measurement.

To illuminate these 3 factors, one should consider what the authors identify as the most common biomarker used in stroke trials: the measurement of the core infarct volume to exclude pa-

tients who are unlikely to benefit from a treatment or intervention. There is strong evidence that this is an appropriate measure. If a large infarct is already present, arterial recanalization may be futile and possibly harmful by risking hemorrhage, reperfusion injury, or malignant edema. Nevertheless, many trials have failed despite the use of this measure. This brings up reason 2: Was the wrong infarct size selected? To help explore this possibility, one should consider an absurd example—exclusion of only those patients who have an identifiable infarct that is the size of the entire MCA territory or larger. Clearly, it would be difficult to show that a treatment is beneficial because so many patients would be admitted into the trial who would have no possibility of benefiting.

What is the best measurement criterion for infarct size to use as a threshold? As noted in the article, a core infarct involving one-third of the MCA territory (~100 mL) has been the most commonly used threshold, but there is now substantial evidence that this volume threshold is probably too high. The multicenter Diffusion and Perfusion Imaging Evaluation for Understanding Stroke Evolution 2 trial³ demonstrated that patients presenting with DWI lesion volumes of <70 mL had better outcomes when undergoing endovascular treatment. This lower volume threshold was also found to lead to better outcomes in 3 single-center studies.⁴⁻⁶ Evidence that one-third of the MCA territory is too large also comes from the failed Mechanical Retrieval and Recanalization of Stroke Clots Using Embolectomy trial,⁷ which used a threshold of 90 mL. Thus, perhaps an infarct involving “one-third of the MCA territory” is wrong.

The final possible reason for poor patient selection is that the imaging method produces errors that are too large to be adequate for the task. Again consider core infarct size. Does the chosen imaging biomarker measure the core infarct with sufficient precision to be useful? There is general agreement with much evidence that unenhanced CT is inadequate for this purpose. There is also general agreement with strong animal and human evidence that DWI does, in fact, reliably measure the core infarct. On the other hand, no animal studies have shown that a single hemodynamic measurement corresponds to infarcted tissue. Moreover, CTP-derived images have inherently poor signal-to-noise ratios, which result in large measurement errors.⁸ Perhaps it would be wise to hold off on the use of perfusion CT (PCT) in stroke trials

until it has been rigorously validated in animal stroke models and measurement errors are reduced.

Against this logic is the clear preference for the use of PCT over DWI as is evident in the review by Harston et al.² The principal justification is that PCT is widely available and readily accessible to patients with stroke, while MR imaging is much less so. Thus, it appears that this decision is based on “practicality” rather than scientific evidence. This possibility raises important ethical questions. Should we use a less effective tool because it is practical, or should we make the necessary effort to make available to our patients with stroke the tool that clearly benefits them?

Rigorous standards for validation of imaging biomarkers are missing, and they are unlikely to be forthcoming without a demand for them by the stroke clinical research community. Such rigor would likely result in the abandonment of imaging biomarkers that perform poorly. However, the other result would be progress toward more homogeneity in the use of imaging biomarkers, and ultimately better outcomes in patients with acute stroke whom we treat.

REFERENCES

1. Berkhemer OA, Fransen PS, Beumer D, et al. **A randomized trial of intraarterial treatment for acute ischemic stroke.** *N Engl J Med* 2015; 372:11–20
2. Harston GW, Rane, N, Shaya S, et al. **Imaging biomarkers in acute ischemic stroke trials: a systematic review.** *AJNR Am J Neuroradiol* 2015;36:839–43
3. Lansberg MG, Straka M, Kemp S, et al. **MRI profile and response to endovascular reperfusion after stroke (DEFUSE 2): a prospective cohort study.** *Lancet Neurol* 2012;11:860–67
4. Simonsen CZ, Sorensen LH, Karabegovic S, et al. **MRI before intraarterial therapy in ischemic stroke: feasibility, impact, and safety.** *J Cereb Blood Flow Metab* 2014;34:1076–81
5. Wisco D, Uchino K, Saqqur M, et al. **Addition of hyperacute MRI AIDS in patient selection, decreasing the use of endovascular stroke therapy.** *Stroke* 2014;45:467–72
6. Yoo AJ, Verduzco LA, Schaefer PW, et al. **MRI-based selection for intraarterial stroke therapy: value of pretreatment diffusion-weighted imaging lesion volume in selecting patients with acute stroke who will benefit from early recanalization.** *Stroke* 2009;40:2046–54
7. Kidwell CS, Jahan R, Gornbein J, et al. **A trial of imaging selection and endovascular treatment for ischemic stroke.** *N Engl J Med* 2013;368:914–23
8. Schaefer PW, Souza L, Kamalian S, et al. **Limited reliability of computed tomographic perfusion acute infarct volume measurements compared with diffusion-weighted imaging in anterior circulation stroke.** *Stroke* 2015;46:419–24

R.G. González

Massachusetts General Hospital and Harvard Medical School
Boston, Massachusetts

<http://dx.doi.org/10.3174/ajnr.A4269>

Memory Part 2: The Role of the Medial Temporal Lobe

F.D. Raslau, I.T. Mark, A.P. Klein, J.L. Ulmer, V. Mathews, and  L.P. Mark

The medial temporal lobe plays a central role in memory processing and is more than just the hippocampus.¹ The hippocampal formation, which forms the upper segment of the medial temporal lobe, is a heterogeneous structure consisting of the Ammon horn or Cornus Ammonis (Cornus Ammonis area 1 to Cornus Ammonis area 4) and the dentate gyrus appearing as 2 interlocking *U*'s on a coronal image. The collapsed portion of the temporal horn of the lateral ventricle forms the superior border of the hippocampal formation. The slightly more dilated lateral aspect of the temporal horn forms the lateral margin, while the ambient cistern is at the medial border.²

The parahippocampal gyrus, positioned just inferior to the hippocampus, forms the other major component of the medial temporal lobe (Fig 1). The parahippocampal gyrus is the most medial of the group of 3 gyri that form the inferior surface of the temporal lobe. The collateral sulcus forms the lateral border of the parahippocampal gyrus, while the ambient cistern is at the medial margin. The parahippocampal gyrus can be subdivided into anterior and posterior components. The anterior portion, sometimes referred to as the rhinal cortex,³⁻⁵ consists of medial and lateral parts, the entorhinal (Brodmann area 28) and perirhinal (Brodmann area 35) cortices, respectively. The border between the entorhinal and perirhinal cortices is located at the junction between the inferior surface of the parahippocampal gyrus and the inferior aspect of the collateral sulcus (Fig 2).^{6,7} The superior aspect of the collateral sulcus demarcates the position of the lateral margin of the perirhinal cortex. In other words, the perirhinal cortex forms the medial bank of the collateral sulcus.⁸ The posterior component of the parahippocampal gyrus consists of the parahippocampal cortex, which is not synonymous with the parahippocampal gyrus. The entorhinal, perirhinal, and parahippocampal cortices to-

gether, therefore, make up the parahippocampal gyrus. The subiculum is transitional cortex that bridges the Ammon horn of the hippocampal formation (allocortex) with the parahippocampal gyrus (isocortex).² The subiculum can be further subdivided into the subiculum proper, presubiculum, and parasubiculum.

The organization of the medial temporal lobe suggests a hierarchic format in which information is initially collected through the perirhinal and parahippocampal cortices, passes to the entorhinal cortex, and ultimately reaches the hippocam-

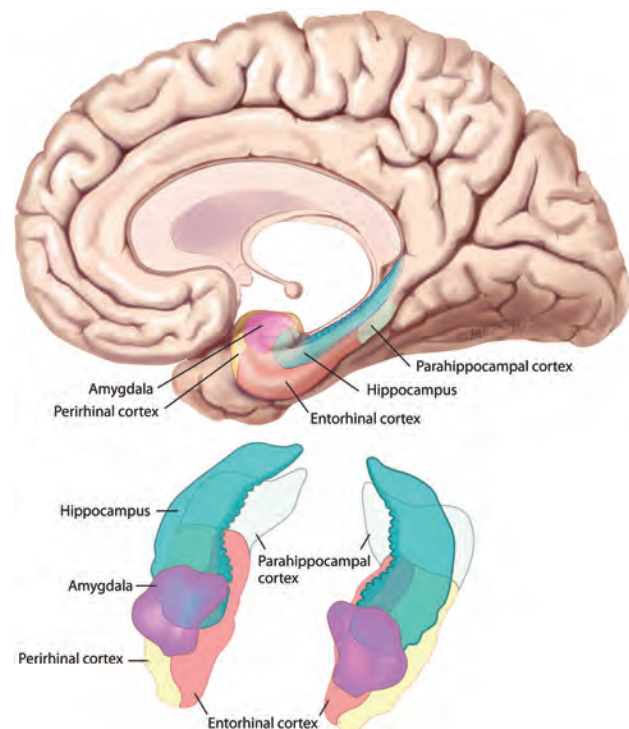


FIG 1. The medial temporal lobe consists of the hippocampal formation (blue-green) superiorly and the parahippocampal gyrus inferiorly. The entorhinal (brown) and perirhinal (yellow) cortices form the medial and lateral components, respectively, of the anterior portion of the parahippocampal gyrus, while the parahippocampal cortex (off-white) forms the posterior portion. Adapted with permission from Purves D, Brannon E, Cabeza R, et al. *Principles of Cognitive Neuroscience*. Sunderland, MA: Sinauer Associates; 2008.

From the Department of Radiology (F.D.R.), University of Kentucky, Lexington, Kentucky; Morsani College of Medicine (I.T.M.), University of South Florida, Tampa, Florida; and Department of Radiology (A.P.K., J.L.U., V.M., L.P.M.), Medical College of Wisconsin, Milwaukee, Wisconsin.

Please address correspondence to Leighton P. Mark, MD, Froedtert Hospital, Department of Radiology, Neuroradiology Section, 9200 West Wisconsin Ave, Milwaukee, WI 53226; e-mail: lmark@mcw.edu

<http://dx.doi.org/10.3174/ajnr.A4169>

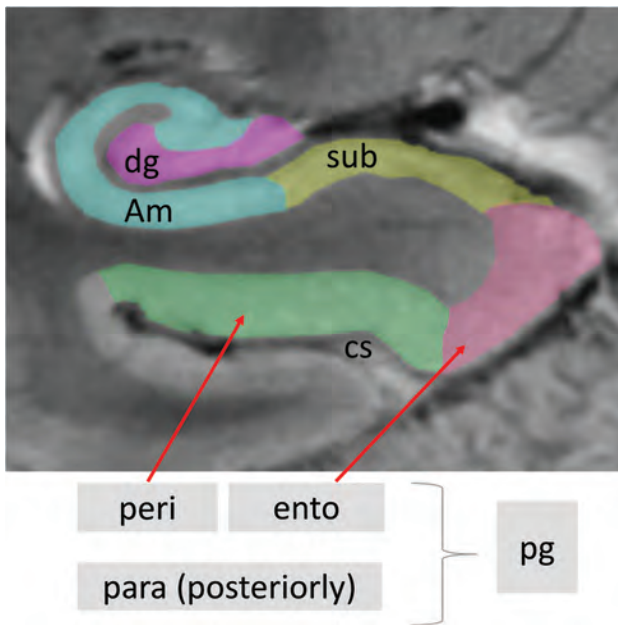


FIG 2. Coronal T2-weighted MR image of the right medial temporal lobe. The Ammon horn (Am) is blue, interlocking with the dentate gyrus (dg) in lavender. The perirhinal cortex (peri) in green is lateral to the entorhinal cortex (ento) in pink. The subiculum (sub) in yellow links the Ammon horn with the entorhinal cortex. Note that the sulcus just lateral to the perirhinal cortex is the collateral sulcus (cs) and the apex or superior most portion of the collateral sulcus marks the position of the lateral margin of the perirhinal cortex, while the inferior aspect of the sulcus marks the border between the perirhinal and entorhinal cortices. The parahippocampal gyrus (pg) consists of the perirhinal, entorhinal, and parahippocampal (para) cortices.

pal formation, which forms major output projections via the fornix (Fig 3).⁹ The parahippocampal gyrus, however, does not merely funnel information to the hippocampus.¹⁰ A large network of connections both within and among the subregions of the parahippocampal gyrus performs extensive information processing on its own and among subregions before any of the information reaches the hippocampus. Exteroceptive (external to the organism) information is processed by the parahippocampal gyrus via the ventral and dorsal streams (Fig 4). The ventral stream from the occipital lobe consists of visual information in terms of object recognition, while the dorsal stream from the parietal lobe carries spatial context information to the parahippocampal gyrus. Interoceptive (internal to the organism) signals carrying information such as emotions and motivation from the medial prefrontal cortex, nucleus accumbens, and amygdala project to the rostral hippocampal formation and rhinal cortex regions. This information from multiple sources is combined and ultimately output via the fornix from the hippocampal formation.

Closer inspection of the medial temporal subregions has revealed additional layers of complexity and organization. The entorhinal cortex, for example, can be seen to have distinctive medial and lateral regions that differ histologically and physiologically.¹¹ The medial entorhinal cortex (Brodmann area 28b) is actively involved in the processing of spatial information from the dorsal stream, whereas the lateral entorhinal cortex (Brodmann area 28a) does so with the object-recognition information from the ventral stream. Furthermore, the

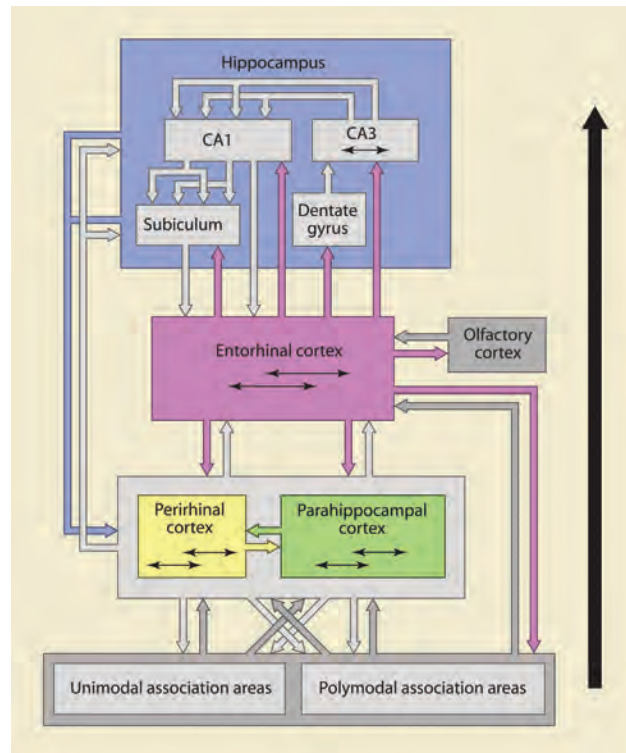


FIG 3. The net flow of information is from the perirhinal and parahippocampal cortices to the entorhinal cortex and then to the hippocampal formation, but considerable information processing occurs within and among the subregions of the parahippocampal gyrus before hippocampal formation involvement. Adapted with permission from Lavenex P, Amaral DG. Hippocampal-neocortical interaction: a hierarchy of associativity. *Hippocampus* 2000;10:420–30, John Wiley and Sons.

rhinal cortex functionally differentiates familiar and novel information input, where more familiar items are given fewer resources for encoding compared with new items. The rhinal cortex, therefore, functions as a gatekeeper of the declarative memory system by optimizing memory-encoding resources to novel information.¹²

In recent years, investigators have also postulated 2 cortical systems (anterior and posterior temporal) for memory-guided behavior involving the perirhinal and parahippocampal cortices.¹³ The anterior temporal system consists of the perirhinal cortex, temporopolar cortex, lateral orbital frontal cortex, and amygdala, while the posterior temporal system includes the parahippocampal cortex, retrosplenial cortex (Brodmann areas 29 and 30), anterior thalamic nuclei, mammillary bodies, pre- and parasubiculum, and components of the so-called default network, of which the retrosplenial cortex is a part, including the posterior cingulate gyrus, precuneus, angular gyrus, and ventral medial prefrontal cortex. The anterior system is more involved in object and face recognition, conceptual identity, and salience, while the posterior system focuses on scene recognition, location, trajectory, temporal context and order, and situations.

Semantic dementia involves more of the anterior temporal system, and patients often show the deficits in fine-grain object recognition. Alzheimer disease often involves more of the posterior temporal system and is frequently associated with deficits in

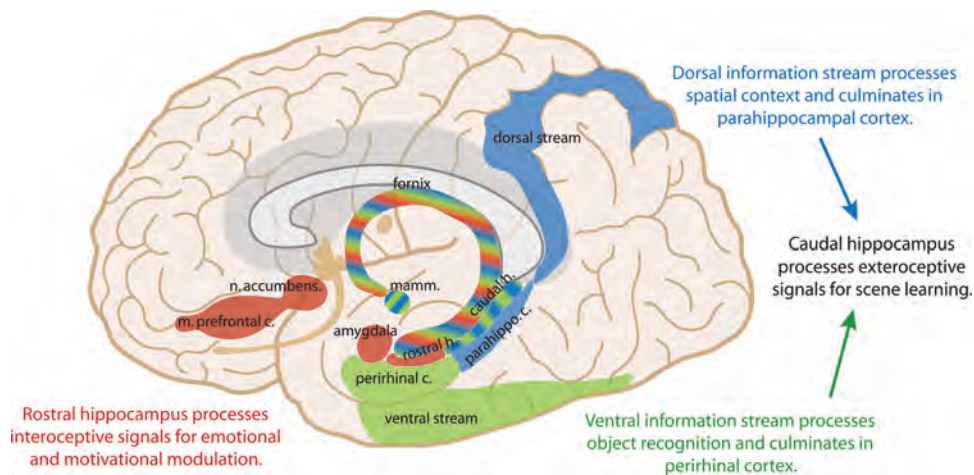


FIG 4. Medial temporal lobe processing of exteroceptive and interoceptive signals for memory formation. The ventral stream from the occipital lobe projects information about object recognition, while the dorsal stream from the parietal lobe conveys spatial information. The rostral interoceptive signals convey emotions and motivations.

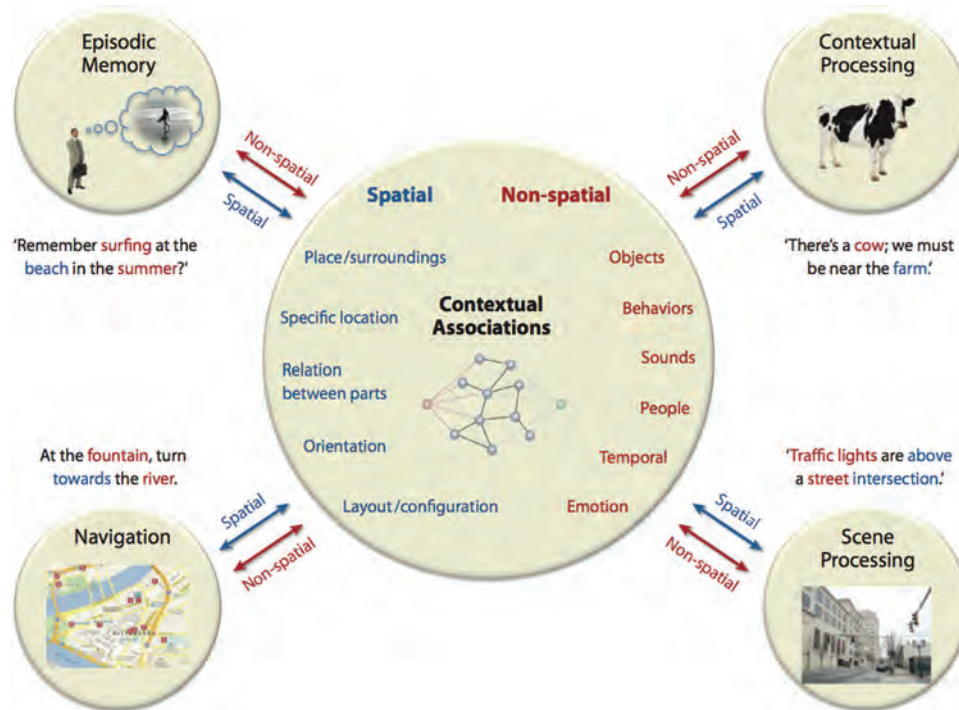


FIG 5. The parahippocampal cortex functions involve more than just spatial processing. The connections with the different areas of the frontal, parietal, and temporal lobes, including the default network, position the parahippocampal cortex as a critical component in processing contextual associations, which are fundamental aspects of higher cognitive functions. Adapted with permission from Aminoff EM, Kveraga K, Bar M. The role of the parahippocampal cortex in cognition. *Trends Cogn Sci* 2013;17:379–90, Elsevier.

scene discrimination. In this same fashion, detailed evaluation reveals that the parahippocampal cortex functions are much more complex than just the processing of spatial layout information. The parahippocampal cortex is part of a larger network that connects regions of the frontal, parietal, and temporal lobes. This includes auditory association areas of the superior temporal gyrus, the polymodal association areas (such as the retrosplenial cortex, lateral inferior parietal lobule, dorsal bank of the superior temporal sulcus), temporal pole, perirhinal cortex, parahippocampal cortex itself, entorhinal cortex, medial prefrontal cortex, dorsal lateral prefrontal cortex, orbital prefrontal cortex, in-

sula, and so forth. It is best to think of the major role of the parahippocampal cortex as facilitating contextual associations, which are the principal elements underlying many higher level cognitive processes (Fig 5).¹⁴

In summary, the medial temporal lobe occupies a central position in the intersection of multiple neuronal networks. Its anatomic complexity within its subregions and with other cerebral structures reflects the multifaceted nature of memory. Its functions, however, are more than those associated with declarative memory and are now known to be wide-ranging and include higher level cognitive functions, especially with the connections

with the retrosplenial cortex and default network as demonstrated by resting-state fMRI studies.

The next Functional Vignette will be the last installment on memory and will showcase clinical cases in which memory is affected when key anatomic structures are involved.

ACKNOWLEDGMENTS

The authors express our deepest gratitude to Jean Augustinack, PhD, Harvard Medical School, Massachusetts General Hospital, Martinos Faculty, for her invaluable advice on the anatomy of the perirhinal and entorhinal cortices.

REFERENCES

1. Amaral DG. **Introduction: what is where in the medial temporal lobe?** *Hippocampus* 1999;9:1–6
2. Duvernoy HM, Cattin TP, Naidic C, et al. *The Human Hippocampus: Functional Anatomy, Vascularization and Serial Sections with MRI*. 3rd ed. Berlin: Springer-Verlag; 2005:232
3. Meunier M, Hadfield W, Bachevalier J, et al. **Effects of rhinal cortex lesions combined with hippocampectomy on visual recognition memory in rhesus monkeys.** *J Neurophysiol* 1996;75:1190–1205
4. Murray EA, Mishkin M. **Visual recognition in monkeys following rhinal cortical ablations combined with either amygdalectomy or hippocampectomy.** *J Neurosci* 1986;6:1991–2003
5. Liu Z, Richmond BJ, Murray EA, et al. **DNA targeting of rhinal cortex D2 receptor protein reversibly blocks learning of cues that predict reward.** *Proc Natl Acad Sci U S A* 2004;101:2336–41
6. Augustinack JC, Huber KE, Stevens AA, et al. **Predicting the location of human perirhinal cortex, Brodmann's area 35, from MRI.** *Neuroimage* 2013;64:32–42
7. Augustinack JC, van der Kouwe AJ, Fischl B. **Medial temporal cortices in ex vivo magnetic resonance imaging.** *J Comp Neurol* 2013; 521:4177–88
8. Feczko E, Augustinack JC, Fischl B, et al. **An MRI-based method for measuring volume, thickness and surface area of entorhinal, perirhinal, and posterior parahippocampal cortex.** *Neurobiol Aging* 2009;30:420–31
9. Lavenex P, Amaral DG. **Hippocampal-neocortical interaction: a hierarchy of associativity.** *Hippocampus* 2000;10:420–30
10. Purves D, Brannon E, Cabeza R, et al. *Principles of Cognitive Neuroscience*. Sunderland, MA: Sinauer Associates; 2008
11. Burgalossi A, Brecht M. **Cellular, columnar and modular organization of spatial representations in medial entorhinal cortex.** *Curr Opin Neurobiol* 2014;24:47–54
12. Fernández G, Tendolkar I. **The rhinal cortex: 'gatekeeper' of the declarative memory system.** *Trends Cogn Sci* 2006;10:358–62
13. Ranganath C, Ritchey M. **Two cortical systems for memory-guided behavior.** *Nat Rev Neurosci* 2012;13:713–26
14. Aminoff EM, Kveraga K, Bar M. **The role of the parahippocampal cortex in cognition.** *Trends Cogn Sci* 2013;17:379–90

Evaluating Blood-Brain Barrier Permeability in Delayed Cerebral Infarction after Aneurysmal Subarachnoid Hemorrhage

J. Ivanidze, K. Kesavabhotla, O.N. Kallas, D. Mir, H. Baradaran, A. Gupta, A.Z. Segal, J. Claassen, and P.C. Sanelli



ABSTRACT

BACKGROUND AND PURPOSE: Patients with SAH are at increased risk of delayed infarction. Early detection and treatment of delayed infarction remain challenging. We assessed blood-brain barrier permeability, measured as permeability surface area product, by using CTP in patients with SAH with delayed infarction.

MATERIALS AND METHODS: We performed a retrospective study of patients with SAH with delayed infarction on follow-up NCCT. CTP was performed before the development of delayed infarction. CTP data were postprocessed into permeability surface area product, CBF, and MTT maps. Coregistration was performed to align the infarcted region on the follow-up NCCT with the corresponding location on the CTP maps obtained before infarction. Permeability surface area product, CBF, and MTT values were then obtained in the location of the subsequent infarction. The contralateral noninfarcted region was compared with the affected side in each patient. Wilcoxon signed rank tests were performed to determine statistical significance. Clinical data were collected at the time of CTP and at the time of follow-up NCCT.

RESULTS: Twenty-one patients with SAH were included in the study. There was a statistically significant increase in permeability surface area product in the regions of subsequent infarction compared with the contralateral control regions ($P < .0001$). However, CBF and MTT values were not significantly different in these 2 regions. Subsequent follow-up NCCT demonstrated new delayed infarction in all 21 patients, at which time 38% of patients had new focal neurologic deficits.

CONCLUSIONS: Our study reveals a statistically significant increase in permeability surface area product preceding delayed infarction in patients with SAH. Further investigation of early permeability changes in SAH may provide new insights into the prediction of delayed infarction.

ABBREVIATIONS: BBBP = blood-brain barrier permeability; DCI = delayed cerebral ischemia; PS = permeability surface-area product

Aneurysmal subarachnoid hemorrhage is a devastating illness with an average case fatality rate of 51% and approximately one-third of survivors needing life-long care.¹ Patients who survive are at high risk for developing sequelae of cerebral vasospasm

and delayed cerebral ischemia (DCI), leading to delayed infarction, which occurs in 40%–70% of patients with SAH, representing the leading cause of post-SAH morbidity and mortality.² Recent studies reported a dissociation of angiographic vasospasm and poor neurologic outcome, supporting the assumption that infarction rather than vasospasm might reflect the ultimate end point of different proischemic pathomechanisms, including microvascular and neuronal dysfunction.³

Early and delayed microcirculatory dysfunction after SAH is increasingly thought to be associated with DCI resulting in delayed infarction, in the absence of proximal vasospasm.⁴ Microvascular dysfunction can be assessed by using CTP. CTP parameters currently used in clinical practice are MTT, CBF, and CBV,⁵ which provide useful findings regarding the presence and extent of DCI.^{5–10} However, screening tools are lacking for earlier detection of patients at particularly high risk of developing delayed infarction from DCI to prompt therapeutic pre-emptive measures to minimize the impending morbidity and mortality. Currently, the assessment of patients with SAH for DCI relies primar-

Received July 23, 2014; accepted after revision November 5.

From the Departments of Radiology (J.I., K.K., O.N.K., D.M., H.B., A.G., P.C.S.), Neurology (A.Z.S.), and Public Health (P.C.S.), Weill Cornell Medical College, New York-Presbyterian Hospital, New York, New York; and Department of Neurology (J.C.), New York-Presbyterian Hospital, Columbia University Medical Center, New York, New York.

This work was supported by grant number 5K23NS058387 from the National Institute of Neurological Disorders and Stroke, a component of the National Institutes of Health. The content of this article is solely the responsibility of the authors and does not necessarily represent the official view of the National Institute of Neurological Disorders and Stroke or the National Institutes of Health.

Paper previously presented at: Annual Meeting of the Radiological Society of North America, December 1–6, 2013; Chicago, Illinois.

Please address correspondence to Jana Ivanidze, MD, PhD, Department of Radiology, New York-Presbyterian Hospital–Weill Cornell Medical Center, 525 E 68th St, Starr 8A, New York, NY 10065; e-mail: jai9018@nyp.org

Indicates open access to non-subscribers at www.ajnr.org

Evidence-Based Medicine Level 1.

<http://dx.doi.org/10.3174/ajnr.A4207>

ily on clinical examination, transcranial Doppler sonography, and NCCT. Clinical examination is limited because symptoms can be variable and difficult to detect,¹¹ while transcranial Doppler sonography is limited by poor sensitivity and specificity.¹²⁻¹⁴ Although NCCT can detect delayed infarction, the management and treatment goals in patients with SAH are to prevent these sequelae of DCI.

Blood-brain barrier permeability (BBBP) is known to increase in certain conditions such as ischemia, malignancy, infection, and autoimmune disease.¹⁵ On the molecular level, the BBB is composed of the neurovascular unit, comprising tight junctions between astrocytes and vascular endothelial cells. Permeability surface-area product (PS), derived from CTP, measures the diffusion of contrast from the vascular into the interstitial space, thus providing an indirect measure of BBBP.¹⁶ Although several reports describe the high sensitivity and specificity of the CTP-derived CBF and/or MTT to detect perfusion abnormalities in DCI,^{5,7-10,17,18} alterations of the BBBP have not yet been studied in this context.

We hypothesized that BBBP increases before delayed infarction in patients with SAH. The purpose of this study was to assess whether alterations in BBBP, measured as PS by using CTP, precede development of infarction related to DCI after SAH.

MATERIALS AND METHODS

Study Population

A retrospective analysis was performed on consecutive patients with SAH enrolled in a prospective diagnostic accuracy trial at our institution. SAH was determined by a combination of NCCT, CTA, DSA, and/or CSF analysis. In this prospective study design, CTP was performed during the baseline period on days 0–3 following aneurysmal rupture with day zero defined as the day of the initial hemorrhagic event, to assess baseline cerebral perfusion and to compare it with later perfusion examinations for interval change. A follow-up CTP was performed on the day of new focal neurologic deficits or on days 6–8 in asymptomatic patients. Institutional review board approval was obtained.

In our study, inclusion criteria were the following: 1) patients with delayed infarction related to DCI detected on NCCT, and 2) CTP, including assessment of PS performed before infarction. Follow-up NCCT was obtained as a standard of care at our institution to assess complications of SAH, including repeat hemorrhage, hydrocephalus, and new infarction.

Patients with SAH were classified as having DCI according to published criteria from recent expert consensus,¹⁹ consisting of a radiologic and clinical component. These criteria included either a new infarction on CT or MR imaging within 6 weeks after SAH or clinical manifestations of new focal neurologic impairment or a decrease of at least 2 points on the Glasgow Coma Scale. Regions of delayed infarction were defined as new areas of ischemia not present on imaging up to 48 hours after aneurysm occlusion and not attributable to other causes such as surgical clipping, endovascular treatment, ventricular catheter placement, and intraparenchymal hematoma.¹⁹ This definition has been used to effectively exclude primary brain damage from SAH and/or surgical interventions.¹⁹ Delayed infarction was dictated in the clinical reports of the NCCT by board-certified neuroradiologists on ser-

vice at our institution. A second independent board-certified neuroradiologist blinded to all clinical and imaging data confirmed the presence and exact location of the infarcted region in each case for inclusion in this study.

Exclusion criteria were the following: 1) patients with an infratentorial infarction, given that the posterior fossa is not adequately imaged on CTP; and 2) severe motion degradation limiting CTP postprocessing.

Data collection included detailed review of each patient's clinical chart and recording of each patient's demographic characteristics, clinical symptoms at presentation, aneurysm location, clinical symptoms at the time of CTP and NCCT, infarction location, and modified Rankin Scale clinical outcome score. Subsequently, these clinical data were grouped and analyzed across all 21 patients.

CTP Image Acquisition, Postprocessing, and Analysis

Routine NCCT was performed from the foramen magnum to the vertex by using the following parameters: 120 kV(peak), 250 mAs, 1.0 rotation time, and 5.0-mm collimation. Extended CTP to measure PS was performed on a LightSpeed Discovery 750 64-section scanner (GE Healthcare, Milwaukee, Wisconsin) by using axial shuttle mode with the following parameters: 80 kVp, 400 mAs, 0.4 rotation time, 5.0-mm collimation with 17 cine cycles and 2.8-second interscan delay for the first pass. The second-pass technique included 10 cine cycles with a 10-second interscan delay. A total of 90 mL of nonionic contrast was intravenously administered at 4.0 mL/s followed by a 30-mL saline bolus.

All CTP data were postprocessed by using CT Perfusion 4D software (GE Healthcare) for generation of PS, CBF, and MTT maps. PS represents the flow across the blood vessel wall, from the intravascular space to the extravascular extracellular space, and thus constitutes a measure of BBBP. Its units are milliliter \times milliliter⁻¹ \times minute⁻¹ (volume of liquid per volume of tissue per minute). PS measurements are derived from the tail of the tissue attenuation curve obtained after the first pass of contrast. In normal cerebral vasculature, PS is negligible.²⁰

The follow-up NCCT showing the delayed infarction was used for ROI placement within the exact infarct location. Using the symmetry tool in AW2 software (GE Healthcare), we generated a "mirror ROI" in the corresponding location on the contralateral side of the brain to serve as the control for each patient. Figure 1A illustrates the ROI placement in a representative patient.

Using the integrated registration tool in the AW2 software, we performed coregistration of the preinfarction CTP, and corresponding follow-up NCCT was performed in 3 planes for each patient. Integrated registration enabled propagation of the ROIs in the regions of subsequent infarction and the contralateral control from each follow-up NCCT onto the respective CTP maps obtained before infarction. Figure 1B illustrates coregistration of the NCCT from Fig 1A with the preinfarction CTP. CBF, MTT, and PS values were then measured within the ROI in the regions of subsequent infarction and the contralateral control. Statistical analysis included Wilcoxon signed rank tests for each CTP parameter to determine whether statistically significant differences in CTP parameter means (with 95% confidence intervals) were

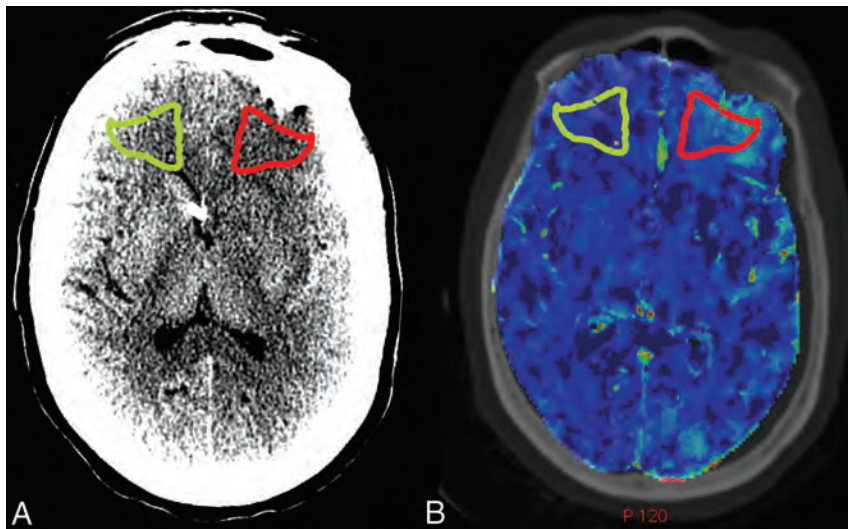


FIG 1. ROI placement and coregistration in a representative patient. *A*, NCCT of a representative patient with SAH demonstrates ROI placement in the region of a new left frontal infarction, which was not present on admission (red) and the contralateral control ROI (green). *B*, Coregistration of the NCCT from *A* with the preinfarction CTP yields matched ROI placement on the PS map and the CBF and MTT maps (not shown).

Quantitative results of PS, CBF, and MTT in the region of subsequent infarction and contralateral control region^a

	Subsequent Infarction	Contralateral Control	P Value
PS (mL × mL ⁻¹ × min ⁻¹)	0.56 (0.45–0.68)	0.35 (0.25–0.45)	<.0001
CBF (mL × 100 g ⁻¹ × min ⁻¹)	17.22 (14.00–20.43)	17.39 (14.78–20.00)	.7048
MTT (sec)	10.85 (8.78–12.92)	10.06 (7.42–12.70)	.128

^a Mean values are shown with 95% confidence intervals (in parentheses).

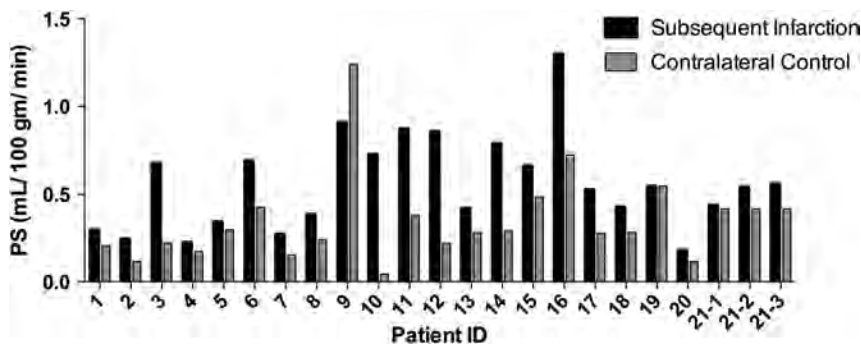


FIG 2. PS values in the regions of subsequent infarction versus respective contralateral control regions for each individual patient.

present between the regions of subsequent infarction and contralateral controls.

RESULTS

Clinical Characteristics of the Study Population

Twenty-one patients with SAH with 23 delayed infarctions in the anterior circulation were included in the analysis. Patients were excluded if they had infratentorial infarctions (*n* = 1) or if severe motion artifacts impeded CTP postprocessing (*n* = 2). The mean age was 50 years (range, 35–88 years) with 76% (16/21) women and 76% (16/21) with anterior circulation aneurysms. The mean Hunt and Hess score at presentation was 3. NCCT performed at the time of the CTP examination did not demonstrate infarction

in any of the patients included in this study. The median day for performing CTP after aneurysmal rupture was day zero (range, 0–3 days, with 71% [15/21] of patients undergoing their CTP on day 0 of admission). At the time of the preinfarction CTP, only 10% (2/21) of patients had developed new focal neurologic deficits not present on their admission clinical examination, while the remaining 90% (19/21) of patients had an unchanged clinical examination compared with their admission status. Follow-up NCCT demonstrated a new infarction at 4 days after CTP (range, 1–7 days) with 91% (21/23) MCA infarctions and 9% (2/23) anterior cerebral artery infarctions. By the time the NCCT showed the infarction, 38% (8/21) of patients exhibited new focal neurologic deficits. The median modified Rankin Scale score at the time of discharge was 3 (range, 0–6), indicating moderate disability.

CTP Analysis

There was a statistically significant increase in PS in the region of subsequent infarction on the preinfarction CTP, compared with the contralateral control region (Table) in 96% of infarctions (22/23). Figure 2 demonstrates the consistency of elevated PS before infarction across the entire study population. However, no significant difference was seen for CBF and MTT between the regions of subsequent infarction and contralateral controls (Table). Figure 3 demonstrates PS elevation preceding the development of subsequent delayed infarction in a representative patient. In addition, the tissue attenuation curves representing the region of subsequent infarction and the contralateral control region demonstrate an elevation of the

tail of the tissue attenuation curve (extended pass) in the region of subsequent infarction (Fig 3D).

DISCUSSION

Currently, the assessment of patients with SAH for DCI and delayed infarction is challenging, given the need to rely on clinical examination, transcranial Doppler sonography, and NCCT data to initiate early treatment and prognosticate patient outcomes. The value of clinical examination is limited due to the potential subjectivity of symptom assessment, low specificity of symptoms, and the frequent incidence of a depressed level of consciousness in patients in the intensive care unit, which can limit the perfor-

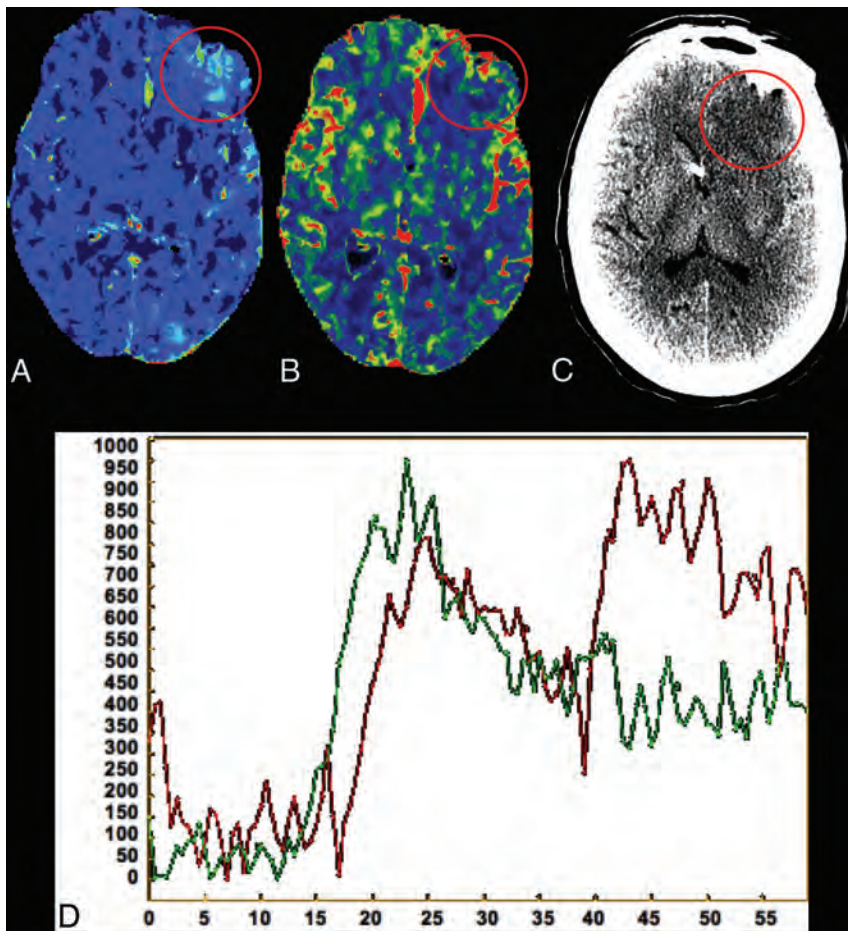


FIG 3. CTP performed on day zero of admission in a representative patient with SAH (same patient as shown in Fig 1). *A*, Elevated PS is demonstrated in the left frontal region (circled in red) compared with the contralateral side. *B*, CBF is not significantly different in the same region compared with the contralateral side. Follow-up NCCT (*C*) reveals an infarction in the exact location of the increased PS seen 2 days prior in this patient. *D*, Tissue attenuation curves representing the region of subsequent infarction (red) and the contralateral control region (green) obtained in this patient, demonstrating an elevation of the tail of the tissue attenuation curve (extended pass) in the region of subsequent infarction.

mance of reliable neurologic examinations.¹¹ Transcranial Doppler sonography is also limited by poor sensitivity and specificity.¹²⁻¹⁴ Thus, there is a strong need for the development and validation of novel imaging strategies allowing identification of patients with SAH at high risk for delayed infarction.

In this study, we have shown that increased PS assessed by CTP precedes the development of delayed infarction seen on NCCT in patients with SAH. These findings were present in 91% (21/23) of regions of subsequent infarction and were statistically significant across the entire study population. Most important, at the time of the preinfarction CTP, the perfusion parameters of CBF and MTT (the most sensitive parameters currently available to clinically assess perfusion deficits¹⁷) were not statistically different in the region of subsequent infarction compared with the contralateral control region. Furthermore, only 10% of patients manifested new focal neurologic deficits at the time of the preinfarction CTP, suggesting that an elevation in PS values could represent an early indicator of subsequent infarction. Thus, the detection of BBBP changes may prove a more sensitive method to detect delayed infarction related to DCI compared with conventional NCCT and

CTP parameters of CBF and MTT, and before clinical symptoms. Furthermore, at the time of follow-up NCCT demonstrating the subsequent infarction, more patients (38%) had developed new focal neurologic deficits. Our findings are similar to those in prior studies reporting the development of neurologic deficits in up to 40% of patients with DCI.^{21,22} Moreover, patients with DCI have been shown to have a statistically increased rate of permanent deficits and worse clinical outcomes compared with patients without DCI.^{21,22}

The BBB is composed of endothelial cells connected by tight junctions, providing an effective barrier against paracellular permeability. Transient or permanent cerebral injury can lead to alteration in molecular signaling pathways, such as the ubiquitin-proteasome pathway, leading to BBB disruption and degradation of the extracellular matrix, resulting in vasogenic edema.²³ Experimental data have demonstrated increased BBBP and dysfunction of the endothelium and vascular components of the brain associated with the development of DCI and poor outcomes in animal models.¹⁵ Moreover, a decrease in BBB disruption and an associated decrease in the effects of cerebral ischemia were seen in animal models treated with novel pharmaceutical agents that stabilize the BBB.^{24,25} BBBP increase and cerebral ischemia thus appear to be closely intertwined; however, understanding the temporal resolution of these 2

pathophysiologic processes remains challenging. In human subjects, perfusion CT and MR imaging have been introduced as tools to measure BBBP.^{16,26}

Although significant differences existed in PS values in the regions of subsequent infarction versus respective contralateral control regions, our study is limited by its small size and retrospective nature. Future studies are needed to establish the clinical value of monitoring PS as a predictor of delayed infarction related to DCI and poor outcomes and to compare PS values in patients with and without DCI, thus expanding our understanding of the utility of PS for prognostication in patients with SAH.

CONCLUSIONS

Our data indicate that the measurement of BBBP using CTP-derived PS has the potential to become a significant marker for the prediction of delayed infarction related to DCI before the onset of clinical symptoms and before alterations seen in MTT and CBF. Our results emphasize the need for continued prospective investigation of BBBP alteration in DCI to develop a clinical indicator for prediction and prognosis of SAH-related morbidity and mor-

tality. Large prospective studies are needed to further validate these initial findings and to provide insight into the underlying pathomechanisms leading to delayed infarction related to DCI after SAH. More important, such future investigations could aid in the development of new strategies targeting the prevention of delayed infarction after SAH.

Disclosures: Jana Ivanidze—RELATED: Grant: National Institute of Neurological Disorders and Stroke (5K23NS058387)*; UNRELATED: Employment: New York-Presbyterian Hospital—Weill Cornell Medical College, Comments: Postgraduate Year-4 Radiology Resident; Grants/Grants Pending: Radiological Society of North America Resident Research Grant, Omar N. Kallas—RELATED: Grant: National Institute of Neurological Disorders and Stroke (5K23NS058387)*; Ajay Gupta—UNRELATED: Grants/Grants Pending: I have active support provided for other neuroradiology-related grants from the Association of University Radiologists GE Radiology Research Academic Fellowship, the Foundation of the American Society of Neuroradiology Scholar Award, and CTSC National Institutes of Health grant UL1TR00457. Pina C. Sanelli—RELATED: Grant: National Institute of Neurological Disorders and Stroke.* *Money paid to the institution.

REFERENCES

- Hop JW, Rinkel GJ, Algra A, et al. **Case-fatality rates and functional outcome after subarachnoid hemorrhage: a systematic review.** *Stroke* 1997;28:660–64
- Mocco J, Ransom ER, Komotar RJ, et al. **Racial differences in cerebral vasospasm: a systematic review of the literature.** *Neurosurgery* 2006;58:305–14
- Petzold GC, Einhaupl KM, Dirnagl U, et al. **Ischemia triggered by spreading neuronal activation is induced by endothelin-1 and hemoglobin in the subarachnoid space.** *Ann Neurol* 2003;54:591–98
- Dreier JP, Ebert N, Priller J, et al. **Products of hemolysis in the subarachnoid space inducing spreading ischemia in the cortex and focal necrosis in rats: a model for delayed ischemic neurological deficits after subarachnoid hemorrhage?** *J Neurosurg* 2000;93:658–66
- Sanelli PC, Ugorec I, Johnson CE, et al. **Using quantitative CT perfusion for evaluation of delayed cerebral ischemia following aneurysmal subarachnoid hemorrhage.** *AJNR Am J Neuroradiol* 2011;32:2047–53
- Dankbaar JW, Rijdsdijk M, van der Schaaf IC, et al. **Relationship between vasospasm, cerebral perfusion, and delayed cerebral ischemia after aneurysmal subarachnoid hemorrhage.** *Neuroradiology* 2009;51:813–19
- Dankbaar JW, de Rooij NK, Velthuis BK, et al. **Diagnosing delayed cerebral ischemia with different CT modalities in patients with subarachnoid hemorrhage with clinical deterioration.** *Stroke* 2009;40:3493–98
- Dankbaar JW, de Rooij NK, Rijdsdijk M, et al. **Diagnostic threshold values of cerebral perfusion measured with computed tomography for delayed cerebral ischemia after aneurysmal subarachnoid hemorrhage.** *Stroke* 2010;41:1927–32
- Aralasmak A, Akyuz M, Ozkaynak C, et al. **CT angiography and perfusion imaging in patients with subarachnoid hemorrhage: correlation of vasospasm to perfusion abnormality.** *Neuroradiology* 2009;51:85–93
- Wintermark M, Ko NU, Smith WS, et al. **Vasospasm after subarachnoid hemorrhage: utility of perfusion CT and CT angiography on diagnosis and management.** *AJNR Am J Neuroradiol* 2006;27:26–34
- Schmidt JM, Wartenberg KE, Fernandez A, et al. **Frequency and clinical impact of asymptomatic cerebral infarction due to vasospasm after subarachnoid hemorrhage.** *J Neurosurg* 2008;109:1052–59
- Carrera E, Schmidt JM, Oddo M, et al. **Transcranial Doppler for predicting delayed cerebral ischemia after subarachnoid hemorrhage.** *Neurosurgery* 2009;65:316–23; discussion 323–24
- Lysakowski C, Walder B, Costanza MC, et al. **Transcranial Doppler versus angiography in patients with vasospasm due to a ruptured cerebral aneurysm: a systematic review.** *Stroke* 2001;32:2292–98
- Naval NS, Thomas CE, Urrutia VC. **Relative changes in flow velocities in vasospasm after subarachnoid hemorrhage: a transcranial Doppler study.** *Neurocrit Care* 2005;2:133–40
- Yan J, Li L, Khatibi NH, et al. **Blood-brain barrier disruption following subarachnoid hemorrhage may be facilitated through PUMA induction of endothelial cell apoptosis from the endoplasmic reticulum.** *Exp Neurol* 2011;230:240–47
- Kishore S, Ko N, Soares BP, et al. **Perfusion-CT assessment of blood-brain barrier permeability in patients with aneurysmal subarachnoid hemorrhage.** *J Neuroradiol* 2012;39:317–25
- Mir DI, Gupta A, Dunning A, et al. **CT perfusion for detection of delayed cerebral ischemia in aneurysmal subarachnoid hemorrhage: a systematic review and meta-analysis.** *AJNR Am J Neuroradiol* 2014;35:866–71
- Killeen RP, Mushlin AI, Johnson CE, et al. **Comparison of CT perfusion and digital subtraction angiography in the evaluation of delayed cerebral ischemia.** *Acad Radiol* 2011;18:1094–100
- Vergouwen MD, Vermeulen M, van Gijn J, et al. **Definition of delayed cerebral ischemia after aneurysmal subarachnoid hemorrhage as an outcome event in clinical trials and observational studies: proposal of a multidisciplinary research group.** *Stroke* 2010;41:2391–95
- Jain R, Ellika SK, Scarpace L, et al. **Quantitative estimation of permeability surface-area product in astroglial brain tumors using perfusion CT and correlation with histopathologic grade.** *AJNR Am J Neuroradiol* 2008;29:694–700
- Sanelli PC, Anumula N, Gold R, et al. **Outcomes-based assessment of a new reference standard for delayed cerebral ischemia related to vasospasm in aneurysmal subarachnoid hemorrhage.** *Acad Radiol* 2012;19:1066–74
- Sanelli PC, Anumula N, Johnson CE, et al. **Evaluating CT perfusion using outcome measures of delayed cerebral ischemia in aneurysmal subarachnoid hemorrhage.** *AJNR Am J Neuroradiol* 2013;34:292–98
- Jin R, Yang G, Li G. **Molecular insights and therapeutic targets for blood-brain barrier disruption in ischemic stroke: critical role of matrix metalloproteinases and tissue-type plasminogen activator.** *Neurobiol Dis* 2010;38:376–85
- Germanò A, d'Avella D, Imperatore C, et al. **Time-course of blood-brain barrier permeability changes after experimental subarachnoid haemorrhage.** *Acta Neurochir (Wien)* 2000;142:575–80; discussion 580–81
- Jin X, Liu J, Yang Y, et al. **Spatiotemporal evolution of blood brain barrier damage and tissue infarction within the first 3h after ischemia onset.** *Neurobiol Dis* 2012;48:309–16
- Hoffmann A, Bredno J, Wendland MF, et al. **Validation of in vivo magnetic resonance imaging blood-brain barrier permeability measurements by comparison with gold standard histology.** *Stroke* 2011;42:2054–60

Evaluation of Virtual Noncontrast Images Obtained from Dual-Energy CTA for Diagnosing Subarachnoid Hemorrhage

X.Y. Jiang, S.H. Zhang, Q.Z. Xie, Z.J. Yin, Q.Y. Liu, M.D. Zhao, X.L. Li, and X.J. Mao



ABSTRACT

BACKGROUND AND PURPOSE: The virtual noncontrast images generated with iodine subtraction from dual-energy CTA images are expected to replace the true noncontrast images for radiation-dose reduction. This study assessed the feasibility of virtual noncontrast images for diagnosing SAH.

MATERIALS AND METHODS: Eighty-four patients with or without SAH underwent true noncontrast brain CT (the criterion standard for diagnosing SAH). Among them, 37 patients underwent an additional head dual-energy angiography, and the other patients underwent head and neck dual-energy angiography. Virtual noncontrast images were produced on a dedicated dual-energy postprocessing workstation and reconstructed in orientation and section width identical to those in true noncontrast images. The findings on the virtual noncontrast and true noncontrast images were compared at both the individual level and the lesion level. Image noise of the virtual noncontrast and true noncontrast images was also measured and compared. The volume CT dose index and dose-length product were recorded for the radiation-dose analysis.

RESULTS: The sensitivity, specificity, positive predictive value, and negative predictive value of virtual noncontrast images at the individual level and the lesion level were 94.5%, 100%, 100%, 90.6% and 86.7%, 96.9%, 91.8%, 94.8%, respectively. The agreement in the diagnosis of SAH on true noncontrast and virtual noncontrast images reached 92.3% at the individual level and 85.1% at the lesion level. The virtual noncontrast images showed a higher image noise level. The volume CT dose index and dose-length product were obviously reduced without the true noncontrast brain CT scan.

CONCLUSIONS: Virtual noncontrast images are a reliable tool for diagnosing SAH, with the advantage of reducing the radiation dose.

ABBREVIATIONS: TNC = true noncontrast; VNC = virtual noncontrast

Subarachnoid hemorrhage is defined as the extravasation of blood into the spaces filled with CSF in the central nervous system.¹ The characteristic appearance of extravasated blood on CT is hyperattenuated, which is markedly different from the CT attenuation of brain tissue, CSF, and bone.^{1,2} Therefore noncontrast CT is the criterion standard for diagnosing SAH. Rupture of an intracranial aneurysm is the major cause of SAH and accounts for approximately 80% of nontraumatic SAH cases.³ CTA is a fast, noninvasive, and readily available method to screen for the presence of an aneurysm.⁴ As a result, patients with suspected SAH

should undergo a noncontrast CT scan of the brain for the diagnosis of SAH, followed by CTA to look for the underlying cause of the SAH. Both examinations are considered necessary. A recent article comparing diagnostic strategies for patients in the emergency department with suspected SAH showed that CT along with CTA was considered the most sensitive and rapid test for diagnosing aneurysm, but had the highest radiation exposure.⁵ However, the limitation of a large amount of radiation exposure to patients might be overcome by the advent of dual-energy. Dual-energy simultaneously acquires datasets at 2 different photon spectra in a single acquisition.⁶ Images postprocessed with 3-material decomposition can be used to differentiate iodine from other materials,⁷ and virtual noncontrast (VNC) images can be created by removing the iodine-containing voxels of dual-energy CTA images. If VNC images can replace true noncontrast (TNC) images, the radiation dose can potentially be reduced. To our knowledge, few studies have compared VNC and TNC images in SAH.⁸ The purpose of our study was to assess the utility of VNC images obtained

Received October 2, 2014; accepted after revision November 9.

From the Departments of Radiology (X.Y.J., Z.J.Y., Q.Y.L., M.D.Z., X.L.L., X.J.M.) and Pediatrics (Q.Z.X.), Affiliated Hospital of Binzhou Medical University, Shandong, P.R. China; and Department of Radiology (S.H.Z.), Shandong Cancer Hospital and Institute, Shandong, P.R. China.

Please address correspondence to Xing Yue Jiang, MD, Department of Radiology, Affiliated Hospital of Binzhou Medical University, 661 Second Huanghe Rd, Binzhou, Shandong 256603, P.R. China; e-mail: xyjiang188@sina.com

<http://dx.doi.org/10.3174/ajnr.A4223>

from dual-energy CTA for diagnosing SAH compared with TNC images.

MATERIALS AND METHODS

Patients

Between May 2012 and January 2013, 55 patients with SAH and 29 patients who were suspected of having head disease but were diagnosed as not having SAH were included in the study. The group with SAH (case group) included 29 men and 26 women with an age range of 23–79 years; mean age, 57 ± 12 years; median age, 58 years. The non-SAH group (control group) included 22 men and 7 women with an age range of 14–76 years; mean age, 51 ± 12 years; median age, 50 years. All patients underwent TNC brain CT with either additional head dual-energy CTA ($n_{\text{SAH}} = 27$, $n_{\text{non-SAH}} = 10$) or head and neck dual-energy CTA ($n_{\text{SAH}} = 28$, $n_{\text{non-SAH}} = 19$) with available datasets.

In the case group ($n = 55$), 25 patients had SAH only and the rest had other intracranial changes in addition to SAH as follows: cerebral hemorrhage ($n = 15$), lacunar infarction or cerebral infarction ($n = 8$), lacunar infarction and cerebral hemorrhage ($n = 2$), epidural hematoma ($n = 1$), cerebral hemorrhage and subdural hematomas ($n = 1$), arachnoid cyst ($n = 1$), hydrocephalus ($n = 1$), and subdural collection of fluid ($n = 1$). The causes for SAH included aneurysm (33 cases were diagnosed or suspected by CTA and 26 were confirmed by surgery or DSA), definite history of head injury ($n = 6$), vascular malformation ($n = 1$), and unclear causes ($n = 15$). The interval between the onset of SAH and the CT examination was in the range of 4–391 hours, with a mean of 57.57 ± 89.43 hours and a median of 19.50 hours; 67.27% of patients had a time interval of <24 hours, and 72.73% of patients had a time interval of <48 hours.

In the control group ($n = 29$), there were 9 patients with essentially normal findings, 17 with lacunar infarction, 1 with subdural collection of fluid, 1 with a history of a cerebral hemorrhage operation 16 months previously, and 1 with a vascular malformation of the cerebellar hemisphere (but without SAH). The CTA findings in the control group included the following: normal findings ($n = 4$), atherosclerosis ($n = 19$), suspicious aneurysm ($n = 5$, without confirmation by an operation or DSA), and vascular malformation ($n = 1$).

This study was approved by our institutional review board, and all patients or their relatives provided written informed consent before the CT examination.

CT Data Acquisition and Postprocessing

All examinations were performed by using a second-generation dual-source CT scanner (Somatom Definition Flash; Siemens, Erlangen, Germany). TNC scans were obtained in a single-energy mode, and CTA was performed in a dual-energy mode.

The TNC brain CT was performed in all patients by using an axial scan technique with a collimation of 128×0.6 mm and a tube voltage of 120 kV. The current flow-dose modulation (CARE Dose4D; Siemens) was enabled with a range of 256–436 mAs.

For CTA scans, we used 2 different tube voltages and currents simultaneously: tube A at 140 kV and tube B at 100 kV. Dose modulation (CARE Dose4D, Siemens) was enabled with a range of 110–140 and 107–157 mAs for tube A and tube B, respectively;

a rotation time of 0.28 seconds per rotation; 128×0.6 mm collimation with a z-flying focal spot; and a pitch of 0.9. An automated power injector (Stellant D; MedRad, Indianola, Pennsylvania) was used to administer 60 mL of contrast material (ioversol, 320 g I/100 mL) at a rate of 4 mL/s and followed by 20 mL of saline solution into the antecubital vein via an 18-ga catheter. The CT scan was triggered by a bolus-tracking technique with the ROI placed in the common carotid artery at the level of C4 and the image acquisition started 4 seconds after the attenuation reached the predefined threshold (100 Hounsfield units). Scan direction was cranial-caudal. The examination region of head dual-energy CTA and head and neck dual-energy CTA was from the cranial end of the skull to the inferior margin of the mandible and from the cranial end of the skull to the arcus aortae, respectively.

TNC images were reconstructed with a 5-mm thickness/interval in the main console and were transferred to the PACS. For each dual-energy CTA examination, we reconstructed 2 image datasets with one at 140 kV and another at 100 kV with a 0.75-mm thickness/0.5-mm interval and transferred them to the workstation (syngo MultiModality; Siemens) for further processing. Images were loaded onto a dedicated dual-energy postprocessing workstation (syngo MultiModality Workplace, Version 2010A; Siemens). The VNC images were produced with a dual-energy-analysis material-decomposition software (syngo Dual Energy Brain Hemorrhage; Siemens) and were reconstructed with orientation and section width identical to those of the TNC images. The findings on VNC images were compared with those on the TNC images.

CT Image Analysis

Diagnosis of SAH. Two experienced radiologists (X.Y.J., X.J.M., with 19 and 12 years' experience in neuroradiology, respectively) who were blinded to the patient clinical data were asked to analyze the performance of the TNC and VNC images in consensus, respectively (including case group and control group; note the cases were mixed and labeled by patient identification). There was an interval of 2 months between the evaluation of TNC and VNC images. The evaluations were recorded in a table. We divided the subarachnoid space into 27 sections, including symmetric framework (cistern of the pontocerebellar angle, pontine cistern, ambient cistern, tentorium of the cerebellum, suprasellar cistern, cistern of the lateral fossa of the cerebrum, and lateral ventricle), asymmetric framework (cistern of the cerebral longitudinal fissure, third ventricle, fourth ventricle), and cortical sulci (in units of lobes: frontal lobe, parietal lobe, occipital lobe, temporal lobe, and insula). For the symmetric framework and lobe, each side was counted as an individual section. The TNC images were used as the criterion standard for diagnosing SAH, and the sensitivity, specificity, positive predictive value, negative predictive value, and κ value were calculated accordingly. Statistical analyses were performed at the individual (patient) and lesion levels (each bleeding section representing a lesion).

Objective Evaluation of Image Quality. For objective evaluation of image quality, image noise⁹ of the TNC images and VNC images was measured as the SD of a 1-cm² ROI placed in homogeneous and normal regions of white matter on the left

centrum ovale. For the same patient, the ROI would be placed in the same region of the same section on the TNC and VNC images. For all measurements, the size and shape of the ROIs were kept constant.

Subjective Evaluation of Image Quality. The image quality was rated by a radiologist (M.D.Z, with 27 years' experience in neuro-radiology) blinded to the patient clinical data by using a 3-point scale: 1 = excellent, when the VNC images were comparable with TNC images; 2 = sufficient, when VNC images were usable in the detection of SAH; and 3 = insufficient, when the VNC images were insufficient for the detection of SAH.

Radiation Dose. The CT dose index and dose-length product displayed on the CT system were used to calculate the radiation dose.

Statistical Analyses

The McNemar test was used to compare TNC and VNC images at the individual level, whereas at the lesion level, the Wilcoxon matched-pairs signed rank sum test was used. The Cohen κ statistic was used to assess the agreement of the diagnostic results between the TNC and VNC images. The guidelines of Landis and Koch¹⁰ were followed to interpret κ values, and the scale is listed as the following: 0.00–0.20 indicated slight agreement; 0.21–0.40, fair agreement; 0.41–0.60, moderate agreement; 0.6–0.80, substantial agreement; and 0.80–1.00, almost perfect agreement.

Image noise of the TNC and VNC images was calculated and expressed as mean \pm SD. Results were tested for statistical significance by using the paired *t* test.

The radiation dose of head dual-energy CTA, head and neck dual-energy CTA, and TNC CT was calculated and expressed as mean \pm SD.

P values < .05 were statistically significant. All statistics were performed with a statistical software program (SPSS, Version 16.0; IBM, Armonk, New York).

RESULTS

Diagnosis of the SAH

At the Individual Level. The number of cases with SAH diagnosed on TNC and VNC images is presented in Table 1.

As reported in Table 1, VNC images failed to show SAH in 3 patients (false-negative results), whereas no patient was misdiagnosed with SAH. No statistical difference was found in diagnosing SAH between the TNC and VNC images (*P* = .250). An almost perfect agreement in the diagnosis of SAH on TNC and VNC images was demonstrated (κ value = 0.923, *P* < .001).

We studied the 3 patients (who had false-negative results) retrospectively and found that they had a long interval of 8, 11, and 12 days between the onset of SAH and CTA examinations. At the same time, each of the 3 patients had just 1, 2, or 4 lesions, respectively. All patients had been confirmed to have SAH by CT in another hospital and then were transferred to our hospital for further evaluation and management when their conditions were stabilized. The increased time interval between the onset of SAH and the CTA examination allowed most of the SAH to be absorbed. The attenuation of the bleeding became very low, and there were only a few remaining lesions, which made it difficult for VNC images to detect these lesions. Compared with TNC images, some of the lesions could be found on VNC images (Fig 1A, -B); but some of the lesions could not be found on VNC images, even after comparing them with those on TNC images retrospectively (Fig 1C, -D). Of the 3 patients, 1 patient was found to have an aneurysm of the anterior communicating artery and the other 2 patients had negative findings on CTA examinations.

At the Lesion Level. The number of lesions with SAH detected on TNC and VNC images is presented in Table 2.

There were 648 lesions detected on TNC images, and 612 lesions on VNC images. There was no statistical difference in detecting lesions between TNC and VNC images (*P* = .121). VNC images missed 86 lesions in total (false-negative results) and misdiagnosed 50 sections with SAH in total (false-positive results).

Table 1: Cases of SAH detected on TNC and VNC images at the individual level

VNC	TNC		Total
	Positive	Negative	
Positive	52	0	52
Negative	3	29	32
Total	55	29	84

Table 2: Number of SAH lesions detected on TNC and VNC images at the lesion level

VNC	TNC		Total
	Positive	Negative	
Positive	562	50	612
Negative	86	1570	1656
Total	648	1620	2268

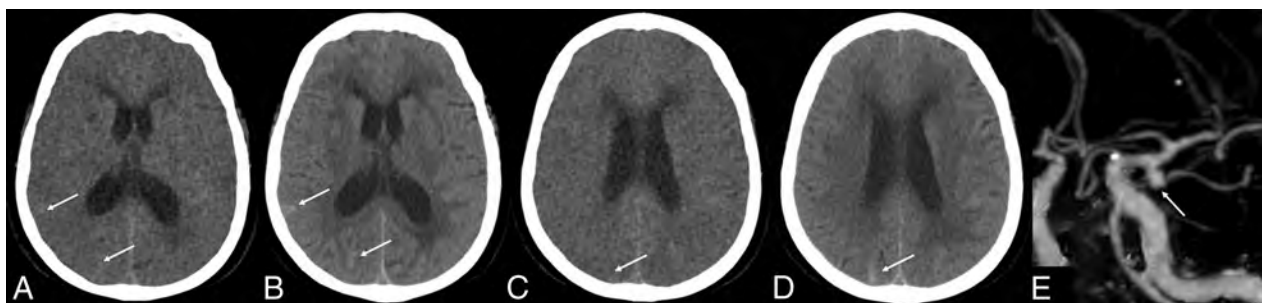


FIG 1. A 71-year-old woman with SAH missed on VNC images. The onset time of SAH was 12 days prior. CTA shows an aneurysm of the left MCA. A and C, VNC image; B and D, TNC image; E, CTA image.

The diagnosis of SAH on TNC and VNC images reached an almost perfect agreement of 85.1% (κ value = 0.851, $P < .001$).

We divided the patients (case group) into 3 groups according to the number of lesions: group 1 with ≤ 3 lesions ($n = 5$), group 2 with ≤ 5 lesions ($n = 8$), and group 3 with > 5 lesions ($n = 42$). In group 1, there were 2 patients in whom the diagnosis of SAH was missed on VNC images; in group 2, there was 1 patient in whom the diagnosis of SAH was missed. No patient was misdiagnosed in group 3.

Evaluation of VNC Images for Diagnosing SAH

As shown in Table 3, the sensitivity, specificity, positive predictive value, and negative predictive value of VNC images were high at both the individual level and the lesion level, with the individual level higher than the lesion level, except in regard to the negative predictive value.

Objective Evaluation of Image Quality. The VNC images showed a higher image noise level and markedly reduced contrast between gray and white matter. The mean image noise of TNC and VNC images was 2.98 ± 0.41 and 3.35 ± 0.59 , respectively, and a significant difference was observed ($t = -5.286$, $P < .001$).

Subjective Evaluation of Image Quality. As for the image quality, 56 sets of VNC images were of excellent quality, 28 were sufficient, and no set was insufficient. The average rating was 1.33, indicating limited image quality noted on VNC images.

Radiation Dose. The radiation doses of head dual-energy CTA, head and neck dual-energy CTA, and the TNC CT scan are presented in Table 4.

The volume CT dose index and dose-length product were sig-

Table 3: Evaluation of VNC images for diagnosing SAH

VNC Images	Sensitivity (%)	Specificity (%)	Positive Predictive Value (%)	Negative Predictive Value (%)
At the individual level	94.5	100	100	90.6
At the lesion level	86.7	96.9	91.8	94.8

Table 4: Radiation dose

	Dual-Energy CTA		
	Head	Head and Neck	TNC Brain CT
CTDI _{vol} (mGy)	9.06 \pm 0.52	10.43 \pm 0.38	55.71 \pm 7.28
DLP (mGy \times cm)	229.11 \pm 41.50	398.44 \pm 21.71	773.49 \pm 104.06

Note:—CTDI_{vol} indicates volume CT dose index; DLP, dose-length product.

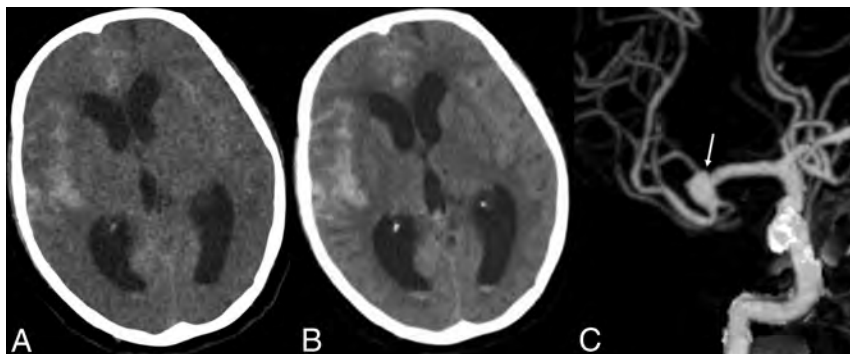


FIG 2. A 78-year-old woman. The onset time of SAH was 17 hours prior. CTA shows an aneurysm in the right MCA. A, VNC image; B, TNC image; C, CTA image.

nificantly lower by using the dual-energy protocol and replacing TNC brain CT with VNC, leading to a radiation-dose reduction of 80.31%–89.92% and 58.98%–83.13%, respectively.

DISCUSSION

The analysis of dual-energy data enables material decomposition, which is the process of separating the materials within each image voxel.¹¹ Material decomposition typically entails a selection of 3 materials of interest with the software available with dual-source dual-energy scanners. As such, VNC images can be generated by extracting iodine from other materials.⁶

VNC images had been studied primarily in the abdominal aorta and in patients after endovascular repair.¹² To date, many studies of the clinical application of VNC images have been performed, mainly in the abdomen for characterizing renal masses,¹³ applications in pancreatic CT,¹⁴ and detecting urinary or biliary stones.^{15,16} Most of those studies proved that VNC images were useful and feasible, though the imaging quality was inferior to that in the TNC images. Very few studies were performed on the detection of intracranial bleeding.⁸ Our study focused on evaluating the value of VNC images in diagnosing SAH. Compared with the previous studies, the present study had the following advantages: First, only SAH was studied and discussed in this study, while the previous studies discussed SAH, combining intracerebral and subdural bleeding, which was easier to detect on VNC images. Second, the subarachnoid space was divided into 27 sections, enabling the quantification of lesions of SAH. In our study, we found that there was some difficulty in using VNC images to correctly diagnose SAH when the number of lesions was ≤ 3 , because in 2 of 5 patients (40%) in group 1, SAHs were missed. It was easy for VNC images to diagnose SAH when the number of lesions was > 5 because all of the patients in group 3 were correctly diagnosed. Third, patients with negative findings were included; therefore, the results were more convincing.

In our study, although VNC images showed a higher image noise level and markedly reduced contrast between gray and white matter compared with the TNC images, VNC images detected SAH in almost all patients and most of the lesions. There was no significant difference between VNC and TNC images in detecting SAH at both individual and lesion levels, proving the diagnostic value of VNC images in SAH. The high negative predictive value of VNC images indicated that the absence of SAH in a patient could be stated confidently, while the higher positive predictive value indicated that the diagnosis of the existence of SAH should be certain. An almost perfect agreement for the diagnosis of SAH between TNC and VNC images was achieved, especially at the individual level. Compared with the TNC images, almost identical locations, extent, and sizes of subarachnoid bleeding were displayed on the VNC images, and only the margin of hemorrhagic focus was not as clear as that seen in the TNC images (Fig 2), probably due to the relatively high noise in VNC images.

In addition, we found that the VNC images showed better conspicuity of

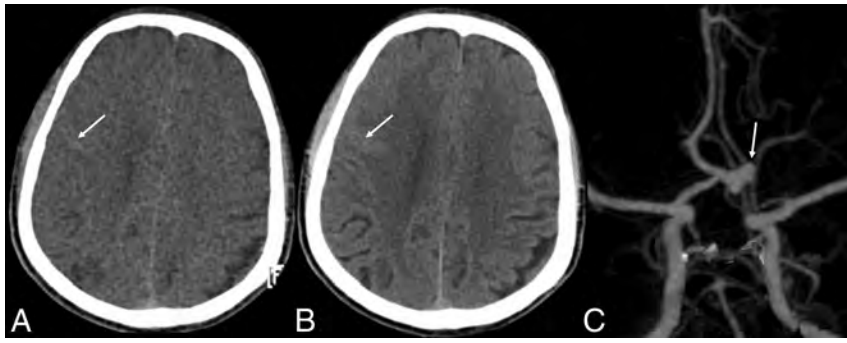


FIG 3. A 58-year-old man. The onset time of SAH was 2.5 days prior. CTA and DSA show an aneurysm of the anterior communicating artery. Both VNC and TNC images find SAH, but the cortical sulci of right frontal lobe appears to have slightly higher attenuation on the VNC images than on TNC images. A, VNC image; B, TNC image; C, CTA image.

hemorrhagic focus than the TNC images in a few patients, especially on the surface of the brain. This may be explained by the overall markedly reduced contrast between gray and white matter on the VNC images. The attenuation of gray matter was decreased at the same time, so the hemorrhagic focus in the cortical sulci and schizencephaly was more clearly depicted in the VNC images (Fig 3). In a study of assessment of VNC images in patients with gallstones or bile duct stones also found that the VNC images showed better stone conspicuity than the TNC images in some patients.¹⁶

At the individual level, there was no false-positive diagnosis for SAH, while SAH in 3 patients was missed on the VNC images. In a retrospective study, we compared the TNC and VNC images of the 3 patients and found that the missed diagnoses were mainly due to the rather small size of bleeding and the relatively low number of bleeding sites on the VNC images. Of course, the higher image noise level could also be one of the reasons. As mentioned above, all 3 patients had a long interval between the onset of SAH and the CTA examination. At the time of CTA, most of the SAH was absorbed with very low residual attenuation of the bleeding and very few remaining lesions. Therefore when the hemorrhagic focus of SAH was very small with very low attenuation, it was difficult to differentiate a small lesion from artifacts on the VNC images. However, in general, VNC images could satisfy the clinical requirements for diagnosing SAH with high sensitivity and specificity because most patients usually had enough lesions and clear enough signal on VNC images, especially during the acute stage when most SAHs were diagnosed.

At the lesion level, there were 50 false-positive lesions and 86 false-negative lesions. The most frequent sites for false-positive lesions were the occipital lobe (18%), suprasellar cistern (16%), tentorium of the cerebellum, and the frontal lobe (both were 12%), while the frequent false-negative lesions were in the lateral ventricle (15%), parietal lobe, and ambient cistern (both accounted for 13%). The VNC images tended to have decreased attenuation and amount of blood in the lateral ventricle (Fig 2). Although the ambient cistern is a common place for aneurysmal SAH and also a frequent site for the false-negative lesions, in our study, there were no patients with SAH in the ambient cistern that was missed. The reason may be that when aneurysmal SAH occurred, the bleeding was not only in the ambient cistern but also in the interhemispheric cistern, the cistern of the lateral sulcus, and so forth, which were easy to observe on VNC images.

As described above, the sensitivity and specificity for the diagnosis of SAH on VNC at the lesion level were not as good as at the individual level. However, the study also indicated positional and quantitative differences in the “lesions” between TNC and VNC images, and these might be due to the following reasons: First, higher image noise level and more artifacts on VNC images might affect the images and cause a false appearance. Second, in some patients, the level of the section on the VNC images was not exactly the same as that on the TNC images, which resulted in positional differences, especially for the cortical sulci. Finally, the subjective error of observers

could also influence the diagnostic results. Nevertheless, the difference at the lesion level between VNC and TNC images did not have a significant effect on the diagnosis of SAH at the individual level for most patients.

In terms of radiation dose, this study indicated an obvious reduction of volume CT dose index and dose-length product when replacing TNC with VNC images. Compared with subtraction CTA, which is required to provide noncontrast CT as a mask, dual-energy CTA has the advantage that images from 1 single CT acquisition can be used to remove bone structures. This advantage reduced the radiation dose to the patients and eliminated misregistration caused by patient movement during 2 scans. Morhard et al¹⁷ and Zhang et al¹⁸ compared both the bone removal results of conventional and dual-energy-based techniques and the diagnostic value for intracranial aneurysms and ultimately concluded that dual-energy-based bone removal led to a significant reduction of radiation dose and that dual-energy CTA had a comparable diagnostic accuracy for the detection of intracranial aneurysms.

There were some limitations to this study. First, SAH was diagnosed solely on the basis of the imaging manifestation without combining the medical history and clinical symptoms, which might affect the diagnostic accuracy. Second, in some cases, the interval of the onset of SAH and CT was too long to show hemorrhage clearly; this interval might affect the sensitivity. Third, the same radiologist reviewed the TNC and VNC images with a 2-month interval, which may have led to bias in the study.

CONCLUSIONS

Despite the higher image noise level, the VNC images were a reliable tool to diagnose SAH, with the advantage of reducing the radiation dose. However, we should be aware of the possible false-negative results when the ictus is not acute. Regardless of the limitations, VNC has the potential to become a valid clinical tool in diagnosing patients with possible SAH.

REFERENCES

1. Papanagiotou P, Roth C, Körner H, et al. **Diagnostic imaging of subarachnoid hemorrhage** [in German]. *Radiologe* 2011;51:100–05
2. Biller J, Godersky JC, Adams HP Jr. **Management of aneurysmal subarachnoid hemorrhage**. *Stroke* 1988;19:1300–05

3. Meyers PM, Schumacher HC, Higashida RT, et al, for the American Heart Association. **Indications for the performance of intracranial endovascular neurointerventional procedures: a scientific statement from the American Heart Association Council on Cardiovascular Radiology and Intervention, Stroke Council, Council on Cardiovascular Surgery and Anesthesia, Interdisciplinary Council on Peripheral Vascular Disease, and Interdisciplinary Council on Quality of Care and Outcomes Research.** *Circulation* 2009;119:2235–49
4. Hoh BL, Cheung AC, Rabinov JD, et al. **Results of a prospective protocol of computed tomographic angiography in place of catheter angiography as the only diagnostic and pretreatment planning study for cerebral aneurysms by a combined neurovascular team.** *Neurosurgery* 2004;54:1329–40
5. Farzad A, Radin B, Oh JS, et al. **Emergency diagnosis of subarachnoid hemorrhage: an evidence-based debate.** *J Emerg Med* 2013;44:1045–53
6. Achenbach S, Ropers D, Kuettner A, et al. **Contrast-enhanced coronary artery visualization by dual-source computed tomography: initial experience.** *Eur J Radiol* 2006;57:331–35
7. Johnson TR, Krauss B, Sedlmair M, et al. **Material differentiation by dual energy CT: initial experience.** *Eur Radiol* 2007;17:1510–17
8. Ferda J, Novák M, Mírka H, et al. **The assessment of intracranial bleeding with virtual unenhanced imaging by means of dual-energy CT angiography.** *Eur Radiol* 2009;19:2518–22
9. Reimann AJ, Davison C, Bjarnason T, et al. **Organ-based computed tomographic (CT) radiation dose reduction to the lenses: impact on image quality for CT of the head.** *J Comput Assist Tomogr* 2012;36:627
10. Landis JR, Koch GG. **The measurement of observer agreement for categorical data.** *Biometrics* 1977;33:159–74
11. Ko JP, Brandman S, Stember J, et al. **Dual-energy computed tomography: concepts, performance, and thoracic applications.** *J Thorac Imaging* 2012;27:7–22
12. Chandarana H, Godoy MC, Vlahos I, et al. **Abdominal aorta: evaluation with dual-source dual-energy multidetector CT after endovascular repair of aneurysms: initial observations.** *Radiology* 2008;249:692–700
13. Song KD, Kim CK, Park BK, et al. **Utility of iodine overlay technique and virtual unenhanced images for the characterization of renal masses by dual-energy CT.** *AJR Am J Roentgenol* 2011;197:W1076–82
14. Mileto A, Mazziotti S, Gaeta M, et al. **Pancreatic dual-source dual-energy CT: is it time to discard unenhanced imaging?** *Clin Radiol* 2012;67:334–39
15. Moon JW, Park BK, Kim CK, et al. **Evaluation of virtual unenhanced CT obtained from dual-energy CT urography for detecting urinary stones.** *Br J Radiol* 2012;85:e176–81
16. Kim JE, Lee JM, Baek JH, et al. **Initial assessment of dual-energy CT in patients with gallstones or bile duct stones: can virtual nonenhanced images replace true nonenhanced images?** *AJR Am J Roentgenol* 2012;198:817–24
17. Morhard D, Fink C, Graser A, et al. **Cervical and cranial computed tomographic angiography with automated bone removal: dual energy computed tomography versus standard computed tomography.** *Invest Radiol* 2009;44:293–97
18. Zhang LJ, Wu SY, Poon CS, et al. **Automatic bone removal dual-energy CT angiography for the evaluation of intracranial aneurysms.** *J Comput Assist Tomogr* 2010;34:816–24

Dual-Energy CTA to Diagnose Subarachnoid Hemorrhage: Ready for Prime Time?

In the article published in this issue of the *American Journal of Neuroradiology*, “Evaluation of Virtual Noncontrast Images Obtained from Dual-Energy CTA for Diagnosing Subarachnoid Hemorrhage,”¹ the authors studied 84 patients, including 55 with subarachnoid hemorrhages (SAHs), by using standard (true) noncontrast head CT (TNC), dual-energy CT (DECT) angiography, and a virtual noncontrast CT (VNC) derived from the DECT angiography. The goal was to compare the ability of VNC to detect SAH by using TNC as the criterion standard (100% presumed sensitivity). Comparisons were made at the “individual level” (ie, based on the CT as a whole for a given patient) and on the “lesion level” on the basis of 27 different subarachnoid-designated regions on the CT scan. Image noise between the 2 modalities was also compared as was radiation dosage. The authors found no statistical difference in SAH detection between VNC and TNC, with VNC having very high sensitivity and specificity. There were, however, 3 patients with subarachnoid hemorrhages on TNC that were missed on VNC, and there were 86 “lesion level” misses. Image noise was higher for VNC, and radiation dosage was higher for TNC. The authors concluded that VNC is an effective technique to detect SAH with less radiation.

This publication is important in that it focuses attention on the radiation dosage as part of diagnostic neuroradiologic imaging. It is important for clinicians to be aware of the radiation dosages of tests we order or at the least to be aware of the comparative doses of tests that might yield similar sensitivities and specificities. DECT angiography has been used for other disease entities outside the central nervous system, and only very few publications have touched on its use within the central nervous system, including 1 article on unruptured aneurysms² and another on a heterogeneous collection of intracranial bleeds.³ The effort here to use DECT as the initial evaluation tool to diagnose SAH is creative and unique. Radiation is potentially detrimental, particularly for younger patients. The carcinogenic effect of even 1 CT scan has been documented and is the subject of considerable research attention.⁴ With the average age of 55 years for SAH from aneurysmal rupture in this country, radiation exposure is very relevant. Any effort at reducing the dose is welcome.

Nevertheless, one must very carefully perform a risk/benefit

analysis for any dose reduction in terms of potential compromise in missed diagnoses and the ultimate harm to patients of such misses. This is the crux of interpreting the use of VNC as opposed to TNC as the initial test of choice in the work-up of suspected SAH. An estimated 80%–85% of atraumatic SAH is caused by a ruptured cerebral aneurysm. However, not all are.^{5,6} The morbidity and mortality of aneurysmal SAH are still quite high despite advances in neurocritical care and endovascular and microsurgical aneurysm repair techniques. The missed diagnosis of even 1 aneurysmal rupture could lead to rerupture, with a significant possibility of neurologic devastation or death and might outweigh any potential benefit from radiation spared.

Thus, the missed diagnoses of 3 patients with SAH by using VNC in this study bear some discussion. First, the clinical importance lies in the ability of VNC to detect SAH at the “individual” and not the “lesion” level. We are in the business of treating patients, not CT scans. The authors used 2 statistical techniques to demonstrate the utility of VNC in assessing SAH: 1) the McNemar test with a κ statistic, which measures agreement or reliability; and 2) sensitivity and specificity with their associated positive predictive and negative predictive values, which measure validity. If we accept noncontrast CT as the criterion standard for evaluating SAH, then we only need to report sensitivity and specificity to make this point.

The finding of 94.5% sensitivity at the “individual” level is quite high. However, is it adequate for detection of SAH when the consequence for a missed diagnosis is potentially dire and the risks of the additional radiation possibly quite acceptable in this setting? Confidence intervals would have been helpful here to emphasize the point that this statistic is associated with sampling variation and that the true value of sensitivity can conceivably be lower. Of course, one could debate whether a noncontrast CT scan, which itself has a certain sensitivity and specificity for detecting SAH, is, in fact, the criterion standard for diagnosing SAH. Is MR imaging better? How about a spinal tap? The question is, of course, controversial. The McNemar test showed an “almost perfect” agreement between the 2 tests, documenting that much of the time, the 2 tests agree. However again, much of the time may not be good enough if missing a cerebral aneurysm rupture is one

of these times. A significant time lag between the ictus and the 3 missed SAHs on CT attests to the notion that the sensitivity of CT for SAH drops with time and that a low threshold for timely CT when SAH is suspected is justified. Using VNC to detect SAH with reduced radiation bears future investigation.

Part of the methodology of this study is a clinical algorithm whereby DECT angiography is obtained as a first technique to work-up a potential SAH, looking for both cerebral aneurysms and SAH. This approach is somewhat contrary to that used by many for the evaluation of suspected aneurysmal SAH.^{5,7} Typically, the effort is to diagnose SAH first and only secondarily to determine the etiology. Therefore, if the CT finding is negative, for example, typically a spinal tap is performed to try to determine whether there has been a hemorrhage.⁸ Obtaining a CTA first puts the cart before the horse in that incidental vascular lesions may be encountered. Alternatively, often either no imaging or MR imaging, which avoids radiation altogether, would suffice. The utility of finding incidental vascular lesions is ambiguous, and such findings may open Pandora's box because the management of such lesions is very controversial. The management of SAH is less controversial; therefore, an effort to establish this diagnosis, neutralizing a vascular cause by using endovascular or surgical means to prevent rebleeding, should be paramount. Therefore, in deciding whether the reduction in radiation risk associated with the use of DECT angiography is worthwhile, one must also weigh in the following: 1) the risk associated with a possible missed SAH diagnosis; 2) the risk associated with increased radiation accompanying a potentially lower imaging threshold for performing CTA in the evaluation of potential SAH (assuming that clinicians view the DECT angiography as affording 2 diagnostic tests for the radiation cost of 1); 3) the risk associated with uncovering incidental vascular lesions; and 4) nephrotoxic and allergic risks associated

with DECT angiography. This risk/benefit analysis is beyond the scope of this study and this "Commentary" but would be a welcome addition to future work on this topic.

ACKNOWLEDGMENTS

I would like to acknowledge the assistance of Katherine Freeman, DrPH, with the statistical analysis of this publication.

REFERENCES

1. Jiang XY, Zhang SH, Xie QZ, et al. **Evaluation of virtual noncontrast images obtained from dual-energy CTA for diagnosing subarachnoid hemorrhage.** *AJNR Am J Neuroradiol* 2015;36:855–60
2. Zhang LJ, Wu SY, Poon CS, et al. **Automatic bone removal dual-energy CT angiography for the evaluation of intracranial aneurysms.** *J Comput Assist Tomogr* 2010;34:816–24
3. Ferda J, Novak M, Mirka H, et al. **The assessment of intracranial bleeding with virtual unenhanced imaging by means of dual-energy CT angiography.** *Eur Radiol* 2009;19:2518–22
4. Brenner DJ, Hall EJ. **Computed tomography: an increasing source of radiation exposure.** *N Engl J Med* 2007;357:2277–84
5. Brisman JL, Song JK, Newell DW. **Cerebral aneurysms.** *N Engl J Med* 2006;355:928–39
6. Kumar S, Goddeau RP Jr, Selim MH, et al. **Atraumatic convexal subarachnoid hemorrhage: clinical presentation, imaging patterns, and etiologies.** *Neurology* 2010;74:893–99
7. Wijdicks EF, Kallmes DF, Manno EM, et al. **Subarachnoid hemorrhage: neurointensive care and aneurysm repair.** *Mayo Clin Proc* 2005;80:550–59
8. Edlow JA, Caplan LR. **Avoiding pitfalls in the diagnosis of subarachnoid hemorrhage.** *N Engl J Med* 2000;342:29–36

J.L. Brisman

Winthrop University Hospital
Lake Success, New York

<http://dx.doi.org/10.3174/ajnr.A4293>

Neurovascular Manifestations in Hereditary Hemorrhagic Telangiectasia: Imaging Features and Genotype-Phenotype Correlations

T. Krings, H. Kim, S. Power, J. Nelson, M.E. Faughnan, W.L. Young, K.G. terBrugge, and the Brain Vascular Malformation Consortium HHT Investigator Group



ABSTRACT

BACKGROUND AND PURPOSE: Hereditary hemorrhagic telangiectasia is an autosomal dominant disease that presents in 10%–20% of patients with various brain vascular malformations. We aimed to report the radiologic features (phenotype) and the genotype-phenotype correlations of brain vascular malformations in hereditary hemorrhagic telangiectasia.

MATERIALS AND METHODS: Demographic, clinical, genotypic, and imaging information of 75 patients with hereditary hemorrhagic telangiectasia with brain arteriovenous malformations enrolled in the Brain Vascular Malformation Consortium from 2010 to 2012 were reviewed.

RESULTS: Nonshunting, small, superficially located conglomerates of enhancing vessels without enlarged feeding arteries or draining veins called “capillary vascular malformations” were the most commonly observed lesion (46 of 75 patients; 61%), followed by shunting “nidus-type” brain AVMs that were typically located superficially with a low Spetzler-Martin Grade and a small size (32 of 75 patients; 43%). Direct high-flow fistulous arteriovenous shunts were present in 9 patients (12%). Other types of vascular malformations (dural AVF and developmental venous anomalies) were present in 1 patient each. Multiplicity of vascular malformations was seen in 33 cases (44%). No statistically significant correlation was observed between hereditary hemorrhagic telangiectasia gene mutation and lesion type or lesion multiplicity.

CONCLUSIONS: Depending on their imaging features, brain vascular malformations in hereditary hemorrhagic telangiectasia can be subdivided into brain AVF, nidus-type AVM, and capillary vascular malformations, with the latter being the most common phenotype in hereditary hemorrhagic telangiectasia. No genotype-phenotype correlation was observed among patients with this condition.

ABBREVIATIONS: CVM = capillary vascular malformation; HHT = hereditary hemorrhagic telangiectasia

Hereditary hemorrhagic telangiectasia (HHT) or Rendu-Weber-Osler disease is a familial disorder that occurs with a prevalence of approximately 1/10,000.^{1–3} The diagnostic certainty of HHT is determined by the number of characteristic clinical findings present in an individual patient. These clinical findings

are the following: 1) nosebleeds, 2) mucocutaneous telangiectasias (of the lips, oral cavity, nose, or fingers), 3) AVMs (of the lungs, the gastrointestinal system, or the CNS), and 4) an affected first-degree relative. In “definite” HHT, 3 of these clinical criteria are present, while “suspected” or “unlikely” HHT diagnoses consist of 2 or 1 item present, respectively. It is estimated that 10%–20% of patients with HHT have brain vascular malformations⁴ with additional neurovascular complications from pulmonary AVMs (stroke and cerebral abscess).⁵

HHT is inherited as an autosomal dominant disorder, caused by mutation in 1 of 3 genes identified to date: *endoglin* (*HHT1*) on chromosome 9q34; *activin receptor-like kinase 1* or *ALK1* (*HHT2*) on chromosome 12q13; and *SMAD4* on chromosome 18q21 (juvenile polyposis, HHT overlap syndrome).^{6–10} The associated

Received August 26, 2014; accepted after revision October 8.

From the Division of Neuroradiology (T.K., S.P., K.G.t.B.), Department of Medical Imaging, and Division of Neurosurgery (T.K.), Department of Surgery, Toronto Western Hospital, University of Toronto, Toronto, Ontario, Canada; Department of Anesthesia and Perioperative Care (H.K., J.N., W.L.Y.), Center for Cerebrovascular Research, and Department of Epidemiology and Biostatistics (H.K.), University of California San Francisco, San Francisco, California; Division of Respiratory (M.E.F.), Department of Medicine and Li Ka Shing Knowledge Institute, St. Michael's Hospital, Toronto, Ontario, Canada; and Division of Respiratory (M.E.F.), Department of Medicine, University of Toronto, Toronto, Ontario, Canada.

The Brain Vascular Malformation Consortium (U54NS065705) is a part of the National Institutes of Health Rare Diseases Clinical Research Network, supported through collaboration between the National Institutes of Health Office of Rare Diseases Research at the National Center for Advancing Translational Sciences and the National Institute of Neurological Disorders and Stroke. Other financial support to M. Faughnan is from the Nelson Arthur Hyland Foundation and the Li Ka Shing Knowledge Institute.

The content of this article is solely the responsibility of the authors and does not necessarily represent the official views of the National Institutes of Health.

Please address correspondence to Timo Krings, MD, PhD, Division of Neuroradiology, Department of Medical Imaging, Toronto Western Hospital, 399 Bathurst St, 3 McL, Toronto, ON, M5T 2S8, Canada; e-mail: Timo.Krings@uhn.ca

Indicates open access to non-subscribers at www.ajnr.org

Indicates article with supplemental on-line table.

<http://dx.doi.org/10.3174/ajnr.A4210>

gene products are expressed in endothelial cells and are part of the transforming growth factor- β signaling pathway, thus involved in angiogenesis and vascular remodeling. Endothelial cells lacking functioning *endoglin* or *ALK1* form abnormal vessels and abnormal connections between vessels.⁶ Early HHT genotype-phenotype correlation studies demonstrated an association between *endoglin* mutation and brain AVMs,¹¹⁻¹³ though more recent studies have demonstrated that brain AVMs can be present with all HHT genotypes.^{14,15} No studies to date have addressed HHT brain AVM phenotypes and their correlation with genotype, to our knowledge.

To date, in the 2 largest single-center series of brain AVMs in HHT with 52 and 14 patients, respectively, 3 different distinct phenotypes of brain vascular malformations were described independently: 1) high-flow “single-hole” pial fistulas, 2) “classic” nidus-type brain AVMs, and 3) “micro-AVM” or “capillary vascular malformations,” defined as small lesions without clear evidence of a shunt.^{5,16}

The aim of the present series was 2-fold: 1) to identify the different radiologic and, in particular angiographic features of brain vascular malformations in HHT, and to subclassify them into different types, and 2) to determine whether there is a genotype-phenotype correlation between the HHT gene mutation and the type of vascular malformation.

MATERIALS AND METHODS

Study Population

We analyzed data from patients recruited to the HHT Project of the Brain Vascular Malformation Consortium. Patients with HHT with a confirmed clinical HHT diagnosis by the Curaçao criteria¹⁷ or a confirmed genetic diagnosis were enrolled as part of the Brain Vascular Malformation Consortium HHT Project as previously described (<http://rarediseasesnetwork.epi.usf.edu/BVMC>).¹⁸ All patients provided written, informed consent, including consent for genetic studies. The study protocol was approved by each institutional review board. Data collected included age, sex, family relationships, genetic testing results (mutated gene: *ACVRL1*, *ENG*, *SMAD4*, and unknown), clinical presentation, and symptoms. Patients were screened for AVM and other HHT clinical features according to standard clinical practice and international HHT guidelines.¹⁹ The Brain Vascular Malformation Consortium HHT cohort targets patients positive for brain AVM but enrolls all HHT cases in a 1:4 ratio, respectively. Cohort characteristics are otherwise similar to those in other cohorts.^{12,14}

Between 2010 and 2012, comprehensive data were available for 384 recruited patients with HHT, 125 of whom had brain AVMs, with sufficient diagnostic imaging available for review in 75 of these patients with brain AVMs. All patients provided written, informed consent, and the study protocol was approved by each institutional review board.

Data Collection

Epidemiologic data collected included age at enrollment and diagnosis, sex, and HHT mutation type. Radiologic data included MR imaging (with contrast-enhanced sequences in at least 2 planes on 1.5T or 3T scanners) and angiography with multiphase

biplanar selective 4-vessel angiography. The angiographic parameters that were identified for every patient who was identified with a brain vascular malformation are listed in the On-line Table. In addition to location, size in the largest dimension, and eloquence (as determined by the Spetzler-Martin classification), specific information about feeding arteries (such as the degree of dilation, number, type [choroidal versus pial], associated aneurysms, and so forth), the nidus (glomus versus fistula, diffuse versus sharp, perinidal angiogenesis, and so forth), and the draining veins (associated pouches, degree of dilation, associated stenosis, number, deep versus superficial, and so forth) was noted. Images were reviewed by 2 of the authors (T.K. and S.P.) in consensus; in cases of disagreement, a third neuroradiologist (K.G.t.B.) reviewed the case.

On the basis of previous work and our observations in the present study, we were able to subclassify 3 types of vascular malformations: the pial arteriovenous fistula (defined by the absence of an intervening nidus between the feeding artery and draining vein in the presence of a shunt), the nidus-type AVM (defined by the presence of a shunt with early filling of a vein through a dilated network of abnormal vessels), and a “capillary malformation,” in which no shunt was visible on angiography and no dilated feeding arteries or veins were identified; just a blush of abnormal vessels was seen in the capillary phase. Vascular malformations that did not fit into any of these categories (developmental venous anomalies, dural arteriovenous fistulas, pontine capillary telangiectasias, cavernomas, and so forth) were specifically sought and, if present, were recorded.

Statistical Tests

We tested for differences of age at diagnosis, sex, and HHT gene mutation (*ALK1* versus *endoglin*) between patients with AVFs and those without AVFs. Similarly, we tested for differences in characteristics between patients with capillary vascular malformations (CVMs) and those without and for patients with AVMs and those without. Additionally, we checked whether age, sex, or HHT gene mutation was associated with lesion multiplicity (≥ 2 lesions of any type). Comparisons involving age were tested with 2-sample *t* tests, allowing for unequal variances, while comparisons involving sex or mutation differences were tested by using Fisher exact tests. We considered *P* values $< .05$ to be statistically significant. All analyses were performed using STATA/SE 13.1 (StataCorp, College Station, Texas).

RESULTS

A summary of demographic and clinical features of the 75 HHT subjects with brain AVMs is presented in Table 1. The average age at enrollment for these subjects was 37 years, and the average age at brain malformation diagnosis was 30 years. Women were slightly more prevalent in the sample (55%). HHT gene mutation status was available for 60% of participants, and among those, 60% had an *endoglin* mutation.

On the basis of the criteria described in the “Materials and Methods” section, we identified 3 different types of vascular malformations: capillary vascular malformations, AVMs, and AVFs. Table 2 details the distribution of these lesions across subjects. Capillary vascular malformations were the most commonly

Table 1: Overview of 75 subjects with HHT and brain vascular malformations

Characteristic	Summary ^a
Demographics	
Female sex	41/75 (55%)
Age at enrollment (yr) (n = 75)	36.6 ± 19.9
Age at brain malformation diagnosis (yr) (n = 68)	30.1 ± 19.7
HHT-related symptoms	
Epistaxis	66/73 (90%)
Anemia	20/72 (28%)
GI bleeding	5/67 (7%)
Pulmonary AVM	45/69 (65%)
Liver VM	4/66 (6%)
HHT-causing mutation	
<i>ALK1</i>	13/45 (29%)
<i>Endoglin</i>	27/45 (60%)
<i>SMAD4</i>	1/45 (2%)
All test findings negative	4/45 (9%)

Note:—GI indicates gastrointestinal; VM, vascular malformations.

^a Summary is the No. of observations with specified value over the total No. (and the percentage) or the mean ± SD.

Table 2: Brain vascular malformation phenotypes of 75 subjects with HHT

	Capillary Vascular Malformation		
	0	1	2+
0 AVMs/AVFs	1 (1%) ^a	17 (23%)	18 (24%) ^b
1 AVM	20 (27%)	5 (7%)	3 (4%)
2 AVMs	1 (1%)	0 (0%)	1 (1%)
1 AVF	4 (5%)	1 (1%)	0 (0%)
2 AVFs	1 (1%)	1 (1%)	0 (0%)
1 AVM and 1 AVF	2 (3%)	0 (0%)	0 (0%)

^a This individual had 1 dural arteriovenous fistula only.

^b One individual in this group had a developmental venous anomaly.

Table 3: Characteristics of 80 capillary vascular malformations

Characteristic	Summary ^a
Size of maximal dimension (mm) (n = 80)	4.8 ± 2.1
Lobe	
Frontal	30/80 (38%)
Parietal	16/80 (20%)
Occipital	14/80 (18%)
Temporal	10/80 (13%)
Cerebellum	7/80 (9%)
Brain stem	2/80 (3%)
Thalamus/basal ganglia	1/80 (1%)
Location	
Deep	3/80 (4%)
Subcortical	14/80 (18%)
Superficial	63/80 (79%)
MRI visible	66/71 (93%)

^a Summary is the No. of observations with specified value over the total No. (and the percentage) or the mean ± SD.

observed lesion, with 61% of subjects having ≥ 1 CVM. Forty-three percent of subjects had ≥ 1 AVM, and 12% had ≥ 1 AVF. One subject had a dural arteriovenous fistula, and 1 subject had a developmental venous anomaly. Multiplicity of lesions was common: Thirty-three (44%) subjects had ≥ 2 brain malformations.

Tables 3–5 present the typical imaging features of the different vascular malformations: CVMs were identified as lesions that had no dilated feeder and no dilated draining veins (Figs 1–3). Eighty of these lesions were identified in 46 patients. All of these lesions were < 1 cm; most were located in the superficial supratentorial

Table 4: Characteristics of 34 AVMs

Characteristic	Summary ^a
Size of maximal dimension (mm) (n = 34)	18.3 ± 5.3
Eloquent	13/34 (38%)
Deep venous drainage	5/31 (16%)
Spetzler-Martin score	
1	16/31 (52%)
2	12/31 (39%)
3	2/31 (6%)
4	1/31 (3%)
5	0/31 (0%)
Lobe	
Frontal	14/34 (41%)
Parietal	5/34 (15%)
Occipital	4/34 (12%)
Temporal	5/34 (15%)
Cerebellum	2/34 (6%)
Brain stem	2/34 (6%)
Thalamus/basal ganglia	2/34 (6%)
Location	
Deep	4/34 (12%)
Subcortical	5/34 (15%)
Superficial	25/34 (74%)
Nidus en passage (vs terminal)	2/20 (10%)
Diffuse nidus (vs sharp)	6/34 (18%)
Pial-to-pial collateralization	5/31 (16%)
Moyamoya-type changes	0/33 (0%)
Stenoses on arteries	0/31 (0%)
Type, pial (vs choroidal)	33/34 (97%)
Associated aneurysms	0/30 (0%)
Multiple draining veins	3/29 (10%)
Venous ectasia	8/31 (26%)
Venous reflux	1/29 (3%)
Pseudophlebitic pattern	0/29 (0%)

^a Summary is the No. of observations with specified value over the total No. (and the percentage) or the mean ± SD.

Table 5: Characteristics of 11 AVFs

Characteristic	Summary ^a
Single hole with pouch	10/11 (91%)
Lobe	
Frontal	4/11 (36%)
Parietal	0/11 (0%)
Occipital	3/11 (27%)
Temporal	3/11 (27%)
Cerebellum	0/11 (0%)
Brain stem	0/11 (0%)
Thalamus/basal ganglia	1/11 (9%)
Location	
Deep	1/11 (9%)
Subcortical	0/11 (0%)
Superficial	10/11 (91%)
Pial-to-pial collateralization	3/11 (27%)
Moyamoya-type changes	1/11 (9%)
Stenoses on arteries	1/11 (9%)
Type, pial (vs choroidal)	2/11 (18%)
Associated aneurysms	2/11 (18%)
Multiple draining veins	5/11 (45%)
Venous ectasia	11/11 (100%)
Venous reflux	0/11 (0%)
Pseudophlebitic pattern	3/11 (27%)

^a Summary is the No. of observations with specified value over the total No. (and the percentage).

brain. On MR imaging, they appeared as small foci of “fluffy” enhancement without abnormal vascular dilation. There was no edema surrounding these vascular malformations. Thirty-four

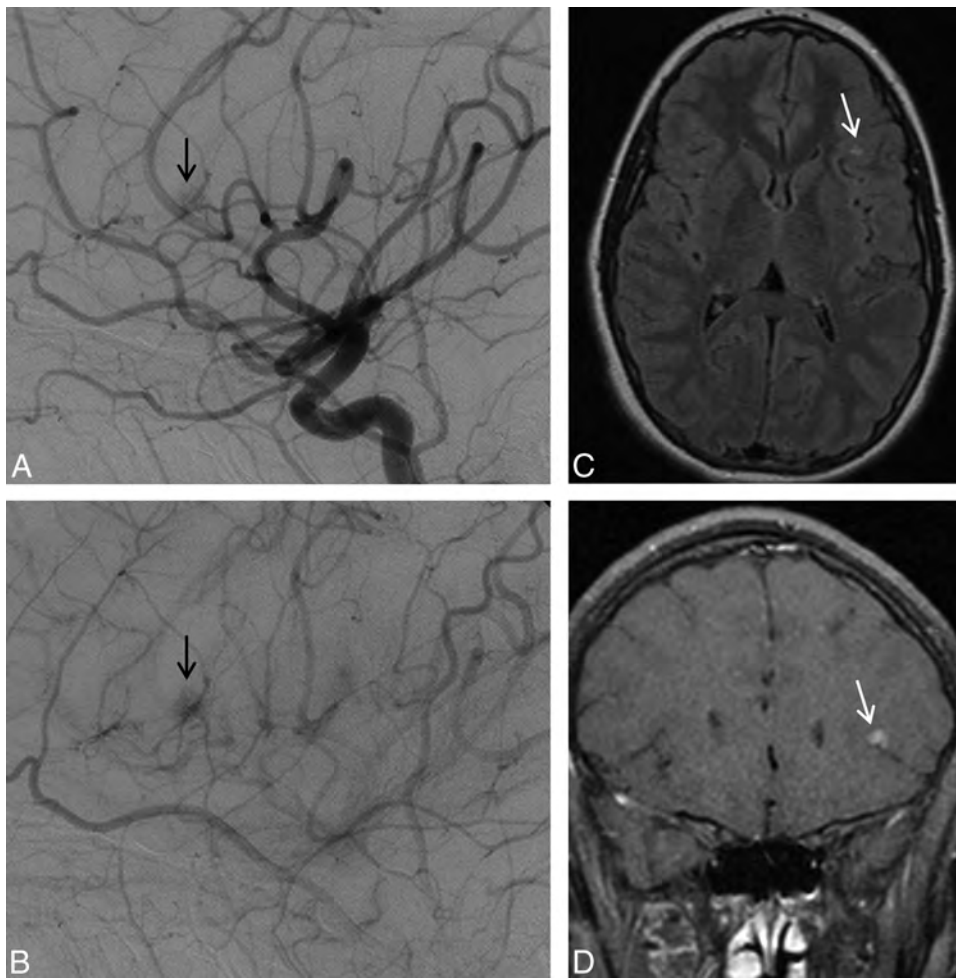


FIG 1. Left ICA angiogram, lateral view, depicts typical features of a capillary vascular malformation in the left frontal opercular region, with a subcentimeter vascular blush identified in the arterial (A) persisting into early venous phase (B, arrow), without evidence of arteriovenous shunting. On MR imaging, this appears as a focal region of hyperintensity on axial T2 FLAIR imaging (C, arrow), with fluffy enhancement on coronal gadolinium-enhanced T1-weighted imaging (D, arrow). No dilated arterial feeder or dilated draining vein is seen.

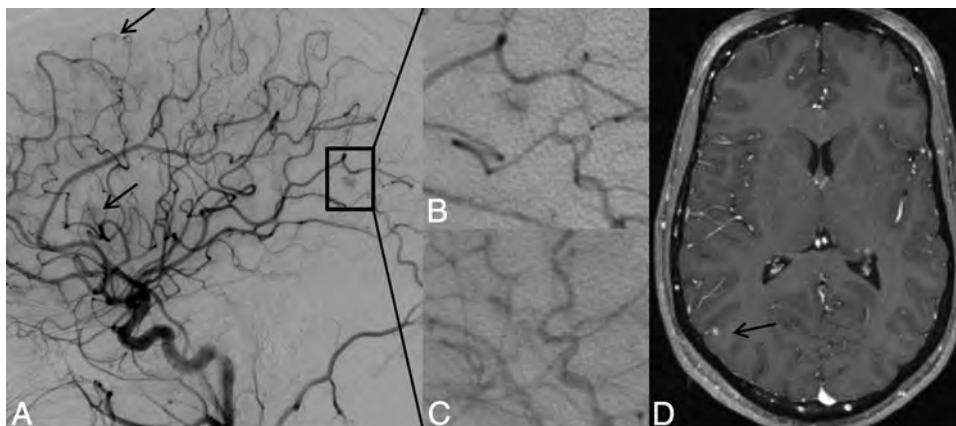


FIG 2. Lateral projection of right ICA angiogram (A–C) and axial T1-weighted gadolinium-enhanced MR imaging (D) demonstrate the typical imaging features of a capillary vascular malformation in a 17-year-old male patient with HHT. A focal subcentimeter blush (arrows) is identified on the arterial phase of a right carotid angiogram, in the frontal, temporal, and parietal regions, in keeping with multiple capillary telangiectasia. Magnified view of the right parietal lesion shows typical angiographic features, with vascular blush identified in the arterial (B) persisting into early venous phase (C); no arteriovenous shunting, dilated arterial feeder, or dilated draining vein are seen. MR imaging appearance of the right parietal lesion demonstrates the typical features of fluffy contrast enhancement in a superficial cortical/subcortical location, without abnormal vascular dilation (D, arrow).

AVMs were present in 32 patients (Figs 4 and 5). As the major differentiating factor from CVMs, the AVMs had enlarged feeding arteries and draining veins and a shunt was visible on angiogra-

phy. In all, an intervening nidus of abnormal vessels was identified. Lesions were almost always <3 cm and rarely (in 2 cases) <1 cm. They had a compact, well-defined nidus and were mainly

located supratentorially and superficially. Given the superficial location and the small size, their Spetzler-Martin grade was typically 1–2, with the higher grades mainly driven by their potential location in eloquent cortex. Feeding arteries were almost always pial vessels (we encountered only 1 choroidal AVM in this series) and were classically fed by terminal-type feeders. Associated aneurysms or other signs of high flow (pial-to-pial collaterals, venous ectasias, and so forth) were uncommon. On the venous side, venous reflux or corkscrew-like dilated veins as signs of long-standing venous hypertension were typically absent. Eleven AVFs were present in 9 patients; these were typically high-flow single-hole macrofistulas that were located in the supratentorial superficial brain with significant venous ectasia

and signs of high flow with consecutive perilesional hypoxemia (Figs 6 and 7).

We found that patients with AVFs tended to be diagnosed at younger ages than those without AVFs ($P = .028$); the average age at diagnosis for patients with AVFs was 15 years compared with an average age of 32 years for patients without AVFs. There was no significant association between the presence of AVFs and sex ($P = .723$) or HHT gene mutation ($P = 1.000$). No significant difference was observed with age, sex, or HHT gene mutation in those patients with capillary vascular malformations versus no CVMs or in patients with AVMs versus those without AVMs. Lesion multiplicity was also not significantly associated with age ($P = .736$), sex ($P = .484$), or HHT gene mutation ($P = 1.000$).

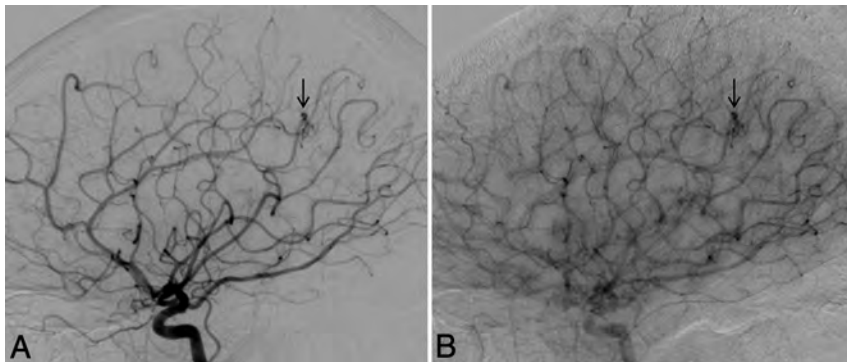


FIG 3. Lateral view of a right ICA angiogram in a 43-year-old male patient with HHT demonstrates a capillary vascular malformation in the right anterior parietal region. A subcentimeter blush is seen in the arterial phase (A, arrow), which persists in the late arterial phase (B) without evidence of arteriovenous shunting.

DISCUSSION

We report herein the largest series and most comprehensive description of brain AVM phenotype among patients with HHT.

On the basis of radiologic and angiographic information, we were able to subclassify 3 different brain vascular malformations in patients with HHT that had some common and distinctive imaging features: The common finding was that brain vascular malformations in HHT tended to be located in supratentorial and superficial compartments. Deep or infratentorial locations were

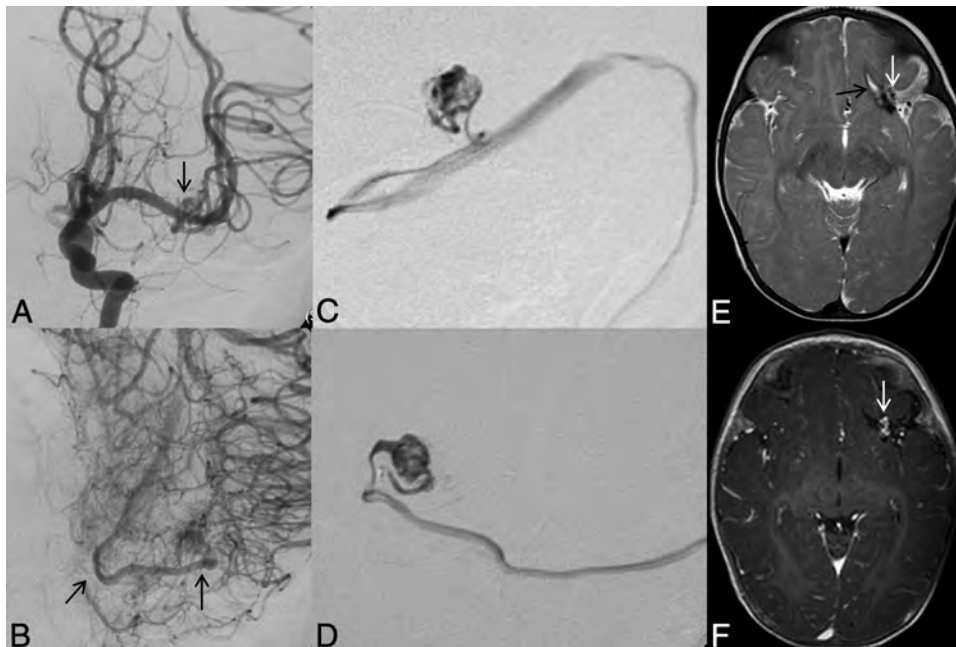


FIG 4. Left ICA catheter angiogram (A and B), microcatheter injection (C and D), axial T2-weighted (E), and contrast-enhanced T1-weighted MR imaging (F) demonstrate imaging findings of a typical arteriovenous malformation. Anteroposterior projection of a left ICA injection demonstrates filling of the AVM nidus through an enlarged anterior temporal branch of the left MCA in the early arterial phase (A, arrow). There is arteriovenous shunting with early venous drainage through an enlarged left inferior temporal vein (B, arrows). Microcatheter injection in frontal (C) and lateral (D) projections demonstrates a typical glomerular well-defined compact nidus supplied by a single terminal arterial feeder with shunting into a dilated vein. MR imaging shows the superficial location of the AVM, with vascular flow voids seen on T2-weighted imaging (E, arrow) and enhancement on postgadolinium T1-weighted imaging (F, arrow). Evidence of previous hemorrhage related to AVM rupture, with a slit-like hematoma cavity in the left inferior frontal lobe, and surrounding hemosiderin staining (E, black arrow).

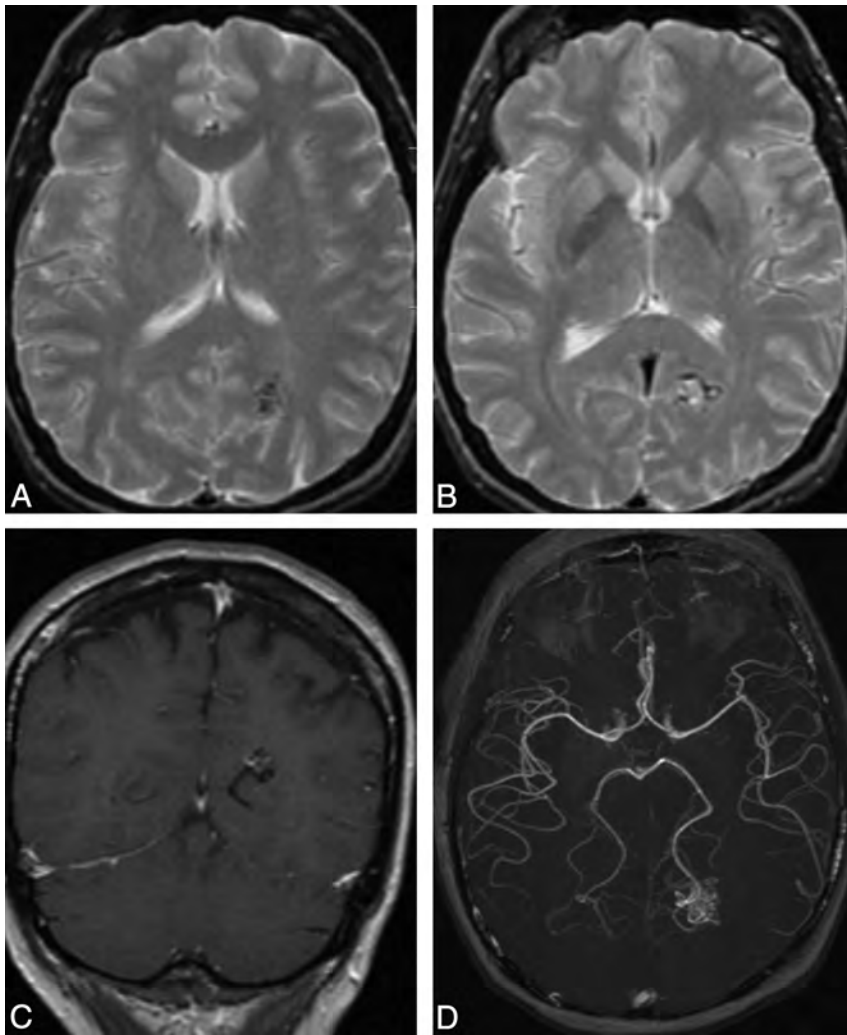


FIG 5. Typical MR imaging features of an arteriovenous malformation in a 50-year-old male patient with HHT. Axial T2-weighted imaging demonstrates a cluster of flow voids in the left occipital lobe, in keeping with a vascular nidus (A). A linear flow void of the dilated draining vein is seen inferior to the nidus on axial T2 (B) and coronal postcontrast T1-weighted imaging (C). Axial MRA MIP demonstrates a compact glomerular-type nidus in the left occipital lobe (D).

atypical. This finding corresponds well with the literature: In the Bicêtre series, 61 of 68 brain vascular malformations (90%) were located superficially and 45 of 68 lesions (66%) were supratentorial.¹⁶ Lesion identification by MR imaging was always possible for the AVMs and AVFs; however, a few capillary vascular malformations could not be detected by MR imaging alone. Distinguishing features among the 3 subtypes were the presence or absence of a shunt and, if a shunt was present, whether the abnormal arteriovenous communication was direct (ie, fistulous) or through a network (or nidus).

Pial AVFs typically had a high shunt volume and therefore often led to massive enlargement of the feeding arteries, significant venous ectasia, and, due to locoregional hypoxemia, secondary changes such as perinidal angiogenesis. We presume that the relatively higher proportion of direct fistulas in the Bicêtre series was related to a referral bias because these lesions tend to be more commonly found in children.¹⁶ Brain AVMs in our series tended to be small (typically <3 cm in their largest diameter and, in 2 cases, <1 cm), and because their location was typically superficial,

their Spetzler-Martin grade tended to be low. Again, this is in keeping with the findings in previous literature. The so-called capillary vascular malformations did not present with dilated vessels (neither on the feeding artery nor the draining venous side) and demonstrated a focal area of fluffy enhancement on MR imaging.

In this article, we introduce the term “capillary vascular malformation” for those vascular malformations that do not exhibit enlarged arteries or veins on MR imaging and in which no true shunt is present on angiography. These vascular malformations have been previously coined “micro-AVMs,” which may lead to the assumption that they behave in a manner similar to true brain AVMs. However, because these vascular lesions differ from “AVMs” in their angioarchitecture, one may hypothesize that they also behave differently in their clinical presentation, an assumption that is founded on the combined experience of the Toronto⁵ and the Bicêtre¹⁶ articles, in which no hemorrhages were encountered for these types of malformations. While in AVMs an arteriovenous shunt is present due to lack of a true capillary bed, the term “capillary malformation” tries to highlight the absence of a shunt and the presence of a capillary bed that is abnormally dilated (and thus visible as a blush within the capillary phase of the angiography and faint enhancement on MR imaging).

We found, similar to findings in previous series,²⁰ no significant sex predilection, a rather young overall age at presentation, and a high propensity for multiplicity of brain lesions if present. Our proportion of multiplicity (33 in 75 patients = 44%) was very similar to numbers reported previously (23 of 56 patients = 39% in the series of Bharatha et al²⁰; 16 of 44 = 36% in the Bicêtre series, when taking into account only the cerebral manifestations¹⁶). Given a rate of approximately 1% multiplicity of brain vascular malformations in the non-HHT population, our data support the previously described high predictive value of AVM multiplicity for the diagnosis of HHT.

Our observations are in keeping with previous reports on the neurovascular manifestations in HHT, but we think that proof of findings of these single-center studies from a multicenter consortium is still necessary and worthwhile reporting. To date, most studies on brain vascular malformations in HHT do not subclassify the different types of vascular malformations. However, it is quite conceivable that the various types will have different natural histories and therefore warrant different treatments. In neither of the 2 larger

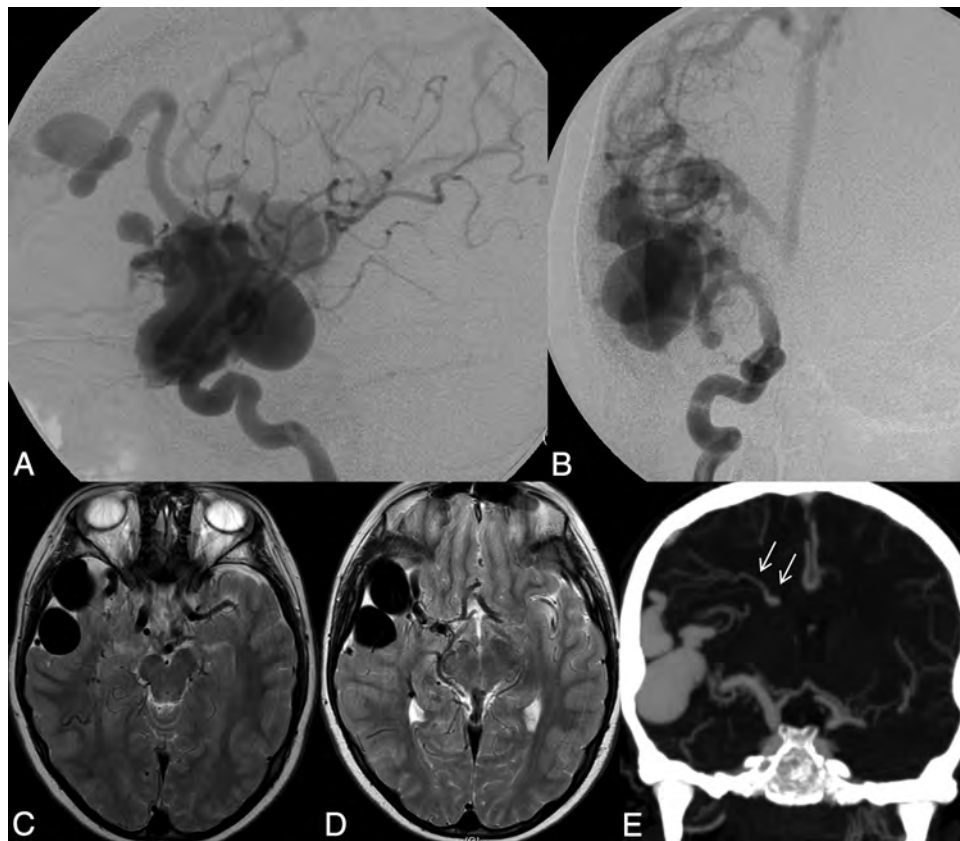


FIG 6. Right ICA catheter angiogram in lateral (A) and frontal (B) projections demonstrates 2 separate high-flow single-hole pial arteriovenous fistulas, 1 in the right frontal lobe and 1 in the right temporal lobe. Arterial supply to each fistula is through a single enlarged right MCA branch, which empties directly into a large venous pouch. Venous drainage is superficial, with both fistulas draining through enlarged cortical veins to the superior sagittal sinus. On axial T2-weighted MR imaging (C and D) venous pouches appear as flow voids and exert mass effect on the adjacent right temporal lobe. Evidence of venous congestion with venous reflux through dilated transmedullary veins to the deep venous system is demonstrated on a coronal reconstruction of CTA (arrows).

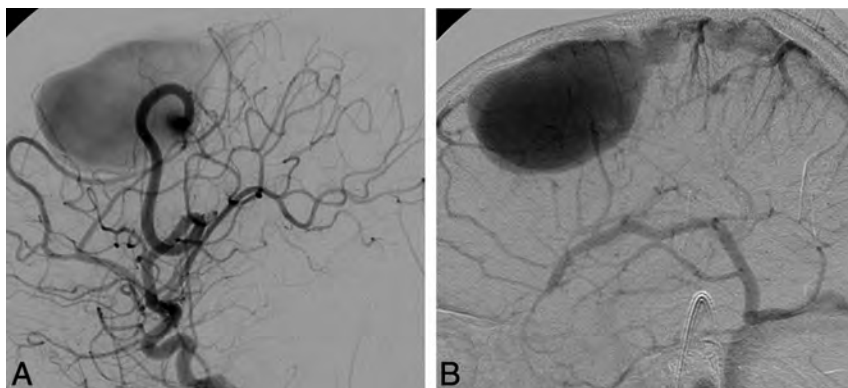


FIG 7. Lateral view of a left ICA angiogram in an 8-year-old male patient with HHT. Angiography in early arterial (A) and venous (B) phases demonstrates a high-flow single-hole pial arteriovenous fistula in the left frontal lobe. Arterial supply is through a single enlarged prefrontal branch of the left MCA, which empties directly into a large venous pouch. Venous drainage is superficial through an enlarged cortical vein to the superior sagittal sinus.

series that reported clinical data of the various types of brain vascular malformations in HHT were there any hemorrhages reported for patients with capillary vascular malformations.²¹

Whether the rate of hemorrhage of vascular malformations associated with HHT is different from that of sporadic brain

AVMs in the non-HHT population remains a matter of debate²²: In Dutch and American HHT populations, a hemorrhagic risk of <1% was reported,^{22,23} a risk that was deemed significantly smaller than the presumed risk of hemorrhage in the population with sporadic AVM. However, in a retrospective study of 22,061 patient-years, similar hemorrhage rates between both groups (approximately 2.0% per patient-year) were found.²⁴ Finally, Morgan et al²⁵ stated that, in particular, infants and children are at high risk of sudden intracranial hemorrhage, which was further supported by the Bicêtre series,¹⁶ in which only 13 of the 50 patients had no symptoms attributable to their neurovascular manifestations. However,

because these 2 latter studies are single-center studies, data may be biased due to referral base.

A potential problem of the large-scale population-based studies is that the type of vascular malformation was not further evaluated. It was assumed that all HHT-related brain vascular malformations be-

have similarly. However, one may argue that the difference in overall bleeding rates in HHT vascular malformations compared with sporadic AVMs observed in some studies may be driven mainly by the capillary vascular malformations (ie, the most often encountered and most benign type of vascular malformation in HHT), thus biasing the results to false low rates of hemorrhage. Thus, if the presented subclassification of brain vascular malformation in HHT proves to be reflected in clinical manifestations, treatment strategies will have to be altered and individualized to the type of vascular malformation, with a more aggressive treatment in arteriovenous fistulas and/or nidus-type AVMs compared with CVMs.

HHT gene mutation information was available for 60% of our patients, and we did not observe a statistically significant association with HHT gene mutation and the type of vascular malformation or the occurrence of multiplicity. This finding fits with the clinical observation that members of the same family can present with different HHT phenotypes, though they have the same type of mutation. An important caveat of our study is that we do not have genetic information for all patients included. However, our results are also in accordance with previous reports that found brain vascular malformations to be present in all types of mutations.¹⁴

CONCLUSIONS

Our study identified several different types of brain vascular malformations in patients with HHT, which may have different natural history and treatment risks. Future studies should focus on describing the hemorrhage risks associated with these different HHT brain vascular malformations.

APPENDIX

The Brain Vascular Malformation Consortium HHT Investigator Group comprises: Murali Chakinala, Marie E. Faughnan, James R. Gossage, Katharine Henderson, Vivek Iyer, Raj Kasthuri, Helen Kim, Timo Krings, Michael T. Lawton, Doris Lin, Johannes Jürgen Mager, Justin McWilliams, Jamie McDonald, Ludmila Pawlikowska, Jeffrey Pollak, Felix Ratjen, Karen Swanson, Karel G. ter Brugge, Dilini Vethanayagam, Andrew White, Robert I. White Jr, Pearce Wilcox, and William L. Young (†).

†Deceased.

Disclosures: Helen Kim—RELATED: Grant: National Institutes of Health (U54 NS065705). *Comments: salary support. Jeffrey Nelson—RELATED: Grant: National Institutes of Health (U54 NS065705). *Comments: salary support. Marie E. Faughnan—RELATED: Grant: National Institutes of Health—National Institute of Neurological Disorders and Stroke National Center for Advancing Translational Sciences. Comments: detailed in the article. *Money paid to the institution.

REFERENCES

- Bideau A, Plauchu H, Brunet G, et al. **Epidemiological investigation of Rendu-Osler disease in France: its geographical distribution and prevalence.** *Popul* 1989;44:3–22
- Kjeldsen AD, Vase P, Green A. **Hereditary haemorrhagic telangiectasia: a population-based study of prevalence and mortality in Danish patients.** *J Intern Med* 1999;245:31–39
- Dakeishi M, Shioya T, Wada Y, et al. **Genetic epidemiology of hereditary hemorrhagic telangiectasia in a local community in the northern part of Japan.** *Hum Mutat* 2002;19:140–48
- Fulbright RK, Chaloupka JC, Putman CM, et al. **MR of hereditary hemorrhagic telangiectasia: prevalence and spectrum of cerebrovascular malformations.** *AJNR Am J Neuroradiol* 1998;19:477–84
- Matsubara S, Mandzia JL, ter Brugge K, et al. **Angiographic and clinical characteristics of patients with cerebral arteriovenous malformations associated with hereditary hemorrhagic telangiectasia.** *AJNR Am J Neuroradiol* 2000;21:1016–20
- Marchuk DA, Srinivasan S, Squire TL, et al. **Vascular morphogenesis: tales of two syndromes.** *Hum Mol Genet* 2003;12(Spec No 1):R97–112
- Guttmacher AE, Marchuk DA, White RI Jr. **Hereditary hemorrhagic telangiectasia.** *N Engl J Med* 1995;333:918–24
- Showlin CL, Hughes JM, Tuddenham EG, et al. **A gene for hereditary haemorrhagic telangiectasia maps to chromosome 9q3.** *Nat Genet* 1994;6:205–09
- McAllister KA, Baldwin MA, Thukkani AK, et al. **Six novel mutations in the endoglin gene in hereditary hemorrhagic telangiectasia type I suggest a dominant-negative effect of receptor function.** *Hum Mol Genet* 1995;4:1983–85
- McAllister KA, Grogg KM, Johnson DW, et al. **Endoglin, a TGF-beta binding protein of endothelial cells, is the gene for hereditary haemorrhagic telangiectasia type I.** *Nat Genet* 1994;8:345–51
- Bayrak-Toydemir P, McDonald J, Markewitz B, et al. **Genotype-phenotype correlation in hereditary hemorrhagic telangiectasia: mutations and manifestations.** *Am J Med Genet A* 2006;140:463–70
- Letteboer T, Mager J, Snijder R, et al. **Genotype phenotype relationship in hereditary hemorrhagic telangiectasia.** *J Med Genet* 2006;43:371–77
- Sabbà C, Pasculli G, Lenato G, et al. **Hereditary hemorrhagic telangiectasia: clinical features in ENG and ALK1 mutation carriers.** *J Thromb Haemost* 2007;5:1149–57
- Nishida T, Faughnan M, Krings T, et al. **Brain arteriovenous malformations associated with hereditary hemorrhagic telangiectasia: gene-phenotype correlations.** *Am J Med Genet A* 2012;158A:2829–34
- Gallione C, Aylsworth A, Beis J, et al. **Overlapping spectra of SMAD4 mutations in juvenile polyposis (JP) and JP-HHT syndrome.** *Am J Med Genet A* 2010;152A:333–39
- Krings T, Ozanne A, Chng SM, et al. **Neurovascular phenotypes in hereditary haemorrhagic telangiectasia patients according to age: review of 50 consecutive patients aged 1 day–60 years.** *Neuroradiology* 2005;47:711–20
- Showlin CL, Guttmacher AE, Buscarini E, et al. **Diagnostic criteria for hereditary hemorrhagic telangiectasia (Rendu-Osler-Weber syndrome).** *Am J Med Genet* 2000;91:66–67
- Akers AL, Ball KL, Clancy M, et al. **Brain vascular malformation consortium: overview, progress and future directions.** *J Rare Disord* 2013;1:5
- Faughnan ME, Palda VA, Garcia-Tsao G, et al. **International guidelines for the diagnosis and management of hereditary hemorrhagic telangiectasia.** *J Med Genet* 2011;48:73–87
- Bharatha A, Faughnan M, Kim H, et al. **Brain arteriovenous malformation multiplicity predicts the diagnosis of hereditary hemorrhagic telangiectasia: quantitative assessment.** *Stroke* 2012;43:72–78
- Krings T, Ozanne A, Chng S, et al. **Hereditary hemorrhagic telangiectasia.** *Clin Neuroradiol* 2006;16:76–90
- Maher CO, Piepgras DG, Brown RD Jr, et al. **Cerebrovascular manifestations in 321 cases of hereditary hemorrhagic telangiectasia.** *Stroke* 2001;32:877–82
- Willemsse RB, Mager JJ, Westermann CJ, et al. **Bleeding risk of cerebrovascular malformations in hereditary hemorrhagic telangiectasia.** *J Neurosurg* 2000;92:779–84
- Easey AJ, Wallace GM, Hughes JM, et al. **Should asymptomatic patients with hereditary haemorrhagic telangiectasia (HHT) be screened for cerebral vascular malformations? Data from 22,061 years of HHT patient life.** *J Neurol Neurosurg Psychiatry* 2003;74:743–48
- Morgan T, McDonald J, Anderson C, et al. **Intracranial hemorrhage in infants and children with hereditary hemorrhagic telangiectasia (Osler-Weber-Rendu syndrome).** *Pediatrics* 2002;109:E12

Pixel-by-Pixel Comparison of Volume Transfer Constant and Estimates of Cerebral Blood Volume from Dynamic Contrast-Enhanced and Dynamic Susceptibility Contrast-Enhanced MR Imaging in High-Grade Gliomas

P. Alcaide-Leon, D. Pareto, E. Martinez-Saez, C. Auger, A. Bharatha, and A. Rovira

ABSTRACT

BACKGROUND AND PURPOSE: Estimates of blood volume and volume transfer constant are parameters commonly used to characterize hemodynamic properties of brain lesions. The purposes of this study were to compare values of volume transfer constant and estimates of blood volume in high-grade gliomas on a pixel-by-pixel basis to comprehend whether they provide different information and to compare estimates of blood volume obtained by dynamic contrast-enhanced MR imaging and dynamic susceptibility contrast-enhanced MR imaging.

MATERIALS AND METHODS: Thirty-two patients with biopsy-proved grade IV gliomas underwent dynamic contrast-enhanced MR imaging and dynamic susceptibility contrast-enhanced MR imaging, and parametric maps of volume transfer constant, plasma volume, and CBV maps were calculated. The Spearman rank correlation coefficients among matching values of CBV, volume transfer constant, and plasma volume were calculated on a pixel-by-pixel basis. Comparison of median values of normalized CBV and plasma volume was performed.

RESULTS: Weak-but-significant correlation ($P < .001$) was noted for all comparisons. Spearman rank correlation coefficients were as follows: volume transfer constant versus CBV, $\rho = 0.113$; volume transfer constant versus plasma volume, $\rho = 0.256$; CBV versus plasma volume, $\rho = 0.382$. We found a statistically significant difference ($P < .001$) for the estimates of blood volume obtained by using dynamic contrast-enhanced MR imaging (mean normalized plasma volume, 13.89 ± 11.25) and dynamic susceptibility contrast-enhanced MR imaging (mean normalized CBV, 4.37 ± 4.04).

CONCLUSIONS: The finding of a very weak correlation between estimates of microvascular density and volume transfer constant suggests that they provide different information. Estimates of blood volume obtained by using dynamic contrast-enhanced MR imaging are significantly higher than those obtained by dynamic susceptibility contrast-enhanced MR imaging in human gliomas, most likely due to the effect of contrast leakage.

ABBREVIATIONS: DCE–MR imaging = dynamic contrast-enhanced MR imaging; DSC–MR imaging = dynamic susceptibility contrast-enhanced MR imaging; K^{trans} = volume transfer constant; V_p = plasma volume; ρ = Spearman rank correlation coefficient

Characterization of the hemodynamics of glial tumors by MR perfusion is very relevant because tumor aggressiveness and growth are associated with both endothelial hyperplasia and neovascularization.¹

The 2 most common MR perfusion techniques used in clinical

practice are dynamic susceptibility contrast-enhanced MR imaging (DSC–MR imaging) and dynamic contrast-enhanced MR imaging (DCE–MR imaging).² CBV is usually calculated from DSC–MR imaging data, while the volume transfer constant (K^{trans}) is usually obtained by using DCE–MR imaging. Both CBV and the volume transfer constant have demonstrated good discriminative power in distinguishing low- and high-grade tumors³ and utility in predicting prognosis.^{4–6}

K^{trans} is defined as the volume transfer constant between plasma and interstitial space. It is often used as a synonym for permeability, but, as defined by Tofts et al,⁷ “the measured transfer constant is a potentially intractable combination of flow, permeability, and surface area.” The physiologic significance of K^{trans} depends on the balance between capillary permeability and blood flow in the tissue of interest. When permeability

Received August 14, 2014; accepted after revision November 9.

From the Department of Radiology, MR Unit (P.A.-L., D.P., C.A., A.R.), and Department of Pathology (E.M.-S.), Hospital Vall d'Hebron, Barcelona, Spain; and Department of Medical Imaging (A.B.), St Michael's Hospital, Toronto, Ontario, Canada.

This work was supported by a grant from the Spanish Society of Radiology (Beca SERAM Industria) in the form of salary for the principal investigator (P.A.-L.).

Please address correspondence to Paula Alcaide-Leon, MD, Hospital Vall d'Hebron, MR Unit, Radiology, Passeig Vall d'Hebron, 119–129, 08035, Barcelona, Spain; e-mail: paulaalcaideleon@hotmail.com

<http://dx.doi.org/10.3174/ajnr.A4231>

is very high, the amount of contrast that leaks out of the vessels depends on the amount of contrast that gets to the capillaries per unit of time. In this situation, K^{trans} is equal to the blood plasma flow per unit volume of tissue (Fig 1). In cases of low permeability, the transfer constant equals the permeability surface area product between blood plasma and the extravascular-extracellular space, per unit volume of tissue.

In the brain, most cases are surface area product-limited,⁷ so K^{trans} depends on both the leakiness of the vessels and the total surface of leaky capillaries. The problem is that the contribution of each factor to the measured K^{trans} is a priori unknown. The transfer constant measured in a voxel may be high due to very leaky vessels, a high number of leaky capillaries within the voxel, or a combination of both (Fig 2).

We suggest that within-voxel comparison of blood volume estimates and K^{trans} would provide valuable information about physiologic meaning of K^{trans} in high-grade gliomas. The correlation between K^{trans} and CBV has been previously assessed in gliomas by Law et al.⁸ Regions with maximal CBV and maximal K^{trans} were compared in each tumor to obtain a weak-but-positive correlation. However, they did not compare parameters of the

same tumor region because their main goal was to correlate maximal values of the parameters with tumor grade. A similar approach was followed by Provenzale et al.⁹ They reported a high correlation between CBV and the degree of contrast enhancement, which was defined by the authors as a relative measure of permeability. Again the CBV and K^{trans} values used for comparison were obtained from different tumor regions. Results about the correlation between K^{trans} and CBV are, therefore, based on indirect methods and are controversial.

The purpose of this study was to compare values of K^{trans} and CBV in high-grade gliomas on a pixel-by-pixel basis to determine whether they provide different physiologic information. The second aim was to compare estimates of blood volume obtained by DCE-MR imaging and DSC-MR imaging.

MATERIALS AND METHODS

Subjects

We retrospectively reviewed data obtained from 35 consecutive patients with a histopathologic diagnosis of intracranial diffuse astrocytoma with necrosis and/or vascular proliferation (grade IV)¹⁰ who underwent surgery with biopsy or surgical resection at our institution between April 2010 and April 2013 and had pre-operative DSC-MR imaging and DCE-MR imaging data suitable for evaluation obtained in the same setting. None of the patients included in the study had undergone surgery or biopsy of their brain tumor. Some were on steroids, but information about steroid treatment was not always available for this retrospective cohort of patients. Significant displacement of the patient's head between DCE-MR imaging and DSC-MR imaging acquisitions leading to inaccurate coregistration of both sets of images was an exclusion criterion; 3 patients were excluded for this reason (final, $n = 32$). Histopathologic evaluation was performed by 2 experienced neuropathologists and was based on the World Health Organization 2007¹⁰ criteria. Approval was obtained from the ethics committee of Vall d'Hebron Hospital, which waived patient consent for this retrospective study.

MR Imaging

MR imaging studies were performed on a 3T MR imaging system (Magnetom Trio; Siemens, Erlangen, Germany) by using a 32-

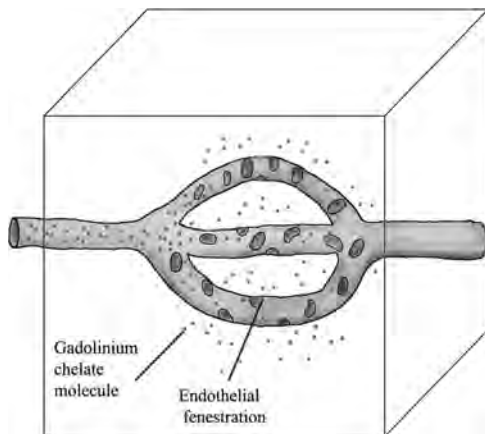


FIG 1. Schematic illustrating flow-limited contrast extravasation. Due to high permeability, the rate of leakage within the voxel depends on the amount of plasma reaching the voxel per unit of time (plasma flow). The venous blood would be “clean” of contrast.

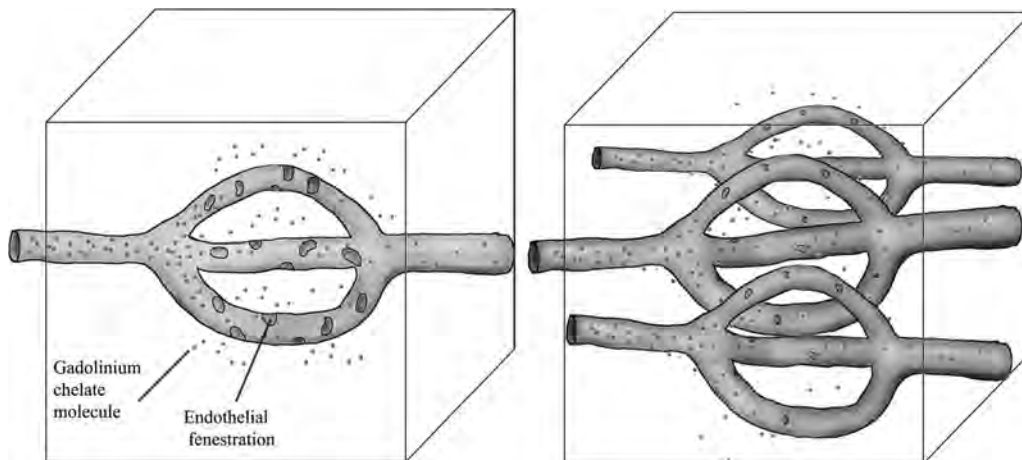


FIG 2. Schematic illustrating 2 voxels with similar K^{trans} values: the first one showing high permeability and low surface area and the second one with low permeability and high surface area.

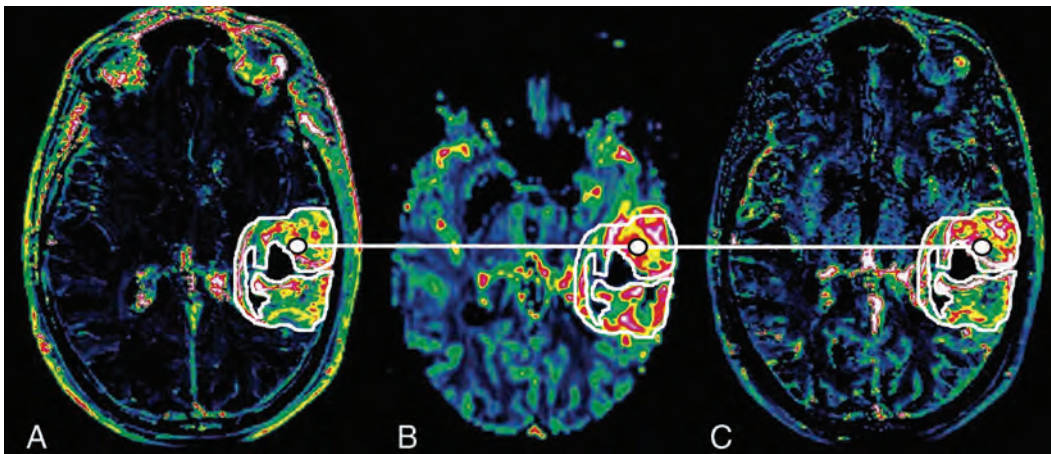


FIG 3. K^{trans} (A), CBV (B), and Vp (C) maps through the center of a grade IV glioma. The white line connects corresponding pixels for the correlation study.

channel head coil. In a few patients, an 8-channel head coil had to be used instead due to large head size or claustrophobia.

Routine anatomic TSE T2 was performed in all patients before dynamic series (TR/TE, 6100/91 ms; in-plane voxel size, $0.5 \times 0.4 \times 0.4$ mm; section thickness, 5 mm). Ten sections were selected for DCE-MR imaging to cover the tumor on the basis of T2-weighted images. Sixty consecutive volumes were acquired in 3 minutes 40 seconds (temporal resolution, 6 seconds) by using a T1-weighted sequence (TR/TE, 7.19/2.55 ms; flip angle, 12° ; section thickness, 3.0 mm; matrix, 320×320 ; in-plane voxel size, $1.8 \times 0.7 \times 3.0$ mm). After the first phase was acquired, an intravenous bolus of gadobutrol (Gadovist, 1 mmol/mL; Bayer Schering Pharma, Berlin, Germany) was injected at a dose of 5 mL by using an autoinjector (Spectris Solaris MR injector; MedRad, Indianola, Pennsylvania) at a rate of 5 mL/s followed immediately by a 20-mL continuous saline flush injected at a rate of 5 mL/s.

DSC-MR imaging was performed in the transverse plane by using a gradient-echo echo-planar sequence (TR/TE, 1450/45 ms; flip angle, 90° ; FOV, 230 mm; section thickness, 5.0 mm; matrix, 128×128 ; in-plane voxel size, $1.8 \times 1.8 \times 5$ mm). The imaging was performed during the first pass of 5 mL of gadobutrol (Gadovist, 1 mmol/mL), and a series of 60 multisection acquisitions was acquired at 2.9-second intervals during the first pass of contrast agent by using the same autoinjector used for DCE-MR imaging. Administration of contrast material before DSC is known to minimize T1 effects on CBV measurements.¹¹

Image Analysis

DSC and DCE perfusion MR imaging data were transferred to an independent workstation and processed by using the software nordicICE (Version 2.3; NordicNeuroLab, Bergen, Norway). Image processing was performed by 1 of the authors (P.A.-L., with 2 years' experience in neuroradiology). DSC perfusion MR images were used in the production of CBV maps on a voxel-by-voxel basis by use of established tracer kinetic models applied to the first-pass data. To reduce the recirculation effects, the $\Delta R2^*$ curves were fitted to a γ -variate function, which is an approximation of the first-pass response as it would appear in the absence of recirculation or leakage. The dynamic curves were mathematically corrected to reduce contrast-agent leakage effects.¹² The be-

ginning and the end of the first-pass bolus were determined through inspection of the time-signal intensity curve, and care was taken to exclude any recirculation-related signal intensity. Manual arterial input function detection was used for calculation.

DCE perfusion MR images were used for the steady-state T1 kinetic analysis. This analysis was based on the extended model of Tofts et al,⁷ which yields estimates of plasma volume (Vp) and K^{trans} . Semiautomated arterial input function detection was used for calculation. The native T1 was not measured, but a fixed value of 1000 ms was assumed. CBV, K^{trans} , and Vp maps were automatically coregistered by using nordicICE. This software performs rigid transformation of the datasets by maximization of mutual information.¹³

For each tumor, ROIs were manually drawn on K^{trans} maps, including the entire contrast-enhanced region. ROIs were copied to corresponding CBV and Vp maps, and a list of pixel values of the ROIs organized by spatial coordinates was obtained for each map (K^{trans} , CBV, and Vp) by using the software package Jim (Version 3.0; Xinapse Systems, West Bergholt, United Kingdom). A 20- to 50-mm² ROI was manually drawn on the contralateral normal-appearing white matter for each tumor used to normalize CBV and Vp (normalized CBV = CBV / CBV of normal-appearing white matter; and normalized VP = VP / VP of normal-appearing white matter). Figure 3 illustrates an example of manually drawn ROIs around enhancing tumor in K^{trans} (Fig 3A), posteriorly copied to CBV (Fig 3B) and Vp (Fig 3C) maps. Values of pixels in the same tumor location were compared in the correlation study.

Visual inspection of coregistered maps was performed, and 3 patients were excluded from the study because adequate coregistration was impossible to achieve (final, $n = 32$). Sections including susceptibility artifacts due to bone, air, or calcification on CBV maps were excluded. In enhancing tumors, pixels with K^{trans} values < 0.01 were also excluded from the analysis. This threshold was used to avoid nonenhancing regions that had been previously included in the manually drawn ROIs by mistake. Pixels with normalized CBV and/or Vp < 0.5 (half of contralateral normal-appearing white matter) were also excluded because they most likely represented nonenhancing necrotic or edematous areas.

Table 1: Median, maximum, minimum, and interquartile range of nCBV, nVp, and K^{trans} values

	nCBV	nVp	K^{trans} (min^{-1})
Median	3.787	13.2	0.1841
Interquartile range	2.887–5.187	7.806–18.755	0.127–0.3125
Range	1.420–11.271	4.769–62.293	0.0471–0.987

Note:—nCBV indicates normalized CBV; nVp, normalized Vp.

Table 2: Results of the correlation study performed in a randomly selected sample of 40% (104,171 pixels)

	CBV and K^{trans}	Vp and K^{trans}	Vp and CBV
Spearman rank correlation coefficients	0.113 ($P < .001$)	0.256 ($P < .001$)	0.382 ($P < .001$)

Statistical Analysis

Statistical analysis was performed by using SPSS (IBM, Armonk, New York). Mean values of Vp, CBV, and K^{trans} of enhancing voxels were calculated for each patient. Values of Vp, CBV, and K^{trans} were tested for normality and were found to be non-normally distributed. The Kolmogorov-Smirnov test was used for assessing normality. The Spearman ρ test was used to calculate rank correlation coefficients between corresponding values of K^{trans} and CBV, K^{trans} and Vp, and CBV and Vp in each pixel. The Spearman rank correlation coefficient can take values from +1 to -1. A Spearman coefficient of +1 indicates a perfect association. A Spearman coefficient of zero indicates no association between ranks, and a coefficient of -1 indicates a perfect negative association of ranks. The closer the Spearman coefficient is to zero, the weaker the association is between the ranks. Due to large sample size (260,610 pixels), the correlation study was performed for a randomly selected sample of 40%. Comparison between median values of CBV and Vp was made by using the Wilcoxon signed-rank test.

RESULTS

The mean age of the 32 patients (20 men, 12 women) was 54 years (range, 36–78 years). Total number of enhancing pixels selected was 260,610. The number of pixels selected in each tumor ranged between 489 and 36,385, with an average of 6377.5.

Mean values of normalized CBV, normalized Vp, and K^{trans} were obtained for each tumor. The distribution of these resulting values was non-Gaussian. Median, maximum, and minimum values and the interquartile ranges of normalized CBV, normalized Vp, and K^{trans} values are shown in Table 1. The difference between the median values of the normalized estimates of cerebral blood volume and plasma blood volume obtained from DSC-MR imaging and DCE-MR imaging, respectively, was statistically significant ($P < .001$). Results of the correlation study between the parameters CBV, K^{trans} , and Vp are listed in Table 2.

DISCUSSION

Values of K^{trans} , Vp, and CBV obtained in our study have to be interpreted on the basis of all enhancing regions of tumors being included. Most studies in the field of perfusion in human gliomas select small ROIs including maximal CBV values. This difference may explain the presence of low mean CBV compared with those reported in the literature for grade IV tumors.¹⁴

When we compared Vp and CBV means, a difference between the T1 and T2* perfusion approaches was evident with blood

volume estimates obtained from DSC-T2 sequences much lower than those obtained from DCE-T1 acquisitions. This difference has been shown by several groups.^{15,16} Our results are, therefore, consistent with their hypothesis of blood volume overestimation when the DCE-T1 approach is used and underestimation when the DSC-T2 method is used. This mismatch is thought to be caused by contrast leakage. On DSC-T2, extravascular contrast causes T1 shortening competing with signal drop caused by intravascular contrast. As a result, blood volume is underestimated. In our case, this effect of leakage has been minimized by preloading with contrast before DSC-MR imaging acquisition and performing mathematic corrections to reduce contrast-agent leakage effects. In the case of the DCE-T1 method, extravascular contrast increases the signal of tissue, leading to artificially elevated blood volume values.

We found a very weak positive correlation between Vp and K^{trans} . Both parameters were obtained from the same sequence, so alignment between both maps was perfect. This low correlation suggests that VP and K^{trans} are providing different information.

A very weak positive correlation between CBV and K^{trans} was found. The correlation was weaker than that between Vp and K^{trans} , most likely due to the lack of perfect alignment between CBV and K^{trans} maps. CBV values were obtained from DSC-MR imaging, whereas K^{trans} and Vp were calculated from the same set of dynamic series. In the case of CBV and K^{trans} , automated interpolation and coregistration of maps had to be performed before the analysis. Visual inspection revealed coregistration not completely accurate between K^{trans} and CBV maps, mostly due to spatial distortions resulting from susceptibility effects in the T2*WI acquisition. Haroon et al¹⁶ reported the same problem when trying to correlate CBV derived from T1 and T2* sequences in brain tumors.

Correlation between the 2 estimates of microvascular density (CBV and VP) is also significant and stronger than that between K^{trans} and CBV and K^{trans} and VP. Figure 4 shows an area in the posterior aspect of the tumor showing high CBV and VP values but not particularly elevated K^{trans} values. Such a low correlation ($\rho = 0.382$) for 2 parameters, Vp and CBV, which are supposed to provide the same physiologic information (microvessel density), is somewhat surprising. This may be partially explained by slight spatial misregistration as discussed above. Another phenomenon that can account for this low correlation is microscopic hemosiderin deposition, which is known to be present in high-grade gliomas and cause signal loss in T2* sequences. Although areas of blooming and voxels with very low values were excluded, small effects from microscopic hemosiderin would still be present. Another difference inherent in the techniques that could account for the low correlation is blooming on DSC-MR imaging. The T2* approach relies on dephasing of the protons within a voxel caused by the intravascular contrast, but the dephasing effect extends to surrounding voxels as well. T1 shortening caused by intravascular contrast on DCE-MR imaging does not extend to surrounding voxels to the same extent.

Few studies correlating K^{trans} and blood volume in brain tumors have been published, and most take for granted that K^{trans} represents permeability. Tofts et al⁷ argue that in the brain, K^{trans} depends on both the leakiness of the vessels and the total surface

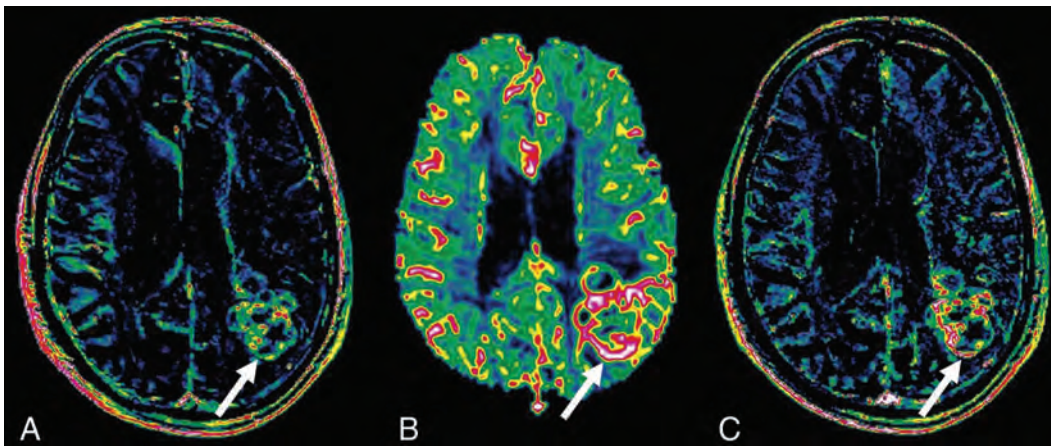


FIG 4. K^{trans} (A), CBV (B), and Vp (C) maps through the center of a grade IV glioma. The arrow points toward an area in the posterior aspect of the tumor showing high CBV and Vp values but only mildly elevated K^{trans} values.

of leaky capillaries, but the contribution of each factor to the K^{trans} value is unknown. Estimates of blood volume cannot be used directly as surrogate markers for the surface area of the vessels because it also depends on the diameter of the vessels, which is unknown. Two different tissues may have the same blood volume but different endothelial surface area, depending on the size of the vessels. Thinner but more numerous vessels have higher surface than a smaller number of larger vessels even if the blood volume is the same. Therefore, we cannot reliably conclude that K^{trans} is entirely reflecting permeability, but at least we can tell that it is providing different information than estimates of microvessel density.

Correlation studies between K^{trans} and CBV have been performed before but never, to our knowledge, on a pixel-by-pixel basis. In a small study including 12 patients with high-grade gliomas, Provenzale et al⁹ reported a high correlation between CBV obtained from DSC-MR imaging and maximal enhancement from DCE-MR imaging ($\rho = 0.794$, $P < .001$). They did not assess K^{trans} but instead measured an indirect expression of K^{trans} , the degree of contrast enhancement using the maximum signal-intensity algorithm. They did not compare parameters from the same tumor region but compared the region with the highest CBV values and the region with the highest “maximal enhancement” values. Patankar et al³ compared maximal values of CBV and K^{trans} obtained from a DCE-MR imaging study in 39 patients and found a high correlation ($\rho = 0.688$, $P < .001$). In a larger study including 73 subjects, Law et al⁸ found a weak-but-positive correlation between K^{trans} and CBV with a ρ of 0.266. In this case, both parameters were obtained from the same DSC sequence by using a first-pass pharmacokinetic model. Again parameters were not extracted from the same tumor region. They actually pointed out that the regions of maximal CBV elevation did not directly correspond to the regions of maximal K^{trans} . In our study K^{trans} , Vp, and CBV values used for comparison were extracted from the same tumor areas.

Our results provide important information regarding imaging biomarkers of angiogenesis in high-grade gliomas. A deep understanding of the physiologic significance of the parameters obtained with DCE and DSC perfusion is very important because both techniques are used in the assessment of antiangiogenic ther-

apies^{17,18} and in the differentiation between posttreatment changes and recurrent tumor.¹⁹⁻²² The assessment of the blood-brain barrier has also gained importance because it provides valuable information regarding brain drug penetration. New therapies have emerged, such as focused sonography, that cause a temporary increase of blood-brain barrier permeability to maximize the delivery of chemotherapy within the brain tumor.²³ Our results confirm that K^{trans} and CBV provide very different information, suggesting that it would be worthwhile to perform both DSC- and DCE-MR imaging studies in the setting of gliomas on a routine basis.

One of the main limitations of this study is the lack of T1 mapping for the calculation of contrast concentration in tissue. Our protocol did not include precontrast T1 sequences for T1 mapping calculation, so a fixed baseline T1 value had to be used for K^{trans} calculation. Some studies have shown K^{trans} estimates to vary on the basis of native T1 values²⁴; however, others have used assumptions similar to those used in this study (fixed T1 value), assuming that this is a minor limitation.²⁵ Another limitation is the inaccurate alignment of maps obtained from DCE-MR imaging (Vp and K^{trans}) and DSC-MR imaging (CBV). This misalignment problem leads to an artifactual decrease in the correlation between CBV and K^{trans} values and between CBV and Vp. Misregistration may be causing a decrease in the values of the correlation coefficients but not in all cases because Vp and K^{trans} maps are obtained from the same sequence, so alignment is perfect between these maps. A fact that is proving the reliability of the results is that the correlation between CBV and Vp is higher than that between K^{trans} and the estimates of microvessel attenuation (CBV and Vp), even though CBV and Vp are obtained from different sequences and therefore subject to misregistration. The correlation between CBV and Vp is higher as expected because both parameters have the same physiologic meaning. The temporal resolution used in our DSC-MR imaging studies (2.9 seconds) is lower than the recommended <1.5 seconds.²⁶ This difference may cause a decrease in the accuracy of the CBV estimation.

CONCLUSIONS

The finding of only weak correlation between estimates of blood volume (Vp and CBV) and K^{trans} suggests that they provide dif-

ferent physiologic information and that a protocol combining DCE- and DSC-MR imaging may provide complementary information in the imaging work-up of high-grade tumors. Estimates of microvascular attenuation derived from DCE-MR imaging tend to be higher than values of CBV obtained by using DSC-MR imaging, most likely due to overestimation caused by leakage.

Disclosures: Paula Alcaide-Leon—RELATED: Grant: Beca “SERAM Industria” de la Sociedad Española de Radiología Médica; UNRELATED: Employment: Novartis,* Comments: currently a Research Fellow in multiple sclerosis at St Michael’s Hospital. This fellowship is funded by Novartis. Alex Rovira—UNRELATED: Consultancy: Novartis, Bayer, Biogen; Payment for Lectures (including service on Speakers Bureaus): Novartis,* Bayer,* Genzyme,* Bracco,* Biogen,* Stendhal*; Payment for Development of Educational Presentations: Novartis,* MS Forum. *Money paid to the institution.

REFERENCES

- Burger PC. Malignant astrocytic neoplasms: classification, pathologic anatomy, and response to treatment. *Semin Oncol* 1986;13:16–26
- Lüdemann L, Warmuth C, Plotkin M, et al. Brain tumor perfusion: comparison of dynamic contrast enhanced magnetic resonance imaging using T1, T2, and T2* contrast, pulsed arterial spin labeling, and H2(15)O positron emission tomography. *Eur J Radiol* 2009;70:465–74
- Patankar TF, Haroon HA, Mills SJ, et al. Is volume transfer coefficient (Ktrans) related to histologic grade in human gliomas? *AJNR Am J Neuroradiol* 2005;26:2455–65
- Mills SJ, Patankar TA, Haroon HA, et al. Do cerebral blood volume and contrast transfer coefficient predict prognosis in human glioma? *AJNR Am J Neuroradiol* 2006;27:853–58
- Bisdas S, Kirkpatrick M, Giglio P, et al. Cerebral blood volume measurements by perfusion-weighted MR imaging in gliomas: ready for prime time in predicting short-term outcome and recurrent disease? *AJNR Am J Neuroradiol* 2009;30:681–88
- Cao Y, Tsien CL, Nagesh V, et al. Survival prediction in high-grade gliomas by MRI perfusion before and during early stage of RT [corrected]. *Int J Radiat Oncol Biol Phys* 2006;64:876–85
- Tofts PS, Brix G, Buckley DL, et al. Estimating kinetic parameters from dynamic contrast-enhanced T(1)-weighted MRI of a diffusible tracer: standardized quantities and symbols. *J Magn Reson Imaging* 1999;10:223–32
- Law M, Yang S, Babb JS, et al. Comparison of cerebral blood volume and vascular permeability from dynamic susceptibility contrast-enhanced perfusion MR imaging with glioma grade. *AJNR Am J Neuroradiol* 2004;25:746–55
- Provenzale JM, York G, Moya MG, et al. Correlation of relative permeability and relative cerebral blood volume in high-grade cerebral neoplasms. *AJR Am J Roentgenol* 2006;187:1036–42
- Louis DN, Ohgaki H, Wiestler OD, et al. The 2007 WHO classification of tumours of the central nervous system. *Acta Neuropathol* 2007;114:97–109
- Paulson ES, Schmainda KM. Comparison of dynamic susceptibility-weighted contrast-enhanced MR methods: recommendations for measuring relative cerebral blood volume in brain tumors. *Radiology* 2008;249:601–13
- Boxerman JL, Schmainda KM, Weisskoff RM. Relative cerebral blood volume maps corrected for contrast agent extravasation significantly correlate with glioma tumor grade, whereas uncorrected maps do not. *AJNR Am J Neuroradiol* 2006;27:859–67
- Wells WM 3rd, Viola P, Atsumi H, et al. Multi-modal volume registration by maximization of mutual information. *Med Image Anal* 1996;1:35–51
- Aronen HJ, Gazit IE, Louis DN, et al. Cerebral blood volume maps of gliomas: comparison with tumor grade and histologic findings. *Radiology* 1994;191:41–51
- Bruening R, Kwong KK, Vevea MJ, et al. Echo-planar MR determination of relative cerebral blood volume in human brain tumors: T1 versus T2 weighting. *AJNR Am J Neuroradiol* 1996;17:831–40
- Haroon HA, Patankar TF, Zhu XP, et al. Comparison of cerebral blood volume maps generated from T2* and T1 weighted MRI data in intra-axial cerebral tumours. *Br J Radiol* 2007;80:161–68
- Jalali S, Chung C, Foltz W, et al. MRI biomarkers identify the differential response of glioblastoma multiforme to anti-angiogenic therapy. *Neuro Oncol* 2014;16:868–79
- Sorensen AG, Batchelor TT, Zhang WT, et al. A “vascular normalization index” as potential mechanistic biomarker to predict survival after a single dose of cediranib in recurrent glioblastoma patients. *Cancer Res* 2009;69:5296–300
- Fatterpekar GM, Galheigo D, Narayana A, et al. Treatment-related change versus tumor recurrence in high-grade gliomas: a diagnostic conundrum—use of dynamic susceptibility contrast-enhanced (DSC) perfusion MRI. *AJR Am J Roentgenol* 2012;198:19–26
- Shin KE, Ahn KJ, Choi HS, et al. DCE and DSC MR perfusion imaging in the differentiation of recurrent tumour from treatment-related changes in patients with glioma. *Clin Radiol* 2014;69:e264–72
- Sugahara T, Korogi Y, Tomiguchi S, et al. Post-therapeutic intra-axial brain tumor: the value of perfusion-sensitive contrast-enhanced MR imaging for differentiating tumor recurrence from nonneoplastic contrast-enhancing tissue. *AJNR Am J Neuroradiol* 2000;21:901–09
- Mangla R, Singh G, Ziegelitz D, et al. Changes in relative cerebral blood volume 1 month after radiation-temozolomide therapy can help predict overall survival in patients with glioblastoma. *Radiology* 2010;256:575–84
- Yang FY, Ko CE, Huang SY, et al. Pharmacokinetic changes induced by focused ultrasound in glioma-bearing rats as measured by dynamic contrast-enhanced MRI. *PLoS One* 2014;9:e92910
- Guo JY, Reddick WE, Rosen MA, et al. Dynamic contrast-enhanced magnetic resonance imaging parameters independent of baseline T10 values. *Magn Reson Imaging* 2009;27:1208–15
- Jung SC, Yeom JA, Kim JH, et al. Glioma: application of histogram analysis of pharmacokinetic parameters from T1-weighted dynamic contrast-enhanced MR imaging to tumor grading. *AJNR Am J Neuroradiol* 2014;35:1103–10
- Essig M, Shiroishi MS, Nguyen TB, et al. Perfusion MRI: the five most frequently asked technical questions. *AJR Am J Roentgenol* 2013;200:24–34

Diffusion and Perfusion MRI to Differentiate Treatment-Related Changes Including Pseudoprogression from Recurrent Tumors in High-Grade Gliomas with Histopathologic Evidence

A.J. Prager, N. Martinez, K. Beal, A. Omuro, Z. Zhang, and R.J. Young



ABSTRACT

BACKGROUND AND PURPOSE: Treatment-related changes and recurrent tumors often have overlapping features on conventional MR imaging. The purpose of this study was to assess the utility of DWI and DSC perfusion imaging alone and in combination to differentiate treatment-related effects and recurrent high-grade gliomas.

MATERIALS AND METHODS: We retrospectively identified 68 consecutive patients with high-grade gliomas treated by surgical resection followed by radiation therapy and temozolomide, who then developed increasing enhancing lesions indeterminate for treatment-related changes versus recurrent tumor. All lesions were diagnosed by histopathology at repeat surgical resection. ROI analysis was performed of the enhancing lesion on the ADC and DSC maps. Measurements made by a 2D ROI of the enhancing lesion on a single slice were recorded as ADC_{Lesion} and $rCBV_{\text{Lesion}}$, and measurements made by the most abnormal small fixed diameter ROI as ADC_{ROI} and $rCBV_{\text{ROI}}$. Statistical analysis was performed with Wilcoxon rank sum tests with $P = .05$.

RESULTS: Ten of the 68 patients (14.7%) had treatment-related changes, while 58 patients (85.3%) had recurrent tumor only ($n = 19$) or recurrent tumor mixed with treatment effect ($n = 39$). DWI analysis showed higher ADC_{Lesion} in treatment-related changes than in recurrent tumor ($P = .003$). DSC analysis revealed lower relative cerebral blood volume ($rCBV_{\text{Lesion}}$ and $rCBV_{\text{ROI}}$ in treatment-related changes ($P = .003$ and $P = .011$, respectively). Subanalysis of patients with suspected pseudoprogression also revealed higher ADC_{Lesion} ($P = .001$) and lower $rCBV_{\text{Lesion}}$ ($P = .028$) and $rCBV_{\text{ROI}}$ ($P = .032$) in treatment-related changes. Applying a combined ADC_{Lesion} and $rCBV_{\text{Lesion}}$ model did not outperform either the ADC or rCBV metric alone.

CONCLUSIONS: Treatment-related changes showed higher diffusion and lower perfusion than recurrent tumor. Similar correlations were found for patients with suspected pseudoprogression.

ABBREVIATIONS: AUC = area under the curve; HGG = high-grade glioma; HR = hazard ratio; NL = normal contralateral white matter; MGMT = O6-methylguanine-DNA methyltransferase; PSR = percentage signal recovery; rCBV = relative cerebral blood volume; ROC = receiver operating characteristic; RT = radiation therapy

Differentiating treatment-related changes from recurrent tumor in treated patients with high-grade glioma (HGG) remains challenging due to overlapping clinical and radiologic features. Both may present with new and/or increasing enhancing mass

lesions and fulfill standard response criteria for progression.¹ Radiation therapy (RT) and chemotherapy can increase capillary permeability and alter the blood-brain barrier, leading to increased leakiness of contrast agent and increased contrast enhancement in the absence of tumor.^{2,3} At histopathology, these treatment-related changes are characterized by vascular dilation, fibrinoid necrosis, and endothelial damage of normal cerebral vasculature.⁴ In contrast, recurrent tumors are characterized by the presence of tumor cells, increased cellularity, and vascular proliferation.⁵⁻⁷

Treatment-related changes may be clinically separated into early pseudoprogression and late radiation necrosis on the basis of timing. Pseudoprogression usually develops <6 months after RT with self-limited enhancing lesions that spontaneously stabilize and resolve without any new treatment. Patients who develop pseudoprogression have been described as having improved survival,^{3,8-10} due to favorable correlation with methylated O6-methylguanine-DNA methyltransferase (MGMT) promoter sta-

Received August 23, 2014; accepted after revision October 20.

From the Departments of Radiology (A.J.P., R.J.Y.), Neurology (N.M., A.O.), Radiation Oncology (K.B.), Epidemiology and Biostatistics (Z.Z.), and the Brain Tumor Center (K.B., A.O., R.J.Y.), Memorial Sloan Kettering Cancer Center, New York, New York.

This work was supported by a Department of Radiology Seed Grant, Memorial Sloan Kettering Cancer Center (R.J.Y.); the Summer Medical Student Fellowship, Memorial Sloan Kettering Cancer Center (A.J.P.); and the Memorial Sloan Kettering Cancer Center Epidemiology and Biostatistics Core (P30 CA008748).

Paper previously presented at: Annual Meeting of the American Society of Neuro-radiology, May 18–23, 2013; San Diego, California.

Please address correspondence to Robert J. Young, MD, Department of Radiology, Memorial Sloan Kettering Cancer Center, 1275 York Ave, New York, NY 10065; e-mail: youngr@mskcc.org

Indicates open access to non-subscribers at www.ajnr.org

<http://dx.doi.org/10.3174/ajnr.A4218>

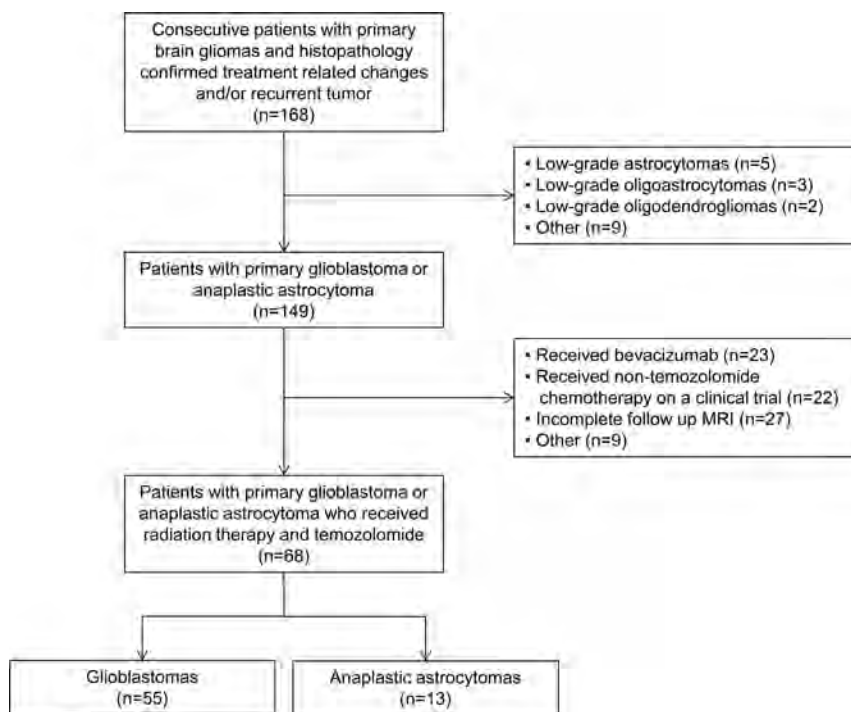


FIG 1. Description of patient cohort.

tus.¹¹ In contrast, radiation necrosis usually occurs >12–18 months after RT, with progressive enhancing lesions that are associated with worsened morbidity. Although pseudoprogression and radiation necrosis are thought to represent distinct clinical and pathophysiologic mechanisms,¹¹ they share many histologic similarities such as inflammatory infiltrates and necrosis, which translate into similar imaging characteristics.⁹

Diffusion and perfusion MR imaging provide physiologic information that is not available with conventional MR imaging. DWI measures the motility of water molecules and alterations in the balance of intracellular and extracellular water restricted by cell membranes and other structures.¹² Areas of diffusion restriction in tumors are correlated with increased tumor cellularity and/or inflammatory processes. DSC MR imaging perfusion is a complementary technique that provides independent information on neoangiogenesis, vascular attenuation, and microvascular leakiness.^{2,13} While both techniques have been examined individually in patients with suspected treatment-related changes, few studies have examined the utility of combining these 2 techniques. The purpose of this study was to assess the utility of DWI and DSC perfusion imaging in differentiating treatment-related changes and recurrent tumor. We hypothesized that the combination of DWI and DSC predictors would improve diagnostic accuracy over either alone.

MATERIALS AND METHODS

Patients

This retrospective study was granted a waiver of informed consent by the hospital institutional review board. In compliance with all Health Insurance Portability and Accountability Act regulations, we queried a hospital data base for patients with histopathologic evidence of HGG according to revised World Health Organization criteria. As summarized in Fig 1, the final patient cohort

consisted of 68 consecutive patients with HGG according to the following inclusion criteria: 1) diagnosis of primary glioblastoma or anaplastic astrocytoma, 2) treatment with RT and temozolomide (Temodar), 3) new and/or increasing enhancing mass lesions at follow-up MR imaging suspicious for treatment-related changes versus recurrent tumor, and 4) brain MR imaging, including contrast T1-weighted imaging with DWI and/or DSC perfusion, ≤ 35 days before subsequent resection of the enhancing mass lesion.

The 68 patients consisted of 51 men (75%) and 17 women (25%) with a median age of 54.9 years (range, 22.6–79.4 years). Chart review was performed by an experienced neuro-oncologist blinded to the DWI and DSC results. At initial diagnosis, patients underwent gross total resection of all enhancing tumors ($n = 41$, 60.3%), subtotal resection of the enhancing tumors ($n = 24$, 35.3%), or biopsy ($n = 3$, 4.4%). When available, MGMT promoter status was determined by review of results from real-time polymerase chain reaction amplification. Most patients ($n = 66$, 97.1%) received partial brain RT to 5940–6000 cGy in 30–33 fractions during 6 weeks. In 2 patients (2.9%), partial brain RT was administered to 4005 cGy in 15 fractions during 3 weeks, which is an equivalent alternative for the elderly or patients with deconditioning.¹⁴ All patients except 1 received concomitant temozolomide, and all patients received adjuvant temozolomide at standard ($n = 62$, 91.2%) or alternative doses according to an ongoing clinical trial ($n = 6$, 8.8%).¹⁵ Patients were followed to determine overall survival.

Lesion Diagnosis

In each case, the lesion diagnosis was determined by histopathology at repeat surgical resection. Treatment-related changes were defined as necrotizing treatment effects with the complete absence of tumor. Recurrent tumor was defined as any amount of tumor (ie, pure tumor and tumor admixed with necrotizing treatment effects).

MR Imaging Parameters

MR images were obtained by using 1.5T and 3T magnets (Signa Excite and Discovery 750; GE Healthcare, Milwaukee, Wisconsin). In addition to the DWI and DSC parameters described below, standard T1-weighted, T2-weighted, FLAIR, and triplanar contrast T1-weighted images were obtained. A trained operator (with 2 years' experience in MR imaging postprocessing) blinded to clinical status (eg, symptomatic or asymptomatic) and lesion diagnosis performed DWI and DSC analysis under the direct supervision of a board-certified radiologist with a Certificate of Added Qualification in neuroradiology (with 14 years' experience).

DWI

DWI was performed by using single-shot echo-planar imaging with b -values = 0 and 1000 s/mm². The DWI data were transferred along with the anatomic data to an off-line workstation (Advantage Workstation; GE Healthcare) and were analyzed by using commercial software (FuncTool 4.6; GE Healthcare). ADC maps were calculated, coregistered with the axial contrast T1-weighted images, and then displayed as overlays. The contrast images were inspected, and the section containing the maximum diameter of the enhancing lesion was selected for subsequent ROI analysis. We manually drew a 2D-ROI around the entire enhancing lesion on a single section, while excluding blood vessels and areas of hemorrhagic, cystic, and/or necrotic-appearing change. The ROI was transferred to the ADC map, and the mean value was recorded as ADC_{Lesion}. In addition, up to 4 small circular ROIs (approximately 0.5 mm²) were manually drawn in the enhancing lesion on the same contrast section, transferred to the ADC map, and adjusted as necessary to target areas with visually low ADC values; the single minimum ADC measurement was recorded as ADC_{ROI}. This technique has been described as the most accurate and reproducible way to obtain ROI-based measurements.¹⁶⁻¹⁸ The ADC_{Ratio} was calculated by dividing the ADC_{ROI} by the ADC_{normal contralateral white matter (NL)} obtained from measuring a similar small circular ROI in the contralateral normal brain.

DSC

DSC was performed by using gradient-echo echo-planar images with TR = 1000–1200 ms, TE = 40–50 ms, matrix = 128 × 128, flip angle = 60°, section thickness = 5 mm, intersection gap = 0, sections = 12–18. Multisection image data were acquired every second for a total of 60 seconds with the contrast injection beginning at 10 seconds. Gadopentetate dimeglumine (Magnevist; Bayer HealthCare Pharmaceuticals, Wayne, New Jersey) was power-injected through a peripheral intravenous catheter at doses standardized by patient body weight (0.2 mL/kg body weight, to a maximum of 20 mL) at 2–5 mL/s and immediately followed by a 20-mL saline flush at the same rate. No preload contrast was administered.

The DSC data were transferred along with the anatomic data to an off-line workstation (Advantage Workstation) and were analyzed by using commercial software (FuncTool 4.6). T2*-weighted signal intensity–time curves were derived on a voxel-by-voxel basis. Post hoc correction for leakage was performed by using γ -variate curve fitting to approximate the curve without recirculation and leakage.¹⁹ Cerebral blood volume maps were calculated, coregistered with the contrast T1-weighted images, and displayed as overlays. ROI analysis for CBV was performed in a manner similar to that of ADC. A single contrast section containing the maximum diameter of the enhancing lesion was selected, and an ROI was drawn around the entire enhancing lesion. Areas of hemorrhage, blood vessels, susceptibility artifacts, and cystic or necrotic change were excluded. The control CBV_{NL} was initially placed in the normal white matter contralateral to the enhancing lesion. The relative CBV of the lesion (rCBV_{Lesion}) was calculated by dividing the CBV_{Lesion}, drawn around the entire

enhancing lesion on a single section, by the CBV_{NL}. Next, 4 small (approximately 0.5 mm²) circular ROIs were drawn in the enhancing lesion, transferred to the CBV map, adjusted as necessary to target the areas with the visually highest CBV, and the ROI with the maximal CBV abnormality was measured and selected as the CBV_{ROI}. The location of the small ROI for CBV was often the same as the location of the small ROI for ADC because the 2 were placed to target different biologic processes. The CBV_{ROI} was divided by the CBV_{NL} to yield the relative CBV_{ROI} (rCBV_{ROI}). The signal intensity–time curve of the CBV_{ROI} was also used to determine S_0 = precontrast baseline signal intensity, S_{min} = minimum signal intensity at the peak of contrast bolus, and S_1 = end signal intensity at 60 seconds. These values were then used to calculate the percentage signal recovery (PSR_{ROI}) = $(S_1 - S_{min}) / (S_0 - S_{min})$. PSR_{ROI} is a measure of permeability influenced by leakage of contrast and the size of the extravascular space,²⁰ with lower PSR reflecting higher permeability.

Statistical Analysis

Comparisons between treatment-related change and recurrent tumor groups were performed by using Wilcoxon rank sum tests. Optimal threshold values for ADC_{Lesion} and rCBV_{Lesion} were obtained by area under the curve (AUC) analysis derived from the receiver operating characteristic (ROC) curves and maximizing the sum of sensitivity and specificity. Overall survival analysis was performed by fitting a univariate Cox model to report the hazard ratio (HR) with P values. Multivariate analysis was not performed due to the small number of events (treatment-related changes). Statistical significance was set at $P = .05$.

To specifically examine patients with possible pseudoprogression, we performed an analysis for the subset of patients who developed new and/or increasing enhancing lesions <6 months (<180 days) after completion of RT. Similar Wilcoxon rank sum tests and ROC and AUC analyses were performed.

RESULTS

The cohort consisted of patients with HGG with glioblastoma ($n = 55$, 80.9%) and anaplastic astrocytoma ($n = 13$, 19.1%). MGMT promoter status was known for 31 patients (46%), with more unmethylated ($n = 19$, 61%) than methylated ($n = 12$, 39%) tumors. During follow-up, all patients developed a new and/or increasing enhancing lesion suspicious for recurrent tumor or treatment-related change and underwent repeat surgery. The mean interval from the end of RT to the repeat surgery was 6.1 months (range, 0.4–40.4 months), with patients undergoing gross total resection of the entire enhancing lesion ($n = 38$, 55.9%) or subtotal resection of the enhancing lesion ($n = 30$, 44.1%). Subsequent histopathology revealed treatment-related changes ($n = 10$, 14.7%) or recurrent tumor ($n = 58$; 85.3%, consisting of $n = 19$ tumor only and $n = 39$ tumor admixed with necrotizing treatment effects). Of the patients with treatment-related changes, most had gross total resections ($n = 6$, 60%). Due to evolving MR imaging standards of care during the study period, all 68 patients underwent DWI and most patients ($n = 41$, 60.3%) underwent both DWI and DSC.

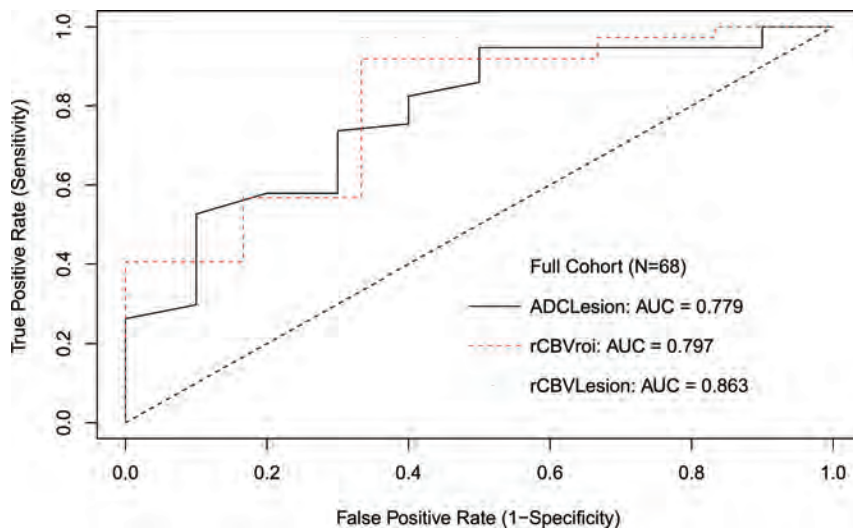


FIG 2. ROC curve for all patients.

Table 1: Diffusion and perfusion results in all patients^a

	Treatment-Related Change (Median)	Recurrent Tumor (Median)	P Value	Survival Analysis	
				HR	P Value
ADC _{Lesion}	0.00159	0.00138	.003 ^b	3.547	.104
ADC _{ROI}	0.0012	0.0011	.13	0.437	.352
ADC _{Ratio}	1.538	1.471	.37	0.515	.283
rCBV _{Lesion}	1.015	1.81	.003 ^b	1.286	.183
rCBV _{ROI}	1.7	2.98	.011 ^b	1.316	.019 ^b
PSR _{ROI}	0.84	0.85	.53	0.204	.036 ^b

^a ADC is reported in mm²/s; rCBV and PSR are unitless.

^b Significant values.

DWI

Diffusion analysis showed higher ADC_{Lesion} in treatment-related change ($P = .003$). An ADC_{Lesion} threshold of ≤ 0.00149 mm²/s to optimize both sensitivity and specificity in declaring tumor had 73.7% sensitivity, 70% specificity, and AUC = 0.779. ADC_{Lesion} ≤ 0.0016 mm²/s had 94.7% sensitivity and 50% specificity to maximize sensitivity for tumor, while ADC_{Lesion} ≤ 0.00139 mm²/s had 52.6% sensitivity and 90% specificity to maximize specificity. ROC curves are shown in Fig 2.

DSC

For perfusion, both rCBV_{Lesion} ($P = .003$) and rCBV_{ROI} ($P = .011$) were lower in treatment-related change. An optimized rCBV_{Lesion} threshold of ≥ 1.27 had 86.5% sensitivity and 83.3% specificity with AUC = 0.863 to declare tumor. This AUC was not significantly better than the best AUC derived from DWI, with $P = .36$. With a commonly applied threshold ≥ 1.75 ,^{9,21,22} rCBV_{Lesion} had 56.8% sensitivity and 83.3% specificity. An optimized rCBV_{ROI} of ≥ 1.74 showed 91.9% sensitivity and 66.7% specificity with AUC = 0.797. Results are summarized in Table 1 and Fig 3.

DWI and DSC

An analysis was performed for the subset of patients ($n = 41$) with both DWI and DSC data. Using ADC_{Lesion} ≤ 0.00149 mm²/s and rCBV_{Lesion} ≥ 1.27 to predict recurrent tumor, we found 51.2% sensitivity (21/41 recurrent tumors correctly identified) and 100% specificity (8/8 treatment-related changes correctly identified).

fied). This combined model was not significantly better than rCBV_{Lesion} alone.

Pseudoprogession

For patients ($n = 51$) who developed worsening lesions <6 months after RT, histopathology revealed pseudoprogession in 8 (15.7%) patients and recurrent tumor in 43 (84.3%) patients. Due to low numbers of known MGMT status ($n = 21/51$, 41.2%), particularly in the pseudoprogession group ($n = 3$), further stratification by MGMT status was not performed.

All patients had DWI available for analysis, and most ($n = 33$, 64.7%) had both DWI and DSC available, though only half of the patients with pseudoprogession ($n = 4$) had DSC. For DWI,

ADC_{Lesion} was higher in pseudoprogession ($P = .001$), while ADC_{ROI} and ADC_{Ratio} were not different ($P > .12$). The ADC_{Lesion} had an AUC of 0.839, and a threshold of >0.0016 mm²/s showed 63% specificity and 95% sensitivity. Results are summarized in Table 2 and Fig 4, and ROC curves are shown in Fig 5.

For DSC, rCBV_{Lesion} ($P = .028$) and rCBV_{ROI} ($P = .032$) were lower for pseudoprogession. The AUC for rCBV_{Lesion} was 0.804, and for rCBV_{ROI} it was 0.795. The best threshold for rCBV_{Lesion} to predict pseudoprogession was <1.07 with 75% specificity and 100% sensitivity, and for rCBV_{ROI} it was <1.74 with 75% specificity and 92.9% sensitivity.

A subanalysis was performed to evaluate a combined DWI and DSC model for the patients at risk for pseudoprogession. When using ADC_{Lesion} ≤ 0.0016 and rCBV_{Lesion} ≥ 1.07 to predict recurrent tumor, we found 93.1% sensitivity (21/41 recurrent tumors correctly identified) and 83.3% specificity (5/6 treatment-related changes correctly identified). This finding was not significantly better than rCBV_{Lesion} alone. Representative T1-weighted imaging, DWI, ADC maps, and rCBV maps for pseudoprogession and recurrent tumors are shown in Figs 6 and 7.

Survival

For all patients, the predictors of overall survival were rCBV_{ROI} (HR = 1.32, $P = .019$) and PSR_{ROI} (HR = 0.204, $P = .036$). For the subset of patients with suspected pseudoprogession presenting with enhancing lesions <6 months after completing RT, the predictors of overall survival were ADC_{Lesion} (HR = 5.563, $P = .047$), rCBV_{ROI} (HR = 1.557, $P = .009$), and PSR_{ROI} (HR = 0.166, $P = .04$). The other diffusion and perfusion metrics were not significant ($P > .10$).

DISCUSSION

We found higher diffusion and lower perfusion values in treatment-related changes than in recurrent tumor in patients with HGGs as confirmed by histopathology. These results probably reflect the lower cellularity and vascularity of treatment-related changes, respectively, and suggest that DWI and DSC are useful tools in discriminating treatment-related changes from recurrent

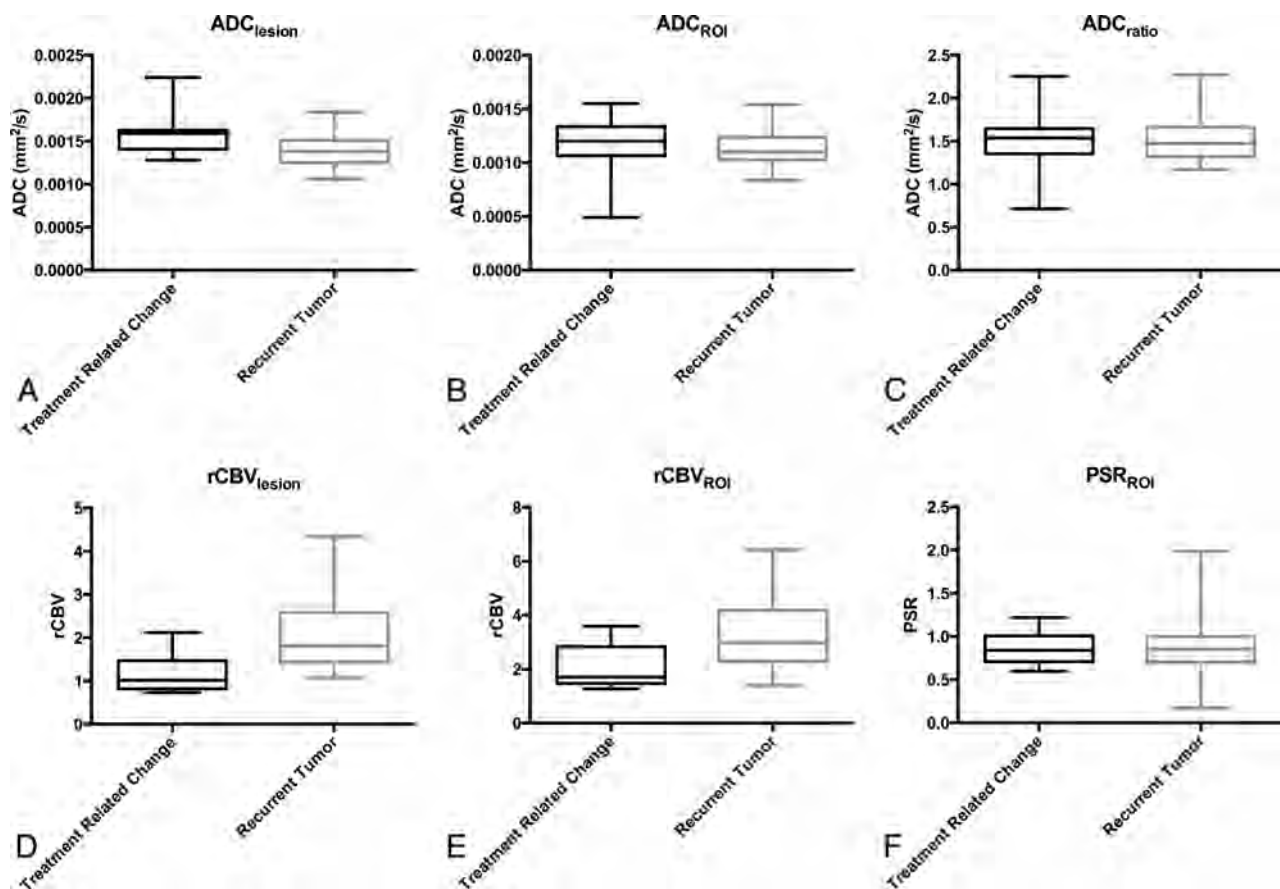


FIG 3. Box-and-whisker plots for parameters in Table 1.

Table 2: Diffusion and perfusion results in patients < 6 months from RT^a

	Treatment-Related Change (Median)	Recurrent Tumor		Survival Analysis	
		(Median)	P Value	HR	P Value
ADC _{Lesion}	0.00162	0.00139	.001 ^b	5.563	.047 ^b
ADC _{ROI}	0.0012	0.0011	.128	0.653	.651
ADC _{Ratio}	1.585	1.482	.288	0.703	.595
rCBV _{Lesion}	0.88	1.76	.028 ^b	1.382	.233
rCBV _{ROI}	1.625	2.575	.032 ^b	1.563	.009 ^b
PSR _{ROI}	0.80	0.87	.467	0.166	.040 ^b

^a ADC is reported in mm²/s; rCBV and PSR are unitless.

^b Significant values.

tumor. DSC outperformed DWI in predicting treatment-related changes, while the combination of DSC and DWI yielded higher specificity at the expense of lowered sensitivity.

DWI has been shown to be helpful in determining treatment response, with several studies describing higher mean ADC values or ADC ratios than those in recurrent tumors.^{12,23} Other articles have applied ADC histogram analysis²⁴ and 3-layer patterns of ADC analysis,²⁵ though these techniques are not commercially available and have not been incorporated into clinical practice. ADC may be decreased with treatment-related changes, possibly due to cellular inflammatory factors and abundant polymorphonuclear lymphocytes.^{23,25} Our results suggest that these inflammatory-related decreases in ADC are less marked than those that occur in recurrent tumors due to high cellularity.

DSC has also been described as useful for distinguishing treat-

ment-related changes from recurrent tumor.^{9,26-28} Alterations in perfusion parameters may occur due to inflammation and vascular changes, including vascular elongation, aneurysmal formation, and proliferation of endothelial cells in response to radiation injury. In patients with glioblastoma with suspected radiation necrosis at a mean of >300 days after RT, Barajas et al²⁶ found lower rCBV ($P < .01$) and higher PSR ($P < .05$) in the necrosis group. In patients with glioblastoma with suspected pseudoprogression at a mean of 133 days after RT, Young et al⁹ reported similar results with lower rCBV ($P = .009$) and higher PSR ($P = .039$). These studies indicate that despite possible differences in the underlying pathophysiologic processes for early pseudoprogression and late radiation necrosis and the very different clinical courses and implications, the 2 entities share common imaging features along a spectrum of treatment-related changes—and that similarities on conventional scans may also translate into similarities on advanced MR imaging by using DSC as well as DWI.

Few studies have examined the combination of DWI and DSC imaging for distinguishing treatment-related changes and recurrent tumor. In 38 patients with primary brain tumor, Fink et al²⁹ reported that rCBV (AUC = 0.917, $P < .001$) outperformed ADC_{Ratio} (AUC = 0.726, $P = .035$) in determining postradiation injury. Patients in their study had a mix of HGGs ($n = 20$) and low-grade gliomas ($n = 17$) as well as an ependymoma, however, who received a variety of chemotherapy agents and inconsistently underwent RT ($n = 6$, no RT). In addition, their median interval for clinical and radiological follow-up was 17.6 months with a

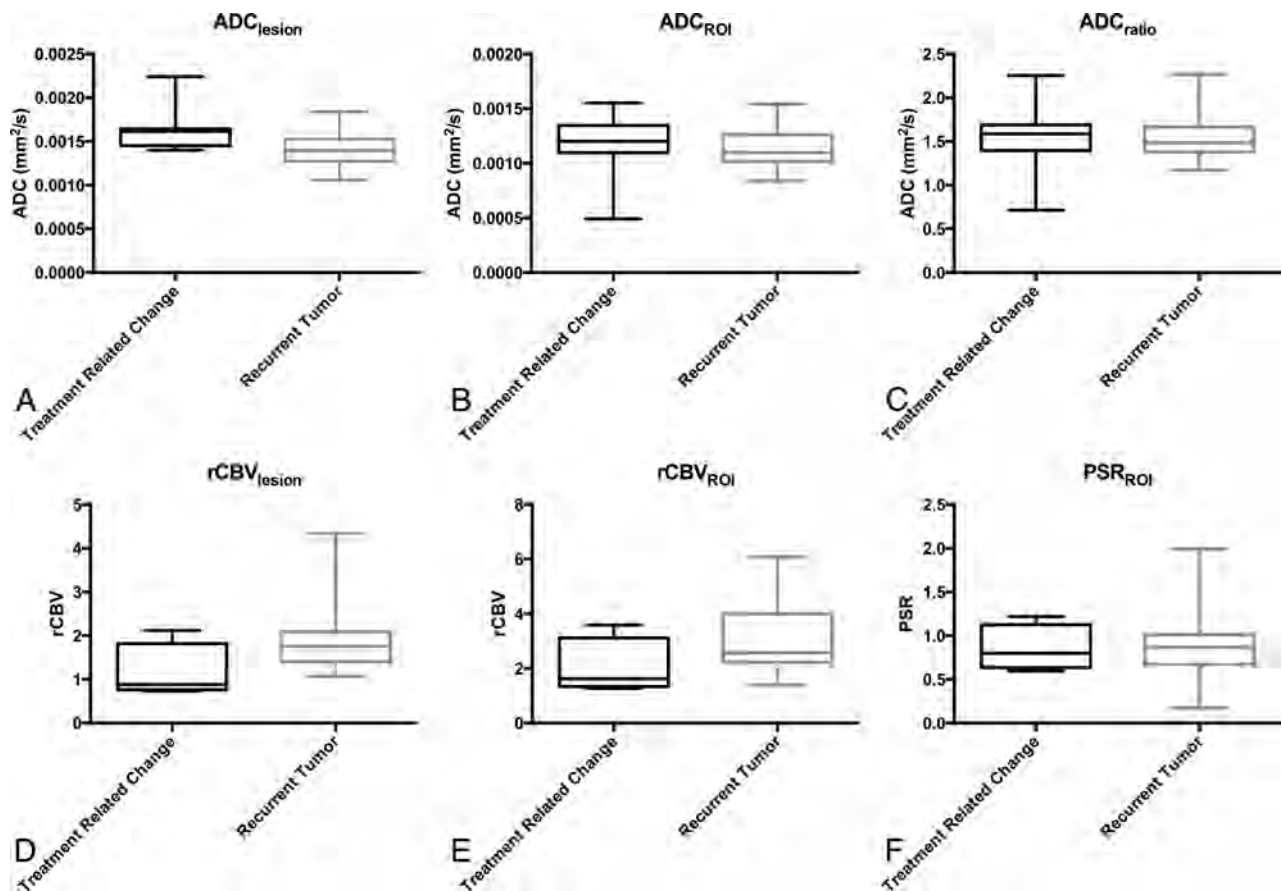


FIG 4. Box-and-whisker plots for parameters in Table 2.

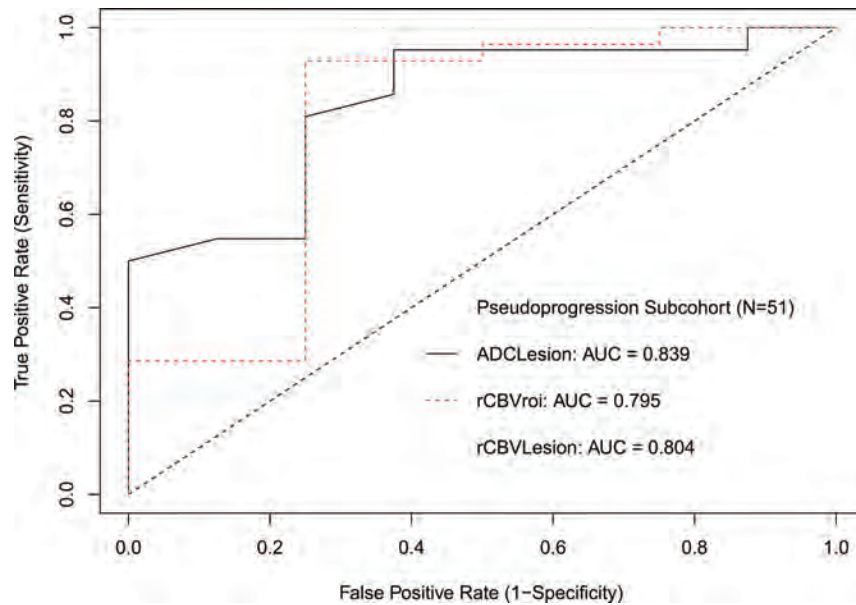


FIG 5. ROC curve for patients <6 months after RT.

wide range (1.2–164.5 months), and only 35% were confirmed by histopathology. A small study of 8 patients with glioma ($n = 7$, HGG) by Bobek-Billewicz et al,³⁰ also reported lower rCBV in radiation injury (median, 13 months; range, 3–70 months) with insignificant results for ADC probably due to their small cohort.

We used histopathology as the reference standard against

which the imaging results were tested. Because all patients in this study underwent gross total or subtotal resections rather than biopsies, the likelihood of sampling error was lessened. The power of our study may have been affected by the fewer patients (14.7%) determined to have treatment-related changes at repeat surgery. This number probably reflects our definition of recurrent tumor as any amount of tumor at histopathologic analysis, with treatment-related changes having a relatively conservative definition as the complete absence of any identifiable tumor. We did not attempt to stratify by fraction of tumor versus fraction of treatment-related changes because there is no standard definition of how little tumor is permissible to diagnose treatment-related changes rather than recurrent tumor. We also did not attempt to distinguish

active (eg, mitotic figures, vascular proliferation, necrosis with pseudopalisading) and inactive (ie, quiescent) tumor. The literature definition of treatment-related changes is inconsistently described as “necrosis without evidence of tumor,”³¹ “pure treatment-related necrosis,”³² “ $\leq 20\%$. . . neoplasm,”²⁷ “no to minimal identifiable tumor,”¹⁰ “ $< 1\%$ viable tumor,”²⁰ or simply

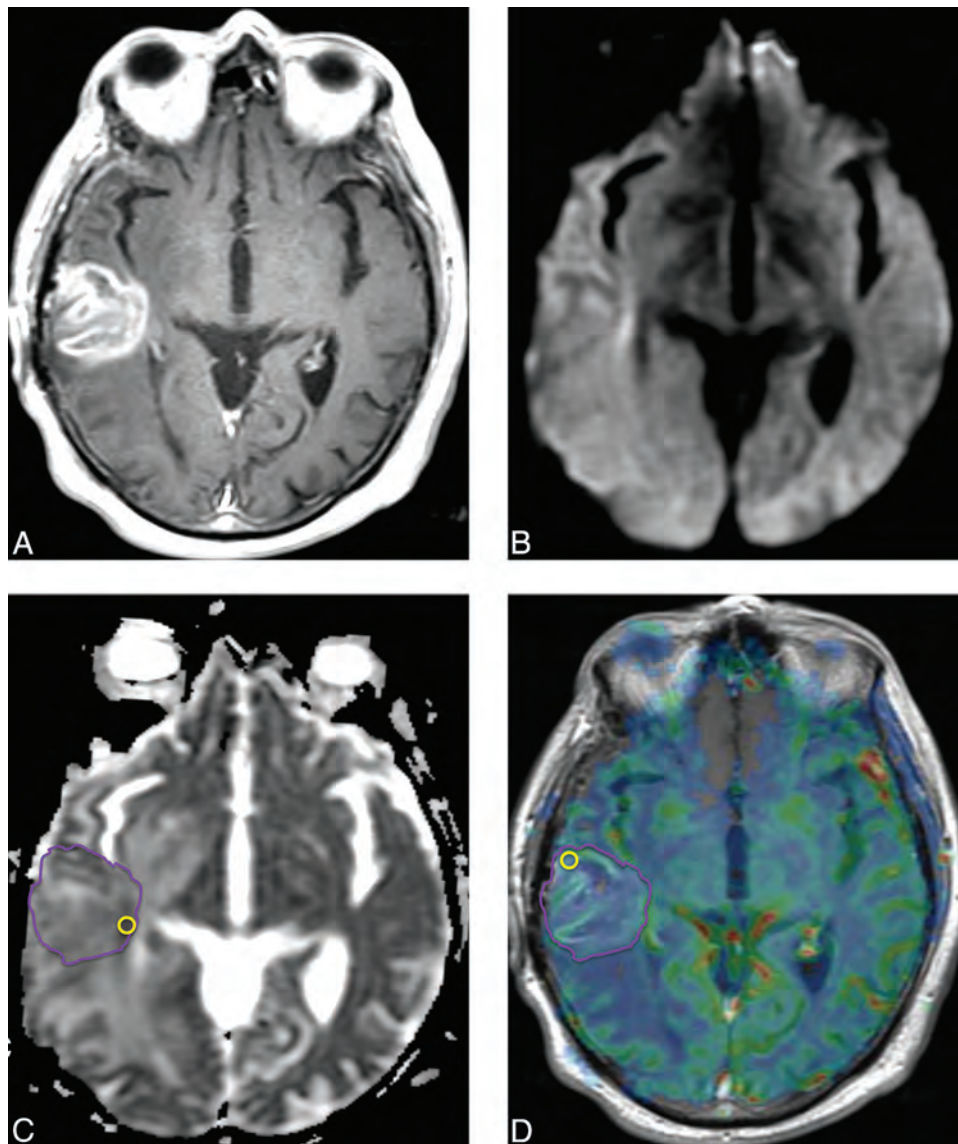


FIG 6. Pseudoprogression. Six months following RT with concomitant and adjuvant temozolomide, this patient with glioblastoma developed a new heterogeneously enhancing mass lesion in the right posterior temporal lobe on a contrast T1-weighted image (A) with no diffusion restriction on DWI (B) or ADC (C). $ADC_{\text{Lesion}} = 0.00142 \text{ mm}^2/\text{s}$. An rCBV map overlaid on a contrast T1-weighted image (D) shows no increase in perfusion. $rCBV_{\text{Lesion}} = 1.41$. Repeat surgery confirmed treatment-related changes.

“at pathologic analysis.”³³ Despite these limitations, histopathology remains the reference standard and is often considered preferable to clinical and radiologic definitions, which are more subjective and influenced by patient signs, symptoms, medications, and follow-up.

Both DWI and DSC may be useful in differentiating treatment-related changes from recurrent tumor, with DSC performing slightly better as a predictor. We found increased specificity when both ADC_{Lesion} and $rCBV_{\text{ROI}}$ were applied in a combined model for all patients, though the increase in specificity (100%) was accompanied by a decrease in sensitivity (51%). While the clinical dilemma is usually to accurately identify treatment-related changes, for which the high specificity should be helpful, the decrease in sensitivity for only an incremental increase in specificity limits the usefulness of combining the 2 metrics. For the subgroup of patients at <6 months after RT at risk for pseudoprogression, the specificity and sensitivity when using both

ADC_{Lesion} and $rCBV_{\text{ROI}}$ were slightly better (but not significantly better) than $rCBV_{\text{ROI}}$ alone. Compared with DSC, DWI has the distinct advantage of widespread adoption into routine imaging protocols, as well as being a rapid-acquisition, noncontrast technique with highly reproducible results. We, therefore, suggest that whenever possible, patients with suspected treatment-related changes should undergo both DSC and DWI.

A few potential limitations were encountered. First, this was a retrospective study in which only 60.3% had both DWI and DSC imaging, which may have decreased our evaluation of the combined diffusion and perfusion model. In addition, fewer patients had treatment-related changes, and only 4 of 8 patients with pseudoprogression had DSC data available for analysis. Despite the small sample sizes, we detected significant differences in diffusion and perfusion metrics and suggest that DSC may be a useful technique for detecting pseudoprogression. Second, there was some heterogeneity in MR imaging scanner field strengths and contrast

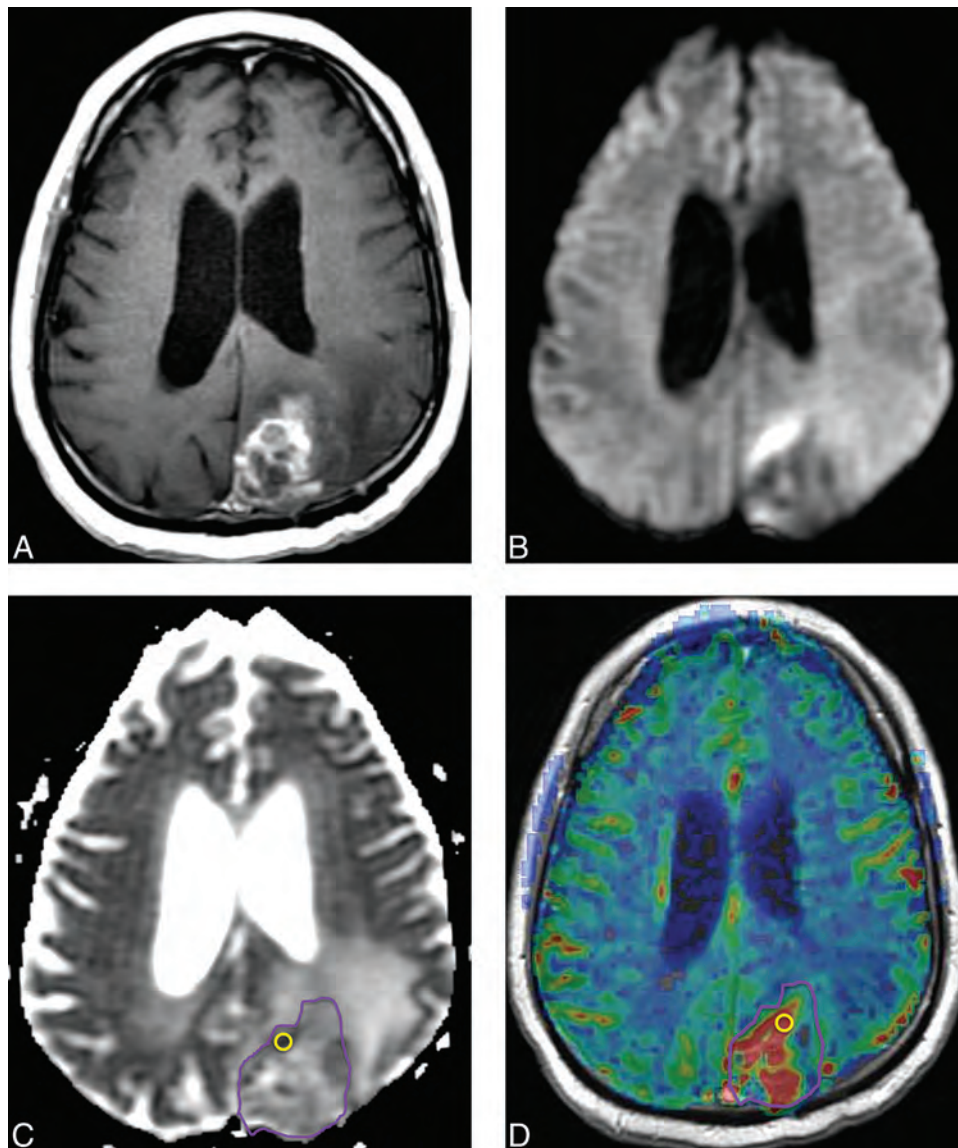


FIG 7. Recurrent tumor. Five months later after RT with concomitant and adjuvant temozolomide, this patient with glioblastoma developed a new heterogeneously enhancing mass lesion in the left occipital lobe on a contrast T1-weighted image (A) with heterogeneously increased signal on DWI (B) and decreased ADC (C). $ADC_{\text{Lesion}} = 0.00123 \text{ mm}^2/\text{s}$. rCBV map (D) shows hyperperfusion. $rCBV_{\text{Lesion}} = 2.78$. Repeat surgery confirmed recurrent tumor.

injection rates that may have affected DSC perfusion time curves, though such variability was minimized by standardized scan parameters, contrast dose, and postprocessing techniques. Third, there may have been a clinical bias to preferentially recommend surgery for patients with large enhancing lesions, mass effect, and/or worsening signs/symptoms. Patients who have treatment-related changes, particularly pseudoprogression, are more likely to be asymptomatic⁸ and therefore more likely to undergo follow-up rather than repeat surgery. While this outcome may have decreased the power of our results, we still found significant results for both DWI and DSC. Fourth, <50% of our patients had known MGMT status, which was still emerging as the standard of care during the time of the study. Because studies have shown positive correlations between MGMT status and pseudoprogression,^{8,11} this correlation is an attractive area for future study. Fifth, we used two 2D-ROI measurements that encompassed the

entire lesion and targeted the areas of maximal abnormality. These techniques are rapid, reproducible, robust by using commercial software, and are commonly used in clinical practice.^{17,18} Although some authors have implemented 3D volumetric measurements,³⁴ these tools often require additional technical expertise and are not widely available.

CONCLUSIONS

DWI and DSC may be helpful in differentiating treatment-related changes and recurrent HGGs. We found that DSC may outperform DWI alone and in combination to predict treatment-related changes as distinguished from recurrent tumor. We suggest that both DSC and DWI be used to improve specificity.

Disclosures: Alisa J. Prager—RELATED: Grant: Memorial Sloan Kettering Cancer Center Medical Student Summer Fellowship Research Program.* Antonio Omuro—

UNRELATED: Consultancy: Roche, Novocure, CarThera. Zhigang Zhang—RELATED: Grant: National Institutes of Health Core Grant P30 CA008748.* *Money paid to the institution.

REFERENCES

1. Wen PY, Macdonald DR, Reardon DA, et al. Updated response assessment criteria for high-grade gliomas: response assessment in neuro-oncology working group. *J Clin Oncol* 2010;28:1963–72
2. Hygino da Cruz LC Jr, Rodriguez I, Domingues RC, et al. Pseudoprogession and pseudoresponse: imaging challenges in the assessment of posttreatment glioma. *AJNR Am J Neuroradiol* 2011;32:1978–85
3. Brandes AA, Franceschi E, Tosoni A, et al. MGMT promoter methylation status can predict the incidence and outcome of pseudoprogession after concomitant radiochemotherapy in newly diagnosed glioblastoma patients. *J Clin Oncol* 2008;26:2192–97
4. Hopewell JW, Calvo W, Jaenke R, et al. Microvasculature and radiation damage. *Recent Results Cancer Res* 1993;130:1–16
5. Sugahara T, Korogi Y, Kochi M, et al. Correlation of MR imaging-determined cerebral blood volume maps with histologic and angiographic determination of vascularity of gliomas. *AJR Am J Roentgenol* 1998;171:1479–86
6. Oh BC, Pagnini PG, Wang MY, et al. Stereotactic radiosurgery: adjacent tissue injury and response after high-dose single fraction radiation. Part I. Histology, imaging, and molecular events. *Neurosurgery* 2007;60:31–44; discussion 44–45
7. Wesseling P, Ruiters DJ, Burger PC. Angiogenesis in brain tumors; pathobiological and clinical aspects. *J Neurooncol* 1997;32:253–65
8. Brandsma D, van den Bent MJ. Pseudoprogession and pseudoresponse in the treatment of gliomas. *Curr Opin Neurol* 2009;22:633–38
9. Young RJ, Gupta A, Shah AD, et al. MRI perfusion in determining pseudoprogession in patients with glioblastoma. *Clin Imaging* 2013;37:41–49
10. Young RJ, Gupta A, Shah AD, et al. Potential utility of conventional MRI signs in diagnosing pseudoprogession in glioblastoma. *Neurology* 2011;76:1918–24
11. Brandsma D, Stalpers L, Taal W, et al. Clinical features, mechanisms, and management of pseudoprogession in malignant gliomas. *Lancet Oncol* 2008;9:453–61
12. Hein PA, Eskey CJ, Dunn JF, et al. Diffusion-weighted imaging in the follow-up of treated high-grade gliomas: tumor recurrence versus radiation injury. *AJNR Am J Neuroradiol* 2004;25:201–09
13. Mangla R, Kolar B, Zhu T, et al. Percentage signal recovery derived from MR dynamic susceptibility contrast imaging is useful to differentiate common enhancing malignant lesions of the brain. *AJNR Am J Neuroradiol* 2011;32:1004–10
14. Roa W, Brasher PM, Bauman G, et al. Abbreviated course of radiation therapy in older patients with glioblastoma multiforme: a prospective randomized clinical trial. *J Clin Oncol* 2004;22:1583–88
15. Clarke JL, Iwamoto FM, Sul J, et al. Randomized phase II trial of chemoradiotherapy followed by either dose-dense or metronomic temozolomide for newly diagnosed glioblastoma. *J Clin Oncol* 2009;27:3861–67
16. Cha S, Knopp EA, Johnson G, et al. Intracranial mass lesions: dynamic contrast-enhanced susceptibility-weighted echo-planar perfusion MR imaging. *Radiology* 2002;223:11–29
17. Wetzel SG, Cha S, Johnson G, et al. Relative cerebral blood volume measurements in intracranial mass lesions: interobserver and intraobserver reproducibility study. *Radiology* 2002;224:797–803
18. Young R, Babb J, Law M, et al. Comparison of region-of-interest analysis with three different histogram analysis methods in the determination of perfusion metrics in patients with brain gliomas. *J Magn Reson Imaging* 2007;26:1053–63
19. Rosen BR, Belliveau JW, Vevea JM, et al. Perfusion imaging with NMR contrast agents. *Magn Reson Med* 1990;14:249–65
20. Barajas RF, Chang JS, Sneed PK, et al. Distinguishing recurrent intra-axial metastatic tumor from radiation necrosis following gamma knife radiosurgery using dynamic susceptibility-weighted contrast-enhanced perfusion MR imaging. *AJNR Am J Neuroradiol* 2009;30:367–72
21. Law M, Young RJ, Babb JS, et al. Gliomas: predicting time to progression or survival with cerebral blood volume measurements at dynamic susceptibility-weighted contrast-enhanced perfusion MR imaging. *Radiology* 2008;247:490–98
22. Al-Okaili RN, Krejza J, Woo JH, et al. Intraaxial brain masses: MR imaging-based diagnostic strategy—initial experience. *Radiology* 2007;243:539–50
23. Asao C, Korogi Y, Kitajima M, et al. Diffusion-weighted imaging of radiation-induced brain injury for differentiation from tumor recurrence. *AJNR Am J Neuroradiol* 2005;26:1455–60
24. Chu HH, Choi SH, Ryoo I, et al. Differentiation of true progression from pseudoprogession in glioblastoma treated with radiation therapy and concomitant temozolomide: comparison study of standard and high-b-value diffusion-weighted imaging. *Radiology* 2013;29:831–40
25. Cha J, Kim ST, Kim HJ, et al. Analysis of the layering pattern of the apparent diffusion coefficient (ADC) for differentiation of radiation necrosis from tumour progression. *Eur Radiol* 2013;23:879–86
26. Barajas RF Jr, Chang JS, Segal MR, et al. Differentiation of recurrent glioblastoma multiforme from radiation necrosis after external beam radiation therapy with dynamic susceptibility-weighted contrast-enhanced perfusion MR imaging. *Radiology* 2009;253:486–96
27. Gasparetto EL, Pawlak MA, Patel SH, et al. Posttreatment recurrence of malignant brain neoplasm: accuracy of relative cerebral blood volume fraction in discriminating low from high malignant histologic volume fraction. *Radiology* 2009;250:887–96
28. Hu LS, Baxter LC, Smith KA, et al. Relative cerebral blood volume values to differentiate high-grade glioma recurrence from posttreatment radiation effect: direct correlation between image-guided tissue histopathology and localized dynamic susceptibility-weighted contrast-enhanced perfusion MR imaging measurements. *AJNR Am J Neuroradiol* 2009;30:552–58
29. Fink JR, Carr RB, Matsusue E, et al. Comparison of 3 Tesla proton MR spectroscopy, MR perfusion and MR diffusion for distinguishing glioma recurrence from posttreatment effects. *J Magn Reson Imaging* 2012;35:56–63
30. Bobek-Billewicz B, Stasik-Pres G, Majchrzak H, et al. Differentiation between brain tumor recurrence and radiation injury using perfusion, diffusion-weighted imaging and MR spectroscopy. *Folia Neuropathol* 2010;48:81–92
31. Chamberlain MC, Glantz MJ, Chalmers L, et al. Early necrosis following concurrent Temodar and radiotherapy in patients with glioblastoma. *J Neurooncol* 2007;82:81–83
32. Kong DS, Kim ST, Kim EH, et al. Diagnostic dilemma of pseudoprogession in the treatment of newly diagnosed glioblastomas: the role of assessing relative cerebral blood flow volume and oxygen-6-methylguanine-DNA methyltransferase promoter methylation status. *AJNR Am J Neuroradiol* 2011;32:382–87
33. Suh CH, Kim HS, Choi YJ, et al. Prediction of pseudoprogession in patients with glioblastomas using the initial and final area under the curves ratio derived from dynamic contrast-enhanced T1-weighted perfusion MR imaging. *AJNR Am J Neuroradiol* 2013;34:2278–86
34. Cha J, Kim ST, Kim HJ, et al. Differentiation of tumor progression from pseudoprogession in patients with posttreatment glioblastoma using multiparametric histogram analysis. *AJNR Am J Neuroradiol* 2014;35:1309–17

Discrimination of Tumorous Intracerebral Hemorrhage from Benign Causes Using CT Densitometry

Y.S. Choi, T.H. Rim, S.S. Ahn, and S.-K. Lee



ABSTRACT

BACKGROUND AND PURPOSE: Differentiation of tumorous intracerebral hemorrhage from benign etiology is critical in initial treatment plan and prognosis. Our aim was to investigate the diagnostic value of CT densitometry to discriminate tumorous and nontumorous causes of acute intracerebral hemorrhage.

MATERIALS AND METHODS: This retrospective study included 110 patients with acute intracerebral hemorrhage classified into 5 groups: primary intracerebral hemorrhage without (group 1) or with antithrombotics (group 2) and secondary intracerebral hemorrhage with vascular malformation (group 3), brain metastases (group 4), or primary brain tumors (group 5). The 5 groups were dichotomized into tumorous (groups 4 and 5) and nontumorous intracerebral hemorrhage (groups 1–3). Histogram parameters of hematoma attenuation on nonenhanced CT were compared among the groups and between tumorous and nontumorous intracerebral hemorrhages. With receiver operating characteristic analysis, optimal cutoffs and area under the curve were calculated for discriminating tumorous and nontumorous intracerebral hemorrhages.

RESULTS: Histogram analysis of acute intracerebral hemorrhage attenuation showed that group 1 had higher mean, 5th, 25th, 50th, and 75th percentile values than groups 4 and 5 and higher minimum and 5th percentile values than group 2. Group 3 had higher 5th percentile values than groups 4 and 5. After dichotomization, all histogram parameters except maximum and kurtosis were different between tumorous and nontumorous intracerebral hemorrhages, with tumors having lower cumulative histogram parameters and positive skewness. In receiver operating characteristic analysis, 5th and 25th percentile values showed the highest diagnostic performance for discriminating tumorous and nontumorous intracerebral hemorrhages, with 0.81 area under the curve, cutoffs of 34 HU and 44 HU, sensitivities of 65.6% and 70.0%, and specificities of 85.0% and 80.0%, respectively.

CONCLUSIONS: CT densitometry of intracerebral hemorrhage on nonenhanced CT might be useful for discriminating tumorous and nontumorous causes of acute intracerebral hemorrhage.

ABBREVIATIONS: ICH = intracerebral hemorrhage; NECT = nonenhanced CT

The incidence of intracerebral hemorrhage (ICH) is 10–20 cases per 100,000 worldwide.^{1–3} ICH has a high mortality rate with case-fatality rates of 34.6% at 7 days and 59.0% at 1 year.⁴ Intracerebral hemorrhage is classified as either primary or secondary on the basis of the underlying cause of bleeding. Primary ICH accounts for 78%–88% of ICH cases and is caused by spontaneous rupture of small vessels associated with chronic hyperten-

sion or amyloid angiopathy.⁵ Secondary ICH can occur in association with vascular malformations or tumors.¹ Tumors account for 10% of all spontaneous ICH cases.^{6,7} Earlier discrimination of tumorous etiology from nontumorous causes of acute ICH might be helpful to determine appropriate imaging follow-up and avoid delays in long-term management of tumorous ICH, though acute management would not differ.

Nonenhanced CT (NECT) is the standard investigation tool for acute ICH. Because most patients with ICH with tumors have a solid enhancing portion, contrast-enhanced CT or contrast-enhanced MR imaging are indicated when secondary ICH with tumor is suspected.^{8–10} However, enhancement of secondary ICH can be obscured by surrounding high attenuation or various T1 signal intensities from hematoma; these make diagnosis of secondary ICH difficult.^{10–12} Dual-energy CT offers better differentiation between ICH of tumor and nontumor etiology because of better visualization

Received September 5, 2014; accepted after revision November 9.

From the Department of Radiology and Research Institute of Radiological Science (Y.S.C., S.S.A., S.-K.L.) and Department of Ophthalmology, Institute of Vision Research (T.H.R.), College of Medicine, Yonsei University, Seoul, Korea.

Please address correspondence to Seung-Koo Lee, MD, PhD, Department of Radiology, College of Medicine, Yonsei University, 50 Yonsei-ro, Seodaemun-gu, Seoul 120-752, Korea; e-mail: SLEE@yuhs.ac

Indicates open access to non-subscribers at www.ajnr.org

<http://dx.doi.org/10.3174/ajnr.A4233>

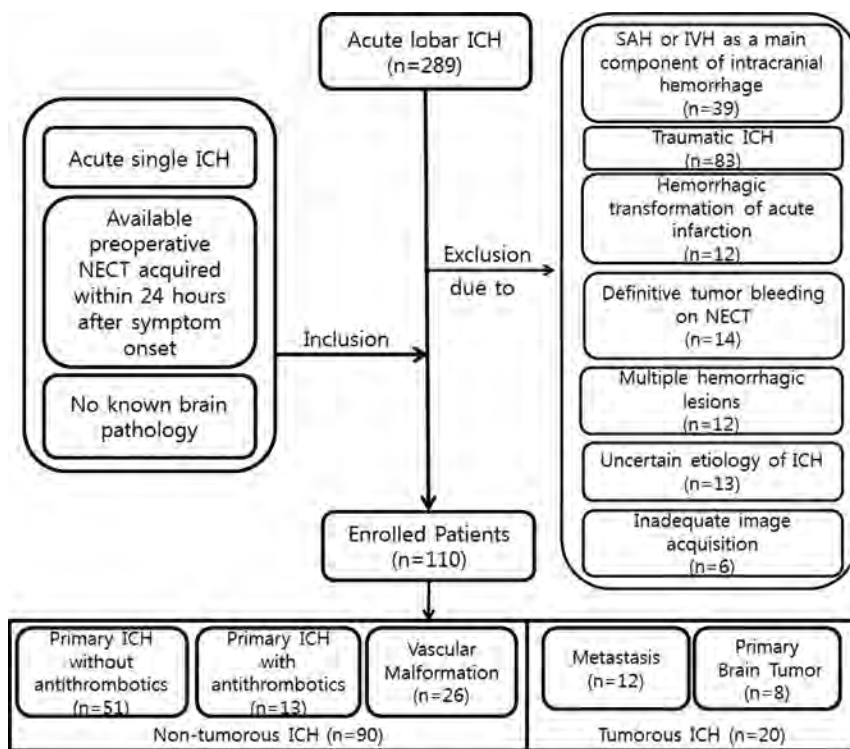


FIG 1. Flowchart of study population enrollment. IVH indicates intraventricular hemorrhage.

of the enhancing lesion within a high-attenuation hemorrhage.^{13,14} However, dual-energy CT is less available than single-energy CT. Thus, a more practical tool with widespread availability in the emergency setting is necessary for early and better discrimination of acute ICH from tumorous-versus-nontumorous causes.

We hypothesized that the attenuation of tumorous ICH differs from that of nontumorous ICH on NECT with the presence of solid lesions. We investigated the diagnostic value of CT densitometry of acute ICH to discriminate tumorous and nontumorous causes of acute ICH.

MATERIALS AND METHODS

This retrospective study was approved by our institutional review board, which waived the requirement for informed consent.

Patient Selection

From November 2005 through September 2013, 289 patients with acute subcortical or lobar hemorrhage were reviewed. The study population enrollment process is summarized in Fig 1. Inclusion criteria were the following: 1) acute single subcortical or lobar ICH, 2) available preoperative NECT acquired within 24 hours after symptom onset, 3) no known brain pathology with hemorrhage risk such as AVM or brain tumor, and 4) pathologically or clinically confirmed causes of acute ICH. Nonpathologically proved cases were confirmed by imaging follow-up (eg, complete disappearance of the hematoma without an underlying lesion on follow-up imaging in cases of primary ICH; vascular malformation confirmed on follow-up CTA, MRA, or conventional angiography in cases of secondary ICH with vascular malformation; and serial growing of the mass or enhancing tumor tissue on follow-up imaging in cases of secondary ICH with tumor). Patients

with initial outpatient NECT images were included if they met the inclusion criteria and had images of adequate quality. To include clinically confusing patients only, we excluded patients with clinical or NECT imaging findings implicating certain underlying causes of ICH, either primary or secondary. Exclusion criteria consisted of intraventricular hemorrhage or SAH as a main component of intracranial hemorrhage ($n = 39$), traumatic ICH ($n = 83$), or hemorrhagic transformation of acute infarction ($n = 12$), and patients with definitive tumorous ICH with gross cystic or solid portions ($n = 14$) or multiple hemorrhagic lesions ($n = 12$).^{9,15} Additionally, we also excluded cases of uncertain-cause ICH in patients who were either not sufficiently followed up with imaging or whose condition was not pathologically proved and could not be retrospectively classified as tumorous or nontumorous ICH ($n = 13$). Patients with initial outpatient NECT images of inadequate image quality were also excluded ($n = 6$).

The study cohort of 110 patients was classified into 5 groups according to underlying causes and antithrombotic medication status: 1) primary ICH and not taking antithrombotics; 2) primary ICH with antithrombotic use within 3 months before the CT scan; 3) secondary ICH due to vascular malformation such as AVM, cavernous angioma, or dural arteriovenous fistula; 4) secondary ICH due to brain metastases; and 5) secondary ICH due to primary brain tumors.

These 5 groups were later combined and dichotomized into patients with nontumorous ICH (groups 1, 2, and 3) and patients with tumorous ICH (groups 4 and 5).

Image Acquisition and Analysis

Among the 110 patients, the CT scans of 67 were obtained in our hospital. CT examinations were performed with voltage from 100 to 120 kV and current from 130 to 250 mA. CT scans of the other 43 patients were performed at other hospitals, with voltage from 100 to 120 kV and current from 100 to 300 mA.

Image analysis was by consensus by 2 neuroradiologists (Y.S.C., with 6 years of experience in brain CT reading; and S.-K.L., with 24 years of experience in brain CT reading) who were blinded to the clinical information. An ROI was drawn on all NECT axial images containing the entire ICH volume by using a semiautomatic method, with thresholding of Hounsfield unit values as described elsewhere¹⁶ and depicted in Fig 2. For drawing ROIs, a lower limit of 25–40 HU and an upper limit of 130 HU were used as thresholds. For ICH adjacent to the skull, skull stripping was performed before drawing the ROI by masking pixels higher than 130 HU. Image analysis used the Medical Image Processing, Analysis, and Visualization software package (Version 7.0; National Institutes of Health, Bethesda, Maryland).

Statistical Analysis

Demographic data were compared among the 5 groups by using 1-way analysis of variance for continuous data and a χ^2 test for categorical data. Histogram parameters were extracted from Hounsfield unit values of ROIs, which were minimum, 5th, 25th, 50th, 75th, 95th percentiles, maximum values, skewness, and kurtosis. Histogram parameters were compared among the 5 groups by using 1-way analysis of variance with post hoc pair-wise comparison with Bonferroni correction of *P* values. To confirm the association between hematoma attenuation and time interval from

symptom onset to CT scan, we used multivariate linear regression after adjusting for possible confounders, including age and sex.

Histogram parameters were compared by *t* test or nonparametric Wilcoxon rank sum test between tumorous and nontumorous ICHs after dichotomization of the study population according to the results of the Shapiro-Wilk test for normalized distribution.

Receiver operating characteristic analysis was performed to determine the optimal cutoff values for histogram parameters to discriminate tumorous and nontumorous ICHs. The optimal cutoff value was determined by maximizing the Youden index and calculating the area under the curve. All calculated *P* values were 2-sided, and results were considered significant if the *P* value was $<.05$. We performed statistical analysis with STATA 12.1 (StataCorp, College Station, Texas).

RESULTS

Study Population

Demographic data of the study population are in Table 1. Among the 110 study patients (mean age, 53.4 years; range, 2.7–88.1 years), 64 had primary ICH and were classified in groups 1 or 2. Thirteen of 64 were classified as group 2, consisting of 6 patients taking warfarin, 5 taking aspirin, and 2 taking clopidogrel. Among 46 patients with secondary ICH, 26 were classified into group 3 with vascular malformation (AVM, *n* = 21; cavernous angioma, *n* = 2; and dural AVF, *n* = 3), 12 were classified into group 4 with brain metastasis (hepatocellular carcinoma, *n* = 7; lung cancer, *n* = 3; breast cancer, *n* = 1; thyroid cancer, *n* = 1), and 8 were classified into group 5 with primary brain tumors (glioblastoma, *n* = 6; anaplastic astrocytoma, *n* = 1; and ependymoma, *n* = 1). Eighty-two of 110 cases were nonpathologically confirmed by complete disappearance of the hematoma in cases of primary ICH (*n* = 57); follow-up by CTA, MRA, or conventional angiography in cases of secondary ICH with vascular malformation (*n* = 18); and serial growing of the mass or enhancing tumor on follow-up imaging in cases of secondary ICH with tumor (*n* = 7).

Ages were significantly different among the 5 groups ($P < .01$), and patients in group 3 were significantly younger than those in the other 4 groups in post hoc pair-wise comparison. Sex and time interval from symptom onset to CT were not significantly different.

Histogram Analysis of ICH Attenuation

Comparisons of histogram parameters among the 5 groups are listed in Table 2 and Fig 3, and representative cases of histogram analysis in tumorous and nontumorous ICH are shown in Fig 2. No significant correlation was observed between histogram parameters and symptom onset–CT time interval within 24 hours. In histogram analysis of

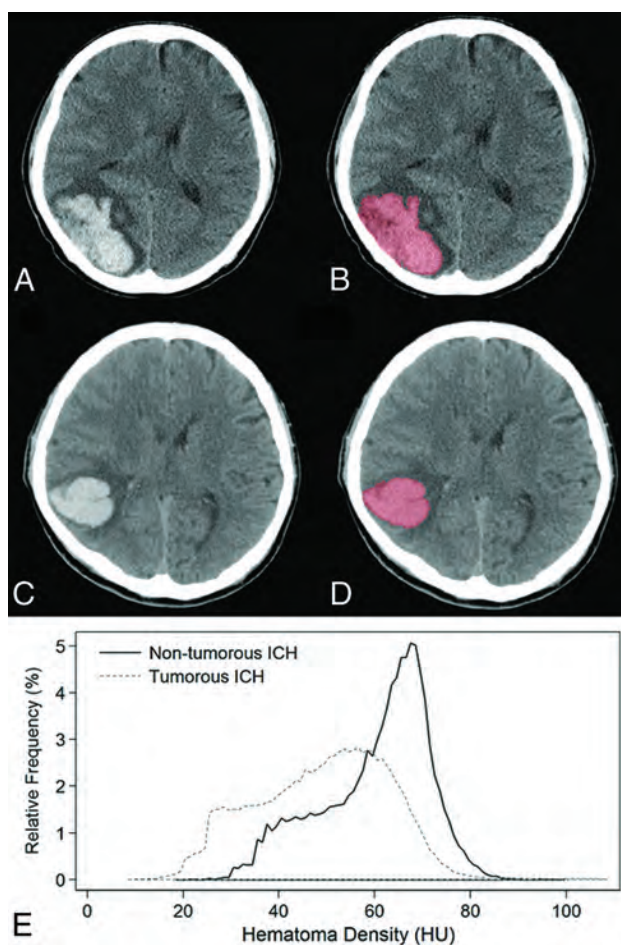


FIG 2. Representative cases of semiautomatic segmentation of tumorous (A and B) and nontumorous (C and D) ICHs and their relative frequency histogram of hematoma attenuation (E). ICH was segmented with a semiautomatic method based on a voxel-intensity threshold of 40–130 HU. On histogram analysis, the 5th and 25th percentile values were 26 HU and 38 HU in tumorous ICHs and 40 HU and 65 HU in nontumorous ICHs, respectively, and were discriminated correctly by using our histogram analysis.

Table 1: Demographic data of study population (n = 110)

Parameter	Nontumorous ICH (n = 90)		Tumorous ICH (n = 20)			P Value ^a
	Primary ICH (n = 64)		Secondary ICH (n = 46)			
	Without Antithrombotics (n = 51)	With Antithrombotics (n = 13)	Vascular Malformation (n = 26)	Metastasis (n = 12)	Primary Brain Tumor (n = 8)	
Age (year)	57.0 ± 20.4	66.8 ± 11.7	31.0 ± 20.9	56.8 ± 14.9	47.9 ± 20.9	<.01
Gender (M:F)	29:22	8:5	14:12	9:3	4:4	.75
Onset–CT interval time (hours)	10.0 ± 8.2	15.2 ± 7.1	8.5 ± 7.8	7.0 ± 6.4	9.5 ± 7.1	.08

^a Difference among the 5 groups tested by 1-way analysis of variance or χ^2 test.

Table 2: Differences in histogram parameters for ICH attenuation among the 5 groups

Parameter	Primary ICH without Antithrombotics (n = 51)	Primary ICH with Antithrombotics (n = 13)	Vascular Malformation (n = 26)	Metastasis (n = 12)	Primary Brain Tumor (n = 8)	P Value ^a
Mean	57.31 ± 7.40	52.64 ± 7.35	54.12 ± 6.96	46.94 ± 9.07	45.08 ± 10.34	<.01
Minimum	21.65 ± 9.65	11.69 ± 9.52	18.62 ± 7.05	14.83 ± 8.50	9.00 ± 5.29	<.01
Percentiles						
5th	37.73 ± 6.70	30.38 ± 7.38	35.56 ± 5.53	28.50 ± 6.26	26.38 ± 6.50	<.01
25th	49.47 ± 8.36	42.77 ± 9.14	45.85 ± 7.05	38.58 ± 8.50	34.38 ± 8.00	<.01
50th	58.78 ± 8.46	54.00 ± 8.71	55.35 ± 8.31	47.42 ± 10.32	44.38 ± 11.65	<.01
75th	65.73 ± 7.42	62.92 ± 6.71	62.65 ± 7.95	55.00 ± 10.57	54.13 ± 14.88	<.01
95th	73.02 ± 7.02	71.15 ± 5.51	70.00 ± 7.38	64.58 ± 9.02	67.25 ± 11.65	<.01
Maximum	99.33 ± 16.46	104.69 ± 17.67	94.31 ± 18.47	92.08 ± 14.05	122.00 ± 65.95	.29
Skewness	-0.32 ± 0.35	-0.18 ± 0.50	-0.13 ± 0.56	0.05 ± 0.47	0.63 ± 0.66	<.01
Kurtosis	2.64 ± 0.52	2.95 ± 0.96	3.00 ± 2.11	2.96 ± 1.21	4.11 ± 2.47	<.01

^a Difference among the 5 groups tested using 1-way analysis of variance before pair-wise comparison.

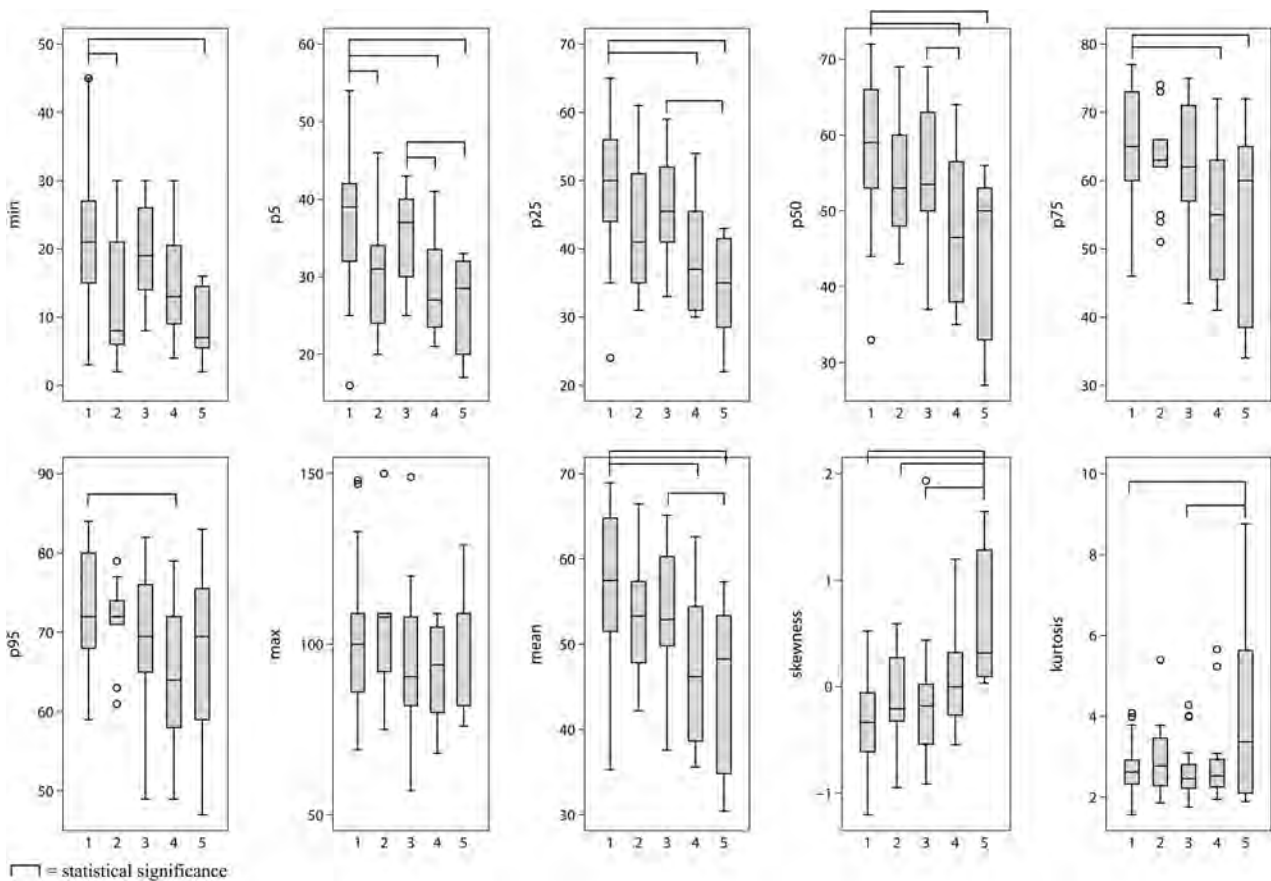


FIG 3. Differences among the 5 groups in histogram parameters of ICH attenuation are list on the x-axis of each boxplot: 1) primary ICH without antithrombotics, 2) primary ICH with antithrombotics, 3) secondary ICH due to vascular malformation, 4) secondary ICH due to brain metastasis, and 5) secondary ICH due to primary brain tumor.

ICH attenuation, group 1 was significantly higher than group 4 with brain metastasis and group 5 with primary brain tumor in the 5th, 25th, 50th, and 75th percentile values. Group 1 was also significantly higher than group 4 in the 95th percentile value. For primary ICH, group 2, with patients taking antithrombotic medication, was significantly lower than group 1 for the minimum and 5th percentile values. Five of 13 patients of group 2 showed blood-fluid levels within the ICH, and all 5 of these patients were on warfarin. Group 3, with patients with vascular malformations, was significantly higher than groups 4 and 5 for 5th percentile values and was higher than group 5 for 25th and 50th percentile values. Maximum values were not significantly different among the 5 groups. Group 5 showed signifi-

cantly higher kurtosis than groups 1 and 3. Groups 1, 2, and 3 showed negative skewness, and groups 4 and 5 showed positive skewness with significant differences.

After dichotomization into tumorous and nontumorous ICHs, all histogram parameters except maximum value and kurtosis were significantly different between tumorous and nontumorous ICHs (Fig 4). Tumorous ICH had lower cumulative histogram parameters and was positively skewed.

Receiver Operating Characteristic Analysis

In receiver operating characteristic analysis (Table 3), all presumptive parameters distinguishing tumorous and nontumorous

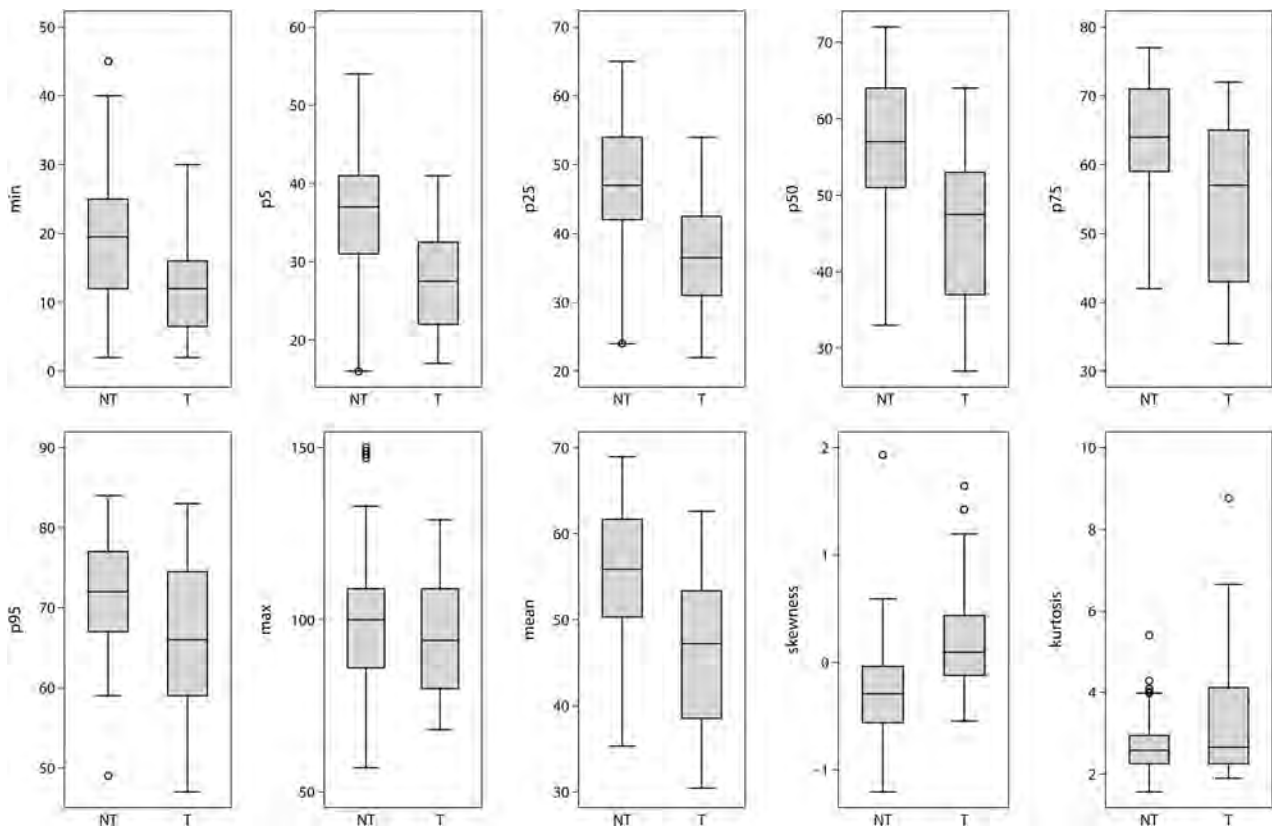


FIG 4. Differences in histogram parameters of ICH attenuation in tumor and nontumorous ICHs. All histogram parameters except maximum value and kurtosis were significantly different between tumorous and nontumorous ICHs. Tumors had lower cumulative histogram parameters and positive skewness. NT indicates nontumorous ICHs; T, tumorous ICHs.

Table 3: Diagnostic performance of ICH attenuation histogram parameters for discriminating tumor and nontumorous ICHs

Parameter	Az Value	95% CI	Cutoff Value ^a	Sensitivity (%)	Specificity (%)
Minimum Percentiles	0.71	0.59–0.84	17	62.2	85.0
5th	0.81	0.72–0.91	34	65.6	85.0
25th	0.81	0.71–0.92	44	70.0	80.0
50th	0.78	0.66–0.89	53	65.6	75.0
75th	0.74	0.60–0.87	60	72.2	65.0
95th	0.69	0.54–0.84	63	90.0	45.0
Mean	0.78	0.66–0.90	49.11	81.1	65.0
Skewness	0.78	0.67–0.88	-0.02	75.0	25.0

Note:—Az indicates area under the receiver operating characteristic curve.

^a Determined by maximizing the Youden index.

ICHs showed good diagnostic performance with area under the curve values above 0.7 (Fig 5). The 5th and 25th percentile values showed the highest diagnostic performance with area under the curve values of 0.81 and optimal cutoff values at 34 HU and 44 HU, respectively, with 65.6% sensitivity and 85.0% specificity for the 5th percentile value and 70.0% sensitivity and 80.0% specificity for the 25th percentile value. The receiver operating characteristic curve of 5th and 25th percentile values showed no significant differences after adjusting for symptom onset to CT time interval, with age and sex as covariates.

DISCUSSION

For acute ICH, we investigated the ability of CT densitometry to discriminate between tumors and nontumorous causes of ICH. With

NECT only, tumorous and nontumorous ICHs were differentiated with good diagnostic performance by using histogram analysis of acute ICH attenuation. Among the examined histogram parameters, the 25th and 5th percentile values had excellent diagnostic value with area under the curve values above 0.8. The study population was confined to patients with lobar ICH, in whom secondary ICH is relatively frequent and primary lobar ICH is not negligible, accounting for 15%–25% of hypertensive spontaneous ICH,^{1,17} making determining a treatment strategy difficult.

Maximum value, unlike the other parameters, was not significantly different among the 5 groups and had poor diagnostic value. This result was because we set an upper limit of 130 HU for thresholding to draw an ROI; maximum values were fixed at 130 HU in case of hematomas adjacent to the skull causing partial volume artifacts. However, these pixels with partial volume artifacts account for a relatively small portion of the hematoma, so the other histogram parameters minimized this problem. Groups showing high attenuation by cumulative histogram parameters, such as groups 1 and 3, showed relatively lower kurtosis. This result might be because highly attenuated acute hematoma had considerable interspersed low-attenuated voxels that were counted on voxelwise histogram analysis. In this context, the higher kurtosis with wider variance seen for group 5 might be attributable to a higher but variable proportion of tumor tissue with lower attenuation within the hematoma. After dichotomization, a higher trend for kurtosis was observed for tumorous than for nontumorous ICH, though this result was not significant.

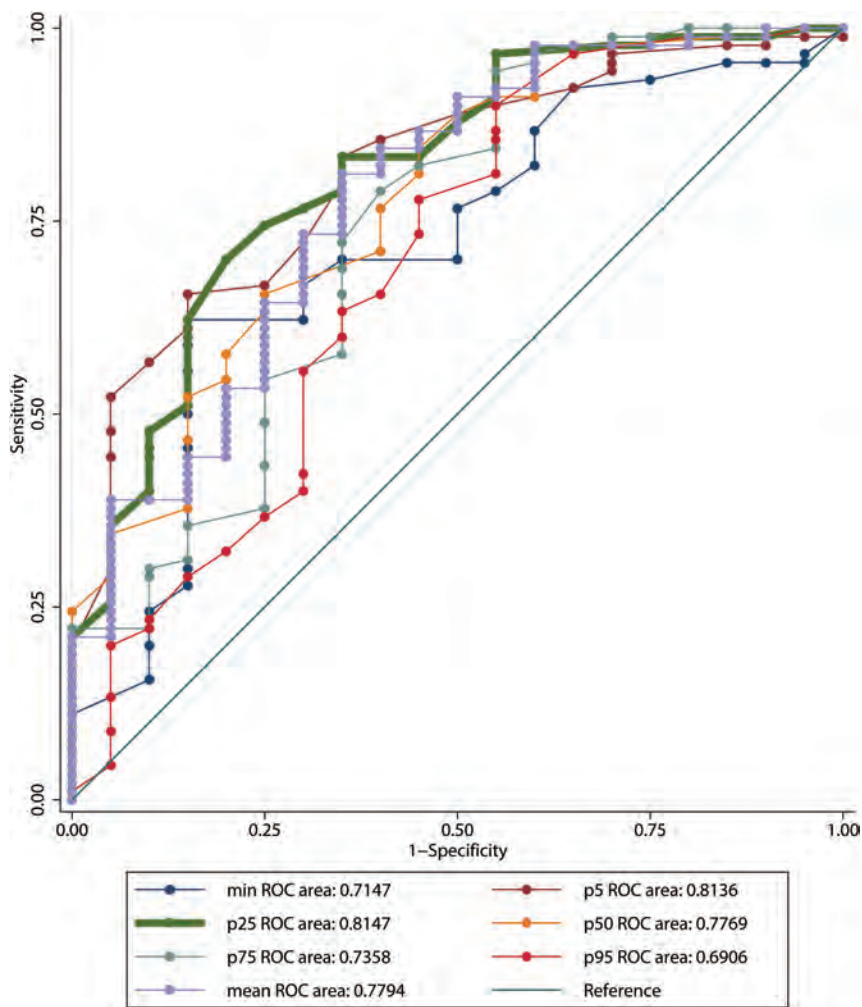


FIG 5. Receiver operating characteristic curves of histogram parameters for discrimination of tumor and nontumorous ICHs.

As shown in Fig 2, tumorous ICH showed a higher relative frequency of hematoma attenuation at lower Hounsfield unit values than nontumorous ICH, leading to positive skewness and relatively lower Hounsfield unit values of tumorous ICHs for all cumulative histogram parameters except the maximum value. One possible explanation for this trend is that a solid tumor lesion within the hematoma might be clustered at lower Hounsfield unit values, though solid tumor lesions are difficult to detect by visual inspection after excluding patients with definitive tumorous ICH with gross cystic and solid lesions. Our receiver operating characteristic analysis showed the 5th and 25th percentile values to be the best parameters for differentiating the attenuation of hematomas between tumorous and nontumorous ICHs. We propose that histogram analysis is a useful tool for detecting hidden solid tumor lesions within acute ICH, which might be helpful in establishing appropriate imaging follow-up and avoiding delays in long-term management of tumorous ICHs. Vascular malformation, another common cause of secondary ICH,^{6,7} showed relatively higher attenuation, similar to that of primary ICH, and thus could be discriminated from tumorous ICH. One explanation for this result is that rupture of abnormal vessels is the main pathophysiology of acute bleeding. Therefore, as

in primary ICH, a solid lesion occupies a smaller proportion in vascular malformations than in tumors.

In the primary ICH group composed of groups 1 and 2, hematoma attenuation was lower in group 2 with antithrombotics, though this result was significant only for the minimum and 5th percentile values. Five of 13 patients with antithrombotic medication showed blood-fluid levels in our study, and all 5 were on anticoagulants (warfarin). Lower attenuation at minimum and 5th percentile values might be because of this fluid-blood interface, which has been reported to result from uncondensed blood and can be seen in acute ICH of patients treated with anticoagulants within the first 12 hours.^{18,19} The lower and heterogeneous attenuation of primary ICH in patients treated with antithrombotics made differentiating primary ICH from tumorous ICH difficult. Therefore, clinicians should consider the possibility of misdiagnosis when examining acute ICH in patients with antithrombotic medication. In patients treated with anticoagulants, the fluid-blood interface uniquely seen in these patients might be helpful in diagnosis.

In routine clinical settings, prognosis and management of secondary ICH depend on the underlying etiology of ICH, while those of primary ICH depend on hematoma growth, initial ICH volume, and expansion into the ventricles.²⁰ Contrast-enhanced CT or MR imaging is performed when secondary ICH, especially tumorous ICH, is suspected. NECT is often undertaken serially to confirm resolution of primary ICH. However, high attenuation on CT and varying T1 intensity on MR imaging for acute hematoma can mask enhancing lesions of ICH on CT and MR imaging.^{11,12} Previous studies^{13,14} showed that dual-energy CT improves detection of enhancement within highly attenuated hemorrhage, but dual-energy CT or even single-energy contrast-enhanced CT and MR imaging are not always used as the initial imaging technique in patients with acute ICH. Serial follow-up with NECT takes time to confirm complete ICH resolution and might cause diagnostic delay. Being suspicious of tumor bleeding before complete ICH resolution might be helpful in determining appropriate imaging follow-up strategies and avoiding delays in long-term management of tumorous ICH, though acute management would not differ. In this context, our study has value in that NECT is a standard technique initially performed on patients with acute ICH in routine clinical settings. To our knowledge, this is the first study investigating the use of NECT for discriminating tumorous and nontumorous ICHs by using CT densitometry.

This study had several limitations. First, the CT protocols were heterogeneous because we included CT scans obtained at other hospitals in the study population. The voltage used in CT scans obtained at other hospitals was similar to that used for CT at our hospital, which was from 100 to 120 kV. The heterogeneous CT protocols probably did not affect our results because attenuation of a lesion changes depending on the voltage used in CT, and attenuation of the lesions would be similar if the voltages used in CT are similar. In addition, attenuation of solid lesions and hemorrhage does not change substantially as voltage increases, in contrast to the attenuation of iodine and calcification.¹³ A second limitation was that the ROIs in our study were subjectively drawn and could be regarded as cumbersome. However, semiautomatic methods of Hounsfield unit value thresholding has been used in previous studies^{16,21} and partially mitigated this limitation. In our experience, it took, on average, 8–10 minutes for an experienced neuroradiologist to segment and analyze a hematoma. Third, only a small number of patients with tumorous ICHs (groups 4 and 5) were included. In addition, the heterogeneity of primary malignancies in group 4 (secondary ICH with brain metastasis) is related to the heterogeneous cellularity of brain metastasis. Hence, it is likely for hypercellular brain metastasis to cause less low attenuation in hematomas and false-negatives in the histogram analysis we proposed. This small number and heterogeneity of patients resulted from the strict exclusion criteria, including multiple hemorrhagic lesions, gross solid or cystic lesions, and the initial CT scan obtained >24 hours after symptom onset because we tried to include clinically confusing cases only. Nonetheless, the strict exclusion criteria can also be a limitation of our study because this study does not reflect the unselected patients who present with acute ICH in the emergency department. Fourth, the number of patients taking antithrombotic medications was relatively small, confined to the primary ICH group. Subsequently, the effect of antithrombotic medication was not fully stratified in all groups. This grouping was because all patients with secondary ICH taking antithrombotic medication were excluded due to other exclusion criteria. Nonetheless, patients taking antithrombotic medication tended to have lower attenuation in acute primary ICH in our study. If this is the case for tumorous ICH, attenuation of tumor ICH with antithrombotic medication would be more likely opposite of expectations for primary ICH; thus, antithrombotic medication would not affect the diagnostic performance of CT densitometry. However, the subgroup of patients taking antithrombotic medications included patients with both antiplatelets and anticoagulants, which also can be a limitation of our study. Patients treated with anticoagulants are more prone to have unclotted components in their hematomas, which might have contributed more to the lower hematoma attenuation, than patients taking antiplatelets.^{22,23} Fifth, no validation has been performed in this study, which needs further investigation.

CONCLUSIONS

We investigated the diagnostic value of CT densitometry for discriminating tumors and nontumorous causes of acute ICH. Histogram parameters for acute ICH attenuation were significantly different for tumorous and nontumorous ICHs. The 5th and 25th

percentile values showed the highest diagnostic performance, with area under the curve values above 0.8, sensitivities of 65.6% and 70.0%, and specificities of 85.0% and 80.0%, respectively. CT densitometry of acute ICH on NECT was a useful tool for discriminating tumorous and nontumorous ICH in patients with acute ICHs of unclear origin.

REFERENCES

1. Qureshi AI, Tuhim S, Broderick JP, et al. **Spontaneous intracerebral hemorrhage.** *N Engl J Med* 2001;344:1450–60
2. Broderick JP, Brott T, Tomsick T, et al. **The risk of subarachnoid and intracerebral hemorrhages in blacks as compared with whites.** *N Engl J Med* 1992;326:733–36
3. Furlan AJ, Whisnant JP, Elveback LR. **The decreasing incidence of primary intracerebral hemorrhage: a population study.** *Ann Neurol* 1979;5:367–73
4. Sacco S, Marini C, Toni D, et al. **Incidence and 10-year survival of intracerebral hemorrhage in a population-based registry.** *Stroke* 2009;40:394–99
5. Foulkes MA, Wolf PA, Price TR, et al. **The Stroke Data Bank: design, methods, and baseline characteristics.** *Stroke* 1988;19:547–54
6. Scott M. **Spontaneous intracerebral hematoma caused by cerebral neoplasms: report of eight verified cases.** *J Neurosurg* 1975;42:338–42
7. Fewel ME, Thompson BG Jr, Hoff JT. **Spontaneous intracerebral hemorrhage: a review.** *Neurosurg Focus* 2003;15:E1
8. Destian S, Sze G, Krol G, et al. **MR imaging of hemorrhagic intracranial neoplasms.** *AJR Am J Roentgenol* 1989;152:137–44
9. Atlas SW, Grossman RI, Gomori JM, et al. **Hemorrhagic intracranial malignant neoplasms: spin-echo MR imaging.** *Radiology* 1987;164:71–77
10. Licata B, Turazzi S. **Bleeding cerebral neoplasms with symptomatic hematoma.** *J Neurosurg Sci* 2003;47:201–10; discussion 210
11. Inamasu J, Kuramae T, Nakatsukasa M. **Glioblastoma masquerading as a hypertensive putaminal hemorrhage: a diagnostic pitfall.** *Neurol Med Chir (Tokyo)* 2009;49:427–29
12. Meyer JR, Gorey MT. **Differential diagnosis of nontraumatic intracranial hemorrhage.** *Neuroimaging Clin North Am* 1998;8:263–93
13. Kim SJ, Lim HK, Lee HY, et al. **Dual-energy CT in the evaluation of intracerebral hemorrhage of unknown origin: differentiation between tumor bleeding and pure hemorrhage.** *AJNR Am J Neuroradiol* 2012;33:865–72
14. Phan CM, Yoo AJ, Hirsch JA, et al. **Differentiation of hemorrhage from iodinated contrast in different intracranial compartments using dual-energy head CT.** *AJNR Am J Neuroradiol* 2012;33:1088–94
15. Gildersleeve N Jr, Koo AH, McDonald CJ. **Metastatic tumor presenting as intracerebral hemorrhage: report of 6 cases examined by computed tomography.** *Radiology* 1977;124:109–12
16. Ko SB, Choi HA, Carpenter AM, et al. **Quantitative analysis of hemorrhage volume for predicting delayed cerebral ischemia after subarachnoid hemorrhage.** *Stroke* 2011;42:669–74
17. Caplan LR. **Intracerebral haemorrhage.** *Lancet* 1992;339:656–58
18. Hart RG, Boop BS, Anderson DC. **Oral anticoagulants and intracranial hemorrhage facts and hypotheses.** *Stroke* 1995;26:1471–77
19. Cervera A, Amaro S, Chamorro A. **Oral anticoagulant-associated intracerebral hemorrhage.** *J Neurol* 2012;259:212–24
20. Davis S, Broderick J, Hennerici M, et al. **Hematoma growth is a determinant of mortality and poor outcome after intracerebral hemorrhage.** *Neurology* 2006;66:1175–81
21. Ko SB, Choi HA, Parikh G, et al. **Multimodality monitoring for cerebral perfusion pressure optimization in comatose patients with intracerebral hemorrhage.** *Stroke* 2011;42:3087–92
22. Gökçe E, Beyhan M, Acu B. **Evaluation of oral anticoagulant-associated intracranial parenchymal hematomas using CT findings.** *Clin Neuroradiol* 2014 Jan 29. [Epub ahead of print]
23. Pflieger MJ, Hardee EP, Contant C, et al. **Sensitivity and specificity of fluid-blood levels for coagulopathy in acute intracerebral hematomas.** *AJNR Am J Neuroradiol* 1994;15:217–23

Dilated Perivascular Spaces in the Basal Ganglia Are a Biomarker of Small-Vessel Disease in a Very Elderly Population with Dementia

T.P. Hansen, J. Cain, O. Thomas, and A. Jackson

ABSTRACT

BACKGROUND AND PURPOSE: Dilated perivascular spaces have been shown to be a specific biomarker of cerebral small-vessel disease in young patients with dementia. Our aim was to examine the discriminative power of dilated cerebral perivascular spaces as biomarkers of small-vessel disease in a very elderly population of patients with dementia.

MATERIALS AND METHODS: We studied healthy volunteers ($n = 65$; mean age, 78 ± 5.6 years) and subjects with vascular dementia ($n = 39$; mean age, 76.9 ± 7.7 years) and Alzheimer disease ($n = 47$; mean age, 74.1 ± 8.5 years). We compared white matter hyperintensity and 2 semiquantitative perivascular space scoring systems (perivascular space-1 and perivascular space-2). Intra- and interobserver agreement was assessed by using a weighted Cohen κ statistic. Multinomial regression modeling was used to assess the discriminative power of imaging features to distinguish clinical groups.

RESULTS: White matter hyperintensity scores were higher in vascular dementia than in Alzheimer disease ($P < .05$) or healthy volunteers ($P < .01$). The perivascular space-1 score was higher in vascular dementia and Alzheimer disease than in healthy volunteers ($P < .01$). The perivascular space-2 score in the centrum semiovale showed no intergroup differences. However, perivascular space-2 in the basal ganglia was higher in vascular dementia than in Alzheimer disease ($P < .05$) or healthy volunteers ($P < .001$) and higher in Alzheimer disease than in healthy volunteers ($P < .001$). Modeling of dementia versus healthy volunteers, Alzheimer disease versus healthy volunteers, and vascular dementia against Alzheimer disease demonstrated perivascular space-2_{basal ganglia} as the only imaging parameter with independent significant discriminative power ($P < .01$, $P < .01$, and $P < .05$) with areas under the receiver operating characteristic curve of 0.855, 0.774, and 0.71, respectively. Modeling of vascular dementia versus healthy volunteers showed that perivascular space-2_{basal ganglia} ($P < .01$) and the modified Scheltens score ($P < .05$) contributed significant, independent discriminatory power, accounting for 34% and 13% of the variance in the model respectively.

CONCLUSIONS: Dilated perivascular spaces remain a valuable biomarker of small-vessel disease in an elderly population.

ABBREVIATIONS: AD = Alzheimer disease; BG = basal ganglia; CSOV = centrum semiovale; Norm = healthy volunteers; PVS = dilated perivascular spaces; ROC = receiver operating characteristic; SVD = small-vessel disease; VaD = vascular dementia

Alzheimer disease (AD) and vascular dementia (VaD) account for approximately 80% of dementias.¹ They can occur separately but are more likely to coexist with increasing age.² Vascular dementia is multifactorial in nature and may result from thrombotic or embolic large-vessel occlusion with consequent cortical infarction or, more commonly, cerebral small-vessel disease (SVD) with ischemic injury to deep brain structures and cerebral

white matter.^{3,4} While segmental infarction and hemorrhages can be identified on MR imaging, there is a pressing need for reliable biomarkers of SVD.⁵ Potential imaging biomarkers include deep white matter hyperintensities, dilated perivascular spaces (PVS), lacunar stroke, cerebral microbleeds, and cerebral atrophy.⁵

Histologically, PVS are a feature of moderate-to-severe SVD.⁶ Imaging studies have shown them to be highly discriminative for diseases associated with SVD, including lacunar stroke,⁷ treatment-resistant late-onset depression,⁸ and vascular dementia.⁶ In each of these cases, PVS provided greater discriminative power than deep white matter hyperintensity scores. A study of 32 healthy elderly subjects also showed that PVS scoring correlated with Framingham stroke risk when deep white matter hyperintensity scores did not.⁹

This study builds on previous studies of PVS in young patients

Received May 14, 2014; accepted after revision December 1.

From the Centre for Imaging Sciences (T.P.H., J.C., A.J.), Wolfson Molecular Imaging Centre, University of Manchester, Greater Manchester, UK; and Salford Royal NHS Foundation Trust (O.T.), Salford, UK.

Please address correspondence to Alan Jackson, PhD, MB, ChB, Wolfson Molecular Imaging Centre, 27 Palatine Rd, Withington, Manchester, M20 3LJ, UK; e-mail: Alan.Jackson@Manchester.ac.uk; @Profajackson

<http://dx.doi.org/10.3174/ajnr.A4237>

with dementia⁶ and older patients with lacunar stroke.⁷ Both SVD and imaging features of vascular disease are increasingly common with advanced age and are commonly found in healthy subjects and in patients with primary neurodegenerative disorders such as AD. These findings are reflected with the scoring systems used by previous authors. Patankar et al,⁶ working in young patients with early-onset dementia, used a scoring system designed to detect early SVD on the basis of the presence of small numbers of PVS in the basal ganglia, with higher scores corresponding to both an increased number and location farther from the brain surface. In elderly individuals, PVS throughout the basal ganglia are increasingly common so that the discriminatory power of this scoring system is likely to be reduced. Consequently, Doubal et al,⁷ comparing PVS in older patients with lacunar and cortical stroke, used a scoring system based on the maximum number of PVS in any single axial section through the basal ganglia and centrum semiovale.

In this study, we examined the utility of PVS and deep white matter hyperintensities as biomarkers of SVD in a very elderly population and compared the discriminative power of the previously described PVS scoring systems to discriminate AD from VaD.

MATERIALS AND METHODS

The South Manchester local research ethics committee approved the project, and all subjects gave informed consent. Consent was gained with the help of caregivers for those lacking full capacity.

Patient Selection

We recruited 3 groups of subjects: 1) AD, 2) VaD, and 3) healthy age-matched controls (Norm). Specialists in geriatric psychiatry performed clinical recruitment across Greater Manchester, and all patients satisfied the criteria for dementia in the *Diagnostic and Statistical Manual of Mental Disorders*, 4th ed. Patients with Alzheimer disease fulfilled the National Institute of Neurologic and Communicative Disorders and Stroke–Alzheimer disease and Related Disorders Association criteria,¹⁰ and patients with vascular dementia fulfilled the National Institute of Neurologic Disorders and Stroke–Association Internationale pour la Recherche et l'Enseignement en Neurosciences criteria for vascular dementia.¹¹ Those with mixed AD and VaD and those receiving anticoagulant treatment were excluded.¹²

Control Subjects

Control subjects were recruited from the general practices at which patients were registered. They were matched for age, sex, and socioeconomic status. Control subjects with significant cognitive abnormalities were excluded (see below). To avoid selection bias, we did not include vascular risk factors in the inclusion/exclusion criteria.

Exclusion Criteria

Patients scoring <10 (severe dementia) on Mini-Mental State Examinations were excluded because they were considered unlikely to have the capacity to give consent for the study. Controls with a diagnosis of dementia or with Mini-Mental State Examinations scores of <24 were excluded because they may have had underly-

Table 1: Modified version of Scheltens scoring scheme used in the study

Subscale	Range of Scores	Definition of Scores
1) Periventricular		
Frontal	0/1/2	0 = absent
Occipital	0/1/2	1 ≤ 5 mm
Bands on lateral ventricle	0/1/2	2 ≥ 5 and <10 mm
Subtotal score	≤6	
2) Deep white matter		
Frontal	0/1/2/3/4/5/6	
Parietal	0/1/2/3/4/5/6	
Occipital	0/1/2/3/4/5/6	
Temporal	0/1/2/3/4/5/6	0 = none
Subtotal score	0–24	1 ≤ 3 mm, n ≤ 5 2 ≤ 3 mm, n > 5
3) Basal ganglia		
Caudate	0/1/2/3/4/5/6	3 = 4–10 mm, n ≤ 5
Lentiform nucleus	0/1/2/3/4/5/6	4 = 4–10 mm, n > 6
Thalamus	0/1/2/3/4/5/6	5 ≥ 11 mm, n > 1
Subtotal score	0–18	6 = confluent
4) Subtentorial		
Cerebellum	0/1/2/3/4/5/6	
Mesencephalon	0/1/2/3/4/5/6	
Medulla	0/1/2/3/4/5/6	
Pons	0/1/2/3/4/5/6	
Subtotal score	0–24	
Total score	0–72	

ing dementia or other cognitive impairment. In addition, following MR imaging, controls with evidence of silent infarction demonstrated on T1 and FLAIR images were excluded from the study.

Neuroimaging

All subjects were scanned by using a 1.5T whole-body scanner with a birdcage head coil receiver (ACS-NT, Power Track 6000 gradient subsystem; Philips Healthcare, Best, the Netherlands). Sequences included the following: 1) 3D volume fluid-attenuated inversion recovery (TR/TE/T1 = 11,000/140/2600 ms, section thickness = 3.0 mm), and 2) 3D volume T1-weighted inversion recovery (TR/TE/T1 = 6850/18/300 ms, section thickness = 3.0 mm). For all sequences, the matrix was 256 × 256, and the FOV was 230 × 230 mm.

Images were transferred to a stand-alone Macintosh personal computer (Apple, Cupertino, California) workstation and viewed by using a clinical workstation application (OsiriX, <http://www.osirix-viewer.com>).¹³

Image Analysis

White matter lesions were scored by using a modified Scheltens score previously validated in our laboratory.¹⁴ The independent scoring of the putamen and globus pallidus was replaced with a composite score for the lentiform nucleus on the basis of poor reproducibility and interrater agreement (Table 1). Scoring was performed by an experienced neuroradiologist (A.J.) by using T1 inversion recovery and FLAIR images.

Axial T1 inversion recovery images were used to visualize dilated PVS. Although most studies use heavily T2-weighted images, previous reports have demonstrated high conspicuity of PVS by using this very heavily T1-weighted sequence.^{6,8} Two previously described scoring systems were used. The first, described by Patankar et al in 2005,⁶ counts total PVS with a total score of 5 in

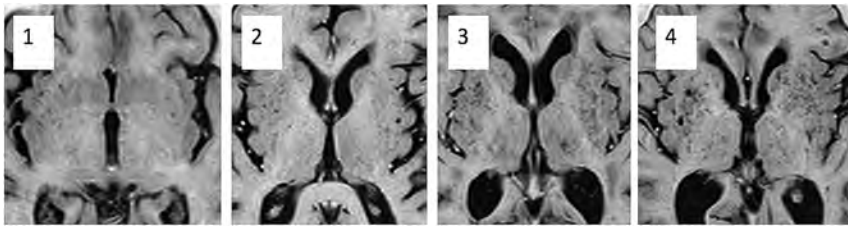


FIG 1. Images show dilated perivascular spaces in the basal ganglia corresponding to PVS-2_{BG} scores of 1–4.

Table 2: Demographic and imaging biomarker data for individual diagnostic groups^a

Group	Healthy	AD	VaD
No.	65	47	39
Age (yr)	78 (5.6)	74.1 (8.5)	76.9 (7.7)
Modified Scheltens score	12.50 (2.5)	13.16 (2.34)	22.76 (2.84)
PVS-1	5.87 (0.21)	6.03 (0.14)	6.34 (0.16)
PVS-2 _{BG}	2.1 (0.5)	2.22 (0.09)	2.471 (0.87)
PVS-2 _{CSOV}	2.51 (0.13)	2.61 (0.10)	2.53 (0.15)

^a Data are mean values (SD).

Table 3: Inter- and intraobserver variation for PVS scores^a

	Modified Scheltens Score			
	PVS-1	PVS-2	PVS-2 _{BG}	
Interobserver Agreement				
Rater 1 vs 2	0.82	0.79	0.92	0.91
Rater 1 vs 3	0.91	0.84	0.89	0.86
Rater 2 vs 3	0.88	0.82	0.83	0.90
Intraobserver agreement				
Rater 1	0.82	0.87	0.92	0.90
Rater 2	0.86	0.96	0.84	0.86

^a Data represent weighted Cohen κ statistics. All ratings were very good, except 0.70, which was good.

the basal ganglia (BG; PVS-1_{BG}) and a total score of 2 in the centrum semiovale (CSOV; PVS-1_{CSOV}). In the CSOV, 0 indicated none; 1, <5 per side; and 2, >5 on 1 or both sides. In the basal ganglia, 0 indicated PVS present only in the substantia innominata and <5 PVS on either side; 1, PVS only in the substantia innominata but >5 dilated on either side; 2, 0–5 PVS in the lentiform nucleus on either side; 3, 5–10 PVS in the lentiform or 0–5 in the caudate nucleus on either side; 4, >10 in the lentiform nucleus and <5 in the caudate nucleus on either side; 5, >10 in the lentiform nucleus and >5 in the caudate nucleus on either side. Care was taken to ensure that PVS were not counted twice by following their continuity through sections. PVS-1_{BG} and PVS-1_{CSOV} were combined to create a cumulative score (PVS-1).

The second scoring system was adapted from Doubal et al, 2010.⁷ The BG (PVS-2_{BG}) and CSOV (PVS-2_{CSOV}) were scored separately; then, the scores were combined to produce a total score (PVS-2). In each structure, the section with most PVS visible was selected and the number was counted on the side of the brain with the greatest number. Scores were as follows; 0 = no PVS, 1 = 1–10, 2 = 11–20, 3 = 21–30, 4 = 31–40, and so on. The original Doubal score had 3 = 21–40, and 4 (>40 PVS) was the maximum score (Fig 1).

Inter- and Intraobserver Variation Studies

An initial inter- and intraobserver variation study was performed to assess the reliability of each component of the scoring systems.

All subjects with dementia (47 with AD and 39 with VaD) and the first 31 healthy control subjects, selected by the recruitment date, were included in the interobserver study ($n = 117$). All cases were scored in random order by 3 experienced neuroradiologists. One observer (A.J.) then repeated the scoring on all cases with 7 days between the sessions. The study assessed all components of the modified Scheltens score (Table 1)¹⁴ and the 2 previously described scoring systems for the presence of dilated PVS.^{6,7}

Statistical Analysis

Statistical analyses were performed in SPSS, Version 20.0 (IBM, Armonk, New York) and InStat (GraphPad Software, San Diego, California). Inter- and intraobserver agreements were assessed by using a weighted Cohen κ statistic. Standard definitions for the interpretation of the κ statistic were adopted. The agreement strength was defined as very good, $\kappa = 0.81$ –1.00; good, $\kappa = 0.61$ –0.80; moderate, $\kappa = 0.41$ –0.60; fair, $\kappa = 0.21$ –0.40; and poor, $\kappa < 0.20$. Tests for group differences used ANOVA for scalar variables with post hoc tests for between-group differences by using the Tamahane test, with significance adjusted to $P < .01$ to compensate for type 1 effects. Correlations among imaging variables were assessed by using the Spearman rank correlation coefficient.

Four data models were constructed to assess the contribution of imaging features to the separation of individuals with dementia from controls, those with VaD from controls, those with AD from controls, and those with AD from those with VaD. Data were standardized for each scenario to produce z scores. Multinomial logistic regression modeling was performed in Wizard Pro (<http://wizard.evanmiller.org/>), treating diagnosis as the outcome class (1 = AD, 2 = VaD, and 3 = Norm). Imaging biomarker scores were entered as covariates in the model if they showed a correlation with diagnosis at a significance of <.05. Variables were then sequentially removed from the model on the basis of the significance of their contribution to the model until all remaining variables were significant at the $P < .05$ level. Patient age and sex were entered as covariates in the model. Receiver operating characteristic (ROC) curves were generated by using the classifier for each model and the area under the ROC curve, and the observed sensitivity and specificity and positive and negative predictive values were calculated.

RESULTS

The final study group consisted of 151 subjects; 47 with AD (mean age, 74.1 \pm 8.5 years), 39 with VaD (mean age, 76.9 \pm 7.7 years), and 65 Norm (mean age, 78 \pm 5.6 years). Demographic and imaging biomarker data are shown in Table 2. Inter- and intraobserver variation studies showed good to very good agreement for modified Scheltens, PVS-1, and PVS-2 scores (Table 3).

The modified Scheltens score was higher in VaD than in AD ($P < .01$) or Norm ($P < .01$), but there was no significant difference between AD and Norm (Fig 2A).

The PVS-1 score was higher in VaD and AD than in Norm

($P < .01$). The PVS-2 score in the centrum semiovale showed no intergroup differences. However, PVS-2 in the basal ganglia was higher in VaD than in AD ($P < .05$) or in Norm ($P < .001$) and higher in AD than in Norm ($P < .001$, Fig 2B).

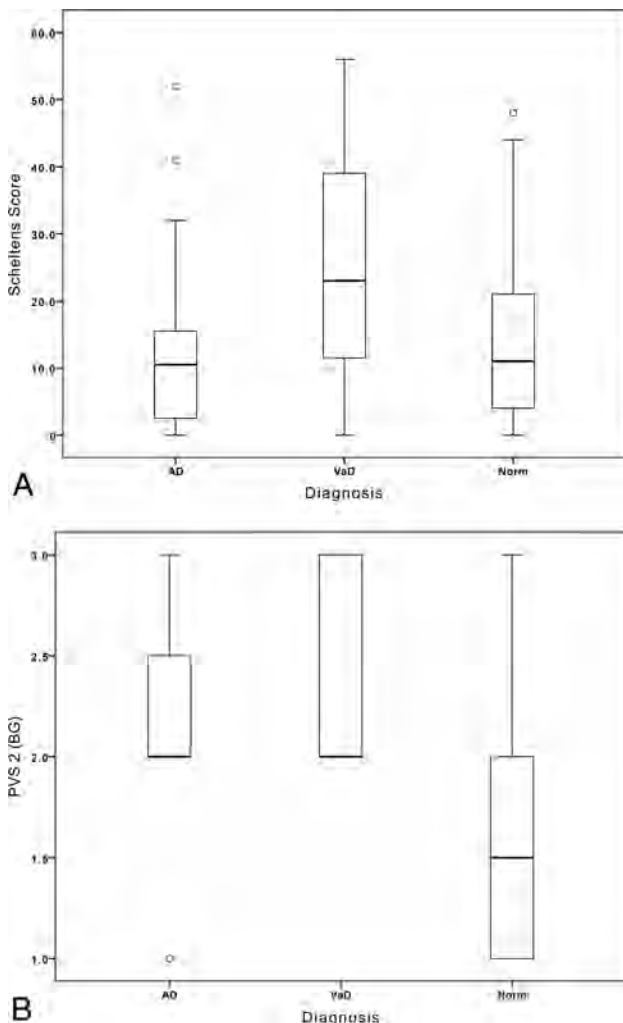


FIG 2. A, Boxplot shows the Scheltens white matter scores for the 3 subject groups. B, Boxplot shows the PVS-2_{BG} scores for the basal ganglia in the 3 subject groups.

There were strong correlations among the modified Scheltens score, PVS-1 ($\rho = 0.334$, $P < .001$), and PVS-2 ($\rho = 0.347$, $P < .001$) and between PVS-1 and PVS-2 ($\rho = 0.374$, $P < .001$).

Results from multinomial regression modeling are summarized in Table 4. PVS-2_{BG} was the only imaging parameter with independent significant discriminative power ($P < .001$) to distinguish patients with dementia (VaD and AD combined) from healthy controls. The area under the ROC curve was 0.855.

Modeling of AD against Norm also demonstrated PVS-2_{BG} as the only imaging parameter with independent significant discriminative power ($P < .01$) with an area under the ROC curve of 0.774. Modeling of VaD against Norm showed that PVS-2_{BG} ($P < .01$) and the modified Scheltens score ($P < .05$) contributed significant, independent discriminatory power, accounting for 34% and 13% of the variance in the model, respectively. The resulting model produced an area under the ROC of 0.93. Finally, modeling of VaD against AD demonstrated PVS-2_{BG} as the only imaging parameter with independent significant discriminative power ($P < .05$), with an area under the ROC curve of 0.71.

DISCUSSION

The presence of dilated PVS, particularly in the basal ganglia, is a cardinal component of the histologic features of SVD.⁶ Visualization of PVS by using MR imaging has been shown to correlate with a number of clinical features characterized by SVD, including VaD in a population with early-onset,⁶ treatment resistance in late-onset depression,⁸ lacunar stroke syndrome,¹⁵ and high stroke risk in healthy individuals.⁹ Furthermore, PVS appear more specific for SVD and have greater discriminative power than the severity of associated white matter hyperintensities in all these cases. PVS dilation has been quantified by using semiquantitative scoring systems, of which 2 have been described. The first, designed to identify early mild-moderate SVD, is based on the presence and location of small numbers of PVS in the basal ganglia, recognizing that PVS in the lentiform nucleus are an early sign of SVD and that the presence of PVS deeper along the path of the striothalamic

Table 4: Results of the multinomial linear regression for each of the 4 scenarios^a

Model	Healthy vs Dementia	Healthy vs AD	Healthy vs VaD	AD vs VaD
Variables entered in the model	PVS-1 PVS-2 _{BG} Modified Scheltens	PVS-1 PVS-2 _{BG} Modified Scheltens	PVS-1 PVS-2 _{BG} Modified Scheltens	PVS-1 PVS-2 _{BG} Modified Scheltens
Variables included in the model	PVS-2 _{BG} Modified Scheltens	PVS-2 _{BG} Modified Scheltens	PVS-2 _{BG} Modified Scheltens	PVS-2 _{BG} Modified Scheltens
PVS-2 _{BG} z score/ β coefficient (significance)	-3.074/-1.094 (<.001)	-3.161/-1.002 (<.01)	-2.623/-1.956 (<.01)	2.212/0.757 (<.05)
Modified Scheltens z score/ β coefficient (significance)	-1.928/-1.221 (NS)	-1.82/-0.951 (NS)	-2.537/-2.727 (<.05)	1.674/0.498 (NS)
Area under ROC curve	0.855	0.774	0.928	0.7135
Sensitivity (%)	94.1	78.9	91.8	65.3
Specificity (%)	71.1	73.6	84.6	71.4
Positive predictive value (%)	83.1	75.0	83.8	80.0
Negative predictive value (%)	88.9	77.8	91.7	54.1

Note:—NS indicates not significant.

^a Diagnoses were treated as categories (AD = 1, VaD = 2, and Healthy = 3). Patient age and sex were entered as covariates in each model. All imaging variables were standardized by calculation of z scores (β /standard error) and were entered into the model if they showed a baseline correlation with the diagnosis with significance $< .05$. Individual z score, β coefficients, and significance are given for each imaging variable in the final model.

arteries indicates increased severity.⁶ The second is based on the observation that in more severe SVD, extensive PVS in the basal ganglia are common, making the first scoring system insensitive to differences between patient groups, especially in older individuals. This scoring system simply counts the number of PVS in the basal ganglia and centrum semiovale on the most severely affected side of the most severely affected section.⁷

In this study, we have examined the discriminative power of deep white matter hyperintensities and PVS scoring systems to separate elderly patients with clinical VaD from healthy controls and patients with AD. Before the study, we had hypothesized that the diagnostic specificity of PVS seen in a young population with dementia¹⁵ would be lost in older patients with increasing frequency of incidental SVD in asymptomatic subjects^{5,7,9} and in those with AD.^{3,16-18} In fact, we have shown that PVS scores retain significant discriminative power to distinguish VaD, AD, and healthy subjects and explain a greater component of the variation between groups than white matter hyperintensity scores. Despite close correlations between PVS-1 and PVS-2 scores, PVS-2 was the more powerful discriminant, and the PVS-1 displayed no independent significant discriminative power.

The identification of PVS-2_{BG} as a powerful discriminator among groups in elderly patients with dementia, providing greater discriminative power than the severity of white matter hyperintensity, is initially counterintuitive. The perception that vascular dementia would be associated with increased white matter injury appears to be supported by the observed data with higher white matter hyperintensity scores in the vascular dementia group. There is, however, no observed group difference in white matter hyperintensity scores between healthy controls and those with AD, both showing values similar to those observed in healthy elderly subjects in previous studies.² In contrast, there is clear evidence of significantly increased numbers of dilated perivascular spaces in the basal ganglia in both AD and, to a more significant extent, in VaD. Dilatation of perivascular spaces is a primary histologic feature of small-vessel disease and has been shown in previous studies to be a more discriminative indicator of the presence of small vessel disease in a number of disease states.^{6,8} In contrast, although deep white matter hyperintensities clearly correlate with the presence of small-vessel disease, a number of other etiologic factors may also be implicated in their production.

An alternative consideration is that the discriminative power of the white matter scoring system will depend on the sensitivity to change over any given portion of the disease process. Observations of deep white matter hyperintensity in normal aging and neurodegenerative diseases demonstrate a predilection for lesions in the deep hemispheric white matter, whereas in subcortical vascular dementia, the frequency of white matter lesions in the basal ganglia and brain stem is significantly higher.^{2,5} Deep white matter hyperintensity accounts for a maximum of only 24/72 on the Scheltens score,¹⁴ whereas the average Scheltens score in patients with VaD in the current study was >22. Furthermore, increases in the deep white matter hyperintensity score depend on the development of large or confluent lesions and can be insensitive to the pres-

ence of numerous lesions, each <1 cm in diameter.¹⁴ It may be that in the presence of extensive deep white matter lesions such as those occurring with advancing age, the Scheltens score becomes less sensitive to increases in severity.

CONCLUSIONS

In summary, these findings indicate that PVS dilation remains a useful biomarker of SVD even in an elderly population and demonstrates greater specificity for discrimination among VaD, AD, and healthy individuals than white matter scoring schemes. Our findings also indicate that the PVS-2_{BG} scoring scheme is preferable in an elderly population.

ACKNOWLEDGMENTS

The authors gratefully acknowledge the major contribution of Nitin Purundare, MD, who sadly died before the completion of this study.

Disclosures: John Cain—UNRELATED: Grants/Grants Pending: Wellcome Trust clinical fellowship. Alan Jackson—RELATED: Grant: Wellcome Trust.* Comments: funded the initial data collection and patient recruitment; UNRELATED: Consultancy: Hoffmann-LaRoche pharmaceuticals, Comments: advisory expert on imaging studies in antiangiogenic studies in lions. *Money paid to the institution.

REFERENCES

1. Kelley RE, Minagar A. **Memory complaints and dementia.** *Med Clin North Am* 2009;93:389–406, ix
2. Mills S, Cain J, Purundare N, et al. **Biomarkers of cerebrovascular disease in dementia.** *Br J Radiol* 2007;80(Spec No 2):S128–45
3. Wardlaw JM, Smith C, Dichgans M. **Mechanisms of sporadic cerebral small vessel disease: insights from neuroimaging.** *Lancet Neurol* 2013;12:483–97
4. Moorhouse P, Rockwood K. **Vascular cognitive impairment: current concepts and clinical developments.** *Lancet Neurol* 2008;7:246–55
5. Wardlaw JM, Smith EE, Biessels GJ, et al. **Neuroimaging standards for research into small vessel disease and its contribution to ageing and neurodegeneration.** *Lancet Neurol* 2013;12:822–38
6. Patankar TF, Mitra D, Varma A, et al. **Dilatation of the Virchow-Robin space is a sensitive indicator of cerebral microvascular disease: study in elderly patients with dementia.** *AJNR Am J Neuroradiol* 2005;26:1512–20
7. Doubal FN, MacLulich AM, Ferguson KJ, et al. **Enlarged perivascular spaces on MRI are a feature of cerebral small vessel disease.** *Stroke* 2010;41:450–54
8. Patankar TF, Baldwin R, Mitra D, et al. **Virchow-Robin space dilatation may predict resistance to antidepressant monotherapy in elderly patients with depression.** *J Affect Disord* 2007;97:265–70
9. Selvarajah J, Scott M, Stivaros S, et al. **Potential surrogate markers of cerebral microvascular angiopathy in asymptomatic subjects at risk of stroke.** *Eur Radiol* 2009;19:1011–18
10. McKhann G, Drachman D, Folstein M, et al. **Clinical diagnosis of Alzheimer's disease: report of the NINCDS-ADRDA Work Group under the auspices of Department of Health and Human Services Task Force on Alzheimer's Disease.** *Neurology* 1984;34:939–44
11. Román GC, Tatemichi TK, Erkinjuntti T, et al. **Vascular dementia: diagnostic criteria for research studies: report of the NINDS-AIREN International Workshop.** *Neurology* 1993;43:250–60
12. Purundare N, Burns A, Daly KJ, et al. **Cerebral emboli as a potential cause of Alzheimer's disease and vascular dementia: case-control study.** *BMJ* 2006;332:1119–24
13. Rosset A, Spadola L, Ratib O. **OsiriX: an open-source software for navigating in multidimensional DICOM images.** *J Digit Imaging* 2004;17:205–16

14. Scheltens P, Barkhof F, Leys D, et al. **A semiquantitative rating scale for the assessment of signal hyperintensities on magnetic resonance imaging.** *J Neurol Sci* 1993;114:7–12
15. Patankar T, Widjaja E, Chant H, et al. **Relationship of deep white matter hyperintensities and cerebral blood flow in severe carotid artery stenosis.** *Eur J Neurol* 2006;13:10–16
16. Varma AR, Laitt R, Lloyd JJ, et al. **Diagnostic value of high signal abnormalities on T2 weighted MRI in the differentiation of Alzheimer's, frontotemporal and vascular dementias.** *Acta Neurol Scand* 2002;105:355–64
17. Esiri MM, Joachim C, Sloan C, et al. **Cerebral subcortical small vessel disease in subjects with pathologically confirmed Alzheimer disease: a clinicopathologic study in the Oxford Project to Investigate Memory and Ageing (OPTIMA).** *Alzheimer Dis Assoc Disord* 2014;28:30–35
18. Jellinger KA, Attems J. **Is there pure vascular dementia in old age?** *J Neurol Sci* 2010;299:150–54

Increased Number of White Matter Lesions in Patients with Familial Cerebral Cavernous Malformations

M.J. Golden, L.A. Morrison, H. Kim, and B.L. Hart



ABSTRACT

BACKGROUND AND PURPOSE: Familial cerebral cavernous malformations, an autosomal dominant disorder, result in excess morbidity and mortality in affected patients. The disorder is most prevalent in the Southwest United States, where the affected families are most often carriers of the *CCM1-KRIT1* Common Hispanic Mutation. The brain and spinal cord parenchyma in these individuals is usually affected by multiple cavernous malformations. Previous studies have shown abnormalities of endothelial cell junctions and the blood-brain barrier in cerebral cavernous malformations. Endothelial cell abnormalities have also been described in pathologic studies of white matter hyperintensities. We compared the prevalence of white matter hyperintensities in a population with known familial cerebral cavernous malformations.

MATERIALS AND METHODS: We examined 191 subjects with familial cerebral cavernous malformations who were enrolled into an institutional review board–approved study. All carry the same Common Hispanic Mutation in the *CCM1* gene. Each subject underwent 3T MR imaging, including gradient recalled-echo, SWI, and FLAIR sequences. The number of cavernous malformations and the number of nonhemorrhagic white matter hyperintensities were counted. Subjects older than 60 years of age were excluded due to the high prevalence of white matter lesions in this population, and children younger than 6 were excluded due to potential sedation requirements. Logistic regression analysis was performed to determine the prevalence of abnormal white matter hyperintensities in those with familial cerebral cavernous malformations compared with healthy controls or those with sporadic cerebral cavernous malformation within the familial cerebral cavernous malformations group; it was also performed to evaluate the associations between abnormal white matter hyperintensities and age, sex, headaches, thyroid disease, diabetes, hypertension, hyperlipidemia, seizure history, or modified Rankin Scale score.

RESULTS: Familial *CCM1* carriers have a higher prevalence of abnormal white matter hyperintensities (15.4%) compared with both control populations (2.1% and 2.5%, respectively) ($P < .05$). Logistic regression showed no statistical association with sex, headaches, hyperlipidemia, hypertension, thyroid disease, seizure history, number of cerebral cavernous malformations, or modified Rankin Scale score among those with familial cerebral cavernous malformation. An expected correlation with age was shown.

CONCLUSIONS: Familial *CCM1* carriers have not only an increased number of cerebral cavernous malformations but also an increased number of white matter T2 hyperintensities, spatially distinct from cerebral cavernous malformations, which exceeded that of a healthy population. Clinical findings did not explain the association with abnormal white matter hyperintensities in the familial cerebral cavernous malformation population. To our knowledge, these relationships have not been previously reported. This finding suggests an additional manifestation of endothelial abnormalities in this population.

ABBREVIATIONS: CCM = cerebral cavernous malformation; fCCM = familial cerebral cavernous malformations; WMHI = white matter hyperintensities

Familial cerebral cavernous malformations (fCCM) constitute an autosomal dominant disorder with variable penetrance.¹

This condition occurs throughout the world but is especially prevalent in the Southwestern United States.^{2,3} Repeated hemorrhages cause significant morbidity and mortality in affected indi-

Received August 20, 2014; accepted after revision October 22.

From the Departments of Radiology (M.J.G., B.L.H.) and Neurology (L.A.M.), University of New Mexico, Albuquerque, New Mexico; and Departments of Anesthesiology and Perioperative Care (H.K.) and Epidemiology and Biostatistics (H.K.), University of California, San Francisco, San Francisco, California.

Dr Golden was supported as a trainee by the Brain Vascular Malformation Consortium. The Brain Vascular Malformation Consortium is supported by a grant from the National Institutes of Health (U54 NS065705) and is a part of the National Institutes of Health Rare Disease Clinical Research Network, supported through a collaboration between the National Institutes of Health Office of Rare Diseases

Research at the National Center for Advancing Translational Science and the National Institute of Neurologic Disorders and Stroke.

Paper previously presented at: Annual Meeting of the American Society of Neuroradiology and the Foundation of the ASNR Symposium, May 17–22, 2014; Montreal, Quebec, Canada.

Please address correspondence to Blaine L. Hart, MD, Department of Radiology, MSC10 5530, 1 University of New Mexico, Albuquerque, NM 87131-0001; e-mail: bhart@salud.unm.edu

Indicates open access to non-subscribers at www.ajnr.org

<http://dx.doi.org/10.3174/ajnr.A4200>

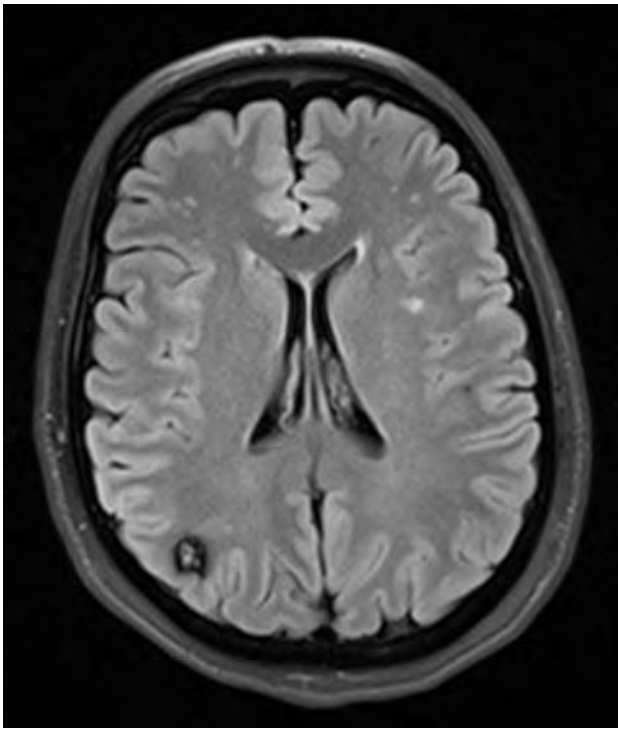


FIG 1. FLAIR images obtained in a 39-year-old patient with fCCM demonstrate a large number of WMHI. Also note the CCM in the right parietal lobe.

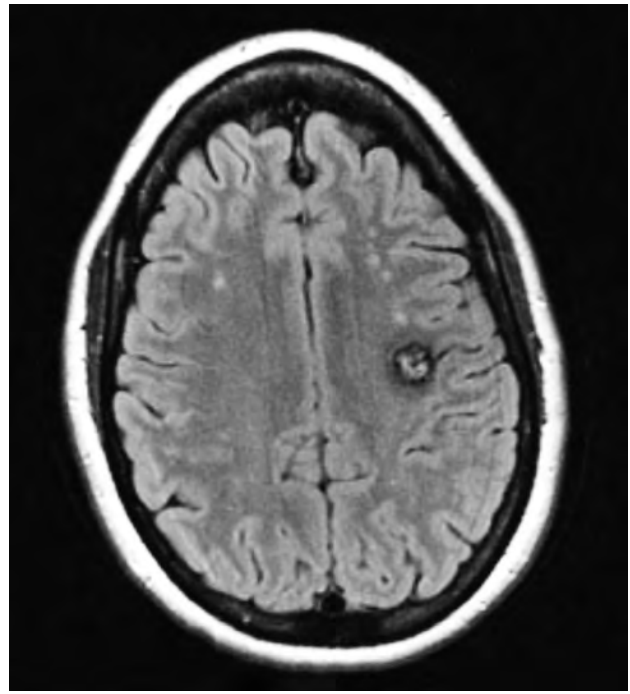


FIG 2. FLAIR images from this 26-year-old patient show numerous WMHI in addition to the CCM located in the posterior left frontal lobe.

viduals and families. Patients present with hemorrhage, seizures, headaches, and/or focal neurologic deficits, and some patients ultimately die from associated complications.

Imaging evaluation of these patients often focuses on the presence, location, and size of the vascular malformations.^{2,4} Blood-breakdown products within the cerebral cavernous malformations (CCMs) are best evaluated with susceptibility-sensitive MR imaging, specifically SWI and T2 gradient recalled-echo sequences. However, FLAIR and T2-weighted sequences sometimes disclose additional findings. We have noted an unexpected number of T2 white matter hyperintensities (WMHI) in some of these patients (Figs 1 and 2). Although such WMHI are generally considered nonspecific on MR imaging, the association of WMHI with a wide variety of conditions with small-vessel disease raised the question of their significance in familial CCM. We tested the hypothesis that increased WM lesions are present in patients with fCCM. We compared the prevalence of T2 WMHI in patients with fCCM with those in a healthy control group and with patients with sporadic CCMs and evaluated whether confounding factors related to small-vessel disease could explain this association.

MATERIALS AND METHODS

All parts of this study were performed with institutional review board approval. After informed consent, 191 subjects were enrolled into an ongoing study of fCCM with the Common Hispanic Mutation (Q455X mutation) recruited as part of the Brain Vascular Malformation Consortium CCM Project.⁵ Brain MR imaging at 3T was performed on all subjects, including T2 gradient recalled-echo, T2 FSE (both with 3-mm section thickness),

SWI (1.5-mm section thickness), and FLAIR imaging (4-mm section thickness). CCMs were counted and characterized on the SWI and gradient recalled-echo sequences by a neuroradiologist with extensive CCM research experience as part of the overall study plan. Children younger than of 6 years of age were not eligible to participate in this study due to the potential need for sedation for MR imaging.

WMHI were counted on the FLAIR sequences, with concurrent reference to T2 sequences. All subjects older than 60 years of age (28 total) were excluded from this retrospective review of white matter lesions, given the known high correlation of WMHI with advancing age.^{6,7} One subject was excluded because the study MR imaging was terminated before FLAIR imaging; 149 subjects remained (56 male, 93 female; 6–59 years of age). There is no universally accepted measure of a “normal” number of white matter changes. They are known to increase with age; indeed, age is the strongest factor associated with WMHI. A common rule of thumb is that 1 WMHI per decade of life is considered unremarkable.⁸ Guidelines for normal or unremarkable WMHI become less useful with increasing patient age. For purposes of this study, the number of WMHI was considered abnormally high if there were >5, or unusually large or confluent lesions were seen in any individual younger than 40 years of age, or >10 lesions were seen in anyone between 40 and 60 years of age.

A control group of 47 healthy volunteers younger than 60 years of age who gave informed consent and were carefully screened to eliminate a history of disease were evaluated for WMHI. This control population was evaluated on the same 3T magnet, and demographics closely resembled those of the fCCM population.

Additionally, a group of 39 patients younger than 60 years of

Table 1: Frequency distribution of WMHI in patients with fCCM

WMHI No.	Frequency	%
0	88	59%
1	14	9%
2	10	7%
3–10	20	13%
11–20	3	2%
21–30	5	3%
31–40	5	3%
41–50	2	1%
51+	2	1%

age (including both 3T and 1.5T MR imaging, part of an institutional review board–approved study) was identified as having sporadic CCMs; each patient had only 1 lesion present in the brain and lacked clinical or family history evidence of fCCM. Any patient with multiple CCMs was excluded from this control group because this finding was suspicious for a familial pattern of CCMs (Common Hispanic Mutation or otherwise). FLAIR imaging was then evaluated, and abnormal white matter lesions were counted.

For the control groups, all FLAIR images were reviewed by a neuroradiology fellow and the same neuroradiologist who originally read the fCCM MR imaging studies. Infrequent differences were resolved by a consensus read. The prevalence of abnormal WMHI in patients with fCCM was compared with that in the 2 control groups by using logistic regression to account for age and sex.

Descriptive statistics, including proportions for categorical variables and means, SDs, ranges, and interquartile ranges for continuous variables, were computed. Logistic regression analysis was preformed to evaluate whether the abnormal status of WMHI differed between patients with fCCM and the 2 control groups while adjusting for age and sex; results are reported as odds ratios with associated 95% confidence intervals. Among patients with fCCM only, the Fisher exact test (categorical variable) or Wilcoxon rank sum test (continuous variable) was performed to compare the univariate association of abnormal WMHI with the number of CCMs, age, sex, hyperlipidemia (physician diagnosed or taking medication), hypertension (physician diagnosed or the subject taking medications at the initial examination⁹), headaches, seizures, thyroid disease, diabetes, and modified Rankin Scale score as a measure of overall neurologic disability. The distribution of CCM and WMHI lesions is heavily right-skewed; thus, values were log-transformed before parametric analysis to avoid the effects of overly influential observations. Clinical factors found to have a $P \leq .10$ in univariate analysis were tested in a multivariate logistic regression model adjusting for age and sex. All P values reported are 2-sided, and we considered $P < .05$ to be statistically significant.

RESULTS

Twenty-three of 149 (15.4%) patients in the fCCM group (mean age, 33.1 years; range, 6–59 years) had an abnormal number of WMHI. Healthy control subjects (mean age, 31.3 years; range, 21–46) had a prevalence of 2.1% (1/48) (Table 1). Patients with sporadic CCM (mean age, 28.1 years; range, 4–56 years) had white matter abnormalities at a prevalence of 2.5% (1/39). Thus,

Table 2: Association of abnormal WMHI and characteristics in 149 patients with fCCM^a

fCCM Characteristic	Abnormal WMHI (n = 23)	Normal WMHI (n = 126)	P Value
Sex (No.) (%)			
Female	18 (78)	75 (60)	.11
Male	5 (22)	51 (40)	
Age (yr) (mean) (SD)	23 (41)	32 (16)	.01
Headaches (No.) (%)			
Yes	15 (65)	79 (64)	1.00
No	8 (35)	45 (36)	
Seizures (No.) (%)			
Yes	11 (48)	48 (39)	.49
No	12 (52)	76 (61)	
Thyroid (No.) (%)			
Yes	3 (13)	9 (7)	.40
No	20 (87)	115 (93)	
Diabetes (No.) (%)			
Yes	2 (9)	12 (10)	1.00
No	21 (91)	112 (90)	
Hyperlipidemia (No.) (%)			
Yes	7 (30)	17 (13)	.06
No	16 (70)	109 (87)	
Hypertension (No.) (%)			
Yes	6 (26)	15 (12)	.10
No	17 (74)	109 (88)	
Modified Rankin Scale (No.) (%)			
0	4 (17)	46 (37)	.33
1	10 (44)	37 (30)	
2	7 (30)	27 (22)	
3	2 (9)	11 (9)	
4	0 (0)	2 (2)	
CCM lesions			
Median (IQR)	29 (29)	11 (39)	.08
Mean (SD)	60 (122)	42 (96)	

Note:—IQR indicates interquartile range.

^a Note that some numbers for characteristics do not add up to column totals due to missing data.

the prevalence of abnormal WMHI was significantly higher in the fCCM group compared with either control group (1-sided $P < .05$).

The prevalence of abnormal WMHI in the healthy control group was nearly identical to the sporadic CCM rate. These 2 populations were then pooled together and compared with the fCCM population. The age and sex distribution were similar between the groups, but logistic regression was further used to evaluate the rate of abnormal WMHI between the fCCM and the pooled control group to correct for sex and age. The odds ratio of patients with fCCM having abnormal quantities of WMHI was 8.3 (95% CI, 1.03–66.9) compared with the combined group, and it was statistically significant ($P < .05$).

Second, we evaluated potential clinical factors within the fCCM group that could explain the increased prevalence of abnormal WMHI (Table 2). No statistically significant association was found with sex ($P = .11$), headaches ($P = 1.00$), seizure ($P = .49$), thyroid disease ($P = .40$), hyperlipidemia ($P = .06$), diabetes ($P = 1.00$), or hypertension ($P = .10$). Age did demonstrate a positive association ($P = .01$), an expected result. We found no association of abnormal WMHI with neurologic disability as measured by the modified Rankin Scale score ($P = .33$).

The patients with fCCM with abnormal WMHI tended to have a greater number of CCM lesions, though this was not statistically significant ($P = .08$). Including age in a logistic regression model explains away the association between WMHI and the number of CCMs ($P = .98$), likely because both WMHI and CCM lesions are strongly correlated with increasing age. A multivariable logistic regression model with hyperlipidemia, hypertension, number of CCMs, age, and sex as predictors of abnormal WMHI status yielded no statistically significant associations.

DISCUSSION

Our study showed a significant increase in WMHI in patients with fCCM compared with healthy controls and with patients with sporadic CCM, which, to the best of our knowledge, has not been previously reported. Bright spots on T2-weighted MR images have been an uncertainty in brain imaging since the inception of MR imaging. This challenge is reflected in the various terms that have been used such as white matter hyperintensities (a purely descriptive term), leukoaraiosis, chronic microvascular changes, chronic microangiopathy, white matter changes of aging, and unidentified bright objects. Such lesions are known to correlate with patient age and can additionally be caused by demyelination, edema, and gliosis, including causes of microvascular change such as hypertension, lupus erythematosus, migraines, seizures, or other vasculopathies. FLAIR hyperintensities may sometimes accompany perivascular spaces. Although some of the WMHI in this study could be associated with perivascular spaces, typical radially oriented perivascular spaces were generally distinguishable by using both FSE T2 and FLAIR on the 3T system. Moreover, changes associated with perivascular spaces are likely to affect all groups in the study to a similar degree. Considerable research has been done on the significance of WMHI in the elderly population. Volumetric measurements have often been used in research studies of elderly patients, in whom the T2 changes are frequently confluent. The presence of focal WMHI in a young or middle-aged population is a common finding in the routine clinical practice of radiology.

Interpretation of the literature on this finding is challenging because of the varying technical factors used in different reports, including field strength and MR imaging sequences used, as well as varying subject ages; such factors are not always specified in the literature. The frequency of WMHI varies widely in the literature, but several authors reported a rate between 0.5% and 5% for a young healthy population.^{10,11} We were able to use a control group of healthy volunteers who were scanned on the same MR imaging system as our fCCM study group, avoiding some of the technical limitations of historical controls. The findings of the additional control group from clinical studies of patients with sporadic CCM appeared very similar to those of the healthy control group, despite a mix of 3T and 1.5T studies. Both groups thus appear very similar to those in literature reports of healthy subjects, but our study confers the added advantage of clearly defined and comparable technical factors.

A variety of pathologic correlates likely exist for the T2 hyperintensities seen on MR imaging. However, we examined possible causes of microvascular changes for association with abnormal WMHI within the fCCM group, and none were found to be sig-

nificantly associated with abnormal WMHI status. Seizure disorders are reported to be associated with increased numbers of WMHI,¹²⁻¹⁴ and seizures are common complications of CCMs. However, the prevalence of WMHI within the fCCM group was nearly identical for those with and without seizure history.

Hypertension and hyperlipidemia were both present at higher frequencies in patients with fCCM with abnormal WMHI but were not found to be significant predictors of abnormal WMHI status in either univariate or multivariate analysis. Both of these variables were derived from patient self-reports of either physician diagnosis or the patient taking medications for these conditions. We did not have detailed information available on the length of the diagnosis or the details of treatment, which may have limited our ability to detect significant associations with these clinically important variables.

Although we could not find an explanation for the increased prevalence of abnormal WMHI with typical clinical factors of microvascular changes, it is well-known that patients with fCCM have underlying endothelial dysfunction.¹⁵⁻¹⁷ Additionally, CCMs demonstrate abnormal ultrastructural characteristics,¹⁸ and this abnormal physiology is known to result in a compromised blood-brain barrier.¹⁹ In vivo human permeability studies have shown that the transfer rate (influx constant) is increased in CCMs.²⁰ Reviews of neuropathologic information about WMHI in older individuals (not those with fCCM) have shown structural abnormalities and compromise of the blood-brain barrier.²¹ The influx constant has also been shown to be increased in nonspecific WMHI in brain white matter in permeability studies of subjects with vascular cognitive impairment.²⁰ Endothelial abnormalities caused by the mutations in fCCM may be a factor in WMHI seen in patients with fCCM.

The increased prevalence of WMHI in fCCM is modest and is not clearly correlated with the number of CCM lesions, especially after accounting for age. Moreover, we did not find a correlation of WMHI with disability as measured by the modified Rankin Scale score. Our definition of abnormal WMHI served as a pragmatic and conservative measure for this study. Although we have not observed T2 WMHI to precede the formation of CCMs, a causal relationship cannot be excluded, and further longitudinal studies will be needed. It is possible that endothelial abnormalities in fCCM predispose to a higher risk of WMHI when combined with other, more common risk factors for microvascular disease. Clinically, when unexpected numbers of WMHI are observed in patients with fCCM, common causes such as hypertension should be considered. If such factors are not found, however, it appears that the fCCM condition itself may be associated with increased WMHI.

The results of our study, combined with historical studies, lead us to hypothesize that underlying endothelial abnormalities in the fCCM population could result in increased permeability with resultant increased hemorrhage, new lesion formation of cerebral cavernous malformations, and increased formation of WMHI. These 2 separate findings may be different manifestations of a common underlying process. Future neuropathologic studies and/or in vivo permeability studies will offer further insight into the mechanisms for these findings.

CONCLUSIONS

Subjects with fCCM have an increased prevalence of abnormal WMHI compared with healthy control populations and those with sporadic CCMs. Additionally, no single clinical factor could be associated with patients with fCCM. We found no association between abnormal WMHI and sex, hypertension, headache, thyroid disease, seizures, diabetes or hyperlipidemia, number of CCMs, or modified Rankin Scale scores among patients with fCCM. CCMs and WMHI may be separate and distinct outcomes of underlying endothelial dysfunction in patients with fCCM.

ACKNOWLEDGMENTS

We thank Herbert Davis and Ron Schrader from the University of New Mexico and Jeffrey Nelson from the University of California, San Francisco, for help with statistical analysis; Cheryl Aine, MD, of the University of New Mexico for providing data from healthy control volunteers; and Beth Baca, MSW, for patient recruitment, coordination, and data management.

Disclosures: Michael J. Golden—RELATED: Grant: National Institutes of Health,* Comments: This research was funded through a National Institutes of Health grant; Employment: University of New Mexico, Comments: salary as a PGY-7 Neuroradiology Fellow. Leslie A. Morrison—RELATED: Grant: National Institute of Neurologic Disorders and Stroke/National Institutes of Health.* Blaine L. Hart—RELATED: Grant: National Institutes of Health (U54 NS065705).* Helen Kim—RELATED: Grant: National Institutes of Health, Comments: support received individually and by institution.* *Money paid to the institution.

REFERENCES

1. Rivera PP, Willinsky RA, Porter PJ. **Intracranial cavernous malformations.** *Neuroimaging Clin N Am* 2003;13:27–40
2. Kattapong VJ, Hart BL, Davis LE. **Familial cerebral cavernous angiomas: clinical and radiologic studies.** *Neurology* 1995;45:492–97
3. Gunel M, Awad IA, Finberg K, et al. **A founder mutation as a cause of cerebral cavernous malformation in Hispanic Americans.** *N Engl J Med* 1996;334:946–51
4. Zabramski JM, Wascher TM, Spetzler RF, et al. **The natural history of familial cavernous malformations: results of an ongoing study.** *J Neurosurg* 1994;80:422–32
5. Akers AL, Ball KL, Clancy M, et al. **Brain vascular malformation consortium: overview, progress and future directions.** *J Rare Disord* 2013;1:5
6. Christiansen P, Larsson HB, Thomsen C, et al. **Age dependent white matter lesions and brain volume changes in healthy volunteers.** *Acta Radiol* 1994;35:117–22
7. Vernooij MW, Ikram MA, Tanghe HL, et al. **Incidental findings on brain MRI in the general population.** *N Engl J Med* 2007;357:1821–28
8. Osborn AG. *Osborn's Brain: Imaging, Pathology, and Anatomy.* Salt Lake City: Amirsys; 2012
9. Liao D, Cooper L, Cai J, et al. **Presence and severity of cerebral white matter lesions and hypertension, its treatment, and its control: the ARIC Study—Atherosclerosis Risk in Communities Study.** *Stroke* 1996;27:2262–70
10. Hopkins RO, Beck CJ, Burnett DL, et al. **Prevalence of white matter hyperintensities in a young healthy population.** *J Neuroimaging* 2006;16:243–51
11. Katzman GL, Dagher AP, Patronas NJ. **Incidental findings on brain magnetic resonance imaging from 1000 asymptomatic volunteers.** *JAMA* 1999;282:36–39
12. Eriksson SH, Stepney A, Symms MR, et al. **Ultra-fast low-angle rapid acquisition and relaxation enhancement (UFLARE) in patients with epilepsy.** *Neuroradiology* 2001;43:1040–45
13. Jansen JFA, Vlooswijk MC, Majoie HM, et al. **White matter lesions in patients with localization-related epilepsy.** *Invest Radiol* 2008;43:552–58
14. Wieshmann UC. **Clinical application of neuroimaging in epilepsy.** *J Neurol Neurosurg Psychiatry* 2003;74:466–70
15. Stockton RA, Shenkar R, Awad IA, et al. **Cerebral cavernous malformations proteins inhibit Rho kinase to stabilize vascular integrity.** *J Exp Med* 2010;207:881–96
16. Glading A, Han J, Stockton RA, et al. **KRIT-1/CCM1 is a Rap1 effector that regulates endothelial cell cell junctions.** *J Cell Biol* 2007;179:247–54
17. Schneider H, Errede M, Ulrich NH, et al. **Impairment of tight junctions and glucose transport in endothelial cells of human cerebral cavernous malformations.** *J Neuropathol Exp Neurol* 2011;70:417–29
18. Tu J, Stoodley MA, Morgan MK, et al. **Ultrastructural characteristics of hemorrhagic, nonhemorrhagic, and recurrent cavernous malformations.** *J Neurosurg* 2005;103:903–09
19. Clatterbuck RE, Eberhart CG, Crain BJ, et al. **Ultrastructural and immunocytochemical evidence that an incompetent blood-brain barrier is related to the pathophysiology of cavernous malformations.** *J Neurol Neurosurg Psychiatry* 2001;71:188–92
20. Hart BL, Taheri S, Rosenberg GA, et al. **Dynamic contrast-enhanced MRI evaluation of cerebral cavernous malformations.** *Trans Stroke Res* 2013;4:500–06
21. Young VG, Halliday GM, Kril JJ. **Neuropathologic correlates of white matter hyperintensities.** *Neurology* 2008;71:804–11

Pituitary-Targeted Dynamic Contrast-Enhanced Multisection CT for Detecting MR Imaging–Occult Functional Pituitary Microadenoma

M. Kinoshita, H. Tanaka, H. Arita, Y. Goto, S. Oshino, Y. Watanabe, T. Yoshimine, and Y. Saitoh



ABSTRACT

BACKGROUND AND PURPOSE: Although resection of a tumor by trans-sphenoidal surgery is considered the criterion standard for successful surgical treatment of functional pituitary microadenoma, MR imaging occasionally fails to visualize and identify the tumor and supplementary imaging modalities are necessary. We tested the possibility of dynamic contrast-enhanced multisection CT of the pituitary gland accompanying image reconstruction of contrast agent dynamics to identify the localizations of microadenomas and compared the diagnostic performance with conventional pituitary-targeted MR imaging.

MATERIALS AND METHODS: Twenty-eight patients with surgically confirmed functional pituitary microadenomas (including growth hormone–, adrenocorticotrophic hormone–, and prolactin-secreting adenomas) who underwent pituitary-targeted dynamic contrast-enhanced multisection CT were retrospectively investigated. We undertook image reconstruction of the dynamics of the contrast agent around the pituitary gland in a voxelwise manner, visualizing any abnormality and enabling qualification of contrast dynamics within the tumor.

RESULTS: Fifteen cases were correctly diagnosed by MR imaging, while dynamic contrast-enhanced multisection CT correctly diagnosed 26 cases. The accuracy of localization was markedly better for adrenocorticotrophic hormone–secreting microadenomas, increasing from 32% on MR imaging to 85% by dynamic contrast-enhanced multisection CT. Compared with the normal pituitary gland, adrenocorticotrophic hormone–secreting adenoma showed the least difference in contrast enhancement of the different functional microadenomas. Images acquired at 45–60 seconds after contrast agent injection showed the largest difference in contrast enhancement between an adenoma and the normal pituitary gland.

CONCLUSIONS: Dynamic contrast-enhanced multisection CT combined with image reconstruction of the contrast-enhanced dynamics holds promise in detecting MR imaging–occult pituitary microadenomas.

ABBREVIATIONS: ACTH = adrenocorticotrophic hormone; AUC = area under the curve; DCE = dynamic contrast-enhanced; MCT = multisection CT; PRL = prolactin; rAUC = relative AUC

Pituitary microadenoma often shows uncontrolled production of pituitary hormones and causes endocrine disorders such as Cushing disease, acromegaly, and hyperprolactinemia. Although

pharmacotherapy has recently played a more pivotal role in treating functional pituitary microadenoma,^{1,2} resection of the tumor by trans-sphenoidal surgery is still considered the criterion standard.³ Because these tumors tend to be relatively small, precise preoperative identification of a microadenoma is one of the crucial elements for successful surgical treatment of this disease.⁴

MR imaging with or without contrast agent is most commonly used for this purpose, and dynamic contrast-enhanced techniques are sometimes applied for better tumor visualization.^{5,6} Moreover, the magnetic field strength typically applied in MR imaging has recently increased from 1.5T to 3T, and clearer imaging of microadenomas has thus been anticipated.⁴ Such effort, however, often fails to correctly depict the microadenoma, and other modalities such as methionine positron-emission tomography have been suggested to meet this need.⁴ Methionine PET does indeed hold promise for the visualization of microadenoma but is not yet widely clinically available, and a more clinically accessible technique is necessary for better visualization of this entity. The present study investigated the possi-

Received September 24, 2014; accepted after revision November 2.

From the Departments of Neurosurgery (M.K., H.A., Y.G., S.O., T.Y., Y.S.) and Radiology (H.T., Y.W.), Osaka University Graduate School of Medicine, Osaka, Japan; Department of Neurosurgery (M.K.), Osaka Medical Center for Cancer and Cardiovascular Diseases, Osaka, Japan; and Department of Neuromodulation and Neurosurgery (Y.S.), Osaka University Graduate School of Medicine, Center of Medical Innovation and Translational Research, Osaka, Japan.

This work was supported by the Aichi Cancer Research Foundation, the SENSHIN Medical Research Foundation, the Life Science Foundation of Japan, and the Japan Society for the Promotion of Science KAKENHI (25462256).

Please address correspondence to Youichi Saitoh, MD, PhD, Department of Neuromodulation and Neurosurgery, Osaka University Graduate School of Medicine, Center of Medical Innovation and Translational Research, 2-2 Yamadaoka, Suita, Osaka 565-0871, Japan; e-mail: neurosaitoh@mbk.nifty.com

Indicates open access to non-subscribers at www.ajnr.org

Indicates article with supplemental on-line tables.

<http://dx.doi.org/10.3174/ajnr.A4220>

bility of dynamic contrast-enhanced multisection CT (DCE-MCT) of the pituitary gland accompanying image reconstruction of contrast agent dynamics to identify the location of a microadenoma and compared the diagnostic performance with conventional pituitary-targeted MR imaging.

MATERIALS AND METHODS

Patient Characteristics

The selected patients for this study consisted of a consecutive series of all those with endocrinopathy treated by surgery who had undergone both pituitary-targeted dynamic contrast-enhanced multisection CT and MR imaging as presurgical studies. As a result, pituitary-targeted DCE-MCT was performed for 28 patients with functional pituitary microadenoma at Osaka University Hospital between 2004 and 2014 as a preoperative assessment. Patient characteristics are shown in On-line Table 1. The underlying pathology was adrenocorticotropic hormone (ACTH)-secreting adenoma in 13 cases, growth hormone-secreting adenoma in 6, and prolactin (PRL)-secreting adenoma in 9. The institutional review board of the local ethics committee approved research use of the collected data (institutional review board number: 12491), and written consent was waived for this study.

Preoperative MR Imaging

MR imaging was performed at either 1.5T (Signa Genesis/Excite; GE Healthcare, Milwaukee, Wisconsin; or Magnetom Vision Plus; Siemens, Erlangen, Germany) or 3T (Signa HDxt; GE Healthcare; or Achieva/Ingenia; Philips Healthcare, Best, the Netherlands). Six patients were scanned at 1.5T; and 22, at 3T. Standard T1- and T2-weighted images and gadolinium-enhanced T1-weighted images targeting the pituitary gland were obtained. The dynamic contrast-enhanced technique was not included for MR imaging in the current study. Axial, coronal, and sagittal images were routinely obtained for gadolinium-enhanced T1-weighted imaging. Section thickness was 3 mm, with section spacing ranging from 0.3 to 0.6 mm. Detailed parameters for MR imaging are listed in On-line Table 2. The final diagnostic report from board-certified neuroradiologists was referenced for defining the tumor location. The surgeons (M.K., S.O., Y.S.) and the first author (M.K.) confirmed the radiologists' official report by observing the actual MR imaging.

Preoperative Dynamic Contrast-Enhanced Multisection CT

Pituitary-targeted dynamic contrast-enhanced multisection CT was performed by using either a Discovery CT750 HD, LightSpeed Ultra, or LightSpeed VCT system (GE Healthcare). A schematic presentation of the protocol is provided in Fig 1. One hundred milliliters of 300-mg I/mL contrast agent was injected intravenously with an injection rate of 5 mL/s, and MCT was acquired at 30, 45, 60, and 90 seconds after contrast agent injection. MCT was acquired at 60, 90, 120, and 150 seconds after contrast agent injection for 2 cases and at 40, 80, and 120 seconds for 1 case for technical reasons (On-line Table 1). Approximately 3 seconds were required to acquire each phase in a gapless 3D volume. Subsequently, pituitary-targeted axial images were reconstructed at a special resolution of 0.3/0.3/0.6 mm with no section gap.

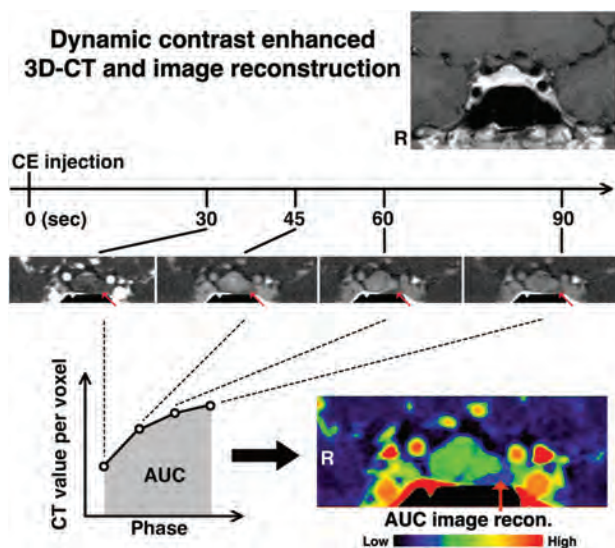


FIG 1. Schematic presentation for DCE-MCT image acquisition and reconstruction. DCE-MCT was performed at 30, 45, 60, and 90 seconds after contrast agent injection. Subsequently, the “AUC image” was reconstructed in 3D. A representative case of a PRL-secreting pituitary microadenoma (case 20) is illustrated. The red arrows indicate the microadenoma, which was confirmed by surgical removal of the lesion.

Image Reconstruction of Contrast Agent Dynamics and Statistical Analysis

The dynamics of the contrast agent around the pituitary gland were calculated by summation of the acquired multiphase MCT in a voxelwise manner by using software developed in-house on Matlab (MathWorks, Natick, Massachusetts). An ROI was placed preoperatively at the normal pituitary gland and the suspected adenoma by the first author (M.K.) on the reconstructed area under the curve (AUC) images without referring to MR imaging, followed by calculation of ROI statistics. A paired *t* test, 2-way analysis of variance, or 1-way ANOVA with a Tukey multiple comparison test was performed by using GraphPad Prism software, Version 5.0 (GraphPad Software, San Diego, California).

Trans-Sphenoidal Surgery and Verification of the Adenoma

Judgment of tumor location was preoperatively performed by using both MR imaging and DCE-MCT with AUC-reconstructed images. When MR imaging and DCE-MCT led to conflicting results, a surgical approach to the tumor was planned so that both sides within the sella turcica could be explored. Endoscope-assisted trans-sphenoidal surgery was performed in all cases by 3 neurosurgeons specializing in pituitary surgery (M.K., S.O., Y.S.). Histologic or endocrinologic confirmation was undertaken to confirm the presence or absence of a hormone-secreting functional adenoma at the surgical location.

RESULTS

Diagnostic Efficacy of MR Imaging and DCE-MCT for Functional Pituitary Microadenoma

Representative cases are shown in Figs 1 and 2. Figure 1 shows a case of PRL-secreting microadenoma. Contrast-enhanced MR imaging failed to identify tumor within the sella turcica, while

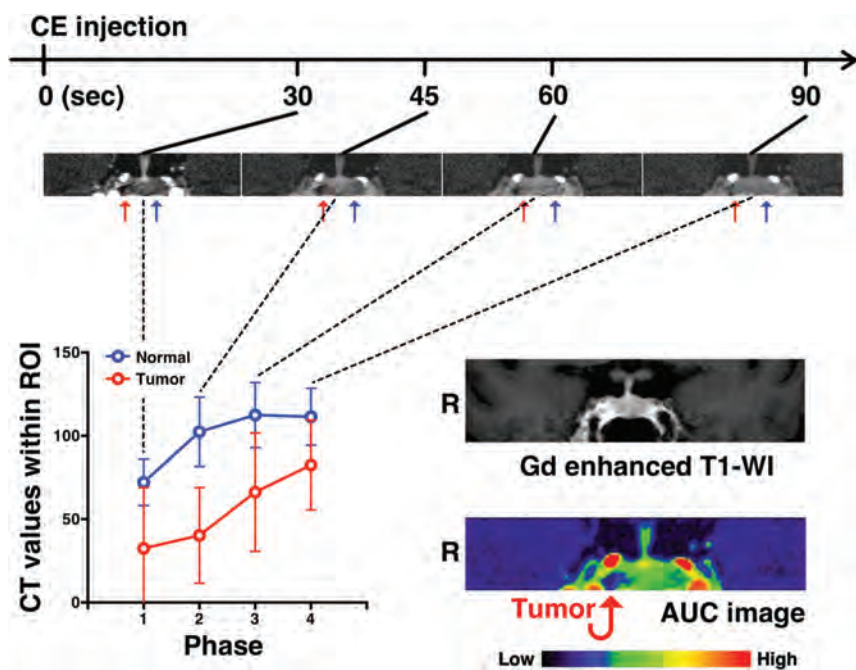


FIG 2. A representative case of ACTH-secreting pituitary microadenoma. DCE-MCT analysis of an ACTH-secreting pituitary microadenoma (case 12) is presented. Abnormal contrast agent dynamics are observed on the right side of the pituitary gland, though no abnormality is evident on MR imaging. The red arrows indicate the microadenoma, which was confirmed by surgical removal of the lesion. The blue arrows indicate a normal pituitary gland.

Comparison of MRI and CT for correct localization diagnosis of functional microadenomas

Hormone Secreted	No. of Cases	Correct Diagnosis by MRI	Correct Diagnosis by CT
ACTH	13	4	11
GH	6	6	6
PRL	9	5	9
Total	28	15	26

Note:—GH indicates growth hormone.

DCE-MCT clearly showed decreased and delayed contrast enhancement on the left side of the pituitary gland. Abnormal contrast agent dynamics were much more easily appreciated on the reconstructed AUC image. Figure 2 shows a case of ACTH-secreting microadenoma. Contrast-enhanced MR imaging again failed to identify the presence of tumor, while DCE-MCT along with the reconstructed AUC image clearly suggested a lesion located on the right side of the pituitary gland. Diagnostic performances of MR imaging and DCE-MCT for each type of functional pituitary microadenoma are listed in the Table and On-line Table 1. Overall, 15 of the 28 cases were correctly diagnosed by MR imaging, while DCE-MCT correctly diagnosed 26 cases (Table). The accuracy of location prediction was markedly improved for ACTH-secreting microadenoma, increasing from 32% (4/13) with MR imaging to 85% (11/13) with DCE-MCT.

Comparison of Contrast-Enhancement Dynamics between the Normal Pituitary Gland and a Functional Pituitary Microadenoma by DCE-MCT

The dynamics of contrast enhancement were compared between the normal pituitary gland and a functional pituitary microadenoma by looking into differences in the AUC retrieved by DCE-

MCT. ROIs were placed on either the normal-appearing pituitary gland or the adenoma, the locations of which were confirmed postoperatively. AUC was significantly decreased in the microadenoma compared with the normal pituitary gland (Fig 3A). Relative AUC (rAUC) was subsequently calculated for each lesion, as $rAUC = AUC_{adenoma} / AUC_{pituitary}$. When contrast-enhanced dynamics are equal between the adenoma and the normal pituitary gland, the rAUC will thus be 1. Fig 3B shows that ACTH-secreting adenomas presented with a significantly higher rAUC compared with PRL-secreting adenomas, and the rAUC of ACTH-secreting adenoma was close to 1. A trend was also seen for the growth hormone-secreting adenoma to show lower rAUC than the ACTH-secreting adenoma. These results suggest that the contrast-enhanced dynamics of ACTH-secreting microadenomas are relatively similar to those of the normal pituitary gland compared with PRL- or growth hormone-secreting microadenomas. This finding was

also confirmed by analyzing the ratio of contrast enhancement compared with the normal pituitary gland in each phase during DCE-MCT. The ACTH-secreting adenoma showed the least contrast-enhancement differences compared with the normal pituitary gland (Fig 3C). These differences were significant ($P = .01$, 2-way ANOVA). In addition, the time phase that showed the largest difference in contrast enhancement between the adenoma and the normal pituitary gland was 45–60 seconds after contrast agent injection, irrespective of the secreted hormone.

DISCUSSION

Successful surgical treatment of functional pituitary microadenoma largely relies on accurate identification of the tumor within the sella turcica.⁴ These relatively small tumors represent a challenge to both neuroradiologists and neurosurgeons in locating them, resulting in a greater potential for insufficient treatment of the lesion. The criterion standard technique used for lesion localization is MR imaging,^{5–7} and some clinical investigations have suggested contrast-enhanced CT,^{8,9} super-selective venous sampling of pituitary hormone levels,^{10–12} and methionine PET⁴ as useful modalities to supplement MR imaging findings. The clinical values of these additional presurgical studies, however, remain undetermined, and conflicting results have been reported. For example, one report has claimed that venous sampling of ACTH at the inferior petrosal sinus is informative for determining adenoma location,¹² while others have reported results to the contrary.¹¹ Methionine PET has also been proposed as a promising imaging technique to identify MR imaging-occult ACTH-secreting microadenomas. MR imaging-registered methionine PET was previously reported

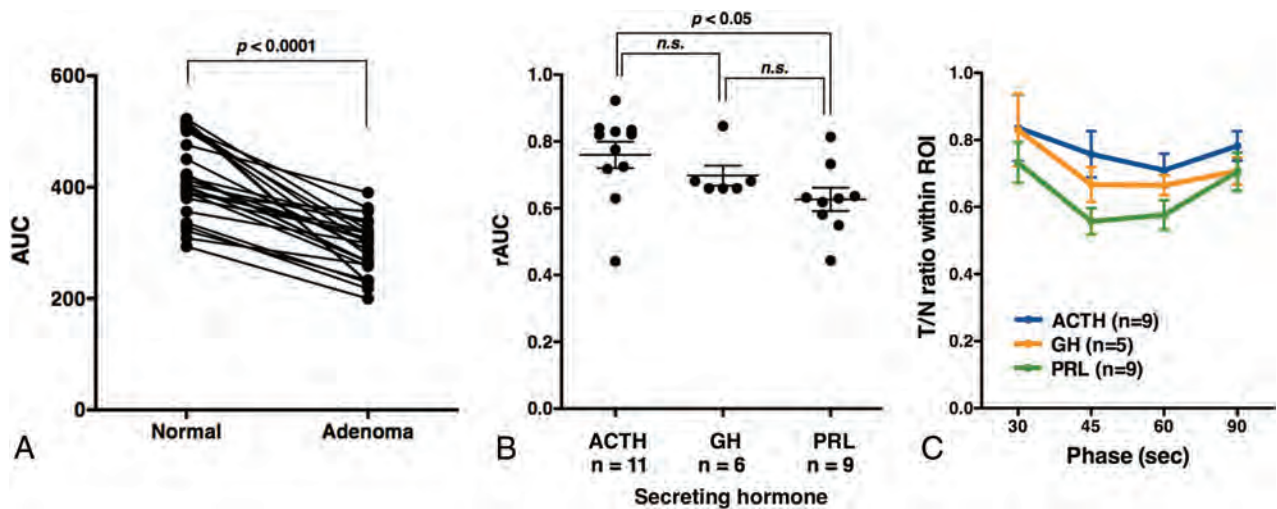


FIG 3. Contrast agent dynamics of pituitary microadenomas assessed by AUC. **A**, Adenomas show significantly lower AUC compared with the normal pituitary gland ($P < .0001$, paired *t* test). **B**, ACTH-secreting pituitary microadenomas show significantly higher rAUC compared with PRL-secreting microadenomas ($P < .05$, 1-way ANOVA with a Tukey multiple comparison), suggesting that contrast agent dynamics within ACTH-secreting microadenomas are similar to those of the normal pituitary gland. GH indicates growth hormone. **C**, The ratio of CT values of adenomas to those of the normal pituitary gland (tumor/node ratio [T/n ratio]) is plotted as a function of the time phase during DCE-MCT. Twenty-three cases in which CT acquisition was performed at 30, 45, 60, and 90 seconds were collected. The most significant drop was observed at 45–60 seconds, irrespective of the secreted hormone. In addition, ACTH-secreting adenomas showed the highest tumor/node ratio among the 3 hormones, indicating the least contrast between the adenoma and normal pituitary gland (2-way ANOVA, $P = .01$).

as showing superb performance in detecting ACTH-secreting microadenomas, of which identification was significantly difficult by using MR imaging alone.⁴ The availability of methionine PET, however, remains limited, and more extensive studies are required to confirm the clinical value of methionine PET for diagnosing functional microadenoma.

MR imaging shows several technical limitations in elucidating the presence of microadenoma. The above-mentioned small size of the tumor is one. To guarantee sufficient image quality, we usually select a section thickness of 3 mm for pituitary imaging. Given the sizes of microadenomas, which are <10 mm, there is a high chance of overlooking the lesion. In addition to the problem of size, pituitary adenoma imaging by using a contrast agent largely relies on the adenomas showing much less contrast enhancement than the normal pituitary gland. As Fig 3B suggests, an ACTH-secreting microadenoma, in particular, shows contrast-enhanced dynamics similar to that of the normal pituitary gland, which seems likely to contribute to failed detection of the lesion on MR imaging. Although the dynamic contrast-enhanced technique is often applied on MR imaging to overcome this issue, scanning time usually required to obtain each dynamic phase ranges from 20 to 30 seconds⁶ or is shortened into 12–20 seconds in some cases, but it is not possible to obtain a gapless 3D image as in MCT. Figure 3C, in particular, highlights this problem. The most suitable time phase to obtain sufficient contrast between an adenoma and the normal pituitary gland is 45–60 seconds after contrast agent injection. This adenoma/normal pituitary gland contrast will rapidly diminish within the subsequent 30 seconds. Both spatial and temporal resolution must, therefore, be sufficiently high to visualize the presence of the adenoma.

The proposed CT-based imaging technique has the potential to overcome these technical difficulties associated with MR imaging, mainly due to the superior temporal resolution of CT compared with MR imaging. Each phase of MCT can be acquired in a

full 3D image within 3 seconds, which provides satisfactory spatial and temporal resolution. The idea of using DCE-MCT for microadenoma detection has been proposed before.^{8,9} To better visualize contrast-enhancement dynamics in a voxelwise manner, the present study applied image reconstruction. The resulting AUC images provided intuitive images for clinicians to identify lesions with abnormal contrast-enhancement dynamics.

Limitations of the current study should be mentioned. First, this study was not a direct comparison between DCE-MR imaging and DCE-MCT. The patient cohort for this study did not have DCE-MR imaging as presurgical imaging for pituitary microadenomas. Further study is necessary to critically evaluate the clinical value of DCE-MCT with an image-reconstruction technique compared with conventional DCE-MR imaging. Another concern is the MR image quality of the current study. Previous studies reported exhibiting 66%–100% sensitivity in detecting ACTH-secreting microadenoma^{6,7} with the aid of DCE-MR imaging. The sensitivity of the current study for detecting ACTH-secreting microadenomas was as low as 32%, which may suggest that MR images of the current study might have been suboptimized compared with the past literature reports. In addition, although it is intriguing to contemplate why ACTH-secreting microadenomas show different contrast-enhanced dynamics compared with other functional microadenomas as shown in Fig 3C, the pathology of the blood supply to microadenomas is unfortunately not yet well-understood, making it difficult to reach any conclusive argument on this matter.

In summary, the present results show that DCE-MCT images along with AUC images can help identify microadenomas and improve the overall detection of those lesions compared with MR imaging alone. Although this study was not a direct comparison between DCE-MR imaging and DCE-MCT, it seems valid to conclude that DCE-MCT is a noninvasive diagnostic technique, which, along with the reported AUC reconstruction method,

could be recommended as a supplementary diagnostic technique for MR imaging–occult functional microadenoma.

CONCLUSIONS

Dynamic contrast-enhanced multisection CT combined with image reconstruction of the contrast-enhanced dynamics holds promise in detecting MR imaging–occult pituitary microadenoma. Because surgical outcomes are highly reliant on accurate preoperative identification of the adenoma, the proposed technique should contribute to better surgical outcomes for functional pituitary microadenomas.

Disclosures: Manabu Kinoshita—*RELATED: Grant:* Research Grant from the Life Science Foundation of Japan,* Scientific Research (C) from the Japan Society for the Promotion of Science,* Research Grant from the SENSHIN Medical Research Foundation,* Research Grant from the Aichi Cancer Research Foundation*; *UNRELATED: Grants/Grants Pending:* Research Grant from the Japanese Foundation for Multidisciplinary Treatment of Cancer.* Yoshiyuki Watanabe—*UNRELATED: Grants/Grants Pending:* Toshiba Medical Japan,* *Comments:* research fund about 320-row CT; *Payment for Lectures (including service on Speakers Bureaus):* GE Healthcare, Bayer Pharmaceutical. Youichi Saitoh—*UNRELATED: Consultancy:* Teijin Pharma; *Payment for Lectures (including service on Speakers Bureaus):* Teijin Pharma. *Money paid to the institution.

REFERENCES

1. Colao A, Boscaro M, Ferone D, et al. **Managing Cushing's disease: the state of the art.** *Endocrine* 2014;47:9–20
2. Suda K, Inoshita N, Iguchi G, et al. **Efficacy of combined octreotide and cabergoline treatment in patients with acromegaly: a retrospective clinical study and review of the literature.** *Endocr J* 2013; 60:507–15
3. Starke RM, Raper DM, Payne SC, et al. **Endoscopic vs microsurgical transsphenoidal surgery for acromegaly: outcomes in a concurrent series of patients using modern criteria for remission.** *J Clin Endocrinol Metab* 2013;98:3190–98
4. Ikeda H, Abe T, Watanabe K. **Usefulness of composite methionine–positron emission tomography/3.0-Tesla magnetic resonance imaging to detect the localization and extent of early-stage Cushing adenoma.** *J Neurosurg* 2010;112:750–55
5. Lee HB, Kim ST, Kim HJ, et al. **Usefulness of the dynamic gadolinium-enhanced magnetic resonance imaging with simultaneous acquisition of coronal and sagittal planes for detection of pituitary microadenomas.** *Eur Radiol* 2012;22:514–18
6. Portocarrero-Ortiz L, Bonifacio-Delgadillo D, Sotomayor-González A, et al. **A modified protocol using half-dose gadolinium in dynamic 3-Tesla magnetic resonance imaging for detection of ACTH-secreting pituitary tumors.** *Pituitary* 2010;13:230–35
7. Kasaliwal R, Sankhe SS, Lila AR, et al. **Volume interpolated 3D-spoiled gradient echo sequence is better than dynamic contrast spin echo sequence for MRI detection of corticotropin secreting pituitary microadenomas.** *Clin Endocrinol* 2013;78:825–30
8. Abe T, Izumiyama H, Fujisawa I. **Evaluation of pituitary adenomas by multidirectional multislice dynamic CT.** *Acta Radiol* 2002;43: 556–59
9. Bonneville JF, Cattin F, Gorczyca W, et al. **Pituitary microadenomas: early enhancement with dynamic CT—implications of arterial blood supply and potential importance.** *Radiology* 1993;187:857–61
10. Batista D, Gennari M, Riar J, et al. **An assessment of petrosal sinus sampling for localization of pituitary microadenomas in children with Cushing disease.** *J Clin Endocrinol Metab* 2006;91: 221–24
11. Lefournier V, Martinie M, Vasdev A, et al. **Accuracy of bilateral inferior petrosal or cavernous sinuses sampling in predicting the lateralization of Cushing's disease pituitary microadenoma: influence of catheter position and anatomy of venous drainage.** *J Clin Endocrinol Metab* 2003;88:196–203
12. Teramoto A, Yoshida Y, Sanno N, et al. **Cavernous sinus sampling in patients with adrenocorticotrophic hormone–dependent Cushing's syndrome with emphasis on inter- and intracavernous adrenocorticotrophic hormone gradients.** *J Neurosurg* 1998;89:762–68

Clinical Utility of Arterial Spin-Labeling as a Confirmatory Test for Suspected Brain Death

K.M. Kang, T.J. Yun, B.-W. Yoon, B.S. Jeon, S.H. Choi, J.-h. Kim, J.E. Kim, C.-H. Sohn, and M.H. Han



ABSTRACT

SUMMARY: Diagnosis of brain death is made on the basis of 3 essential findings: coma, absence of brain stem reflexes, and apnea. Although confirmatory tests are not mandatory in most situations, additional testing may be necessary to declare brain death in patients in whom results of specific components of clinical testing cannot be reliably evaluated. Recently, arterial spin-labeling has been incorporated as part of MR imaging to evaluate cerebral perfusion. Advantages of arterial spin-labeling include being completely noninvasive and providing information about absolute CBF. We retrospectively reviewed arterial spin-labeling findings according to the following modified criteria based on previously established confirmatory tests to determine brain death: 1) extremely decreased perfusion in the whole brain, 2) bright vessel signal intensity around the entry of the carotid artery to the skull, 3) patent external carotid circulation, and 4) “hollow skull sign” in a series of 5 patients. Arterial spin-labeling findings satisfied the criteria for brain death in all patients. Arterial spin-labeling imaging has the potential to be a completely noninvasive confirmatory test to provide additional information to assist in the diagnosis of brain death.

ABBREVIATION: ASL = arterial spin-labeling

Brain death is defined as irreversible loss of brain and brain stem function. The diagnosis of brain death is made on the basis of 3 essential findings: coma, absence of brain stem reflexes, and apnea.¹ Sometimes it is very difficult to make the clinical diagnosis, however, due to confounding factors such as uncertain reliability of neurologic examination or an inability to use the apnea test.² For example, patients with trauma to the eyes or ears, neuromuscular paralysis, or heavy sedation may not be amenable to appropriate neurologic assessment. In addition, patients who are carbon dioxide retainers cannot undergo an apnea test.³ In these cases, additional confirmatory tests are helpful to determine the diagnosis. Confirmatory tests for brain death can be divided into those that demonstrate loss of bioelectrical activity and those that show absence of CBF. As a test to demonstrate the loss of

bioelectrical activity, electroencephalography is used in many countries and remains one of the most well-validated confirmatory tests.¹ Although electroencephalography is sensitive to hypothermia, drugs, or extreme hypotension and confounding artifacts can appear in the environment of the intensive care unit because of the presence of multiple devices, this technique is still used extensively as a confirmatory test to diagnose brain death.^{1,2}

Another category of confirmatory test involves demonstrating the absence of CBF.³ Bernat⁴ emphasized that the surest way to demonstrate irreversible global loss of clinical brain function is to show complete absence of intracranial blood flow. Cerebral angiography was the first technique used to demonstrate the absence of intracranial circulation distal to the intracranial portions of the internal carotid and vertebral arteries in brain death.⁵ Other techniques used to determine the absence of CBF include cerebral intravenous DSA, intravenous radionuclide angiography, SPECT, echoencephalography, measurement of arm-to-retina circulation time, ophthalmic artery pressure measurement, xenon-enhanced CT, MRA, CTA, CT perfusion, and transcranial Doppler sonography.⁶ The preferred confirmatory test for CBF is angiography or a radiotracer method.^{2,3} However, cerebral angiography is invasive with the risk of vessel injury. Furthermore, both angiography and radiotracer methods require not only an injection of exogenous material such as contrast media or radioisotopes but also additional exposure to radiation.

Arterial spin-labeling (ASL) is a noninvasive MR imaging

Received August 15, 2014; accepted after revision November 11.

From the Institute of Radiation Medicine (K.M.K., T.J.Y., S.H.C., J.-h.K., C.-H.S., M.H.H.), Seoul National University Medical Research Center, Seoul, Republic of Korea; Departments of Radiology (K.M.K., T.J.Y., S.H.C., J.-h.K., C.-H.S., M.H.H.), Neurology (B.-W.Y., B.S.J.), and Neurosurgery (J.E.K.), and Clinical Research Center for Stroke (B.-W.Y., B.S.J.), Clinical Research Institute, Seoul National University Hospital, Seoul, Republic of Korea.

Please address correspondence to Tae Jin Yun, MD, Department of Radiology, Seoul National University Hospital, 101, Daehangno, Jongno-gu, Seoul 110-744, Korea; e-mail: radiologyyun@gmail.com

 Indicates open access to non-subscribers at www.ajnr.org

 Indicates article with supplemental on-line table.

<http://dx.doi.org/10.3174/ajnr.A4209>

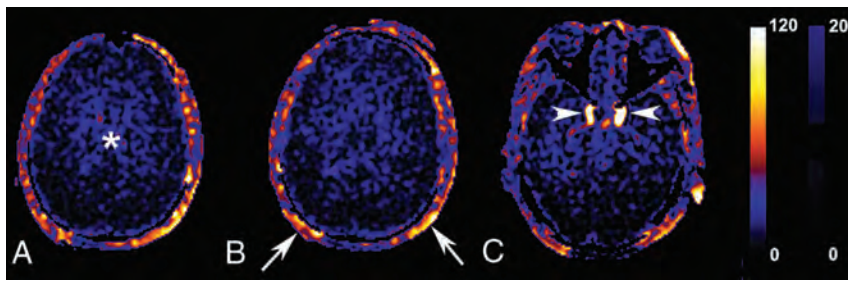


FIG 1. Representative arterial spin-labeling images for each criterion: extremely decreased perfusion in the whole brain (*asterisk, A*); patent external carotid circulation and the hollow skull sign (*arrows, B*), and bright vessel signal intensity around the entry of the carotid artery to the skull (*arrows, C*). The darker signal intensity in the bilateral parieto-occipital lobes seems to be due to the long transit time exceeding that of the postlabeling decay. Scale units: $\text{mL} \times 100 \text{ g}^{-1} \times \text{min}^{-1}$.

method to evaluate cerebral perfusion that does not require injection of any exogenous contrast agent or tracers.⁷ Instead, it uses endogenous arterial water labeled by radiofrequency pulses as a freely diffusible tracer. Therefore, there is no radiation exposure with ASL. In addition, ASL is beneficial in terms of resource allocation compared with DSC or radionuclide scans because it has lower cost and is time-efficient. Furthermore, because ASL can provide information regarding CBF values noninvasively, it is quite appropriate for the unique clinical setting of suspected brain death, in which the patient's family frequently refuses any additional invasive examinations. One case has been previously reported on the use of ASL to evaluate brain death.⁸ The purpose of this study was to investigate the potential of ASL as a confirmatory test to determine brain death.

MATERIALS AND METHODS

Case Series

This retrospective study was approved by our institutional review board. Informed consent was waived. After reviewing our radiology data base from June 2010 to April 2014, we identified 5 patients with clinically diagnosed brain death who underwent ASL MR imaging. These 5 patients (3 men and 2 women; median age, 60 years; range, 48–75 years) form the basis of this study, though a case report based on 1 of these 5 subjects was published previously.⁸ The brain deaths occurred following the return of spontaneous circulation after cardiac arrest ($n = 2$), large cerebral infarction ($n = 1$), encephalitis ($n = 1$), and systemic lupus erythematosus encephalopathy ($n = 1$).

The diagnosis of brain death was made on the basis of 3 clinical findings: coma (with a known cause), absence of brain stem reflexes, and apnea.² These 3 clinical findings need to be present to make the definitive diagnosis. The brain death diagnosis was made by at least 2 neurologists according to criteria established by local law. The prerequisites to determine brain death were an irreversible and proximate cause of coma; deep coma without spontaneous respiration; and no evidence of a neurologic state that could mimic brain death, including drug intoxication or poisoning, use of sedatives, metabolic or endocrine abnormalities, hypothermia, and shock. Furthermore, there was no return of the above neurologic functions after 6 hours of observation. In addition, all patients showed generalized continuous low-voltage background activity on electroencephalography.

All patients were clinically brain dead before acquisition of MR imaging. Even though the patients were already diagnosed as being brain dead by clinical criteria, the physicians requested MR imaging to determine the irreversible cause of coma and to evaluate the features of brain parenchyma, intracranial arteries, and perfusion. The mean interval between ASL imaging and brain death in the 5 patients was 3 days (range, 1–7 days). All patients underwent MR imaging on a 1.5T unit (Signa HDTx; GE Healthcare, Milwaukee, Wisconsin) by using an 8-channel head coil to acquire ASL perfusion MR imaging. MR imaging

sequences including T1WI, T2WI, FLAIR, DWI (b factors, 0 and 1000 mm^2/s^2), and ASL were acquired. The ASL protocol applied was as follows: ASL sequence parameters: TR, 4225 ms; TE, 9.9 ms; FOV, $24 \times 24 \text{ cm}^2$; section thickness, 5 mm; NEX, 3; and number of interleaved sections, 32. Pseudocontinuous spin-labeling for 1.5 seconds before a post-spin-labeling delay of 1.5 seconds was applied. Three of the 5 patients underwent 3D TOF MRA, whereas 2 patients underwent contrast-enhanced MRA with subsequent maximum-intensity-projection reconstruction during the MR imaging examination. Specific parameters for MR imaging sequences are provided in the On-line Table.

Two neuroradiologists (K.M.K. and T.J.Y., with 6 and 12 years of experience in neuroradiology, respectively) reviewed the ASL images with consensus. The ASL findings for diagnosing the absence of CBF were made on the basis of the findings from previous studies by using reference standard tests, radionuclide scans, and cerebral angiography.^{3,9–16} The ASL findings used to assess the absence of intracranial blood flow were the following: 1) extremely decreased perfusion in the whole brain, 2) bright vessel signal intensity around the entry of the carotid artery to the skull suggesting flow stagnation, and 3) patent external carotid circulation corresponding to the findings of brain death on conventional angiography.³ In addition, we reviewed the “hollow skull sign,” which was defined as a finding of extremely impaired cerebral perfusion with preserved perfusion in the distribution of the external carotid artery on ASL images. The finding was modified from the hollow skull sign described in scintigraphy for the diagnosis of brain death.^{10,12,16,17}

Figure 1 shows representative images of each criterion.

All images were spatially normalized to the ethnicity-specific T1 template before determining CBF by using SPM5 software (<http://www.fil.ion.ucl.ac.uk/spm/software/spm5>) and custom scripts in Matlab 7.6.0, R2008 (MathWorks, Natick, Massachusetts). CBF values were measured in ethnicity-specific volume of interest for whole-brain parenchyma by a neuroradiologist (T.J.Y., with 12 years of experience in neuroradiology).^{18–20}

Extremely impaired perfusion was detected in the whole brain in all 5 cases. In addition, bright signal intensity was observed at the cavernous or petrous ICA levels in all cases. The bright signal intensity occurred at the unilateral petrous ICA in 2 patients and at the bilateral cavernous or petrous ICAs in 3 patients. In contrast, perfusion supplied by the external carotid artery branches

ASL findings in 5 patients in whom brain death was diagnosed

Case	Age (yr)	Sex	Causes	ASL Findings					
				Extremely Decreased Perfusion in the Whole Brain	Bright Vessel Signal Intensity around the Entry of Carotid Artery to the Skull (\pm Level)	External Carotid Circulation	Hollow Skull Sign	CBF (Mean \pm SD, $\text{mL} \times 100 \text{ g}^{-1} \times \text{min}^{-1}$)	MRA
1	71	M	Cardiac arrest	+	+, Rt petrous ICA	+	+	10.0 ± 2.3	NV
2	60	M	Cardiac arrest	+	+, Bilateral cavernous ICAs	+	+	8.5 ± 3.2	NA
3	75	F	Cerebral infarction	+	+, Lt petrous ICA	+	+	7.0 ± 4.5	NV
4	50	M	Encephalitis	+	+, Rt cavernous ICA and Lt petrous ICA	+	+	7.5 ± 6.4	NV
5	48	F	SLE encephalopathy	+	+, Rt petrous ICA and Lt cavernous ICA	+	+	6.9 ± 2.8	NA

Note.—Lt indicates left; NA, not available; NV, no visualization of intracranial arterial flow; Rt, right; SLE, systemic lupus erythematosus; +, present.

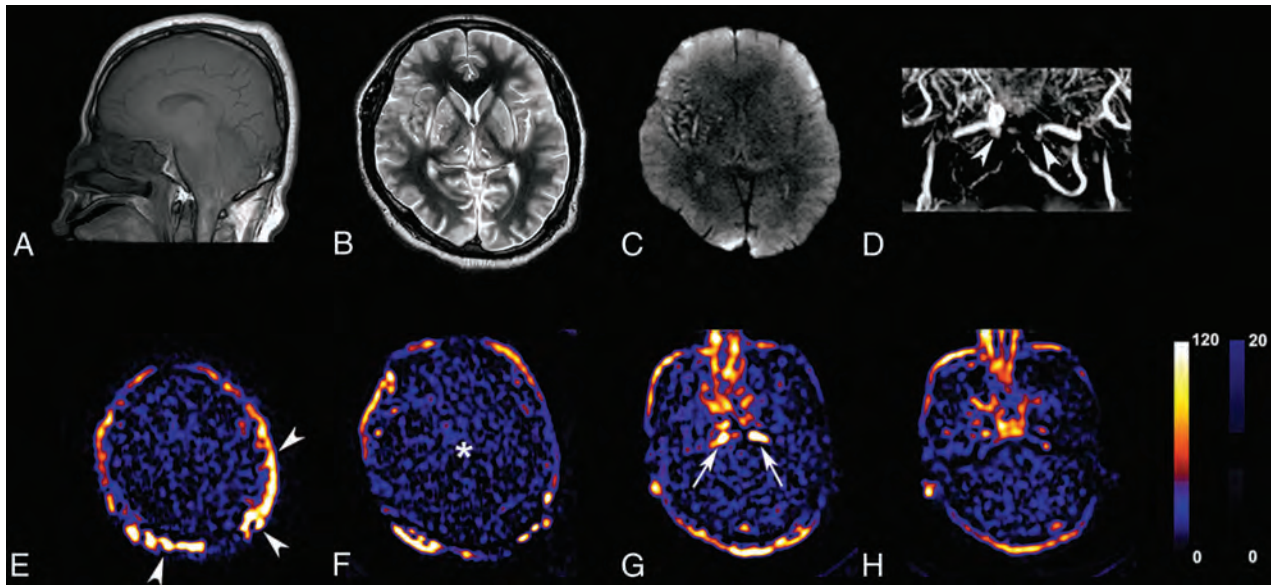


FIG 2. Representative MR imaging and arterial spin-labeling images in a 50-year-old man with brain death. Sagittal TIWI (A) shows tonsillar impaction in the foramen magnum. Axial T2WI (B) reveals gyral swelling with decreased ventricle size, and DWI (C) shows diffuse hyperintensity involving the whole brain. Contrast-enhanced MRA (D) shows an abrupt cutoff in the bilateral ICAs around the entries of carotid arteries to the skull (arrowheads, D) and the absence of intracranial arterial flow. The ASL images (E–H) satisfy all ASL criteria supporting brain death: extremely decreased perfusion in the whole brain (asterisk, F), bright signal intensity in the ICA around the entry of the carotid artery into the skull suggesting flow stagnation (arrows, G), and patent external carotid circulation and the hollow skull sign (arrowheads, E). Scale units: $\text{mL} \times 100 \text{ g}^{-1} \times \text{min}^{-1}$.

was normal in all cases. In addition, the hollow skull sign was seen in all patients on ASL. No intracranial arterial flow was detected on MRA in 3 patients (Table). The CBF values for the whole-brain parenchyma ranged from 6.9 to $10.0 \text{ mL} \times 100 \text{ g}^{-1} \times \text{min}^{-1}$, with a mean value of $8.0 \pm 1.3 \text{ mL} \times 100 \text{ g}^{-1} \times \text{min}^{-1}$, and all CBF values were $<15 \text{ mL} \times 100 \text{ g}^{-1} \times \text{min}^{-1}$ (Table). Representative MR images, including ASL in patients who were brain dead, are shown in Figs 2 and 3. ASL and MRA images of a healthy subject and a patient who was brain dead or with cardiac arrest are shown in Fig 4.

DISCUSSION

Brain death is a clinical diagnosis based on neurologic assessment and confirmatory tests conducted according to the situation. In our study, all brain death cases showed severe compromise in the intracranial circulation and patent external carotid artery perfusion. Very bright vessel signal intensity in the ICA around the entry of carotid artery to the skull without signal intensity in the intracerebral circulation was also observed. This “bright vessel signal” represents labeled blood with a notable transit delay, presumably secondary to elevated intracranial pressure, especially

when relatively normal external carotid artery blood flow is seen. This finding corresponds to visualizing the extracranial ICA with no visualization of the anterior circulation beyond the level of the supraclinoid ICAs on conventional angiography.³ In cases of patients showing unilateral bright vessel signals, there had been chronic occlusion in the contralateral ICA. Therefore, we assume that the bright vessel signal around the entry of the carotid artery to the skull might not be seen in cases of chronic stenoses in the bilateral ICAs.

According to the criteria we used, ASL revealed the absence of CBF in brain death by both visual and quantitative analysis. Because the absence of CBF is generally accepted as a definite sign of brain death,^{3,5,11,12,16} ASL has the potential to be a noninvasive and reliable confirmatory test for diagnosing brain death. However, the assessment of criteria should be performed carefully and strictly. If either the absence of intracranial flow or the preservation of extracranial flow is not observed, then the case should not be diagnosed as brain death. We had a 20-year-old female patient who experienced cardiac arrest during an MR imaging examination. Because the patient had a myocardial infarction after acqui-

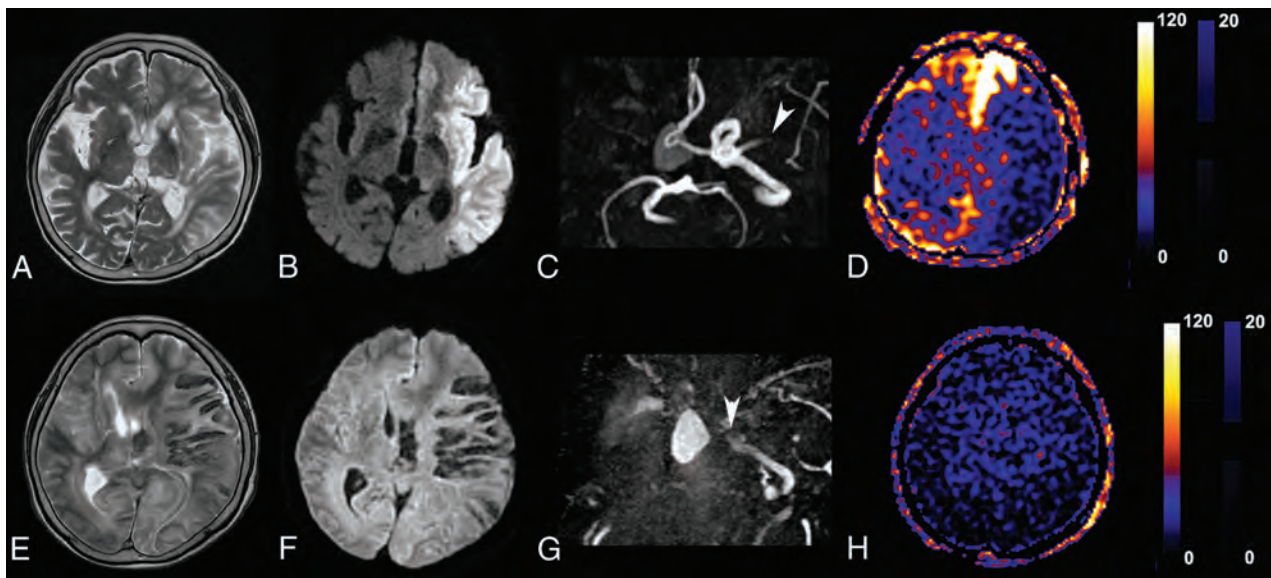


FIG 3. Representative arterial spin-labeling images in a 75-year-old woman with brain death following an infarct. The images in the *upper row* were acquired when the patient was admitted with an infarct. The images in the *lower row* were acquired when the patient was declared brain dead. T2WI (A) shows hyperintense parenchymal swelling in the left MCA territory, and DWI (B) demonstrates increased signal intensity in the corresponding area. TOF MRA (C) reveals total occlusion in the left proximal MCA (*arrowhead*). The patient also had chronic stenosis in the right proximal ICA. Although cerebral perfusion is severely impaired in the left MCA territory on the ASL image (D), the CBF values in other areas of the brain are preserved. T2WI (E) and DWI (F) performed shortly after the diagnosis of brain death depict diffuse gyral swelling and diffusion hyperintensity, respectively, in the whole brain. TOF MRA (G) shows an abrupt cutoff of the left distal ICA (*arrowhead*) and absence of intracranial vessels. ASL image (H) demonstrates markedly decreased CBF in the whole brain. Scale units: $\text{mL} \times 100 \text{ g}^{-1} \times \text{min}^{-1}$.

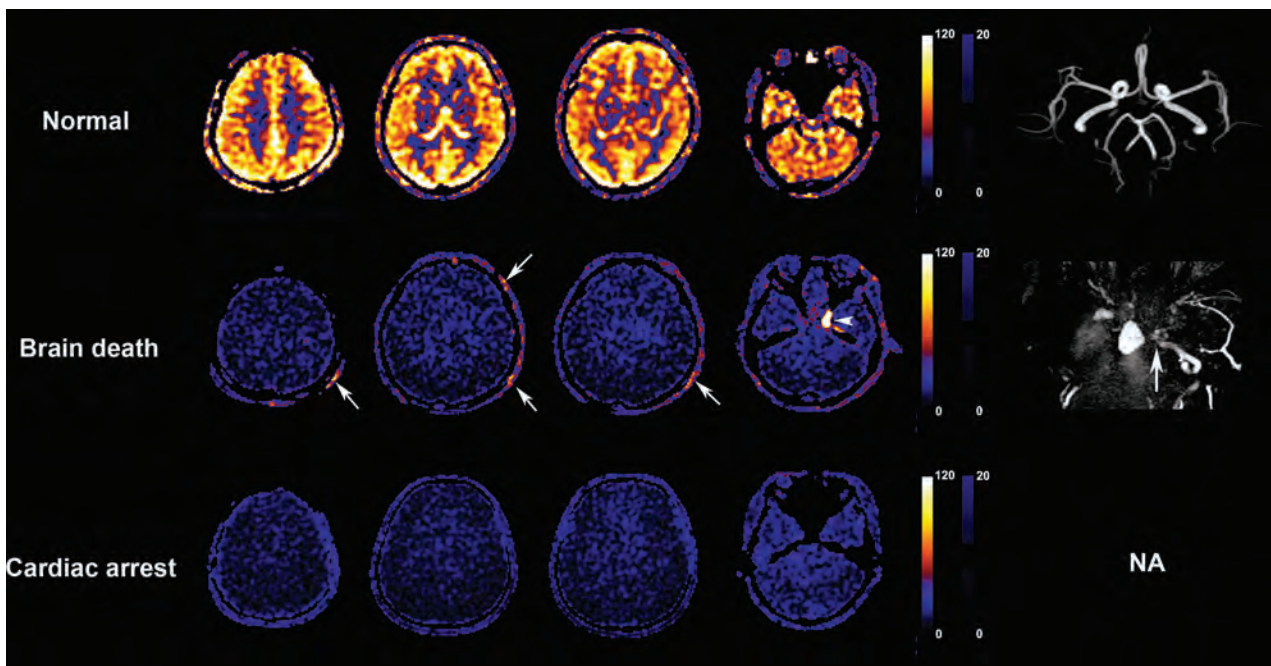


FIG 4. Representative arterial spin-labeling images in a healthy subject, a patient with brain death, and a patient who had cardiac arrest during an MR imaging examination. These figures show representative ASL and MRA images in a 46-year-old woman as a healthy subject (*upper row*), a 75-year-old woman with brain death (*middle row*), and a 20-year-old woman who had sudden cardiac arrest just before the acquisition of ASL images during an MR imaging examination (*bottom row*). ASL images from the patient with brain death show extremely impaired brain perfusion in the whole brain, bright vessel signal intensity around the level of entry of the carotid artery to the skull (*arrowhead*), and patent external carotid circulation (*arrows*) compared with the ASL images from the healthy subject. An MRA image in the patient with brain death (*right column of middle row*) shows an abrupt cutoff in the left distal ICA (*arrow*). Although the ASL images from the patient with cardiac arrest also show extremely impaired brain perfusion in the whole brain, there is neither bright vessel signal intensity around the entry of carotid artery to the skull nor patent external carotid circulation. Even though TOF MRA acquired just before the cardiac arrest had normal findings, acquisition of contrast-enhanced MRA after cardiac arrest failed. Scale units: $\text{mL} \times 100 \text{ g}^{-1} \times \text{min}^{-1}$. NA indicates not available.

sition of TOF intracranial MRA, the intracranial MRA findings were normal. However, ASL images acquired immediately after the myocardial infarction showed extremely impaired extracranial flow and extremely decreased CBF calculated at $8.62 \text{ mL} \times 100 \text{ g}^{-1} \times \text{min}^{-1}$, resulting from severely impaired cardiac output (Fig 4). The ASL findings of this patient and patients with brain death were different in that external carotid artery perfusion was always preserved in brain death. In addition, insufficient labeling of arterial flow caused by atherosclerosis or stent placement at the level of labeling might prevent demonstrating signals for both intracranial and extracranial flow on ASL. Therefore, both intracranial circulatory cessation and preserved external carotid artery perfusion are necessary to determine the cessation of intracranial flow in cases of brain death.

In contrast to other perfusion techniques, including dynamic susceptibility contrast MR perfusion and SPECT, ASL provides an absolute CBF value. In the present study, the CBF values in the whole brain parenchyma ranged from 6.9 to $10.0 \text{ mL} \times 100 \text{ g}^{-1} \times \text{min}^{-1}$. Even though there is no established threshold or CBF cutoff that defines brain death, according to several reports, minimal CBF in viable brain is $15 \text{ mL} \times 100 \text{ g}^{-1} \times \text{min}^{-1}$.^{21–25} Although quantifying CBF with ASL could help reveal the lack of CBF in cases of brain death, a postlabel delay of 1.5 seconds used in our study might be relatively short in the setting of markedly prolonged transit.^{26,27} In such cases, one should use caution in applying absolute quantitative CBF values across practice settings. Using a multidelayer longer postlabel decay time may be helpful in overcoming this limitation.^{26,27} Furthermore, there is no well-defined threshold or CBF cutoff that defines irreversible and/or definite brain death. Future work may further explore such a possible threshold.

In our study, we observed the hollow skull sign with ASL in all patients with brain death. The hollow skull sign was originally a scintigraphic finding to confirm brain death.¹² Now, it serves as a secondary sign of brain death. Among scintigraphic examinations for brain death, SPECT imaging provides information additional to that of planar imaging.¹⁸ SPECT imaging has some benefit for differentiating scalp, parotid, or neck muscle uptake from brain uptake. In addition, evaluation of the posterior fossa is better with SPECT imaging than with planar imaging because of its tomographic nature. Furthermore, ASL provides not only the same advantages as SPECT without injecting exogenous material, it also has other potential advantages such as resource allocation, lower cost, and time-efficiency compared with DSC and radionuclide scans. Therefore, ASL seems to be a promising method to replace scintigraphic methods.

The concept of brain death is often difficult for families to accept when dealing with a tragic loss. Grieving family members are understandably occasionally against any invasive test to confirm brain death. Hence, easily applied clinical tools that help a patient's kin understand brain death are needed. In our study, we introduced 4 ASL findings to determine brain death. These findings are fairly straightforward features to interpret. We think that applying ASL in cases of suspected brain death can help family members accept the grave condition of the patient so that they might be approached about possible organ donation before organ viability becomes a concern.

Our study had several limitations. First, there is selection bias because this is a clinical report for a case series of patients with known brain death. Future studies need to be performed prospectively to determine diagnostic accuracy and clinical effectiveness. Second, only a limited number of patients with brain death were evaluated. Thus, we could not perform a statistical analysis to investigate the diagnostic accuracy of ASL to determine brain death. Perfect diagnostic accuracy is an essential prerequisite as a brain death diagnostic tool because the presence of a false-positive case would be unacceptable. Further studies with a larger sample size and a prospective design are required to validate whether ASL imaging could be used to determine brain death. Third, ASL requires transfer of a critically ill patient to the MR imaging scanner. Its lack of portability is a major limitation of ASL as a confirmatory test for brain death. Finally, a postlabel delay of 1.5 seconds used in our study might be relatively short in the setting of severely impaired cerebral perfusion.

CONCLUSIONS

ASL imaging has the potential to serve as a noninvasive confirmatory test to provide additional information to assist in the diagnosis of brain death.

ACKNOWLEDGMENTS

We would like to thank So Young Yun (Seoul National University Hospital, Seoul, South Korea), who assisted with recruitment of the subjects.

Disclosures: Tae Jin Yun—RELATED: Grant: National Research Foundation of Korea (NRF-2013RIA1A2008332). *Money paid to the institution.

REFERENCES

1. Wijdicks EF. **The diagnosis of brain death.** *N Engl J Med* 2001; 344:1215–21
2. Wijdicks EF, Varelas PN, Gronseth GS, et al. **Evidence-based guideline update: determining brain death in adults—report of the Quality Standards Subcommittee of the American Academy of Neurology.** *Neurology* 2010;74:1911–18
3. Heran MK, Heran NS, Shemie SD. **A review of confirmatory tests in evaluating brain death.** *Can J Neurol Sci* 2008;35:409
4. Bernat JL. **On irreversibility as a prerequisite for brain death determination.** *Adv Exp Med Biol* 2004;550:161–67
5. Bücheler E, Käufer C, Dux A. **Cerebral angiography to determine brain death** [in German]. *Fortschr Geb Rontgenstr Nuklearmed* 1970; 113:278–96
6. Machado C. **Diagnosis of brain death.** *Neurol Int* 2010;2:e2
7. Wolf RL, Detre JA. **Clinical neuroimaging using arterial spin-labeled perfusion magnetic resonance imaging.** *Neurotherapeutics* 2007;4:346–59
8. Yun TJ, Sohn CH, Yoon BW, et al. **Brain death evaluation of cerebral blood flow by use of arterial spin labeling.** *Circulation* 2011;124: 2572–73
9. Bradac G, Simon R. **Angiography in brain death.** *Neuroradiology* 1974;7:25–28
10. Abdel-Dayem HM, Bahar RH, Sigurdsson GH, et al. **The hollow skull: a sign of brain death in Tc-99m HM-PAO brain scintigraphy.** *Clin Nucl Med* 1989;14:912–16
11. Wieler H, Marohl K, Kaiser K, et al. **Tc-99m HMPAO cerebral scintigraphy: a reliable, noninvasive method for determination of brain death.** *Clin Nucl Med* 1993;18:104–09
12. Orrison WW Jr, Champlin AM, Kesterson OL, et al. **MR 'hot nose sign' and 'intravascular enhancement sign' in brain death.** *AJNR Am J Neuroradiol* 1994;15:913–16

13. Bonetti M, Ciritella P, Valle G, et al. **^{99m}Tc HM-PAO brain perfusion SPECT in brain death.** *Neuroradiology* 1995;37:365–69
14. Ishii K, Onuma T, Kinoshita T, et al. **Brain death: MR and MR angiography.** *AJNR Am J Neuroradiol* 1996;17:731–35
15. Qureshi AI, Kirmani JF, Xavier AR, et al. **Computed tomographic angiography for diagnosis of brain death.** *Neurology* 2004;62:652–53
16. Sinha P, Conrad GR. **Scintigraphic confirmation of brain death.** *Semin Nucl Med* 2012;42:27–32
17. Al-Shammri S, Al-Feeli M. **Confirmation of brain death using brain radionuclide perfusion imaging technique.** *Med Princ Pract* 2004;13:267–72
18. Lee JS, Lee DS, Kim J, et al. **Development of Korean standard brain templates.** *J Korean Med Sci* 2005;20:483–88
19. Collins DL, Neelin P, Peters TM, et al. **Automatic 3D intersubject registration of MR volumetric data in standardized Talairach space.** *J Comput Assist Tomogr* 1994;18:192–205
20. Yun TJ, Sohn CH, Han MH, et al. **Effect of carotid artery stenting on cerebral blood flow: evaluation of hemodynamic changes using arterial spin labeling.** *Neuroradiology* 2013;55:271–81
21. Powers WJ, Grubb RL, Darriet D, et al. **Cerebral blood flow and cerebral metabolic rate of oxygen requirements for cerebral function and viability in humans.** *J Cereb Blood Flow Metab* 1985;5:600–08
22. Latchaw RE, Yonas H, Hunter GJ, et al. **Guidelines and recommendations for perfusion imaging in cerebral ischemia: a scientific statement for healthcare professionals by the Writing Group on Perfusion Imaging, from the Council on Cardiovascular Radiology of the American Heart Association.** *Stroke* 2003;34:1084–104
23. Astrup J. **Energy-requiring cell functions in the ischemic brain: their critical supply and possible inhibition in protective therapy.** *J Neurosurg* 1982;56:482–97
24. Schuier F, Hossmann K. **Experimental brain infarcts in cats. II. Ischemic brain edema.** *Stroke* 1980;11:593–601
25. Jones TH, Morawetz RB, Crowell RM, et al. **Thresholds of focal cerebral ischemia in awake monkeys.** *J Neurosurg* 1981;54:773–82
26. Qiu D, Straka M, Zun Z, et al. **CBF measurements using multidelay pseudocontinuous and velocity-selective arterial spin labeling in patients with long arterial transit delays: comparison with xenon CT CBF.** *J Magn Reson Imaging* 2012;36:110–19
27. Alsop DC, Detre JA, Golay X, et al. **Recommended implementation of arterial spin-labeled perfusion MRI for clinical applications: a consensus of the ISMRM perfusion study group and the European consortium for ASL in dementia.** *Magn Reson Med* 2014 Apr 8. [Epub ahead of print]

Disrupted Resting-State Functional Connectivity in Progressive Supranuclear Palsy

M.C. Piattella, F. Tona, M. Bologna, E. Sbardella, A. Formica, N. Petsas, N. Filippini, A. Berardelli, and P. Pantano

ABSTRACT

BACKGROUND AND PURPOSE: Studies on functional connectivity in progressive supranuclear palsy have been restricted to the thalamus and midbrain tegmentum. The present study aims to evaluate functional connectivity abnormalities of the subcortical structures in these patients. Functional connectivity will be correlated with motor and nonmotor symptoms of the disease.

MATERIALS AND METHODS: Nineteen patients with progressive supranuclear palsy (mean age, 70.93 ± 5.19 years) and 12 age-matched healthy subjects (mean age, 69.17 ± 5.20 years) underwent multimodal MR imaging, including fMRI at rest, 3D T1-weighted imaging, and DTI. fMRI data were processed with fMRI of the Brain Software Library tools by using the dorsal midbrain tegmentum, thalamus, caudate nucleus, putamen, and pallidum as seed regions.

RESULTS: Patients had lower functional connectivity than healthy subjects in all 5 resting-state networks, mainly involving the basal ganglia, thalamus, anterior cingulate, dorsolateral prefrontal and temporo-occipital cortices, supramarginal gyrus, supplementary motor area, and cerebellum. Compared with healthy subjects, patients also displayed subcortical atrophy and DTI abnormalities. Decreased thalamic functional connectivity correlated with clinical scores, as assessed by the Hoehn and Yahr Scale and by the bulbar and mentation subitems of the Progressive Supranuclear Palsy Rating Scale. Decreased pallidum functional connectivity correlated with lower Mini-Mental State Examination scores; decreased functional connectivity in the dorsal midbrain tegmentum network correlated with lower scores in the Frontal Assessment Battery.

CONCLUSIONS: The present study demonstrates a widespread disruption of cortical-subcortical connectivity in progressive supranuclear palsy and provides further insight into the pathophysiologic mechanisms of motor and cognitive impairment in this condition.

ABBREVIATIONS: ACC = anterior cingulate cortex; DLPF = dorsolateral prefrontal cortex; dMT = dorsal midbrain tegmentum; FA = fractional anisotropy; FC = functional connectivity; MD = mean diffusivity; PSP = progressive supranuclear palsy; SMA = supplementary motor area

Progressive supranuclear palsy (PSP) is one of the most common forms of atypical parkinsonism, characterized by early-onset postural instability, falls, and oculomotor abnormalities. Patients with PSP often have cognitive impairment, involving frontal executive functions and language, and behavioral symptoms, including apathy and social withdrawal or disinhibition.^{1,2} The pathologic changes in PSP include neuronal degeneration and τ immune-reactive depositions in the basal ganglia, dien-

cephalon, brain stem, and cerebellum, with limited involvement of the neocortex.³

MR imaging has detected several structural changes in PSP, which mainly involve the midbrain, thalamus, basal ganglia, frontal cortex, and white matter bundles, reflecting the underlying neurodegenerative processes present in this condition.⁴⁻⁷ However, the relationship between brain abnormalities and clinical manifestations is still unclear.

The resting-state fMRI technique is a method used to investigate spontaneous neuronal activity at rest.⁸ Spontaneous neuronal activity is identified by slow fluctuations in the blood oxygen level–dependent signal and is represented by spatial maps of correlations of these blood oxygen level–dependent signal fluctuations within anatomically separate brain regions, also defined as maps of functional connectivity (FC).⁸ FC in PSP has previously been explored in 2 studies with a limited focus on the thalamus⁹ and dorsal midbrain tegmentum (dMT) regions.¹⁰ Both studies reported functional disconnection between each of these struc-

Received July 18, 2014; accepted after revision November 11.

From the Department of Neurology and Psychiatry (M.C.P., F.T., E.S., A.F., N.P., A.B., P.P.), Sapienza University of Rome, Italy; Neuromed Institute Istituto Di Ricovero e Cura a Carattere Scientifico (M.B., A.B., P.P.), Pozzilli, Italy; and Department of Psychiatry and FMRI Centre (N.F.), University of Oxford, United Kingdom.

Please address correspondence to Maria Cristina Piattella, MD, Department of Neurology and Psychiatry, Sapienza University of Rome, Viale dell'Università, 30-00185 Rome, Italy; e-mail: mcpiattella@gmail.com

<http://dx.doi.org/10.3174/ajnr.A4229>

tures and some cortical, subcortical, and cerebellar sites.^{9,10} It is unknown whether FC abnormalities also affect other key subcortical areas in PSP.³ Owing to the widespread degeneration of subcortical structures in PSP,³ the FC of the caudate nucleus, putamen, and pallidum may also be affected in this condition. Due to the basal ganglia involvement in motor and cognitive functions, through the parallel interconnections with the frontal cortex,^{11,12} understanding FC abnormalities of the caudate nucleus, putamen, and pallidum in PSP would provide further information on the pathophysiologic mechanisms of the disease. To achieve this goal, we evaluated the FC from the caudate, putamen, and pallidum nuclei, in addition to the thalamus and dMT. The ultimate aim of this article was to investigate possible correlations between cortical-subcortical network disruption and clinical scores of disease severity.

MATERIALS AND METHODS

Subjects

We enrolled 19 patients who were diagnosed with PSP (9 women; mean age, 70.93 ± 5.19 years) according to the National Institute for Neurological Disorders and Society for PSP criteria¹³ and were consecutively referred to the Department of Neurology and Psychiatry at the Sapienza University of Rome, between January 2011 and October 2012. All the patients were clinically classified as having Richardson syndrome, one of the subtypes of PSP,^{1,14} by experienced neurologists (A.B. and M.B.). Exclusion criteria were other neurologic, psychiatric, and systemic diseases and general contraindications to MR imaging. Patients were clinically evaluated (by A.F.) by using the Unified Parkinson's Disease Rating Scale,¹⁵ the Frontal Assessment Battery,¹⁶ the Hoehn and Yahr Scale,¹⁷ the Mini-Mental State Examination,¹⁸ and the PSP Rating Scale and its subscales.¹⁹ All patients also underwent a multimodal MR imaging study (by M.C.P. and F.T.), which included resting-state fMRI, diffusion tensor imaging, and volumetric imaging. Twelve healthy subjects (9 women; mean age, 69.17 ± 5.20 years) with no history of neurologic or psychiatric disease at the time of the examination constituted the control group.

Participants provided their written informed consent. The study protocol was approved by the institutional review board of Sapienza University of Rome and complied with the Health Insurance Portability and Accountability Act.

MR Imaging Acquisition

A standardized protocol was performed on a 3T scanner (Magnetom Verio; Siemens, Erlangen, Germany). The 12-channel head coil of the manufacturer designed for parallel imaging (generalized autocalibrating partially parallel acquisitions) was used for signal reception. A multiplanar T1-weighted localizer with section orientation parallel to the subcallosal line was acquired at the beginning of each MR imaging examination. The MR imaging protocol included the following sequences for all the subjects: 1) blood oxygen level–dependent single-shot echo-planar images (TR = 3000 ms, TE = 30 ms, flip angle = 89° , FOV = 192, matrix = 64×64 , 50 axial sections 3-mm-thick, no gap, 120 volumes, acquisition time = 6 minutes 11 seconds), with all patients and healthy subjects being instructed to close their eyes and

stay awake during the resting-state fMRI acquisitions; 2) DTI acquired with a single-shot echo-planar spin-echo sequence with 30 directions (TR = 12,200 ms, TE = 94 ms, FOV = 192 mm, matrix = 96×96 , $b = 0$ and 1000 s/mm², 72 axial sections 2-mm-thick, no gap, acquisition time = 13 minutes 15 seconds); 3) a high-resolution 3D T1-weighted MPRAGE sequence (TR = 1900 ms, TE = 2.93 ms, flip angle = 9° , FOV = 260 mm, matrix = 256×256 , 176 sagittal sections 1-mm-thick, no gap, acquisition time = 3 minutes 48 seconds); and 4) dual turbo spin-echo, proton-attenuation, and T2-weighted images (TR = 3320 ms, TE = 10/103 ms, FOV = 220 mm, matrix = 384×384 , 25 axial sections 4-mm-thick, 30% gap). The dual turbo spin-echo sequences were obtained to exclude subjects with brain alterations due to concomitant diseases.

Image Processing and Data Analysis

Data analysis was carried out by using the fMRI of the Brain Software Library (FSL), Version 4.1.9 (<http://www.fmrib.ox.ac.uk/fsl>).

Preprocessing. Single-subject preprocessing and group analysis were performed by using the fMRI Expert Analysis Tool, Version 5.98, part of FSL (<http://fsl.fmrib.ox.ac.uk/fsl/fslwiki/FEAT>). The first 3 volumes of the 120 resting-state blood oxygen level–dependent volumes were discarded to obtain a steady-state of the blood oxygen level–dependent signal. In brief, preprocessing consisted of head-motion correction, brain extraction, spatial smoothing by using a Gaussian kernel of full width at half maximum of 5 mm, and high-pass temporal filtering equivalent to a period of 100 seconds. Functional data were registered to structural images (within-subject) and Montreal Neurological Institute standard space (to allow higher level group comparisons) by using the FMRIB Linear Image Registration Tool (<http://www.fmrib.ox.ac.uk/>) and Nonlinear Image Registration Tool (<http://fsl.fmrib.ox.ac.uk/fsl/fslwiki/FNIRT>) and then were optimized by using a boundary-based registration approach.²⁰

Functional Connectivity (Seed Description, Time-Series Extraction, and Higher Level Analysis). Individual seed-ROI masks of the thalami, caudate, putamen, and pallidum nuclei were obtained from each subject's high-resolution T1-weighted structural scan by using FMRIB's Integrated Registration and Segmentation Tool (<http://fsl.fmrib.ox.ac.uk/fsl/fslwiki/FIRST>),²¹ an automatic subcortical segmentation program. Each image was visually inspected in the coronal plane to ensure accuracy. Left and right masks of each of the 4 nuclei of interest (thalamus, caudate, putamen, and pallidum) were merged to obtain a single bilateral mask. In addition, a 4-mm-radius spheric ROI was placed on the dMT; it was centered according to the coordinates (5, –15, –8) of a previous study.¹⁰ Each ROI was registered to functional coordinate space and was used to extract the related time course after having preprocessed the raw fMRI data. Time-series were averaged across all voxels for each seed ROI. Each time-series was separately fed into the fMRI Expert Analysis Tool and produced individual participant-level correlation maps of all voxels that were positively or negatively correlated with each of the seeds. Afterward, higher level (group level) analysis was performed by using FMRIB's Local Analysis of Mixed Effects (<http://fsl.fmrib.ox.ac.uk/fsl/fslwiki/FEAT>).²² The general linear model was

applied to test for group averages and differences between the 2 groups (patients and controls) by using a 2-sample unpaired *t* test. The Z-statistic images were thresholded by using clusters determined by $Z > 2.3$, and a whole-brain family-wise-error-corrected cluster significance threshold of $P < .05$ was applied to the super-threshold clusters. Anatomic localization of significant clusters was established according to the Harvard-Oxford Structural Atlas, the Juelich histologic atlas, and the Oxford Thalamic Connectivity Probability Atlas included in the FSL (<http://www.fmrib.ox.ac.uk/fsl/data/atlas-descriptions.html>).

Nuisance Signal Regression and Covariates of No Interest Included in the Model. To account for potential indeterminate noise,^{23,24} we also identified seeds of CSF and white matter on each individual functional EPI, and their time courses were added as covariates of no interest (nuisance) into each of the seed-ROI voxelwise correlation analyses to remove nonneural contributions to the blood oxygen level-dependent signal and thus enhance specificity. Similarly, the age of the study participants and volumes of the specific seeds were entered as nuisance covariates. Finally, structural maps were used as additional covariates on a voxel-by-voxel basis to account for potential gray matter differences. Very briefly, GM images of each subject were extracted by using FMRIB's Integrated Registration and Segmentation Tool,²¹ registered in standard space, smoothed to match the fMRI data, demeaned within each group, and added to the model used to analyze fMRI data.

To visualize a unique image common to areas of functional abnormalities shared by the 5 maps of FC, we first performed a transformation of between-group difference maps in binary data; then, we performed a voxel-by-voxel sum of the 5 binarized maps. In the final image, we attributed a different color to each voxel value (range, 0–5). Finally, parameter estimates in individual functional connectivity maps, within a group mask of each of the 5 functional connectivity maps, were used to correlate functional connectivity with both clinical scores and structural damage (brain volumes and DTI parameters) in the patient group.

Structural MR Imaging. T1 3D images were processed by using SIENA/X (part of FSL), a fully automated and accurate method for measuring cross-sectional changes in brain volume.²⁵ This automated method also provided values of normalized cortical volume.

Subcortical volumes (ie, the caudate, putamen, pallidum, thalamus nuclei, and the brain stem) were estimated through FMRIB's Integrated Registration and Segmentation Tool.²¹ Subcortical volumes were corrected for individual differences in intracranial volume by an individual scale factor obtained by SIENA/X.

Diffusion MR Imaging. Eddy current correction was used to preprocess raw DTI images to correct for distortions due to the gradient directions applied. Subsequently, DTIFit, part of FMRIB's Diffusion Toolbox (http://fsl.fmrib.ox.ac.uk/fsl/fsl-4.1.9/fdt/fdt_dtifit.html), was used to fit a diffusion tensor model at each voxel and generate fractional anisotropy (FA), mean diffusivity (MD), axial diffusivity, and radial diffusivity maps. Axial diffusivity was calculated from the eigenvalues in the principal direction of water flow (λ_1). The 2 minor axes (λ_2 and λ_3) were averaged to compute radial diffusivity. The average of all 3 (λ_1 , λ_2 , and λ_3) eigenvalues was used to calculate MD. Briefly, MD and FA are mainly

affected by myelin content and, to a lesser extent, FA, by axonal attenuation,²⁶ while axial diffusivity and radial diffusivity are considered measures of axonal and myelin integrity, respectively.²⁷ Voxelwise statistical analysis of FA, MD, radial diffusivity, and axial diffusivity data was performed by using a Tract-Based Spatial Statistics tool (<http://fsl.fmrib.ox.ac.uk/fsl/fslwiki/TBSS>).²⁷

All diffusion and FA maps of patient and healthy subject cohorts were first aligned into a common space by using the Non-linear Image Registration Tool. The most representative diffusion maps were selected automatically as the target, and diffusion maps of all subjects were nonlinearly registered to this. Following this step, all images were transformed into Montreal Neurological Institute standard space. The mean FA image was generated and thinned to create a mean FA skeleton, which represents the centers of all tracts common to the subjects. Each subject's aligned FA data were then projected onto this skeleton, and the resulting data were fed into voxelwise general linear modeling cross-subject statistics. We used a threshold of 0.2 for creation of a mean FA skeleton to include the major WM tracts but exclude peripheral tracts, which may cause significant intersubject variability and/or partial volume effects with GM and CSF. A voxel-by-voxel permutation nonparametric test (5000 permutations) was used to assess group-related differences by using threshold-free cluster enhancement, which avoids using an arbitrary threshold for the initial cluster formation.²⁸ In addition to FA data, MD, axial diffusivity, and radial diffusivity were also analyzed by using Tract-Based Spatial Statistics in an analogous fashion. The results were corrected for multiple comparisons and reported at a significance level of $P < .05$.

Statistical Analysis

The statistical analysis was performed by using SPSS software, Version 16.0 (IBM, Armonk, New York). All values are reported as mean \pm SD or median and range as appropriate. Unpaired *t* tests and χ^2 tests were used to evaluate any differences between groups, after Bonferroni correction for multiple comparisons.

Correlations between clinical and radiologic variables were investigated by backward stepwise regression.

RESULTS

Demographic, clinical, and radiologic characteristics of the 19 patients with PSP are shown in Table 1. There were no statistically significant differences in age and sex distribution between patients and healthy subjects (Table 1).

Functional Connectivity

The dMT, thalamus, caudate, putamen, and pallidum were chosen as ROIs in both patients and healthy subjects, and the FC patterns were identified in each region (Fig 1). Patients with PSP had lower FC than healthy subjects in all 5 functional connectivity maps (Fig 2).

FC in the dMT functional connectivity map was significantly reduced in the left dorsolateral prefrontal cortex (DLPF) and supramarginal gyrus, as well as in the pregenual anterior cingulate cortex, bilaterally.

FC in the thalamic functional connectivity map was decreased in the basal ganglia and thalamus, dorsolateral prefrontal cortex,

Table 1: Clinical and radiologic characteristics of 19 patients with PSP and of 12 healthy subjects

	Healthy Subjects ^a (n = 12)	Patients with PSP ^a (n = 19)	P Value ^b
Age (yr)	69.172 ± 5.201	70.933 ± 5.196	.356
Male/female ^c	3/9	10/9	.158
UPDRS	—	27.625 ± 17.952	NA
FAB	—	11.187 ± 3.799	NA
H&Y	—	2.9 ± 1.065	NA
MMSE	29.135 ± 0.8	24.325 ± 3.886	NA
PSPRS	—	35.823 ± 16.994	NA
History	—	7.706 ± 3.820	NA
Mentation	—	3.647 ± 2.597	NA
Bulbar	—	3.117 ± 1.996	NA
Ocular	—	7.706 ± 2.932	NA
Limb	—	4.176 ± 3.486	NA
Gait	—	9.235 ± 5.750	NA
Thalamus V (mm ³)	9.483 ± 0.840	8.005 ± 0.657	<.0001 ^d
Caudate V (mm ³)	4.380 ± 0.373	3.962 ± 0.477	.015
Putamen V (mm ³)	5.992 ± 0.472	4.835 ± 0.575	<.0001 ^d
Pallidum V (mm ³)	2.404 ± 0.472	1.857 ± 0.293	.0004 ^d
Brain stem V (mm ³)	14.906 ± 1.652	12.618 ± 1.603	.0006 ^d
Intracranial V (mm ³)	1620.661 ± 163.482	1549.769 ± 114.184	.165
Cortical V (mm ³)	600.423 ± 41.923	576.789 ± 49.823	.167
Mean FA	0.508 ± 0.019	0.441 ± 0.030	<.0001 ^d
Mean MD (mm × sec ⁻²) × 10 ⁻³	0.689 ± 0.026	0.762 ± 0.030	<.0001 ^d
Mean RD (mm × sec ⁻²) × 10 ⁻³	0.478 ± 0.029	0.561 ± 0.034	<.0001 ^d
Mean AD (mm × sec ⁻²) × 10 ⁻³	1.049 ± 0.032	1.154 ± 0.056	<.0001 ^d

Note:—UPDRS indicates Unified Parkinson's Disease Rating Scale; FAB, Frontal Assessment Battery; H&Y, Hoehn and Yahr Scale; MMSE, Mini-Mental State Examination; PSPRS, PSP Rating Scale; V, volume (left and right values of subcortical volumes are averaged); RD, radial diffusivity; AD, axial diffusivity; —, not available; NA = not applicable.

^a Values are reported as mean ± SD.

^b Differences between groups were assessed by t test.

^c Differences between groups were assessed by χ^2 .

^d Statistically significant values after Bonferroni correction for multiple comparisons.

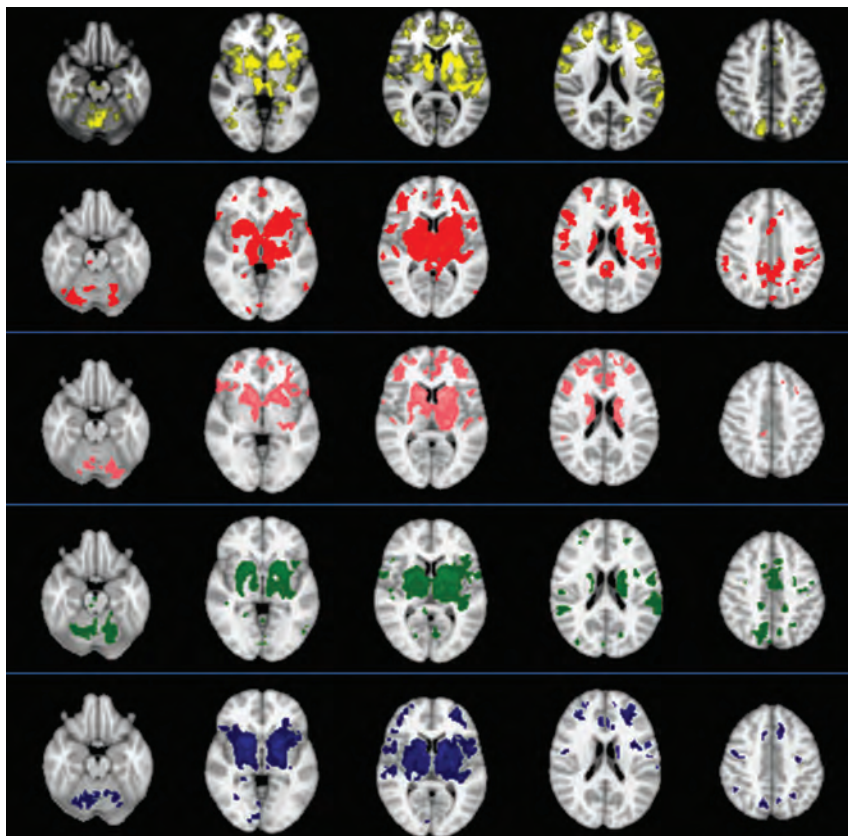


FIG 1. Maps of functional connectivity obtained from 5 seeds, ie, the dorsal midbrain tegmentum (yellow), thalamus (red), caudate (pink), putamen (green), and pallidum (blue)—in 12 healthy subjects (1-sample t test, $P < .05$, corrected for family-wise error). The images are presented according to radiologic orientation.

anterior cingulate cortex (ACC), supplementary motor area (SMA), and precentral gyrus, bilaterally, and in the left temporo-occipital cortex and left cerebellar Crus I.

FC in the caudate nucleus functional connectivity map was significantly lower in clusters located in the thalamus and caudate, ACC, and pre-SMA, bilaterally, and in the left DLPF and temporo-occipital cortex; FC was also decreased in the posterior lobe of the cerebellum (Crus I, lobules VI, VIIb, VIIIa, VIIIb, IX).

FC in the putamen functional connectivity map was significantly reduced in the thalamus and caudate, ACC, SMA, postcentral and supramarginal gyri, precuneus, and temporo-occipital and occipital cortices, bilaterally; the cerebellum was also bilaterally affected (Crus I, Crus II, lobules VI, VIIb, VIIIa, VIIIb, IX).

Finally, FC in the pallidum functional connectivity map was reduced in the basal ganglia and thalamus, DLPF, ACC and SMA, supramarginal gyrus, precuneus, temporo-occipital and occipital cortices, bilaterally, and in the cerebellum (Crus I, lobules VI, VIIb, VIIIa) bilaterally, though to a greater degree on the right side.

To identify common brain areas having reduced FC across all 5 functional connectivity maps, we overlapped results obtained from each map separately (Fig 3). We obtained images showing voxels of significantly decreased FC in 4 results (located in the thalamus, caudate, and ACC, bilaterally, and the left DLPF and temporo-occipital cortex) and in 3 results (located in the left supramarginal gyrus and in the SMA and cerebellar Crus I, lobules VI, VIIb and VIIIb, bilaterally). No focus of decreased FC in any of the 5 functional maps was identified.

Structural Damage

Patients with PSP had significantly lower subcortical structure volumes than healthy subjects, whereas no significant difference emerged between the 2 groups in cerebral cortex volumes (Table 1).

Patients also had significantly lower mean FA and significantly higher MD, radial diffusivity, and axial diffusivity values than healthy subjects (Table 1).

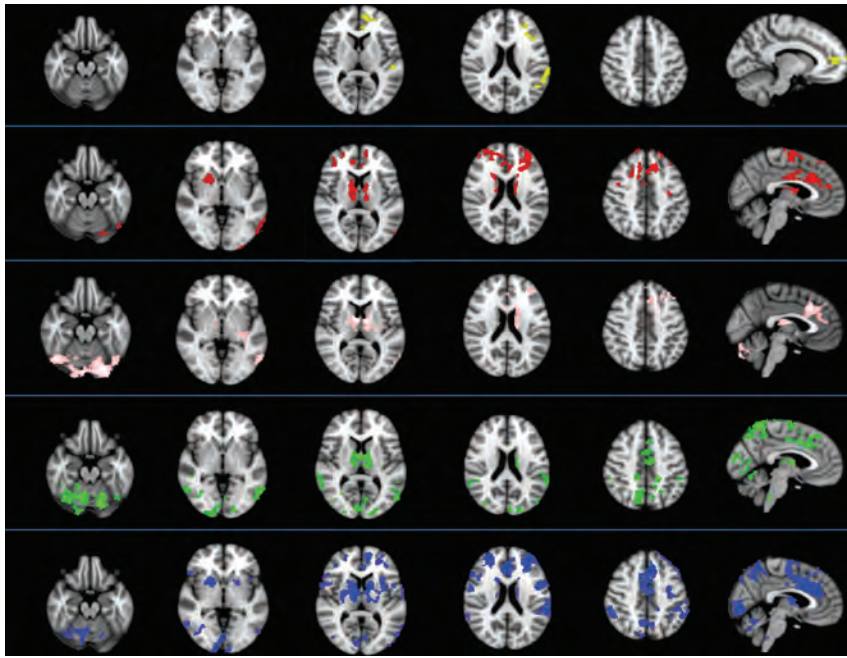


FIG 2. Differences between 19 patients with progressive supranuclear palsy and 12 healthy subjects in functional connectivity obtained from 5 seeds (2-sample *t* test, $P < .05$, corrected for family-wise error). Patients with PSP had significantly lower FC than healthy subjects in all 5 FC maps—that is, the dorsal midbrain tegmentum (yellow), thalamus (red), caudate (pink), putamen (green), and pallidum (blue). The images are presented according to radiologic orientation.

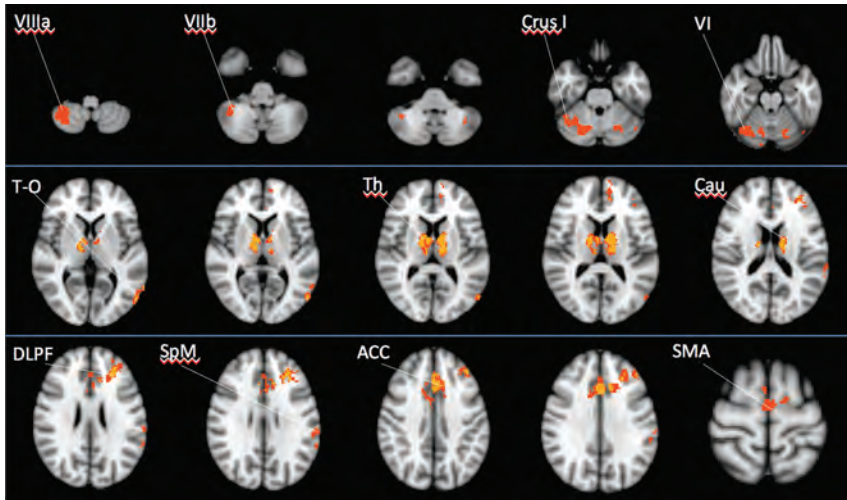


FIG 3. Images showing common areas of functional abnormalities shared by the 5 maps of FC. Different colors show the number of abnormal FC maps: in yellow, voxels of decreased FC in 4 maps; and in orange, voxels of decreased FC in 3 maps. Voxels of decreased FC in 2 maps are not shown. No focus of decreased FC in any of the 5 maps was identified. The images are presented according to radiologic orientation.

Correlation Analysis

FC estimates did not correlate with regional subcortical volumes and DTI parameters. The correlation analysis between the parameter estimates of FC within each of the 5 functional connectivity maps and clinical measures, as assessed by the Unified Parkinson's Disease Rating Scale, Frontal Assessment Battery, Hoehn and Yahr scale, Mini-Mental State Examination, and PSP Rating Scale and its subscales, yielded significant results (Table 2). Estimates of thalamic FC were inversely correlated with the Hoehn and Yahr Scale and the bulbar and mentation subitems of the PSP

Rating Scale scores ($P \leq .05$). Estimates of pallidum FC were directly correlated with Mini-Mental State Examination scores ($P = .03$), and estimates of the dMT FC were directly correlated with Frontal Assessment Battery scores ($P = .04$). Overall, these results indicated that decreased FC was associated with more severe manifestations of the disease. Conversely, regional subcortical volumes and DTI parameters did not correlate with clinical scores of disease severity.

DISCUSSION

The main finding of this study is that all the networks we evaluated—dMT, thalamus, caudate, putamen, and pallidum—exhibited lower FC in patients with PSP than in healthy subjects in several subcortical and cortical areas. Cortical disconnection mainly involved the frontal cortex (DLPF, ACC, SMA, precentral gyrus) and parietal (supramarginal gyrus and precuneus), temporal, and occipital cortices; the basal ganglia, thalamus, and cerebellum were also affected. Disruption of specific brain regions (ie, the thalamus, caudate, ACC, SMA, and cerebellum on both sides and the DLPF, temporo-occipital cortex, and supramarginal gyrus on the left side) was a common finding in the various functional connectivity maps analyzed.

Following a previous observation by Gardner et al,¹⁰ who first found reduced dMT FC in the cerebellum, thalamus, striatum, and frontal and parietal cortices in patients with PSP, in the present study, we provide further evidence showing that FC in the dMT functional connectivity map is reduced in the left DLPF and supramarginal gyrus and in the pregenual anterior cingulate cortex, bilaterally. Moreover, in the present study, we did not find any region of enhanced dMT FC, which is in keeping with previous results.¹⁰ With regard to thalamic FC, we confirmed the reduced connectivity in the premotor cortex, SMA, thalamus, basal ganglia, and cerebellum previously described by Whitwell et al⁹ in patients with PSP. Unlike us, however, they did not detect decreased FC in the ACC and found increased FC in regions surrounding the perisylvian fissure.⁹ These discrepancies between the 2 studies are likely due to differences in the methodology used for the data analysis or in the selection of patients or both.

Table 2: Significant correlations between parameter estimates of FC maps and clinical scores in patients with PSP

	Clinical Scales ^a	β	P Value	95% CI	R ²
Thalamus	Bulbar	-5.89	.04	-11.57 to -0.20	0.19
Thalamus	Mentation	-8.02	.05	-16.20 to -0.15	0.27
Thalamus	H&Y	-3.51	.03	-6.60 to -0.40	0.53
Pallidum	MMSE	12.23	.03	1.19-23.27	0.52
dMT	FAB	42.16	.04	2.24-82.08	0.26

Note:—FAB indicates Frontal Assessment Battery; H&Y, Hoehn and Yahr Scale; MMSE, Mini-Mental State Examination.

^a Bulbar and Mentation are subitems of the PSP Rating Scale.

With respect to the previous studies,^{9,10} we evaluated FC also from the caudate nucleus, putamen, and pallidum and found that functional disruption was a consistent finding in PSP and extensively involved multiple subcortical and cortical areas. The thalamus, caudate, ACC, DLPF, and SMA are part of the parallel circuits that connect the basal ganglia and frontal cortex and are implicated in motor and cognitive functions,^{29,30} with the putamen mainly being connected to motor cortical areas¹² and the caudate nucleus mainly being involved in cognitive frontal circuits.³⁰ The decrease in thalamic FC we observed in all the functional connectivity maps, with the exception of the dMT, highlights the key role of the thalamus, which is an important integration center of networks related to emotional, cognitive, and motor functions³¹ in the pathophysiology of PSP. We also observed that the FC was abnormal in a specific region of the ACC in all the functional connectivity maps, with the exception of the dMT. This finding supports the concept of an overlap between different domains (ie, motor, cognitive, and emotional functions in the ACC).^{30,32} The DLPF, which plays a key role in executive functions,³³ was disconnected from the thalamus and pallidum bilaterally and from the dMT and caudate on the left side alone. This asymmetric FC likely reflects hemispheric functional specialization in executive functions between the left and right DLPF.³⁴ Last, the SMA was disconnected in the putamen, pallidum, and thalamic functional connectivity maps, while a region in the medial superior frontal cortex corresponding to the pre-SMA³⁵ was disconnected in the caudate functional connectivity map. The functional alterations we observed are in agreement with anatomic interconnections among the putamen, SMA, and motor cortices on 1 side and among the caudate, pre-SMA, and prefrontal cortex on the other side.^{35,36}

In addition to areas belonging to the subcortical-frontal circuits, the decrease in FC was consistently observed in the cerebellum and in the left temporo-occipital cortex and supramarginal gyrus, thereby suggesting a functional involvement of connections between basal ganglia and cortical areas other than frontal ones in the pathophysiology of PSP. The basal ganglia receives projections from widespread regions of the cerebral cortex, including the parietal and temporal lobes.³⁷ Furthermore, although the main interactions between the basal ganglia-cortical and cerebellum-cortical loops occur largely at the cortical level,³³ recent evidence points to direct connections between the cerebellum and basal ganglia.^{38,39}

In this study, patients with PSP displayed a gray matter volume decrease in subcortical structures and DTI abnormalities in white matter compared with healthy subjects, which is in keeping with

the results of previous studies.⁵⁻⁷ These structural abnormalities did not correlate with FC. Although it is commonly assumed that FC reflects structural connectivity, the relationship between the 2 is rather complex⁴⁰: FC can be observed, for example, between regions with no or few anatomic connections, owing to the dynamic reorganization capabilities of functional connections in the brain.⁴¹

Regarding the clinical impact of MR imaging structural abnormalities, previous studies that investigated possible relationships between cerebral atrophy measurements and disease severity generally failed to detect a significant correlation.^{5,9} There are few reports of correlations between regional measurements of DTI parameters and clinical scores.⁴² In the present study, neither regional brain volumes nor mean DTI metrics correlated with the clinical severity of patients with PSP. These observations suggest that the severity of clinical impairment may be due to a functional disruption of subcortical-cortical circuits rather than to structural abnormalities. To evaluate the effects of functional abnormalities on clinical severity, we investigated a possible correlation between disease severity clinical scores and parameter estimates of FC. We observed that thalamic FC was associated with both motor and cognitive abnormalities, as shown by correlations with Hoehn and Yahr Scale scores and with the bulbar and mentation subitems of the PSP Rating Scale; the pallidum FC correlated with the Mini-Mental State Examination and the dMT FC correlated with Frontal Assessment Battery changes. This latter finding is in keeping with the significant relationship between FC of the dMT network and the severity of cognitive impairment, found by Gardner et al.¹⁰ The present observations suggest that FC abnormalities in PSP might be developed as surrogate biomarkers of motor and cognitive abnormalities in PSP.

This study has certain limitations. First, we used a seed-based analysis, which is intrinsically flawed from a methodologic point of view owing to the a priori choice of the brain areas to correlate with the rest of the brain.⁸ Second, the seeds of our study included each of the 5 subcortical structures as a whole, with no distinction being made between the various components and nuclei. This drawback is related to the spatial resolution of the blood oxygen level-dependent images, which is insufficient to yield a reliable parcellation. Third, because we studied a homogeneous group of patients affected by Richardson syndrome,¹ and not by other PSP subtypes, the conclusion of our study cannot be extended to other subtypes of PSP. Last, we did not perform a follow-up study; therefore, further investigations are needed to clarify whether FC abnormalities in PSP are useful measures to predict the clinical outcome in this condition.

CONCLUSIONS

Our data on PSP clearly point to widespread functional alterations involving 5 different functional connectivity maps. Some of these abnormalities are strictly correlated with the severity of clinical impairment, suggesting that the characterization of patterns and dynamics of brain networks may shed light on pathophysiological and clinical changes in patients with PSP.

Disclosures: Nikolaos Petsas—UNRELATED: Consultancy; Federazione Italiana Sclerosi Multipla (fellowship).* Patrizia Pantano—UNRELATED: Grants/Grants Pending; Federazione Italiana Sclerosi Multipla.* *Money paid to the institution.

REFERENCES

- Colosimo C, Bak TH, Bologna M, et al. **Fifty years of progressive supranuclear palsy.** *J Neurol Neurosurg Psychiatry* 2014;85:938–44
- Steele JC, Richardson JC, Olszewski J. **Progressive supranuclear palsy: a heterogeneous degeneration involving the brain stem, basal ganglia and cerebellum with vertical gaze and pseudobulbar palsy, nuchal dystonia and dementia.** *Arch Neurol* 1964;10:333–59
- Dickson DW, Ahmed Z, Algom AA, et al. **Neuropathology of variants of progressive supranuclear palsy.** *Curr Opin Neurol* 2010;23:394–400
- Quattrone A, Nicoletti G, Messina D, et al. **MR imaging index for differentiation of progressive supranuclear palsy from Parkinson disease and the Parkinson variant of multiple system atrophy.** *Radiology* 2008;246:214–21
- Saini J, Bagepally BS, Sandhya M, et al. **Subcortical structures in progressive supranuclear palsy: vertex-based analysis.** *Eur J Neurol* 2013;20:493–501
- Shi HC, Zhong JG, Pan PL, et al. **Gray matter atrophy in progressive supranuclear palsy: meta-analysis of voxel-based morphometry studies.** *Neurol Sci* 2013;34:1049–55
- Stamelou M, Knake S, Oertel WH, et al. **Magnetic resonance imaging in progressive supranuclear palsy.** *J Neurol* 2011;258:549–58
- Fox MD, Raichle ME. **Spontaneous fluctuations in brain activity observed with functional magnetic resonance imaging.** *Nat Rev Neurosci* 2007;8:700–11
- Whitwell JL, Avula R, Master A, et al. **Disrupted thalamocortical connectivity in PSP: a resting-state fMRI, DTI, and VBM study.** *Parkinsonism Relat Disord* 2011;17:599–605
- Gardner RC, Boxer AL, Trujillo A, et al. **Intrinsic connectivity network disruption in progressive supranuclear palsy.** *Ann Neurol* 2013;73:603–16
- Alexander GE, Crutcher MD, DeLong MR. **Basal ganglia-thalamocortical circuits: parallel substrates for motor, oculomotor, “pre-frontal” and “limbic” functions.** *Prog Brain Res* 1990;85:119–46
- Bonelli RM, Cummings JL. **Frontal-subcortical circuitry and behavior.** *Dialogues Clin Neurosci* 2007;9:141–51
- Litvan I, Agid Y, Calne D, et al. **Clinical research criteria for the diagnosis of progressive supranuclear palsy (Steele-Richardson-Olszewski syndrome): report of the NINDS-SPSP international workshop.** *Neurology* 1996;47:1–9
- Williams DR, Lees AJ. **Progressive supranuclear palsy: clinicopathological concepts and diagnostic challenges.** *Lancet Neurol* 2009;8:270–79
- Goetz CG, Fahn S, Martinez-Martin P, et al. **Movement Disorder Society-sponsored revision of the Unified Parkinson’s Disease Rating Scale (MDS-UPDRS): process, format, and clinimetric testing plan.** *Mov Disord* 2007;22:41–47
- Dubois B, Slachevsky A, Litvan I, et al. **The FAB: a Frontal Assessment Battery at bedside.** *Neurology* 2000;55:1621–26
- Hoehn MM, Yahr MD. **Parkinsonism: onset, progression, and mortality.** *Neurology* 1998;50:318
- Folstein MF, Folstein SE, McHugh PR. **“Mini-mental state”: a practical method for grading the cognitive state of patients for the clinician.** *J Psychiatr Res* 1975;12:189–98
- Golbe LI, Ohman-Strickland PA. **A clinical rating scale for progressive supranuclear palsy.** *Brain* 2007;130(pt 6):1552–65
- Greve DN, Fischl B. **Accurate and robust brain image alignment using boundary-based registration.** *Neuroimage* 2009;48:63–72
- Patenaude B, Smith SM, Kennedy DN, et al. **A Bayesian model of shape and appearance for subcortical brain segmentation.** *Neuroimage* 2011;56:907–22
- Woolrich MW, Behrens TE, Smith SM. **Constrained linear basis sets for HRF modelling using variational Bayes.** *Neuroimage* 2004;21:1748–61
- Gavrilescu M, Shaw ME, Stuart GW, et al. **Simulation of the effects of global normalization procedures in functional MRI.** *Neuroimage* 2002;17:532–42
- Macey PM, Macey KE, Kumar R, et al. **A method for removal of global effects from fMRI time series.** *Neuroimage* 2004;22:360–66
- Smith SM, Zhang Y, Jenkinson M, et al. **Accurate, robust, and automated longitudinal and cross-sectional brain change analysis.** *Neuroimage* 2002;17:479–89
- Song SK, Sun SW, Ramsbottom MJ, et al. **Dysmyelination revealed through MRI as increased radial (but unchanged axial) diffusion of water.** *Neuroimage* 2002;17:1429–36
- Smith SM, Jenkinson M, Johansen-Berg H, et al. **Tract-based spatial statistics: voxelwise analysis of multi-subject diffusion data.** *Neuroimage* 2006;31:1487–505
- Smith SM, Nichols TE. **Threshold-free cluster enhancement: addressing problems of smoothing, threshold dependence and localisation in cluster inference.** *Neuroimage* 2009;44:83–98
- DeLong MR, Wichmann T. **Circuits and circuit disorders of the basal ganglia.** *Arch Neurol* 2007;64:20–24
- Alexander GE, DeLong MR, Strick PL. **Parallel organization of functionally segregated circuits linking basal ganglia and cortex.** *Annu Rev Neurosci* 1986;9:357–81
- Haber SN, Calzavara R. **The cortico-basal ganglia integrative network: the role of the thalamus.** *Brain Res Bull* 2009;78:69–74
- Paus T. **Primate anterior cingulate cortex: where motor control, drive and cognition interface.** *Nat Rev Neurosci* 2001;2:417–24
- Middleton FA, Strick PL. **Cerebellar projections to the prefrontal cortex of the primate.** *J Neurosci* 2001;21:700–12
- Kaller CP, Rahm B, Spreer J, et al. **Dissociable contributions of left and right dorsolateral prefrontal cortex in planning.** *Cereb Cortex* 2011;21:307–17
- Zhang S, Ide JS, Li CR. **Resting-state functional connectivity of the medial superior frontal cortex.** *Cereb Cortex* 2012;22:99–111
- Kim JH, Lee JM, Jo HJ, et al. **Defining functional SMA and pre-SMA subregions in human MFC using resting state fMRI: functional connectivity-based parcellation method.** *Neuroimage* 2010;49:2375–86
- Middleton FA, Strick PL. **The temporal lobe is a target of output from the basal ganglia.** *Proc Natl Acad Sci U S A* 1996;93:8683–87
- Hoshi E, Tremblay L, Féger J, et al. **The cerebellum communicates with the basal ganglia.** *Nat Neurosci* 2005;8:1491–93
- Wu T, Hallett M. **The cerebellum in Parkinson’s disease.** *Brain* 2013;136(pt 3):696–709
- Damoiseaux JS, Greicius MD. **Greater than the sum of its parts: a review of studies combining structural connectivity and resting-state functional connectivity.** *Brain Struct Funct* 2009;213:525–33
- O’Reilly JX, Croxson PL, Jbabdi S, et al. **Causal effect of disconnection lesions on interhemispheric functional connectivity in rhesus monkeys.** *Proc Natl Acad Sci U S A* 2013;110:13982–87
- Wang J, Wai Y, Lin W-Y, et al. **Microstructural changes in patients with progressive supranuclear palsy: a diffusion tensor imaging study.** *J Magn Reson Imaging* 2010;32:69–75

WEB Treatment of Intracranial Aneurysms: Feasibility, Complications, and 1-Month Safety Results with the WEB DL and WEB SL/SLS in the French Observatory

L. Pierot, J. Moret, F. Turjman, D. Herbreteau, H. Raoult, X. Barreau, S. Velasco, H. Desal, A.-C. Januel, P. Courtheoux, J.-Y. Gauvrit, C. Cognard, S. Soize, A. Molyneux, and L. Spelle

ABSTRACT

BACKGROUND AND PURPOSE: Safety analyses in the French Observatory have shown that treatment of intracranial aneurysms by using flow disruption with the Woven EndoBridge Device (WEB) is safe, with low morbidity and no mortality. The objective of this study was to analyze treatment feasibility, complications, and safety results in patients treated with the Woven EndoBridge Device Dual-Layer (WEB DL) and Woven EndoBridge Device Single-Layer/Single-Layer Sphere (WEB SL/SLS) in the French Observatory.

MATERIALS AND METHODS: Patients with bifurcation aneurysms were included in this prospective, multicenter good clinical practices study. A medical monitor independently analyzed procedural and clinical data. The study started with the WEB DL, and secondarily, the WEB SL/SLS was authorized in the study.

RESULTS: Between November 2012 and January 2014, 10 French centers included 62 patients with 63 aneurysms. Thirty patients with 31 aneurysms were treated with the WEB DL, and 32 patients with 32 aneurysms, with the WEB SL/SLS. The percentage of anterior communicating artery aneurysms treated with WEB SL/SLS was significantly higher (37.5%) compared with WEB DL (12.9%) ($P = .04$). The WEB SL/SLS was more frequently used in aneurysms of <10 mm than the WEB DL (respectively, 96.9% and 67.7%; $P = .002$). Morbidity was similar in both groups (WEB DL, 3.3%; WEB SL/SLS, 3.1%), and mortality was 0.0% in both groups.

CONCLUSIONS: This comparative study shows increased use of WEB treatment in ruptured, small, and anterior communicating artery aneurysms when using WEB SL/SLS. There was a trend toward fewer thromboembolic complications with the WEB SL/SLS. With both the WEB DL and WEB SL/SLS, the treatment was safe, with low morbidity and no mortality.

ABBREVIATIONS: AcomA = anterior communicating artery; DL = Dual-Layer; SL = Single-Layer; SLS = Single-Layer Sphere; WEB = Woven EndoBridge Device

Endovascular treatment is the preferred therapeutic option for ruptured aneurysms that are anatomically suitable for endovascular coil treatment, supported by randomized studies, espe-

cially in locations less suitable for surgery.^{1,2} It also has an important place in the management of unruptured aneurysms that are judged appropriate for treatment.³ Complex aneurysms (fusiform, wide-neck, large, or giant) are often untreatable or difficult to treat with standard coiling. For these complex cases, endovascular techniques such as balloon-assisted coiling, stent-assisted coiling, or flow diversion have been used with good results.⁴⁻⁹

Flow disruption is a new endovascular approach, which involves placement of a Woven EndoBridge Device (WEB; Sequent Medical, Aliso Viejo, California), which modifies the blood flow at the level of the neck and induces intra-aneurysmal thrombosis. The WEB was designed initially to treat wide-neck and bifurcation aneurysms. The initial clinical results have shown that treatment is feasible with a low level of complications, low morbidity, and no mortality.¹⁰⁻¹⁴ The device has been progressively developed from a dual-layer version (WEB Dual-Layer [DL] aneurysm embolization system; Sequent Medical) to single-layer versions (WEB Single-Layer [SL] and WEB Single-Layer Sphere [SLS]).

Received August 8, 2014; accepted after revision October 24.

From the Department of Neuroradiology (L.P., S.S.), Hôpital Maison-Blanche, Université Reims-Champagne-Ardenne, Reims, France; Department of Neuroradiology (J.M., L.S.), Hôpital Beaujon, Assistance Publique-Hôpitaux de Paris, Clichy, France; Department of Neuroradiology (F.T.), Centre Hospitalier Universitaire Lyon, Lyon, France; Department of Neuroradiology (D.H.), Centre Hospitalier Universitaire Tour, Tours, France; Department of Neuroradiology (H.R., J.-Y.G.), Centre Hospitalier Universitaire Rennes, Rennes, France; Department of Neuroradiology (X.B.), Centre Hospitalier Universitaire Bordeaux, Bordeaux, France; Department of Neuroradiology (S.V.), Centre Hospitalier Universitaire Poitiers, Poitiers, France; Department of Neuroradiology (H.D.), Centre Hospitalier Universitaire Nantes, Nantes, France; Department of Neuroradiology (A.-C.J., C.C.), Centre Hospitalier Universitaire Toulouse, Toulouse, France; Department of Neuroradiology (P.C.), Centre Hospitalier Universitaire Caen, Caen, France; and Department of Neuroradiology (A.M.), Oxford Neurovascular and Neuroradiology Research Unit, Oxford Radcliffe Hospital, Oxford, United Kingdom.

Please address correspondence to Laurent Pierot, MD, Department of Neuroradiology, Hôpital Maison-Blanche, 45 rue Cognacq-Jay, 51092 Reims Cedex, France; e-mail: lpierot@gmail.com

<http://dx.doi.org/10.3174/ajnr.A4230>

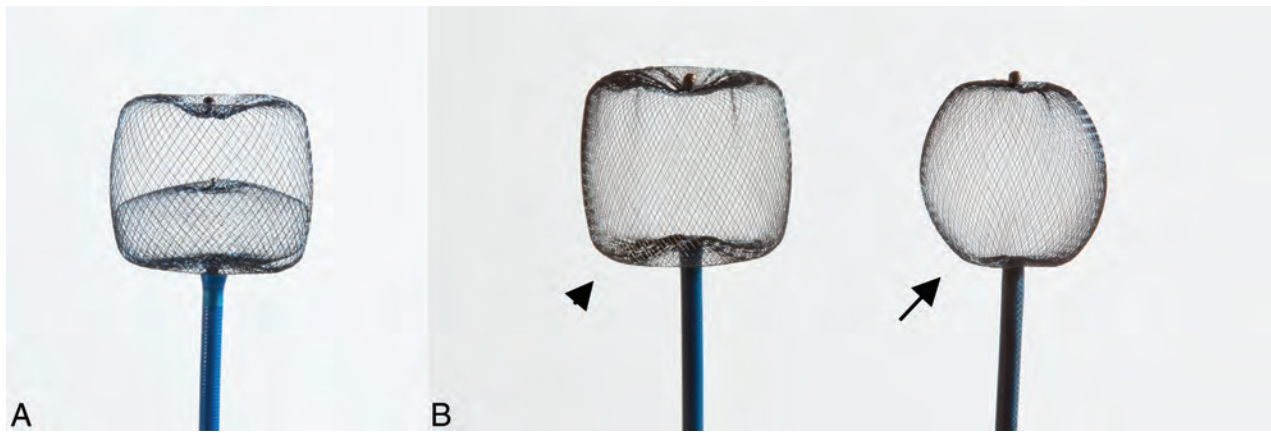


FIGURE. A, WEB DL. B, WEB SL (arrowhead) and SLS (arrow).

The French Observatory is a prospective, multicenter observational study of consecutive cases, with independent monitoring, across 10 French centers.

It has 2 major objectives:

- 1) To carefully evaluate the safety of this treatment with an independent assessment of all adverse events and morbidity/mortality.
- 2) To evaluate the efficacy of this treatment at 12 and 24 months with independent core lab adjudication.

Patients treated with both WEB DL and WEB SL/SLS were included in the French Observatory. The present analysis reports the feasibility of treatment, adverse events, and morbidity/mortality at 1 month in patients treated with WEB DL and WEB SL/SLS.

MATERIALS AND METHODS

The study received required national regulatory authorization: approval from the Reims Institutional Review Board, the Consultative Committee of Information Processing in Health Care Research program, and the National Commission for Data Processing and Freedom. Written informed consent was obtained for all patients. The study has been declared on Clinicaltrials.gov (NCT01975233).

Trial Design

The French Observatory is a single-arm, prospective, consecutive, multicenter, observational, French study confined to the evaluation of WEB treatment for bifurcation aneurysms.

The study protocol had the following inclusion criteria:

- Patients of 18–75 years of age, able to consent and comply with 30-day, 1-year, and 2-year follow-up.
- Aneurysm status: ruptured (Hunt and Hess 1, 2, or 3), unruptured, and recanalized.
- Aneurysm location: bifurcation aneurysms located at the basilar artery, middle cerebral artery, anterior communicating artery, and internal carotid artery terminus.
- Aneurysm morphology: able to be treated with available WEB sizes, and dome-to-neck ratio greater ≥ 1 .

In each participating institution, the treatment decision and its technique (surgery or endovascular treatment) were decided

on a case-by-case basis by a local multidisciplinary team, including neurosurgeons, neuroanesthesiologists, neurologists, and neuroradiologists. The selection of aneurysms treated with the WEB device was performed autonomously in each center by the interventional neuroradiologists according to the study protocol.

Study follow-up was conducted at 30 days (safety/mRS), 12 months (safety/mRS and imaging per standard of care), and 24 months (safety/mRS and imaging per standard of care). All imaging was evaluated by an independent core lab to assess the adequacy of occlusion.

The study was initiated with the WEB DL device, and an amendment was approved when the WEB SL and SLS were available, making these devices usable in the study.

WEB Devices

WEB devices (Figure) are retrievable, electrothermally detachable, nitinol braids that are placed within the sac of the aneurysm to disrupt the flow at the level of the neck and create aneurysmal thrombosis.

WEB DL, which received CE Mark in 2010, contains a second nitinol braid that is proximally placed inside the first nitinol braid and provides a double-layer high-attenuation mesh coverage at the neck to achieve rapid intraprocedural stasis. The WEB DL is available in diameters between 5 and 11 mm and heights between 3 and 9 mm and has a barrel shape designed to treat wide-neck bifurcation aneurysms (ie, the WEB is wider than it is tall). With the double layers, WEB DL devices contain 216 or 288 total wires, depending on device size. More important, a given WEB DL contains 2 or 3 different-diameter wires braided into the device in a proprietary process called MicroBraid (Sequent Medical).

WEB SL and WEB SLS, which received CE Mark in 2013, represent an evolution of the MicroBraid technology. WEB SL and SLS are available in an expanded range of diameters between 4 and 11 mm and heights between 3 and 9 mm. Markedly different from the WEB DL, the WEB SL and SLS devices vary from 144 wires in 4-mm-diameter devices up to 216 wires in 11-mm-diameter devices. With a more spherical shape, WEB SLS is designed to treat ~ 1.5 –2 dome-to-neck-ratio aneurysms and aneurysms with V-shaped or tapered necks. Unlike the WEB SL, which is available in multiple heights at any given width, WEB SLSs are singularly

available in sizes between 4 and 11 mm (ie, the heights of WEB SLSs are slightly less than their diameters due to the inclusion of the distal and proximal marker recesses). The increasing wire count in a single, braided layer—combined with multiple wire diameters—allows the WEB SL and SLS to achieve rapid contrast stasis and to balance radial force with conformability.¹⁵ This uniform response may be important clinically in that small and large WEB devices must have an appropriate radial force to remain where they are deployed (ie, WEB radial force is greater than the parent artery blood flow force) but must remain soft enough to conform safely to the aneurysm (ie, WEB radial force is less than the compressive force on the aneurysm from the subarachnoid space).

Since late 2012, VIA catheters have been available from Sequent Medical, designed specifically for the WEB. During 2010 through late 2012, WEB DL 5- to 7-mm diameters were used primarily with Rebar-27 (Covidien, Irvine, California), and WEB DL 8- to 11-mm diameters were used with DAC 038 (Stryker, Fremont, California). From late 2012 to the present, WEB procedures were performed with the VIA-27 (WEB DL 5–7 mm, WEB SL/SLS 4–9 mm), VIA-33 (WEB DL 8–9 mm, WEB SL/SLS 10–11 mm), and DAC 038 (WEB DL 10 and 11 mm). Taken together, the WEB SL/SLS and the VIA catheters provide complete systems for WEB delivery, retrieval, deployment, and detachment in aneurysms ~3 to ~10 mm in diameter.

Procedural Modalities

The treatment of aneurysms with the WEB was performed with techniques similar to those used in the treatment of aneurysms with coils (eg, general anesthesia, intraoperative treatment with intravenous heparin, single or double femoral approach). Pre-, intra-, and postoperative antiplatelet therapy was managed in each center as indicated for their standard endovascular treatment with coils (or stent and coils if this approach was a potential alternative treatment).

After accurate evaluation of aneurysm anatomy (aneurysm morphology, aneurysm transverse diameter and height, and neck size) by the treating physician by using MRA and DSA, it was determined whether the treatment with the WEB was indicated and device sizing was appropriate.

We usually used a triaxial access: a long introducer sheath placed in the internal carotid artery or vertebral artery, a distal access catheter placed in the intracranial portion of the ICA or vertebral artery, and a microcatheter placed in the aneurysm. The WEB device chosen according to aneurysm measurements was then positioned in the aneurysmal sac. A control angiogram was performed to check the position of the device in the aneurysm and to evaluate flow stagnation inside the aneurysm. If the position was not satisfactory, the device was resheathed and repositioned. If the size was not appropriate, the device was resheathed and another device was deployed into the aneurysm. When the right-sized device was correctly positioned, a final DSA run was performed. Treatment with ancillary devices (balloon, coils, and stent) was authorized if deemed necessary by the treating physician.

Data Collection

Each center completed a patient file with the following data: patient age and sex; aneurysm status; aneurysm characteristics, in-

cluding location, size, and neck size; date of the procedure; type of device used (DL or SL/SLS); occurrence of a complications during or after the procedure; and use of an additional device during the procedure (coils, remodeling balloons, stents, or flow diverters). A preoperative Hunt and Hess grade was collected in case of ruptured aneurysms. mRS was collected before treatment (unruptured/re canalized aneurysms) and at 1 month (all patients).

All adverse events were collected in this good clinical practices series, even if no specific treatment was needed. Thromboembolic events were diagnosed intraoperatively by angiography regardless of type (clotting near the neck of the aneurysm, clotting in the distal branches, and parent vessel occlusion). Postoperative thromboembolic events were diagnosed by MR imaging and/or digital subtraction angiography performed in cases of sudden neurologic compromise. Intraoperative rupture was diagnosed by the exit of the tip of the coil or the microcatheter outside the limit of the aneurysmal sac and/or extravasation of contrast media. Adverse events were reported even if no clinical modification was associated with them.

Data Analysis

Clinical data were independently monitored and analyzed including all adverse events. Morbidity was defined as mRS of >2 when the preoperative mRS was ≤2 (or in case of ruptured aneurysm) and as an increase of 1 point when the preoperative the mRS was >2. Population, adverse events, and morbidity/mortality were compared in the DL and SL/SLS groups.

Statistical Analysis

Continuous variables were described as mean ± SD with extreme values and categorical variables as a number and percentage. Categorical variables and quantitative variables were compared between patients with WEB DL and WEB SL/SLS devices by using Mann-Whitney *U* tests, χ^2 tests, or Fisher exact tests, as appropriate. A *P* value < .05 was considered significant. Analyses were conducted by using MedCalc statistical software for Windows (Version 11.4.3.0; MedCalc Software, Mariakerke, Belgium).

RESULTS

Population

Patients were included in French Observatory between November 2012 and January 2014.

Thirty patients (women, 23; 76.7%) aged 33–71 years (mean, 55.6 ± 8.9 years) with 31 aneurysms were treated with the WEB DL. Thirty-two patients (women, 16; 50.0%) aged 33–74 years (mean, 57.4 ± 10.3 years) with 32 aneurysms were treated with WEB SL or WEB SLS.

In the DL group, aneurysms were ruptured (2/31, 6.5%), unruptured (26/31, 83.9%), and recanalized (3/31, 9.6%). They were located on the MCA (19/31, 61.3%), basilar artery (6/31, 19.4%), ICA terminus (2/31, 6.5%), and anterior communicating artery (AcomA) (4/31, 12.9%). Aneurysm size was <10 mm in 21/31 aneurysms (67.7%). Neck size was >4 mm in 29/31 aneurysms (93.5%). Four patients (13.3%) received single (3 patients) or dual (1 patient) antiplatelet treatment before the procedure. Dur-

Aneurysm characteristics, treatment complications, and morbidity and mortality in patients treated with WEB DL and WEB SL (and SLS)

	WEB DL	WEB SL/SLS	P Value
Patients	30	32	
Age (mean) (yr)	55.6 ± 8.9	57.4 ± 10.3	.86
Female	24/30 (80.0%)	16/32 (50.0%)	.20
Aneurysms	31	32	
Ruptured	2/31 (6.5%)	5/32 (15.6%)	.42
AcomA	4/31 (12.9%)	12/32 (37.5%)	.04
Aneurysm <10 mm	21/31 (67.7%)	31/32 (96.9%)	.002
Neck >4 mm	29/31 (96.5%)	28/32 (87.5%)	.67
Antiplatelet treatment ^a			
Before treatment	4/30 (13.3%)	11/32 (34.4%)	.07
During treatment	22/30 (73.3%)	20/32 (62.5%)	.42
After treatment	26/30 (86.7%)	22/32 (68.8%)	.13
Treatment feasibility	30/31 (96.8%)	32/32 (100.0%)	.49
Adjunctive treatment	4/30 (13.3%)	3/32 (9.4%)	.70
Adverse events			
Device problems	3/30 (10.0%)	2/32 (6.3%)	.66
TE ^b	7/30 (23.3%)	3/32 (9.4%)	.17
IOR	1/30 (3.3%)	0/32 (0.0%)	.48
Morbidity/mortality			
Morbidity	1/30 (3.3%)	1/32 (3.1%)	1
Mortality	0/30 (0.0%)	0/32 (0.0%)	1

Note:—TE indicates thromboembolic event/appearance of thrombus; IOR, intraoperative rupture.

^a One or 2 medications.

^b DL group: no clinical deficit in 3, transient deficits in 3, permanent deficit in 1. SL group: no deficit in 1, transient deficits in 2.

ing the procedure, 22 patients (73.3%) received antiplatelet treatment (single, 14; dual, 8). After the procedure, 26 patients (86.7%) received antiplatelet treatment (single, 18; dual, 8).

In the SL/SLS group, aneurysms were ruptured (5/32, 15.6%), unruptured (25/32, 78.1%), and recanalized (2/32, 6.3%). They were located on the MCA (13/32, 40.6%), basilar artery (3/32, 9.4%), ICA terminus (4/32, 12.5%), and AcomA (12/32, 37.5%). Aneurysm size was <10 mm in 31/32 aneurysms (96.9%). Neck size was >4 mm in 28/32 aneurysms (87.5%). Eleven patients (34.4%) received single (4 patients) or dual (7 patients) antiplatelet treatment before the procedure. During the procedure, 20 patients (62.5%) received antiplatelet treatment (single, 12; dual, 8). After the procedure, 22 patients (68.8%) received antiplatelet treatment (single, 13; dual, 9).

Patient and aneurysm populations are statistically compared in the Table.

Treatment Feasibility

Technical success (deployment of the WEB in the target aneurysm) was achieved in 30/31 aneurysms (96.8%) in the DL group and in 32/32 aneurysms (100.0%) in the SL/SLS group. One treatment failure occurred in the DL group: it was impossible to deploy the WEB, which was stuck in the microcatheter. The aneurysm was treated with coils.

Adjunctive Treatments

Adjunctive devices were used in 4/30 aneurysms (13.3%) in the DL group (coiling in 3 cases and stent placement in 1 case) and in 3/32 aneurysms (9.4%) in the SL/SLS group (coiling in 1 case and stent placement in 2 cases).

Technical Problems and Adverse Events

Technical problems were encountered in 3/30 patients (9.7%) in the DL group (detachment problem, 1; WEB protrusion, 1; WEB stuck in microcatheter, 1) and 2/32 patients (6.3%) in the SL/SLS group (WEB protrusion, 2). All events were clinically asymptomatic.

Thromboembolic events or any appearance of thrombus was reported in 7/30 patients (23.3%) in the DL group (with no clinical deficit in 3, transient deficits in 3, and a permanent deficit in 1) and in 3/32 patients (9.4%) in SL/SLS group (with no deficit in 1 and a transient deficit in 2). In both groups, there was no evidence of a statistical relationship between antiplatelet medication and the occurrence of thromboembolic events.

Intraoperative rupture occurred in 1 patient (3.3%) in the DL group and zero patients in the SL/SLS group. The intraoperative rupture was not symptomatic.

One patient (3.3%) had an intracranial hemorrhage 2 days after WEB DL treatment related to dual antiplatelet therapy with no clinical worsening.

Statistical comparison for technical complications and adverse events between the DL and SL/SLS groups is shown in the Table.

Mortality/Morbidity at 1 Month

There was no mortality in the series. One patient in each group had mRS >2 at 1 month, leading to a morbidity of 3.3% in the DL group and 3.1% in the SL/SLS group. Morbidity was related to a thromboembolic event in the DL group and to an increase of a pre-existing aneurysm mass effect in the SL group.

DISCUSSION

The present analysis shows that indications for the WEB DL and WEB SL/SLS are slightly different. Fewer thromboembolic complications or any appearance of thrombus was observed after treatment with the WEB SL/SLS (9.4% versus 23.3% in the DL group), but with such small numbers, this difference was not significant ($P = .14$). Morbidity was low and similar in both groups, (3.3% with the WEB DL and 3.1% with the WEB SL/SLS). There was no mortality.

For similar-sized devices, moving from a dual-layer to a single-layer device improves the device profile with several potential advantages, including a decrease in size of the microcatheter used for the placement of the device and improved navigability of the device in the microcatheter. Other potential advantages are easier deployment of the device in the aneurysm sac, better conformability of the device to the aneurysm, and improved retrievability of the device.

The present analysis shows a change in the way the WEB device is used. Of note, there was a trend toward an increased percentage of ruptured aneurysms treated in the cohort, 6.5% with WEB DL and 15.6% with WEB SL/SLS, though again, the trend was not significant ($P = .42$). The use of antiplatelet drugs is not mandatory when using this technique, making the WEB potentially suitable for use in the treatment of ruptured aneurysms, which present difficulties for standard coil treatment or stent-assisted coiling.^{16,17} Larger series are needed to determine the exact place of WEB treatment in the management of ruptured aneurysms.

The percentage of AcomA aneurysms treated with the WEB SL/SLS was significantly higher (37.5%) in this series compared

with the WEB DL (12.9%) ($P = .04$). The lower device profile offered by the WEB SL/SLS is the single most important factor making it more suitable for aneurysms in this location. Entering the A1 segment of the anterior cerebral artery with a 0.027- to 0.033-inch microcatheter is not always simple, and the anatomy of the anterior communicating artery complex is transiently modified when the microcatheter is in the A1 segment and when the device is pushed into the microcatheter, making correct positioning of the device sometimes more difficult. The improvement of the WEB SL/SLS device profile consequently makes the procedure easier and increases the feasibility of treating more wide-neck anterior communication artery aneurysms.

In this study, both the WEB DL and WEB SL/SLS devices were used in predominantly wide-neck aneurysms (respectively, 96.5% and 87.5%). The WEB SL/SLS was more frequently used in aneurysms of <10 mm than the WEB DL (respectively, 96.9% and 67.7%; $P = .002$), probably as a result of reduced catheter profile and better conformability of the device.

Treatment success was high with both the WEB DL and WEB SL/SLS (respectively, 96.8% and 100.0%). Adjunctive devices were used in a similar percentage of cases in both the DL and SL/SLS groups (respectively, 13.3% and 9.4%). Coiling was used in 3 aneurysms after WEB DL treatment and in 1 aneurysm after WEB SL/SLS treatment, in case of incomplete treatment with the WEB. In all these cases, the device was undersized, with inappropriate filling of the aneurysm creating 2 different sometimes combined situations: 1) The device was not completely applied against the aneurysm wall; in this case, it was possible to catheterize the space between the aneurysm wall and the device and to deploy some coils. 2) An aneurysm remnant was left in place close to the neck; in this case, it was possible to fill the aneurysm remnant with coils by using the remodeling technique.⁴

Stent placement was used in 1 aneurysm after WEB DL treatment and in 2 aneurysms after WEB SL in case of WEB protrusion.

Device problems were encountered in a similar percentage of aneurysms with the WEB DL (10.0%) and WEB SL (6.3%). Fewer thromboembolic events were reported in the WEB SL/SLS group (9.4%) than in the WEB DL group (20.0%), but the difference was not statistically significant ($P = .14$). This phenomenon probably has several explanations, including the learning curve with the WEB device relating singularly to the procedure and WEB sizing (the WEB DL was used at the beginning of the experience and the WEB SL/SLS, after the WEB DL) and refinement of the antiplatelet medication protocol (because antiplatelet treatments were slightly different between the WEB DL and WEB SL, but not significantly).¹⁷

Very important, the observed clinical morbidity in patients treated with the WEB DL and WEB SL/SLS was similar and low with both devices (respectively, 3.3% and 3.1%). Mortality was 0.0% in both groups. Given the population of complex aneurysms treated, regardless of the device used, the treatment is safe.

This comparative study has some limitations. First, both devices were not used during the same period. The French Observatory started with the WEB DL at the beginning of the clinical experience with WEB, and the WEB SL/SLS was introduced half-

way through the study. When using the WEB SL/SLS, the physicians were more familiar (learning curve) with flow-disruption procedures and WEB sizing. Second, both groups are small, with a small number of patients. This size limits any statistical comparison between the groups, but to date, the French Observatory is the largest good clinical practices study and the only study in which patients were treated with both the WEB DL and the WEB SL/SLS. Third, the number of ruptured aneurysms was not sufficient to perform subgroup analysis of ruptured-versus-unruptured aneurysms. Fourth, because the reason for using the WEB was not collected in the series, it is not possible to analyze precisely the framework of situations in which the WEB was used.

CONCLUSIONS

This comparative study suggests that there is increasing use of flow disruption with the WEB SL/SLS in ruptured, small, and AcomA aneurysms. With both the WEB DL and the WEB SL/SLS, treatment is safe, with low morbidity (respectively, 3.3% and 3.1%) and no mortality. The next step is to evaluate the efficacy of the WEB DL and WEB SL/SLS in terms of protection against bleeding and rebleeding and the stability of aneurysm occlusion.

Disclosures: Laurent Pierot—RELATED: Consulting Fee or Honorarium: Sequent; UNRELATED: Consultancy: Codman, Covidien, MicroVention, Stryker; OTHER: proctoring and consultant agreement (Sequent), Principal Investigator for WEBCAST and the French Observatory. Jacques Moret—UNRELATED: Board Membership: Covidien; Consultancy: Covidien, MicroVention; OTHER RELATIONSHIPS: My son works for Covidien. Francis Turjman—UNRELATED: Consultancy: Codman, Covidien, Balt; Grants/Grants Pending: Covidien*; Payment for Lectures (including service on Speakers Bureaus): Codman,* Covidien*; Payment for Development of Educational Presentations: Codman,* Covidien*; Travel/Accommodations/Meeting Expenses Unrelated to Activities Listed: Codman, Covidien, Stryker. Denis Herbreteau—RELATED: Other: Sequent (proctor); UNRELATED: Travel/Accommodations/Meeting Expenses Unrelated to Activities Listed: Sequent,* Comments: World Federation of Interventional and Therapeutic Neuroradiology (Buenos Aires, Val d'Isère). Xavier Barreau—RELATED: Fees for Participation in Review Activities such as Data Monitoring Boards, Statistical Analysis, Endpoint Committees, and the Like: Sequent; UNRELATED: Consultancy: MicroVention, Stryker, Covidien. Anne-Christine Januel—RELATED: Support for Travel to Meetings for the Study or Other Purposes: Sequent,* Comments: support occasionally for meetings; OTHER: Sequent (proctoring). Jean Yves Gauvrit—RELATED: core lab agreement for a European WEB series (Sequent). Christopher Cognard—RELATED: Consulting Fee or Honorarium: Sequent (proctoring); UNRELATED: Consultancy: Stryker, Codman, Sequent, MicroVention, Covidien. Andrew Molyneux—RELATED: Support for Travel to Meetings for the Study or Other Purposes: Sequent, Comments: in connection with study design and adverse event adjudication (adverse event adjudication agreement); Fees for Participation in Review Activities such as Data Monitoring Boards, Statistical Analysis, Endpoint Committees, and the Like: Sequent Medical, Comments: for time conducting independent evaluation of adverse events and study-design advice. Laurent Spelle—UNRELATED: Consultancy: Sequent, Stryker, Covidien; Travel/Accommodations/Meeting Expenses Unrelated to Activities Listed: Stryker, Covidien, Sequent; OTHER: Sequent (proctoring). *Money paid to the institution.

REFERENCES

1. Molyneux A, Kerr R, Stratton I, et al; International Subarachnoid Aneurysm Trial (ISAT) Collaborative Group. **International Subarachnoid Aneurysm Trial (ISAT) of neurosurgical clipping versus endovascular coiling in 2143 patients with ruptured intracranial aneurysms: a randomised trial.** *Lancet* 2002;360:1267–74
2. Cognard C, Pierot L, Anxionnat R, et al; Clarity Study Group. **Results of embolization used as the first treatment choice in a consecutive nonselected population of ruptured aneurysms: clinical results of the Clarity GDC study.** *Neurosurgery* 2011;69:837–41; discussion 842
3. Pierot L, Spelle L, Vitry F; ATENA Investigators. **Immediate clinical outcome of patients harboring unruptured intracranial aneurysms**

- treated by endovascular approach: results of the ATENA study. *Stroke* 2008;39:2497–504
4. Pierot L, Cognard C, Spelle L, et al. **Safety and efficacy of balloon remodeling technique during endovascular treatment of intracranial aneurysms: critical review of the literature.** *AJNR Am J Neuroradiol* 2012;33:12–15
 5. Pierot L, Spelle L, Leclerc X, et al. **Endovascular treatment of unruptured intracranial aneurysms: comparison of safety of remodeling technique and standard treatment with coils.** *Radiology* 2009;251:846–55
 6. Pierot L, Cognard C, Anxionnat R, et al; CLARITY Investigators. **Remodeling technique for endovascular treatment of ruptured intracranial aneurysms had a higher rate of adequate postoperative occlusion than did conventional coil embolization with comparable safety.** *Radiology* 2011;258:546–53
 7. Shapiro M, Becske T, Sahlein D, et al. **Stent-supported aneurysm coiling: a literature survey of treatment and follow-up.** *AJNR Am J Neuroradiol* 2012;33:159–63
 8. Pierot L. **Flow diverter stents in the treatment of intracranial aneurysms: where are we?** *J Neuroradiol* 2011;38:40–46
 9. Berge J, Biondi A, Machi P, et al. **Flow-diverter Silk stent for the treatment of intracranial aneurysms: 1-year follow-up in a multicenter study.** *AJNR Am J Neuroradiol* 2012;33:1150–55
 10. Pierot L, Liebig T, Sychra V, et al. **Intrasaccular flow-disruption treatment of intracranial aneurysms: preliminary results of a multicenter clinical study.** *AJNR Am J Neuroradiol* 2012;33:1232–38
 11. Lubicz B, Mine B, Collignon L, et al. **WEB device for endovascular treatment of wide-neck bifurcation aneurysms.** *AJNR Am J Neuroradiol* 2013;34:1209–14
 12. Pierot L, Klisch J, Cognard C, et al. **Endovascular WEB flow disruption in middle cerebral artery aneurysms: preliminary feasibility, clinical, and anatomical results in a multicenter study.** *Neurosurgery* 2013;73:27–34; discussion 34–35
 13. Lubicz B, Klisch J, Gauvrit JY, et al. **WEB-DL endovascular treatment of wide-neck bifurcation aneurysms: short- and midterm results in a European study.** *AJNR Am J Neuroradiol* 2014;35:432–38
 14. Papagiannaki C, Spelle L, Januel AC, et al. **WEB intrasaccular flow disruptor—prospective, multicenter experience in 83 patients with 85 aneurysms.** *AJNR Am J Neuroradiol* 2014;35:2106–11
 15. Mine B, Pierot L, Lubicz B. **Intrasaccular flow-diversion for treatment of intracranial aneurysms: the Woven EndoBridge.** *Expert Rev Med Devices* 2014;11:315–25
 16. Caroff J, Mihalea C, Dargento F, et al. **Woven Endobridge (WEB) Device for endovascular treatment of ruptured intracranial wide-neck aneurysms: a single-center experience.** *Neuroradiology* 2014;56:755–61
 17. Spelle L, Liebig T. **Letter to the editor.** *Neuroradiol J* 2014;27:369

Challenges of the WEB Device for Intracranial Aneurysms: How to Widen the Spectrum and Compare Favorably

The authors undertook a prospective, multicenter study investigating the feasibility and safety of a new intra-aneurysmal flow disruptor, the WEB device (Sequent Medical, Aliso Viejo, California) in a cohort of 63 aneurysms. Two different models (WB DL and SL/SLS) were used, showing low overall morbidity and no mortality, with potential superiority of the newer SL/SLS model.

The authors must be commended for a thorough investigation of this important device, in which sound and comprehensive data acquisition during the initial safety and feasibility phase can facilitate detailed and longer follow-up studies, which are much needed for future efficacy interpretation.

The WEB device was primarily developed for treatment of wide-neck aneurysms, which may not be amenable to stand-alone coiling or even stent placement plus coiling. The authors convincingly demonstrated the feasibility of this new technique in a large subgroup of both ruptured and unruptured aneurysms, potentially widening the indication for endovascular treatment. To better understand the applicability of this new approach, documentation of the degree of immediate occlusion (even with adjunctive treatments) is essential; unfortunately, these results were not included in the current study. Although a control angiogram was obtained after device placement to determine flow stagnation (or filling adjacent to the deployed device), only the technical success rate (deployment of the WEB device in the target aneurysm) was provided. While analysis of technical feasibility is a prerequisite for any new technique to be investigated, analysis of success/efficacy will be the invariable next step to better determine the value of intra-aneurysmal flow disruption. The authors will continue data collection up to 24 months after treatment, and we will be eagerly awaiting any short-term follow-up results on aneurysm occlusion to compare with their recent retrospective analysis with an aneurysm occlusion rate of 56.9%.¹ We are hopeful that data acquisition will be continued even beyond this point because newer data imply increasing relevance of particularly long-term durability up to 10 years.

A major clinical drawback for more complex endovascular treatment with stent or flow-diverter placement—apart from a

potential increase in the operative complication rate—is the frequent necessity for (prolonged and/or double) antiplatelet treatment. Counteracting the thrombogenic effect of additional intraluminal devices can significantly increase the risk profile of any subsequent open surgical procedure, if not prohibiting it all together, a clinical dilemma not infrequently encountered, particularly in patients with ruptured aneurysms requiring temporary or permanent CSF diversion. If the WEB device can indeed facilitate the treatment of more wide-neck aneurysms with fewer parent artery constructs, it will be crucial to see additional data on the actual need for antiplatelet treatment with the WEB device.

In this study, the incidence of thromboembolic events was found to be in the range of 9%–23%, depending on the type of device used and diagnosed by MR imaging and/or DSA. Routine MR imaging within 24 hours after the procedure in all patients may clarify the exact rate and type of this particular complication, also in the context of a particular antiplatelet regimen. If a much-needed decrease in these events can be achieved only with an intensification of antiplatelet treatment, the advantage of this new device may, in part, be limited to the ascribed ease of use and application. In this regard, the discrepancy in complication rates between the devices used (WEB DL versus SL/SLS) will also warrant further attention, and the effect of user experience/efficacy and learning curve will have to be separated from a device-related risk profile (SL/SLS with more rapid contrast stasis and a balanced radial force with conformability).

Reduction of periprocedural complications—independent from an individual learning curve—and an increase in efficacy are the basis for offering any new technique to future patients. This holds true in view of a potentially benign natural course with smaller, unruptured aneurysms, in which treatment recommendation must be based on the premise of a particularly low interventional risk profile with convincing long-term durability. Also, new and convincing evidence from large-volume, high-competence centers now suggests clinical equipoise for surgical treatment of anterior circulation aneurysms with

longer follow-up,² supported by other centers and data registries.^{3,4} With this compelling new technique of intra-aneurysmal flow disruption proficiently introduced by the authors, both the safety and long-term durability will have to compare favorably with what, for many, is currently considered the gold standard of treatment for wide-neck (MCA) aneurysms: surgical clipping.

REFERENCES

1. Papagiannaki C, Spelle L, Januel AC, et al. **WEB intrasaccular flow disruptor—prospective, multicenter experience in 83 patients with 85 aneurysms.** *AJNR Am J Neuroradiol* 2014;35:2106–11
2. Spetzler RF, McDougall C, Zabramski J, et al. **The Barrow Ruptured Aneurysm Trial: 6-year results.** In: *Proceedings of the 82nd Annual*

Scientific Meeting of the American Association of Neurological Surgeons, San Francisco, California. April 5–9, 2014

3. Bakker NA, Metzemaekers JD, Groen RJ, et al. **International Subarachnoid Aneurysm Trial 2009: endovascular coiling of ruptured intracranial aneurysms has no significant advantage over neurosurgical clipping.** *Neurosurgery* 2010;66:961–62
4. Gonda DD, Khalessi AA, McCutcheon BA, et al. **Long-term follow-up of unruptured intracranial aneurysms repaired in California.** *J Neurosurg* 2014;120:1349–57

G.A. Schubert

Department of Neurosurgery
Cerebrovascular Section
RWTH Aachen University
Aachen, Germany

<http://dx.doi.org/10.3174/ajnr.A4206>

Uncertainty and Agreement Regarding the Role of Flow Diversion in the Management of Difficult Aneurysms

T.E. Darsaut, J.-C. Gentric, C.M. McDougall, G. Gevry, D. Roy, A. Weill, and J. Raymond



ABSTRACT

BACKGROUND AND PURPOSE: The role of flow diversion in the management of aneurysms remains unknown. We sought to evaluate the community agreement regarding indications for flow diversion.

MATERIALS AND METHODS: A portfolio of 35 difficult aneurysm cases was sent to 40 clinicians with varying backgrounds and experience. Responders were asked whether they considered flow diversion a treatment option, whether other options were possible, whether recruitment in a randomized trial would be considered, and to select their final choice. Agreement was studied by using κ statistics.

RESULTS: Decisions for flow diversion were more frequent ($n = 300$, 39%) than decisions to coil ($n = 163$, 21.2%), to observe ($n = 121$, 15.7%), to occlude the parent vessel ($n = 102$, 13.2%), or to clip ($n = 66$, 8.6%). Sidewall aneurysm morphology was associated with flow diversion as the final choice ($P = .001$). Interjudge agreement was fair at best ($\kappa < 0.3$) for all cases and all judges, despite high certainty levels (range, 7.2–8.9 \pm 2.0 on a 0–10 scale). Agreement was no better within specialties or with more experience. All patients were judged to have other treatment options. Judges were willing to offer trial participation in 417 of 741 (56.3%) scenarios, more frequently when the aneurysm was sidewall ($P = .001$) or in the anterior circulation ($P = .028$).

CONCLUSIONS: Individuals did not agree regarding the indications for flow diversion. There is sufficient uncertainty to justify trials designed to protect patients from the potential risks of premature adoption of an innovation.

ABBREVIATIONS: BST = best standard treatment; CL = confidence level; FD = flow diversion; FIAT = Flow diversion In Aneurysm Treatment; RCT = randomized controlled trial

Flow diversion (FD) of intracranial aneurysms is an innovative therapeutic approach.^{1–3} The introduction of surgical innovations involves a process of trial and error when entering unknown territory.⁴ The early adoption of innovations can result in spectacular advances or unexpected complications: FD has been shown to be capable of arterial reconstruction in patients with giant aneurysms who previously might have been treated only with parent vessel occlusion, but FD has also been associated with the rupture of unruptured aneurysms.^{5,6} Using flow diversion

also means working with new devices, which may also introduce unexpected adverse events. For example, embolism of material used to coat endovascular delivery tools has been implicated in the occurrence of fatal parenchymal hemorrhages, occurring at a distance from the aneurysm.⁷

Although there have been enthusiastic proponents for early adoption of FD,^{8–11} others have urged restraint,^{12,13} at least until reliable information becomes available. To minimize the potential harm associated with innovations, progressive steps have recently been proposed, including the careful selection of well-informed participants, when interventions are still considered “experimental.”¹⁴ Important questions that immediately arise are the following: 1) In what context are these experimental interventions to be offered, care or research? and 2) On what basis will patients be selected?

The approach regulatory agencies used to approve the first flow diverters was a registry of consecutive but carefully selected patients.¹ Alternatively, beginning with a randomized trial would have been a prudent option.¹² Long ago, Chalmers¹⁵ suggested that we should “randomize the first patient” to give each patient a chance to receive the best therapy until the best therapy is identi-

Received October 16, 2014; accepted after revision November 6.

From the Division of Neurosurgery (T.E.D., C.M.M.), Department of Surgery, University of Alberta Hospital, Mackenzie Health Sciences Centre, Edmonton, Alberta, Canada; Department of Radiology (J.-C.G., D.R., A.W., J.R.), Centre Hospitalier de l'Université de Montréal, Notre-Dame Hospital, Montreal, Quebec, Canada; and Laboratory of Interventional Neuroradiology (G.G., J.R.), Centre Hospitalier de l'Université de Montréal, Notre-Dame Hospital Research Centre, Montreal, Quebec, Canada.

Please address correspondence to Jean Raymond, MD, CHUM–Notre-Dame Hospital, Interventional Neuroradiology, 1560 Sherbrooke East, Pavillon Simard, Room Z12909, Montreal, Quebec, Canada H2L 4M1; e-mail: jean.raymond@umontreal.ca

Indicates article with supplemental on-line appendix.

<http://dx.doi.org/10.3174/ajnr.A4201>



Case 3
53 M
43 mm unruptured cavernous ICA aneurysm
Ophthalmoplegia
Passed Test Balloon Occlusion

1. Is Flow diversion (\pm coils) an option for this patient ?
 Yes No
2. Any other option that you would conceivably offer this patient ? Choose one :
 No, only FD \pm coils
 Coiling \pm stenting
 Parent vessel occlusion \pm bypass
 Surgical clipping
 Observation
3. Would you be willing to recruit *this* patient in an RCT that would give a 50% chance of FD and a 50% chance of Best Standard Treatment Yes No
4. Final best treatment choice:
 Flow diversion
 Coiling \pm stenting
 Parent vessel occlusion \pm bypass
 Surgical clipping
 Observation
5. Confidence level in your selection of final treatment choice:

<input type="checkbox"/>									
0%	20%	40%	60%	80%	100%				

FIG 1. Example. One of the 35 cases, corresponding vignette, and survey questions that were presented to judges is illustrated.

fied. In these situations, we have proposed care trials.¹⁶ The Flow diversion In Aneurysm Treatment (FIAT) study was conceived and designed to guide the ethical introduction of FD into daily clinical management of patients with difficult aneurysms.¹⁷ FIAT is meant to be offered to any patient for whom the use of FD is contemplated.

Should patients receive FD in the context of a registry or of a trial? It still remains unclear to whom FD should be offered. By definition, no one really knows because a proper comparative evaluation of FD efficacy and safety has yet to be performed for any group of patients.

To help with this dilemma, we sought to explore the opinions of clinicians and study agreement within the neurointerventional community regarding the use of FD. Furthermore, a survey of opinions may inform trial design considerations.

MATERIALS AND METHODS

This study, which involved anonymous colleagues questioned on images of anonymous patients, was considered by our institutional review board committee and approval was deemed to not be required.

Patients

A portfolio of 35 clinical cases of difficult aneurysms was prepared, along with a short clinical vignette, such as the following: a 53-year-old man, 43-mm unruptured cavernous ICA aneurysm, ophthalmoplegia, passed test balloon occlusion. Respondents were asked a series of 5 questions: 1) whether they considered FD (\pm coils) to be a treatment option; 2) whether there was another treatment choice they would conceivably offer the patient (respondents could select from the following: i) no, FD \pm coils only, ii) coiling \pm stent placement, iii) parent vessel occlusion \pm bypass, iv) surgical clipping, or v) observation); 3) whether they would consider offering the patient a randomized trial given a 50% chance of treatment with FD or a 50% chance of “best stan-

ard treatment” (BST), 4) their best final choice (same options as question 2), and 5) their confidence level regarding their final choice on a scale of 0–10 (Fig 1).

All cases were selected either from the FIAT trial ($n = 14$), comparing FD with BST, or were patients treated with FD outside the randomized controlled trial (RCT) ($n = 21$), but raters were not informed of the source of the cases. All cases had thus been judged by at least 1 clinician to be a candidate for FD. In reality, 28 of the 35 patients had been treated with FD. The 7 other patients had also been judged appropriate for FD but had been allocated to BST. Our aims were the following: 1) to ensure that we had included cases appropriate for flow diversion, 2) to assess whether other treatment options would be chosen as preferable or possible, and 3) to assess the community willingness to participate in a trial such as FIAT.

Raters

The e-mailed or paper portfolio (On-line Appendix) was addressed to 40 clinicians, selected because they had presented or published on flow diverters or were on a list of potential FIAT participants, and all received responses were included. We did not require participants to have performed a minimum number of FDs. In the end, the survey was independently evaluated by 22 practicing interventionists with the following demographic information: 16 radiologists and 6 cross-trained neurosurgeons, able to deliver surgical and endovascular care. Respondents were from academic centers in North America (Canada and the United States) ($n = 16$) or Europe ($n = 6$). Clinicians had been in practice for 0–5 years ($n = 6$), 5–10 years ($n = 3$), or >10 years ($n = 13$). Nine judges (41%) had previous experience in >15 patients with flow diverters. Repeatedly responding to the same questionnaire can be a painful experience. Four senior raters (with >20 years of experience), selected on the basis of previous mutual collaborations, were commissioned to respond to the questionnaire twice, >3 months apart, to generate the intraobserver evaluations.

Statistics

κ statistics were calculated by using SPSS software (Version 20; IBM, Armonk, New York). The κ values reflect agreement beyond chance, with a score of zero no better than flipping a coin, 1 representing perfect agreement, and -1 representing perfect disagreement. κ values were interpreted according to Landis and Koch¹⁸: ≤ 0.0 , poor; 0–0.2, slight; 0.21–0.4, fair; 0.41–0.6, moderate; 0.61–0.8, substantial; and 0.81–1.0, almost perfect agreement. Confidence in decision-making along a scale of 0–10 was analyzed with ANOVAs. Multiple comparisons among confidence levels according to treatment choices were adjusted according to Bonferroni. A Mann-Whitney or Kruskal-Wallis test was done (according to the number of categories of the independent

Table 1: Patient and aneurysm characteristics

	All Cases	Patients in RCTs	Others
Patients (No.)	35	14	21
Male/female	14/21	4/10	10/11
Mean age (yr)	52.4 ± 14.5	49.6 ± 18.0	54.3 ± 11.3
Aneurysms			
Mean size (range) (mm)	23.5 ± 12.9 (3–55)	22.6 ± 9.5 (5–40)	24.1 ± 14.8 (3–55)
Anterior circulation	26 (74%)	12 (86%)	14 (67%)
Extradural carotid	10 (29%)	5 (36%)	5 (24%)
Intradural carotid	15 (43%)	7 (50%)	8 (38%)
Posterior circulation	9 (26%)	2 (14%)	7 (33%)
Intradural vertebral	6 (17%)	1 (7%)	5 (24%)
Basilar	3 (9%)	1 (7%)	2 (10%)
Proximal ^a aneurysms	23 (66%)	9 (64%)	14 (66%)
Proximal ^a aneurysms, passed TBO	11 (48%)	3 (33%)	8 (38%)
Sidewall aneurysm	17 (49%)	5 (36%)	12 (57%)
Recurrent aneurysms	5 (14%)	2 (14%)	3 (14%)
Ruptured (recent SAH)	4 (11%)	1 (7%)	3 (14%)
Symptomatic aneurysms	20 (57%)	6 (43%)	14 (67%)

Note:—TBO indicates test balloon occlusion.

^a Proximal indicates cavernous, ophthalmic, and intradural vertebral locations.

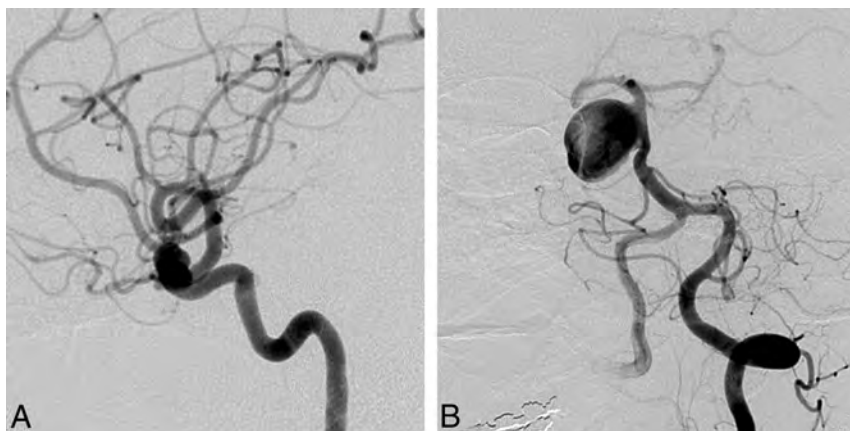


FIG 2. Responses to question 4 (best final management choice). FD was commonly selected as the best final treatment choice for anterior circulation (A, 9-mm asymptomatic paraophthalmic aneurysm; 10 votes for FD) or sidewall aneurysms (B, 38-mm asymptomatic sidewall basilar trunk aneurysm; 12 votes for FD).

variable) to compare the distribution of FD choices among different groups of aneurysms or patients (extra-/intradural, anterior/posterior circulation; neck size; randomized in FIAT or not; and sidewall versus bifurcation versus fusiform aneurysms) or different groups of raters (background; FD experience or years of experience). Exploratory comparisons between proportions of treatment choices for patients in FIAT or not in FIAT were performed by using χ^2 tests and among mean confidence levels by using paired Student *t* tests. χ^2 tests were also used to compare willingness to recruit patients in a RCT, adjusted for multiplicity according to Bonferroni.

RESULTS

Patient and aneurysm characteristics are presented in Table 1.

Final Management Decisions with Confidence Levels (Questions 4 and 5)

Of 752 responses (97.7% of 770 possible responses; 2.3% missing responses) to question 4, which asked clinicians to make a final choice, decisions to use FD were more frequent ($n = 300$, 39%) than decisions to coil ($n = 163$, 21.2%), to observe ($n = 121$,

15.7%), to occlude the parent vessel ($n = 102$, 13.2%), or to surgically clip ($n = 66$, 8.6%).

Clinicians were generally confident that they had selected the best option (mean confidence levels [CLs] between 7.2 and 8.9). CLs were not significantly different for radiologists or surgeons ($P = .09$), for more or less experienced clinicians ($P = .22$), or for those having more or less FD experience ($P = .11$). CLs varied according to treatment choices ($P = .012$); clinicians showed more confidence when they chose observation (8.9) than FD (7.7, $P = .043$). FD was considered the best option by at least 1 clinician (minimum = 1, maximum = 18) for each case, but the same treatment option was not chosen unanimously for any single case. The most common final choice was different overall for patients in FIAT compared with those patients not randomized to FIAT: Clinicians favored FD in 36.6% of patients randomized to FIAT, whereas 42.2% of those not randomized to FIAT were selected for FD. The main difference was that responders chose observation more frequently for patients randomized to FIAT (23.5%) than for the patients treated outside the trial (11.0%) ($P = .0001$). The only characteristic associated with a FD choice was sidewall aneurysm morphology ($P = .001$). For 11 (31%) of 35 cases, FD was selected most frequently as the best final treatment choice. Ten of 11 (91%) of these

cases were proximal carotid aneurysms (perhaps corresponding to American on-label use); the other was a 38-mm basilar trunk sidewall aneurysm (Fig 2).

Interrater agreement regarding the best treatment choice was “poor” to “slight” for all clinicians (in the range of $\kappa = 0.0$ –0.2) and no better among neurosurgeons or among radiologists or when responders were experienced or had performed >15 FD treatments (Table 2). Agreement was no better when answers were dichotomized (FD versus any other option). Intrarater agreement at least 3 months apart was better ($\kappa = 0.387$ –0.634) (Table 2).

Is FD an Option for This Case? (Question 1)

FD was always an option (mean, 16 ± 4 positive responses to question 1; minimum = 7, maximum = 21 of 22 responders). Anterior location ($P = .025$) and sidewall morphology ($P = .001$) were aneurysm characteristics associated with considering FD as a treatment option.

The 2 cases with the highest number of dissenting raters, who did not consider FD to be an option, were the following: an inci-

Table 2: Inter- and intraobserver agreement regarding question 4 (best final management choice)

	Categories ^a	All Cases (n = 35)	Patients in RCTs (n = 14)	Others (n = 21)
Interobserver agreement				
All raters (n = 22)	5	0.219 ± 0.017	0.225 ± 0.020	0.190 ± 0.025
	2	0.111 ± 0.018	0.151 ± 0.036	0.072 ± 0.020
Surgeons (n = 6)	5	0.252 ± 0.025	0.202 ± 0.043	0.271 ± 0.033
	2	0.114 ± 0.084	0.063 ± 0.131	0.148 ± 0.109
>10 years' experience (n = 13)	5	0.210 ± 0.019	0.203 ± 0.030	0.199 ± 0.025
	2	0.062 ± 0.030	0.120 ± 0.050	0.024 ± 0.038
>15 FD experiences (n = 9)	5	0.182 ± 0.029	0.258 ± 0.042	0.116 ± 0.040
	2	0.093 ± 0.032	0.201 ± 0.055	0.018 ± 0.040
Intraobserver agreement				
Rater 1	5	0.465 ± 0.115	0.432 ± 0.162	0.465 ± 0.163
	2	0.634 ± 0.109	0.340 ± 0.178	0.463 ± 0.195
Rater 2	5	0.387 ± 0.112	0.421 ± 0.175	0.333 ± 0.143
	2	0.243 ± 0.175	0.176 ± 0.272	0.271 ± 0.208
Rater 3	5	0.501 ± 0.104	0.246 ± 0.141	0.629 ± 0.124
	2	0.382 ± 0.114	0.263 ± 0.154	0.442 ± 0.160
Rater 4	5	0.634 ± 0.109	0.509 ± 0.178	0.707 ± 0.129
	2	0.651 ± 0.129	0.571 ± 0.198	0.712 ± 0.153

^aThe number 5 indicates that answers were treated as 5 categories: FD, coiling, observation, occlusion of the parent vessel, and surgical clipping. The number 2 indicates that answers were treated as 2 categories: flow diversion versus all other treatment groups.

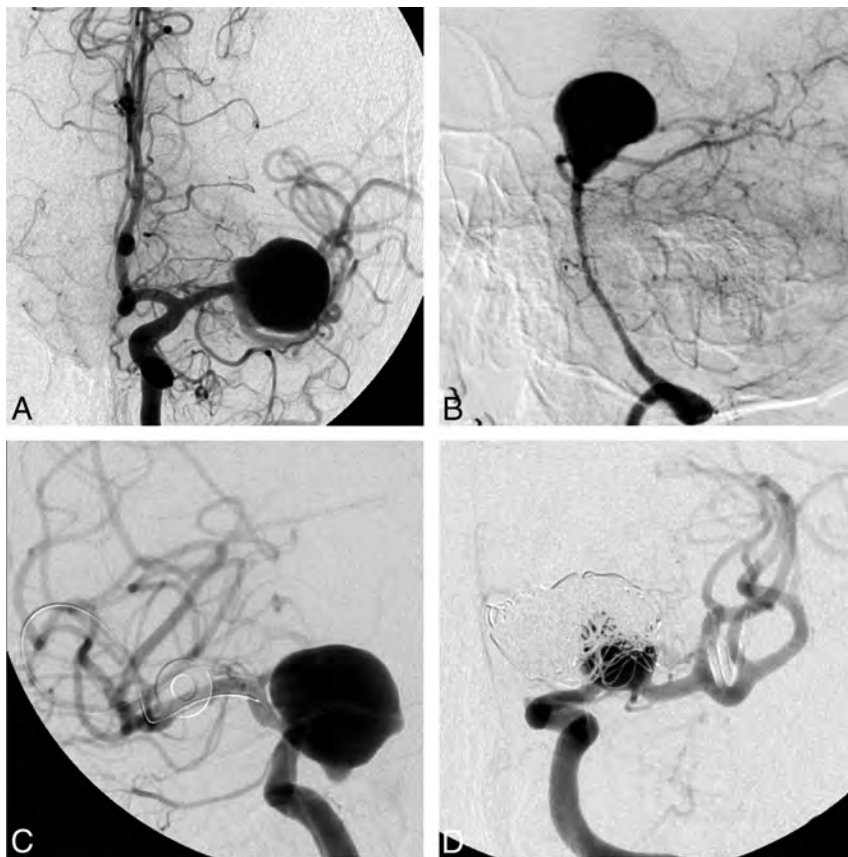


FIG 3. Responses to question 1 (Is flow diversion an option?). FD was considered an option by at least 7 judges in all cases. The cases in which flow diversion was most frequently judged not to be a viable option were a 20-mm MCA bifurcation aneurysm (A, 15/22 “no” votes) and a 38-mm basilar tip aneurysm (B, 14/22 “no” votes). The cases in which flow diversion was least frequently thought not to be an option, with only 1/22 “no” votes each, were a 22-mm ophthalmic segment aneurysm (C) and a recurrent previously coiled carotid bifurcation aneurysm (D).

dental 20-mm MCA aneurysm in a 56-year-old woman (case 20, n = 15 negative answers) and a 67-year-old woman with headaches and a 38-mm unruptured basilar tip aneurysm (case 10, n =

low (Table 4). Clinicians were more willing to recruit a patient in an RCT when the lesion was in the anterior circulation (P = .028) or when the aneurysm featured a sidewall morphology (P = .001).

14). On the other hand, there were 6 cases for which a single “No, FD is not an option” response (of 22 raters) was obtained (Fig 3).

The judgment of whether FD was a treatment option did not feature significant agreement for any group of raters or for any group of patients (Table 3).

For This Patient’s Aneurysm, Are There Treatment Alternatives? (Question 2)

Treatment options other than FD were considered viable by at least some clinicians for all 35 cases. The greatest number of clinicians who judged that FD was the only possible option was 5 of 22 judges for a blister aneurysm in a 45-year-old man. All other cases had ≤4 votes for “FD is the only option,” with an overall mean of 1.85 judges considering that FD was the only appropriate treatment for an aneurysm (Fig 4).

Are Clinicians Willing to Recruit This Particular Patient in a Trial? (Question 3)

Respondents were willing to offer trial participation in 417 of 741 (56.3%) responses to question 3. The percentage of positive responses was 60.7% from surgeons, 54.6% from radiologists (P = .146), 52.3% from senior clinicians, 61.2% from junior clinicians (P = .022), 52.9% from clinicians with the largest FD experience compared with 65.1% from clinicians with less experience (P = .016), 52.9% for patients in FIAT, and 58.3% for those not in FIAT (P = .022). Given the multiplicity of testing, none of these P values were significant. In 74% of patients with proposed participation in question 3, FD was selected as the best option in question 4. Clinicians not willing to offer participation were more confident in their treatment choice (8.7 ± 1.3) than clinicians willing to offer participation (7.5 ± 1.5, P = .005).

In 4 cases, more than half of the raters showed willingness to include that patient in a RCT, all of which featured aneurysms in ophthalmic or paraophthalmic locations (Fig 5). Interrater agreement regarding recruitment in an RCT was poor; intrarater agreement was also

DISCUSSION

The main finding of this survey was that if FD is frequently chosen as the best option for patients with difficult aneurysms, there was poor agreement regarding indications. Choices of FD as the best therapy were more frequent for sidewall and anterior circulation aneurysms, but the same patients were uniformly considered to have other treatment options. Substantial variability existed in deciding how to best manage these patients. Discrepant recommendations were made at the individual level, and clinicians' decisions did not follow according to their number of years in practice, specialty backgrounds, or experience with FD. Wide discrepancies were present within all subgroups of decision-makers and for all sorts of patients. If the best management decision for an individual patient is the consensus of a panel of clinicians, it appears reasonable to conclude that for most patients, one decision cannot rationally be justified over another. Nonetheless, individuals had high confidence levels regarding their treatment choices. Clinicians were willing to recruit patients in a randomized trial in half of the cases, but agreement regarding who should be enrolled was poor.

When reliable evidence is absent, the selection of patients for an innovative therapy can be based on various considerations. The first and perhaps most intuitive approach is to restrict the use of the unproven device to patients for whom conventional options are (relatively) contraindicated because risks are considered prohibitive or because efficacy of other management choices is expected to be low.^{13,19} One drawback of this strategy is that it is unlikely to portray the device in a good light because difficult cases are also more likely to have poor outcomes, compared with “stan-

dard cases.” Furthermore, if access to the device under strict conditions is truly enforced, a proper comparative evaluation cannot be done when users claim there are no viable alternative treatment options with which to compare results.²⁰ Here, we see that restricting the use of FD to patients with aneurysms because they have “no other choice” really applies to very few patients; the answers to question 2 suggests that FD is rarely the sole possible treatment option.

Another approach to introducing an innovation is to restrict early use of the novelty to cases with the best chance of success, as judged from a priori reasoning, clinical intuition, or animal studies. In a sense, this is what was done for FD.¹ The concept of the device makes it ideal for sidewall aneurysms. The success of FD with sidewall aneurysms yet failing in bifurcation or giant fusiform aneurysms has been confirmed in animal models.²¹⁻²³ Early series and meta-analyses have suggested that FD is associated with good outcomes in proximal carotid aneurysms; results were not as good in fusiform or bifurcation aneurysms of the posterior circulation.^{1,12,24,25} Perhaps most unsurprising, our survey confirms that anterior circulation and sidewall dispositions are aneurysm characteristics associated with frequent FD choices. However, 2 major difficulties exist with using this approach to decide who should receive a new treatment or device. First, comparisons among different patients treated with the same method cannot provide the evidence necessary to support treatment decision-making for individual patients: The fact that FD works better in proximal carotid compared with basilar aneurysms cannot be used to suggest that FD should not be performed for basilar aneurysms or should be used for anterior circulation aneurysms.

To make rational treatment choices based on evidence, we need a valid comparison among similar patients treated by different treatments, showing better results with FD compared with an alternative. Second, if a registry of selected patients eligible for standard treatment options is suggested, it remains unclear why FD should be chosen over established alternatives. Although in some cases, authors claimed patients were “untreatable” by standard means, and even though in most early series patients and aneurysms were carefully selected, few patients with aneurysms truly have no other manage-

ment option, as shown by this survey. An approach that restricts FD use to patients considered to have the best chance of success may not be in the best interest of current patients because with narrow selection, some patients with truly difficult aneurysms in need of innovative treatments are denied a chance to receive the novelty. Those with more favorable characteristics for FD, enthusiastically selected to be offered the new treatment, are exposed to unknown risks but under pressure to accept. These patients, treatable by other means, may have had as good an outcome with standard therapy. In our view, these patients should have offered participation in a trial comparing the innovation with standard treatment until the best treatment is identified.

Table 3: Interrater agreement regarding question 1 (Is FD an option in this case?)

	All Cases (n = 35)	Patients in RCTs (n = 14)	Others (n = 21)
All raters (n = 22)	0.136 ± 0.052	0.162 ± 0.070	0.110 ± 0.075
Surgeons (n = 6)	0.042 ± 0.121	0.013 ± 0.147	0.036 ± 0.191
>10 years' experience (n = 13)	0.070 ± 0.070	0.078 ± 0.101	0.062 ± 0.097
>15 FD experiences (n = 9)	0.131 ± 0.084	0.135 ± 0.137	0.128 ± 0.106

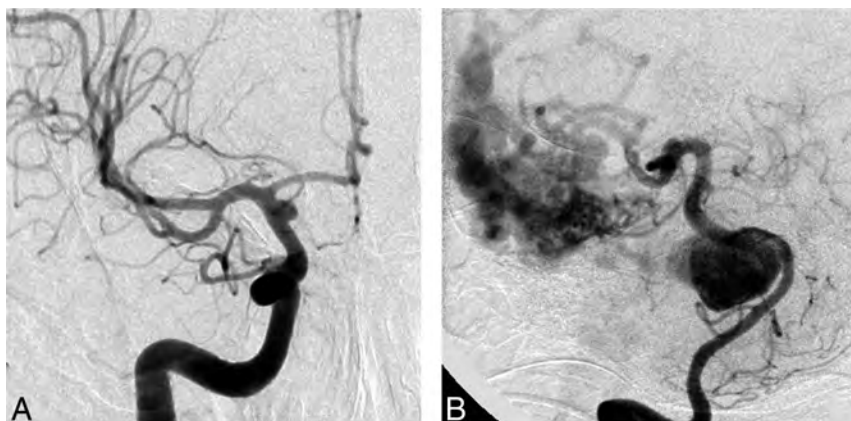


FIG 4. Responses to question 2 (Any other treatment option?). In all cases, judges were able to find a viable alternative to flow diversion. The cases with the largest number of votes for “No, flow diversion only” were a ruptured supraclinoid carotid blister aneurysm (A, 5 votes) and a giant basilar aneurysm with an associated AVM (B, 4 votes). All other aneurysm-patient combinations were thought to have >1 treatment option.

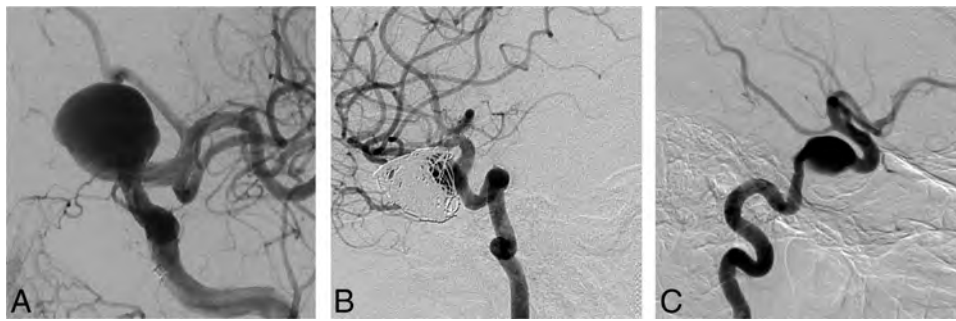


FIG 5. Responses to question 2 (Would you recruit this patient in a RCT?). Aneurysm-patient combinations, which more than half of judges were willing to include in a randomized trial, were all ophthalmic or paraophthalmic: for example, a 22-mm ophthalmic segment in a 57-year-old patient (A, 18/22 votes for trial participation) and a recurrent giant ophthalmic artery aneurysm in a 37-year-old patient (B, 20/22 votes). The case with the fewest number of judges willing to randomize was a 16-mm asymptomatic cavernous aneurysm in a 79-year-old patient (C, 4/22 votes).

Table 4: Inter- and intrarater agreement regarding question 3 (Would you recruit this patient in a RCT?)

	All Cases (n = 35)	Patients in RCTs (n = 14)	Others (n = 21)
Interrater agreement			
All raters (n = 22)	0.162 ± 0.023	0.170 ± 0.031	0.154 ± 0.033
Surgeons (n = 6)	0.190 ± 0.062	0.161 ± 0.077	0.180 ± 0.101
>10 years' experience (n = 13)	0.121 ± 0.023	0.133 ± 0.041	0.109 ± 0.030
>15 FD experiences (n = 9)	0.168 ± 0.032	0.179 ± 0.058	0.142 ± 0.046
Intrarater agreement			
Rater 1	0.229 ± 0.160	0.263 ± 0.154	0.250 ± 0.238
Rater 2	0.687 ± 0.145	0.625 ± 0.240	0.729 ± 0.180
Rater 3	0.249 ± 0.205	0.440 ± 0.305	0.000 ± 0.000
Rater 4	0.370 ± 0.217	0.264 ± 0.313	0.462 ± 0.305

A survey of prevalent opinions on treatment choices can be instructive in the context of a conventional trial: It may help in the design of the trial, in determining selection criteria, or in fixing the comparative interventions. It may also instruct the notion of community equipoise²⁶ and indicate whether a trial is likely to be successfully completed. For example, answers to question 1 (Is FD an option for this patient?) could have been used to determine exclusion criteria had we found patients for whom “no” was a unanimous answer. In these types of trials, the priority is to come up with an answer to a precise research question.

In the context of surgical innovations, we believe these notions need to be revised because they presuppose knowledge that has yet to be discovered. Looking for agreement before initiating the trial is putting the cart before the horse. In the absence of reliable knowledge, on what basis would agreement be constructed? Waiting for agreement regarding indications is at the root of the “it is always too early until it is too late” phenomenon, leading to decades of medical history in which interventions are practiced without evidence that they are beneficial.²⁷

Care trials such as FIAT differ from conventional trials.¹⁶ In the presence of little agreement and scant knowledge, they provide a prudent, orderly way to introduce innovations, to assist in the care of patients in the presence of uncertainty. They prioritize the protection of patients being offered promising but unvalidated therapies because the unknown implies potential risks. The trial is constructed on a principle of prudence: Novel therapies should be offered only within the trial until they are either shown to be beneficial and adopted to replace standard

options or are shown to be harmful and abandoned. With FIAT, a patient for whom the treating physician considers using FD is a potential study participant. The treating physician is asked to select another option (BST), and the patient is allocated to either treatment with FD or BST. Thus, the patient has a 50% chance of receiving the promising FD, hypothesized but not yet proved better, but also a balanced 50% chance of receiving BST and avoiding the potential morbidity that might arise from using barely tested treatments that may entail risks.^{15,28} FIAT also includes a registry for patients with no other therapeutic option, but as this survey showed, this opt-out should not need to be used frequently.

Our survey may also inform whether the condition of “clinical equipoise” exists regarding the use of FD.²⁶ While many clinicians may believe that equipoise requires an absence of preference or think that there is no reason to lean toward one treatment or another in this particular patient, this understanding is both conceptually odd and ethically irrelevant.²⁶ According to Freedman,²⁶ who introduced and popularized the concept, clinical equipoise occurs when “there is no consensus within the clinical expert community about the comparative merits of the alternatives to be tested.” If this survey shows that such a condition is met for FD, we believe that for a clinician to use FD or any surgical innovation, the correct approach is to replace the notion of clinical equipoise with the notion that in the absence of a good exemptive reason, a clinician should only use an unvalidated intervention within the context of a declared care trial.¹⁶

The widespread discrepancies in management decisions shown in this survey should provide the evidence for collective community uncertainty needed to proceed with a trial. The choices patients and clinicians face are not care versus research. The use of FD in the care of patients is far from being established therapy. Controversy also remains regarding coiling or stent-assisted coiling versus open surgery for the treatment of difficult aneurysms. Randomized clinical trials are required if physicians want to properly counsel their patients regarding the relative risks and benefits of potential management options in the future. In the meantime, a more immediate goal is to enable experimentation with a promising innovation in the care of patients with difficult aneurysms while attempting to minimize the risks to patients who are exposed to the innovation.

Limitations

There were several limitations of this study. The questionnaire was submitted to 40 experts. Only 22 answers (55%) were received. The responders were not a random sample of a population of experts, and there is no reason to believe that they are representative of such a population, if it could be defined. We can only conjecture that results reflect the opinions of a self-selected group of clinicians who took the time and energy to respond. Some participants had little experience with FD, and one may question the significance of their opinions. However, agreement among more experienced participants was equally poor. The portfolio was artificially constructed. Absolute numbers of choices are thus not meaningful, but we were careful to present cases that are currently at least considered for FD. Agreement regarding particular cases (reliability) does not mean accuracy (in other words everyone could be wrong). Finally, answering a questionnaire and caring for real patients represent different contexts for decision-making; we can only speculate about how seriously the responders imagined they were dealing with important clinical decisions. Clinical decision-making in practice is rarely performed by a single individual in isolation and typically takes into consideration opinions from collaborators and patient preferences.

CONCLUSIONS

Wide variability and poor agreement exist regarding the indications for FD. This uncertainty should provide ample room for participation in trials designed to safely introduce promising technology in the care of patients with difficult aneurysms.

Disclosures: Daniel Roy—UNRELATED: Grants/Grants Pending: Stryker,* MicroVention,* Covidien,* Codman,* Comments: fellowship support. Alain Weill—UNRELATED: Grants/Grants Pending: MicroVention,* Stryker,* Covidien,* Codman,* Comments: We receive support from these entities in our academic fund for fellowship support; Payment for Lectures (including service on Speakers Bureaus): MicroVention,* Comments: We received money from MicroVention in our academic fund for a lecture I gave at the Asian Australasian Federation of Interventional and Therapeutic Neuroradiology 2014 conference ("Bailout in Aneurysm Treatment"). Jean Raymond—UNRELATED: Grant: Canadian Institute of Health Research,* Johnson & Johnson,* Comments: Canadian Institute of Health Research: funding for the Collaborative Unruptured Endovascular versus Surgery trial; Johnson & Johnson: unrestricted research funding for the Does Embolization with Larger coils lead to better Treatment of Aneurysms trial (investigator-initiated study). *Money paid to the institution.

REFERENCES

1. Becske T, Kallmes DF, Saatci I, et al. **Pipeline for uncoilable or failed aneurysms: results from a multicenter clinical trial.** *Radiology* 2013;267:858–68
2. Lylyk P, Miranda C, Ceratto R, et al. **Curative endovascular reconstruction of cerebral aneurysms with the Pipeline embolization device: the Buenos Aires experience.** *Neurosurgery* 2009;64:632–42; discussion 642–43; quiz N6
3. Nelson PK, Lylyk P, Szikora I, et al. **The Pipeline embolization device for the intracranial treatment of aneurysms trial.** *AJNR Am J Neuroradiol* 2011;32:34–40
4. Barkun JS, Aronson JK, Feldman LS, et al. **Evaluation and stages of surgical innovations.** *Lancet* 2009;374:1089–96
5. Darsaut TE, Rayner-Hartley E, Makoyeva A, et al. **Aneurysm rupture after endovascular flow diversion: the possible role of persistent flows through the transition zone associated with device deformation.** *Interv Neuroradiol* 2013;19:180–85
6. Kulcsár Z, Houdart E, Bonafé A, et al. **Intra-aneurysmal thrombosis**

- as a possible cause of delayed aneurysm rupture after flow-diversion treatment. *AJNR Am J Neuroradiol* 2011;32:20–25
7. Hu YC, Deshmukh VR, Albuquerque FC, et al. **Histopathological assessment of fatal ipsilateral intraparenchymal hemorrhages after the treatment of supraclinoid aneurysms with the Pipeline embolization device.** *J Neurosurg* 2014;120:365–74
 8. Chalouhi N, Starke RM, Yang S, et al. **Extending the indications of flow diversion to small, unruptured, saccular aneurysms of the anterior circulation.** *Stroke* 2014;45:54–58
 9. Crobbedu E, Lanzino G, Kallmes DF, et al. **Marked decrease in coil and stent utilization following introduction of flow diversion technology.** *J Neurointerv Surg* 2013;5:351–53
 10. Jabbour P, Chalouhi N. **The era of flow diverters in aneurysm treatment.** *Neurosurgery* 2014;74:E341–42
 11. Fang S, Lanzino G. **Paraclinoid aneurysms: is there a new endovascular standard?** *Neurol Res* 2014;36:314–22
 12. Arrese I, Sarabia R, Pintado R, et al. **Flow-diverter devices for intracranial aneurysms: systematic review and meta-analysis.** *Neurosurgery* 2013;73:193–99; discussion 199–200
 13. van Rooij WJ, Sluzewski M, van der Laak C. **Flow diverters for unruptured internal carotid artery aneurysms: dangerous and not yet an alternative for conventional endovascular techniques.** *AJNR Am J Neuroradiol* 2013;34:3–4
 14. McCulloch P, Altman DG, Campbell WB, et al. **No surgical innovation without evaluation: the IDEAL recommendations.** *Lancet* 2009;374:1105–12
 15. Chalmers TC. **Randomize the first patient.** *N Engl J Med* 1977;296:107
 16. Raymond J, Darsaut TE, Altman DG. **Pragmatic trials used as optimal medical care: principles and methods of care trials.** *J Clin Epidemiol* 2014;67:1150–56
 17. Raymond J, Darsaut TE, Guilbert F, et al. **Flow diversion in aneurysms trial: the design of the FIAT study.** *Interv Neuroradiol* 2011;17:147–53
 18. Landis JR, Koch GG. **The measurement of observer agreement for categorical data.** *Biometrics* 1977;33:159–74
 19. Toma AK, Robertson F, Wong K, et al. **Early single centre experience of flow diverting stents for the treatment of cerebral aneurysms.** *Br J Neurosurg* 2013;27:622–28
 20. Raymond J, Darsaut TE. **Stenting for intracranial aneurysms: how to paint oneself into the proverbial corner.** *AJNR Am J Neuroradiol* 2011;32:1711–13
 21. Sadasivan C, Cesar L, Seong J, et al. **An original flow diversion device for the treatment of intracranial aneurysms: evaluation in the rabbit elastase-induced model.** *Stroke* 2009;40:952–58
 22. Raymond J, Darsaut TE, Makoyeva A, et al. **Endovascular treatment with flow diverters may fail to occlude experimental bifurcation aneurysms.** *Neuroradiology* 2013;55:1355–63
 23. Darsaut TE, Bing F, Salazkin I, et al. **Flow diverters failing to occlude experimental bifurcation or curved sidewall aneurysms: an in vivo study in canines.** *J Neurosurg* 2012;117:37–44
 24. Kulcsár Z, Ernemann U, Wetzel SG, et al. **High-profile flow diverter (Silk) implantation in the basilar artery: efficacy in the treatment of aneurysms and the role of the perforators.** *Stroke* 2010;41:1690–96
 25. Siddiqui AH, Abila AA, Kan P, et al. **Panacea or problem: flow diverters in the treatment of symptomatic large or giant fusiform verte-brobasilar aneurysms.** *J Neurosurg* 2012;116:1258–66
 26. Freedman B. **Equipoise and the ethics of clinical research.** *N Engl J Med* 1987;317:141–45
 27. Buxton MJ. **Problems in the economic appraisal of new health technology: the evaluation of heart transplants in the UK.** In: Drummond MF, ed. *Economic Appraisal of Health Technology in the European Community.* Oxford: Oxford University Press; 1987:103–18
 28. Cloft HJ. **What is all of the hype about?** *AJNR Am J Neuroradiol* 2008;29:1604

Anterior Choroidal Artery Patency and Clinical Follow-Up after Coverage with the Pipeline Embolization Device

E. Raz, M. Shapiro, T. Becske, D.W. Zumofen, O. Tanweer, M.B. Potts, H.A. Riina, and P.K. Nelson

ABSTRACT

BACKGROUND AND PURPOSE: Endoluminal reconstruction with the Pipeline Embolization Device is an effective treatment option for select intracranial aneurysms. However, concerns for the patency of eloquent branch arteries covered by the Pipeline Embolization Device have been raised. We aimed to examine the patency of the anterior choroidal artery and clinical sequelae after ICA aneurysm treatment.

MATERIALS AND METHODS: We prospectively analyzed all patients among our first 157 patients with ICA aneurysms treated by the Pipeline Embolization Device who required placement of at least 1 device across the ostium of the anterior choroidal artery. The primary outcome measure was angiographic patency of the anterior choroidal artery at last follow-up. Age, sex, type of aneurysm, neurologic examination data, number of Pipeline Embolization Devices used, relationship of the anterior choroidal artery to the aneurysm, and completeness of aneurysm occlusion on follow-up angiograms were also analyzed.

RESULTS: Twenty-nine aneurysms requiring placement of at least 1 Pipeline Embolization Device (median = 1, range = 1–3) across the anterior choroidal artery ostium were identified. At angiographic follow-up (mean = 15.1 months; range = 12–39 months), the anterior choroidal artery remained patent, with antegrade flow in 28/29 aneurysms (96.5%), while 24/29 (82.7%) of the target aneurysms were angiographically occluded by 1-year follow-up angiography. Anterior choroidal artery occlusion, with retrograde reconstitution of the vessel, was noted in a single case. A significant correlation between the origin of the anterior choroidal artery from the aneurysm dome and failure of the aneurysms to occlude following treatment was found.

CONCLUSIONS: After placement of 36 Pipeline Embolization Devices across 29 anterior choroidal arteries (median = 1 device, range = 1–3 devices), 1 of 29 anterior choroidal arteries was found occluded on angiographic follow-up. The vessel occlusion did not result in persistent clinical sequelae. Coverage of the anterior choroidal artery origin with the Pipeline Embolization Device, hence, may be considered reasonably safe when deemed necessary for aneurysm treatment.

ABBREVIATIONS: AchoA = anterior choroidal artery; PED = Pipeline Embolization Device

Flow diversion with the Pipeline Embolization Device (PED; Covidien, Irvine, California) has been shown to be an effective treatment option for complex intracranial aneurysms of the internal carotid artery.^{1–4} Fundamentally, the safety and effectiveness of the device in the cerebral vasculature depends on its ability to differentially facilitate aneurysm occlusion without symptomatically compromising branch vessel patency. Branch vessel flow

depends on the arterial-venous pressure gradient and composite impedance of the vascular territory subserved by the branch.⁵ Although placement of single PEDs across the origins of branch vessels is not expected to affect vascular resistance in the jailed (covered) artery,^{6,7} the intrinsic thrombogenicity of the implant has caused concern for the patency of jailed branch arteries.^{5,6,8} Several studies have shown that coverage of the ophthalmic artery is clinically safe,^{9,10} but coverage of the anterior choroidal artery (AchoA) has not yet been systematically evaluated. Several reports have suggested that >50% compromise of the luminal cross-sectional area is required before flow in branch arteries is diminished significantly,^{11,12} reflecting a degree of branch ostial coverage lower than that expected from deployment of a single PED (between 18% and 36% surface metal coverage) as determined from benchtop analysis.¹³ Even when PEDs are overlapped, metal

Received August 7, 2014; accepted after revision October 29.

From the Bernard and Irene Schwartz Interventional Neuroradiology Section (E.R., M.S., T.B., D.W.Z., M.P.B., H.A.R., P.K.N.), Department of Radiology, and Departments of Neurology (M.S., T.B.) and Neurosurgery (D.W.Z., O.T., M.B.P., H.A.R., P.K.N.), New York University School of Medicine, New York, New York.

Please address correspondence to Peter Kim Nelson, MD, Department of Radiology, New York University School of Medicine, 660 First Ave, 2nd Floor New York, NY 10016; e-mail: peter.nelson@nyumc.org; @eytanraz

<http://dx.doi.org/10.3174/ajnr.A4217>

coverage is not reasonably expected to exceed 40% for any 2 devices.¹⁴ We therefore hypothesized that coverage of the AchoA with PED is unlikely to cause occlusion of this eloquent vessel territory.

MATERIALS AND METHODS

This study was an institutional review board–approved retrospective analysis of prospectively acquired data. Inclusion criteria were the following: 1) presence of an intracranial internal carotid artery aneurysm treated by placement of ≥ 1 PED, and 2) coverage of the AchoA with at least 1 PED.

We recorded the following baseline data: age, sex, neurologic examination before and after the procedure, location of the aneurysm (according to Shapiro et al¹⁵), relationship of the AchoA to the aneurysm, and the number of PEDs implanted across the origin of the AchoA. At follow-up, the interval from the index procedure, aneurysm occlusion status, patency of the AchoA, and neurologic examination findings were recorded. Baseline and follow-up neurologic assessments were performed in a nonblinded fashion by 2 board-certified neurologists (T.B., M.S.).

Treatment Protocol

Procedures were performed with the patient under general anesthesia, typically by using a triaxial system in a fashion previously described.² The AchoA was covered by as many PEDs as was thought necessary to achieve a subjectively satisfactory balance between treatment of the aneurysm and AchoA coverage, with the result that in most cases coverage of the AchoA was minimized to a single device. Neurologic status was assessed before treatment, immediately after treatment, at discharge, and at follow-up clinical visits.

All patients received dual antiplatelet coverage. During the intervention, patients additionally underwent anticoagulation by intravenous boluses of heparin sodium, targeting an increase in activated coagulation time of twice baseline. Patients continued with clopidogrel (75 mg daily) and acetylsalicylic acid (325 mg daily) for a minimum of 180 days after treatment. Antiplatelet therapy was not explicitly modified from our standard PED–aneurysm treatment protocol (which uses testing with the VerifyNow P2Y12 assay [Accumetrics, San Diego, California] to establish suitable inhibition at the time of treatment). In those patients in whom the AchoA arose from the aneurysm fundus, posttreatment heparinization at 500–700 IU/h was continued for 4–5 days.

Follow-Up Protocol

As with other patients treated by us with the PED, subjects of this investigation were scheduled for follow-up clinical and angiographic evaluations at 6 months and 1 and 3 years (± 2 months) postembolization. We evaluated the longest angiographic follow-up when > 1 instance of follow-up was available.

Imaging Evaluation

All pre- and posttreatment angiograms were reviewed by 5 neurointerventionalists in consensus (T.B., P.K.N., E.R., M.S., D.W.Z.). We carefully evaluated the following: the aneurysm site; descriptive features of the AchoA, such as hyperplastic variant¹⁶

Table 1: Study population^a

	No. or Mean (SD)
Age (yr)	57.6 (13.6)
Sex (M/F)	7/21
Aneurysm side (R/L)	16/13
Aneurysm site	
Paraophthalmic	17
PcomA	10
AchoA	1 (2 bystander)
Terminus	1

Note:—R indicates right; L, left; PcomA, posterior communicating artery.

^a Our study population included 28 patients with 29 aneurysms, with coverage of the anterior choroidal artery with at least 1 PED.

or origin from the aneurysm dome¹⁷; occlusion or patency of the aneurysm; and status of the AchoA at follow-up.

Statistics

The data are expressed as mean \pm SD or as median and range. When appropriate, analyses were performed by using a Fisher exact test. A *P* value $< .05$ was considered statistically significant.

RESULTS

Between August 2008 and May 2013, we treated 157 patients with ICA aneurysms with PED constructs. Of these, 28 patients with 29 ICA aneurysms requiring placement of at least 1 PED across the origin of the AchoA were identified. None of these patients developed any sustained postprocedural neurologic deficits. Clinical and angiographic follow-up data were available for all patients through at least 1 year. To date, no patient in this cohort has been lost to follow-up. Baseline demographic and clinical data for the 28 identified patients are shown in Table 1. Eighty-two PEDs were implanted successfully in this cohort, of which 36 PEDs were placed across the ostium of the AchoA in developing a therapeutic construct (mean per aneurysm = 1.24 ± 0.57 , median = 1, range = 1–3). The mean time to last angiographic follow-up was 15.1 months with a range of 12–39 months. Representative examples of pre- and posttreatment angiograms are shown in Figs 1 and 2.

At follow-up, impairment of the AchoA flow was noted in 2 patients. Asymptomatic occlusion of the AchoA occurred in 1 individual (3.4%), who was continued on clopidogrel for 1 year. In another patient, the angiographic opacification of the AchoA at follow-up was judged sluggish, secondary to an ostium stenosis. In the case of AchoA occlusion (Fig 3), the AchoA originated from the lateral fundus of a large aneurysm, which was covered with 3 PEDs. After treatment, the patient was maintained on heparin, 500 IU/h, for 5 days before being discontinued. Within hours of stopping heparin, the patient experienced a transient episode (5 minutes) of contralateral weakness and hemianopsia, consistent with an AchoA syndrome. An urgent angiogram was obtained, demonstrating occlusion of the aneurysm and the AchoA (Fig 3D) with collateral reconstitution of the AchoA territory via anastomoses with the ipsilateral posterior lateral choroidal and medial lenticulostriate arteries. The patient had no further symptoms and was discharged home on postoperative day 9, neurologically intact. At 6-month and 1-year follow-ups, the aneurysm and AchoA ostium were fully closed (Fig 3E), with the distal AchoA collaterally reconstituted through more robust anastomoses with

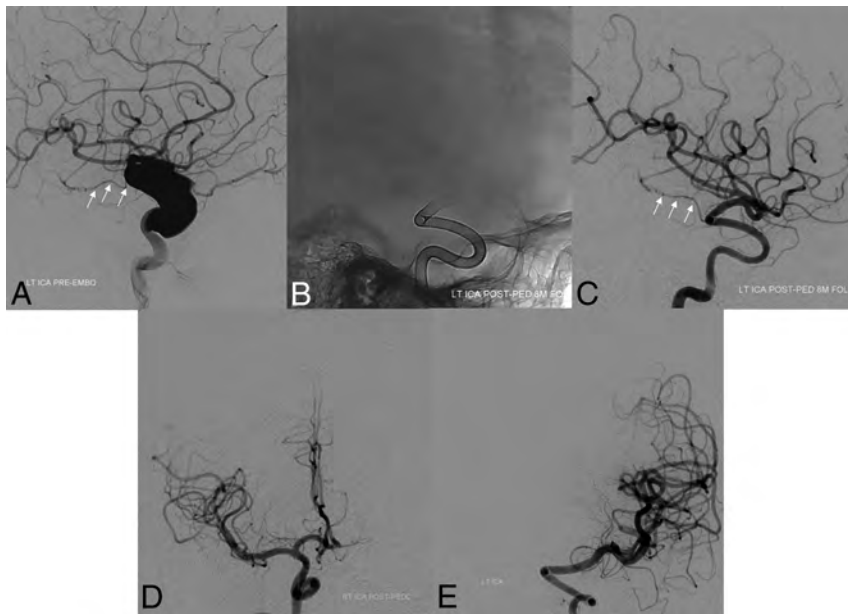


FIG 1. Baseline pretreatment digital subtraction angiogram (lateral projection, A) demonstrating a large dysplastic ICA aneurysm with preserved antegrade flow in the anterior choroidal artery (white arrows). In an initial posttreatment follow-up angiogram after placement of a PED, unsubtracted mask (B) and arterial phase DSA in a lateral projection (C) demonstrate complete occlusion of the aneurysm with preservation of antegrade flow within the anterior choroidal artery (white arrows). Follow-up DSAs demonstrate reconstruction of the left ICA with smooth uniform neointimal overgrowth of the minimally porous endoluminal device construct. Eighteen-month follow-up DSAs (frontal projections) demonstrate a contralateral supply of the left anterior cerebral artery from the right ICA (D) and persistent occlusion of the left ICA aneurysm (E).

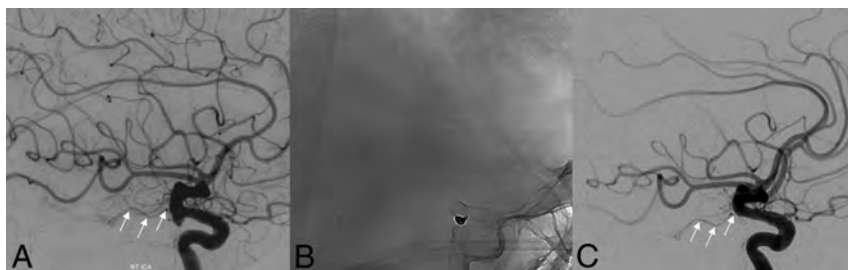


FIG 2. Baseline lateral DSA projection (A) demonstrating a posterior communicating artery aneurysm and normal flow in the anterior choroidal artery (white arrows). One-year follow-up angiography after placement of a PED and coils, unsubtracted mask (B) and DSA (C), confirm occlusion of the aneurysm with preservation of antegrade flow within the anterior choroidal artery (white arrows).

a medial lenticulostriate branch of the right A1 segment (Fig 3F) and the ipsilateral posterior lateral choroidal artery (Fig 3H). A comparison of baseline features between patients with impaired AchoA flow at follow-up and those with normal flow is shown in Table 2. No occlusion of the AchoA was observed among patients with double-device coverage ($n = 3$) or in the other 2 patients with triple coverage of the AchoA. No clinical signs or symptoms of AchoA occlusion were present at follow-up in any patients. As of the time of this writing, no new deficits were noted in the 2 patients with compromised AchoAs.

The AchoA originated from the aneurysm fundus in 4 aneurysms (Table 3). Two of these included the aforementioned cases of AchoA occlusion and flow restriction/stenosis. Three of these 4 aneurysms were incompletely occluded at follow-up; this scenario suggests that persistent runoff into the AchoA may be a potential

contributing factor for incomplete closure of aneurysms treated with the PED.

DISCUSSION

Minimally porous endoluminal devices such as the PED have provided a conceptual paradigm shift in the treatment of cerebral aneurysms.¹⁻⁴ Nevertheless, one of the major concerns related to use of such devices is the risk of potential critical branch vessel occlusion.¹⁸ Various in vitro and animal model studies have attempted to reproduce human in vivo conditions to explore the effect of PED placement on covered branch status. Jailed lumbar segmental vessels reportedly remained patent^{18,19} following single-device placement of PEDs within the rabbit aorta. Histologic evaluation of PEDs 6 months after implantation has typically demonstrated near-uniform neointimal overgrowth of the device, interrupted by uncovered “pores” at origins of branch vessels.¹⁹ This observation is supported in part by the demonstration of persistent patency in most ophthalmic arteries chronically covered by single PEDs.^{2,3,9,10}

Furthermore, while Puffer et al¹⁰ reported that ~25% of ophthalmic arteries covered by PEDs were occluded on follow-up imaging and ~18% were occluded in the Budapest PED experience,³ neurologic sequelae of such ophthalmic artery occlusion are demonstrably rare. For the ophthalmic artery, the infrequency of symptomatic occlusions likely reflects the rich collateral support available through anastomoses with orbital branches of the external carotid artery; additionally, the cases in which the ophthalmic artery was occluded serve to

illustrate the potential for use of such devices in facilitating asymptomatic vascular remodeling in the treatment of complex aneurysms. Moreover, the apparent infrequency of symptomatic orbital thromboembolic events following coverage with a PED,¹ even in cases in which the artery is incorporated into the target aneurysm, is reassuring. Nevertheless, the sufficiency of collateral support for the AchoA²⁰ has been poorly studied and remains disturbingly unpredictable,²¹ particularly considering the neurologic eloquence of this vascular territory and the knowledge that ischemic infarctions due to perforator occlusion have been described in other territories.²² Although a role for balloon test occlusion, supplemented by simultaneous angiographic assessment of collateral support, might be of use in identifying patients in whom collateral support is immediately sufficient, it is unlikely that much insight into the consequences of slowly progressive,

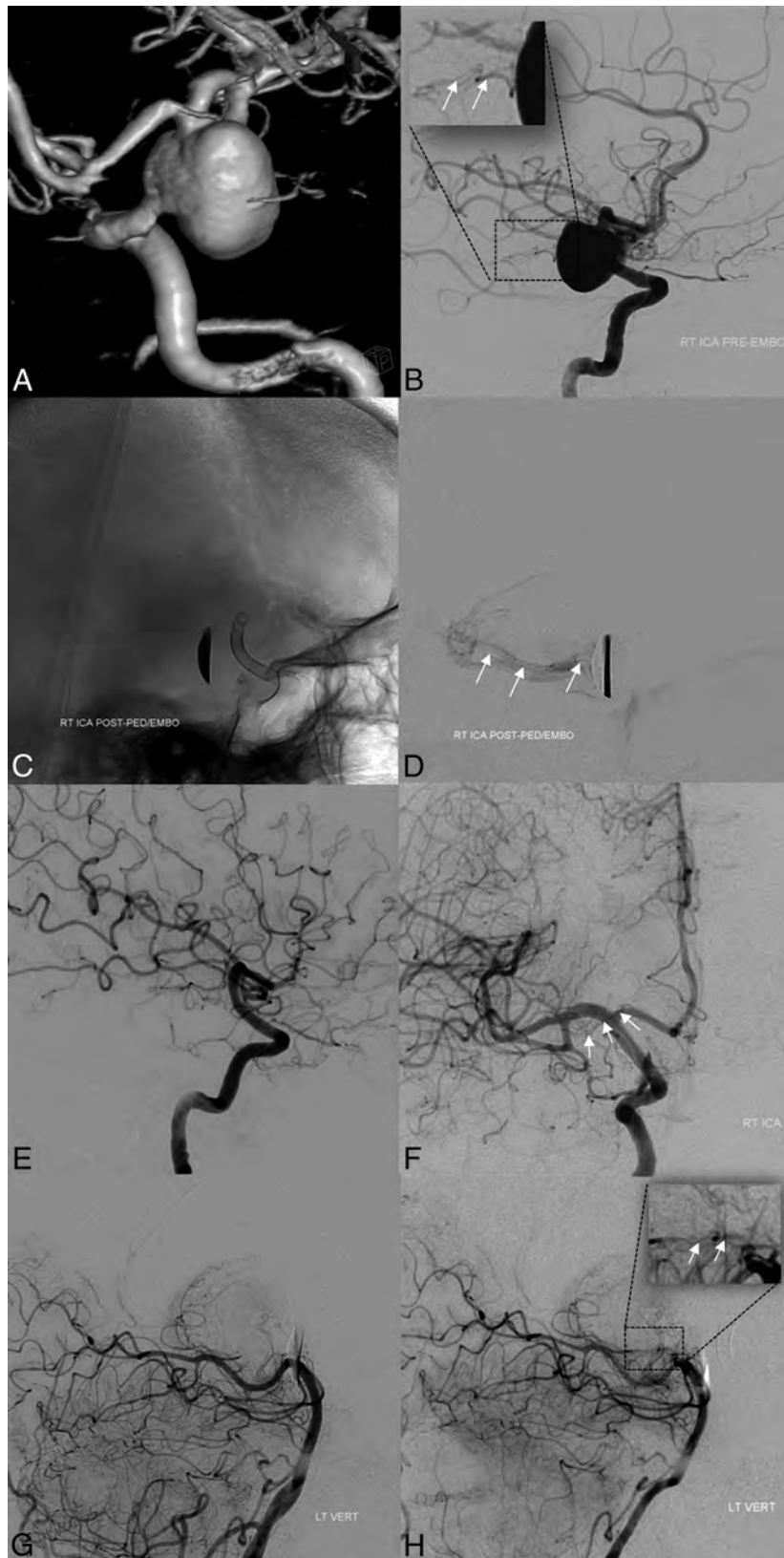


FIG 3. Baseline pretreatment 3D-DSA (A) and lateral projection DSA (B) demonstrating a large anterior choroidal artery aneurysm. Note the origin of the AchoA from the aneurysm fundus (*white arrows* in inset, B). Immediate posttreatment images, after placement of PED, unsubtracted mask (C) and delayed image DSA (D), demonstrate coverage of the AchoA origin and residual antegrade opacification of the AchoA territory (*white arrows*, D). Follow-up angiography (E and F) confirms complete occlusion of the aneurysm and AchoA origin; the AchoA is opacified retrogradely (*white arrows*, F). Baseline pretreatment (G) and follow-up (H) DSAs of the left vertebral artery (lateral projections) demonstrate the collateral opacification of the AchoA through anastomoses with the posterior lateral choroidal artery at follow-up (inset in H, *white arrows*; compare with the inset in B, not visualized at baseline (G)).

Table 2: AchoA status

	AchoA Status	
	Open	Impaired
Aneurysms (No.)	27 (93.1%)	2 (6.9%)
Mean age (SD) (yr)	57.9 (14.0)	53.5 (4.9)
Sex (M/F)	7/20	1/1
Mean PED covering AchoA (No.)	1.25 (0.6)	2 (1.4)
Aneurysm occlusion at follow-up (No.)	24 (88.8%)	1 (50%)
Mean (SD) follow-up (mo)	15.1 (7.1)	15.5 (4.9)

Table 3: AchoA origin from the dome and association with aneurysm occlusion at follow-up^a

	Aneurysm		
	Closed	Open	Total
AchoA origin from the aneurysm fundus (No.)	1	3	4
AchoA origin outside of the aneurysm fundus (No.)	24	1	25
Total	25	4	29

^a Fisher exact test: 2-tailed *P* value = .0043.

delayed occlusion of the AchoA for individuals with poor collateral support at the time of treatment would be gained. None of our patients underwent test occlusion of the AchoA before treatment.

The present study provides some reassurance that strategically limited PED coverage of the AchoA is infrequently associated with symptomatic flow impairment or vessel occlusion. In this series, no permanent clinical sequelae resulted from coverage of the AchoA by a PED through a mean of 15.1 months of follow-up. A single AchoA occlusion was seen. In this patient, transient symptoms suggestive of an AchoA syndrome developed on postoperative day 5 following discontinuation of heparin (which had been continued during a prolonged period specifically to prevent acute aneurysm thrombosis in this patient). However, the symptoms regressed spontaneously within minutes, coinciding with angiographically confirmed collateral reconstitution of the occluded AchoA by mechanisms previously described.¹⁶ Another asymptomatic patient was observed at 1 year postprocedure to have subjectively sluggish antegrade flow within the AchoA, associated with origin stenosis of the vessel; however, this patient remains clinically asymptomatic through 3 years. The median number of PEDs covering the choroidal segment in this series was 1, with double ($n = 3$) or triple ($n = 3$) coverage being the exception. In 1 case of triple coverage, the AchoA and its associated aneurysm were occluded. In the remaining 2 triple-coverage cases, antegrade flow was maintained through the 1-year follow-up angiograms. Thus, multidevice coverage may be justified if in the judgment of the operator, such a construct is necessary for aneurysm treatment (Fig 1).

Although a margin of safety may exist in covering neurologically eloquent branches such as the AchoA, judicious treatment should be focused on limiting such coverage. Toward this goal, the degree of absolute metal coverage may be minimized by strategic selection of PED size in developing a therapeutic construct. The functional metal coverage projected by an individual PED varies substantially depending on its size relative to the parent vessel, regional curvature, and other conditions of deployment (with realized values between 18% and 36%). This variation pro-

vides the opportunity to minimize judiciously eloquent branch coverage.^{13,14} From this perspective, the porosities of devices covering the AchoA is likely lower than that expected in a straight-vessel model, due to the relative oversizing of devices for the choroidal segment to match the diameter of the ICA at the more proximal landing zone and because the AchoA typically arises from an outer curvature of the supraclinoid ICA, causing individual device pores of the PED to be further opened.²³

In our cohort, 4 AchoAs originated from the aneurysm fundus. Of these, 2 AchoAs were impaired at follow-up and only 1 aneurysm was angiographically occluded at 1-year follow-up. These results raise the possibility that persistent runoff into branches originating from the aneurysm proper may prevent complete aneurysm obliteration by mechanisms similar to those responsible for continued patency of normal side branches. In studies by Raz et al⁹ and Puffer et al,¹⁰ branch origin from the dome was an independent factor associated with lack of aneurysm occlusion at follow-up.

We acknowledge the following limitations of this study: First, the requisite angiographic follow-up was 1 year. Thus, it may be argued that during a longer term, AchoA occlusion may be underestimated. Also, the small number of patients with 2 or 3 PEDs across the artery ostium ($n = 5$) limits the power of analysis correlating PED number and vessel status.

CONCLUSIONS

Our experience demonstrates the overall safety and efficacy of PED placement across the AchoA, with expectation of a few incidences of postprocedural AchoA occlusion. None of the patients in the current series reported permanent symptoms related to AchoA coverage following PED treatment.

Disclosures: Maksim Shapiro—UNRELATED: Consultancy: Pipeline proctor and consultant for Covidien; Payment for Development of Educational Presentations: Covidien. Tibor Becske—UNRELATED: Consultancy: Covidien/ev3 (I am a consultant with Covidien, the manufacturer of the device in question); Payment for Lectures (including service on Speakers Bureaus): Covidien/ev3 (I have given a presentation); Payment for Development of Educational Presentations: Covidien/ev3, Comments: I participated in development of FDA-mandated training for US neurointerventionalists in the use of the Pipeline device. Daniel W. Zumofen—UNRELATED: Grants/Grants Pending: personal scholarship from the Fund Helmut Hartweg and the Swiss Academy of Medical Science, Comments: 1-year personal scholarship from the Fund Helmut Hartweg and the Swiss Academy of Medical Science to cofinance my fellowship at the New York University School of Medicine; Travel/Accommodations/Meeting Expenses Unrelated to Activities Listed: Swiss Neurosurgery Update, Comments: invited guest speaker at the Swiss Neurosurgery Update in January 2014 in Basel, Switzerland. Travel and accommodation expenses were covered by the meeting organization; not related to present work; no conflict of interest; Other: Stryker, Covidien, Penumbra, Medtronic, Comments: I went to the 2014 national fellowship courses organized by Stryker, Covidien, Penumbra, and Medtronic. Traveling and accommodation expenses were covered by the companies; not related to present work; no conflict of interest. Peter K. Nelson—RELATED: Consulting Fee or Honorarium: Covidien; UNRELATED: Consultancy: Covidien.

REFERENCES

1. Becske T, Kallmes DF, Saatci I, et al. Pipeline for uncoilable or failed aneurysms: results from a multicenter clinical trial. *Radiology* 2013;267:858–68
2. Nelson PK, Lylyk P, Szikora I, et al. The Pipeline embolization device for the intracranial treatment of aneurysms trial. *AJNR Am J Neuroradiol* 2011;32:34–40
3. Szikora I, Berentzi Z, Kulcsar Z, et al. Treatment of intracranial aneurysms by functional reconstruction of the parent artery: the Bu-

- dapest experience with the Pipeline embolization device. *AJNR Am J Neuroradiol* 2010;31:1139–47
4. Lylyk P, Miranda C, Ceratto R, et al. **Curative endovascular reconstruction of cerebral aneurysms with the Pipeline embolization device: the Buenos Aires experience.** *Neurosurgery* 2009;64:632–42; discussion 642–43; quiz N6
 5. Fiorella D, Lylyk P, Szikora I, et al. **Curative cerebrovascular reconstruction with the Pipeline embolization device: the emergence of definitive endovascular therapy for intracranial aneurysms.** *J Neurointerv Surg* 2009;1:56–65
 6. Appanaboyina S, Mut F, Löhner, et al. **Computational modelling of blood flow in side arterial branches after stenting of cerebral aneurysms.** *International Journal of Computational Fluid Dynamics* 2008;22:669–76
 7. Cebral JR, Raschi M, Mut F, et al. **Analysis of flow changes in side branches jailed by flow diverters in rabbit models.** *Int J Numer Method Biomed Eng* 2014;30:988–99
 8. Seong J, Wakhloo AK, Lieber BB. **In vitro evaluation of flow diverters in an elastase-induced saccular aneurysm model in rabbit.** *J Biomech Eng* 2007;129:863–72
 9. Raz E, Tanweer O, Becske T, et al. **Ophthalmic artery patency and clinical follow-up after placement of Pipeline embolization device.** In: *Proceedings of the Annual Meeting of the American Society of Neuroradiology*, San Diego, California. May 18–23, 2013
 10. Puffer RC, Kallmes DF, Cloft HJ, et al. **Patency of the ophthalmic artery after flow diversion treatment of paraclinoid aneurysms.** *J Neurosurg* 2012;116:892–96
 11. Lopes DK, Ringer AJ, Boulos AS, et al. **Fate of branch arteries after intracranial stenting.** *Neurosurgery* 2003;52:1275–78; discussion 1278–79
 12. Wakhloo AK, Tio FO, Lieber BB, et al. **Self-expanding nitinol stents in canine vertebral arteries: hemodynamics and tissue response.** *AJNR Am J Neuroradiol* 1995;16:1043–51
 13. Shapiro M, Raz E, Becske T, et al. **Variable porosity of the Pipeline embolization device in straight and curved vessels: a guide for optimal deployment strategy.** *AJNR Am J Neuroradiol* 2014;35:727–33
 14. Shapiro M, Raz E, Becske T, et al. **Building multidevice Pipeline constructs of favorable metal coverage: a practical guide.** *AJNR Am J Neuroradiol* 2014;35:1556–61
 15. Shapiro M, Becske T, Riina HA, et al. **Toward an endovascular internal carotid artery classification system.** *AJNR Am J Neuroradiol* 2014;35:230–36
 16. Takahashi S, Suga T, Kawata Y, et al. **Anterior choroidal artery: angiographic analysis of variations and anomalies.** *AJNR Am J Neuroradiol* 1990;11:719–29
 17. Kang HS, Kwon BJ, Kwon OK, et al. **Endovascular coil embolization of anterior choroidal artery aneurysms: clinical article.** *J Neurosurg* 2009;111:963–69
 18. Kallmes DF, Ding YH, Dai D, et al. **A second-generation, endoluminal, flow-disrupting device for treatment of saccular aneurysms.** *AJNR Am J Neuroradiol* 2009;30:1153–58
 19. Kallmes DF, Ding YH, Dai D, et al. **A new endoluminal, flow-disrupting device for treatment of saccular aneurysms.** *Stroke* 2007;38:2346–52
 20. Alderazi YJ, Shastri D, Kass-Hout T, et al. **Flow diverters for intracranial aneurysms.** *Stroke Res Treat* 2014;2014:415653
 21. Lee M, Saver JL, Hao Q, et al. **Anterior choroidal artery ischaemic patterns predict outcome of carotid occlusion.** *J Neurol Neurosurg Psychiatry* 2012;83:586–90
 22. van Rooij WJ, Sluzewski M. **Perforator infarction after placement of a Pipeline flow-diverting stent for an unruptured A1 aneurysm.** *AJNR Am J Neuroradiol* 2010;31:E43–44
 23. Bing F, Darsaut TE, Salazkin I, et al. **Stents and flow diverters in the treatment of aneurysms: device deformation in vivo may alter porosity and impact efficacy.** *Neuroradiology* 2013;55:85–92

Prospective Study of Early MRI Appearances following Flow-Diverting Stent Placement for Intracranial Aneurysms

BJ. McGuinness, S. Memon, and J.K. Hope

ABSTRACT

BACKGROUND AND PURPOSE: MR imaging findings of aneurysm enlargement, aneurysm wall enhancement, perianeurysmal edema, and embolic phenomena following deployment of flow-diverting stents may be relevant to those patients who subsequently experience procedure-related intracranial hemorrhage. We sought to document the routine early postoperative MR imaging findings following flow-diverting stent insertion.

MATERIALS AND METHODS: Patients requiring flow-diverting stent placement for treatment or retreatment of cerebral aneurysms were prospectively included in the study during a 26-month period. Early postprocedural MR imaging studies were obtained and compared with preoperative imaging. Patient clinical outcome data were also collected.

RESULTS: There were 34 stent-placement procedures during the study period. Aneurysm mural enhancement and mild new perianeurysmal edema were present in 50% and 14%, respectively. Any DWI lesion was present in 57% of cases. New or possibly new foci of susceptibility effect were found ipsilateral to the stent and not associated with diffusion restriction in 66% of cases. There were 2 cases (6%) of parenchymal hemorrhage and 2 major clinical complications (6%) causing permanent morbidity.

CONCLUSIONS: Asymptomatic aneurysm mural enhancement is frequently seen following flow-diverting stent placement and should not necessarily be interpreted as a sign of impending aneurysm rupture. This finding often persists despite complete aneurysm occlusion. New small brain parenchymal susceptibility foci following stent placement have not previously been reported, to our knowledge, but were common in our series.

Following flow-diverting stent placement to treat intracranial artery aneurysms, complications of delayed aneurysmal and parenchymal hemorrhage, with or without preceding symptomatology, have been described.¹⁻⁵ Speculation remains regarding the etiology of both forms of hemorrhage, with an overall hemorrhage risk of 7% in reported series.⁶ Delayed parenchymal hemorrhages typically occur on the side of the treated aneurysm and at an incidence in excess of that expected due to dual antiplatelet medication alone and from that reported in prior non-flow-diverting-stent literature.^{7,8} MR imaging case reports have identified perianeurysmal edema, aneurysm expansion, and aneurysm wall enhancement in symptomatic patients before delayed aneurysm rupture.^{1,2} It is unknown whether such findings are predic-

tive of subsequent aneurysm rupture. Microembolic change on diffusion imaging is common following angiographic procedures, and hemorrhagic transformation of infarcts is one putative cause of the parenchymal hemorrhages. We sought to document the routine early postprocedural MR imaging findings following flow-diverting stent insertion.

MATERIALS AND METHODS

Study Population

Local institutional ethics approval was obtained for this study. Consecutive patients requiring elective flow-diverting stent placement for the treatment of unruptured cerebral aneurysms or retreatment of previously ruptured aneurysms were prospectively included in the study during a 26-month period from January 2012 to March 2014. Acutely ruptured aneurysms were excluded.

Stent-Placement Procedure

Dual antiplatelet medication (300 mg aspirin and 75 mg clopidogrel) was started 5 days before the intervention; then, clopidogrel was continued for 6 months, and aspirin, life-long. All procedures were performed with the patient under general anes-

Received August 11, 2014; accepted after revision November 3.

From the Department of Radiology (B.J.M., J.K.H.), Auckland City Hospital, Auckland, New Zealand; and Department of Radiology (S.M.), Vancouver General Hospital, Vancouver, British Columbia, Canada.

Please address correspondence to Ben McGuinness, MD, FRANZCR, Radiology Department, Auckland City Hospital, Park Rd, Grafton, Auckland, New Zealand; e-mail: benmcg@gmail.com

<http://dx.doi.org/10.3174/ajnr.A4335>

thetia. A 5000-U heparin bolus was given after femoral puncture; then, smaller boluses were given to keep activated clotting time at 2–3 times the baseline level. Postprocedural heparin was not routinely administered. Stents deployed were the Pipeline Embolization Device (Covidien, Irvine, California) in all cases except for 2, in which the Flow-Redirection Endoluminal Device (MicroVention, Tustin, California) was used. Each stent-placement procedure was performed by 2 of 4 available interventional neuroradiologists with between 7 and 20 years of experience (ie, 2 operators per case).

Postprocedural MR Imaging

Early postprocedural MR imaging studies were planned between 2 and 10 days post-stent placement. All MR imaging scans were obtained on a 1.5T unit (Magnetom Avanto; Siemens, Erlangen, Germany). Scan protocol was sagittal and axial FSE T1, axial and coronal FSE T2, axial FLAIR, axial DWI, and either gradient-echo T2* or SWI also in the axial plane. TOF and dynamic contrast-enhanced MRA (20 mL of gadopentetate dimeglumine, Magnevist; Bayer HealthCare Pharmaceuticals, Wayne, New Jersey) was performed followed by postcontrast axial FSE.

Image Analysis

Images from the early postprocedural MR imaging were interpreted by an experienced neuroradiologist (B.J.M.) and compared with any available pre-stenting imaging. Doubtful findings were resolved by consensus read by a second neuroradiologist (J.K.H.). Aneurysm size, shape, surrounding edema, wall enhancement, and the occurrence of parenchymal DWI-positive lesions or any other signal disturbance were recorded. Aneurysm size was considered stable if the maximum single dimension obtained was the same as or within 1 mm of that on the preprocedural imaging. Perianeurysmal edema was assessed on T2 and FLAIR and was defined as mild if <3-mm maximum thickness, moderate if between 3- and 10-mm thickness, and severe if >10 mm. Aneurysm wall enhancement was defined as a complete rim of enhancement about the aneurysm wall. Pre-existing T1 shortening due to subacute thrombus or coil artifacts was excluded by reviewing the precontrast T1 scans. Enhancement due to intraneurysmal flow was excluded by assessment of the TOF and contrast-enhanced MRA source images. Nodular enhancement was defined as mural enhancing foci of >2 mm thick interspersed with thinner linear mural enhancement.

Clinical and Delayed Follow-Up

Clinical data were prospectively recorded as to neurologic symptomatology and clinical complications, at both the time of the intervention and at follow-up scans. All patients underwent imaging (typically MR imaging but occasionally DSA or CTA at the discretion of the attending interventional neuroradiologist) and clinical follow-up as per our standard protocol, which is 6 months, 1 year, and 2 years following stent placement.

RESULTS

Study Population and Clinical Presentation

Thirty-four elective flow-diverting stent procedures treating 33 aneurysms in 31 patients were performed during the study period (2 patients had a single aneurysm retreated with a flow-diverting

stent during the study period, 1 patient had 2 aneurysms on 1 carotid segment treated with a single stent, and 1 patient had a bilateral paraclinoid aneurysms treated sequentially in 2 procedures). Twenty-seven patients were women, and 4, men, with an average age of 56 years (range, 42–81 years). Median aneurysm pretreatment diameter was 12 mm (mean, 14 mm; range, 5–35 mm). All patients underwent clinical and imaging follow-up between 6 and 24 months. Eight cases were retreatment of previously coiled ruptured aneurysms, and the remainder were for unruptured aneurysms. Overall, 13 patients had coils present in the aneurysm, either deployed at the time of flow diversion or present from a previous coiling procedure. A single flow-diverting stent was used in all cases except for 5 in which between 2 and 4 stents were deployed. Four of the 26 unruptured aneurysms were symptomatic (2 unilateral headache, 1 headache and sixth cranial nerve palsy, 1 fourth cranial nerve palsy). Three aneurysms were in the vertebrobasilar territory with the remainder arising from the carotid artery (3 posterior communicating aneurysms). Four aneurysms were cavernous carotid with the remainder intradural in location.

Complete early postprocedural MR imaging studies were performed in 24 cases (21 patients and 22 aneurysms). Ten patients did not meet study imaging inclusion criteria and are excluded from MR imaging analysis: Four patients did not have MR imaging due to claustrophobia ($n = 2$) and booking errors ($n = 2$), 4 patients did not receive contrast during their scans, and 2 patients had their scans outside the DWI target window (both at day 16). All patients underwent clinical and delayed imaging follow-up, and any patient who experienced clinical complications is discussed in the “Results” section, including any relevant findings from incomplete MR imaging performed.

Early MR Imaging Findings

Aneurysm mural enhancement was present in 11 of 22 (50%) aneurysms measuring 1- to 3-mm thick. Three of these showed nodular wall enhancement, with the remainder being smooth and linear (Fig 1). Mild (≥ 3 mm) perianeurysmal edema was present in 3 aneurysms (14%, Fig 2). In all cases, prior imaging showed that this edema had developed secondary to flow-diverting stent insertion. Two of these patients re-presented to the hospital with headaches at days 5 and 23 postoperatively (another patient without perianeurysmal edema re-presented to the hospital with headache at day 21). Two of these patients with edema were retreated in this series in an attempt to promote aneurysm occlusion. None of the patients with perianeurysmal edema had coils within the treated aneurysm, while 6 of the 11 aneurysms (55%) with mural enhancement had coils. Aneurysm size was stable or within 1 mm of pretreatment dimensions in all cases. Any DWI lesion was present in 13 of 24 cases (57%). Seven cases (30%) had >5 DWI lesions or any lesion >5 mm. Twenty-one of the 24 cases had susceptibility-weighted imaging performed, while 3 had gradient-echo T2. New foci of susceptibility effects ipsilateral to the stent and not associated with diffusion restriction were found in 8 patients (38%) who had susceptibility-weighted sequences performed (Fig 3). A further 28% of these studies (6/21) had susceptibility foci ipsilateral to the stent, which were possibly new but did not have an earlier comparison SWI sequence. All SWI foci were <2 mm and not identifiable on any other sequence.

Clinical Complications

Ten clinical complications occurred in 9 of 34 operations (26%). Eight of these were transient or resolved with appropriate treatment, and 2 patients (6%) experienced permanent morbidity. One of these (parenchymal hemorrhage) was disabling (mRS = 3), and the other (ischemic), nondisabling (mRS = 1). There were no deaths.

There were 3 ischemic and 2 hemorrhagic complications, 3 of 5 cases being transiently symptomatic. Four of these occurred within 48 hours of stent deployment, and 1 at 2 weeks (pontine hemorrhage). Two cases (6%) of symptomatic parenchymal hemorrhage occurred within the treated vascular territory. One of these occurred at approximately 6 hours following stent deployment, resulting in a 4-cm hematoma in the superior left temporal lobe with associated Sylvian subarachnoid hemorrhage and producing expressive and receptive dysphasia. This patient subsequently had MR imaging the following day, which showed 2 small foci of restricted diffusion (<5 mm) remote from the hemorrhage. No new foci of susceptibility effect were identified remote from the hemorrhage. This patient was excluded from the early MR imaging analysis due to not having contrast at the time of her acute scan. The

second case of parenchymal hemorrhage was a 3-mm pontine hemorrhage found on CT at 2 weeks' post-stent deployment when the patient presented to another institution following a syncope episode (Fig 4). There were no lasting clinical sequelae, and no clear cause of the syncope was identified. No DWI or SWI focus was identified at the site of the hemorrhage on the patient's preceding early MR imaging scan at day 2. Both hemorrhages occurred in the vascular territory accessed by the guide catheter, the first case occurring distal to the stented cavernous carotid aneurysm and the second occurring proximal to a posterior cerebral artery aneurysm.

Three patients re-presented to the hospital with headaches without subsequent hemorrhage or neurologic sequelae. One of these patients re-presented to the hospital with headaches twice and was retreated with a flow-diverting stent within this series in an attempt to promote occlusion of the aneurysm. One patient, who also experienced a transient ischemic deficit, required open surgical repair of a femoral artery puncture site, with full recovery.

Delayed Imaging Follow-Up

All patients have had between 6- and 24-month follow-up. Imaging follow-up was with contrast-enhanced MRA in all patients except for 2 in whom CTA was performed. DSA was performed in addition to these studies in 5 cases. Aneurysm occlusion was complete in 19 of 33 aneurysms (58%) and in 14 of 18 (78%) that had at least 12 months of follow-up. Of the 11 aneurysms that showed aneurysm wall enhancement, 2 have resolved in association with aneurysm occlusion, 5 showed stable wall enhancement despite aneurysm occlusion, 3 showed stable wall enhancement in the presence of ongoing aneurysm filling, and 1 case with an occluded aneurysm was not assessable because it was followed with CTA. Of the 3 aneurysms with perianeurysmal edema, 1 resolved in association with aneurysm occlusion and reduction in aneurysm size, 1 is stable with persistent aneurysm filling, and 1 with an occluded aneurysm is not assessable due to CTA follow-up. The areas of new susceptibility foci on early post-stent-insertion MR imaging remain unchanged in size, number, and morphology.

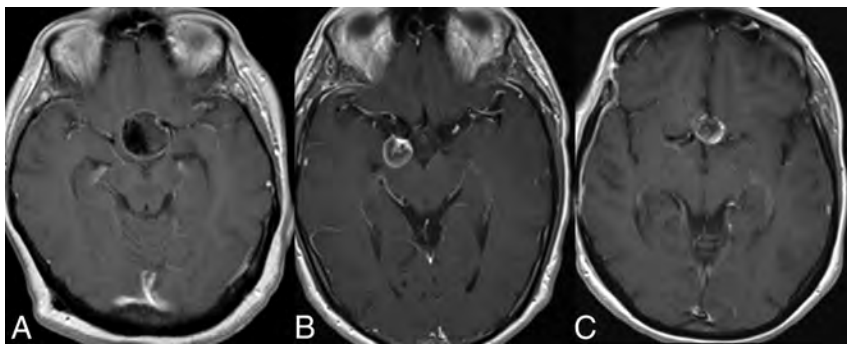


FIG 1. Postcontrast T1-weighted images showing aneurysm mural enhancement following flow-diverting stent placement. A, Smooth linear wall enhancement in a large left paraclinoid aneurysm. B, Linear wall enhancement along with some central aneurysm luminal filling in a large right posterior communicating artery aneurysm. C, Nodular wall enhancement of a left paraclinoid aneurysm.

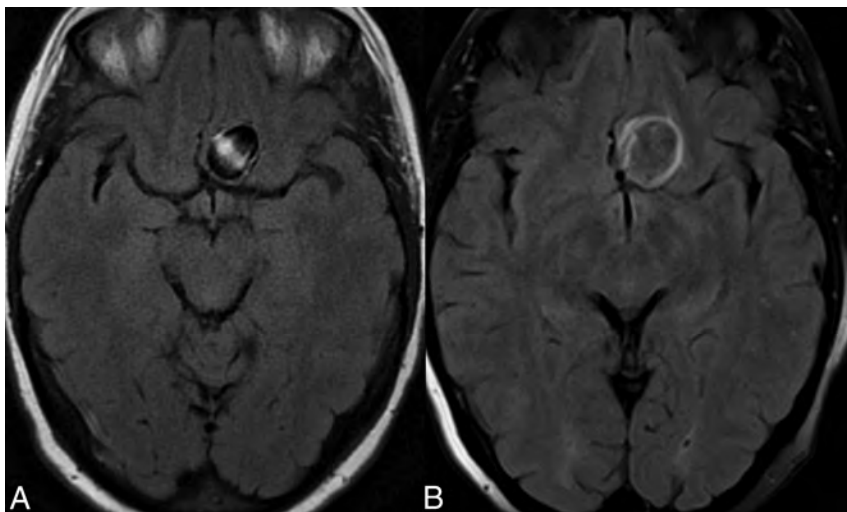


FIG 2. Development of mild perianeurysmal edema following flow-diverting stent placement. A, Axial FLAIR imaging before treatment. B, Corresponding FLAIR image following stent placement shows new perianeurysmal edema.

ture, there is the opportunity for therapeutic intervention such as modifying dual antiplatelet medications, inserting an additional flow-diverting stent, or performing parent artery occlusion. This study has shown that similar to results in the coiling literature, aneurysm mural enhancement is frequently seen on MR imaging in asymptomatic patients who do not proceed to aneurysm rupture.⁹ Aneurysm wall enhancement is thought to represent an inflammatory healing response and, when present following coiling, is usually seen to persist for months to years.⁹ Such an inflammatory response can be responsible for optic nerve or other cranial nerve dysfunction in the absence of aneurysm enlargement. Our series also shows that it can persist for

months to years following flow diversion despite complete aneurysm occlusion.

In the coiling literature, perianeurysmal edema has been observed before treatment in large and often partially thrombosed aneurysms but also in smaller aneurysms following coiling with both HydroCoils (MicroVention) and bare platinum coils.^{9,10} Our study showed that while perianeurysmal edema can occasionally occur following flow diversion, it is usually mild.

There were no cases of delayed aneurysm rupture in our series, and it is not possible to draw any conclusions about predictive findings from postprocedural MR imaging for delayed aneurysm rupture. Previous published case reports of delayed aneurysm

rupture with MR imaging preceding rupture show findings ranging from stable aneurysm size and perianeurysmal edema but with linear wall enhancement to marked aneurysm enlargement and new brain edema.^{1,2} On the basis of our findings and the previous published literature, aneurysm wall enhancement is common and should not be interpreted as a sign of impending rupture. Perianeurysmal edema is a less common finding and would be a more concerning finding, particularly in the symptomatic patient. Two patients in this series with perianeurysmal edema underwent further treatment, one of which resulted in successful aneurysm occlusion and resolution of the edema, while the other aneurysm continues to fill with stable edema.

Foci of restricted diffusion are known to be a common finding after aneurysm embolization and, to a lesser degree, diagnostic cerebral angiography.^{11,12} They are also increasingly recognized after open and endovascular cardiac interventions.^{13,14} The degree to which they are due to gas or thrombotic or other embolic material is unknown; however, the use of heparin and air filters has been shown to reduce their incidence.¹²

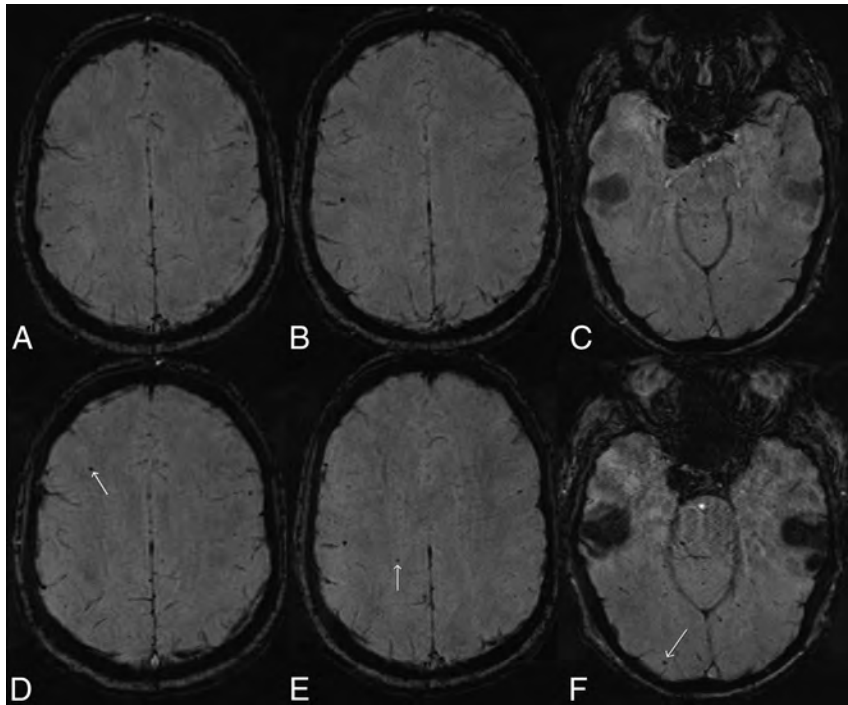


FIG 3. Development of new susceptibility foci in the ipsilateral hemisphere following flow-diverting stent placement for a right posterior communicating artery aneurysm. Axial SWI (top row, A–C) obtained 7 days before deployment of a right supraclinoid ICA flow-diverting stent shows a single susceptibility focus laterally in the superior right parietal lobe (B). Axial SWI obtained 6 days following stent deployment (bottom row, D–F) shows small new susceptibility foci in the superior right frontal lobe (D, arrow), superior right parietal lobe (E, arrow) medial to the pre-existing focus, and in the right occipital pole (F, arrow). The patient had a moderate-sized posterior communicating artery arising from the aneurysm, approximately co-dominant in size with the right P1 segment.



FIG 4. Pontine hemorrhage 2 weeks following flow-diverting stent placement for a large left posterior cerebral artery aneurysm in a 52-year-old man. Axial DWI (A) and SWI (B) performed at 2 days post-stent deployment show 2 small foci of restricted diffusion in the right cerebellar hemisphere but no signal disturbance in the brain stem. Sagittally reformatted noncontrast CT scan (C) obtained 2 weeks after stent deployment following a syncopal episode shows a 3-mm pontine hemorrhage (arrow). Axial DWI (D) and SWI (E) performed at 6 months show the susceptibility effect at the site of the prior pontine hemorrhage.

Diffusion-positive lesions are mostly asymptomatic, but larger or more numerous lesions are associated with ischemic symptoms.¹¹ This was confirmed in our study with 2 of the 3 patients who had ischemic TIA or stroke with MR imaging scans showing a large number of diffusion lesions. The third patient did not have MR imaging, but an early CT scan and delayed MR imaging showed embolic changes that would certainly have been correlated with a large DWI load. Evidence for procedural techniques that minimize the incidence and number of DWI foci is lacking; such techniques will undoubtedly reduce the procedural risk of clinical stroke. Adverse long-term neuropsychological outcomes have been shown with high DWI load following cardiac surgery. Whether this translates to neuroendovascular treatments is unknown, and even if it does, it may still be of lower risk than open neurosurgical alternatives.^{15,16}

There were 2 cases of parenchymal hemorrhage in our series. The first of these was reasonably typical relative to those previously reported in the literature. Proposed mechanisms include unrecognized microwire perforation, hemorrhagic transformation of an infarct, embolized foreign body material, hemodynamic changes secondary to the stent, and hyper-response to dual antiplatelet medication.^{6,17,18} Our second case of parenchymal hemorrhage was atypical, given the size, location, and lack of long-term neurologic morbidity. Most described parenchymal hemorrhages following flow diversion are supratentorial and result in a severe clinical deficit.^{3,5,17} Most interesting, in this case, we had the opportunity of obtaining MR imaging before the brain stem hemorrhage, but it did not show a focus of diffusion restriction or susceptibility effect as a clue to the cause of the hemorrhage. The only caveat was that DWI can fail to detect a small brain stem infarct when performed early after the stroke (day 2 postoperative in this case).¹⁹

New susceptibility foci, which almost always occurred distally within the vascular territory being treated with a flow-diverting stent, were an unexpected finding of this study. There was no correlation of these foci with areas of restricted diffusion. The case illustrated in this article (Fig 3) had an earlier comparison MR imaging that was only 14 days prior, meaning that incidental new microhemorrhages unrelated to the intervention are an implausible explanation. Potential causes include primary microhemorrhages, microhemorrhagic transformation of thromboembolism, gas embolism, or foreign body embolism. On making the observation of these new SWI foci, we reviewed our previous 20 elective non-stent-coiling cases and found the following: Three had definitely new SWI foci compared with a prior SWI study, 4 had probable new foci compared with a prior gradient-echo T2 study, 5 had possibly new foci with no old studies, and 8 had no SWI foci (B.J.M., unpublished data, March 2014). We suspect that this finding is not unique to flow-diverting stents.

CONCLUSIONS

Asymptomatic aneurysm mural enhancement is frequently seen following flow-diverting stent placement and should not necessarily be interpreted as a sign of impending aneurysm rupture. This finding often persists despite complete aneurysm occlusion. Perianeurysmal edema is less common and, particularly when symptomatic, is potentially an indication to perform further

treatment. DWI data suggest a comparable embolic risk to that reported with aneurysm coiling. New small susceptibility foci following stent placement have not been previously reported, to our knowledge, but were common in our series.

Disclosures: Ben J. McGuinness—UNRELATED: Travel/Accommodations/Meeting Expenses Unrelated to Activities Listed: Covidien, Comments: I have attended Covidien-sponsored meetings where flights, accommodation, and meals have been paid. I have not received any direct payment from Covidien and have not been paid to attend these meetings. Sohrabh Memon—UNRELATED: Employment: University of British Columbia; Travel/Accommodations/Meeting Expenses Unrelated to Activities Listed: University of British Columbia Fellow conference stipend.

REFERENCES

- Hampton T, Walsh D, Tolia C, et al. **Mural destabilization after aneurysm treatment with a flow-diverting device: a report of two cases.** *J Neurointerv Surg* 2011;3:167–71
- Chow M, McDougall C, O’Kelly C, et al. **Delayed spontaneous rupture of a posterior inferior cerebellar artery aneurysm following treatment with flow diversion: a clinicopathologic study.** *AJNR Am J Neuroradiol* 2012;33:E46–51
- Cruz JP, Chow M, O’Kelly C, et al. **Delayed ipsilateral parenchymal hemorrhage following flow diversion for the treatment of anterior circulation aneurysms.** *AJNR Am J Neuroradiol* 2012;33:603–08
- O’Kelly CJ, Spears J, Chow M, et al. **Canadian experience with the Pipeline embolization device for repair of unruptured intracranial aneurysms.** *AJNR Am J Neuroradiol* 2013;34:381–87
- Tomas C, Benaissa A, Herbreteau D, et al. **Delayed ipsilateral parenchymal hemorrhage following treatment of intracranial aneurysms with flow diverter.** *Neuroradiology* 2014;56:155–61
- Brinjikji W, Murad M, Lanzino G, et al. **Endovascular treatment of intracranial aneurysms with flow diverters: a meta-analysis.** *Stroke* 2013;44:442–47
- Shapiro M, Becske T, Sahlein D, et al. **Stent-supported aneurysm coiling: a literature survey of treatment and follow-up.** *AJNR Am J Neuroradiol* 2012;33:159–63
- Diener HC, Bogousslavsky J, Brass LM, et al. **Aspirin and clopidogrel compared with clopidogrel alone after recent ischaemic stroke or transient ischaemic attack in high-risk patients (MATCH): randomised, double-blind, placebo-controlled trial.** *Lancet* 2004;364:331–37
- Fanning NE, Willinsky RA, ter Brugge KG. **Wall enhancement, edema, and hydrocephalus after endovascular coil occlusion of intradural cerebral aneurysms.** *J Neurosurg* 2008;108:1074–86
- Craven I, Patel UJ, Gibson A, et al. **Symptomatic perianeurysmal edema following bare platinum embolization of a small unruptured cerebral aneurysm.** *AJNR Am J Neuroradiol* 2009;30:1998–2000
- Kang DH, Kim BM, Kim DJ, et al. **MR-DWI-positive lesions and symptomatic ischemic complications after coiling of unruptured intracranial aneurysms.** *Stroke* 2013;44:789–91
- Bendszus M, Koltzenburg M, Bartsch AJ, et al. **Heparin and air filters reduce embolic events caused by intra-arterial cerebral angiography: a prospective, randomized trial.** *Circulation* 2004;110:2210–15
- Gaita F, Leclercq JF, Schumacher B, et al. **Incidence of silent cerebral thromboembolic lesions after atrial fibrillation ablation may change according to technology used: comparison of irrigated radiofrequency, multipolar nonirrigated catheter and cryoballoon.** *J Cardiovasc Electrophysiol* 2011;22:961–68
- Floyd TF, Shah PN, Price CC, et al. **Clinically silent cerebral ischemic events after cardiac surgery: their incidence, regional vascular occurrence, and procedural dependence.** *Ann Thorac Surg* 2006;81:2160–66
- Barber PA, Hach S, Tippett LJ, et al. **Cerebral ischemic lesions on**

- diffusion-weighted imaging are associated with neurocognitive decline after cardiac surgery. *Stroke* 2008;39:1427–33
16. Scott RB, Eccles F, Molyneux AJ, et al. **Improved cognitive outcomes with endovascular coiling of ruptured aneurysms: neuropsychological outcomes from the International Subarachnoid Aneurysm Trial (ISAT).** *Stroke* 2010;41:1743–47
 17. Deshmukh V, Hu YC, McDougall CG, et al. **Histopathological assessment of delayed ipsilateral parenchymal hemorrhages after treatment of paraclinoid aneurysms with the Pipeline embolization device.** *Neurosurgery* 2012;71:E551–52
 18. Goh C, Churilov L, Mitchell P, et al. **Clopidogrel hyper-response and bleeding risk in neurointerventional procedures.** *AJNR Am J Neuroradiol* 2013;34:721–26
 19. Fukuoka T, Takeda H, Dembo T, et al. **Clinical review of 37 patients with medullary infarction.** *J Stroke Cerebrovasc Dis* 2012; 21:594–99

Association between Venous Angioarchitectural Features of Sporadic Brain Arteriovenous Malformations and Intracranial Hemorrhage

M.D. Alexander, D.L. Cooke, J. Nelson, D.E. Guo, C.F. Dowd, R.T. Higashida, V.V. Halbach, M.T. Lawton, H. Kim, and S.W. Hetts



ABSTRACT

BACKGROUND AND PURPOSE: Intracranial hemorrhage is the most serious outcome for brain arteriovenous malformations. This study examines associations between venous characteristics of these lesions and intracranial hemorrhage.

MATERIALS AND METHODS: Statistical analysis was performed on a prospectively maintained data base of brain AVMs evaluated at an academic medical center. DSA, CT, and MR imaging studies were evaluated to classify lesion side, drainage pattern, venous stenosis, number of draining veins, venous ectasia, and venous reflux. Logistic regression analyses were performed to identify the association of these angiographic features with intracranial hemorrhage of any age at initial presentation.

RESULTS: Exclusively deep drainage (OR, 3.42; 95% CI, 1.87–6.26; $P < .001$) and a single draining vein (OR, 1.98; 95% CI, 1.26–3.08; $P = .002$) were associated with hemorrhage, whereas venous ectasia (OR, 0.52; 95% CI, 0.34–0.78; $P = .002$) was inversely associated with hemorrhage.

CONCLUSIONS: Analysis of venous characteristics of brain AVMs may help determine their prognosis and thereby identify lesions most appropriate for treatment.

Arteriovenous malformations are complex lesions that have variable clinical presentations and prognoses. The most serious clinical manifestation is intracranial hemorrhage. As such, identification of patients and their respective lesion characteristics can help target higher risk lesions for which treatment is most appropriate. The role of venous features in relation to hemorrhagic propensity is incompletely understood. The current study examines the associations among angiographic features of venous components of arteriovenous malformations and presentation with intracranial hemorrhage in a large prospectively maintained cohort.

MATERIALS AND METHODS

The University of California, San Francisco Brain AVM Project data base is a human research protocol–approved, prospectively maintained resource that collects demographic, clinical, and imaging data for patients diagnosed with arteriovenous malformations who were evaluated and treated at this institution. This data base was queried to identify patients with nidus AVMs enrolled between January 2001 and February 2014. Patients with incomplete angiographic records or angiographic characteristics measured after partial treatment were excluded. Additionally, patients with vein of Galen malformations, dural arteriovenous fistulas, non-Galenic pial arteriovenous fistulas, or a hereditary hemorrhagic telangiectasia diagnosis were excluded.

For each patient, the earliest cerebral DSA examination was evaluated by neurointerventional radiologists (S.W.H., D.L.C., C.F.D., R.T.H., V.V.H.), and angioarchitectural features were scored according to a structured format based on recommendations from the Joint Writing Group.¹ All patients with an AVM underwent 2D digital subtraction angiography performed at fast film rates. Initial CT and MR imaging were also examined by a neurointerventional radiologist to identify any current or prior intracranial hemorrhage.

General demographic variables were noted. Venous compartment features recorded included lesion side (right, left, midline), drainage pattern (exclusively deep, not exclusively deep), degree of venous stenosis (0%–24%, 25%–49%, 50%–74%, 75%–99%,

Received July 16, 2014; accepted after revision October 21.

From the Department of Radiology (M.D.A.), University of Washington, Seattle, Washington; and Center for Cerebrovascular Research, Department of Anesthesia and Perioperative Care (J.N., D.E.G., H.K.), Department of Radiology and Biomedical Imaging (D.L.C., C.F.D., R.T.H., V.V.H., S.W.H.), and Department of Neurological Surgery (M.T.L.), University of California, San Francisco, San Francisco, California.

This work was supported, in part, by the National Institutes of Health grant R01 NS034949 to H. Kim.

H. Kim and S.W. Hetts contributed equally to this work.

Please address correspondence to Steven W. Hetts, MD, Neurointerventional Radiology, University of California, San Francisco, 505 Parnassus Ave, L-352, San Francisco, CA 94143; e-mail: steven.hetts@ucsf.edu

Indicates open access to non-subscribers at www.ajnr.org

<http://dx.doi.org/10.3174/ajnr.A4224>

Table 1: Summary statistics of AVM cases^a

Characteristic	Hemorrhage on Noninvasive Imaging		Overall (n = 519)
	Nonhemorrhagic (n = 293 [56%])	Hemorrhagic (n = 226 [44%])	
Age at diagnosis (yr)	36.9 ± 17.2	33.5 ± 19.0	35.4 ± 18.0
Sex			
Female	155 (53)	116 (51)	271 (52)
Male	138 (47)	110 (49)	248 (48)
White ^b			
Yes	170 (58)	113 (50)	283 (55)
No	123 (42)	113 (50)	236 (45)
AVM side			
Right	135 (46)	105 (46)	240 (46)
Left	146 (50)	105 (46)	251 (48)
Midline	12 (4)	16 (7)	28 (5)
Maximum dimension (cm)	3.28 ± 1.58	2.43 ± 1.55	2.92 ± 1.62
Venous drainage			
Not exclusively deep	275 (94)	163 (72)	438 (84)
Exclusively deep	18 (6)	63 (28)	81 (16)
Venous stenosis			
0%–24%	125 (43)	112 (50)	237 (46)
25%–49%	54 (18)	38 (17)	92 (18)
50%–74%	73 (25)	38 (17)	111 (21)
75%–99%	34 (12)	30 (13)	64 (12)
100% (occlusion)	7 (2)	8 (4)	15 (3)
Number of draining veins			
Single	71 (24%)	123 (54%)	194 (37%)
Multiple	222 (76%)	103 (46%)	325 (63%)
Venous ectasia			
Yes	170 (58)	76 (34)	246 (47)
No	123 (42)	150 (66)	273 (53)
Venous reflux			
Yes	105 (36)	46 (20)	151 (29)
No	188 (64)	180 (80)	368 (71)

^a Values are No. (%) or mean ± SD.

^b Ethnicity is included as a variable, as other studies have shown statistically significant differences in the rates of AVM hemorrhage in individuals of different ethnic backgrounds.

occlusion), number of draining veins (single, multiple), presence or absence of venous ectasia, and presence or absence of venous reflux. Venous stenosis was measured as the narrowest diameter divided by the most proximal measureable portion of the vein. Occlusion was noted if a blind-ending vein was visualized exiting the lesion. To identify factors associated with the presence or absence of intracranial hemorrhage at initial presentation, we performed univariable and multivariable logistic regression analyses, generating odds ratios and 95% confidence intervals. Variables that were statistically significant ($P < .05$) in univariable analysis were included in the multivariable analysis to assess which venous compartment features were significant independent predictors of hemorrhagic presentation. All analyses were performed by using STATA/SE 12.0 (StataCorp, College Station, Texas).²

RESULTS

Five hundred nineteen patients were evaluated during the study period. Patient demographics and lesion characteristics are summarized in Table 1. Two hundred twenty-six (43.5%) patients had intracranial hemorrhage identified on noninvasive imaging. Univariable logistic regression analysis identified exclusively deep venous drainage (OR, 5.90; $P < .001$) and a single draining vein (OR, 3.73; $P < .001$) as associated with presentation with intracranial hemorrhage. Age at diagnosis per decade (OR, 0.90; $P = .036$), AVM size per centimeter (OR, 0.69; $P < .001$), the presence

of venous ectasia (OR, 0.37; $P < .001$), and the presence of venous reflux (OR, 0.46; $P < .001$) were inversely related to hemorrhagic presentation. No statistical significance was observed for biologic sex, AVM side, or venous stenosis.

A multivariable logistic regression analysis was performed to evaluate characteristics that were statistically significant in the univariable analysis (results presented in Table 2). Exclusively deep venous drainage remained the most strongly predictive characteristic for intracranial hemorrhage (OR, 3.42; 95% CI, 1.87–6.26; $P < .001$). A single draining vein (OR, 1.98; 95% CI, 1.26–3.08; $P = .002$), venous ectasia (OR, 0.52; 95% CI, 0.34–0.78; $P = .002$), and size (OR, 0.85; 95% CI, 0.74–0.98; $P = .025$) also retained statistical significance. Age at diagnosis ($P = .212$) and venous reflux ($P = .798$) became nonsignificant in the multivariable model.

DISCUSSION

Intracranial hemorrhage accounts for most of the morbidity and mortality caused by brain AVMs. Natural history studies have reported markedly different hemorrhage rates, ranging from 1% to 34% risk of rupture, with multiple previously identified risk factors affecting these rates.³ Among these, numerous

angiographic characteristics of the venous components of these malformations have been noted to affect hemorrhage risk. While certain trends have been identified, disparate results have been reported concerning several venous features. The current study seeks to clarify the role of such venous characteristics by examining a large prospectively maintained series of patients that have been uniformly evaluated on the basis of consensus recommendations.¹

Deep venous drainage is the single characteristic most frequently associated with AVM hemorrhage.^{4–8} The current study supports this widely reported finding, with exclusively deep drainage more commonly associated with hemorrhage than exclusively superficial or mixed superficial and deep venous drainage. This was the strongest predictor noted in this study. Of note, the subgroup of AVMs in our cohort with superficial nidus location and exclusively deep venous drainage (perhaps implying occlusion of previously extant superficial veins) had a particularly high frequency of hemorrhagic presentation (OR, 9.12; $P = .002$).

AVMs with fewer draining veins have shown higher rates of hemorrhage in prior studies.^{9–17} Analysis has varied, with some studies looking at correlations of numbers of draining veins^{14–17} and other studies categorizing or dichotomizing numbers to compare hemorrhagic risks.^{9–13} The current study found that lesions with a single draining vein were more likely to be associated with hemorrhage at the time of initial clinical presentation. This find-

Table 2: Logistic regression analysis (intracranial hemorrhage on presentation as outcome)

Characteristic	Univariable (n = 519)			Multivariable (n = 519)		
	OR	95% CI	P Value	OR	95% CI	P Value
Age at diagnosis (decade)	0.90	(0.82–0.99)	.036	0.93	(0.84–1.04)	.212
AVM size (cm)	0.69	(0.61–0.79)	<.001	0.85	(0.74–0.98)	.025
Exclusively deep venous drainage	5.90	(3.38–10.32)	<.001	3.42	(1.87–6.26)	<.001
Single draining vein	3.73	(2.57–5.43)	<.001	1.98	(1.26–3.08)	.002
Venous ectasia	0.37	(0.26–0.53)	<.001	0.52	(0.34–0.78)	.002
Venous reflux	0.46	(0.31–0.68)	<.001	0.94	(0.59–1.49)	.798
Female sex	0.94	(0.66–1.33)	.722	–	–	–
White ^a	0.72	(0.51–1.03)	.069	–	–	–
AVM side ^b						
Left	0.92	(0.65–1.32)	.668	–	–	–
Middle	1.71	(0.78–3.78)	.182	–	–	–
Venous stenosis ^c	0.94	(0.81–1.09)	.436	–	–	–

Note:— – indicates variables that did not show significance on univariable analysis and were not subjected to multivariable analysis.

^a Ethnicity is included as a variable, as other studies have shown statistically significant differences in the rates of AVM hemorrhage in individuals of different ethnic backgrounds.

^b Right side considered baseline; test results comparing either left or right to middle were not significant ($P = .140$).

^c Tested using ordinal 5-point scale.

ing has face validity: Fewer draining veins mean fewer potential routes for egress of blood from an AVM, thus presumably increasing the likelihood of AVM pressurization and rupture when any given draining vein thromboses.

Venous ectasia has been examined in previous studies, and there is no consensus on the role of ectasia and the risk of hemorrhage. Some studies report increased risk of hemorrhage,^{8,13,18,19} while other reports suggest no impact¹² or a protective role for ectasia.^{11,20} This study found that venous ectasia is inversely related to intracerebral hemorrhage. This finding may reflect an adaptive mechanism whereby such dysmorphism supports either a greater efferent capacitance and/or more functional arterialization of the draining veins. Venous ectasia also appears to develop with time, with older patients more likely to demonstrate this feature than younger patients in our cohort.²¹ In our cohort, exceedingly few patients with ectasia have experienced repeat hemorrhage; we have described one of these patients elsewhere.²²

Similar to ectasia, stenosis or occlusion of draining veins has been examined in prior studies with no resulting consensus. Some studies report increased risk of hemorrhage,^{4,9,18,20,23,24} while other reports suggest no independent effect.^{11,12,25} Venous stenosis offered no predictive value in the current study. Of course, cerebral veins that are completely thrombosed are not directly visible on DSA and only inconsistently identifiable on CT and MR imaging, thus limiting the utility of this measure.

Venous reflux is a less commonly discussed finding but has been suggested to identify lesions more likely to cause hemorrhage, presumably because reflux is an indicator of increased venous pressure.^{18,26} However, venous reflux was inversely related to hemorrhage in univariable analysis in this study. This association did not persist in the multivariable model, suggesting interaction with other variables.

When considering numerous characteristics, there is potential for confounding variables. For example, multiple series have shown that smaller AVMs are more likely to bleed. However, small AVMs are also likely to have fewer draining veins, which also carry an increased association with hemorrhagic risk. Similarly, central lesions are more likely to rupture, but these lesions

are also more likely to have deep draining veins. In the current analysis, age at diagnosis and the presence of venous reflux demonstrated statistical significance in univariable analysis, but their roles were not confirmed in the multivariable analysis. Size persisted as a significant predictor of intracerebral hemorrhage in multivariable analysis, though to a lesser degree than singular venous outflow or deep venous drainage.

While this study identifies an association of venous architectural features with intracranial hemorrhage, it has several limitations. This was a cross-sectional analysis of prospectively enrolled patients in a robustly designed data base, but it examined an outcome that occurred contemporaneously with or before enrollment.

Hemorrhagic association was based solely on imaging features and did not account for clinical features. Furthermore, analysis allowed by this database did not permit differentiation between hemorrhage occurring acutely at the time of enrollment or evidence of prior hemorrhage noted on noninvasive imaging at the time of enrollment. Additionally, the analysis does not distinguish the hemorrhagic location (eg, intraparenchymal versus intraventricular). Furthermore, it is possible that hemorrhage may alter angioarchitectural features in such a way that they differ from what would be identified before the hemorrhage.

Further investigation is warranted for both clinical and angiographic features that can predict AVM hemorrhage, to most accurately stratify hemorrhagic risk and thereby identify patients most suitable for treatment. This is particularly important because of the publication of the A Randomized Trial of Unruptured Brain Arteriovenous Malformations study,²⁷ wherein a relatively short follow-up of previously unruptured AVMs demonstrated inferior outcomes for patients who received therapeutic interventions compared with patients who received conservative medical follow-up.

CONCLUSIONS

Venous factors appear to influence the likelihood that arteriovenous malformations will present with hemorrhage. Exclusively deep venous drainage and a single draining vein were associated with hemorrhage presentation, while venous ectasia was inversely associated with this presentation. Age at diagnosis and venous reflux did not retain statistical significance in a multivariable model. Venous characteristics should be considered when evaluating AVMs and predicting their natural history, thus helping to determine which lesions may be most appropriate for treatment.

ACKNOWLEDGMENTS

The authors wish to acknowledge the contributions of William L. Young, MD, to AVM research in general and to this study in particular. Dr Young was the Founder and Director of the University of California, San Francisco Center for Cerebrovas-

cular Research before his untimely death. The authors also wish to thank Voltaire Gungab for assistance in manuscript preparation.

Disclosures: Jeffrey Nelson—RELATED: Grant: received salary support from National Institutes of Health grant NS034949.* Diana E. Guo—RELATED: Grant: National Institutes of Health (R01 NS034949).* Comments: This grant is paid to Helen Kim, Center for Cerebrovascular Research. Christopher F. Dowd—UNRELATED: Other: MicroVention, Comments: Chief Adjudicator, Flow Re-direction Endoluminal Device trial. Helen Kim—RELATED: Grant: receives salary support from the National Institutes of Health grant R01 NS034949.* UNRELATED: Travel/Accommodations/Meeting Expenses Unrelated to Activities Listed: receive travel reimbursements from National Institutes of Health grant R01 NS034949 when presenting AVM research at conferences/meetings. Steven W. Hetts—RELATED: Grant: National Institutes of Health—National Institute of Neurological Disorders and Stroke.* Comments: brain AVM study funding to Helen Kim and the University of California, San Francisco, Center for Cerebrovascular Research; UNRELATED: Consultancy: Medina Medical, Silk Road Medical, Comments: consulting on medical device design. *Money paid to the institution.

REFERENCES

1. Atkinson RP, Awad IA, Batjer HH, et al. **Reporting terminology for brain arteriovenous malformation clinical and radiographic features for use in clinical trials.** *Stroke* 2001;32:1430–42
2. StataCorp. **2011 Stata Statistical Software: Release 12.** College Station: StataCorp LP
3. Rutledge WC, Ko NU, Lawton MT, et al. **Hemorrhage rates and risk factors in the natural history course of brain arteriovenous malformations.** *Transl Stroke Res* 2014;5:538–42
4. Willinsky R, Lasjaunias P, Terbrugge K, et al. **Brain arteriovenous malformations: analysis of the angio-architecture in relationship to hemorrhage (based on 152 patients explored and/or treated at the hospital de Bicêtre between 1981 and 1986).** *J Neuroradiol* 1988;15:225–37
5. Duong DH, Young WL, Vang MC, et al. **Feeding artery pressure and venous drainage pattern are primary determinants of hemorrhage from cerebral arteriovenous malformations.** *Stroke* 1998;29:1167–76
6. Langer DJ, Lasner TM, Hurst RW, et al. **Hypertension, small size, and deep venous drainage are associated with risk of hemorrhagic presentation of cerebral arteriovenous malformations.** *Neurosurgery* 1998;42:481–86; discussion 487–89
7. Miyasaka Y, Kurata A, Irikura K, et al. **The influence of vascular pressure and angiographic characteristics on haemorrhage from arteriovenous malformations.** *Acta Neurochir (Wien)* 2000;142:39–43
8. Stefani MA, Porter PJ, terBrugge KG, et al. **Angioarchitectural factors present in brain arteriovenous malformations associated with hemorrhagic presentation.** *Stroke* 2002;33:920–24
9. Miyasaka Y, Yada K, Ohwada T, et al. **An analysis of the venous drainage system as a factor in hemorrhage from arteriovenous malformations.** *J Neurosurg* 1992;76:239–43
10. Albert P, Salgado H, Polaina M, et al. **A study on the venous drainage of 150 cerebral arteriovenous malformations as related to hemorrhagic risks and size of the lesion.** *Acta Neurochir (Wien)* 1990;103:30–34
11. Kubalek R, Yin L, Fronhöfer G, et al. **Cerebral arterio-venous malformations: correlation between the angioarchitecture and the bleeding risk** [in German]. *Klin Neuroradiol* 2001;11:97–104
12. Kubalek R, Moghtaderi A, Klisch J, et al. **Cerebral arteriovenous malformations: influence of angioarchitecture on bleeding risk.** *Acta Neurochir (Wien)* 2003;145:1045–52; discussion 1052
13. Lv X, Wu Z, Jiang C, et al. **Angioarchitectural characteristics of brain arteriovenous malformations with and without hemorrhage.** *World Neurosurg* 2011;76:95–99
14. Albert P. **Personal experience in the treatment of 178 cases of arteriovenous malformations of the brain.** *Acta Neurochir (Wien)* 1982;61:207–26
15. Pollock BE, Flickinger JC. **A proposed radiosurgery-based grading system for arteriovenous malformations.** *J Neurosurg* 2002;96:79–85
16. Ji Y, Ding X, Wang ZG. **Analysis of relevant factors of cerebral arteriovenous malformation with hemorrhage** [in Chinese]. *Zhonghua Yi Xue Za Zhi* 2012;92:2488–90
17. Niu H, Cao Y, Wang X, et al. **Relationships between hemorrhage, angioarchitectural factors and collagen of arteriovenous malformations.** *Neurosci Bull* 2012;28:595–605
18. Nataf F, Meder JF, Roux FX, et al. **Angioarchitecture associated with haemorrhage in cerebral arteriovenous malformations: a prognostic statistical model.** *Neuroradiology* 1997;39:52–58
19. Bai J, Dou CW, Wang YJ, et al. **Correlations of angio-architectural factors with cerebral arteriovenous malformation hemorrhage** [in Chinese]. *Zhonghua Yi Xue Za Zhi* 2012;92:2202–04
20. Mansmann U, Meisel J, Brock M, et al. **Factors associated with intracranial hemorrhage in cases of cerebral arteriovenous malformation.** *Neurosurgery* 2000;46:272–79
21. Hetts SW, Cooke DL, Nelson J, et al. **Influence of patient age on angioarchitecture of brain arteriovenous malformations.** *AJNR Am J Neuroradiol* 2014;35:1376–80
22. Alexander MD, Hetts SW, Young WL, et al. **Supernova hemorrhage: obliterative hemorrhage of brain arteriovenous malformations following gamma knife radiosurgery.** *J Neurointerv Surg* 2012;4:364–67
23. Marks MP, Lane B, Steinberg GK, et al. **Hemorrhage in intracerebral arteriovenous malformations: angiographic determinants.** *Radiology* 1990;176:807–13
24. Pasqualin A. **Natural history of cerebral AVM** [in Italian]. *Neuroradiol J* 2002;15:29–40
25. Miyasaka Y, Tanaka R, Kurata A, et al. **The factors influencing haematoma volume due to arteriovenous malformations.** *Acta Neurochir* 1999;141:385–87; discussion 387–88
26. Lasjaunias P, Manelfe C, Chiu M. **Angiographic architecture of intracranial vascular malformations and fistulas—pretherapeutic aspects.** *Neurosurg Rev* 1986;9:253–63
27. Mohr JP, Parides MK, Stapf C, et al; international ARUBA investigators. **Medical management with or without interventional therapy for unruptured brain arteriovenous malformations (ARUBA): a multicentre, non-blinded, randomised trial.** *Lancet* 2014;383:614–21

Quantifying Intracranial Aneurysm Wall Permeability for Risk Assessment Using Dynamic Contrast-Enhanced MRI: A Pilot Study

P. Vakil, S.A. Ansari, C.G. Cantrell, C.S. Eddleman, F.H. Dehkordi, J. Vranic, M.C. Hurley, H.H. Batjer, B.R. Bendok, and T.J. Carroll



ABSTRACT

BACKGROUND AND PURPOSE: Pathological changes in the intracranial aneurysm wall may lead to increases in its permeability; however the clinical significance of such changes has not been explored. The purpose of this pilot study was to quantify intracranial aneurysm wall permeability (K^{trans} , V_L) to contrast agent as a measure of aneurysm rupture risk and compare these parameters against other established measures of rupture risk. We hypothesized K^{trans} would be associated with intracranial aneurysm rupture risk as defined by various anatomic, imaging, and clinical risk factors.

MATERIALS AND METHODS: Twenty-seven unruptured intracranial aneurysms in 23 patients were imaged with dynamic contrast-enhanced MR imaging, and wall permeability parameters (K^{trans} , V_L) were measured in regions adjacent to the aneurysm wall and along the paired control MCA by 2 blinded observers. K^{trans} and V_L were evaluated as markers of rupture risk by comparing them against established clinical (symptomatic lesions) and anatomic (size, location, morphology, multiplicity) risk metrics.

RESULTS: Interobserver agreement was strong as shown in regression analysis ($R^2 > 0.84$) and intraclass correlation (intraclass correlation coefficient > 0.92), indicating that the K^{trans} can be reliably assessed clinically. All intracranial aneurysms had a pronounced increase in wall permeability compared with the paired healthy MCA ($P < .001$). Regression analysis demonstrated a significant trend toward an increased K^{trans} with increasing aneurysm size ($P < .001$). Logistic regression showed that K^{trans} also predicted risk in anatomic ($P = .02$) and combined anatomic/clinical ($P = .03$) groups independent of size.

CONCLUSIONS: We report the first evidence of dynamic contrast-enhanced MR imaging-modeled contrast permeability in intracranial aneurysms. We found that contrast agent permeability across the aneurysm wall correlated significantly with both aneurysm size and size-independent anatomic risk factors. In addition, K^{trans} was a significant and size-independent predictor of morphologically and clinically defined high-risk aneurysms.

ABBREVIATIONS: DCE = dynamic contrast-enhanced; IA = intracranial aneurysm; ISUIA = International Study of Unruptured Intracranial Aneurysms; K^{trans} = contrast-transfer coefficient; V_L = fractional volume of extravascular extracellular space per unit tissue

Intracranial aneurysms (IAs) affect 2%–6% of the population, with nearly 30,000 Americans having an aneurysm rupture each year.¹ Aneurysmal subarachnoid hemorrhage has an approximate

50% mortality, with survivors incurring a tremendous personal and financial burden due to permanent disabilities. Despite the potential devastating effects of IAs, the universal treatment of unruptured IAs still remains controversial. The largest prospective study to date on unruptured IAs, the International Study of Unruptured Intracranial Aneurysms (ISUIA), indicated lower rupture rates than previously suspected.² However, multiple subsequent reports challenged these findings,^{3,4} thus further complicating management decisions. The exact pathogenesis and patho-evolution of IAs is largely unknown, with only a fraction of IAs progressing to rupture annually ($< 2\%$), suggesting potential differences in the pathobiology of ruptured-versus-unruptured IAs. Aneurysm risk stratification has been attempted by identifying specific characteristics of ruptured IAs, including size, location, and morphologic factors (eg, irregular contour⁵ and daughter sacs⁶), but also clinical factors, such as symptomatic lesions, hypertension, smoking, alcohol/drug abuse, and genetic predispositions to aneurysm formation/rupture. However, without absolute

Received July 23, 2014; accepted after revision October 22.

From the Departments of Radiology (P.V., S.A.A., J.V., M.C.H., T.J.C.), Neurosurgery (B.R.B.), and Biomedical Engineering (P.V., C.G.C., T.J.C.), Northwestern University, Chicago, Illinois; Department of Neurological Surgery (C.S.E., H.H.B.), University of Texas-Southwestern, Dallas, Texas; and Department of Economics and Decision Sciences (F.H.D.), Western Illinois University, Macomb, Illinois.

This work was supported by the National Institutes of Health/National Heart, Lung, and Blood Institute R01 HL088437; National Institutes of Health/National Institute of Biomedical Imaging and Bioengineering T32 EB005170, and Radiological Society of North America RSD1207.

Please address correspondence to Timothy J. Carroll, PhD, Departments of Radiology and Biomedical Engineering, Northwestern University, 737 N Michigan Ave, Ste 1600, Chicago, IL 60611; e-mail: t-carroll@northwestern.edu

Indicates open access to non-subscribers at www.ajnr.org

Indicates article with supplemental on-line table.

<http://dx.doi.org/10.3174/ajnr.A4225>

risk-stratification parameters for unruptured IAs, patients and physicians encounter difficult management decisions regarding the risk-benefit analysis for treatment. Aneurysm size measured by CTA, MRA, or DSA is the primary imaging marker of rupture risk and is used for clinical decisions to either treat with coil embolization/microsurgical clipping or offer conservative management with routine imaging follow-up evaluations and clinical risk-factor control.

The pathobiology of IAs and alterations in the aneurysm wall have been shown to involve a multitude of histopathologic changes, such as disruption of the internal elastic lamina, smooth-muscle cell migration, and myointimal hyperplasia leading to irregular surfaces with variable thickness. In fact, direct inspection of the IA wall during surgery has demonstrated heterogeneous features, such as thin translucent regions,⁷ but these are not resolved with noninvasive imaging. Noninvasive CT or MR imaging of the morphologic phenotype of the aneurysm wall may be useful in assessing IA stability. It is plausible, given the aforementioned changes in IA wall histology, specifically apoptosis of endothelial cells, loss of collagen, and remodeling of the extracellular matrix, that contrast agents could extravasate or permeate these compromised areas into the surrounding CSF. This may be interpreted as a macroscopic manifestation of microscopic tracer permeability, which occurs through the capillary bed into tissue. The contrast agent permeability rate (K^{trans}) could then provide a surrogate measure of vessel wall integrity and focal degradation resulting from environmental factors such as hemodynamic stresses, typically assessed with advanced MR imaging acquisitions⁸ and post-processing algorithms.⁹

The purpose of this work was to determine the feasibility of quantifying aneurysm wall permeability by using widely available dynamic contrast-enhanced (DCE)-MR imaging. Our goal was to develop an adjunctive imaging metric to complement existing anatomic and developing flow-based imaging markers of aneurysm risk (size, location, morphology, computational/4D flow dynamics). We report the results of a prospective pilot study comparing aneurysm wall permeability by using DCE-MR imaging with anatomic and clinical metrics that predispose IAs to rupture. We hypothesized that increased IA wall permeability may be associated with IA size, location, morphology, and multiplicity and clinically defined high-risk or symptomatic lesions.

MATERIALS AND METHODS

Institutional review board approval was provided for patient recruitment and study. Informed consent was acquired, and the study was conducted according to Health Insurance Portability and Accountability Act guidelines. Consecutive patients with unruptured IAs reporting for neurosurgical consultation at our institution between July 2011 and July 2013 were prospectively recruited to undergo a contrast-enhanced MR imaging examination, including DCE-MR imaging for kinetic modeling of IA wall permeability to contrast agent. Patient demographics and clinical presentations were acquired by using the electronic medical data base of our institution. Major exclusion criteria were typical contraindications to MR imaging: pregnancy, contrast allergy, renal insufficiency, presence of MR imaging-incompatible implants, and prior IA treatment.

DCE-MR imaging-derived permeability metrics lack a recognized imaging standard of reference. To place reported permeability values in physiologic perspective, previous studies presented derived lesion values with a paired internal control, typically healthy tissue¹⁰⁻¹² (expected to have virtually no permeability) or the choroid plexus¹³ (lacks a blood-brain barrier, with high contrast-uptake rates).¹⁴ We followed a similar approach and present our reported aneurysm wall permeability values with those from paired healthy proximal segments of the middle cerebral artery and the choroid plexus.

Imaging Protocol

All patients were scanned on 3T (Magnetom Trio; Siemens, Erlangen, Germany) or 1.5T (Avanto; Siemens) MR imaging scanners. A 3D time-of-flight MRA sequence was used to localize the IA. IA wall permeability was measured by using a standard DCE-MR imaging protocol. DCE-MR images were acquired by using a standard multiphase 3D gradient-recalled-echo-based pulse sequence that provided volumetric T1-weighted images every 5–8 seconds after contrast agent injection for approximately 10 minutes. Images were acquired by using the following parameters: TR/TE = 2.84/0.8 ms, matrix = 128 × 128–384 × 384, FOV = 190–220 mm, and 24 partitions placed to cover the IA, resulting in voxel dimensions of 0.58 × 0.58 × 2.0 mm—1.48 × 1.48 × 5.0 mm. Section thickness was adjusted from 5 to 2 mm to prevent partial volume contamination for smaller aneurysms. A single dose (0.1-mmol/kg) of T1-shortening contrast agent (gadopentetate dimeglumine, Magnevist; Bayer HealthCare Pharmaceuticals, Wayne, New Jersey) was injected during the DCE acquisition. Precontrast T1 values (T_{10}) of the tissue were found by using a commonly used multi-flip angle routine ($\alpha = 5^\circ, 10^\circ, 12^\circ, 15^\circ, 20^\circ, 25^\circ$) to fit the spoiled gradient-echo equation.^{15,16}

$$1) \quad S(\alpha) = A \sin \alpha \frac{1 - \exp(-TR/T_{10})}{1 - \cos \alpha \exp(-TR/T_{10})}$$

Permeability Modeling

The permeability-limited Modified Tofts Model¹⁷ quantifies the kinetics of a tracer leaking through a semipermeable membrane with the following relationship:

$$2) \quad C(t) = K^{\text{trans}} \int_0^t e^{-k_{\text{ep}}(t-\tau)} C_p(t) d\tau + V_p C_p(t),$$

with K^{trans} dictating the tracer transfer rate from the intravascular into the extracellular extravascular space with units of minute^{-1} ; $k_{\text{ep}} = K^{\text{trans}}/V_L$ in units of minute^{-1} , describing the ratio of the transfer rate (K^{trans}) to the fractional volume of tracer in the extracellular extravascular space (V_L); $C_p(t)$, the intravascular tracer concentration; and V_p , the fractional plasma volume for each voxel. $C(t)$ is measured adjacent to the aneurysm wall in the CSF. A Levenberg-Marquardt algorithm was used to find the K^{trans} , V_L , and V_p in Equation 2 that best fits the measured signal $C(t)$ (Fig 1).

Data Analysis and Imaging Evaluation

A neuroradiologist (S.A.A.) classified IA locations (anterior-versus-posterior circulation as per ISUIA) and smooth-versus-

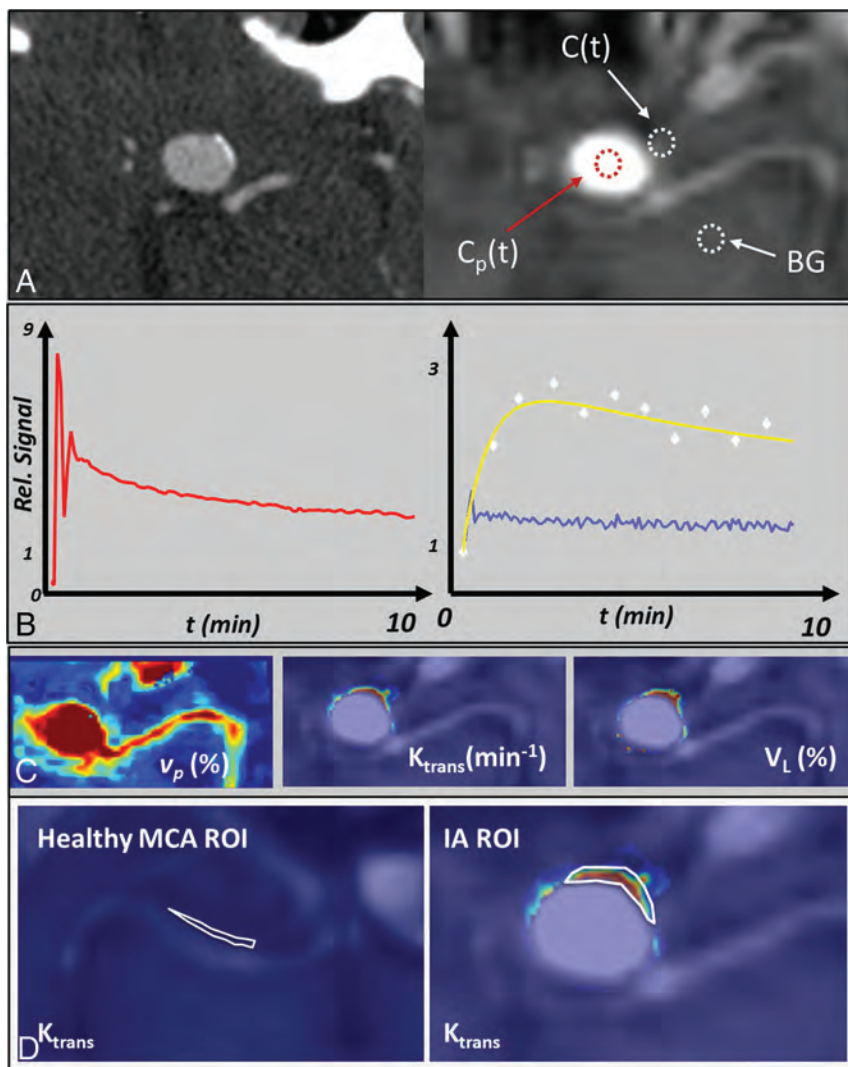


FIG 1. Aneurysm permeability modeling in a 14-mm right ICA aneurysm. In the IA, the signal time course from DCE imaging (A) is used to measure the plasma concentration, $C_p(t)$ (red curve, B). The permeability signal, $C(t)$, is subsequently modeled and fit for every voxel to Equation 2. The signal from a single voxel selected from the white circled region adjacent to the IA (white diamonds, B) and fit (yellow curve, B) are shown. The fitting of all voxels derives permeability parameters (K^{trans} , V_L , and V_p , C). Note the observed signal next to the aneurysm has nearly 3-fold the signal intensity as background (BG) enhancement (blue curve, B). ROIs were placed adjacent to a healthy artery (left panel, D) and the area of highest permeability, next to the IA (right panel, D).

irregular morphology (asymmetries, daughter sacs, blebs, or protrusions) and measured size indices, such as dome height, width, and neck diameter, by using available cross-sectional CTA and 3D rotational DSA datasets on a multiplanar postprocessing Leonardo workstation (Siemens).

Mean values of K^{trans} and V_L were calculated in ROIs containing a minimum of 10 pixels, adjacent to the aneurysm wall. A neuroradiologist (S.A.) and MR imaging physicist (T.J.C.), blinded to the patient clinical data and MR imaging results and each with >10 years of experience in MR image analysis, independently placed ROIs on a single section containing the aneurysm that had the highest permeability values observed (Fig 1D). Scores from both reviewers were averaged to determine the mean permeability for each aneurysm. In the event that there was not significant agreement between observers, IA data would be evaluated independently for each observer. To exclude intraluminal tissue in

K^{trans} modeling, we considered only voxels with a corresponding V_p smaller than 0.5 ($V_p < 0.5$) (ie, the DCE signal of the voxel could not have >50% vascular contamination). Mean K^{trans} and V_L values were also measured adjacent to the wall of a healthy MCA (Fig 1D) and the choroid plexus in each patient as a paired internal control. Permeability modeling and analysis were performed by using in-house software developed in Matlab (MathWorks, Natick, Massachusetts).

Statistical Analysis

Interobserver agreement in measured permeability values was compared by using the Mann-Whitney U Test for continuous variables, linear regression, intraclass correlation statistics, and Bland-Altman analysis. We compared average aneurysm K^{trans} and V_L measurements with those from the paired control MCA and choroid plexus by using paired Student t tests to determine whether our DCE aneurysm measurements were significantly different.

We evaluated wall permeability as a marker of IA rupture risk by comparing it against established clinical and anatomic/imaging metrics. First, IAs were grouped into ISUIA-determined size-based risk categories (<7, 7–12, 13–24, and ≥ 25 mm) and were compared with DCE parameters (K^{trans} , V_L) by using a regression model. Second, IAs were classified into high-risk and low-risk categories by using 2 size-independent risk assessment paradigms. In clinical risk paradigm A, high-risk aneurysms were those that presented with neurologic symptoms relevant to the location of the

aneurysm (headaches, mass effect, cranial neuropathy); asymptomatic aneurysms were low-risk. In risk paradigm B, high-risk aneurysms had 1 of the following 4 imaging/anatomic properties: 1) multilobulated dome or blebs as defined by DSA or CTA, 2) patient presenting with multiple IAs, or 3) located in the posterior circulation; all others were defined as low-risk. Size indices were not used to define the risk profile for any aneurysm in group A or B.

Separate univariate logistic regression analyses were performed for groups A and B. High- and low-risk groups were compared with aneurysm size indices (aspect ratio, maximum IA dome size, neck diameter) and DCE parameters. Patient demographics (age/sex), history of hypertension, hyperlipidemia, tobacco/alcohol abuse, and statin use have been identified by ISUIA as clinical risk contributors to IA rupture. These known risk fac-

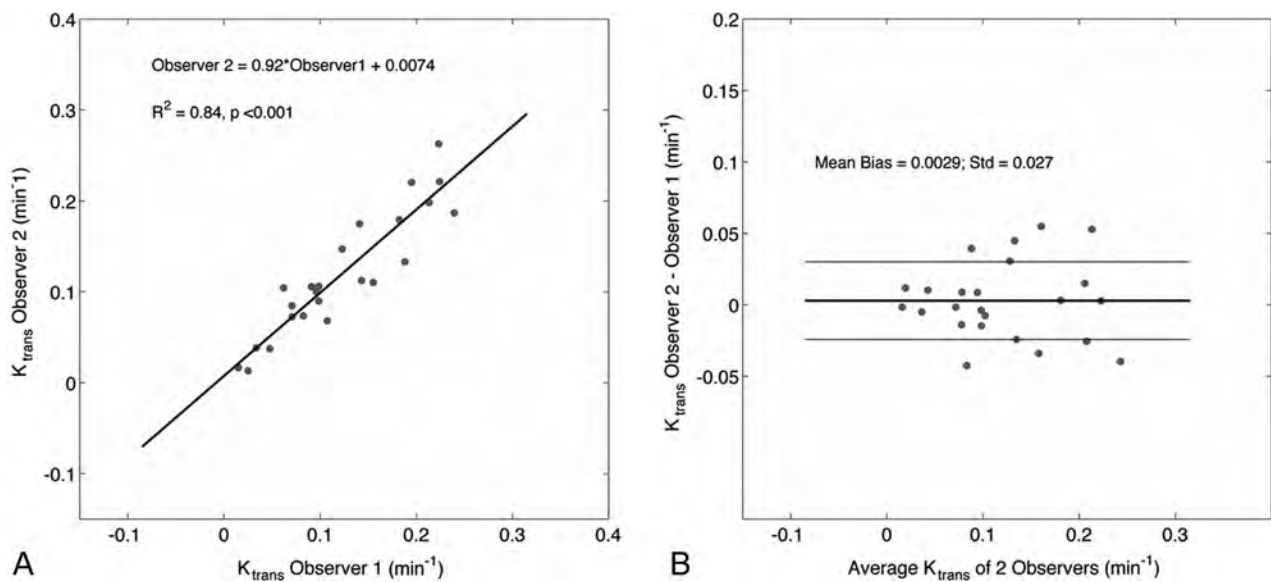


FIG 2. Correlation and Bland-Altman analysis between measured K^{trans} values of both observers reveal strong agreement in derived values. V_L is not shown.

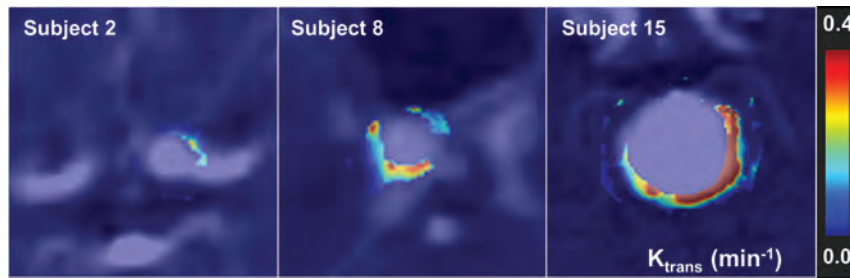


FIG 3. DSA and K^{trans} permeability images demonstrate a broad distribution of wall permeability values. Notice the heterogeneity in K^{trans} both among subjects and within a single IA.

tors were also subjected to univariate logistic regression analysis. Candidate variables for multiple logistic regression analysis were selected on the basis of statistically significant univariable relationships. Multivariable logistic regression analysis was then performed to evaluate independent predictors of risk in the aforementioned risk paradigms/groups. Significance was defined as $<.05$ in all statistical tests.

RESULTS

Patient Demographics

Twenty-five consecutive patients consented to participate in the study and were scanned. Two patients were excluded for the following reasons: significant susceptibility artifacts from a pre-existing intracranial stent ($n = 1$) and severe patient motion during the study ($n = 1$) rendering images nondiagnostic. In total, 27 aneurysms in 23 patients (mean age, 60.7 ± 12.2 years; age range, 30–82 years), 13 women (mean age, 58.8 ± 12.9 years; range, 30–76 years) and 10 men (mean age, 63.1 ± 11.5 years; range, 39–8 years) were included in the study. There was no significant difference between men and women in age ($P = .42$), K^{trans} ($P = .84$), V_L ($P = .91$), or IA size ($P = .65$). All IAs were unruptured when imaged. The On-line Table provides relevant patient demographics, risk factors, and risk-group assignment. Note that the column labeled “Sx

(Group A)” denotes IAs that are symptomatic and therefore in risk category A. Three aneurysms in our cohort were fusiform, and 24 were saccular. To control for potentially different pathology, we performed statistical analyses on saccular and fusiform aneurysms separately. As a result, fusiform IA imaging markers were not used for risk analysis.

Imaging Findings

Interobserver agreement in measurements of K^{trans} and V_L was strong. Independent measurements made by 2 observers were not statistically different from one another (K^{trans} , $P = .89$; V_L , $P = .86$, Mann-Whitney U Test). Furthermore, intraclass correlation coefficients between the 2 observers showed strong and highly significant agreement (K^{trans} : intraclass correlation coefficient = 0.93, $P < .001$; V_L : intraclass correlation coefficient = 0.92, $P < .001$). In Fig 2, measured K^{trans} and V_L values from both observers were highly correlated (K^{trans} : $R^2 = 0.84$, slope = 0.92, intercept = 0.007; V_L : $R^2 = 0.92$, slope = 1.08, intercept = -0.013 , data not shown), and Bland-Altman analysis revealed a small mean bias and little variability over a broad range of values (bias \pm SD: $K^{\text{trans}} = 0.003 \pm 0.03$ minute $^{-1}$; $V_L = 0.3\% \pm 4\%$, data not shown).

Aneurysms were found to have a broad range of associated wall permeability values as shown in a series of 3 subjects in Fig 3. Figure 4 shows a representative case of a 14-mm aneurysm in a 61-year-old man. Initial imaging with DSA and CTA confirmed the presence of a smooth, regular saccular aneurysm of the posterior communicating artery. At the same time, K^{trans} imaging showed an inhomogeneous presentation of contrast agent leakage with $K^{\text{trans}} = 0.22$ minutes $^{-1}$ and 0.19 minutes $^{-1}$ in the anterior (Fig 4C, top arrow) and posterior (Fig 4C, bottom arrow) walls, respectively. The patient elected to forgo treatment. Eighteen months after initial imaging, follow-up CTA was acquired due to

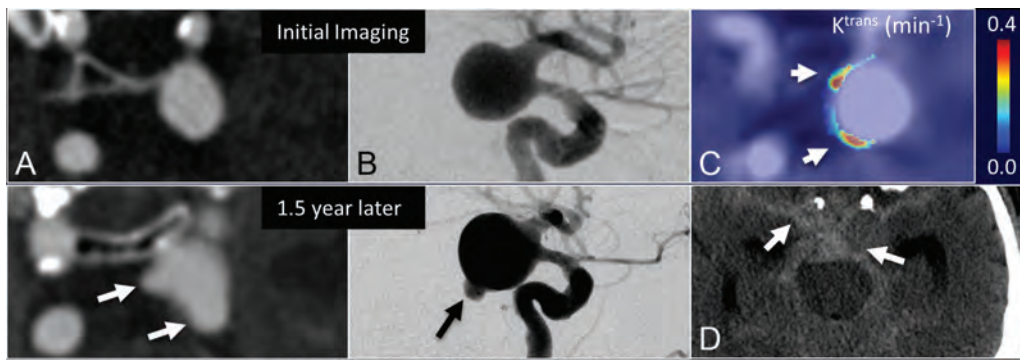


FIG 4. The evolution of an untreated posterior communicating artery IA in a 61-year-old man demonstrates that elevated K^{trans} at baseline correlated with bleb formation. Morphologic changes during 1.5 years are observed on CTA (A) and DSA (B); however, DCE-MR imaging demonstrates 2 regions with high K^{trans} (arrows, C) at the time of imaging—apparently correlating with eventual SAH seen on CT (arrows, D).

symptom onset consistent with SAH. CTA and DSA demonstrated extensive intracranial bleeding deemed to be resulting from 2 newly observed daughter sacs coincidental with areas of prior elevated K^{trans} .

DCE Sensitivity to Pathology

We found that the K^{trans} associated with saccular aneurysm walls was larger than values observed in the normal-appearing MCA (mean, 0.1219 ± 0.0130 minutes⁻¹ versus 0.0053 ± 0.0007 minutes⁻¹, respectively; $P < .001$) and smaller than values found in the choroid plexus (mean, 0.4058 ± 0.0567 minutes⁻¹; $P < .001$). There was a significant difference between saccular IA V_L and that of the parent artery (mean, $13.2\% \pm 2.3\%$ versus $1.3\% \pm 0.2\%$; $P = .0014$), but not between IA V_L and the choroid plexus (mean, $13.5\% \pm 3.7\%$; $P = .85$). Fusiform IAs K^{trans} (mean, 0.0444 ± 0.0065 minutes⁻¹) was significantly larger than that in healthy vessels ($P < .001$) and smaller than that in the choroid plexus ($P = .035$). Similarly, fusiform IA V_L (mean, 8.1 ± 2.3 minutes⁻¹) was larger than that of healthy vessels ($P < .001$) and less, though not significantly, than the V_L measured in the choroid plexus. Fusiform IA K^{trans} and V_L were smaller than saccular IA K^{trans} and V_L , but not significantly ($P = .06$ and $.48$, respectively).

Statistical Analysis of Risk

Linear regression analysis demonstrated that mean aneurysm K^{trans} values increased linearly with successively larger aneurysm-size risk bins (<7, 7–12, 13–24 mm), defined by the ISUIA and shown in Fig 5. In this regression model, the coefficients increased linearly for successive size bins (0.075, 0.1205, and 0.1650; $P < .0001$; $R^2 = 0.74$). A similar regression model with V_L showed no significant increase between healthy vessels and the <7-mm group (coefficient = 0.059, $P = .11$), while the increase for the 7- to 12-mm and 13- to 24-mm groups was 0.1175 ($P = .004$) and 0.1958 ($P < .001$), respectively ($R^2 = 0.44$). A simple linear regression model by using permeability parameters as a response and size of the IA as a predictor showed that for every millimeter increase in IA size, the average K^{trans} increased by 0.005 minutes⁻¹ with a standard error of 0.002 ($P = .02$). IA size and V_L did not have a significant linear correlation ($P = .16$). IA neck diameter and aspect ratio did not have a significant correlation with K^{trans} ($P = .06$ and $P = .15$, respectively) or V_L ($P = .37$ and $.30$, respectively).

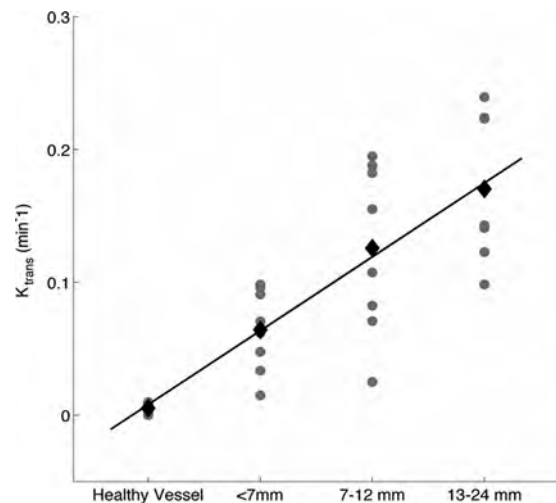


FIG 5. Mean K^{trans} and V_L values (black diamonds) increase linearly with larger ISUIA-determined size/risk bins (<7, 7–12, and 13–24 mm) as shown in the scatterplot. Note that our cohort did not contain aneurysms in the >25-mm size/risk bin. The gray circles represent individual IA permeability values. The black diamonds are the mean for each size bin.

The Table shows the results of univariate and multivariate logistic regression comparing ISUIA-identified clinical risk factors, aneurysm size, neck, aspect ratio, K^{trans} , and V_L in their ability to predict high-risk saccular IAs in groups A, B, and AB (A or B). Within group A, only size and K^{trans} showed significant univariate relationships ($P < .05$). In all risk-assessment paradigms, K^{trans} had the greatest effect in predicting risk. When risk was based on anatomic and imaging markers in group B, K^{trans} was both statistically significant and more effective in predicting a high-risk saccular IA. Most important, when both groups A and B were combined, then a 0.1-minute⁻¹ increase in K^{trans} conferred a 74.3996 increase in the likelihood that the IA was either symptomatic or had high-risk imaging/anatomic features outlined above ($P = .03$), while size had a smaller and statistically insignificant effect ($P = .40$).

DISCUSSION

We have demonstrated the feasibility of a new imaging marker for the evaluation of intracranial aneurysms. We found that K^{trans} and V_L are elevated from baseline across all aneurysms relative to

Results of univariate and multivariate logistic regression of demographic and imaging markers against size-independent risk paradigms^a

	Group A (High Risk = 7, Low Risk = 17)			Group B (High Risk = 15, Low Risk = 9)			Group AB (High Risk = 17, Low Risk = 7)		
	P Value	Coefficient	Standard	P Value	Coefficient	Standard	P Value	Coefficient	Standard
			Error			Error			Error
Univariate analysis									
Sex	.4092	-0.7985	0.9675	.5231	0.5596	0.8763	.9395	-0.0690	0.9090
Age	.4463	-0.0302	0.0396	.1687	0.0563	0.0409	.9774	-0.0011	0.0401
HTN ^b (n = 19)	.9999	27.4910	3.32E + 05	.2560	1.1787	1.0377	.1073	1.7272	1.0724
HLD (n = 17)	.3205	1.1856	1.1934	.2115	1.1632	0.9309	.3504	0.8910	0.9541
Statins (n = 12)	.4784	0.6444	0.9090	.9158	0.0896	0.8473	.8511	0.1699	0.9052
Tobacco									
Current use (n = 5)	.5526	0.6242	1.0511	.9999	27.93	3.32E + 05	.9999	27.4937	3.32E + 05
Past use (n = 11)	.4784	0.6444	0.9090	.9158	0.0896	0.8473	.8511	0.1699	0.9052
Alcohol ^c (n = 3)	.8654	0.2231	1.3166	.2897	-1.3863	1.3093	.1620	-1.1856	1.3276
Imaging markers (n = 24)									
IA size	.0182 ^d	0.2877 ^d	0.1222 ^d	.9583	-0.0036	0.0695	.3962	0.0764	0.0900
IA neck	.0616	0.5743	0.3072	.6545	-0.1061	0.2370	.5223	0.1880	0.2938
K ^{trans}	.0280 ^d	19.5088 ^d	8.8789 ^d	.0243 ^d	23.6481 ^d	10.4975 ^d	.0286 ^d	36.5083 ^d	16.6795 ^d
Aspect ratio	.1074	1.2814	0.7959	.627	0.2073	0.4266	.4511	0.4385	0.5819
V _L	.2286	4.5210	3.7548	.4176	3.3395	4.1195	.3632	4.4843	4.9321
Multivariate analysis									
IA Size	.0337	0.2448	0.1153	.1534	-0.1591	0.1114	.4435	-0.0817	0.1066
K ^{trans}	.1339	18.5544	12.3781	.0231 ^d	33.9634 ^d	14.9545 ^d	.0346 ^d	43.0945 ^d	20.3981 ^d

Note:—HTN indicates hypertension; HLD, hyperlipidemia.

^a Analysis performed on 24 saccular IAs.

^b All patients' hypertension was under control using medication.

^c Current use.

^d Significant ($P < .05$).

normal-appearing arteries. Furthermore, K^{trans} correlates positively with size, morphologic properties, and symptomatology. Logistic regression analysis indicates that K^{trans} may be an independent indicator of rupture risk.

Aneurysm size is one of the most fundamental indications of rupture risk, as found by the ISUIA² and Unruptured Cerebral Aneurysm Study (UCAS).¹⁸ prospective studies, and is frequently used clinically to determine surgical-versus-medical management. Nevertheless, many studies have indicated that various factors independent of IA size are associated with progressing IA pathology and rupture, including other anatomic metrics (morphology, location, multiplicity, aspect ratios, and orientation of the parent artery), clinical risk factors (hypertension, smoking, alcohol/drug abuse, inherited connective tissue diseases), symptomatology, inflammation (matrix metalloproteinases, macrophage infiltration), and hemodynamic flow and stress properties.

In our study, we found that K^{trans} was a strong, significant, and independent determinant of rupture risk based on anatomic and combined clinical/anatomic high-risk subgroups. Aneurysm size was only a statistically significant and independent predictor of rupture risk in the clinically symptomatic subgroup (group A), intuitively due to the effect of aneurysm size on mass effect, but not in the high-risk anatomic subgroup (group B). This difference may indicate that K^{trans} provides clinically relevant information about IA vascular pathology related to high-risk morphologic features, location, and multiplicity (vascular wall predisposition to IA development/progression) that are independent of size. Whether these results independently confer an increased rupture risk or define progressive thinning of an aneurysm wall requires larger prospective patient studies and/or direct intraoperative observation with histologic samples from surgically harvested tissue.

DCE-MR imaging permeability parameters lack a recognized standard of reference; however, we were able to provide internal reference values. In fact, previous studies have paired lesion permeability parameters with a paired internal control such as healthy tissue or the choroid plexus. We followed a similar methodology in our study, and our results closely corroborate the values reported by other groups for permeability in healthy tissue (negligible or zero¹²⁻¹⁴) and K^{trans} values ranging from 0.2 to 0.5 minutes⁻¹ in the choroid plexus.¹⁵

Relevance to Flow Modeling

Hemodynamic flow patterns play an important role in the formation, growth, and eventual rupture of aneurysms. As such, advanced imaging techniques such as 4D-flow^{12,19} and postprocessing algorithms in computational fluid dynamics²⁰ are active areas of research. These studies have shown that local variations of hemodynamic stresses can induce vascular injury,²¹ causing inflammatory responses,²² which, in turn, can lead to internal elastic lamina and tunica thinning, macrophage infiltration,^{23,24} and extracellular matrix remodeling. The net effect is a modification in wall uniformity and thickness, which is readily visible intraoperatively,⁷ though not easily visualized noninvasively. We see DCE-MR imaging playing a role complementary to hemodynamic imaging in this regard. Several studies have already demonstrated that pathologic changes in cervical vessel walls and inflammatory factors correlate with changes in K^{trans} . For example, Kerwin et al²⁵ demonstrated that K^{trans} , by using DCE-MR imaging, had a strong linear correlation with macrophage infiltration in carotid atherosclerotic plaques on histopathologic analysis. As such, DCE-MR imaging may provide important information about a significant component of aneurysm disease—structural

and biologic changes in the wall.²⁵ A future correlation of K^{trans} IA wall permeability with computational fluid dynamics or 4D-flow MR imaging may assist in identifying focal aneurysm regions of high risk or stress.

Limitations

Several limitations were identified in this study. Data were collected from a single center, exposing us to biases in the patient population available at our institution. Furthermore, we were limited to a sample size of 27 aneurysms in this proof-of-principle pilot study. In future studies, we expect to follow untreated IAs for several years and compare DCE metrics of those that progress against those that remain stable. In the future, larger sample sizes must be followed for several years to determine whether contrast agent leakage can be used as an independent or adjunctive predictor of rupture risk.

CONCLUSIONS

In this pilot study, we report the first evidence of DCE-MR imaging-modeled contrast permeability in IAs. We modeled the rate of contrast agent permeability across the IA wall and found that it correlated significantly with size-based and size-independent anatomic/imaging features and clinical assessments of rupture risk. In addition, high-risk aneurysms had higher contrast permeability rates than lower risk aneurysms. More studies comparing K^{trans} in aneurysms with other clinical and hemodynamic risk factors and histopathologic correlation will provide greater insight into the clinical interpretation of K^{trans} and its reflection on aneurysm wall pathology.

Disclosures: Parmede Wakil—RELATED: Grant: National Institutes of Health.* Bernard Bendok—UNRELATED: Grants/Grants Pending: MicroVention.* Comments: support for clinical trial: New Generation Hydrogel Endovascular Aneurysm Treatment Trial. *Money paid to the institution.

REFERENCES

1. Weir B. **Unruptured intracranial aneurysms: a review.** *J Neurosurg* 2002;96:3–42
2. Wiebers DO, Whisnant JP, Huston J 3rd, et al; International Study of Unruptured Intracranial Aneurysms Investigators. **Unruptured intracranial aneurysms: natural history, clinical outcome, and risks of surgical and endovascular treatment.** *Lancet* 2003;362:103–10
3. Ishibashi T, Murayama Y, Urashima M, et al. **Unruptured intracranial aneurysms: incidence of rupture and risk factors.** *Stroke* 2009;40:313–16
4. Juvela S, Porras M, Poussa K. **Natural history of unruptured intracranial aneurysms: probability of and risk factors for aneurysm rupture.** *J Neurosurg* 2008;108:1052–60
5. Frösen J, Piippo A, Paetau A, et al. **Remodeling of saccular cerebral artery aneurysm wall is associated with rupture: histological analysis of 24 unruptured and 42 ruptured cases.** *Stroke* 2004;35:2287–93
6. Dumont AS, Lanzino G, Kassell NF. **Unruptured aneurysms.** *J Neurosurg* 2002;96:52–56; discussion 58–60
7. Kadasi LM, Dent WC, Malek AM. **Cerebral aneurysm wall thickness analysis using intraoperative microscopy: effect of size and gender on thin translucent regions.** *J Neurointerv Surg* 2013;5:201–06
8. Kecskemeti S, Johnson K, Wu Y, et al. **High resolution three-dimensional cine phase contrast MRI of small intracranial aneurysms using a stack of stars k-space trajectory.** *J Magn Reson Imaging* 2012;35:518–27
9. Raschi M, Mut F, Byrne G, et al. **CFD and PIV analysis of hemodynamics in a growing intracranial aneurysm.** *Int J Numer Method Biomed Eng* 2012;28:214–28
10. Provenzale JM, Wang GR, Brenner T, et al. **Comparison of permeability in high-grade and low-grade brain tumors using dynamic susceptibility contrast MR imaging.** *AJR Am J Roentgenol* 2002;178:711–16
11. Jia Z, Geng D, Liu Y, et al. **Low-grade and anaplastic oligodendrogliomas: differences in tumour microvascular permeability evaluated with dynamic contrast-enhanced magnetic resonance imaging.** *J Clin Neurosci* 2013;20:1110–13
12. Cha S, Yang L, Johnson G, et al. **Comparison of microvascular permeability measurements, K^{trans} , determined with conventional steady-state T1-weighted and first-pass T2*-weighted MR imaging methods in gliomas and meningiomas.** *AJNR Am J Neuroradiol* 2006;27:409–17
13. Li KL, Zhu XP, Checkley DR, et al. **Simultaneous mapping of blood volume and endothelial permeability surface area product in gliomas using iterative analysis of first-pass dynamic contrast enhanced MRI data.** *Br J Radiol* 2003;76:39–50
14. Kilgore DP, Breger RK, Daniels DL, et al. **Cranial tissues: normal MR appearance after intravenous injection of Gd-DTPA.** *Radiology* 1986;160:757–61
15. Fram EK, Herfkens RJ, Johnson GA, et al. **Rapid calculation of T1 using variable flip angle gradient refocused imaging.** *Magn Reson Imaging* 1987;5:201–08
16. Deoni SC. **High-resolution T1 mapping of the brain at 3T with driven equilibrium single pulse observation of T1 with high-speed incorporation of RF field inhomogeneities (DESPOT1-HIFI).** *J Magn Reson Imaging* 2007;26:1106–11
17. Tofts PS, Brix G, Buckley DL, et al. **Estimating kinetic parameters from dynamic contrast-enhanced T(1)-weighted MRI of a diffusible tracer: standardized quantities and symbols.** *J Magn Reson Imaging* 1999;10:223–32
18. Zhu FP, Zhang LJ, Lu GM. **Unruptured cerebral aneurysms in a Japanese cohort.** *N Engl J Med* 2012;367:1267–68; author reply 1269
19. Schnell S, Ansari SA, Wakil P, et al. **Three-dimensional hemodynamics in intracranial aneurysms: influence of size and morphology.** *J Magn Reson Imaging* 2014;39:120–31
20. Cebral JR, Vazquez M, Sforza DM, et al. **Analysis of hemodynamics and wall mechanics at sites of cerebral aneurysm rupture.** *J Neurointerv Surg* 2014 May 14. [Epub ahead of print]
21. Mantha A, Karmonik C, Benndorf G, et al. **Hemodynamics in a cerebral artery before and after the formation of an aneurysm.** *AJNR Am J Neuroradiol* 2006;27:1113–18
22. Hashimoto T, Meng H, Young WL. **Intracranial aneurysms: links among inflammation, hemodynamics and vascular remodeling.** *Neurol Res* 2006;28:372–80
23. Hasan DM, Mahaney KB, Magnotta VA, et al. **Macrophage imaging within human cerebral aneurysms wall using ferumoxytol-enhanced MRI: a pilot study.** *Arterioscler Thromb Vasc Biol* 2012;32:1032–38
24. Aoki T, Kataoka H, Ishibashi R, et al. **Impact of monocyte chemoattractant protein-1 deficiency on cerebral aneurysm formation.** *Stroke* 2009;40:942–51
25. Kerwin WS, O'Brien KD, Ferguson MS, et al. **Inflammation in carotid atherosclerotic plaque: a dynamic contrast-enhanced MR imaging study.** *Radiology* 2006;241:459–68

Exploring the Value of Using Color-Coded Quantitative DSA Evaluation on Bilateral Common Carotid Arteries in Predicting the Reliability of Intra-Ascending Aorta Flat Detector CT–CBV Maps

Q. Zhang, R. Xu, Q. Sun, H. Zhang, J. Mao, T. Shan, W. Pan, Y. Deuerling-Zheng, M. Kowarschik, and J. Beilner

ABSTRACT

BACKGROUND AND PURPOSE: Cerebral blood volume, acquired with flat panel detector CT by injecting contrast medium into the ascending aorta, enabled real-time acquisition of brain functional information with remarkable reduction of contrast medium usage comparing to an intravenous injection approach. However, individual vasculature and flow variations cause inhomogeneous contrast medium distribution and unexpected asymmetric perfusion for certain patients even without cerebral circulatory disorders. This work aimed at testing the feasibility of using color-coded quantitative DSA to predict the reliability of flat panel detector CT–based CBV maps by injecting contrast medium into the ascending aorta by exploring the correlation between measurements of color-coded quantitative DSA and the symmetry of CBV maps.

MATERIALS AND METHODS: For 12 patients without perfusion-related cerebral abnormalities, color-coded quantitative DSA at the aortic arch and flat panel detector CT–based CBV maps by injecting contrast medium into the ascending aorta were acquired. In color-coded quantitative DSA, ROIs were defined on the bilateral common carotid arteries. Time-density curves were extracted, and area under the curve values were calculated. To evaluate brain perfusion symmetry, we defined ROIs on the anterior and middle cerebral artery territories in CBV maps, and quantitative CBV values were extracted.

RESULTS: Eight patients demonstrated good perfusion symmetry with relative CBV of 0.96 ± 0.06 , and their relative area under the curve was found to be 0.99 ± 0.02 . For the other 4 patients, CBV from the left hemisphere was significantly lower than that from the right with relative CBV of 0.81 ± 0.09 . This asymmetric perfusion was confirmed by the color-coded quantitative DSA with relative area under the curve values of 0.79 ± 0.03 .

CONCLUSIONS: This preliminary study showed good correlation between relative area under the curve from color-coded quantitative DSA and relative CBV from CBV maps. Color-coded quantitative DSA potentially helped sort out patients whose vascular anatomy could support reliable CBV acquisitions of flat detector CT by injecting contrast medium into the ascending aorta.

ABBREVIATIONS: AUC = area under the curve; CCA = common carotid artery; CCQ-DSA = color-coded quantitative DSA; CM = contrast medium; FPCT = flat panel detector CT; IA-FPCT-CBV = intra-ascending aorta CM injection to acquire FPCT CBV maps; rAUC = relative AUC; rCBV = relative CBV; TDC = time-density curve

Angiographic suites equipped with flat panel detector CT (FPCT) for clinical imaging practice have been increasingly accepted during neurointerventions. This technique offers significant advantages in patient management because the patient does not have to be transferred between different clinical units for diagnosis and treatment, improving clinical workflow and increas-

ing patient safety.^{1–3} Continuous development in imaging technology has led to significant improvement of image acquisition and postprocessing tools in FPCT. Recently, an important brain perfusion parameter, CBV (milliliter/1000 milliliter), can be acquired by using FPCT. It has been suggested that a color-coded CBV map, which displays hemodynamic information in the capillary level of the entire brain parenchyma, provides a measurement of regional CBV variations and information on suspected ischemia, which is of great value for patients with acute ischemic stroke.^{4,5} The CBV value measured with this technique has been validated in a number of clinical studies, proving that the CBV maps generated from FPCT correlated well with CT perfusion maps from multisection CT, which were regarded as ground truth.^{6–9} This technique offered the possibility of obtaining functional information and assessing the viability of the brain tissue during interventional procedures.¹⁰

Received July 21, 2014; accepted after revision October 21.

From the Beijing PLA Military General Hospital (Q.Z., R.X., H.Z., J.M., T.S., W.P.), Affiliated Bayi Brain Hospital, Beijing, China; Healthcare Sector (Q.S., J.B.), Siemens Ltd China, Beijing, China; and Siemens AG (Y.D.-Z., M.K.), Erlangen, Germany.

Please address correspondence to Qiang Zhang, MD, Beijing PLA Military General Hospital, Affiliated Bayi Brain Hospital, No. 5, Nanmencang, Dongcheng District, Beijing, 100700, China; e-mail: vivien-sun1226@hotmail.com; and Ruxiang Xu, MD, Beijing PLA Military General Hospital, Affiliated Bayi Brain Hospital, No. 5, Nanmencang, Dongcheng District, Beijing, 100700, China; e-mail: xuruxiang_bjjz@hotmail.com

<http://dx.doi.org/10.3174/ajnr.A4238>

Table 1: Patient diagnostic and treatment information

Patient No.	Age (yr)	Sex	DSA Diagnosis	Treatment
1	35	Female	Left internal carotid artery aneurysm	Stent-assisted coiling
2	49	Male	Left internal carotid artery aneurysm	Medication
3	46	Male	Sagittal sinus thrombus	Medication
4	43	Male	Sellar mass	–
5	54	Female	Subarachnoid hemorrhage	Medication
6	47	Male	Further investigation needed	Medication
7	50	Male	Mild stenosis on right vertebral artery	–
8	49	Male	Further investigation needed	–
9	37	Male	Further investigation needed	Medication
10	67	Male	Hemorrhage on left occipital lobe	Medication
11	51	Female	Further investigation needed	–
12	64	Female	Glomus jugulare tumor	Medication + lumbar puncture

Advancements in protocols of contrast medium (CM) injection and image acquisition have been further investigated to achieve an optimized whole-brain CBV map acquisition pipeline by using FPCT.^{11–14} A number of studies have demonstrated the feasibility of obtaining CBV maps via intravenous CM injection by using FPCT. However, with this injection protocol, the CM will be diluted during the transit, thus only a small portion of the injected CM contributed to the formation of CBV maps. In contrast, intra-arterial administration has become an attractive method to increase the CM delivery and efficiency and may provide a viable approach for reducing the amount of CM used during FPCT CBV imaging. The feasibility and clinical value of intra-ascending aorta CM injection to acquire FPCT CBV maps (IA-FPCT-CBV) have been tested and confirmed; this approach enabled remarkably reduced CM usage relative to the intravenous CM injection protocol (350 mg I/mL; total amount, 96 mL; 20% diluted versus 60–80 mL, nondiluted) by using FPCT. Moreover, the reliability of this intra-arterial injection approach has also been validated against conventional CT perfusion imaging with intravenous CM injection.¹⁵

However, nonuniform CM distribution could be observed for a number of patients even without cerebral circulatory disorders, causing unexpected asymmetric perfusion in 2 hemispheres, mainly in the territories of the anterior and middle cerebral arteries.^{15,16} A possible explanation for nonuniform distribution could be patients' individual vasculature variations at the aortic arch, high blood flow speed, and the limited length of the ascending aorta.

Currently, color-coded quantitative digital subtraction angiography (CCQ-DSA) could be generated from a conventional DSA sequence at no additional radiation exposure or CM use, which enhanced the recognition of hemodynamic and morphologic findings. This technique provides a means to display temporal information of contrasted blood flow and attenuation for the duration of the DSA acquisition in a single color-coded image. Moreover, this image allowed the creation of a time-density curve (TDC) of a CM bolus in user-defined regions, from which quantitative blood flow information could be also extracted.^{17–19}

This work aimed at exploring the correlation between measurement of CCQ-DSA on the main feeding arteries and symmetry of CBV maps and testing the feasibility of using CCQ-DSA to predict

the reliability of IA-FPCT-CBV on a patient-specific basis before the acquisition.

MATERIALS AND METHODS

Patient Selection

From January 2013 to November 2013, CCQ-DSA at the aortic arch and IA-FPCT-CBV were acquired for 12 patients (8 men, 4 women; mean age, 49.3 ± 9.4 years) without perfusion-related cerebral abnormalities. Detailed diagnostic and treatment information of each patient is listed in Table 1. This study was approved by the hospital ethics committee.

CCQ-DSA and CBV Map Generation

All patients received intravenous sedation and local anesthesia. The Seldinger technique was used to place a 5F sheath into the right femoral artery, and a 5F pigtail catheter was inserted and located at the ascending aorta. A routine conventional DSA sequence (7.5 frames/s) at the aortic arch was then acquired by using a rotational FPCT system (Artis zeego; Siemens, Erlangen, Germany). Thirty milliliters of nondiluted CM (350 mg I/mL) was injected by a power injector (600 psi, Avidia; Imaxeon, Silverwater, New South Wales, Australia) through the pigtail catheter at an injection rate of 15 mL/s. With a commercially available postprocessing software (syngo iFlow; Siemens), this DSA sequence was converted to a CCQ-DSA image, which quantitatively showed the blood flow dynamics.

In addition, a CBV map was acquired by using the same FPCT system. Twenty milliliters of CM diluted by 76 mL of saline to a total volume of 96 mL was injected with a rate of 6 mL/s during 16 seconds. The generation of the CBV map consisted of two 3D image-acquisition steps, including a mask run followed by a fill run. To ensure maximum brain tissue and intravascular contrast enhancement, we started the fill run with an 8-second x-ray delay. During the 3D image acquisition, the C-arm rotated for 200° in 8 seconds, with an angle increment of 0.5°. A total of 397 projection images were generated with an x-ray dose of 0.36 μGy/frame. The reconstruction was performed by using commercially available software (syngo DynaPBV Neuro; Siemens). The fully automatic reconstruction algorithm has been extensively described in detail in another work.²⁰

Quantitative Evaluation

The CCQ-DSA and CBV imaging results were quantitatively reviewed by 2 experienced neuroradiologists, respectively.

On the basis of the DSA sequence (Fig 1A), rectangular ROIs were defined on symmetric bilateral common carotid arteries (CCAs) on the generated CCQ-DSA image. The ROIs were placed approximately 8–10 cm away from the aortic arch, with their sizes approximately 0.02 cm². This selected ROI area could completely cover the artery cross-sections in the radial direction for a short distance, thus having minimal influence from superimposing vessels (Fig 1B). The corresponding TDCs, determined by the number and intensity of colored pixels inside the ROI, were extracted (Fig 1C). The area under curve (AUC) could be calculated from

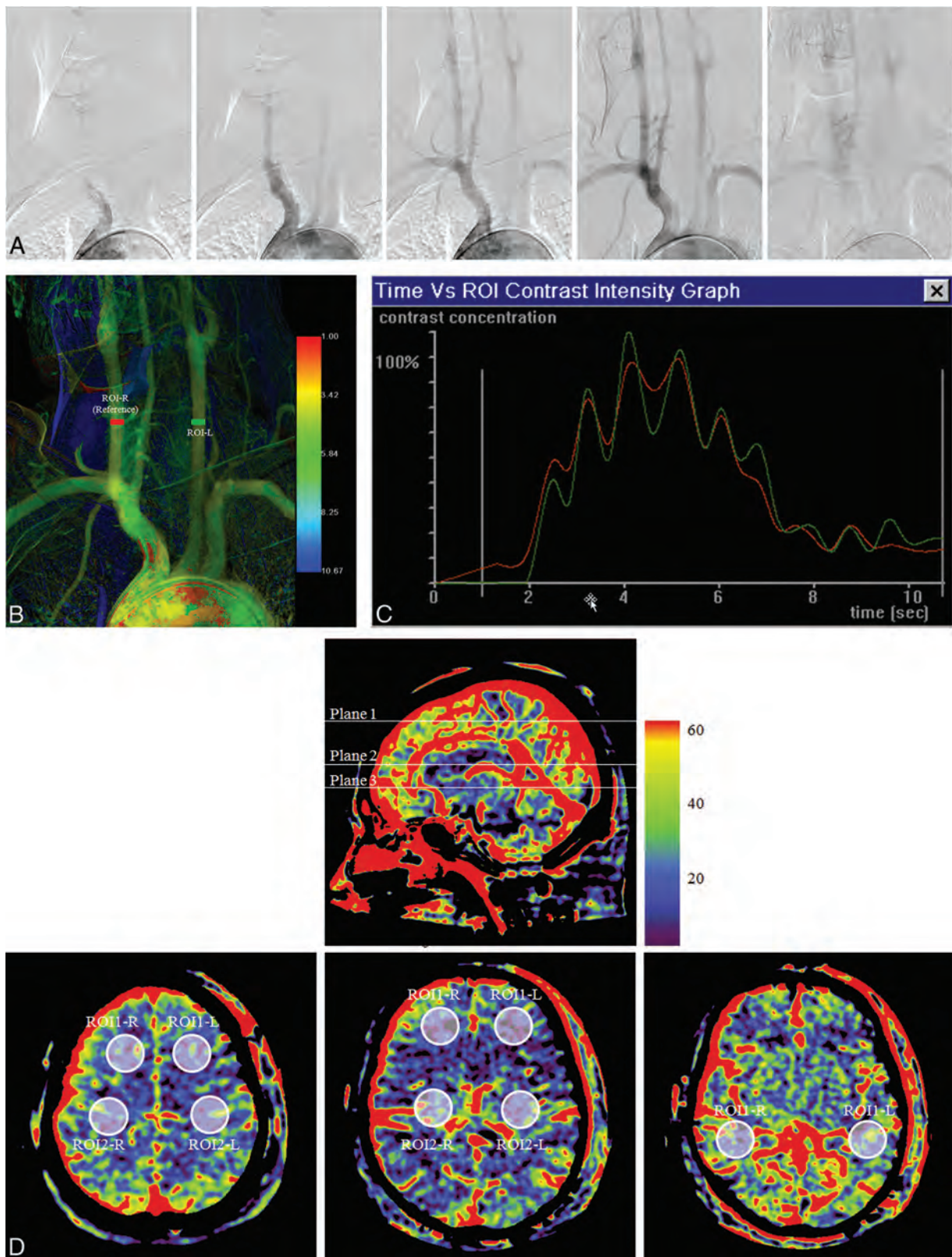


FIG 1. As an example, in patient 5, a conventional DSA sequence at 5 time instances shows the course of CM passing through the aortic arch and its major branching arteries (A). In the generated CCQ-DSA image, ROIs are defined on bilateral CCAs as red (ROI-R) and green (ROI-L) rectangles (B). Corresponding TDCs were extracted from the defined ROI, showing good correlation between the 2 curves (C). On the CBV maps (D), 3 planes were selected (upper panel). The lower panel corresponded to the above planes (left, plane 1; middle, plane 2; right, plane 3), with ROIs defined in pairs (ROI-R on the right hemisphere and ROI-L on the left hemisphere) on each plane covering characteristic anatomic structures to examine rCBV on 2 hemispheres: the frontal and parietal lobes in plane 1; frontal lobe and basal ganglia region in plane 2; and temporal lobe in plane 3.

the TDC, indicating the amount of contrasted blood flowing through the selected ROI during the image acquisition. The AUC of the TDC on the right CCA was regarded as the baseline and was set as reference value 1, and the AUC of the TDC on the left CCA was calculated relative to it. Next, the ratio between the AUC extracted from 2 CCAs, called relative AUC (rAUC), was then obtained by

$$1) \quad rAUC = AUC_{\text{left CCA}} / AUC_{\text{right CCA}}$$

where $AUC_{\text{left CCA}}$ and $AUC_{\text{right CCA}}$ were the areas calculated under the TDC profile from the ROI on the left and the right CCA, respectively.

To evaluate the symmetry of brain perfusion, we selected 3 anatomically characteristic planes crossing the frontal, parietal, and temporal lobes and basal ganglia regions. Circular ROIs with an area of approximately 3.0 cm² were manually defined on axial planes to cover the anterior and middle cerebral artery territories of both hemispheres, with major vessels excluded (Fig 1D). A spatially averaged CBV value in the ROI was extracted, and relative CBV (rCBV) values were then calculated by

$$2) \quad rCBV = CBV_{\text{left hemisphere}} / CBV_{\text{right hemisphere}}$$

Table 2: From the CCQ-DSA images, AUC values calculated for TDCs extracted from ROIs on bilateral CCAs and the AUC ratio between left and right sides

Patient No.	AUC-ROI-R (Reference)	AUC-ROI-L	rAUC
1	1	1.02	1.02
2	1	1.01	1.01
3	1	1.01	1.01
4	1	0.98	0.98
5	1	1.01	1.01
6	1	1.03	1.03
7	1	0.98	0.98
8	1	0.76	0.76
9	1	0.83	0.83
10	1	0.80	0.80
11	1	0.76	0.76
12	1	0.97	0.97

Note:—R indicates right; L, left.

Table 3: Quantitative CBV measurement and perfusion symmetry of patients

Planes	Patient No.											
	1	2	3	4	5	6	7	8	9	10	11	12
Plane 1												
ROI1-R	29	26	27	26	16	18	18	20	23	23	26	20
ROI1-L	28	25	27	24	15	19	18	19	19	22	22	18
rCBV	0.97	0.96	1.00	0.92	0.94	1.06	1.00	0.95	0.83	0.96	0.85	0.90
ROI2-R	22	21	23	19	20	20	17	22	25	16	25	17
ROI2-L	23	20	20	17	20	20	17	15	21	14	28	18
rCBV	1.05	0.95	0.87	0.89	1.00	1.00	1.00	0.68	0.84	0.88	0.72	1.06
Plane 2												
ROI1-R	14	25	20	19	10	13	16	22	24	15	23	18
ROI1-L	14	23	22	20	10	12	16	20	20	14	16	19
rCBV	1.00	0.92	1.10	1.05	1.00	0.92	1.00	0.91	0.83	0.93	0.70	1.06
ROI2-R	29	27	33	34	14	28	28	35	30	34	33	31
ROI2-L	27	24	31	30	13	26	29	27	23	26	27	28
rCBV	0.93	0.89	0.94	0.88	0.93	0.93	1.04	0.77	0.77	0.76	0.82	0.90
Plane 3												
ROI1-R	17	25	24	25	14	21	20	20	20	24	25	23
ROI1-L	17	23	22	23	14	20	19	16	17	20	20	22
rCBV	1.00	0.92	0.92	0.92	1.00	0.95	0.95	0.80	0.85	0.83	0.80	0.96
rCBV with most asymmetry	0.93	0.89	0.87	0.88	0.93	0.92	0.95	0.68 ^a	0.77 ^a	0.76 ^a	0.70 ^a	0.90

^a Significant asymmetric perfusion was detected.

where $CBV_{\text{left hemisphere}}$ and $CBV_{\text{right hemisphere}}$ were the mean CBV values extracted from the ROIs on the left and the right hemispheres, respectively. Thus, perfusion symmetry (1.0 for perfect symmetry) in different anatomic regions could be quantitatively examined.

RESULTS

IA-FPCT-CBV was technically successful, and all the resulting image quality was adequate for evaluation. No adverse physiologic changes caused by CBV map acquisitions were detected for any patient. From the CCQ-DSA images, AUC values for bilateral CCA were extracted from the TDC and are summarized in Table 2. Quantitative CBV evaluation results are listed in Table 3.

For patients 1–7 and 12, CCQ-DSA evaluation showed rAUC values of 0.99 ± 0.02 . From CBV maps, rCBV was found to be 0.96 ± 0.06 . An exemplary case (patient 5) was shown in Fig 1. There was good correlation between the profiles of the TDC extracted from the 2 ROIs, including the wash-in, wash-out phase; pulsatile flow pattern; peak intensity; and duration of contrast enhancement. On the generated CBV maps, correspondence on the perfusion level on 2 hemispheres was visually evident. Quantitative CBV evaluation was performed in 3 planes in the ROIs defined at the frontal, parietal, and temporal lobes and basal ganglia; this evaluation also showed excellent perfusion symmetry for each pair of ROIs.

In 4 patients (patients 8–11), inhomogeneous CM distribution on bilateral CCAs, with an rAUC value of 0.79 ± 0.03 could be observed. Table 3 shows that CBV from the left hemisphere was significantly lower than that from the right hemisphere in certain regions for these patients with an rCBV of 0.81 ± 0.09 . Imaging results of patient 11 are shown as an exemplary case (Fig 2). Differences could be easily detected for TDC comparison. Although the shape of 2 TDCs remained similar, the magnitude was much lower for the curve from the left CCA, resulting in an AUC deviation of 24%. Large CBV variations in multiple regions on 2 hemispheres could be also detected by visual inspection on the CBV

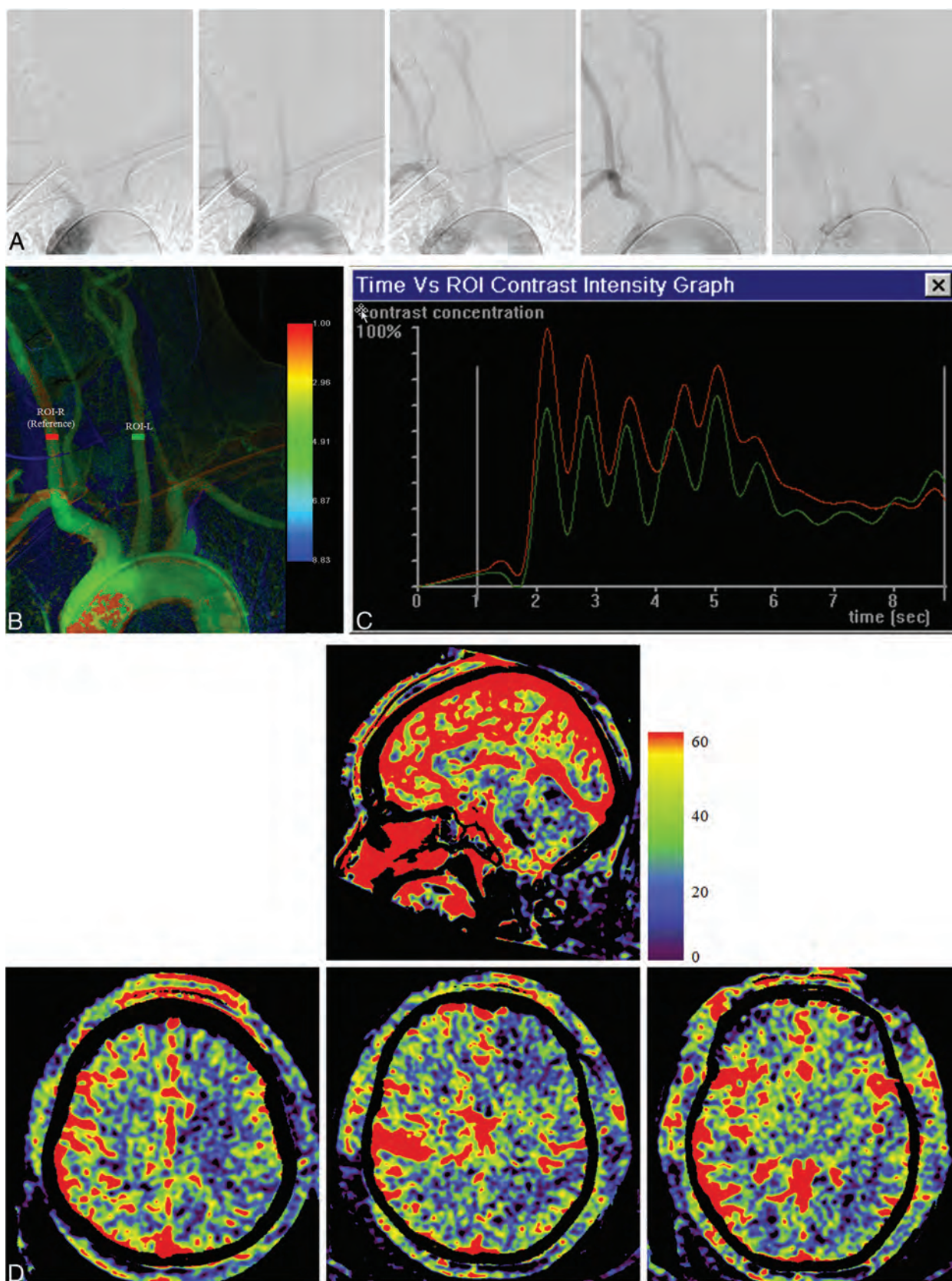


FIG 2. As an example, in patient 11, conventional DSA sequence at 5 time instances shows the course of CM passing through the aortic arch and its major branching arteries (A). In the generated CCQ-DSA image, ROIs were defined on bilateral CCAs (B). Corresponding TDCs were extracted from the defined ROIs, showing large deviations in magnitude between the 2 curves (C). CBV maps evidently show low perfusion levels in plane 1 (lower panel, left) in the parietal lobe, in plane 2 (lower panel, middle) in both the frontal lobe and basal ganglia region, and in plane 3 (lower panel, right) in the temporal lobe (D).

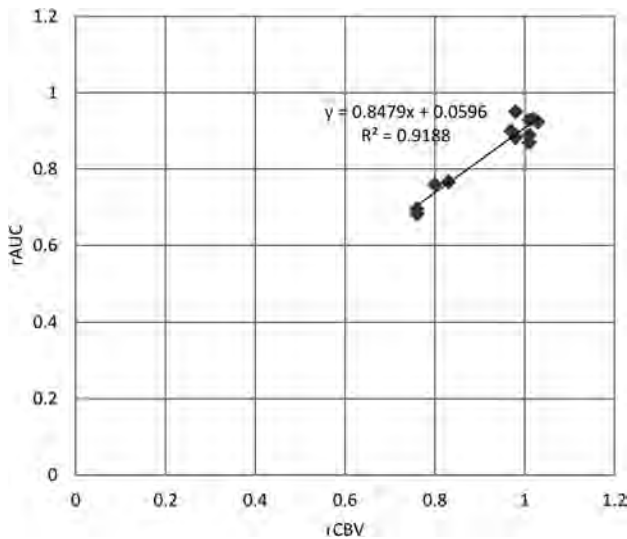


FIG 3. Linear regression analysis shows that rAUC and rCBV with the most asymmetry have approximately a linear relationship.

map. The CBV value in the left hemisphere was significantly lower than that from the right hemisphere with the maximum CBV deviation close to 30%. Specifically, a low perfusion level was mainly detected in plane 1 in the parietal lobe (ROI2), in plane 2 in both the frontal lobe (ROI1) and basal ganglia region (ROI2), and in plane 3 in the temporal lobe (ROI1).

Asymmetric perfusion between 2 hemispheres may only appear in some regions. For each patient, the rCBV with the largest deviation from the perfect symmetry through all the examined regions was used and scatterplots were created against the rAUC. In Fig 3, the relationships between rAUC and rCBV were quantified by linear logistic regression. There was no point lying far from the cluster of data points or far from the regression line, and the high correlation ($R^2 = 0.9188$) indicated an approximate linear relationship between rAUC and rCBV.

DISCUSSION

It has been previously confirmed that CBV maps acquired with FPCT could obtain functional information of the entire brain immediately in the angiographic suite for patients undergoing diagnostic angiography or endovascular treatment. Compared with CT- and FPCT-based perfusion imaging by using an intravenous injection protocol, the IA-FPCT-CBV technique not only enabled real-time monitoring of the brain function, assessments of perfusion parameters during an intervention, and direct evaluation of the treatment outcome but also achieved significant reduction of CM dose, thus potentially minimizing the CM-induced side effects.

The major challenge of this intra-arterial injection protocol was the unexpected asymmetry of perfusion for certain patients between the left/right hemispheres shown on the generated CBV map, which may be caused by nonuniform CM distribution. In fact, for those patients who showed perfusion asymmetry, it could sometimes be observed that a slightly larger portion of CM from the catheter tip flowed through the ostium of the brachiocephalic trunk and then fed into the right CCA and thus the right hemisphere.

Due to the high complexity of the blood flow and CM distributions during transit, it is challenging for the clinicians to visually detect and analyze parameters such as AUC on a conventional monochromatic DSA sequence; this challenge may be an important indicator for physiologic variations. The use of CCQ-DSA with parametric color-coding not only allowed easier visual evaluation but also enabled quantification and estimation of the blood supply to the brain.

In our study, the feasibility of determining CBV symmetry before the acquisition on the basis of CCQ-DSA assessment was investigated. With CCQ-DSA, measurement of the AUC of the TDC in ROIs placed on symmetric CCAs was immediate and quantitative. The CCQ-DSA was generated from the routinely acquired DSA sequence on the aortic arch; thus, no additional CM and x-ray dose was needed. The presented results showed that on the CBV maps, there were no significant differences in CBV values from characteristic regions on the left and right hemispheres for 8 patients. For the other 4 patients, the CBV value was higher on the right hemisphere in ≥ 1 examined region. The same tendency was observed in the AUC measurements of the TDC extracted from bilateral CCAs. We have shown that there is an almost linear relationship between rAUC and rCBV with the most asymmetry, proving that for a specific patient, the use of CCQ-DSA was feasible for predicting whether a reliable IA-FPCT-CBV map could be generated that correctly reflected the perfusion level without inherent bias induced by an intra-arterial injection protocol.

Therefore, the combination of CCQ-DSA could help to sort out patients who are/are not suitable for undergoing IA-FPCT-CBV acquisitions. For those patients who have shown a large discrepancy of AUC values on the bilateral CCAs, an intravenous injection protocol is suggested, or other advanced intra-arterial injection protocols enabling uniform CM distribution need to be further investigated and developed.

The restrictions and limitations of this study should be also mentioned. First, a complete bolus transport consisting of wash-in and wash-out through defined ROIs on CCAs should be included during image acquisition to ensure a correct AUC calculation and comparison. Therefore, the DSA acquisition time has to be long enough, typically 8–10 seconds. Besides, due to the high flow rate in the CCA, the DSA acquisition frame rate of >7.5 frames/s is suggested to make sure that major flow characteristics are well-captured. Second, the CCQ-DSA image is based on the subtraction of a sequence of angiographic images; thus, any patient motion will cause degradation of image quality and subsequent inaccuracies in the quantification results. Therefore, the patient must be well-stabilized to minimize motion-induced artifacts during image acquisition. Third, the catheter position should be carefully controlled with the tip close to the aortic valve. Otherwise, different CM transport distances may bring deviations across patients. Fourth, current available technology of angiographic systems allows only CBV measurement. However, it has been previously demonstrated that cerebral blood flow and cerebral perfusion reserve have also been valuable parameters for achieving comprehensive evaluation on the brain functional changes. Fifth, the number of patients recruited into this study is small; hence, the feasibility of this method was only demonstrated preliminarily.

CONCLUSIONS

IA-FPCT-CBV map acquisition could allow whole-brain perfusion imaging directly in the angiographic suite, but with significantly less CM compared with an intravenous-injection protocol. This preliminary study showed good correlation between the AUC of the TDC at the CCA from CCQ-DSA images and measurements on CBV maps. CCQ-DSA evaluation may be applied before the CBV acquisition in clinics, to help decide whether patients are suitable for undergoing IA-FPCT-CBV acquisitions.

Disclosures: Qi Sun—OTHER RELATIONSHIPS: employee of Siemens, China. Yu Deuerling-Zheng—OTHER RELATIONSHIPS: employee of Siemens. Markus Kowarschik—OTHER RELATIONSHIPS: employee of Siemens. Janina Beilner—OTHER RELATIONSHIPS: employee of Siemens, China.

REFERENCES

1. Kalender W, Kyriakou Y. Flat-detector CT (FD-CT). *Eur Radiol* 2007;17:2767–79
2. Fahrig R, Fox S, Lowrie S, et al. Use of a C-arm system to generate true 3-D computed rotational angiograms: preliminary in vitro and in vivo results. *AJNR Am J Neuroradiol* 1997;18:1507–14
3. Akpek S, Brunner T, Benndorf G, et al. Three-dimensional imaging and cone beam volume CT in C-arm angiography with flat panel detector. *Diagn Interv Radiol* 2005;11:10–13
4. Ahmed AS, Zellerhoff M, Strother CM, et al. C-arm CT measurement of cerebral blood volume: an experimental study in canines. *AJNR Am J Neuroradiol* 2009;30:917–22
5. Bley T, Strother CM, Pulfer KA, et al. C-arm CT measurement of cerebral blood volume in ischemic stroke: an experimental study in canines. *AJNR Am J Neuroradiol* 2010;31:536–40
6. Struffert T, Deuerling-Zheng Y, Kloska S, et al. Flat detector CT in the evaluation of brain parenchyma, intracranial vasculature, and cerebral blood volume: a pilot study in patients with acute symptoms of cerebral ischemia. *AJNR Am J Neuroradiol* 2010;31:1462–69
7. Struffert T, Deuerling-Zheng Y, Engelhorn T, et al. Feasibility of cerebral blood volume mapping by flat panel detector CT in the angiography suite: first experience in patients with acute middle cerebral artery occlusions. *AJNR Am J Neuroradiol* 2012;33:618–25
8. Fiorella D, Turk A, Chaudry I, et al. A prospective, multicenter pilot study investigating the utility of flat detector derived parenchymal blood volume maps to estimate cerebral blood volume in stroke patients. *J Neurointerv Surg* 2014;6:451–56
9. Struffert T, Deuerling-Zheng Y, Kloska S, et al. Cerebral blood volume imaging by flat detector computed tomography in comparison to conventional multislice perfusion CT. *Eur Radiol* 2011;21:882–89
10. Lin CJ, Yu M, Hung SC, et al. In-room assessment of cerebral blood volume for guidance during intra-arterial thrombolytic therapy. *Interv Neuroradiol* 2012;18:463–68
11. Fieselmann A, Ganguly A, Deuerling-Zheng Y, et al. Automatic measurement of contrast bolus distribution in carotid arteries using a C-arm angiography system to support interventional perfusion imaging. In: *Proceedings of SPIE Medical Imaging 2011: Visualization, Image-Guided Procedures, and Modeling*, Orlando, Florida. March 1, 2011;7964:79641W
12. Klostranec JM, Ehtiaty T, Rao S, et al. Comparison of aortic arch and intravenous contrast injection techniques for C-arm cone beam CT. *Acad Radiol* 2013;20:509–18
13. Yasuda R, Royalty K, Pulfer K, et al. C-arm CT measurement of cerebral blood volume using intra-arterial injection of contrast medium: an experimental study in canines. *AJNR Am J Neuroradiol* 2012;33:1696–701
14. Ganguly A, Fieselmann A, Marks M, et al. Cerebral CT perfusion using an interventional C-arm imaging system: cerebral blood flow measurements. *AJNR Am J Neuroradiol* 2011;32:1525–31
15. Zhang Q, Wang B, Han J, et al. Feasibility study of perfusion imaging using flat detector CT with an intra-arterial injection protocol compared to conventional multi-slice perfusion CT with an intravenous injection protocol. *Interv Neuroradiol* 2013;19:409–15
16. Itokawa H, Moriya M, Fujimoto M, et al. Assessment of C-arm cerebral blood volume maps obtained through aortic arch injection with 50% and 30% diluted contrast medium. In: *Proceedings of the Annual Meeting of the American Society of Neuroradiology*, San Diego, California. May 18–23, 2013:426–27
17. Strother CM, Bender F, Deuerling-Zheng Y, et al. Parametric color coding of digital subtraction angiography. *AJNR Am J Neuroradiol* 2010;31:919–24
18. Lin CJ, Hung SC, Guo WY, et al. Monitoring peri-therapeutic cerebral circulation time: a feasibility study using color-coded quantitative DSA in patients with steno-occlusive arterial disease. *AJNR Am J Neuroradiol* 2012;33:1685–90
19. Struffert T, Ott S, Kowarschik M, et al. Measurement of quantifiable parameters by time-density curves in the elastase-induced aneurysm model: first results in the comparison of a flow diverter and a conventional aneurysm stent. *Eur Radiol* 2013;23:521–27
20. Zellerhoff M, Deuerling-Zheng Y, Strother CM, et al. Measurement of cerebral blood volume using angiographic C-arm systems. In: *Proceedings of SPIE Medical Imaging 2009: Biomedical Applications in Molecular, Structural, and Functional Imaging*, Orlando, Florida. February 27, 2009;7262:72620H

Assessing Blood Flow in an Intracranial Stent: A Feasibility Study of MR Angiography Using a Silent Scan after Stent-Assisted Coil Embolization for Anterior Circulation Aneurysms

R. Irie, M. Suzuki, M. Yamamoto, N. Takano, Y. Suga, M. Hori, K. Kamagata, M. Takayama, M. Yoshida, S. Sato, N. Hamasaki, H. Oishi, and S. Aoki



ABSTRACT

BACKGROUND AND PURPOSE: Blood flow in an intracranial stent cannot be visualized with 3D time-of-flight MR angiography owing to magnetic susceptibility and radiofrequency shielding. As a novel follow-up tool after stent-assisted coil embolization, we applied MRA by using a Silent Scan algorithm that contains an ultrashort TE combined with an arterial spin-labeling technique (Silent MRA). The purpose of this study was to determine whether Silent MRA could visualize flow in an intracranial stent placed in the anterior circulation.

MATERIALS AND METHODS: Nine patients treated with stent-assisted coil embolization for anterior circulation aneurysms underwent MRAs (Silent MRA and TOF MRA) and x-ray digital subtraction angiography. MRAs were performed in the same session on a 3T unit. Two neuroradiologists independently reviewed the MRA images and subjectively scored flow in a stent as 1 (not visible) to 4 (excellent) by referring to the latest x-ray digital subtraction angiography image as a criterion standard.

RESULTS: Both observers gave MRA higher scores than TOF MRA for flow in a stent in all cases. The mean score for Silent MRA was 3.44 ± 0.53 , and for TOF MRA, it was 1.44 ± 0.46 ($P < .001$).

CONCLUSIONS: Silent MRA was able to visualize flow in an intracranial stent more effectively than TOF MRA. Silent MRA might be useful for follow-up imaging after stent-assisted coil embolization, though these study results may be only preliminary due to some limitations.

Endovascular therapy for intracranial aneurysms has been widely used since the International Subarachnoid Aneurysm Trial.¹ The number of cases of coil embolization for aneurysms is increasing, and the stent-protection technique has widened the applicability to cases that had been otherwise difficult to treat with conventional coil embolization.² Nevertheless, there is a risk of coil compaction or in-stent restenosis after stent-assisted coil embolization. X-ray digital subtraction angiography is the optimal technique used to examine these adverse events, and it is commonly used as a follow-up tool after using an intracranial stent. However, DSA presents some unavoidable risks related to the catheter procedure, radiation, and contrast media.³⁻⁵

3D time-of-flight MR angiography is widely used for the assessment of cerebral vascular diseases and has also been examined

as a noninvasive substitute for DSA.⁶⁻⁹ These studies generally reported difficulty in visualizing flow in a stent with TOF MRA because of magnetic susceptibility and radiofrequency shielding, though some beneficial aspects were observed in assessing the residual lumen of aneurysms. As a novel follow-up tool after stent-assisted coil embolization, we applied MRA by using a Silent Scan algorithm (GE Healthcare, Milwaukee, Wisconsin) that contains an ultrashort TE combined with an arterial spin-labeling technique (Silent MRA). In this situation, visualizing flow means visualizing arterial geometry and patency. It does not mean directly visualizing blood flow rate. The purpose of this study was to determine whether Silent MRA can visualize flow in an intracranial stent placed at the anterior circulation.

MATERIALS AND METHODS

Patients treated by stent-assisted coil embolization for unruptured aneurysms in the anterior circulation were examined, and 10 consecutive patients who underwent 2 types of MRAs (Silent MRA and TOF MRA) from March 1 to June 30, 2014, were included in this study. One patient with an anterior communicating artery aneurysm was excluded because the patient experienced stent occlusion during the follow-up period. Written informed consent was not required for this study because of its retrospective observational design. All 9 patients were treated with Enterprise VRD (Codman & Shurtleff, Raynham, Massachusetts). Endovas-

Received August 18, 2014; accepted after revision October 29.

From the Departments of Radiology (R.I., M.S., N.T., M.H., K.K., M.T., M. Yoshida, S.S., N.H., S.A.) and Neurosurgery (M. Yamamoto, Y.S., H.O.), Juntendo University Hospital, Tokyo, Japan; and Department of Neuroendovascular Therapy (H.O.), Juntendo University School of Medicine, Tokyo, Japan.

Please address correspondence to Ryusuke Irie, MD, Department of Radiology, Juntendo University Hospital, 3-1-3 Hongo, Bunkyo-ku, Tokyo 113-8431, Japan; e-mail: ririe@juntendo.ac.jp

Indicates open access to non-subscribers at www.ajnr.org

<http://dx.doi.org/10.3174/ajnr.A4199>

Patient data

Case No.	Age (yr)	Sex	Aneurysm Location	Stent Configuration ^a	Interval between DSA and MRA	Aneurysm Occlusion Status	Scores of Silent MRA ^b	Scores of TOF MRA ^b
1	65	F	Rt. ICA paraclinoid	Clinoid-terminal	13 mo	NR	4/3	1/1
2	75	M	Rt. ICA-AchoA	Supraclinoid-MCA	15 mo	CO	4/3	2/2
3	74	F	Rt. ICA paraclinoid	Cavernous-supraclinoid	7 mo	CO	4/4	1/1
4	59	M	Lt. ICA bifurcation	Supraclinoid-MCA	1 day	CO	3/3	2/1
5	45	F	Rt. ICA paraclinoid	Cavernous-terminal	7 mo	CO	4/4	2/2
6	50	F	Rt. ICA paraclinoid	Cavernous-terminal	1 day	NR	4/3	1/1
7	51	F	Lt. ICA cavernous	Cavernous-clinoid	12 mo	CO	2/3	1/1
8	61	F	Rt. ICA-Pcoma	Supraclinoid-terminal	2 days	NR	4/4	2/2
9	64	M	Lt. ICA paraclinoid	Cavernous-supraclinoid	12 mo	NR	3/3	2/1

Note:—AchoA indicates anterior choroidal artery; Pcoma, posterior communicating artery; Clinoid, clinoid segment of ICA; terminal, terminal segment of ICA; supraclinoid, supraclinoid segment of ICA; Cavernous, cavernous segment of ICA; NR, neck remnant; CO, complete occlusion; Rt., right; Lt., left.

^a Proximal-distal marker of a stent.

^b Scores of observers 1/2.

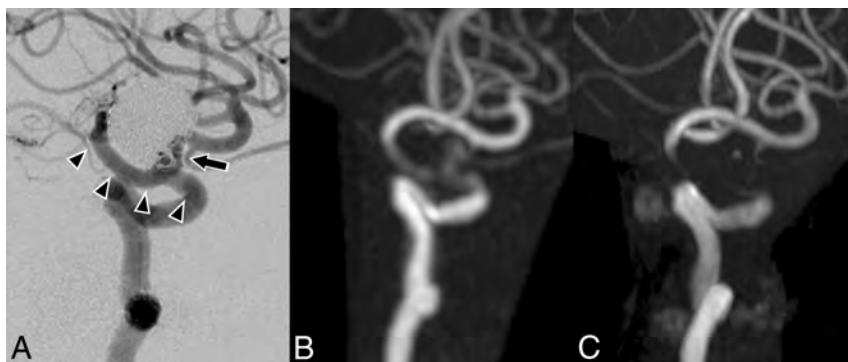


FIG 1. Case 1. A 65-year-old woman with a right paraclinoid internal carotid artery aneurysm was treated by stent-assisted coil embolization in March 2011. The latest DSA was performed in February 2013 (A). Silent MRA (B) and TOF MRA (C) were performed in March 2014. The clinoid-to-terminal segment of the internal carotid artery is covered by a stent (arrowheads). The anatomic outcome of the aneurysm in DSA is a neck remnant (arrow). Our subjective scores of Silent MRA are 4 and 3. The scores of TOF MRA are 1 and 1. In this case, the Silent MRA depiction of the neck remnant is also better than that of TOF MRA.

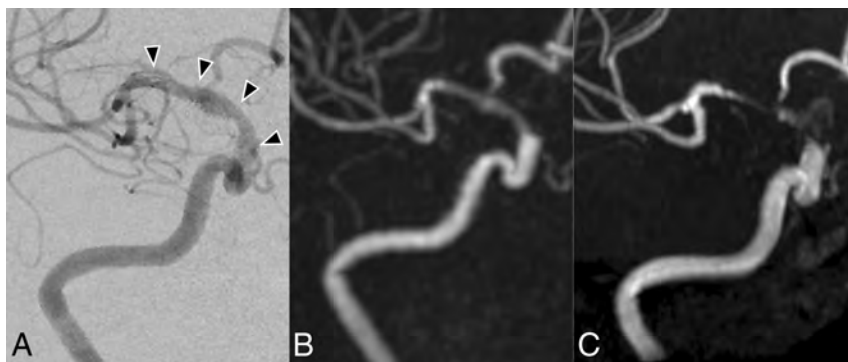


FIG 2. Case 2. A 75-year-old man with a right anterior choroidal artery aneurysm was treated in June 2010. The latest DSA was performed in December 2012 (A). Silent MRA (B) and TOF MRA (C) were performed in March 2014. The supraclinoid segment of the internal carotid artery to middle cerebral artery is covered by a stent (arrowheads). The anatomic outcome of the aneurysm in DSA is complete occlusion. Our subjective scores of Silent MRA are 4 and 3. The scores of TOF MRA are 2 and 2.

cular therapy and examinations were performed with the following angiographic systems: Axiom Artis dTA (Siemens, Erlangen, Germany) until February 2014 and Artis Q BA Twin (Siemens) from March 2014 to present. Anatomic outcomes of the aneurysm in the latest DSA were complete occlusion in 5 cases and neck remnant in 4 cases. Patient data are shown in the Table.

Both MRAs were performed in the same session on a 3T unit (Discovery MR750w; GE Healthcare). Silent MRA is only appli-

cable to 3T MR imaging. The parameters for acquisition in the Silent MRA were as follows: TR/TE, 1116.4/0.016 ms; flip angle, 5°; FOV, 180 × 180 mm; matrix, 150 × 150; section thickness, 1.2 mm; NEX, 1.5; bandwidth, ±20 kHz; and acquisition time, 7 minutes 40 seconds. TOF MRA was performed with the following parameters: TR/TE, 19/2.9 ms; flip angle, 15°; FOV, 200 × 200 mm; matrix, 416 × 192; section thickness, 1.2 mm; NEX, 1; bandwidth, ±41.7 kHz; and acquisition time, 3 minutes 31 seconds. Although the details of the Silent Scan algorithm were undisclosed, the arterial spin-labeling technique is used as a preparation pulse, and data acquisition is based on a 3D radial scan.¹⁰ In the Silent Scan, a control image is first scanned before the labeling pulse, followed by a labeled image. The control and labeled images are subtracted to yield an angiographic image.

Two neuroradiologists independently reviewed the MRAs and rated the visual conditions around the flow in each stent subjectively on a 4-point scale as follows: 1, not visible (almost no signal in the stent); 2, poor (structures are slightly visible but with significant blurring or artifacts, not diagnostic); 3, good (good-quality diagnostic information with minimal blurring or artifacts); or 4, excellent (excellent-quality diagnostic information; the shape of depiction is nearly equal to that of DSA). The scores

of the 2 observers were averaged, and a paired *t* test was performed in the statistical analysis of the subjective scores for flow in a stent. The latest DSA image was used as a reference standard. The average of the interval between the latest DSA and MRAs was 7.33 months (range, 1 day to 15 months), and the interval between the aneurysm treatment and MRAs was 18.67 months (range, 1 day to 45 months). The level of interobserver agreement in the evaluation was analyzed by weighted κ statistics.

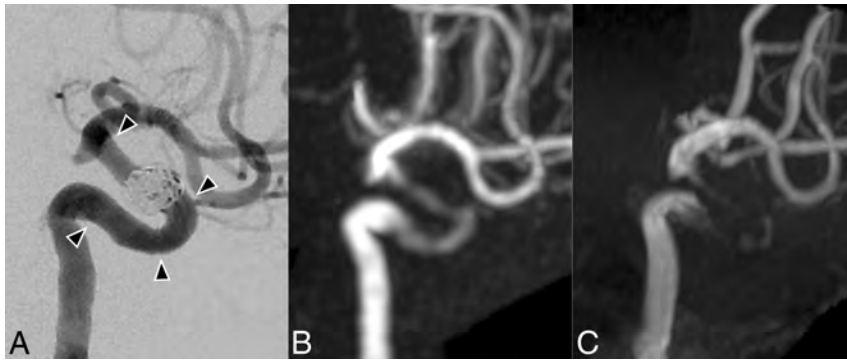


FIG 3. Case 3. A 74-year-old woman with a right paraclinoid internal carotid artery aneurysm was treated in October 2013. A DSA image (A) was obtained right after the treatment. Silent MRA (B) and TOF MRA (C) were performed in May 2014. The cavernous-to-supraclinoid segment of the internal carotid artery is covered by a stent (arrowheads). The anatomic outcome of the aneurysm in DSA is complete occlusion. Our subjective scores of Silent MRA are 4 and 4. The scores of TOF MRA are 1 and 1.

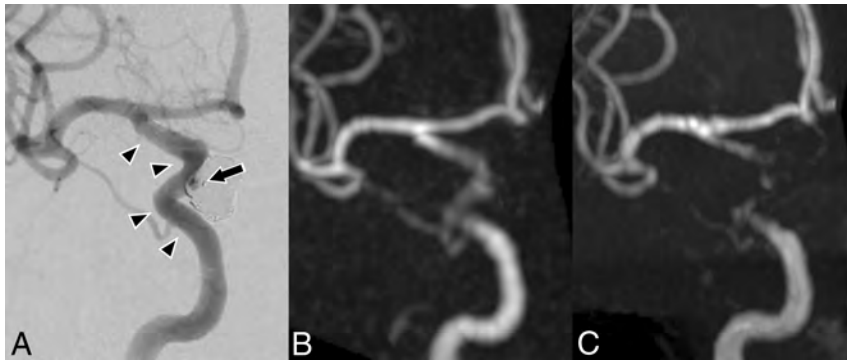


FIG 4. Case 6. A 50-year-old woman with a right paraclinoid internal carotid artery aneurysm was treated in June 2012. Silent MRA (B) and TOF MRA (C) were performed in June 2014, and DSA (A) was performed the next day. The cavernous-to-terminal segment of the internal carotid artery is covered by a stent (arrowheads). The anatomic outcome of the aneurysm in DSA is a small neck remnant (arrow). Our subjective scores of Silent MRA are 4 and 3. The scores of TOF MRA are 1 and 1.

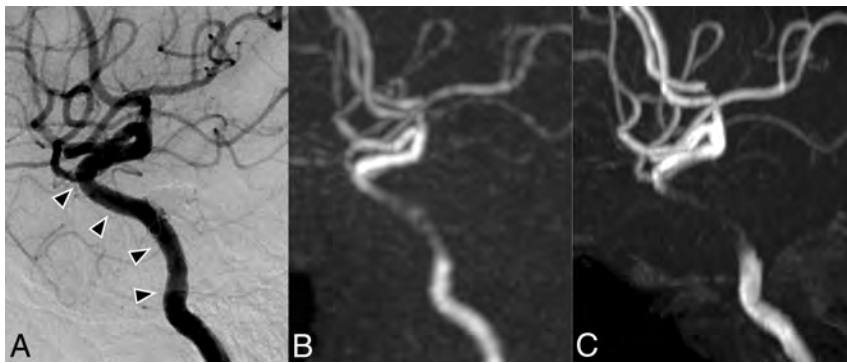


FIG 5. Case 7. A 51-year-old woman with a left cavernous internal carotid artery aneurysm was treated in May 2012. The latest DSA was performed in June 2013 (A). Silent MRA (B) and TOF MRA (C) were performed in June 2014. The cavernous-to-clinoid segment of the internal carotid artery is covered by a stent (arrowheads). The anatomic outcome of the aneurysm in DSA is complete occlusion. In this case, the overall image quality of Silent MRA is not good, but visualization of the flow in a stent is still better than that of TOF MRA. Our subjective scores of Silent MRA are 2 and 3. The scores of TOF MRA are 1 and 1.

RESULTS

The mean score of Silent MRA was 3.44 ± 0.53 , and for TOF MRA, it was 1.44 ± 0.46 ($P < .001$). Both observers gave Silent MRA higher scores than TOF MRA for flow in a stent in all

cases. Interobserver agreement was good ($\kappa = 0.963$). Of note, the Silent MRA depictions of the neck remnant in 4 cases were similar to those of DSA, while TOF MRA showed only a small depiction of the neck remnant. Figures 1–5 show the DSA, Silent MRA, and TOF MRA images for each case, respectively. Silent MRA and TOF MRA images were processed to maximum intensity projections, and surrounding vessels were removed to make them similar to those on DSA.

DISCUSSION

In this study, we found that Silent MRA was superior to TOF MRA for visualizing flow in a stent in all 9 observed patients with anterior circulation aneurysms.

In the anterior circulation, the tortuosity and diameter of the vessel are different from those in the posterior circulation. The effect of magnetic susceptibility by stent or coil may differ between the anterior and posterior circulations. Thus, we believe that there is a need to distinguish these regions when assessing flow in a stent.

The most important characteristic of a Silent Scan is the ultrashort TE (TE = 0.016 ms). Ultrashort TE imaging can decrease magnetic susceptibility and visualize short T2 tissues such as the musculoskeletal system, lung parenchyma, or carotid plaque.^{11–13} In Silent MRA, the ultrashort TE can minimize the phase dispersion of the labeled blood flow signal in the voxel space and decrease magnetic susceptibility. Accordingly, the artifacts from stents or coils are diminished; this change enables visualization of flow in a stent. The effect of the disturbed flow in TOF MRA may also decrease. Gönner et al^{14,15} reported that ultrashort TE reduced the artifacts after coiling or stent placement, though a TE of 2.4 ms was used in that study.

In Silent MRA, the angiographic image is obtained by subtraction of images scanned before and after labeling. Thus, static tissue such as a thrombus cannot be detected in Silent MRA. Conversely, in TOF MRA, thrombus in a stent might be detected as a high-signal-intensity

area. Compared with TOF MRA, Silent MRA images are easy to interpret because they consist of only the labeled blood flow signal. Takayama et al¹⁶ reported that contrast-enhanced MRA is

useful when visualizing flow in a stent, though DSA remains a superior follow-up tool for stent-assisted coil embolization. Also, while rare, contrast agents might induce serious adverse events such as anaphylaxis or nephrogenic systemic fibrosis.

There are some limitations to this study. We only examined flow in a stent, though Mizuki et al¹⁷ reported that Silent MRA was similar to TOF MRA for assessment of flow outside a stent. Wu et al¹⁸ also reported the feasibility of MRA by using arterial spin-labeling and 3D radial scan data acquisition, which might be somewhat similar to Silent MRA. The average interval between MRA and DSA as a standard of reference is quite long (up to 15 months), which limits the validity of this comparison. Thus, MRA images might not reflect the exact condition of flow in a stent. We were also unable to compare Silent MRA and contrast-enhanced MRA. Finally, we included only cases with a closed-cell-design Enterprise stent in this study. Future studies are required to examine open-cell-design stents because the stent form might produce differences in the MRA images.¹⁹

These study results may only be preliminary due to the small number of cases examined, limited to the anterior circulation and only 1 stent design. For potential replacement of TOF or contrast-enhanced MRA for aneurysm follow-up imaging after treatment, one must analyze not only in-stent flow but also aneurysm occlusion status. We have planned a prospective study to define the situations under which Silent MRA can replace TOF MRA.

CONCLUSIONS

Silent MRA could visualize flow in an intracranial stent at the anterior circulation more effectively than TOF MRA. Further studies are required to determine the factors that affect MRA images and the most appropriate scan parameters to visualize flow in a stent. Silent MRA might be useful for the follow-up imaging after stent-assisted coil embolization, though some limitations remain to be examined.

REFERENCES

1. Molyneux A, Kerr R, Stratton J, et al; International Subarachnoid Aneurysm Trial (ISAT) Collaborative Group. **International Subarachnoid Aneurysm Trial (ISAT) of neurosurgical clipping versus endovascular coiling in 2143 patients with ruptured intracranial aneurysms: a randomised trial.** *Lancet* 2002;360:1267–74
2. Mine B, Aljishi A, D'Harcour JB, et al. **Stent-assisted coiling of unruptured intracranial aneurysms: long-term follow-up in 164 patients with 183 aneurysms.** *J Neuroradiol* 2014;41:322–28
3. Ferns SP, Sprengers ME, van Rooij WJ, et al. **Coiling of intracranial aneurysms: a systematic review on initial occlusion and reopening and retreatment rates.** *Stroke* 2009;40:e523–29
4. Kanaan H, Jankowitz B, Aleu A, et al. **In-stent thrombosis and ste-**

- nosis after neck-remodeling device-assisted coil embolization of intracranial aneurysms.** *Neurosurgery* 2010;67:1523–32; discussion 1532–33
5. Mocco J, Fargen KM, Albuquerque FC, et al. **Delayed thrombosis or stenosis following Enterprise-assisted stent-coiling: is it safe? Mid-term results of the interstate collaboration of Enterprise stent coiling.** *Neurosurgery* 2011;69:908–13; discussion 913–14
6. Schaafsma JD, Velthuis BK, Majoie CB, et al. **Intracranial aneurysms treated with coil placement: test characteristics of follow-up MR angiography—multicenter study.** *Radiology* 2010;256:209–18
7. Lavoie P, Gariépy JL, Milot G, et al. **Residual flow after cerebral aneurysm coil occlusion: diagnostic accuracy of MR angiography.** *Stroke* 2012;43:740–46
8. Cho WS, Kim SS, Lee SJ, et al. **The effectiveness of 3T time-of-flight magnetic resonance angiography for follow-up evaluations after the stent-assisted coil embolization of cerebral aneurysms.** *Acta Radiol* 2014;55:604–13
9. Cho YD, Kim KM, Lee WJ, et al. **Time-of-flight magnetic resonance angiography for follow-up of coil embolization with Enterprise stent for intracranial aneurysm: usefulness of source images.** *Korean J Radiol* 2014;15:161–68
10. Alibek S, Vogel M, Sun W, et al. **Acoustic noise reduction in MRI using Silent Scan: an initial experience.** *Diagn Interv Radiol* 2014; 20:360–63
11. Robson MD, Gatehouse PD, Bydder M, et al. **Magnetic resonance: an introduction to ultrashort TE (UTE) imaging.** *J Comput Assist Tomogr* 2003;27:825–46
12. Bergin CJ, Pauly JM, Macovski A. **Lung parenchyma: projection reconstruction MR imaging.** *Radiology* 1991;179:777–81
13. Chan CF, Keenan NG, NIELLES-Vallespin S, et al. **Ultra-short echo time cardiovascular magnetic resonance of atherosclerotic carotid plaque.** *J Cardiovasc Magn Reson* 2010;12:17
14. Gönner F, Heid O, Remonda L, et al. **MR angiography with ultrashort echo time in cerebral aneurysms treated with Guglielmi detachable coils.** *AJNR Am J Neuroradiol* 1998;19:1324–28
15. Gönner F, Lövblad KO, Heid O, et al. **Magnetic resonance angiography with ultrashort echo times reduces the artefact of aneurysm clips.** *Neuroradiology* 2002;44:755–58
16. Takayama K, Taoka T, Nakagawa H, et al. **Usefulness of contrast-enhanced magnetic resonance angiography for follow-up of coil embolization with the Enterprise stent for cerebral aneurysms.** *J Comput Assist Tomogr* 2011;35:568–72
17. Mizuki K, Masui T, Katayama M, et al. **Evaluation of patients of the cerebral vasculature: comparison with Silenz MRA and 3D TOF MRA.** In: *Proceedings of Joint Annual Meeting International Society for Magnetic Resonance in Medicine—European Society for Magnetic Resonance in Medicine and Biology*, Milan, Italy. May 10–16, 2014
18. Wu H, Block WF, Turski PA, et al. **Noncontrast-enhanced three-dimensional (3D) intracranial MR angiography using pseudocontinuous arterial spin labeling and accelerated 3D radial acquisition.** *Magn Reson Med* 2013;69:708–15
19. Choi JW, Roh HG, Moon WJ, et al. **Optimization of MR parameters of 3D TOF-MRA for various intracranial stents at 3.0T MRI.** *Neurointervention* 2011;6:71–77

The Curved MCA: Influence of Vessel Anatomy on Recanalization Results of Mechanical Thrombectomy after Acute Ischemic Stroke

B.J. Schwaiger, A.S. Gersing, C. Zimmer, and S. Prothmann

ABSTRACT

BACKGROUND AND PURPOSE: Vessel anatomy is assumed to influence results of endovascular mechanical thrombectomy using stent retrievers. The purpose of this study was to analyze the influence of vessel curvature on recanalization results in patients with acute ischemic stroke caused by large-vessel occlusion.

MATERIALS AND METHODS: In 159 patients (70 ± 12.8 years of age; 79 women) treated for acute ischemic stroke after carotid T and/or MCA occlusion by using stent retrievers, the following angles were measured in standard anteroposterior angiograms to describe vessel anatomy: first, between the terminal ICA segment and the most downward curved M1 segment conterminous to the proximal face of the thrombus (ICA/M1 angle); second, between the most proximal M1 segment and the segment immediately conterminous to the thrombus (M1/M1 angle); and additionally, in patients with distal M1/proximal M2 occlusion, the angle of the last curvature proximal of the thrombus (M1/M2 angle). Angles of patients with-versus-without successful recanalization were compared.

RESULTS: Patients without successful recanalization (TICI 0–2a) showed significantly larger ICA/M1 angles (mean, $110^\circ \pm 23.8^\circ$ versus $69^\circ \pm 28.7^\circ$, $P < .001$) and significantly larger M1/M1 angles ($56^\circ \pm 29.2^\circ$ versus $29^\circ \pm 26.6^\circ$, $P = .001$) than patients with successful recanalization (TICI 2b/3). In patients without successful recanalization after a distal M1 or proximal M2 occlusion, the M1/M2 angle was significantly larger than that in patients with successful recanalization ($117^\circ \pm 34.3^\circ$ versus $67^\circ \pm 29.5^\circ$, $P = .006$).

CONCLUSIONS: This retrospective analysis showed that mechanical thrombectomy in the anterior circulation was significantly less often successful in patients with large vessel angles. Therefore, vessel curvature significantly influences the results of mechanical thrombectomy with stent retrievers for treatment of acute ischemic stroke. Further work is needed to understand the underlying causality.

ABBREVIATIONS: MT = endovascular mechanical thrombectomy; ROC = receiver operating characteristic

Acute ischemic stroke is one of the leading causes of morbidity and mortality in industrialized countries.¹ While studies suggest that intravenous thrombolysis by using recombinant tissue plasminogen activator is barely effective in large-vessel occlu-

sions,^{2–4} recent studies have shown that endovascular mechanical thrombectomy (MT) by using second-generation devices, known as stent retrievers, is associated with high recanalization rates and substantially improved clinical outcome.^{5–11} However, in approximately 10%–25% of the patients, a successful recanalization (TICI 2b/3) still cannot be achieved.^{5–14} Only a couple of technical factors are understood that may determine the fate of these patients: First, histologic characteristics of thromboemboli may influence recanalization results.¹⁵ Second, thrombus length has been identified as a relevant factor.¹⁶ A recent study presented contradictory results, reporting that the recanalization success of MT was not significantly influenced by clot length.¹⁷ The exact thrombus location, being more proximal or distal within the MCA M1 segment, was demonstrated to be a significant determinant for clinical outcome, however not for recanalization success.¹⁸

To date, no evidence of vessel anatomy influencing recanalization success exists, though experienced interventionalists report that MT with stent retrievers is less likely to be successful in

Received September 30, 2014; accepted after revision November 17.

From the Department of Diagnostic and Interventional Neuroradiology, Klinikum rechts der Isar der Technischen Universität München, Munich, Germany.

Preliminary results previously presented as part of the following contribution to the World Federation of Neuroradiological Societies Symposium Neuroradiologicum, September 7–12, 2014; Istanbul, Turkey: Schwaiger BJ, Kober F, Gersing AS, et al. "The pREset Retriever for Endovascular Treatment of Stroke after MCA Occlusion: Safety and Clinical Outcome."

This work has been performed in accordance with the standards defined by the local ethics committee and the standards laid down in the 1964 Declaration of Helsinki and its later amendments.

Please address correspondence to Benedikt J. Schwaiger, MD, Department of Diagnostic and Interventional Neuroradiology, Klinikum rechts der Isar der Technischen Universität München, Ismaninger Str 22, 81675 Munich, Germany; e-mail: benedikt.schwaiger@tum.de

<http://dx.doi.org/10.3174/ajnr.A4222>

patients with strongly curved vessels. Zhu et al¹⁹ reported that vessel branching and curvature are important determinants of recanalization success; however, their work was based on indirect MR imaging findings and focused on thrombectomy by using the Merci retriever (Concentric Medical, Mountain View, California), a first-generation device, which is now obsolete in most cases. In a previous study on MT by using the pREset thrombus retriever (Phenox, Bochum, Germany), we observed that successful recanalization was significantly less likely in patients with strongly curved MCAs.¹³ Consequently, in this study, we analyzed the influence of vessel anatomy, assessed in anteroposterior angiograms, on recanalization results in a larger sample size. The purpose of this study was also to assess information on prognostic cutoff values and the prevalence of unfavorable MCA anatomy.

MATERIALS AND METHODS

Patients, Therapy Strategy, and CT

In the stroke data base of our institution, we identified patients treated for symptomatic acute ischemic stroke after unilateral occlusion in the anterior circulation by using stent retrievers between July 2011 and April 2014. We included 159 patients (mean age, 70 ± 12.8 years; 79 women) presenting with 1 of the following occlusion types: short-segment carotid T (ICA terminus including proximal MCA) occlusion encompassing only the terminal ICA segment, isolated M1 segment occlusion, combined occlusion of the M1 and the proximal M2, or isolated proximal M2 occlusion.

Patients with proximal and long-segment ICA occlusion, isolated anterior cerebral artery occlusion, or occlusion of >1 intracranial vessel were excluded as well as patients with other vascular pathologies such as pre-existing ICA or intracranial stenosis or dissection, suspected vasculitis, Moyamoya disease, or acute ischemic stroke caused by an endovascular procedure. Patients in whom the occlusion site could not be reached due to proximal vessel anatomy were excluded from the analysis as well.

There were no exclusion criteria regarding the number of devices used and passages of the thrombus or any demographic or clinical parameters.

A neurologic deficit of an NIHSS score of ≥ 4 was required to indicate treatment, following the standard operating procedure of our institution. The NIHSS score was assessed at admission for baseline evaluation of the patient's clinical status.

Preinterventionally, IV rtPA was applied within a timeframe of 4.5 hours after observed symptom onset if no contraindications existed, following the guidelines by the German Society of Neurology.²⁰ Patients received a dose of 0.9-mg rtPA per kilogram of body weight. Ten percent of the total dose was applied as an immediate loading dose; then, the remaining 90% was applied during the following hour, regardless of the starting time of angiography and MT.

MT was performed in patients who presented within a timeframe of 6 hours after symptom onset. Contraindications for MT were intracranial hemorrhage and infarct demarcation of more than one-third of the MCA territory in the most recent CT. Patients with wake-up stroke were included if they presented within 3 hours after discovery and only if there was no infarct demarcation detected by noncontrast CT and there was an MTT/CBV mismatch of $>30\%$ as detected by CT perfusion, according to the standard operating procedure of our institution and recent literature.²¹⁻²³

Time durations were measured from symptom onset to groin puncture, from symptom onset to reperfusion or the end of the procedure in case of unsuccessful recanalization, and from groin puncture to reperfusion or the end of the procedure, respectively.

All patients underwent CT either on a 64- or 256-detector row CT scanner (Brilliance 64/iCT; Philips Healthcare, Best, the Netherlands) immediately at admission, to rule out hemorrhage or infarct demarcation. In addition, CT angiography was performed to verify the occlusion type and to analyze vessel patterns. A further CT or MR imaging was performed routinely within 24 hours after endovascular treatment or in case of any clinical deterioration. The complete imaging data including angiograms were re-evaluated for this study by 2 neuroradiologists in a consensus reading (S.P. and B.J.S.).

Endovascular Treatment and Evaluation

Depending on patient compliance and vigilance, procedures were performed with the patient under either conscious sedation or general anesthesia. An 8F guiding catheter (VISTA BRITE TIP; Cordis, Fremont, California) for cervical access was placed through a short 8F sheath after the femoral artery was punctured. By a 3-axial approach, a 0.054-inch intermediate catheter (5MAX; Penumbra, Alameda, California) containing a 0.021-inch microcatheter (Trevor Pro 18; Stryker, Kalamazoo, Michigan) and a 0.014-inch microwire (Traxcess 14; MicroVention, Tustin, California) was advanced intracranially. The occlusion site was passed with the microwire and the microcatheter, which was placed as close as possible to the proximal thrombus face. In this position, the stent retriever was deployed, covering the proximal and the distal thrombus borders. After a delay of 5 minutes, the device was retrieved under constant manual aspiration into the intermediate catheter. This procedure was repeated until successful recanalization was achieved or it was aborted in case of excessive procedural time and negligible chances for success. In this study, the following stent retrievers were used either as a sole device or in combination with other devices, according to the performing interventionalist's individual decision: Solitaire FR Revascularization Device (Covidien, Irvine, California), Trevor and Trevor ProVue Retriever (Stryker), pREset thrombus retriever, Capture LP (MindFrame, Irvine, California), Aperio Thrombectomy System (Acandis, Pforzheim, Germany), and Separator 3D (Penumbra).

Recanalization results were graded in the final angiogram by using the TICI score. TICI 2b and 3 scores were considered successful recanalization.

Perforation, dissection, thrombus dispersion, and focal or diffuse SAH were determined as procedure-related complications. Stroke-related hemorrhagic events (hemorrhagic infarction and parenchymal hematoma) were characterized separately, according to the methods used in the European Cooperative Acute Stroke Study trials.²⁴ Complications and hemorrhage were defined as clinically relevant if they were associated with an NIHSS increase of ≥ 4 points.

Vessel Anatomy Evaluation

DSA was performed on a biplanar Allura Xper FD scanner (Philips Healthcare). For assessment of vessel anatomy, standard

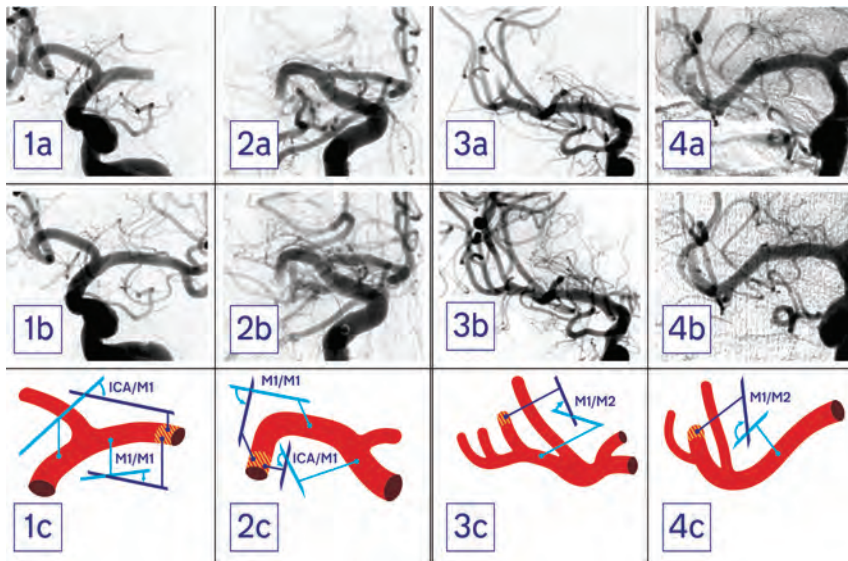


FIG 1. First and second columns (patients 1 and 2) show pre- (a) and postprocedural (b) angiograms of patients with a proximal M1 occlusion as well as schematics of the vessel anatomy (c). The thrombus site is hatched red and yellow. In patient 1, the ICA/M1 was 53° and the M1/M1 was 18°, and he was successfully recanalized (TICI 3). Patient 2 presented with an ICA/M1 of 140° and an M1/M1 of 105°. In this patient, thrombectomy was unsuccessful (TICI 0). Third and fourth columns (patients 3 and 4) show pre- (a) and postprocedural (b) angiograms of patients with a proximal M2 occlusion as well as vessel schematics (c). While patient 3 presented with an M1/M2 angle of 51° and was successfully recanalized (TICI 3), in patient 4, an M1/M2 angle of 128° was measured and thrombectomy was unsuccessful (TICI 1).

Table 1: Epidemiologic, clinical, and technical parameters for all patients and a comparison between subgroups, depending on recanalization success

Parameter	All Patients	TICI 0–2a	TICI 2b/3	P Value
Group/subgroup size	159	24 (15.1%)	135 (84.9%)	
Female sex (No., % of subgroup)	79 (49.7%)	11 (45.8%)	68 (50.4%)	.825
Age (yr, mean)	70 ± 12.8	70 ± 10.7	70 ± 13.2	.964
Wake-up (No., % of subgroup)	30 (18.9%)	3 (12.5%)	27 (20%)	.572
Time symptom onset to puncture (min, mean) ^a	230 ± 80.0	232 ± 82.6	230 ± 79.9	.902
Procedure time (min, mean) ^b	55 ± 35.1	69 ± 38.2	53 ± 34.3	.058
Time onset to recanalization (min, mean) ^c	285 ± 86.9	303 ± 96.7	283 ± 85.4	.349
NIHSS score at admission (median, range)	15 (4–27)	16 (7–24)	14 (4–27)	.198
IV rtPA administered (No., % of subgroup)	112 (70.4%)	15 (62.5%)	97 (71.9%)	.345
General anesthesia applied (No., % of subgroup)	127 (79.9%)	20 (83.3%)	107 (79.3%)	.787
Passages of device (No., median, range)	2 (1–12)	4 (1–10)	2 (1–12)	.008 ^d
<1 Device used (No., % of subgroup)	55 (34.6%)	14 (58.3%)	41 (30%)	.011 ^d

^a Data missing for 24 patients.

^b Data missing for 9 patients.

^c Data missing for 21 patients.

^d Significant at $P < .05$.

anteroposterior projections of the final angiograms were analyzed (Fig 1).

Patients with short-segment carotid T occlusion and proximal M1 occlusion were summarized as having proximal occlusion, while patients with terminal M1 or proximal M2 occlusion were summarized as having distal occlusion. Patients with combined proximal and distal occlusions were assigned to both subgroups.

In patients with a proximal occlusion, we measured 2 angles: first, the angle between the terminal ICA segment and the most downward bent M1 segment (Fig 1, subsequently referred to as the ICA/M1 angle); and second, the angle between the most proximal M1 segment emerging from the carotid T and the M1 segment immediately conterminous to the proximal thrombus face (M1/M1 angle).

In patients with a distal occlusion, in addition to these 2 angles,

a third angle was measured between the vessel segment conterminous to the occlusion site and the segment immediately proximally adjacent to this (M1/M2 angle).

In patients with carotid T occlusion and M1 segment occlusion immediately adjacent to the carotid T, angle measurements were not possible in preinterventional angiograms due to low vessel contrast. Therefore, the frame with the best vessel contrast was selected from the final control angiogram. Thus, correct measurements were possible even in patients with incomplete recanalization after carotid T occlusion ($n = 3$) or M1 segment occlusions adjacent to the carotid T ($n = 7$) due to partially re-established vessel contrast in all cases.

All measurements were performed by using standard PACS tools.

Statistics

In addition to descriptive statistics, the Fisher exact test was used for categorical data and the exact Mann-Whitney U test, for nonparametric testing. The Student t test was used for continuous data. To analyze the influence of the measured angles on the recanalization results, we used logistic regression models, correcting for several covariates. Receiver operating characteristic (ROC) analyses were performed, and the areas under the ROC analysis curves were used to evaluate the diagnostic performance of the measured angles to differentiate patients with-versus-without successful recanalization. The Youden J statistic was used to identify the optimal cutoff values for differentiation of patients.²⁵ Correlations were analyzed by the Pearson r . Statistical analyses were performed by using SPSS, Release 22 (IBM, Armonk, New York) and were supervised by a statistician.

RESULTS

One hundred fifty-nine patients (mean age, 70 ± 12.8 years; 79 women) were included in this study (Table 1). Angle measurements were feasible in final control angiograms of all selected patients, including those with carotid T occlusions.

The median NIHSS score at admission was 15 (range, 4–27). Thirty patients (18.9%) were admitted after presenting with a wake-up stroke with an unknown time from symptom onset to reperfusion, while in the remaining patients, the mean time between observed symptom onset and groin puncture was 230 ± 80.0 minutes. In the latter, the exact time was not documented in 21 cases (16.0%), but it definitely ranged within a time window of

Table 2: Angles, P values, AUCs for ROC analyses, and optimal cutoff values to differentiate TIC1 subgroups and Youden indices for different vessel angles^a

Occlusion Pattern	Group Size	Angle	TICI 0–2a (mean)	TICI 2b/3 (mean)	P	ROC AUC	Cutoff and Youden index
Proximal (carotid T or proximal M1 segment)	125	ICA/M1	110 ± 23.8	69 ± 28.7	.000 ^b	.872 ^d	100° (J = 0.69)
	125	M1/M1	56 ± 29.2	29 ± 26.6	.001 ^b	.759 ^d	36° (J = 0.40)
Distal (distal M1 or proximal M2 segment)	36	M1/M2	117 ± 34.3	67 ± 29.5	.006 ^c	.865 ^d	97° (J = 0.64)

Note:—AUC indicates area under the curve.

^a P values significant at $P < .05$.

^b Corrected for age, sex, and IV rtPA (yes/no).

^c Corrected for age.

^d Significant at $P < .005$.

6 hours. In addition, no infarct demarcation was shown on the CT scan immediately before intervention in these patients.

A successful recanalization (TICI 2b/3) was achieved in 135 patients (84.9%) after an average procedure time of 55 ± 35.1 minutes. TICI 2b/3 was achieved in 29 patients (90.6%) with a carotid T occlusion, in 109 patients (87.2%) with a proximal M1 occlusion, and in 28 patients (77.8%) with a distal M1 or proximal M2 occlusion.

Stent retrievers were used in the following cases: pREset in 91 (57%), Solitaire in 57 (36%), Trevo and Trevo ProVue in 18 (11%), and others (Capture LP, Aperio, and Separator 3D) in 13 (8%).

MT was performed with the patient under conscious sedation in 32 patients (20.1%) and general anesthesia in 127 patients (79.9%). No significant influence of the type of anesthesia on the recanalization results was found ($P > .05$). Patients undergoing general anesthesia had significantly higher NIHSS values than patients treated under conscious sedation (median, 16; range, 4–27 versus 11, 5–22; $P < .001$).

Between subgroups of patients with-versus-without successful recanalization, there were no significant differences in demographic parameters, NIHSS score at admission, time between symptom onset and groin puncture, and procedure time. During MT or at follow-up imaging, we detected the following procedure-related complications: dispersion of the thrombus in 6 patients (3.8%), periprocedural perforation of the vessel in 4 patients (2.5%), and dissection of a vessel in 4 patients (2.5%). A focal SAH was found in 5 patients (3.1%), while diffuse SAH was not found in any patients. According to the European Cooperative Acute Stroke Study classification for hemorrhagic events, there were 10 patients (6.3%) with small petechial hemorrhagic infarction, 3 patients (1.9%) with more confluent petechial hemorrhagic infarction, 5 patients (3.1%) with a parenchymal hematoma with a mild space-occupying effect, and 3 patients (1.9%) with a parenchymal hematoma with a significant space-occupying effect. This latter parenchymal hematoma only occurred in patients with large MCA territory infarctions after hemicraniectomy. None of the described procedure-related complications or hemorrhagic events were associated with an additional relevant clinical deterioration. There were no significant differences between patients with-versus-without successful recanalization regarding complication rates and hemorrhagic events ($P > .05$).

One hundred twenty-five patients were assigned to the subgroup with proximal occlusions. In patients without successful recanalization (TICI 0–2a), the ICA/M1 angle was significantly larger than that in patients with successfully recanalization after correction for age, sex, and IV rtPA application (mean, $110^\circ \pm$

23.8° versus $69^\circ \pm 28.7^\circ$; $P < .001$; Table 2). For differentiating these patients regarding recanalization success, an area under the receiver operating characteristic analysis curve of 0.87 ($P < .001$) was computed for an optimal cutoff of the ICA/M1 angle at 100° (sensitivity, 0.81; specificity, 0.88; Youden $J = 0.69$). By analogy, the M1/M1 angle also differed significantly between patients without-versus-with successful recanalization after correction for age, sex, and IV rtPA application (mean, $56^\circ \pm 29.2^\circ$ versus $29^\circ \pm 26.6^\circ$; $P = .001$). For the M1/M1 angle, ROC analysis provided the corresponding area under the curve of 0.76 ($P = .001$), with an optimal cutoff at 36° (sensitivity, 0.75; specificity, 0.65; Youden $J = 0.40$).

Between the ICA/M1 angle and the M1/M1 angle, a significant correlation was found ($r = 0.54$, $P < .001$).

Thirty-six patients were assigned to the subgroup with distal occlusions. In patients without successful recanalization (TICI 0–2a), the M1/M2 angle was significantly higher than that in patients with successful recanalization after correction for age (mean, $117^\circ \pm 34.3^\circ$ versus $67^\circ \pm 29.5^\circ$; $P = .006$; Table 2). Using ROC analysis, we found an area under the curve of 0.87 ($P = .001$) for the ICA/M1 angle, with an optimal cutoff at 97° (sensitivity, 0.78; specificity, 0.86; Youden $J = 0.64$).

In this subgroup with distal occlusion, no significant differences were found between patients with-versus-without successful recanalization regarding the proximal angles ICA/M1 and M1/M1 ($P > .05$).

After defining an ICA/M1 angle of $>100^\circ$ as a curved MCA, 26 of 125 patients with proximal vessel occlusion were detected (20.8%; mean age, 70 ± 10.4 years; 10 women) who presented with this curved vessel anatomy. In these patients, TICI 2b/3 was significantly less often achieved than in patients with a lower ICA/M1 angle (50.0% versus 97.0%, $P < .001$).

In the subgroup of patients with distal occlusion, 11 of 36 (30.6%; mean age, 69.82 ± 14.2 years; 3 women) had an M1/M2 angle of $>97^\circ$. Compared with patients with lower M1/M2 angles, TICI 2b/3 was significantly less often achieved in these patients (36.4% versus 92.0%, $P = .001$).

There were no significant differences regarding demographic parameters between patients with curved ($>100^\circ$ ICA/M1) and straight ($<100^\circ$ ICA/M1) proximal vessel angles as well as between patients with curved ($>97^\circ$ M1/M2) and straight ($<97^\circ$ M1/M2) distal vessel angles.

For the comparison of different stent retrievers, the seldom-used devices, Capture LP, Aperio, and Separator 3D, were grouped as “others,” while the most frequently used devices, Solitaire FR, pREset, and Trevo/Trevo ProVue were assessed sepa-

rately. We analyzed whether one of the devices was used more frequently in patients who were successfully recanalized despite the presence of curved vessels. None of the devices were significantly over-represented in either subgroup ($P > .05$). In the whole study population, none of the devices were associated with a significantly better recanalization rate or a significantly elevated complication rate ($P > .05$). In patients without successful recanalization, significantly more passages were performed and >1 device was deployed significantly more often than in patients with successful recanalization ($P = .008$ and $P = .011$, respectively).

A strong vessel curvature (ICA/M1 $> 100^\circ$, M1/M1 $> 36^\circ$, M1/M2 $> 97^\circ$, respectively) was associated with neither a significantly higher rate of procedure-related complications such as thrombus dispersion, vessel perforation, or dissection nor hemorrhagic events ($P > .05$, respectively).

In patients with successful recanalization, IV rtPA was not administered significantly more often than in patients with TICI 0–2a (71.9% in TICI 2b/3 versus 62.5% in TICI 0–2a; $P > .05$).

DISCUSSION

In this study, we have shown that vessel anatomy, in particular the curvature of the carotid T and the MCA M1 and M2 segments, has a significant influence on the technical results of MT by using stent retrievers. Patients without successful recanalization (TICI 0–2a) had both significantly larger ICA/M1 and M1/M1 angles in proximal vessel occlusions and significantly larger M1/M2 angles in distal vessel occlusions.

To our knowledge, this phenomenon has not been described in detail before. In patients with acute ischemic stroke after MCA occlusion, Zhu et al¹⁹ assessed the clot configuration by using gradient-echo MR images in axial sections and thus the vessel anatomy within the occlusion site. However, this method provides only indirect information on the vessel curvature, and vessel anatomy proximal to the occlusion site cannot be analyzed.

The relevant geometric details provided by the MCA segment are direction changes toward superior and inferior. Therefore MCA angles are visualized and assessed best in anteroposterior projections.

Furthermore, per se, vascular structures are shown in DSA most precisely; however, only vessel sections passed by intra-arterial contrast agent are visible. Therefore, a limitation of the technique used is that we were only able to measure angles including the most distal vessel segment visualized that was immediately conterminous to the occlusion site. Clot configuration along its entire length and vessel anatomy within the occlusion site could not be analyzed; thus, its influence on recanalization success remains unclear. Further analyses may make use of the microwire passage as an auxiliary marker for vessel anatomy within the occlusion site, or, more directly, of 3D susceptibility-weighted imaging data from patients undergoing MR imaging as a primary stroke imaging technique.

While vessel anatomy assessment based on anteroposterior projections remains an approximation, the most precise angle measurement may be possible in 3D models obtained from CTA. For this analysis, this method has been tested in a small group of patients; however, it proved to be impractical due to the compar-

atively low spatial resolution and the poor vessel contrast immediately adjacent to the occlusion site.

Because this is a retrospective analysis, only assumptions can be made regarding the causal relation between vessel anatomy and successful recanalization. First, when retracting the stent retriever toward the distal-access catheter following a strongly curved vessel segment, the stent-like device may diminish its full spatial extension and thus the grip and interacting forces on the thrombus may be reduced, an effect that has been described as “tapering.”^{12,13} Second, strongly curved vessels may increase friction among the vessel walls, catheters, wires, and device, thus impeding passage and retrieving maneuvers. Third, during the retrieving maneuver, one may observe a change of the vessel anatomy: When applying traction to the pusher wire to which the stent retriever is connected, the expanded device transfers this tension to the vessel anatomy, causing both a folding of vessel segments proximal and an elongation distal to the deployment site. This effect may be more prominent in initially already strongly curved vessels and may increase angles and friction between the thrombus and the vessel wall even more.

On the other hand, curved vessels were not associated with a significantly increased number of periprocedural complications, such as thrombus dispersion, vessel perforation, or intracranial hemorrhage. Therefore, patients with curved vessels apparently do not have an increased periprocedural risk profile if MT is performed.

Regarding different devices, this study did not show any significant superiority of any of the used stent retrievers compared with other models in patients with curved vessels, even though more recently developed stent retrievers have been designed to provide more stability when being retracted around vessel curves and therefore are supposed to avoid the “tapering” phenomenon.^{12,13}

Although vessel curvature significantly influences the results of MT by using stent retrievers, TICI 2b/3 was still achieved in one-half of patients presenting with curved vessels with proximal occlusions and approximately one-third of patients with curved vessels and distal occlusions. Therefore, patients should never be excluded from MT solely on the basis of their vessel angles. However, further development and individualized selection of retrieval devices regarding vessel anatomy may improve the recanalization success in patients with curved vessels. For instance, more bendable devices with a design advanced from the classic stent configuration may perform differently.

Additionally, alternative techniques such as the forced-suction approach, as described in a recent trial, should be assessed in patients with curved vessels because recanalization rates of up to 95% have been reported for this technique.²⁶ A number of studies on suction-based approaches have been published recently, showing inconsistent results; however, none of these studies analyzed vessel anatomy as a factor influencing recanalization success.^{27–29}

Aortic and cervical vessel anatomy may influence recanalization results as well. Especially, older patients with a history of hypertension present with elongated arteries that may impede catheterization and lengthen the procedure duration. Still, no significant influences of age and procedure time on TICI scores were found. Similarly, neither the type of anesthetic nor the NIHSS score at admission significantly influenced the recanalization results. Therefore, we conclude, in this retrospective analysis, that

any possible influence from those parameters on technical results of MT was secondary.

This study focused on intracranial vessel anatomy as 1 factor influencing MT results. It is plausible that other factors (ie, thrombus composition) have a significant influence as well. These should be considered and analyzed in further prospective studies.

Overall, MT significantly improved recanalization rates and clinical outcome in patients with acute ischemic stroke caused by large-vessel occlusion by using stent retrievers.^{5–11} However, in approximately 10%–25% of patients, a successful recanalization (TICI 2b/3) could not be achieved.^{5–14} So far, not many factors are fully understood in determining the recanalization results of these patients. One significant factor is vessel anatomy, as this retrospective study showed.

CONCLUSIONS

In this study, the influence of vessel anatomy, assessed in anteroposterior angiograms, on recanalization results by using stent retrievers in patients with acute ischemic stroke after large-vessel occlusion was described for the first time. It was shown that patients with unsuccessful recanalization (TICI 0–2a) had significantly stronger curved carotid Ts, distal M1 segments, and/or proximal M2 segments than patients with successful recanalization results (TICI 2b/3). Further experimental work is needed to understand the causality of this finding and to develop and analyze new treatment strategies and devices for this patient subgroup.

ACKNOWLEDGMENTS

The authors thank Sebastian Obermeyer for the illustrations and Alexander Hapfelmeier for statistical advice.

Disclosures: Sascha Prothmann—UNRELATED: Consultancy: proctoring for Phenox; Employment: consultant at Klinikum rechts der Isar, Munich.

REFERENCES

1. Seshadri S, Wolf PA. **Lifetime risk of stroke and dementia: current concepts, and estimates from the Framingham Study.** *Lancet Neurol* 2007;6:1106–14
2. Mori E, Yoneda Y, Tabuchi M, et al. **Intravenous recombinant tissue plasminogen activator in acute carotid artery territory stroke.** *Neurology* 1992;42:976–82
3. Saqqur M, Uchino K, Demchuk AM, et al; CLOTBUST Investigators. **Site of arterial occlusion identified by transcranial Doppler predicts the response to intravenous thrombolysis for stroke.** *Stroke* 2007;38:948–54
4. Smith WS, Lev MH, English JD, et al. **Significance of large vessel intracranial occlusion causing acute ischemic stroke and TIA.** *Stroke* 2009;40:3834–40
5. Dávalos A, Pereira VM, Chapot R, et al; Solitaire Group. **Retrospective multicenter study of Solitaire FR for revascularization in the treatment of acute ischemic stroke.** *Stroke* 2012;43:2699–705
6. Nogueira RG, Lutsep HL, Gupta R, et al; TREVO 2 Trialists. **Trevo versus Merci retrievers for thrombectomy revascularisation of large vessel occlusions in acute ischaemic stroke (TREVO 2): a randomised trial.** *Lancet* 2012;380:1231–40
7. Pereira VM, Gralla J, Dávalos A, et al. **Prospective, multicenter, single-arm study of mechanical thrombectomy using Solitaire flow restoration in acute ischemic stroke.** *Stroke* 2013;44:2802–07
8. Saver JL, Jahan R, Levy EI, et al; SWIFT Trialists. **Solitaire flow restoration device versus the Merci retriever in patients with acute ischaemic stroke (SWIFT): a randomised, parallel-group, non-inferiority trial.** *Lancet* 2012;380:1241–49
9. Yoon YH, Yoon W, Jung MY, et al. **Outcome of mechanical thrombectomy with Solitaire stent as first-line intra-arterial treatment in intracranial internal carotid artery occlusion.** *Neuroradiology* 2013; 55:999–1005
10. Zaidat OO, Castonguay AC, Gupta R, et al. **North American Solitaire Stent Retriever Acute Stroke registry: post-marketing revascularization and clinical outcome results.** *J Neurointerv Surg* 2014; 6:584–88
11. Broussalis E, Trinka E, Hitzl W, et al. **Comparison of stent-retriever devices versus the Merci retriever for endovascular treatment of acute stroke.** *AJNR Am J Neuroradiol* 2013;34:366–72
12. Kurre W, Aguilar-Pérez M, Schmid E, et al. **Clinical experience with the pREset stent retriever for the treatment of acute ischemic stroke—a review of 271 consecutive cases.** *Neuroradiology* 2014;56:397–403
13. Schwaiger BJ, Kober F, Gersing AS, et al. **The pREset stent retriever for endovascular treatment of stroke caused by MCA occlusion: safety and clinical outcome.** *Clin Neuroradiol* 2014 Aug 12. [Epub ahead of print]
14. Jansen O, Macho JM, Killer-Oberpfalzer M, et al; TREVO Study Group. **Neurothrombectomy for the treatment of acute ischemic stroke: results from the TREVO study.** *Cerebrovasc Dis* 2013; 36:218–25
15. Yuki I, Kan I, Vinters HV, et al. **The impact of thromboemboli histology on the performance of a mechanical thrombectomy device.** *AJNR Am J Neuroradiol* 2012;33:643–48
16. Gralla J, Burkhardt M, Schroth G, et al. **Occlusion length is a crucial determinant of efficiency and complication rate in thrombectomy for acute ischemic stroke.** *AJNR Am J Neuroradiol* 2008;29:247–52
17. Jindal G, Miller T, Shivashankar R, et al. **Relationship of thrombus length to number of stent retrievals, revascularization, and outcomes in acute ischemic stroke.** *J Vasc Interv Radiol* 2014;25:1549–57
18. Behme D, Kowoll A, Weber W, et al. **M1 is not M1 in ischemic stroke: the disability-free survival after mechanical thrombectomy differs significantly between proximal and distal occlusions of the middle cerebral artery M1 segment.** *J Neurointerv Surg* 2014 Jun 24. [Epub ahead of print]
19. Zhu L, Liebeskind DS, Jahan R, et al. **Thrombus branching and vessel curvature are important determinants of middle cerebral artery trunk recanalization with Merci thrombectomy devices.** *Stroke* 2012;43:787–92
20. Veltkamp R. **Akuttherapie des ischämischen Schlaganfalls.** In: Diener HC, Weimar C, eds. *Leitlinien für Diagnostik und Therapie in der Neurologie.* 5th ed. Stuttgart: Thieme; 2012:307–23
21. Fisher M, Albers GW. **Advanced imaging to extend the therapeutic time window of acute ischemic stroke.** *Ann Neurol* 2013;73:4–9
22. Parsons M, Spratt N, Bivard A, et al. **A randomized trial of tenecteplase versus alteplase for acute ischemic stroke.** *N Engl J Med* 2012;366:1099–107
23. Burton KR, Dhanoa D, Aviv RI, et al. **Perfusion CT for selecting patients with acute ischemic stroke for intravenous thrombolytic therapy.** *Radiology* 2015;274:103–14
24. Berger C, Fiorelli M, Steiner T, et al. **Hemorrhagic transformation of ischemic brain tissue: asymptomatic or symptomatic?** *Stroke* 2001; 32:1330–35
25. Youden WJ. **Index for rating diagnostic tests.** *Cancer* 1950;3:32–35
26. Turk AS, Frei D, Fiorella D, et al. **ADAPT FAST study: a direct aspiration first pass technique for acute stroke thrombectomy.** *J Neurointerv Surg* 2014;6:260–64
27. Kim SK, Yoon W, Moon SM, et al. **Outcomes of manual aspiration thrombectomy for acute ischemic stroke refractory to stent-based thrombectomy.** *J Neurointerv Surg* 2014 May 7. [Epub ahead of print]
28. Kang DH, Kim YW, Hwang YH, et al. **Switching strategy for mechanical thrombectomy of acute large vessel occlusion in the anterior circulation.** *Stroke* 2013;44:3577–79
29. Kass-Hout T, Kass-Hout O, Sun CH, et al. **Clinical, angiographic and radiographic outcome differences among mechanical thrombectomy devices: initial experience of a large-volume center.** *J Neurointerv Surg* 2015;7:176–81

Dual-Lumen Balloon Catheters May Improve Liquid Embolization of Vascular Malformations: An Experimental Study in Swine

J.C. Gentric, J. Raymond, A. Batista, I. Salazkin, G. Gevry, and T.E. Darsaut

ABSTRACT

BACKGROUND AND PURPOSE: Liquid embolic agents are increasingly used to treat vascular malformations. We sought to assess embolization with these agents by using a dual-lumen balloon catheter in an experimental setting.

MATERIALS AND METHODS: Eighteen injections of liquid embolic agents were performed in the rete mirabile of swine. We used 3 methods to control liquid embolic agent reflux: 1) dual-lumen balloon-catheter (group A, $n = 8$); 2) injection of liquid embolic agent after proximal *n*-BCA plug formation through a second microcatheter (group B, $n = 4$); and 3) standard liquid embolic agent injection (group C, controls, $n = 6$). The following outcomes were graded by using ordinal scales by angiography, macrophotography, and radiography of retia after euthanasia: 1) angiographic and pathologic extent of liquid embolic agent embolization of the rete, 2) reflux of liquid embolic agents in the parent artery, and 3) density of liquid embolic agents in the proximal rete. Technical complications were also recorded. A successful injection was defined as an embolization that reached the contralateral rete without reflux into proximal external branches. Exact logistic regression analyses were performed to compare groups.

RESULTS: There were significant differences among groups for reflux ($P = .029$) and liquid embolic agent density in the proximal rete ($P = .014$), while extension to the contralateral rete did not reach statistical significance ($P = .07$). Injections differed among groups ($P = .004$), with dual-lumen balloon-catheter injections more frequently successful compared with control injections ($P = .019$).

CONCLUSIONS: Dual-lumen balloon catheters allowed better liquid embolic agent injections than standard injections.

ABBREVIATIONS: LEA = liquid embolic agent; PHIL = Precipitating Hydrophobic Injectable Liquid

Ethylene-vinyl alcohol copolymer liquid embolic agents (LEAs) have changed the management of vascular malformations such as arteriovenous malformations and dural arteriovenous fistulas.¹⁻⁴ LEAs such as Onyx (Covidien, Irvine, California) can be injected through small microcatheters, and on injection, they precipitate out of the dimethyl-sulfoxide solvent and slowly harden after coming in contact with blood. These agents are cohesive rather than adhesive and perhaps better controlled than other

agents such as *n*-BCA. In many cases, these features (of LEAs such as Onyx/Phil) may permit longer injections and possibly more complete embolizations than other LEAs.¹

The standard method used to control injections is to slowly inject the LEA, allowing some reflux for a short plug proximal to the catheter tip to form and harden, and to wait for the LEA to preferentially move in an antegrade direction deep into the nidus of the malformation. One factor potentially limiting the efficacy of the injection is excessive reflux of LEA back along the catheter, which can enter and occlude unwanted vessels.⁵ Additionally, if a segment of microcatheter that is too long is left in contact with the LEA for too long, the proximal plug may entrap the catheter tip in place. Removal of entrapped catheters has led to intracranial hemorrhages, leading to an FDA warning regarding this aspect of treatment with Onyx.⁶

Several potential solutions to these problems have been proposed. One option is to use 2 microcatheters together: One microcatheter with a detachable tip is used for the injection of the LEA, while the other microcatheter is used to deliver *n*-BCA quickly, intentionally gluing the detachable portion of the first

Received September 2, 2014; accepted after revision November 6.

From the Department of Radiology (J.C.G., J.R., A.B.), Centre Hospitalier de l'Université de Montréal, Notre-Dame Hospital, Montreal, Quebec, Canada; Laboratory of Interventional Neuroradiology (J.R., I.S., G.G.), Centre Hospitalier de l'Université de Montréal, Notre-Dame Hospital Research Centre, Montreal, Quebec, Canada; Division of Neurosurgery (T.E.D.), Department of Surgery, University of Alberta Hospital, Mackenzie Health Sciences Centre, Edmonton, Alberta, Canada; and Equipe d'Accueil 3878 - Groupe d'Etude de la Thrombose en Bretagne Occidentale (J.C.G.), Université de Bretagne Occidentale, Brest, France.

This work was supported by MicroVention, which also supplied catheters and the PHIL prototype liquid embolic. Covidien supplied Onyx and microcatheters.

Please address correspondence to Tim Darsaut, MD, University of Alberta Hospital, 8440 112th St, WMC 2C3.83, Edmonton, Alberta, Canada T6G 2B7; e-mail: tdarsaut@ualberta.ca

<http://dx.doi.org/10.3174/ajnr.A4211>

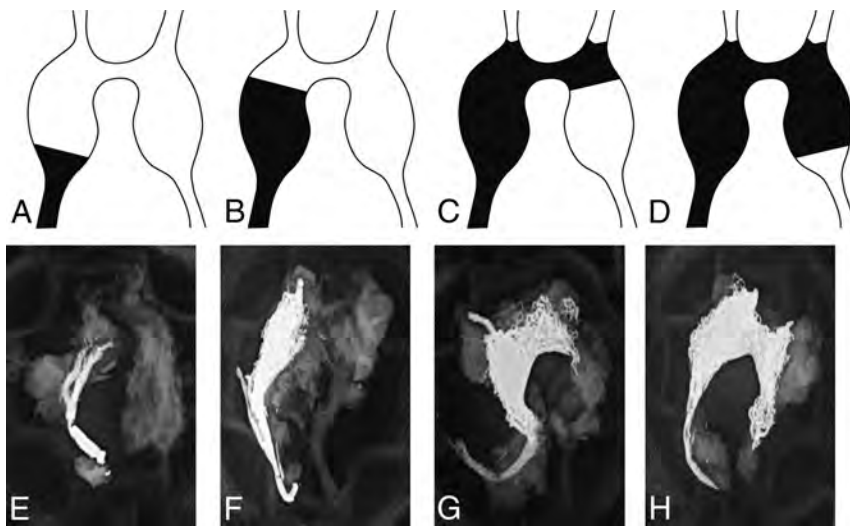


FIG 1. Schematics and radiographs demonstrating the different grades of extent of LEA infiltration through the porcine rete. A and E, Grade I, <50% infiltration of the ipsilateral rete. B and F, Grade II, >50% but <100% infiltration of the ipsilateral rete. C and G, Grade III, complete infiltration through the ipsilateral rete with <50% of the contralateral rete. D and H, Grade IV, complete infiltration through the ipsilateral and >50% of the contralateral rete.

catheter, forming the proximal plug that will prevent reflux of LEA, and ensuring antegrade embolization of the nidus.⁷⁻⁹ Another option is to use a dimethyl-sulfoxide-compatible dual-lumen balloon catheter, in which 1 lumen is used to inflate a balloon and prevent reflux, while the second lumen delivers the embolic agent (Scepter; MicroVention, Tustin, California).^{5,10}

Animal models may be useful to inform clinical applications of embolic agents.¹¹⁻¹⁴ We sought to explore whether using a dual-lumen balloon catheter could improve embolization of the swine rete (a model often used for experimental AVM embolization)^{12,15,16} and prevent excessive reflux compared with more traditional techniques. We hypothesized that the use of the balloon would promote more complete nidus filling with less reflux and fewer complications than other methods.

MATERIALS AND METHODS

Embolization

Protocols for animal experimentation were approved by the Institutional Animal Care Committee in accordance with guidelines of the Canadian Council on Animal Care. All procedures were performed in 20- to 25-kg Yorkshire pigs under general anesthesia. Conventional angiography was performed via femoral puncture. Using a coaxial approach, we navigated microcatheters to the porcine ascending pharyngeal artery, which supplies the rete mirabile. Animals were randomly allocated to be embolized by using 1 of 3 treatment options: 1) Group A animals were embolized by using a dual-lumen balloon catheter ($n = 8$); 2) group B animals were embolized by using a 2-microcatheter technique (1 detachable-tip microcatheter was used for LEA injection [Apollo; Covidien]; the other [Marathon; Covidien] was used for *n*-BCA proximal plug formation [$n = 4$]); and group C were controls using a single-microcatheter technique (the balloon microcatheter, keeping the balloon deflated) ($n = 6$).

Scepter is a dimethyl-sulfoxide- and Onyx-compatible double-lumen balloon catheter. The profile of the Scepter is 2.8F

proximally and 2.1F in its distal segment, with a working lumen inner diameter of 0.0165 inches. The balloon catheter is compatible with up to 0.014-inch guidewires.

Onyx 18 (Covidien) was the LEA used for 11 injections; a prototype LEA (Precipitating Hydrophobic Injectable Liquid [PHIL]; MicroVention) was used for 7 injections. This liquid embolic agent, PHIL, is a 2-component system. The first component is the flushing solution, which is an organic solvent, dimethyl-sulfoxide, and the second component is the liquid embolic agent, a copolymer that is dissolved in dimethyl-sulfoxide.

All injections were performed in random order, either by 2 interventionists (T.E.D. and J.C.G., 5 years of experience each) or by the senior author (J.R., 29 years of experience). All injections were

observed by 2 interventionists. Randomization was performed by flipping a coin for allocation to an experimental group or control and by trying to balance Onyx and prototype LEA injections (1:1) for groups A and C. Thus, the number of injections with Onyx versus PHIL was 4:4 for group A and 3:3 for group C. The number of injections requiring balloon catheters (groups A and C) and LEA and the total number of animals were limited by the availability of material and the total budget for these experiments. Due to these constraints, the resulting final number of animals per group was unequal.

After slowly flushing the microcatheter dead space with dimethyl-sulfoxide and the dimethyl-sulfoxide with the LEA for 2 minutes, we injected the LEA slowly by using fluoroscopic guidance, attempting to reach the contralateral rete, until reflux out of the ascending pharyngeal artery occurred or until the rete was completely filled. Injections were also stopped when the embolic material reached the intracranial circulation. After control angiography, animals were euthanized and the rete mirabile was harvested and immersed in 10% formalin for macroscopic photography and radiographic and pathologic analyses.

Macroscopic photographs and radiographs of the embolized and formalin-fixed specimens were used to score the extent of LEA infiltration within the rete by using a 4-point scale. Grades were adjudicated by 2 readers (J.R. and J.C.G.) as follows: grade I, <50% of the ipsilateral rete; grade II, >50% but <100% of the ipsilateral rete; grade III, complete infiltration through the ipsilateral rete reaching <50% of the contralateral rete; and grade IV, complete infiltration of the ipsilateral and >50% of the contralateral rete (Figs 1 and 2). We studied the reliability of the grading system: Three authors (J.R., T.E.D., and J.C.G.) blindly and independently scored a random sample of 10 rete radiographs from these experiments to provide a measure of interobserver variability.

Reflux was defined as any retrograde filling of the ascending pharyngeal artery proximal to the catheter tip and was graded by

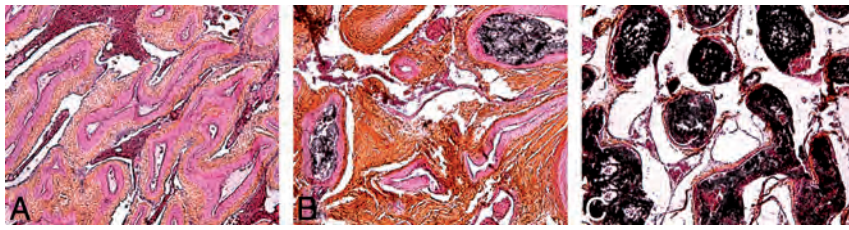


FIG 2. Microscopic pathology of the rete mirabile. Three different specimens are shown as examples of grade 0, no filling (A); grade I, incomplete filling (B); and grade II, complete filling of the proximal rete (C). (Hematoxylin phloxine saffron stain; original magnification $\times 50$.)

Summary of LEA injections

Group and Injection	Reflux	Extent	Density	Technical Complications	LEA Used
Group A: dual-lumen balloon catheter					
1 ^a	2	3	2	No	Onyx 18
2 ^a	1	4	2	No	Onyx 18
3 ^a	1	4	2	No	PHIL
4 ^a	2	3	1	No	PHIL
5 ^a	1	4	2	No	PHIL
6	3	3	1	No	PHIL
7 ^a	2	3	2	No	Onyx 18
8	3	4	2	No	Onyx 18
Group B: double-microcatheter technique					
9	3	2	2	No	Onyx 18
10	3	3	1	Yes	Onyx 18
11	3	4	2	No	Onyx 18
12	3	3	2	Yes	Onyx 18
Group C: single-microcatheter (controls)					
13	3	1	1	No	Onyx 18
14	3	3	1	Yes	PHIL
15	3	3	1	No	PHIL
16	3	1	0	No	Onyx 18
17 ^a	2	4	1	Yes	PHIL
18	3	1	1	No	Onyx 18

^a Denotes a successful injection, defined as an injection with a grade >2 for extent of infiltration without excessive reflux (reflux score of <3).

using a 3-point scale as follows: grade I, acceptable reflux (limited to the distal two-thirds of the ascending pharyngeal artery); grade II, maximal permissible reflux (up to the proximal one-third of the ascending pharyngeal artery); and grade III, reflux into any artery other than the ascending pharyngeal, which was considered unacceptable.

The density of LEAs within the proximal rete mirabile was scored after microscopic examination by the same raters by using a 3-point scale, adjudicated as follows: 0, no filling; 1, partial filling; and 2, total filling of the proximal rete. A successful liquid embolic injection was defined as an injection that reached an extent grade of >2 without excessive reflux (a reflux score of <3). In case of discrepancies between microscopic examination and macrophotographs, a final verdict was established through a consensus session. At the end of each injection and for each microcatheter, the amount of traction required to retrieve the catheter was assessed. Inflated balloon-catheters were deflated under fluoroscopic control. The distal tips of all catheters, including the 0.5-mm distal catheter tip of the Scepter balloon, were examined and photographed by using a stereomicroscope, looking for adherent embolic material or fragments.

Statistics

Groups were compared by exact logistic regression analyses, by using .05 as the threshold for statistical significance. Interobserver agreement in scoring the extension of rete embolization was assessed by using a weighted κ with a 95% confidence interval.¹⁷ The κ values were interpreted according to Altman¹⁸: ≤ 0.20 , poor agreement; 0.21–0.40, fair agreement; 0.41–0.60, moderate agreement; 0.61–0.80, good agreement; and 0.81–1.00, very good agreement.

RESULTS

Results are summarized in the Table and illustrated in Figs 1 and 2.

The extent of rete embolization was >2 in 8/8 dual-lumen balloon animals (group A), 3/4 double-microcatheter animals (group B), and 3/6 single-microcatheter animals (group C) ($P = .073$). There was good (raters 1 versus 3 and 2 versus 3; 70% concordance; $\kappa = 0.8$ [range, 0.625–0.975]) to very good (rater 1 versus 2; 100% concordance; $\kappa = 1$) agreement in scoring extension of embolization between observers. Excessive (or grade 3) reflux occurred in 4/4 group B and 5/6 group C but only in 2/8 group A animals ($P = .029$). The density of LEA differed among groups ($P = .014$), with the rete mirabile of the group A animals found to be more densely filled than that of controls ($P = .019$).

Technical Complications

In 2 injections of the control group, the microcatheter tip was trapped within the LEA plug. In 2 animals treated by using the 2-microcatheter technique (group B), serious complications occurred, with extensive reflux (of LEA in 1 case and *n*-BCA in the other), leading to inadvertent embolization of branches. On 2 occasions during LEA embolization, the inflated balloon moved proximally by approximately 1 cm when the injection pressure was increased to more completely fill the contralateral rete. The retrograde balloon movement was controlled by gently further inflating the balloon. These cases were considered minor problems. Macroscopic inspection of the microcatheters did not reveal any material on balloon surfaces or catheter tips, but there were a few microscopic particles of the LEA mixture in 2 cases. There was no instance of spontaneous balloon deflation, and balloons remained intact in all cases.

The frequency of injections judged to be “successful” differed among groups ($P = .004$), with more successful injections in the dual-lumen-balloon group (group A) animals compared with controls (group C, $P = .019$).

DISCUSSION

The main result of this investigation is that dual-lumen balloon catheters can be used to allow LEA to more readily reach the contralateral rete without excessive reflux compared with single-lumen catheter or 2-microcatheter techniques. The balloon remains intact and can be deflated and retrieved easily at the end of the injection.

There are several important steps to successful injection of LEAs, which have been summarized by Weber et al.¹⁹ Most operators used a “push and plug” technique,²⁰ in which after establishing a small proximal plug of LEA, the operator resumes the injection, assessing under close fluoroscopic guidance whether the LEA is moving antegrade to fill the nidus or refluxing proximally. The operator halted the injection for at least 2 reasons: 1) Too much reflux threatened to fill an unwanted more proximal blood vessel, potentially leading to an ischemic insult; or 2) reflux increased the length of catheter exposed to the solidifying LEA, which can increase the risk of trapping the catheter. In this work, the use of a dual-lumen balloon-mounted catheter effectively mitigated these problems.

The dual-lumen balloon-mounted catheters studied in this work have already been used in human applications, including brain arteriovenous malformations and dural arteriovenous fistulas, leading to several early, enthusiastic clinical reports.^{5,20,21} One potential advantage of the balloon catheter is the ability to inject LEA, perhaps more safely, in the presence of a high-flow shunt.^{9,21,22}

To avoid complications, one must pay close attention, nonetheless, to the radiopaque LEA as it progresses from the microcatheter; retrograde flow can still occur despite an inflated balloon, and antegrade flow of LEA can still fill potentially dangerous anastomotic vessels.

Finally, the dual-lumen balloon catheter cannot be navigated as far distal in the vasculature as a simple microcatheter because it has a larger outer diameter. If an optimal position cannot be reached, a more proximal position from which to perform the injection risks filling of normal vessels “en route” to the nidus, with potential complications.

Limitations

One important limitation of this study is the small number of animals; in addition, groups were of unequal sizes, both affecting the power of statistical analyses. Although the rete mirabile is a plexiform vascular structure, it does not contain arteriovenous shunts. The surgical creation of an arteriovenous fistula can make this model more similar to an AVM.^{23,24} It is unclear whether results would have differed if this more complex model had been used. The persistence of variable antegrade flow from the contralateral ascending pharyngeal artery may have affected the extension of the embolic agent when injected in the contralateral rete. In our hands, the surgical creation of a shunt may also introduce variable flow patterns in the model, from one animal to another. In addition, the shunt may decrease with time in some animals, making timing of experiments critical.

We have used a simple but subjective grading system, rather than a previously published, more objective method, to quantify the extension of LEA embolization.²⁵ Two different LEAs were

used during these experiments, but we think that this had no important effect on results. The use of the prototype agent PHIL was balanced among groups (4 of 8 injections for group A; 3 of 6 injections for group C). The rete is also considerably smaller than many AVMs encountered in patients, and complete occlusion in this experimental setting is more readily achievable. Injection times were also shorter than many injections in clinical embolizations, which can reach 45–60 minutes or more. This shorter period may not have allowed as much LEA hardening as can sometimes be required in the clinical setting; therefore, we may have underestimated the traction forces required for microcatheter removal. Other factors important for successful AVM embolization are not evaluable by using this model, including navigability of the balloon-catheter through tortuous vascular structures. The risks of specific complications such as vascular rupture arising from inflating balloons in dysplastic intracranial AVM feeders could not be assessed. We have not tested, in this model, other LEAs, such as *n*-BCA mixed with Lipiodol (Guerbet, Roissy, France), which cannot be used with the Scepter; the use of these agents may lead to balloon rupture.²⁶

CONCLUSIONS

Balloon catheters may improve the control of LEA embolization in an animal model of vascular malformation.

ACKNOWLEDGMENTS

This publication was made possible in part by an International Fellowship award to Jean-Christophe Gentric by the Société Française de Radiologie.

Disclosures: Jean Raymond—RELATED: Grant: MicroVention provided unrestricted funding for this project.* *Money paid to the institution.

REFERENCES

1. Saatci I, Geyik S, Yavuz K, et al. **Endovascular treatment of brain arteriovenous malformations with prolonged intranidal Onyx injection technique: long-term results in 350 consecutive patients with completed endovascular treatment course.** *J Neurosurg* 2011;115:78–88
2. Pierot L, Cognard C, Herbreteau D, et al. **Endovascular treatment of brain arteriovenous malformations using a liquid embolic agent: results of a prospective, multicentre study (BRAVO).** *Eur Radiol* 2013;23:2838–45
3. van Rooij WJ, Jacobs S, Sluzewski M, et al. **Curative embolization of brain arteriovenous malformations with Onyx: patient selection, embolization technique, and results.** *AJNR Am J Neuroradiol* 2012;33:1299–304
4. Mounayer C, Hammami N, Piotin M, et al. **Nidal embolization of brain arteriovenous malformations using Onyx in 94 patients.** *AJNR Am J Neuroradiol* 2007;28:518–523
5. Jagadeesan BD, Grigoryan M, Hassan AE, et al. **Endovascular balloon-assisted embolization of intracranial and cervical arteriovenous malformations using dual-lumen coaxial balloon microcatheters and Onyx: initial experience.** *Neurosurgery* 2013;73(2 Suppl Operative):ons238–43
6. ev3 Onyx Liquid Embolic System: Safety Communication—Risk of Catheter Entrapment. Posted June 29, 2012. <http://www.fda.gov/Safety/MedWatch/SafetyInformation/SafetyAlertsforHumanMedicalProducts/ucm310199.htm>. Accessed June 19, 2014
7. Shi ZS, Loh Y, Duckwiler GR, et al. **Balloon-assisted transarterial embolization of intracranial dural arteriovenous fistulas.** *J Neurosurg* 2009;110:921–28

8. Newman CB, Hu YC, McDougall CG, et al. **Balloon-assisted Onyx embolization of cerebral single-channel pial arteriovenous fistulas.** *J Neurosurg Pediatr* 2011;7:637–42
9. Andreou A, Ioannidis I, Nasis N. **Transarterial balloon-assisted glue embolization of high-flow arteriovenous fistulas.** *Neuroradiology* 2008;50:267–72
10. Spiotta AM, James RF, Lowe SR, et al. **Balloon-augmented Onyx embolization of cerebral arteriovenous malformations using a dual-lumen balloon: a multicenter experience.** *J Neurointerv Surg* 2014 Aug 12. [Epub ahead of print]
11. Raymond J, Salazkin I, Gevry G, et al. **Interventional neuroradiology: the role of experimental models in scientific progress.** *AJNR Am J Neuroradiol* 2007;28:401–05
12. Murayama Y, Viñuela F, Ulhoa A, et al. **Nonadhesive liquid embolic agent for cerebral arteriovenous malformations: preliminary histopathological studies in swine rete mirabile.** *Neurosurgery* 1998;43:1164–175
13. Natarajan SK, Born D, Ghodke B, et al. **Histopathological changes in brain arteriovenous malformations after embolization using Onyx or N-butyl cyanoacrylate: laboratory investigation.** *J Neurosurg* 2009;111:105–13
14. Spiotta AM, Sivapatham T, Teng Q, et al. **Balloon-augmented carotid artery sacrifice with Onyx: a proof of concept study in a swine model.** *J Neurointerv Surg* 2011;3:390–94
15. Amiridze NS, Darwish R, Griffith GM, et al. **Treatment of arteriovenous malformations with hydrocoils in a swine model.** *Interv Neuroradiol* 2008;14:165–71
16. Levrier O, Mekkaoui C, Rolland PH, et al. **Efficacy and low vascular toxicity of embolization with radical versus anionic polymerization of n-butyl-2-cyanoacrylate (NBCA): an experimental study in the swine.** *J Neuroradiol* 2003;30:95–102
17. Fleiss JL, Levin B, Paik MC. *Statistical Methods for Rates and Proportions.* 3rd ed. New York: Wiley; 2003
18. Altman DG. *Practical Statistics for Medical Research.* London: Chapman and Hall; 1990
19. Weber W, Kis B, Siekmann R, et al. **Endovascular treatment of intracranial arteriovenous malformations with Onyx: technical aspects.** *AJNR Am J Neuroradiol* 2007;28:371–77
20. Paramasivam S, Niimi Y, Fifi J, et al. **Onyx embolization using dual-lumen balloon catheter: initial experience and technical note.** *J Neuroradiol* 2013;40:294–302
21. Orozco LD, Luzardo GD, Buciuic RF. **Transarterial balloon assisted Onyx embolization of pericallosal arteriovenous malformations.** *J Neurointerv Surg* 2013;5:e18
22. Jagadeesan BD, Mortazavi S, Hunter DW, et al. **Endovascular balloon-assisted embolization of high-flow peripheral vascular lesions using dual-lumen coaxial balloon microcatheter and Onyx: initial experience.** *J Vasc Interv Radiol* 2014;25:587–92
23. Siekmann R, Wakhloo AK, Lieber BB, et al. **Modification of a previously described arteriovenous malformation model in the swine: endovascular and combined surgical/endovascular construction and hemodynamics.** *AJNR Am J Neuroradiol* 2000;21:1722–25
24. Massoud TF, Ji C, Viñuela F, et al. **An experimental arteriovenous malformation model in swine: anatomic basis and construction technique.** *AJNR Am J Neuroradiol* 1994;15:1537–45
25. Lieber BB, Wakhloo AK, Siekmann R, et al. **Acute and chronic swine rete arteriovenous malformation models: effect of ethiodol and glacial acetic acid on penetration, dispersion, and injection force of N-butyl 2-cyanoacrylate.** *AJNR Am J Neuroradiol* 2005;26:1707–14
26. Park S, Hwang SM, Lim OK, et al. **Compliant neurovascular balloon catheters may not be compatible with liquid embolic materials: intraprocedural rupture of the protecting balloon during tumor embolization using n-butyl cyanoacrylate and lipiodol mixture.** *J Neurointerv Surg* 2014 Aug 27. [Epub ahead of print]

CT Findings in the External Auditory Canal after Transcanal Surgery

V. Mingkwansook, H.D. Curtin, and H.R. Kelly

ABSTRACT

BACKGROUND AND PURPOSE: Middle ear surgery is often performed through the external auditory canal, and the CT appearance of the external auditory canal after transcanal middle ear surgery can mimic erosive pathology such as carcinoma, external auditory canal cholesteatoma, or necrotizing external otitis. We reviewed the CT findings in a group of patients following transcanal surgery to highlight this potential pitfall in interpretation.

MATERIALS AND METHODS: Twenty-seven temporal bones in 25 patients with a history of a transcanal approach to the middle ear and available postoperative CT imaging were identified. Images were assessed for changes along or involving the walls of the external auditory canal, including widening, irregularity, bony defects, and soft tissue opacification.

RESULTS: Osseous changes along the floor of the external auditory canal were demonstrated in 25 of 27 (92.6%) temporal bone CT scans. Similar changes were present in the superior and anterior walls of the external auditory canal in 21 and 18 temporal bones, respectively. The anterior wall was the most common site for complete bony defects (10 of 27 temporal bones). The posterior wall was the least often involved, with osseous changes in 15 of 27 temporal bones and bony defects in 3 cases. Soft tissue thickening was seen most commonly along the floor. No patient was found to have a superimposed pathologic process of the external auditory canal.

CONCLUSIONS: CT findings in the external auditory canal after transcanal surgery include thinning, irregularity and/or flattening of the bone, soft tissue thickening, and bony wall defects. Although these changes may be subtle, they may mimic pathology and should be included in the differential diagnosis of osseous abnormality of the external auditory canal.

ABBREVIATION: EAC = external auditory canal

Middle ear surgery performed through the external auditory canal (EAC) often involves drilling a portion of the bony canal wall to provide access and necessary exposure.¹⁻³ In the absence of associated transmastoid surgery (such as a canal wall down mastoidectomy), the postoperative status may not be immediately obvious to the interpreting radiologist, and relevant history may not be provided. On CT, such postoperative changes in the external canal can mimic bony and soft tissue changes typically associated with neoplasms, external canal cholesteatoma, or

aggressive infections of the EAC. Prior literature has predominantly focused on the appearance of the middle ear after surgery.⁴⁻¹¹ We describe the CT appearance of the EAC after transcanal surgery so that postoperative change can be included in the differential diagnosis, even in the absence of available history, and erroneous diagnoses may be avoided.

MATERIALS AND METHODS

Patients

This retrospective study was performed in accordance with the Health Insurance Portability and Accountability Act. Twenty-five patients with a history of transcanal middle ear surgery (including 2 patients with a history of bilateral surgery) and subsequent postoperative CT imaging were retrospectively identified from an imaging data base. Postoperative imaging was performed during a 7-year period from July 2007 to April 2014. Confirmation of transcanal surgery with an operative report and/or clinical surgical note describing the alterations/drilling of the EAC was necessary for inclusion. Patients with a history of prior canal wall down mastoidectomy were excluded, given the distinctive appearance

Received August 19, 2014; accepted after revision November 21.

From the Radiology Department (V.M.), Thammasat University Hospital, Pathumthani, Thailand; Department of Radiology (V.M., H.D.C., H.R.K.), Massachusetts Eye and Ear Infirmary/Harvard Medical School, Boston, Massachusetts; and Division of Neuroradiology (H.R.K.), Massachusetts General Hospital/Harvard Medical School, Boston, Massachusetts.

Paper previously presented in part at: Annual Meeting of the American Society of Neuroradiology, May 17-22, 2014; Montréal, Québec, Canada.

Please address correspondence to Hillary R. Kelly, MD, Massachusetts General Hospital, Division of Neuroradiology, 55 Fruit St, GRB-273A, Boston, MA 02114; e-mail: hillary.kelly@mgh.harvard.edu

<http://dx.doi.org/10.3174/ajnr.A4226>

of the removal of the posterosuperior wall of the EAC. Patients with a history of surgery for a primary EAC indication (such as exostosis removal or repair of EAC stenosis) rather than middle ear surgery were also excluded. The electronic medical record was reviewed for otologic history, clinical examination findings, and operative reports, in addition to demographic data.

CT Technique

All 25 patients underwent dedicated temporal bone CT without intravenous contrast. Of 27 temporal bones, 19 were imaged on a 40-section multidetector CT scanner (Somatom Sensation; Siemens, Erlangen, Germany). Scanning parameters were 120 kV(peak), 320 mAs at 0.6-mm collimation, and a 0.55 pitch with helical acquisition extending from just superior to the petrous ridge through the inferior skull base. In pediatric patients, 120 mAs was used to decrease the radiation dose. Data from each ear were reconstructed into 0.6 (section thickness) \times 0.2 mm (reconstruction interval) axial images in a bone algorithm at a display FOV of 100 mm and a matrix of 512 \times 512. The technologist then created standardized axial and coronal reformatted images along the plane of the lateral semicircular canal at the scanner console by using the sagittal images as a reference. The remaining 8 of 27 temporal bones were imaged on a digital volume tomography (conebeam) scanner (3D Accuitomo 170; J. Morita, Osaka, Japan). Scanning parameters were 90 kVp, 8 mA, 30.8-second rotation time, with a 60 \times 60 mm FOV. The raw data voxel size was 0.5 \times 0.08 \times 0.08 mm, and the same standardized reformatted images were created in the axial and coronal planes, as described above.

Image Analysis

The axial and coronal reformatted images from each temporal bone were reviewed on the PACS of our institution. All CT images were independently reviewed by 2 neuroradiologists (V.M. with 4 years of experience and board-certified in Thailand; H.R.K. with 7 years of experience with a Certificate of Added Qualification in neuroradiology). The images were reviewed for cortical change (including flattening of the floor of the EAC with apparent loss of the tympanic sulcus, thinning, and/or irregularity), bony defects, and soft tissue thickening along each EAC wall (anterior, posterior, superior, and inferior). Preoperative imaging was used for comparison if available. Comparison was also made with the contralateral side if imaged and if asymptomatic by history. A bony defect was defined as focal discontinuity of the anterior and/or inferior EAC wall. For the superior and posterior walls, a bony defect was defined as a loss of the bony plate covering the mastoid air cells. Measurement of the maximal defect size of each wall was also performed, by using the axial plane for the anterior and posterior walls and the coronal plane for the superior and inferior walls. Any soft tissue opacity along the bony EAC walls was also recorded. The tympanic membrane was also assessed for thickening and/or calcification. The absence of any ossicles or the presence of an ossicular prosthesis or both were also recorded. Interobserver agreement was calculated by using the κ statistic. Discrepancies were resolved by consensus and with additional adjudication by an experienced head and neck radiologist

(H.D.C., board-certified, with >30 years of experience and a Certificate of Added Qualification in neuroradiology).

RESULTS

Of the 25 patients included in the study, 14 were male and 13 were female, with ages ranging from 8 to 87 years (median age, 47 years). The time interval between operative intervention and CT ranged from 2 months to 30 years (median interval, 4 years). The surgical procedure in 25 of the 27 temporal bones was tympanoplasty, with 7 of these patients also undergoing canal wall up mastoidectomy, 4 undergoing additional canaloplasty, and 3 undergoing additional atticotomy. One operation included canal wall up mastoidectomy and canaloplasty, while a single patient was status/post transcanal resection of a glomus tympanicum. Other than this last patient, the indications for surgery included chronic otitis media, middle ear cholesteatoma, and chronic tympanic membrane perforation. Indications for imaging (as indicated by the imaging requisition submitted by the referring surgeon) included chronic otitis media, evaluate cholesteatoma ($n = 14$); hearing loss with or without additional history of chronic otitis media included ($n = 7$); ear pain and drainage ($n = 2$); tympanic membrane not visible on examination with external canal stenosis, evaluate middle ear involvement ($n = 1$); possible middle ear mass on examination ($n = 1$); otorrhea, evaluate CSF leak ($n = 1$); and recurrent pulsatile tinnitus and feeling of blockage in ear, evaluate recurrent glomus tympanicum ($n = 1$).

Preoperative imaging was only available for comparison in 4 of the 25 patients/27 temporal bones. All 27 temporal bones demonstrated osseous changes along at least 1 wall of the EAC. A widened appearance of the canal was also observed in all 27 temporal bones. The most common site for osseous changes in the EAC was the floor (inferior wall), found in 25 of 27 temporal bones (92.6%). These changes included mild flattening and/or slight irregularity with thinning of the floor and loss of the normal tympanic sulcus (Fig 1) or more extensive bony irregularity mimicking erosive change (Fig 2). The relatively flat and wide appearance of the canal with predominant involvement of the EAC floor and loss of the tympanic sulcus was present in 17 of 25. This was the most common overall finding in the cohort, seen in 63% of cases (17 of 27 total temporal bones). In the 8 cases with more extensive bony irregularity along the floor of the EAC, focal bony defects were present, ranging from 1 to 8.1 mm (average, 3.3 mm). Similar osseous changes were seen in the superior and anterior walls of the EAC in 21 and 18 temporal bones (77.8% and 66.7%, respectively). The anterior wall was the most common location for osseous defects, occurring in 10 of 27 temporal bones (37%). The posterior wall was the least common site for osseous findings, found in 15 of 27 temporal bones (55.6%), with only 3 (11.1%) demonstrating osseous defects.

Soft tissue thickening was also most common along the inferior EAC wall, present in 18 of 27 temporal bones (66.7%). Soft tissue thickening was seen along the anterior, superior, and posterior walls slightly less commonly (14, 12, and 12 temporal bones, respectively). The presence of soft tissue thickening within the EAC did not correlate with the time interval from surgery and was seen in instances of both recent and remote operative interventions.

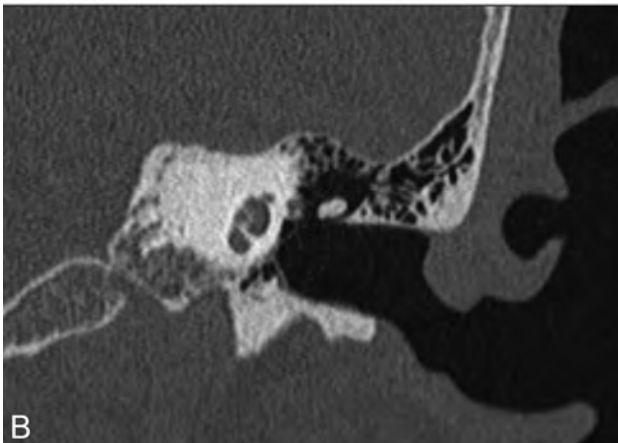
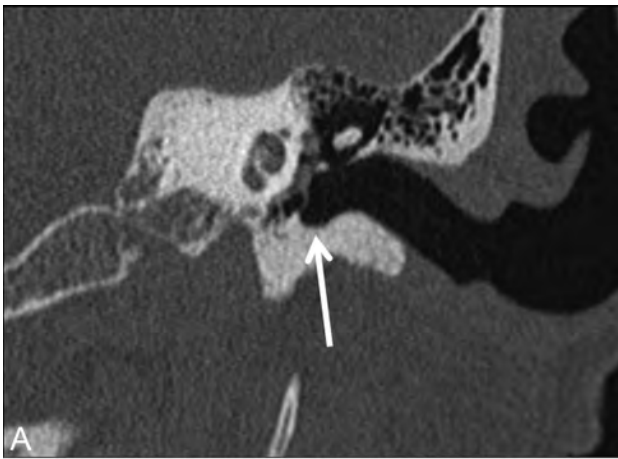


FIG 1. A 59-year-old woman with history of left chronic otitis media and recurrent cholesteatoma status/post left-sided transcanal tympanoplasty. Images were obtained before surgery and 2 years after surgery. The preoperative coronal image (A) demonstrates the normal curvature of the walls of the external auditory canal and the normal tympanic sulcus (arrow), while the postoperative coronal image (B) demonstrates flattening and smoothing of the superior wall and floor of the external canal, with loss of the normal tympanic sulcus inferiorly.

Thickening of the tympanic membrane was also observed in 17 of 27 temporal bones and, in all cases, was associated with prior tympanoplasty. In 4 of these 17, calcification of the tympanic membrane was also present. In the remaining cases, no thickening was demonstrated or the thickness of the tympanic membrane could not be assessed adequately due to adjacent soft tissue attenuation in the external canal or middle ear (3 cases).

In 3 cases, partial ossicular prostheses were in place, with the stapes present but absence of the malleus and incus in all 3. In 2 cases, total ossicular prostheses were present, with absence of all ossicles. In 1 case, the incus was not in the normal position and an osseous structure seen between the stapes and the tympanic membrane was postulated to represent an incus interposition graft. In the remaining 21 temporal bones, the ossicles were present and no prostheses were identified.

Interobserver agreement was excellent ($\kappa = 0.80$; 95% CI, 0.7–0.9). Discrepancies regarding the presence of bony change and/or soft tissue attenuation along ≥ 1 wall of the EAC involved a miss by 1 of the 2 readers for all cases.

In 3 of the official radiology reports, the prior surgical history was not known or postulated by the interpreting radiologist (Fig 3).

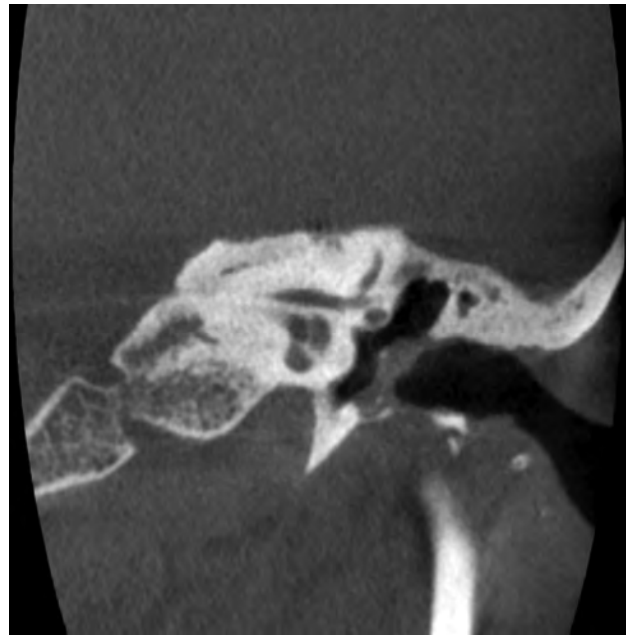


FIG 2. A 59-year-old woman with a history of left chronic otitis media status/post tympanoplasty 8 years before conebeam CT imaging. Irregularity and loss of the normal bony cortex are demonstrated along the EAC floor, with a focal bony defect and mild adjacent soft tissue opacification abutting the tympanic membrane. No active infection or cholesteatoma was present on otologic follow-up.

In the remaining reports, prior surgery in the external canal was postulated, though additional differential diagnostic considerations were included in many cases. In these cases, pathologic processes of the EAC were included in the differential diagnosis, including cholesteatoma, keratosis obturans, and external otitis.

Although a few patients required additional procedures after CT for recurrent middle ear disease, none of the patients included in our study had pathologic findings in the EAC at clinical/surgical follow-up. Only chronic postoperative changes were observed in the EAC in all patients by their referring otologists per the electronic medical record. One patient developed chronic soft tissue stenosis of the EAC after surgery (Fig 3).

DISCUSSION

The EAC is an S-shaped tubular structure, typically 16–25 mm in length and 7–10 mm in diameter, extending from the meatus of the pinna to the tympanic membrane. The lateral one-third is fibrocartilaginous, while the medial two-thirds is osseous, formed by 3 segments of the temporal bone: the squamous, mastoid, and tympanic segments. There are 2 physiologic narrowings in the EAC: one at the isthmus (the junction between fibrocartilaginous and bony portions) and another medially adjacent to the tympanic membrane. At the medial end of the EAC is a rise in the floor of the EAC adjacent to a narrow furrow, the tympanic sulcus.^{12–14}

Surgery is widely used to treat various middle ear conditions, including inflammatory disease, congenital malformations, trauma, and tumors.^{4,5} Surgical approaches to the middle ear through the EAC may involve drilling the bony EAC walls to provide adequate exposure.^{1–3} Extensive literature describes the postoperative appearance of the middle ear after such surgeries^{4–11} and more extensive surgeries involving the external canal,

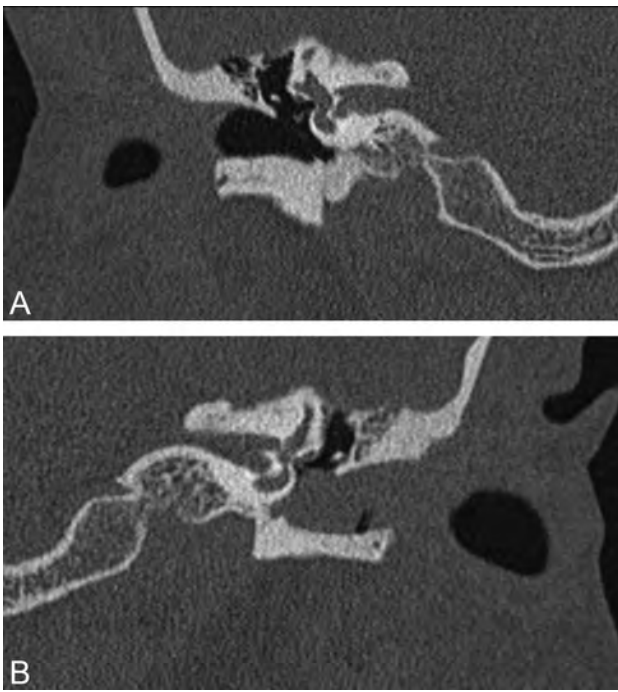


FIG 3. A 51-year-old man with a history of chronic otitis media status/post left tympanoplasty (with total drum replacement) 6 months before multidetector row CT imaging. The normal right temporal bone is shown in the coronal image on the right (A). Coronal image of the left temporal bone (B) demonstrates soft tissue filling the EAC, with smooth “erosion” of the anterior and inferior EAC walls. The patient developed soft tissue stenosis of the EAC postoperatively, related to a hypersensitivity reaction to antibiotic drops, without infection or cholesteatoma on clinical follow-up. The interpreting radiologist did not have the clinical history and interpreted the findings as probable EAC cholesteatoma.

such as canal wall down mastoidectomy. We undertook a detailed description of the CT findings in the EAC after transcanal surgery. Patients with canal wall down mastoidectomy were excluded. The surgeries performed included total drum replacement and atticotomy, with changes that are much more subtle than more extensive tympanomastoid surgeries.

The typical sites for bony removal of the EAC walls at transcanal surgery are the anterosuperior and anteroinferior walls (Fig 4), usually with further dissection of the inferior wall.^{1,2} In our series, osseous changes were observed along the inferior EAC margin most frequently, followed by the superior and anterior walls. The posterior wall was the least commonly observed site for osseous changes, bony defects, and soft tissue opacity. These findings correlate with the typical surgical approaches and may be subtle, with only mild bony changes seen. In these cases, we have found comparison with the contralateral normal side helpful, especially if preoperative images are not available.

In our experience, postoperative findings in the EAC may mimic pathological processes, including cholesteatoma, infection (including malignant [necrotizing] otitis externa), malignancy, radiation necrosis, and granulomatosis with polyangiitis (Wegener granulomatosis). The subtle osseous irregularities may be misinterpreted if the radiologist is not aware of the typical appearance of the EAC after transcanal surgery and/or does not have the clinical history at the time of imaging.

At CT, EAC cholesteatoma commonly presents as a soft tissue

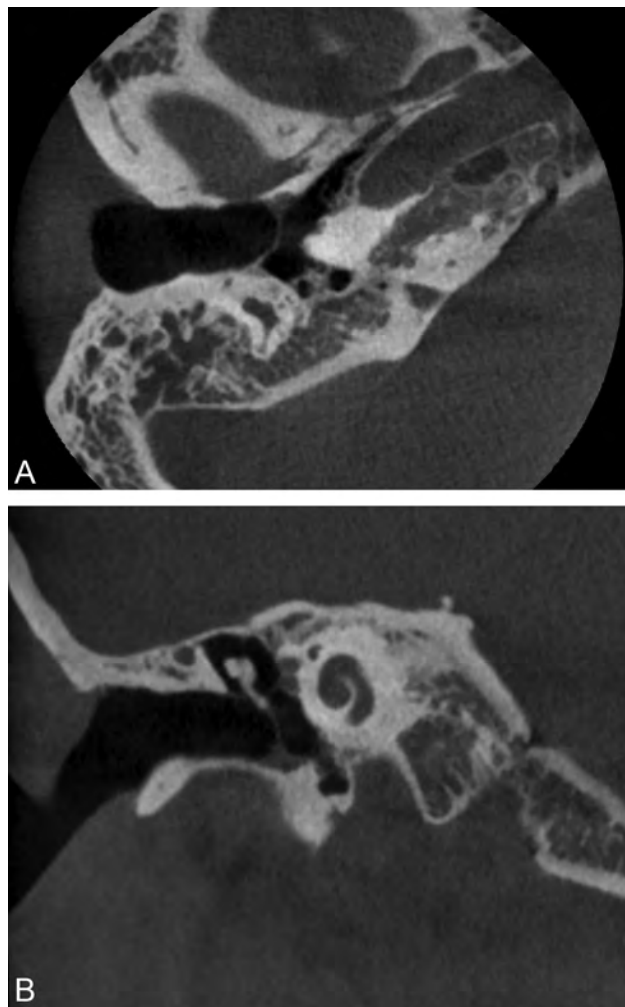


FIG 4. A 20-year-old woman with a history of bilateral chronic otitis media status/post right-sided transcanal tympanoplasty 10 years before conebeam CT. The axial image (A) demonstrates a small bony defect along the anterior wall, while the coronal image (B) demonstrates rounded bony change along floor with soft tissue at the base of the tympanic membrane. No infection or cholesteatoma was present at follow-up.

mass with associated bony erosion and may be either smooth or irregular, with intramural bony fragments.¹⁴⁻¹⁶ The inferior and posterior EAC walls are the most common sites of origin of the soft tissue mass, though they can be circumferential.¹⁵ The amount of soft tissue attenuation material associated with the osseous changes may be minimal because cholesteatoma extends under the periosteum. The osseous changes in EAC cholesteatoma are typically focal, whereas the postoperative changes observed in our cohort typically involved a longer segment of the EAC margin, though findings may overlap significantly and the operative history may help distinguish these 2 entities.

Malignant tumors of the EAC are rare, with squamous cell carcinoma the most common histologic type. The inferior EAC wall is the most common site of disease, followed by the anterior and posterior walls.^{17,18} On CT imaging, EAC squamous cell carcinoma commonly presents as a soft tissue mass, usually with associated bony destruction.^{14,18} In the early stages, however, squamous cell carcinoma may be impossible to radiologically dis-

tinguish from benign disease such as malignant otitis externa and EAC cholesteatoma.¹⁴

Malignant otitis externa is a chronic progressive infection with extensive involvement of tissues beyond the EAC, typically due to *Pseudomonas aeruginosa* infection in elderly patients with diabetes.¹⁹ This entity usually begins along the EAC floor at the osseous-cartilaginous junction as a small area of granulation tissue, followed by chondritis with subsequent involvement of the adjacent soft tissues beneath the skull base. Unlike chronic postoperative changes, at CT there are typically edematous changes of the soft tissue surrounding the EAC and pinna, with obliteration of the normal fat planes inferior to the temporal bone and skull base. The CT appearance of malignant otitis externa may be indistinguishable from malignancy.^{14,19} The changes beyond the EAC and the clinical history should distinguish this entity from postoperative changes.

In our study, osseous changes and soft tissue opacity were most commonly observed along the inferior wall of the EAC in patients postoperatively, with similar findings less commonly demonstrated along the other margins of the EAC. The most common postoperative appearance observed was subtle irregularity and flattening of the external canal, predominantly involving the floor, with loss of the tympanic sulcus (63%). The posterior canal was the least commonly involved, though osseous changes were present in 55.6% of the temporal bones. Such findings along any margin of the EAC may be subtle but, when observed, should not necessarily prompt concern for a pathologic erosive process, particularly after confirmation of the appropriate surgical history. In other cases, a differential diagnosis may be appropriate; however, the interpreting radiologist may be the first to suggest postoperative changes as a possibility and prompt further investigation into the clinical history. None of the patients included in this study had pathologic findings in the EAC on clinical follow-up, other than chronic postoperative changes such as granulation tissue and acquired EAC stenosis.

Additional clues to prior transcanal surgery include thickening and/or calcification of the tympanic membrane, absence of ≥ 1 ossicle, and/or the presence of an ossicular prosthesis. However, these findings were only present in a minority of the cases in our cohort.

Limitations to our study include the retrospective design and the relatively small number of patients. Another possible limitation is that postoperative imaging is usually only performed in symptomatic patients. However, our sample likely reflects a typical referral pattern of an otologic practice and the patients most likely to be seen at temporal bone CT by a radiologist. Preoperative imaging was only available for comparison in 4 of 25 patients. Lack of preoperative imaging is a common occurrence at a large referral center where patients may have undergone surgery elsewhere. In our series, this was a common reason for lack of preoperative imaging. Patients in our cohort were also scanned on either multidetector row CT or conebeam CT, and differences between the 2 techniques could limit the generalizability of our results. Although conebeam CT has a higher resolution for fine bony detail, most patients in this cohort were evaluated with multidetector row CT and this technique is likely sufficient to detect the bony changes observed in this study.

CONCLUSIONS

CT findings in the EAC after transcanal surgery include smooth thinning, irregularity and/or focal defects of the bony walls, and soft tissue thickening. The inferior wall is the most common site for these postoperative changes; however, any of the margins of the EAC may be involved. Such changes at CT should not necessarily prompt concern for a pathologic process, and interpretation should include a thorough review of the clinical examination and surgical history. Knowledge of this typical postoperative appearance may help the radiologist suggest prior surgery and avoid misdiagnosis of external canal disease at CT imaging.

REFERENCES

1. Fisch U, May JS, Linder T. **Tympanoplasty**. In: Fisch U, May JS, Linder T. *Tympanoplasty, Mastoidectomy, and Stapes Surgery*. 2nd ed. New York: Thieme; 2008:2–47
2. Gurr A, Sudhoff H, Hildmann H. **Approaches to the middle ear**. In: Hildmann H, Sudhoff H, eds. *Middle Ear Surgery*. New York: Springer-Verlag; 2006:19–22
3. Rodrigues S, Fagan P, Doust B, et al. **A radiologic study of the tympanic bone: anatomy and surgery**. *Otol Neurotol* 2003;24:796–99
4. Williams MT, Ayache D. **Imaging of the postoperative middle ear**. *Eur Radiol* 2004;14:482–95
5. Kösling S, Bootz F. **CT and MR imaging after middle ear surgery**. *Eur J Radiol* 2001;40:113–18
6. Rao AG, Weissman JL. **Imaging of postoperative middle ear, mastoid, and external auditory canal**. *Semin Ultrasound CT MR* 2002;23:460–65
7. Mukherji SK, Mancuso AA, Kotzur IM, et al. **CT of the temporal bone: findings after mastoidectomy, ossicular reconstruction, and cochlear implantation**. *AJR Am J Roentgenol* 1994;163:1467–71
8. Swartz JD, Goodman RS, Russell KB, et al. **High-resolution computed tomography of the middle ear and mastoid. Part III. Surgically altered anatomy and pathology**. *Radiology* 1983;148:461–64
9. Miracle AC, Mukherji SK. **Conebeam CT of the head and neck. Part 2. Clinical applications**. *AJNR Am J Neuroradiol* 2009;30:1285–92
10. Larson TL, Wong ML. **Imaging of the mastoid, middle ear, and internal auditory canal after surgery: what every radiologist should know**. *Neuroimaging Clin N Am* 2009;19:307–20
11. Ginat DT, Mukherji SK. **Imaging of the postoperative ear and temporal bone**. In: Ginat DT, Westesson PA. *Atlas of Postsurgical Neuro-radiology*. New York: Springer-Verlag; 2012:287–340
12. Curtin HD, Gupta R, Bergeron RT. **Embryology, anatomy and imaging of the temporal bone**. In: Som PM, Curtin HD, eds. *Head and Neck Imaging*. 5th ed. Philadelphia: Elsevier Mosby; 2011:1063–64
13. Fatterpekar GM, Doshi AH, Dugar M, et al. **Role of 3D CT in the evaluation of the temporal bone**. *Radiographics* 2006;26(suppl 1):S117–32
14. Castillo M, Jewells VL, Buchman C. **The external auditory canal and pinna**. In: Swartz JD, Loevner LA, eds. *Imaging of the Temporal Bone*. 4th ed. New York: Thieme; 2009:25–57
15. Heilbrun ME, Salzman KL, Glastonbury CM, et al. **External auditory canal cholesteatoma: clinical and imaging spectrum**. *AJNR Am J Neuroradiol* 2003;24:751–56
16. Malcolm PN, Francis IS, Wareing MJ, et al. **CT appearances of external ear canal cholesteatoma**. *Br J Radiol* 1997;70:959–60
17. Lobo D, Llorente JL, Suarez C. **Squamous cell carcinoma of the external auditory canal**. *Skull Base* 2008;18:167–72
18. Ong CK, Pua U, Chong VF. **Imaging of carcinoma of the external auditory canal: a pictorial essay**. *Cancer Imaging* 2008;8:191–98
19. Curtin HD, Wolfe P, May M. **Malignant external otitis: CT evaluation**. *Radiology* 1982;145:383–88

Predictors of Multigland Disease in Primary Hyperparathyroidism: A Scoring System with 4D-CT Imaging and Biochemical Markers

A.R. Sepahdari, M. Bahl, A. Harari, H.J. Kim, M.W. Yeh, and J.K. Hoang

ABSTRACT

BACKGROUND AND PURPOSE: Multigland disease represents a challenging group of patients with primary hyperparathyroidism. Additional lesions may be missed on imaging because they are not considered or are too small to be seen. The aim of this study was to identify 4D-CT imaging and biochemical predictors of multigland disease.

MATERIALS AND METHODS: This was a retrospective study of 155 patients who underwent 4D-CT and successful surgery with a biochemical cure that compared patients with multigland and single-gland disease. Variables studied included the size of the largest lesion on 4D-CT, the number of lesions prospectively identified on 4D-CT, serum calcium levels, serum parathyroid hormone levels, and the Wisconsin Index (the product of serum calcium and parathyroid hormone levels). Imaging findings and the Wisconsin Index were used to calculate a composite multigland disease scoring system. We evaluated the predictive value of individual variables and the scoring system for multigland disease.

RESULTS: Thirty-six patients with multigland disease were compared with 119 patients with single-gland disease. Patients with multigland disease had significantly lower Wisconsin Index scores, smaller lesion size, and a higher likelihood of having either multiple or zero lesions identified on 4D-CT ($P \leq .01$). Size cutoff of <7 mm had 85% specificity for multigland disease, but including other variables in the composite multigland disease score improved the specificity. Scores of ≥ 4 , ≥ 5 , and ≥ 6 had specificities of 81%, 93%, and 98%, respectively.

CONCLUSIONS: The composite multigland disease scoring system based on 4D-CT imaging findings and biochemical data can identify patients with a high likelihood of multigland disease. Communicating the suspicion for multigland disease in the radiology report could influence surgical decision-making, particularly when considering re-exploration in a previously operated neck or initial limited neck exploration.

ABBREVIATIONS: MGD = multigland disease; PTH = parathyroid hormone; ROC = receiver operating characteristic; SGD = single-gland disease; WIN = Wisconsin Index

Preoperative parathyroid imaging is routinely performed in patients with primary hyperparathyroidism. In the era of minimally invasive parathyroidectomy, the role of imaging is to localize the parathyroid adenoma with high confidence for surgical planning. Although primary hyperparathyroidism is most commonly caused by a single parathyroid adenoma, 10%–30% of patients will have multigland disease (MGD) due to parathyroid hyperplasia or multiple adenomas.^{1,2} This group represents a

challenge for radiologists and surgeons because these patients have a much higher frequency of nonlocalizing imaging studies and failed surgeries.^{2–4}

The technique of multiphase multidetector CT, also known as 4D-CT, may be advantageous in patients with MGD. Several studies have shown 4D-CT to have higher sensitivity than sonography and scintigraphy for localizing abnormal parathyroid glands, due to higher spatial resolution for the detection of small lesions and an improved ability to visualize adenomas in deep or ectopic locations.^{4–7} Selected studies analyzed the subgroup of patients with MGD and found 4D-CT to be superior to sonography and scintigraphy, but the sensitivity of 4D-CT for MGD (32%–53%) was still considerably lower compared with single-gland disease (SGD) (88%–93%).^{4,5,7,8} None of the studies described characteristics of MGD and SGD or attempted to determine predictors of MGD.

Some of the barriers to lesion detection on 4D-CT for MGD

Received September 30, 2014; accepted after revision November 7.

From the Departments of Radiological Sciences (A.R.S., H.J.K.) and Surgery (A.H., M.W.Y.), David Geffen School of Medicine, University of California, Los Angeles, Los Angeles, California; and Departments of Radiology (M.B., J.K.H.) and Radiation Oncology (J.K.H.), Duke University Medical Center, Durham, North Carolina.

Please address correspondence to Jenny K. Hoang, MBBS, Duke University Medical Center, Department of Radiology, Box 3808, Erwin Rd, Durham, NC 27710; e-mail: jennykh@gmail.com; @JennyKHoang

<http://dx.doi.org/10.3174/ajnr.A4213>

include a smaller size than for SGD and overlooking additional lesions after detecting the first lesion. The latter pitfall could be minimized if the radiologist was aware of predictors for MGD that would lead to a more dedicated search for additional lesions. The aim of this study was to identify 4D-CT imaging and biochemical predictors of MGD in patients with primary hyperparathyroidism. Our hypothesis is that the combination of smaller lesion size on imaging and lower serum biochemical markers can predict MGD with high specificity.

MATERIALS AND METHODS

Study Subjects

We performed a retrospective review of 155 patients from 2 academic institutions who had 4D-CT studies performed between October 2009 and December 2013 before successful parathyroid surgery. There were 87 patients from institution A (University of California, Los Angeles) and 68 from institution B (Duke University). Successful surgery was defined as an intraoperative parathyroid hormone (PTH) drop of >50% and at least 6 months of postoperative eucalcemia. Both institutions obtained institutional review board approval with a waiver of consent.

For all patients, medical records were reviewed for patient demographics, history of prior surgery, operative notes, pathology results, imaging findings on 4D-CT, and preoperative serum calcium and PTH levels.

4D-CT Technique

Institution A. Imaging was performed either on a 64–detector row scanner (Somatom Definition; Siemens, Erlangen, Germany) or a 256–detector row scanner (Somatom Definition Flash; Siemens). Scanning included noncontrast, arterial phase, and delayed phase images from the hard palate to the carina. The parameters for all 3 phases were the following: section thickness, 0.6 mm; tube rotation time, 0.5 seconds; pitch factor, 1; FOV, 24 cm; 120 kV(peak); 230 reference milliampere-second with automated tube current modulation (CARE Dose4D; Siemens). Arterial phase images were performed 25 seconds following the initiation of a 100- to 120-mL IV bolus of iohexol, 350-mg iodine/mL (Omnipaque; GE Healthcare, Piscataway, New Jersey), injected through either a 20- or 22-ga antecubital catheter, at either 4 or 3 mL/s. The delayed phase was acquired 30 seconds after the arterial phase ended. All images were reconstructed at 1-mm section thickness in the axial, coronal, and sagittal planes and sent to the PACS.

Institution B. Imaging was performed by using a 64–detector row CT scanner (750 HD; GE Healthcare, Milwaukee, Wisconsin) with 3 imaging phases. Scanning included noncontrast, arterial phase, and delayed phase images. The noncontrast phase covered only the thyroid gland (z-axis from the hyoid bone to the clavicular heads) to reduce radiation exposure. The 2 contrast-enhanced phases were scanned from the angle of the mandible to the carina. The parameters for all 3 phases were the following: 0.625-mm section thickness; tube rotation time, 0.4 seconds; pitch factor, 0.516:1; FOV, 20 cm; 120 kVp; and automatic tube current modulation. Tube current modulation (mA Modulation; GE Healthcare) was used with a noise index of 8, minimum 100

Table 1: MGD scores^a

Criterion	Scoring
No. of candidate lesions identified on 4D-CT	Single lesion: 0 Multiple lesions: 2 No lesions: 2
Maximum diameter of largest lesion on 4D-CT	>13 mm: 0 7–13 mm: 1 <7 mm or no lesion identified: 2
WIN	>1600: 0 800–1600: 1 <800: 2

Note:—WIN indicates serum calcium level (milligram/deciliter) × serum parathyroid hormone level (picogram/milliliter).

^a The composite MGD score includes all 3 components in the Table and ranges from 0 to 6. The 4D-CT MGD score does not include the Wisconsin Index and ranges from 0 to 4.

mA, and maximum 500 mA for the nonenhanced and delayed phases and 700 mA for the arterial phase. Arterial phase images were obtained 25 seconds following initiation of an injection of 75 mL of intravenous iopamidol (Isovue 300; Bracco, Princeton, New Jersey) through a 20-ga antecubital catheter at a rate of 4 mL/s, followed by a 25-mL saline chaser. The delayed phase was acquired 80 seconds from the start of the injection. Before September 2012, studies were performed with only arterial and delayed phases.⁹ Reformatted images were sent to a PACS as 2.5-mm-thick contiguous images in the axial plane for all 3 phases, and 2.5-mm-thick images in the coronal and sagittal planes in the arterial and delayed phases.

Lesion Localization

All parathyroid lesions were classified as correctly or incorrectly localized on 4D-CT by correlating the operative notes with the original radiology reports and using anatomic landmarks reported in both the operative and radiology reports. Radiology reports were generated by 2 board-certified neuroradiologists (9 and 12 years' experience in CT interpretation). Sensitivities for lesion localization were based on these original radiology reports. If surgically confirmed lesions were missed on 4D-CT, the images were rereviewed by the 2 radiologists with knowledge of the surgical findings to determine whether lesions could be seen in retrospect.

Predictors of Multigland Disease

4D-CT imaging and biochemical predictors of MGD were proposed on the basis of prior surgical literature.^{10,11} 4D-CT imaging predictors were the number of lesions identified on the original radiology report and lesion size (maximum diameter in any plane). If multiple candidates were seen on 4D-CT, lesion size was represented by the largest prospectively identified lesion. Biochemical predictors were serum calcium levels (milligram/deciliter), serum PTH levels (picogram/milliliter), and the Wisconsin Index (WIN). The WIN is the product of the serum calcium levels (milligram/deciliter) and PTH levels (picogram/milliliter) and was shown to help discriminate MGD and SGD in a prior study.¹⁰

A composite MGD score was derived on the basis of 4D-CT imaging and biochemical data of lesion size on 4D-CT, number of prospectively detected lesions on 4D-CT, and the WIN. Each variable contributed up to 2 points to the MGD scores (Table 1). The cutoff values used to assign points in the score were based on prior literature for lesion size and ranges of biochemical markers.^{10,12} A

Table 2: Characteristics of patients with MGD and SGD^a

	All subjects	MGD	SGD	P Value
No. of patients	155	36	119	
No. of glands	216	97	119	
Mean age (yr)	60 (range, 14–88)	59	60	
Female	108 (67%)	25 (69%)	83 (70%)	
4D-CT characteristics				
Mean size of abnormal glands (mm)	10.9 (5.9)	8.8 (4.0)	11.7 (6.4)	.002
Median size of abnormal glands (mm) (IQR)	10 (7–13)	8 (6–11)	11 (7–13)	
No. <10 mm (%)	79 (37%)	39 (64%)	40 (34%)	
No. <7 mm (%)	30 (14%)	19 (31%)	11 (9%)	
No. >13 mm (%)	39 (18%)	6 (10%)	33 (28%)	
Prospectively detected lesions				
1	100	10 ^b	90	<.001
≥2	46	20	26	
None	9	6	3	
Biochemical markers				
Serum calcium level (mg/dL)	11.0 (0.7)	10.8 (0.4)	11.1 (0.7)	.07
Serum parathyroid hormone level (pg/mL)	117 (69)	92 (44)	122 (73)	.02
WIN	1279 (744)	1005 (501)	1357 (783)	.01
MGD scores				
Composite MGD score	2.6 (1.6)	4.1 (1.4)	2.2 (1.4)	<.001
4D-CT MGD score	1.6 (1.4)	2.9 (1.1)	1.2 (1.2)	<.001
4D-CT sensitivity based on original radiology reports				
Detection of lesions	167 (77%)	53 (55%)	114 (95%)	
Detection of all lesions in individual patients	126 (81%)	12 (33%)	114 (95%)	

Note:—IQR indicates interquartile range.

^a Values are expressed as mean (SD) except as specified.

^b Twenty-five patients with MGD showed multiple lesions, and 5 showed single lesions after rereview of imaging studies following surgery.

second scoring system, the 4D-CT MGD score, was based on only the 4D-CT imaging variables of lesion size and the number of prospectively detected lesions on 4D-CT. The composite MGD score ranged from 0 to 6. The 4D-CT MGD score ranged from 0 to 4. For both scoring systems, a higher score more strongly favored MGD.

Data Analysis

The characteristics of MGD were compared with those of SGD for individual variables and the scoring system. The Fisher exact test was used to assess differences in patients with MGD and SGD for categorical data. The Student *t* test was used to assess differences between MGD and SGD for continuous variables. Receiver operating characteristic (ROC) analysis was performed to determine the sensitivity and specificity of each feature for predicting MGD. *P* values of <.05 were the threshold used for statistical significance for all tests. The data were entered into an Excel spreadsheet (2007 version; Microsoft, Redmond, Washington). Statistical analyses were performed by using SAS Enterprise (Version 4.2; SAS Institute, Cary, North Carolina).

RESULTS

Study Subjects

Of the 155 patients, 36 had MGD (23 from institution A and 13 from institution B) and 119 had SGD (64 from institution A and 55 from institution B) (Table 2). There were 97 abnormal glands in patients with MGD, resulting in 216 abnormal glands in this study. The mean gland size was 11 ± 6 mm, and the median size was 10 mm (interquartile range, 7–13).

Prior parathyroid surgery had been performed in 9 (25%) patients with MGD and 34 (29%) with SGD. The leading cause of persistent or recurrent hyperparathyroidism in our group was a missed single adenoma. The Fisher exact test showed no significant

difference between MGD and SGD with respect to whether prior surgery had been performed (*P* = .83).

Lesion Localization

Of the 97 abnormal glands seen in 36 patients with MGD, 53 (55%) were identified prospectively and an additional 9 (9%) could be identified in retrospect. The others could not be detected even with knowledge of the surgical findings. Institution A prospectively identified 55% (36/65) of abnormal glands in the setting of MGD. Institution B prospectively identified 53% (17/32) of abnormal glands in the setting of MGD. The sensitivity of detecting all MGD lesions in a patient was 35% (8/23) for Institution A and 31% (4/13) for Institution B.

Of abnormal glands in patients with SGD, 95% (113/119) were identified prospectively. Institution A prospectively identified 95% (62/65) of glands with SGD. Institution B prospectively identified 94% (51/54) of glands with SGD. Of the 6 abnormal glands in SGD that were not identified prospectively, 4 could be identified in retrospect. The missed lesions not seen in retrospect were typically juxtathyroid in location. It is not clear whether they were not seen due to the small size or poor contrast between the adenoma and surrounding tissues.

Predictors of Multigland Disease

MGD had a smaller mean lesion size of 9 mm compared with 12 mm for SGD (*P* = .002). The WIN was lower for MGD at 1005 compared with 1357 for SGD (*P* = .01). Statistically significant differences were also seen for the number of lesions identified prospectively (*P* < .001) and serum PTH levels (*P* = .02).

Despite significant differences between MGD and SGD with respect to multiple continuous variables, ROC analyses of each of these individual variables did not find clinically useful cutoff val-

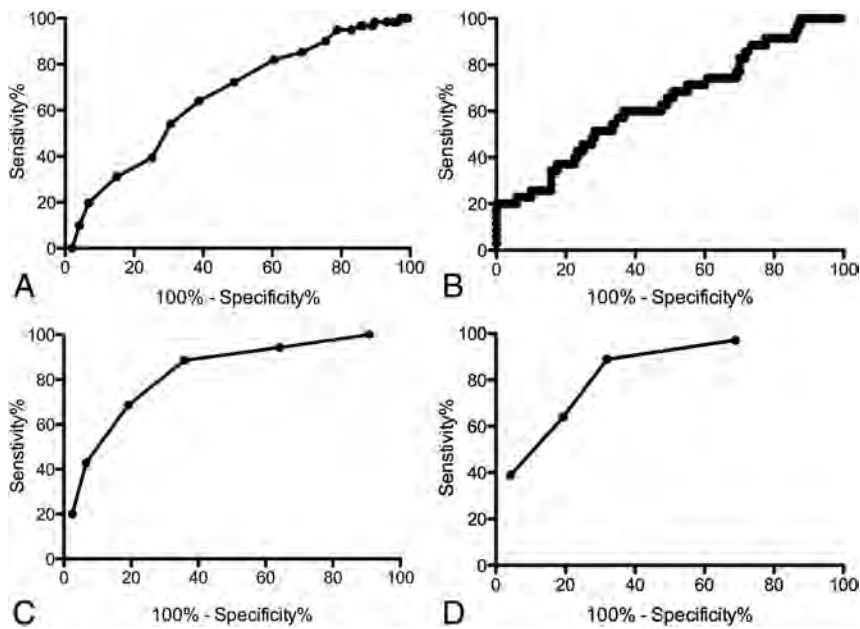


FIG 1. Receiver operating characteristic curves showing performance in predicting MGD for the largest lesion size (A), Wisconsin Index (B), the composite MGD score (C), and the 4D-CT MGD score (D).

Table 3: Performance of the composite MGD score for predicting MGD on the basis of the size of the largest lesion, the number of lesions prospectively identified, and the Wisconsin Index^a

MGD Score	No. of Patients	Sensitivity	Specificity	Positive Predictive Value
≥1	35	100%	9%	24%
≥2	33	94%	36%	30%
≥3	31	89%	64%	43%
≥4	24	69%	81%	51%
≥5	15	43%	93%	65%
6	7	20%	98%	70%

^a There were no patients with scores of zero. One patient did not have recent serologic data.

Table 4: Performance of the 4D-CT MGD score for predicting MGD, based on the size of largest lesion and the number of lesions prospectively identified

MGD Score	No. of Patients	Sensitivity	Specificity	Positive Predictive Value
0	36	100%	0%	23%
≥1	35	97%	31%	30%
≥2	32	89%	68%	46%
≥3	23	64%	81%	50%
4	14	39%	96%	74%

ues. Areas under the ROC curves were <0.66 (Fig 1A, -B). Prospective identification of either multiple or no abnormal glands (rather than a single gland) was 76% sensitive and 72% specific for MGD. Using the median lesion size of ≤10 mm as a size cutoff was only 64% sensitive and 61% specific for MGD.

Cutoff values of 7 and 13 mm used for the scoring systems had higher specificity for MGD and SGD, respectively. A lesion size of <7 mm had a high specificity of 85% for MGD. Conversely, a lesion size of >13 mm had a high specificity for SGD of 85%. The <7 and >13 mm cutoff values both had a low sensitivity of 31%. A WIN of <661 had 90% specificity for MGD but only 26% sensitivity. Similarly, a WIN of >1629 had 91% specificity for SGD but only 23% sensitivity.

The mean composite MGD score was significantly higher for MGD at 4.1 compared with 2.2 for SGD ($P < .001$), with an improved area under the ROC curve of 0.82 (Fig 1C). 4D-CT MGD scores were similarly strongly predictive of MGD ($P < .001$), with an area under the ROC curve of 0.83 (Fig 1D). In the subset of patients without a history of prior surgery, the mean composite MGD score was 4.4 in MGD and 2.4 in SGD ($P < .001$), while the mean 4D-CT MGD score was 3.1 in MGD and 1.6 in SGD ($P < .001$). The sensitivities, specificities, and positive predictive values for MGD versus SGD based on the composite MGD and 4D-CT MGD scores are shown in Tables 3 and 4. High composite MGD scores of ≥4, ≥5, and 6 had specificities of 81%, 93%, and 98%, respectively, for predicting MGD.

Figures 2 and 3 illustrate how the multifactorial composite MGD score can guide interpretation. Figure 2 shows an example of MGD in the setting of only a single prospectively identified lesion, but with a composite MGD score of 4 due to small lesion size and mild biochemical disease. Figure 3 shows an example of SGD in the setting of multiple candidate lesions but a low MGD score of 2.

DISCUSSION

Identifying cases of MGD preoperatively is an important role of parathyroid imaging when considering whether to offer minimally invasive parathyroidectomy rather than traditional bilateral neck exploration as an initial operation. In potential reoperation cases, MGD poses particular challenges due to distorted anatomy and scar tissue, and appropriate preoperative suspicion is essential in guiding surgical decision-making and preoperative counseling. Although prior studies using 4D-CT have described a range of sensitivities and specificities for MGD, typically superior to scintigraphy and sonography, no existing studies compare the imaging characteristics of MGD and SGD on 4D-CT.^{4-8,13} In this study, we found that a size threshold of <7 mm on 4D-CT favors MGD over SGD, but additional imaging and biochemical data can be used to calculate MGD scores and identify a subset of patients with a high likelihood of MGD.

In clinical practice, radiologists will first suspect MGD on the basis of detection of >1 candidate lesion for hyperplastic glands or adenoma. Our study found that identifying multiple lesions on 4D-CT is neither sensitive nor specific for MGD. Almost one-quarter of patients with MGD only had 1 gland seen prospectively (false-negative), while more than one-quarter of patients with SGD had additional less suspicious candidate lesions (false-positive). Thus, the sign of multiple lesions is not sufficient to guide clinical decision-making, and additional criteria are needed for the radiologist to call MGD with confidence.

Another imaging sign of MGD on 4D-CT is smaller lesion size than that in SGD, which corroborates previous reports based on pathology findings.¹⁰ A single cutoff value based on the mean or

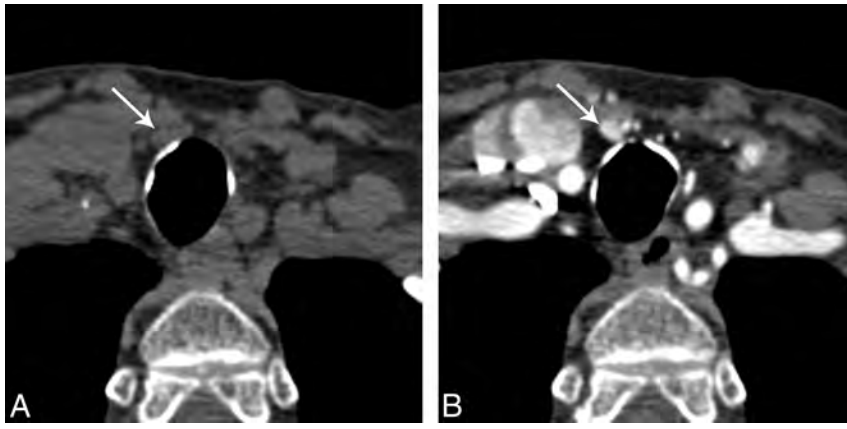


FIG 2. A 78-year-old woman with multigland disease, with a single small candidate lesion. *A*, Axial noncontrast CT just inferior to the thyroid gland shows a 6-mm nodule just deep to the strap muscles on the right (*arrow*). *B*, Axial arterial phase CT scan shows intense enhancement of this nodule. The serum calcium level was 10.1, and the serum parathyroid hormone level was 76. Despite identification of only a single lesion with 4D-CT, the composite MGD score was 4, and the probability of multigland disease was moderate. Surgical exploration revealed hyperplasia of the gland seen here and also hyperplastic bilateral superior parathyroid glands, neither of which could be seen even in retrospect.

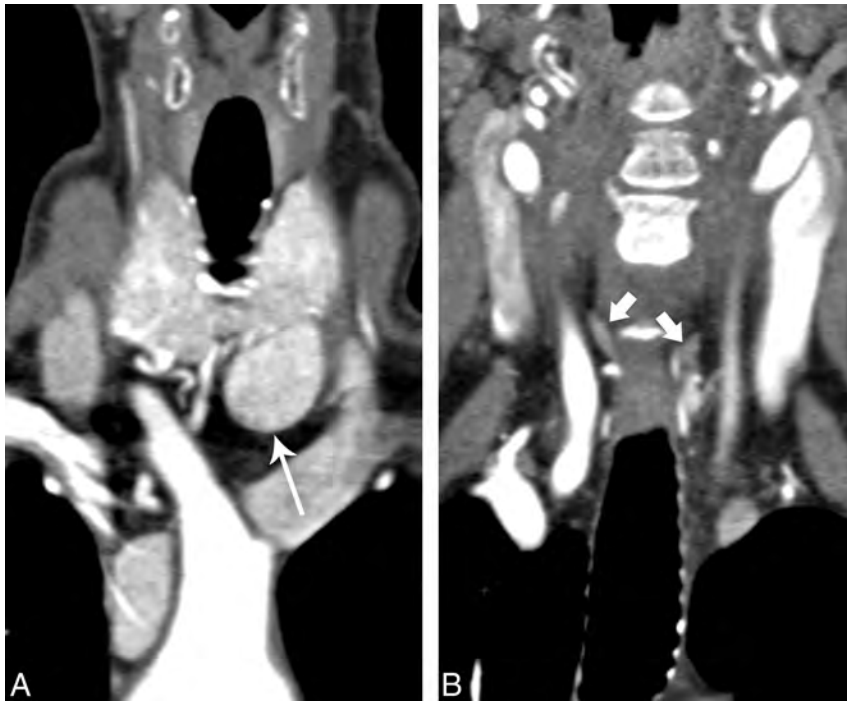


FIG 3. A 67-year-old woman with single-gland disease with multiple prospective candidate lesions. *A*, Coronal arterial phase CT image shows an intensely enhancing nodule in an orthotopic left inferior gland location (*long arrow*), measuring 20 mm in diameter. *B*, Coronal arterial phase CT image posterior to *A*, viewed in the same window width/level, shows ovoid nodular lesions in the orthotopic right and left superior positions (*short arrows*). Despite appropriate location and shape, these lesions show less intense enhancement than is typical of parathyroid adenoma. The serum calcium level is 11.7, and the serum parathyroid hormone level is 211. Despite the presence of multiple candidate lesions, the composite MGD score is only 2 and the findings are predictive of single-gland disease.

median lesion size was not helpful, but categorization of lesions by <7 and >13 mm had higher specificity (85%) for predicting and excluding MGD, respectively. Using size alone is limited for predicting MGD in most patients, however, who have lesions between 7 and 13 mm. Our MGD prediction model improves the ability to predict MGD in more patients by using size in combi-

nation with other variables. Our study found that composite MGD scores of ≥ 4 , ≥ 5 , and ≥ 6 had specificities of 81%, 93%, and 98%, respectively, and could be applied to more patients than a size cutoff of <7 mm. The composite MGD score was also an improvement over biochemical data alone. The cutoff values for WIN that were required to achieve high specificity for either MGD or SGD resulted in very low sensitivities.

The sensitivities for predicting MGD were low for composite MGD scores ≥ 4 , but the scoring system does not aim to detect all patients with MGD. The primary aim is to identify a subset of patients in whom MGD should be suspected. One clinical implication to the radiologist is that a higher composite MGD score may prompt the radiologist to search for additional lesions after the first lesion is found, thereby avoiding “satisfaction of search” errors. However, the radiologist should be aware that even on detailed review, it may not be possible to see the additional lesions; a third of MGD lesions in our study could not be seen on 4D-CT, even with knowledge of the surgical findings. In the setting in which there is a single lesion but a high composite MGD score (ie, small lesion and relatively low serum PTH and calcium levels), the radiologist should still communicate the increased probability of MGD. The surgeon can use this information to counsel the patient about parathyroidectomy. Conversely, when >1 lesion is seen in a patient with a low composite MGD score (ie, a large lesion and high serum PTH and calcium levels), additional smaller lesions can be reported as much less suspicious if they are not clearly abnormal.

Previous clinical models for MGD have also emphasized the value of high specificity rather than high sensitivity.^{10,14} Kebebew et al¹⁴ proposed a multifactorial model based on serum calcium levels, serum PTH levels, and concordant-versus-discordant results of sonography and scintigraphy. Mazeh et al¹⁰ proposed a

multifactorial model for predicting MGD with high specificity, by using a combination of WIN and the weight of the resected parathyroid lesion. Our scoring system offers advantages over these models, which did not include imaging signs and were only helpful to the surgeon for decision-making after imaging was complete, or intraoperatively.

We proposed 2 scoring systems to predict MGD and found both to have similar results in predicting it. For the radiologist, the 4D-CT MGD score has the advantage of using only imaging findings, but the composite MGD score may be more reproducible and reliable. This possibility is because the 4D-CT MGD score is based on only 2 sets of data, lesion size and the ability to visualize additional lesions. The latter characteristic may be interpreted with high interobserver variability because the second lesion may be overlooked if not suspected. In contrast, lesion size and biochemical markers are objective criteria.

There were several limitations to this study. First, this was a retrospective study from 2 academic institutions with 2 different neuroradiologists interpreting the original 4D-CT examinations. There were minor technical differences between the acquisition and reconstruction parameters from the 2 institutions, but imaging protocols were alike with regard to the number of phases acquired and timing of the arterial phase, which we believe are the most important controllable factors. Both institutions achieved similar interpretation accuracy for both SGD and MGD, which is reassuring for confirming the external validity of the data. Second, the characteristics of the lesions were based on the original radiology reports. We did not re-interpret the imaging because we thought there would be recall bias. The fact that we did not re-interpret the imaging studies under blinded conditions is potentially a confounding factor because the original radiology reports were often influenced by clinical information such as surgical history and data from previous sonography and scintigraphy results. However, the use of the original reports is, to some extent, a strength of this study because it reflects the performance of 4D-CT under true clinical conditions. A third potential limitation is the heterogeneity of the study group with respect to whether prior surgery was performed. In theory, there may be differences between patients undergoing initial surgery and those undergoing a reoperation with respect to the presence of MGD, particularly because undertreated MGD is a cause of failed parathyroidectomy. However, these differences did not appear to be a confounding factor in our study. Patients undergoing reoperation were distributed between SGD and MGD in a proportion similar to that of patients undergoing initial exploration, and a missed single adenoma was the leading cause of recurrent/persistent hyperparathyroidism in our group, which was in keeping with findings in the existing literature.^{15,16} Given the importance of determining the probability of MGD in the setting of a potential reoperation, it is essential to include these patients in the analysis.

CONCLUSIONS

4D-CT imaging findings of lesion size and the number of lesions detected can be combined with biochemical data to calculate a composite MGD score. The scoring system can help determine the overall probability of MGD, even if only 1 lesion is detected, and can identify a subset of patients with a high likelihood of MGD. Communicating the suspicion for MGD in the radiology

report could influence surgical decision-making, particularly when considering re-exploration in a previously operated neck or initial limited neck exploration.

REFERENCES

1. Ruda JM, Hollenbeak CS, Stack BC Jr. A systematic review of the diagnosis and treatment of primary hyperparathyroidism from 1995 to 2003. *Otolaryngol Head Neck Surg* 2005;132:359–72
2. Fraker DL, Harsono H, Lewis R. Minimally invasive parathyroidectomy: benefits and requirements of localization, diagnosis, and intraoperative PTH monitoring: long-term results. *World J Surg* 2009;33:2256–65
3. Hoang JK, Sung WK, Bahl M, et al. How to perform parathyroid 4D CT: tips and traps for technique and interpretation. *Radiology* 2014;270:15–24
4. Rodgers SE, Hunter GJ, Hamberg LM, et al. Improved preoperative planning for directed parathyroidectomy with 4-dimensional computed tomography. *Surgery* 2006;140:932–40; discussion 940–41
5. Kukar M, Platz TA, Schaffner TJ, et al. The use of modified four-dimensional computed tomography in patients with primary hyperparathyroidism: an argument for the abandonment of routine sestamibi single-positron emission computed tomography (SPECT). *Ann Surg Oncol* 2015;22:139–45
6. Eichhorn-Wharry LI, Carlin AM, Talpos GB. Mild hypercalcemia: an indication to select 4-dimensional computed tomography scan for preoperative localization of parathyroid adenomas. *Am J Surg* 2011; 201:334–38; discussion 338
7. Galvin PL, Oldan J, Bahl M, et al. Discordant parathyroid 4DCT and scintigraphy results: what factors contribute to missed parathyroid lesions? In: *Proceedings of the Annual Meeting of the American Society of Neuroradiology and the Foundation of the ASNR Symposium*, Montreal, Quebec, Canada. May 17–22, 2014
8. Sepahdari AR, Yeh MW, Rodrigues D, et al. Three-phase parathyroid 4-dimensional computed tomography initial experience: inexperienced readers have high accuracy and high interobserver agreement. *J Comput Assist Tomogr* 2013;37:511–17
9. Gafton AR, Glastonbury CM, Eastwood JD, et al. Parathyroid lesions: characterization with dual-phase arterial and venous enhanced CT of the neck. *AJNR Am J Neuroradiol* 2012;33:949–52
10. Maze H, Chen H, Leverson G, et al. Creation of a “Wisconsin index” nomogram to predict the likelihood of additional hyperfunctioning parathyroid glands during parathyroidectomy. *Ann Surg* 2013;257:138–41
11. McCoy KL, Chen NH, Armstrong MJ, et al. The small abnormal parathyroid gland is increasingly common and heralds operative complexity. *World J Surg* 2014;38:1274–81
12. Siperstein A, Berber E, Barbosa GF, et al. Predicting the success of limited exploration for primary hyperparathyroidism using ultrasound, sestamibi, and intraoperative parathyroid hormone: analysis of 1158 cases. *Ann Surg* 2008;248:420–28
13. Starker LF, Mahajan A, Bjorklund P, et al. 4D parathyroid CT as the initial localization study for patients with de novo primary hyperparathyroidism. *Ann Surg Oncol* 2011;18:1723–28
14. Kebebew E, Hwang J, Reiff E, et al. Predictors of single-gland vs multigland parathyroid disease in primary hyperparathyroidism: a simple and accurate scoring model. *Arch Surg* 2006;141:777–82; discussion 782
15. Shen W, Duren M, Morita E, et al. Reoperation for persistent or recurrent primary hyperparathyroidism. *Arch Surg* 1996;131:861–67; discussion 867–69
16. Udelsman R, Donovan PI. Remedial parathyroid surgery: changing trends in 130 consecutive cases. *Ann Surg* 2006;244:471–79

Postoperative Intraspinial Subdural Collections after Pediatric Posterior Fossa Tumor Resection: Incidence, Imaging, and Clinical Features

J.H. Harreld, N. Mohammed, G. Goldsberry, X. Li, Y. Li, F. Boop, and Z. Patay



ABSTRACT

BACKGROUND AND PURPOSE: Postoperative intraspinal subdural collections in children after posterior fossa tumor resection may temporarily hinder metastasis detection by MR imaging or CSF analysis, potentially impacting therapy. We investigated the incidence, imaging and clinical features, predisposing factors, and time course of these collections after posterior fossa tumor resection.

MATERIALS AND METHODS: Retrospective review of postoperative spine MRI in 243 children (5.5 ± 4.6 years of age) from our clinical data base postresection of posterior fossa tumors from October 1994 to August 2010 yielded 37 (6.0 ± 4.8 years of age) subjects positive for postoperative intraspinal subdural collections. Their extent and signal properties were recorded for postoperative (37/37), preoperative (15/37), and follow-up spine (35/37) MRI. Risk factors were compared with age-matched internal controls ($n = 37$, 5.9 ± 4.5 years of age). Associations of histology, hydrocephalus and cerebellar tonsillar herniation, and postoperative intracranial subdural collections with postoperative intraspinal subdural collections were assessed by the Fisher exact test or χ^2 test. The association between preoperative tumor volume and postoperative intraspinal subdural collections was assessed by the Wilcoxon rank sum test.

RESULTS: The overall incidence of postoperative intraspinal subdural collections was 37/243 (15.2%), greatest ≤ 7 days postoperatively (36%); 97% were seen 0–41 days postoperatively (12.9 ± 11.0 days). They were T2 hyperintense and isointense to CSF on T1WI, homogeneously enhanced, and resolved on follow-up MR imaging (35/35). None were symptomatic. They were associated with intracranial subdural collections ($P = .0011$) and preoperative tonsillar herniation ($P = .0228$).

CONCLUSIONS: Postoperative intraspinal subdural collections are infrequent and clinically silent, resolve spontaneously, and have a distinctive appearance. Preoperative tonsillar herniation appears to be a predisposing factor. In this series, repeat MR imaging by 4 weeks documented improvement or resolution of these collections in 88%.

ABBREVIATIONS: PISC = postoperative intraspinal subdural collections; PISC+ = positive for postoperative intraspinal subdural collections; POD = postoperative day

The importance of MR imaging for the diagnosis of leptomeningeal metastasis in children with posterior fossa tumors, critical for risk stratification and treatment,¹ is well-recognized. MR imaging detects leptomeningeal metastasis in up to 50% of those with false-negative CSF examination findings, which may occur in up to 45% of initial lumbar punctures,² and findings on MR imaging correlate better with survival than CSF results.^{2–4} Al-

though preoperative brain and spine MR imaging are optimal, neurosurgical urgency may dictate deferral until the postoperative period, or repeat spine imaging may be necessary to exclude leptomeningeal metastasis postoperatively. A few case reports and small series have described spinal subdural collections and enhancement on postoperative myelography and MR imaging.^{5–8} These findings were further investigated in a larger series by Warmuth-Metz et al,⁹ who described such findings in children after posterior fossa (7/45) but not supratentorial (0/8) tumor resection. However, due to the limited availability of follow-up imaging, the natural history could not be established.

Received September 26, 2014; accepted after revision November 1.

From the Departments of Radiological Sciences (J.H.H., Z.P.), Biostatistics (X.L., Y.L.), and Surgery (F.B.), St. Jude Children's Research Hospital, Memphis, Tennessee; Department of Imaging Diagnostic (N.M.), Institute of Paediatric, Kuala Lumpur Hospital, Kuala Lumpur, Malaysia; and Department of Radiology (G.G.), McFarland Clinic, Ames, Iowa.

This work was supported in part by grant No. CA21765 from the National Cancer Institute and by the American Lebanese Syrian Associated Charities.

Paper previously presented in part at: Annual Meeting of the American Society of Neuroradiology and the Foundation of the ASNR Symposium, April 21–26, 2012; New York, New York.

Please address correspondence to Zoltan Patay, MD, PhD, St. Jude Children's Research Hospital, Department of Radiological Sciences, 262 Danny Thomas Place, MS-220, Memphis, TN 38105; e-mail: zoltan.patay@stjude.org

Indicates open access to non-subscribers at www.ajnr.org

Indicates article with supplemental on-line table.

<http://dx.doi.org/10.3174/ajnr.A4221>

At St. Jude Children's Research Hospital, enrollment of patients with posterior fossa tumors on long-term therapeutic protocols confers the advantage of follow-up imaging availability. Because most arrive postoperatively and undergo subsequent metastasis-screening MR imaging according to our imaging protocols before enrollment, we see a number of postoperative intraspinal subdural collections (PISC). While these collections do not indicate metastasis,^{6,7,9} they may be misinterpreted by radiologists unfamiliar with their appearance, prompt neurosurgical consult, or hinder metastasis detection in the critical postoperative staging period. We therefore investigated the incidence, imaging and clinical features and course, and associated potentially predisposing factors in patients with PISC after suboccipital tumor resection in a large pediatric cohort.

MATERIALS AND METHODS

Study Population

A retrospective Health Insurance Portability and Accountability Act-compliant, institutional review board-approved clinical data base search conducted with a waiver of consent yielded 304 subjects who underwent resection of posterior fossa tumors between October 1994 and August 2010. Of these, 243 subjects (age range, 1 month to 20 years; mean age, 5.5 ± 4.6 years; 40.3% female; 139 medulloblastomas, 69 ependymomas, 15 atypical teratoid rhabdoid tumors, 5 astrocytomas, 3 glioblastomas, 3 gliomas, 1 medullomyoblastoma, 1 primitive neuroectodermal tumor, 7 rhabdoid tumors) had available postoperative spine MR imaging of sufficient diagnostic quality for detection of PISC. MR imaging review yielded 37 subjects with evidence of PISC (age range, 6 months to 16 years; mean, 6.0 ± 4.8 years; 37.8% female; 24 medulloblastomas, 7 ependymomas, 2 astrocytomas, 4 atypical teratoid rhabdoid tumors). Medical records were reviewed for CSF findings and for evidence of neurologic signs and symptoms related to irritation or compression of intraspinal neural structures at the time of MR imaging. To exclude the influence of age, we then established an age-matched internal control group negative for PISC ($n = 37$; age range, 5 months to 16.6 years; mean, 5.9 ± 4.5 years; 35% female; 27 medulloblastomas, 8 ependymomas, 2 atypical teratoid rhabdoid tumors) for comparative risk factor analysis.

Spine MR Imaging Analysis

Spine MR imaging techniques varied due to the 16-year study time span and multi-institutional imaging protocols. All spine MRIs were performed for metastasis screening and included postcontrast T1WI. All MRIs were reviewed by a board-certified neuroradiologist with a Certificate of Added Qualification (J.H.H., with 4.5 years' experience interpreting pediatric spine MR imaging). A second board-certified neuroradiologist (Z.P., with 18 years' experience interpreting pediatric spine MR imaging) reviewed all MRI in the final cohort (those positive for postoperative subdural collections [PISC+] and controls negative for postoperative subdural collection), equivocal cases, and those ultimately excluded for technical reasons. Differences were resolved in consensus. Both reviewers were blinded to pathology and radiology reports. MRIs of subjects deemed PISC+ on the first postoperative MR imaging or on any MR imaging ≤ 30 days

after surgery were followed until they were negative for PISC. Time from surgery to spine MR imaging was recorded for all examinations. The presence, location (cervical, thoracic, lumbosacral), extent (expressed in number of spinal segments), maximum thickness, and signal properties of PISC were assessed on sagittal postcontrast T1WI (37/37 subjects positive for PISC), precontrast T1WI (13/37) and T2WI (20/37) on postoperative MRIs, and subsequent follow-up spine MRIs in 35/37 subjects positive for PISC; follow-up spine MRIs were unavailable in 2/37 subjects positive for PISC. Signal on T1WI and T2WI was defined as isointense, hyperintense, or hypointense to CSF in the perimedullary subarachnoid space. Preoperative spine MRIs available in 15/37 subjects positive for PISC were assessed for the presence of subdural collections. Original reports from referring institutions were subsequently reviewed.

Brain MR Imaging Analysis

Preoperative brain MRIs of all subjects were evaluated for the location (fourth ventricle or not) and size of the posterior fossa tumor and for hydrocephalus by both subjective assessment and Evans index >90 th percentile.¹⁰ Tonsillar herniation was defined as >5 -mm protrusion of the cerebellar tonsils below the foramen magnum. Incomplete preoperative brain imaging for 1 subject positive for PISC precluded evaluation for tonsillar herniation or Evans index. Tumor volumes were calculated, per ellipsoid volume, as

$$V = \frac{4}{3} \pi \times \frac{L}{2} \times \frac{W}{2} \times \frac{H}{2}.$$

Postoperative brain imaging, CT in 1 subject and MRI in 36/37 subjects, were evaluated for intracranial subdural collections (supratentorial or infratentorial) as visualized on T1WI without (36/36) and with contrast (31/36), T2WI (35/36), noncontrast FLAIR (26/36), and contrast-enhanced FLAIR (18/36) images. Intracranial subdural collections were subjectively graded as nonexistent (0), mild (1), moderate (2), or large (3).

Statistical Analysis

Statistical analyses were performed by using SAS 9.3 software (SAS Institute, Cary, North Carolina). Associations of PISC with tumor histology and grade of intracranial subdural collection were assessed by the Fisher exact test. Association of PISC with tumor volume was evaluated by the Wilcoxon rank sum test. The associations of PISC with tumor location, subjective assessment of hydrocephalus, Evans index >90 th percentile, and the presence of tonsillar herniation and intracranial subdural collection were evaluated by the χ^2 test. Age and time from surgery to MR imaging were compared between all subjects positive and negative for postoperative subdural collections by the Wilcoxon rank sum test. $P < .05$ was considered statistically significant.

RESULTS

The overall incidence of PISC was 37/243 (15.2%). In the overall cohort, subjects positive for PISC were imaged earlier (18 ± 26 days postoperatively) than those without PISC (30 ± 32 days postoperatively) ($P = .0005$), and the incidence rate of PISC fell from 36% for subjects imaged up to 7 days after surgery to 8% in

Percentage risk of PISC in entire cohort (n = 243) by number of days from PFS to MRI

PFS to MRI (days)	PISC+	Total No. Subjects	% PISC+
0–7	15	42	36%
8–14	6	44	14%
15–21	6	48	13%
22–28	5	43	11%
>28	5	66	8%

Note:—PFS indicates posterior fossa surgery.

those imaged after postoperative day (POD) 28 (Table). There was no association of PISC with age ($P = .5033$).

Compared with controls, subjects positive for PISC did not differ significantly in age ($P = .9957$) or time from surgery to MR imaging ($P = .0723$). There was no association between PISC and tumor histology ($P = .4573$). Chart review yielded no neurologic signs or symptoms related to irritation or compression of intraspinal neural structures contemporaneous with the diagnosis of PISC.

Time to Appearance

The time from posterior fossa surgery to the first postoperative MR imaging revealing PISC ranged from 0 to 41 days (mean, 15 ± 17 days) in 36/37 (97%) subjects and was 137 days in a single subject (On-line Table). The time from posterior fossa surgery to the first postoperative MR imaging (mean, 17.6 ± 10.8 days) was 1–49 days in controls. Two subjects with PISC 27 days postoperatively had earlier negative MRI findings on PODs 11 and 20, respectively. No subdural collections were visible on preoperative MRI available in 15/37 subjects positive for PISC.

Time to Resolution

Further follow-up MRIs were available in 35/37 subjects positive for PISC. In 34 subjects, MR imaging demonstrated resolution of PISC between 8 and 472 days (108.2 ± 123.4 days) postoperatively, which was 3–441 days (95 ± 119.5 days) after the first PISC+ MR imaging. In another subject who had residual unresectable ependymoma at the foramen magnum and was diagnosed with PISC on POD 137, PISC persisted on MR imaging 325 days postoperatively. Resolution was documented 5.9 years after surgery, at which time the primary tumor had decreased in size so that the foramen magnum was patent. Otherwise, PISC had resolved in 100% of subjects re-imaged ≥ 57 days after the initial PISC+ MR imaging and had resolved in 12/17 (70.5%) subjects re-imaged between 3 and 28 days after the initial PISC+ MR imaging (On-line Table).

Three subjects with PISC diagnosed 1, 12, and 27 days after surgery had persistent but decreased collections on follow-up MR imaging 17, 6, and 28 days later (PODs 18, 18, and 55), respectively (On-line Table); all had resolved on repeat MR images obtained 35, 84, and 30 days later (PODs 53, 102, and 85), respectively. In 1 subject with PISC 3 days after surgery, PISC persisted at 17 days, with no further follow-up.

Location and Size

Two subjects were excluded from location and size analysis due to imaging limited to the cervical and thoracolumbar spine, respectively, precluding full analysis despite demonstrating PISC. Sub-

dural collections were most frequently thoracic (33/35), followed by lumbosacral (29/35) and cervical (27/35). PISC spanned an average of 18.8 ± 8.7 vertebral bodies at initial diagnosis, and except for a single subject with only ventral collections, all were both dorsal and ventral. PISC measured up to 0.46 ± 0.1 mm in thickness ventrally and 0.43 ± 0.21 mm dorsally, with maximal thickness most frequently at lumbar levels ventrally (19/35) and dorsally (18/35).

Imaging Characteristics

PISC were isointense to CSF on noncontrast T1WI (13/13) (Fig 1), hyperintense (19/20) more frequently than isointense to CSF (1/20) on T2WI, and most frequently hyperintense (enhancing) on postcontrast T1WI (36/37), on which they were most readily visualized (Figs 1 and 2). PISC were isointense to CSF on postcontrast T1WI in 1 subject. They were lobulated on sagittal postcontrast T1WI and T2WI and on axial imaging when available (Fig 2). No hematocrit levels were observed. There was no evidence of associated cord deformity or signal abnormality suggestive of compression in any subject, though prominent lumbar PISC often caused central crowding of the cauda equina without compression (Fig 2).

Associated Imaging Findings

PISC were not associated with preoperative hydrocephalus by either subjective assessment ($P = .0749$) or by Evans index $>90\%$ ($P = .7222$). There was no significant relationship between either tumor volume ($P = .8797$) or fourth ventricular location ($P = .3594$) and the development of PISC.

PISC were significantly associated with preoperative cerebellar tonsillar herniation ($P = .0228$) and with both the presence ($P = .0011$) and magnitude ($P = .0071$) of postoperative intracranial subdural collections; 91.89% of patients with PISC had intracranial subdural collections, compared with 59.46% of controls. Intracranial collections were most frequently mild in both subjects positive for PISC (67.57%) and control subjects (43.24%). Intracranial collections were more frequently associated with tonsillar herniation in subjects positive for PISC than in controls ($P = .0116$).

Correlation with CSF

CSF was obtained an average of 5 days (± 13 days) after the first postoperative MR imaging in 29/37 subjects, 146 days later in 1 subject, 392 days later in another, and unavailable in 6/37. Seven subjects had spinal metastases visible on PISC+ MR imaging; CSF was positive in 2/7, both medulloblastomas. In 1 case, metastases were questionable until resolution of PISC. In another, metastases were previously diagnosed on preoperative MR imaging; CSF was negative for metastases.

In another medulloblastoma case, PISC+ MR imaging and same-day CSF were negative for metastasis, despite CSF positive for metastasis 2 days later. Fluid color was not recorded.

Six subjects underwent lumbar puncture immediately following PISC+ MR imaging negative for metastasis. Collected fluid was yellow (xanthochromic) in 2/6 and negative for malignant cells in 6/6.

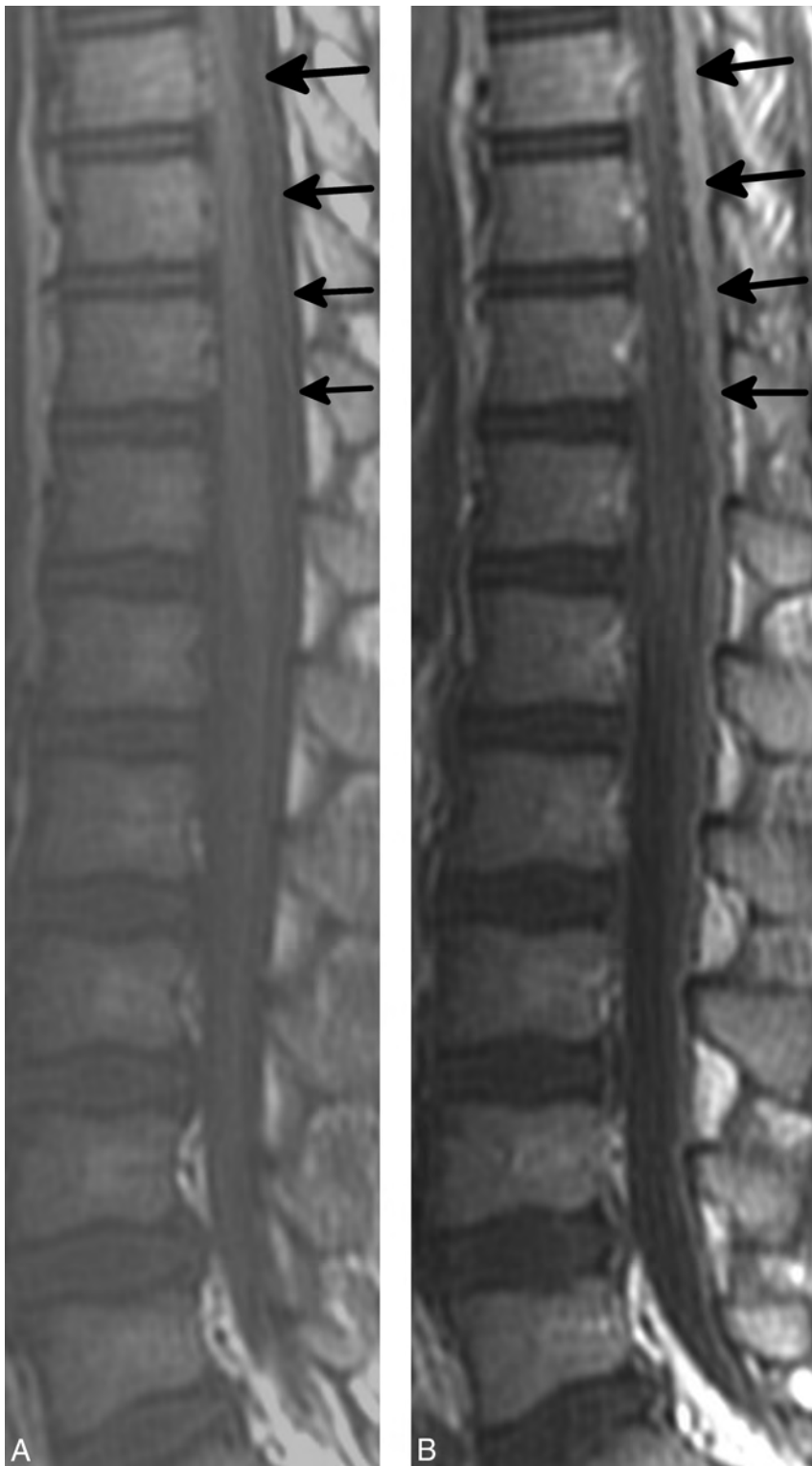


FIG 1. PISC (arrows) appear isointense to CSF on T1WI (A) and enhance on postcontrast T1WI (B).

Diagnosis

PISC were correctly identified on 23/23 MRIs interpreted by radiologists employed by St. Jude Children's Research Hospital, a pediatric cancer specialty hospital. Two PISC+ examinations performed at St. Jude were interpreted by locum tenens radiologists; PISC were incorrectly interpreted as potential metastases in both instances. Of 12 examinations performed and interpreted at

outside referring institutions, PISC were missed in 3, misinterpreted as contrast leakage in 1, misinterpreted as metastasis or potential metastasis in 4, and correctly diagnosed in 4/12. Thus, of 14 examinations interpreted by nonspecialized radiologists, only 4 (28.6%) were correctly interpreted as PISC, and 6/14 (42.9%) were misinterpreted as metastasis or potential metastasis.

DISCUSSION

Enhancing spinal subdural collections have been described in 15.5%–23% of children after posterior fossa surgery,^{7,9} but descriptions of associated factors and natural history have been limited due to sample size and follow-up limitations. In this study, we found PISC in 37 (15.2%) of 243 children imaged after posterior fossa surgery, similar to the 15.5% frequency described by Warmuth-Metz et al.⁹ PISC were associated with both intracranial subdural collections and tonsillar herniation. Although relief of increased intracranial pressure as evidenced by preoperative obstructive hydrocephalus has been suggested as a mechanism,⁹ we found no association of PISC with hydrocephalus either by subjective assessment or by the Evans index.¹⁰

PISC appeared as late as >20 days postoperatively, resolved as early as 8 days after surgery, and had resolved in most (70.5%) subjects imaged up to 28 days after initial PISC+ MR imaging. The incidence of PISC is greatest, 36% in this series, within 1 week after surgery and drops precipitously thereafter. In a single subject with unresectable ependymoma partially obstructing the foramen magnum and leptomeningeal metastasis, PISC persisted for at least 325 days; resolution was documented 5 years after surgery, at which time the primary tumor had decreased in size so that the foramen magnum was again patent. Although the collections were frequently large, significantly effacing CSF, there was no imaging or clinical evi-

dence of compression of spinal neural elements. However, PISC did partially obscure metastases in at least 1 case, resulting in a questionable diagnosis, and may have been sampled rather than CSF to give a false-negative CSF result on lumbar puncture in at least 1 patient who had positive lumbar puncture findings 2 days later. Xanthochromic fluid sampled in 2 additional subjects may

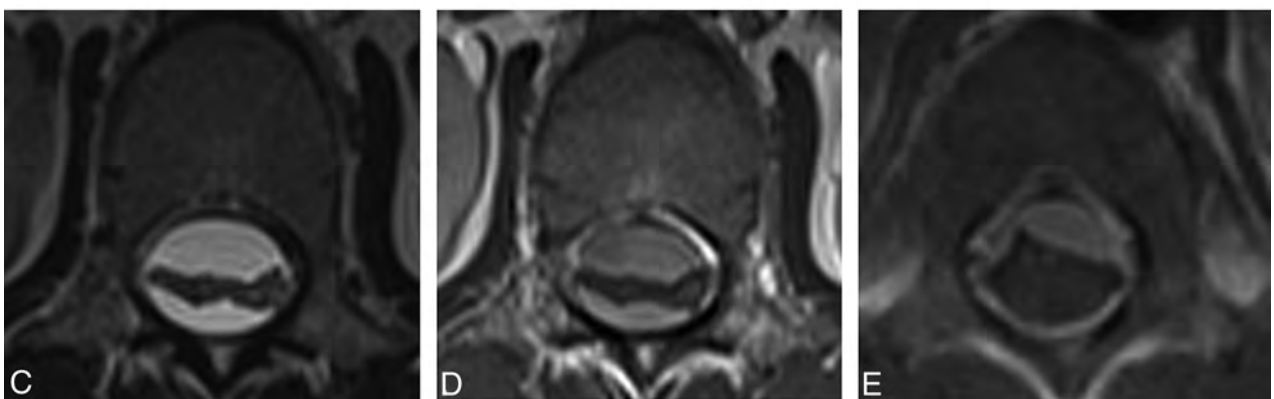


FIG 2. PISC filling the spinal canal appear mildly hyperintense to CSF (*asterisk*) on sagittal T2WI (A) and enhance on postcontrast T1WI (B), POD 10. PISC centrally displace the cauda equina on axial T2WI (C) and postcontrast T1WI (D) in another subject, POD 12. Festooned, enhancing PISC persist on postcontrast T1WI (E) in another subject on POD 41.

also have been subdural rather than CSF.¹¹ Although even lumbar punctures performed under ideal conditions may be falsely negative in up to 45%,² these observations suggest that PISC may render the diagnosis of metastasis more challenging on both MR imaging and CSF examinations; this problem potentially results

in incorrect risk stratification and treatment of the primary pathology. Of equal importance is the potential for misdiagnosis of PISC as metastasis by radiologists unfamiliar with this phenomenon, as occurred in 42.9% of spine MRI interpreted by nonspecialized radiologists in this series, potentially resulting in unrec-

essarily aggressive therapy and attendant increases in associated risks.

Thirty-six of 37 (97.3%) PISC were homogeneously hyperintense on postcontrast T1WI in this series, a characteristic finding. Although most subjects had only high-resolution postcontrast MR imaging as per our institutional leptomeningeal metastasis screening protocol, isointensity to CSF on noncontrast T1WI confirmed enhancement in 13/37, consistent with findings in prior reports.^{6,7,9} Despite this enhancement, the subdural location and lobulated appearance readily distinguish PISC from leptomeningeal metastases, which are subarachnoid in location and typically nodular, though they may diffusely “sugarcoat” the spinal cord.¹

The appearance of PISC is similar to that of spinal subdural collections in patients with spontaneous intracranial hypotension, including a “festooned” appearance on axial imaging due to attachments spanning the “subdural” zone (Fig 2), supporting decreased CSF pressure as a common mechanism.¹²⁻¹⁴ The Monro-Kellie hypothesis, which states that the sum of volumes of intracranial blood, CSF, and tissue must remain constant in an intact cranium, is generally invoked to explain the intracranial subdural collections as compensating for low CSF volumes in spontaneous intracranial hypotension or for sudden loss of intracranial volume postoperatively.^{12,14-18} This hypothesis has been extended to account for intraspinal subdural collections in spontaneous intracranial hypotension and after posterior fossa surgery.^{9,19}

It has been suggested that microtears in the arachnoid layer due to low CSF pressure and retraction of the arachnoid from the dura permit leakage of CSF into the subdural space,¹⁸⁻²⁰ however, such freely communicating CSF collections, termed “hygromas,” do not demonstrate the enhancement observed in PISC.^{6,9,11,21} PISC are more consistent with subdural effusions, which are encapsulated collections of protein-rich, xanthochromatic fluid not in communication with the subarachnoid space; enhancement differentiates them from hygromas.²¹ In actuality, there is no true “subdural space”; subdural effusions form within a relatively weak vascularized fibroblast cell layer, known as the “dural border” cell layer, at the interface of the dura and arachnoid layers,^{13,14,21} due to negative hydrostatic pressure inducing vasodilation and increased permeability in the dural border cell layer, with leakage of plasma and contrast resulting in enhancing subdural effusions.^{6,9,11}

Of all subjects with intracranial subdural collections, cerebellar tonsillar herniation was more frequent in those with PISC, an association not previously described. We therefore hypothesize that sequestration of the intraspinal and intracranial spaces, rather than increased intracranial pressure alone, predisposes patients with tonsillar herniation to PISC via relatively increased intraspinal pressure via a “ball valve” mechanism, followed by an abrupt postoperative pressure decrease. The requirement for compartmental sequestration could explain the absence of PISC in children with supratentorial tumors, which are less commonly associated with tonsillar herniation, though intracranial subdural collections may be present within the same supratentorial compartment postshunting or after decompressive craniotomy.^{17,18}

Limitations of this study include irregular timing of follow-up

spine MRI, occurring up to >1 year after diagnosis of PISC, limiting precise evaluation of the natural history. However, nearly all patients in this series, the largest to date, had follow-up imaging documenting resolution of PISC, and it would be difficult to justify administering contrast and anesthesia to asymptomatic patients for MR imaging for this purpose prospectively. Formal neurologic examinations were not performed because the patients were asymptomatic. CSF pressure measurements are not routinely obtained at lumbar puncture for metastasis detection at St. Jude Children’s Research Hospital, precluding correlation with PISC. Although xanthochromic and false-negative fluid was obtained at lumbar puncture in 3 subjects, subdural fluid was not intentionally sampled; this sampling could be informative in future studies.

CONCLUSIONS

Enhancing postoperative intraspinal subdural effusions occurred in 15.2% of children after posterior fossa tumor resection in this series, resolved spontaneously without neurologic sequelae, and had a characteristic appearance. Abrupt postoperative relief of excessive intraspinal pressure caused by spinal sequestration by tonsillar herniation is the proposed etiology. Preoperative spine MR imaging is ideal, but not always possible. Because time is of the essence for establishing a diagnosis of metastasis, delaying postoperative imaging, as previously suggested,⁶ is not advised because PISC occur infrequently and metastases may be visible despite PISC. However, we do recommend that if subdural collections are detected, MR imaging with contrast be repeated as late as clinically tolerated to re-evaluate leptomeningeal metastasis and potentially confounding lumbar PISC before lumbar puncture. In this series, repeat MR imaging documented improvement or resolution of PISC in 88% by 4 weeks.

Disclosures: Julie H. Harreld—UNRELATED: Grants/Grants Pending: National Cancer Institute,* American Lebanese Syrian Associated Charities,* Comments: St. Jude Children’s Research Hospital is a Comprehensive Cancer Center receiving grant support from the National Cancer Institute, grant No. CA21765. American Lebanese Syrian Associated Charities is the fundraising arm of St. Jude Children’s Research Hospital and supports all clinical and research activities; Travel/Accommodations/Meeting Expenses Unrelated to Activities Listed: Society of Pediatric Radiology; World Federation of Neuroradiological Societies, Comments: Society of Pediatric Radiology supported travel expenses and honorarium for an invited talk in 2013. World Federation of Neuroradiological Societies supported travel expenses for an invited talk in 2014. Frederick Boop—RELATED: Consulting Fee or Honorarium: Vancouver Children’s Hospital*; UNRELATED: Board Membership: Association of Neurological Surgeons*; Employment: Semmes-Murphey Clinic; OTHER RELATIONSHIPS: Board Member; Chairman, Department of Neurosurgery, University of Tennessee Health Science Center. Zoltan Patay—UNRELATED: Consultancy: Guerbet, Comments: one-time advisory board participation in 2013; Grants/Grants Pending: American Lebanese Syrian Associated Charities,* National Cancer Institute CA21765*; Travel/Accommodations/Meeting Expenses Unrelated to Activities Listed: Symposium Neuroradiologicum (Turkey), Third International Congress of NeuroOncology (Algeria), Seventh Arab Radiology Congress (Qatar), Hungarian Neuroradiology Society (Hungary), The Hospital for Sick Children (Canada), Indian Society of Neuroradiology (India), Sao Paulo Radiology Meeting (Brasil), Kuwait International Neuroimaging Conference (Kuwait), Erasmus Course of Magnetic Resonance Imaging (Romania, Belgium), European Course of Pediatric Neuroradiology (Italy), Comments: invited lectures given at mentioned meetings and courses. I received reimbursement of travel and lodging expenses. *Money paid to the institution.

REFERENCES

1. Engelhard HH, Corsten LA. Leptomeningeal metastasis of primary central nervous system (CNS) neoplasms. *Cancer Treat Res* 2005;125:71–85

2. Maroldi R, Ambrosi C, Farina D. **Metastatic disease of the brain: extra-axial metastases (skull, dura, leptomeningeal) and tumour spread.** *Eur Radiol* 2005;15:617–26
3. Terterov S, Krieger MD, Bowen I, et al. **Evaluation of intracranial cerebrospinal fluid cytology in staging pediatric medulloblastomas, supratentorial primitive neuroectodermal tumors, and ependymomas.** *J Neurosurg Pediatr* 2010;6:131–36
4. Pang J, Banerjee A, Tihan T. **The value of tandem CSF/MRI evaluation for predicting disseminated disease in childhood central nervous system neoplasms.** *J Neurooncol* 2008;87:97–102
5. Porto L, Kieslich M, Turowski B, et al. **Spinal subdural haematoma mimicking tethered cord after posterior fossa open surgery.** *Neuroradiology* 2002;44:415–17
6. Shaw DW, Weinberger E, Brewer DK, et al. **Spinal subdural enhancement after suboccipital craniectomy.** *AJNR Am J Neuroradiol* 1996;17:1373–77
7. Kaufman BA, Moran CJ, Park TS. **Spinal magnetic resonance imaging immediately after craniotomy for detection of metastatic disease.** *Pediatr Neurosurg* 1995;23:171–81
8. Wiener MD, Boyko OB, Friedman HS, et al. **False-positive spinal MR findings for subarachnoid spread of primary CNS tumor in postoperative pediatric patients.** *AJNR Am J Neuroradiol* 1990;11:1100–03
9. Warmuth-Metz M, Kuhl J, Krauss J, et al. **Subdural enhancement on postoperative spinal MRI after resection of posterior cranial fossa tumours.** *Neuroradiology* 2004;46:219–23
10. Wilk R, Kluczevska E, Syc B, et al. **Normative values for selected linear indices of the intracranial fluid spaces based on CT images of the head in children.** *Pol J Radiol* 2011;76:16–25
11. Teksam M, Casey SO, McKinney A, et al. **Gadolinium enhancement of spinal subdural collection on magnetic resonance imaging after lumbar puncture.** *Neuroradiology* 2003;45:553–56
12. Chiapparini L, Ciceri E, Nappini S, et al. **Headache and intracranial hypotension: neuroradiological findings.** *Neurol Sci* 2004;25(suppl 3):S138–41
13. Haines DE, Harkey HL, al-Mefty O. **The “subdural” space: a new look at an outdated concept.** *Neurosurgery* 1993;32:111–20
14. Mokri B, Parisi JE, Scheithauer BW, et al. **Meningeal biopsy in intracranial hypotension: meningeal enhancement on MRI.** *Neurology* 1995;45:1801–07
15. Mokri B. **The Monro-Kellie hypothesis: applications in CSF volume depletion.** *Neurology* 2001;56:1746–48
16. Tosaka M, Sato N, Fujimaki H, et al. **Diffuse pachymeningeal hyperintensity and subdural effusion/hematoma detected by fluid-attenuated inversion recovery MR imaging in patients with spontaneous intracranial hypotension.** *AJNR Am J Neuroradiol* 2008;29:1164–70
17. Aarabi B, Chesler D, Maulucci C, et al. **Dynamics of subdural hygroma following decompressive craniectomy: a comparative study.** *Neurosurg Focus* 2009;26:E8
18. Sonmez OF, Temel Y, Visser-Vandewalle V, et al. **A new evaluation method for the intracranial volume changes and subdural effusion of patients following endoscopic third ventriculostomy.** *Clin Neurol Neurosurg* 2013;115:160–64
19. Schievink WI. **Spontaneous spinal cerebrospinal fluid leaks and intracranial hypotension.** *JAMA* 2006;295:2286–96
20. Watanabe A, Horikoshi T, Uchida M, et al. **Diagnostic value of spinal MR imaging in spontaneous intracranial hypotension syndrome.** *AJNR Am J Neuroradiol* 2009;30:147–51
21. Mori K, Maeda M. **Delayed magnetic resonance imaging with GdDTPA differentiates subdural hygroma and subdural effusion.** *Surg Neurol* 2000;53:303–10; discussion 310–11

Incidence of Inadvertent Intravascular Injection during CT Fluoroscopy–Guided Epidural Steroid Injections

P.G. Kranz, T.J. Amrhein, and L. Gray



ABSTRACT

BACKGROUND AND PURPOSE: Inadvertent intravascular injection during epidural steroid injection can result in complications and has been investigated previously with conventional fluoroscopy, but not CT fluoroscopy. The purpose of this study was to determine the incidence of intravascular injections recognized during CT fluoroscopy–guided epidural steroid injection.

MATERIALS AND METHODS: We retrospectively reviewed 575 consecutive CT fluoroscopy–guided epidural steroid injections. Procedures were assessed to determine the incidence of intravascular injection. Cases positive for intravascular injection were classified on the basis of anatomic location, distance from the needle tip, washout pattern, and presence of combined epidural and vascular injection. Cases were also graded as either venous or arterial by using a 5-point scale.

RESULTS: Intravascular injection was observed in 26% of cervical transforaminal epidural steroid injections (7/27), 9% of cervical interlaminar epidural steroid injections (4/47), 8% of lumbar transforaminal epidural steroid injections (22/275), and 2% of lumbar interlaminar epidural steroid injections (4/222). Vessels were most commonly identified close to the needle, but in 30% of cases, they were visualized in the anterior paraspinal soft tissues remote from the needle. Washout was most commonly delayed (86%), though rapid washout occurred in 14% of cases. Simultaneous epidural and vascular injections occurred in 32% of cases. Most visualized vessels were venous, but 2 cases were classified as probably arterial.

CONCLUSIONS: Intravascular injections can be detected with CT fluoroscopy. The incidence in our study was similar to that in previous reports using conventional fluoroscopy. Technical factors such as the “double-tap” on CT fluoroscopy following contrast injection, assessment for discordance between injected and visualized contrast volume, and maintenance of an appropriate FOV facilitate the detection of such events.

ABBREVIATIONS: CTF = CT fluoroscopy; ESI = epidural steroid injection; ILESI = interlaminar epidural steroid injection; TFESI = transforaminal epidural steroid injection

Epidural steroid injections (ESIs) are a commonly performed intervention for patients with degenerative conditions of the spine.¹ Recent attention to rare but potentially catastrophic side effects associated with ESIs has resulted in an increased focus on maximizing the safety of these injections.^{2,3} It is thought that most severe adverse events are vascular, the result of either embolic phenomena during injection of particulate steroid into arteries that supply the spinal cord or brain, or direct vascular injury during needle placement.⁴

The incidence of unintended intravascular needle placement

during procedures performed with conventional fluoroscopy has been previously reported in multiple investigations.^{5–9} Several authors have advocated that real-time fluoroscopy or digital subtraction angiography be used when epidural injections are performed, to maximize the detection of intravascular injections.^{10–12} However, CT fluoroscopy (CTF) guidance, which does not use real-time fluoroscopy or DSA but does offer superior contrast resolution compared with fluoroscopy, has been increasingly used by some practitioners when performing epidural injections because it provides the benefits of cross-sectional needle localization and improved visualization of soft-tissue structures.^{13,14} The ability to detect intravascular injections by using CT guidance has not been previously reported, to our knowledge. Nevertheless, it has been assumed by some authors to be inferior to conventional fluoroscopy in this respect.^{15–17}

The purpose of this investigation was to report the incidence of intravascular injections detected during CTF-guided epidural

Received September 5, 2014; accepted after revision October 21.

From the Department of Radiology, Duke University Medical Center, Durham, North Carolina.

Please address correspondence to Peter G. Kranz, MD, Department of Radiology, Box 3808, Duke University Medical Center, Durham, NC 27710; e-mail: peter.kranz@duke.edu

<http://dx.doi.org/10.3174/ajnr.A4219>

steroid injections. Additionally, we sought to characterize the appearance of intravascular injections to guide proceduralists unaccustomed to observing these injections with CT.

MATERIALS AND METHODS

All consecutive CTF-guided ESIs performed by a single proceduralist at 1 outpatient facility during an 18-month period (January 2013 to June 2014) were retrospectively reviewed. The proceduralist was a board-certified radiologist who holds a Certificate of Added Qualification in neuroradiology and has 7 years' experience performing injections under CTF guidance. The investigation was approved by our local institutional review board and is compliant with Health Insurance Portability and Accountability Act regulations.

Cases were identified by review of departmental procedure schedules and were considered on a per-injection basis (ie, if patients underwent >1 injection in a single visit, each individual injection was considered a separate case for data analysis).

Injection Technique

Injections were performed by using intermittent CTF on a single CT scanner (LightSpeed 16; GE Healthcare, Milwaukee, Wisconsin), equipped with a foot pedal used to trigger acquisition of a set of 3 consecutive fluoroscopic images, using a peak voltage of 120 kV(peak) and a section thickness of 2.5 mm. The tube current and display FOV were selected by the radiologist on a case-by-case basis, depending on the age and body habitus of the patient and the complexity of the local anatomy. In general, the tube current was typically set at 20–60 mA for lumbar injections and approximately 50% higher for cervical injections. The display FOV was

selected to encompass, at minimum, the skin surface of the back to the anterior margin of the vertebral body.

Contrast was used for all injections before injection of steroid. For lumbar injections, undiluted iopamidol containing 200-mg/mL iodine was used (Isovue-M 200; Bracco, Princeton, New Jersey). For cervical injections, a 50% dilution of iopamidol with preservative-free sterile saline was used to achieve a final iodine concentration of 100-mg/mL iodine.¹⁸ The injected contrast volume was approximately 0.2–0.4 mL for the first injection. Repeat injections using larger volumes of contrast (0.5–1.0 mL) were used if the first injection was not sufficient due to either poor visualization or suspected vascular washout. After contrast injection, 2 sets of fluoroscopic images were obtained by using a “double-tap” approach, whereby the foot pedal was pressed immediately following the injection to determine the initial contrast pattern and again 2–3 seconds later to obtain a delayed image to evaluate contrast washout. A 22-ga Quincke Point Spinal Needle (BD Medical, Franklin Lakes, New Jersey) was used for all injections. If blood flash was seen in the needle hub, the needle was repositioned before contrast injection. For transforaminal epidural steroid injections (TFESIs), care was taken to position the needle as far posterior in the neural foramen as possible. An anesthetic test dose was performed during cervical TFESL.¹⁹ Procedures were otherwise performed as previously described.^{13,20,21}

Image Analysis

All consecutive cases of ESIs performed during the study time range were reviewed on a PACS by the radiologist who performed the procedures to identify cases of unintended intravascular injection. Images obtained after contrast injection were compared with preinjection images at the same level to ensure that attenuation related to osseous structures was not misinterpreted as vascular contrast. Findings of cases were considered positive if there was either direct visualization of vascular structures or if there was little-to-no contrast visualized after contrast injection, after checking to ensure the absence of a leak from the connector tubing. Cases that demonstrated intravascular injection were then independently reviewed and confirmed by a second board-certified radiologist who holds a Certificate of Added Qualification in neuroradiology and who has 4 years' experience performing injections under CT fluoroscopy.

Both readers then classified the intravascular contrast in cases positive for it according to its location relative to the spinal canal, distance from the needle tip, and washout pattern. The location of the contrast was categorized into 5 predetermined anatomic regions, as depicted in Fig 1. Multiple locations could be assigned per injection if intravascular contrast was identified in >1 zone simultaneously. The rate of contrast washout was assessed by comparing the immediate CTF image with the delayed image and was classified as one of the following: no washout, rapid washout, or delayed washout. “Rapid washout” was defined as a case in which there was complete

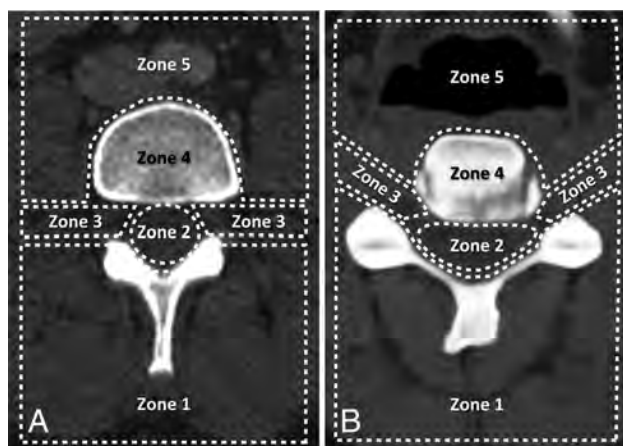


FIG 1. Classification scheme for the location of visualized vessels seen during inadvertent intravascular injection in the lumbar (A) and cervical (B) spine. Regions include the following: posterior paraspinal soft tissues (zone 1), spinal canal (zone 2), foraminal region (zone 3), vertebral body (zone 4), and anterior paraspinal soft tissues (zone 5).

Table 1: Assessment criteria for vessel type seen during intravascular injection

Score	Vessel	Suggestive Features
5	Definite vein	Flow into a specific, anatomically identifiable venous structure
4	Probable vein	Flow into region of known venous structure, flow predominantly away from spinal canal, delayed washout
3	Indeterminate	Not meeting criteria for other categories
2	Probable artery	Flow into region of known arterial structure, flow predominantly toward the spinal canal, rapid washout
1	Definite artery	Flow into a specific, anatomically identifiable arterial structure

Table 2: Frequency of intravascular injection by anatomic zone^a

Injection Type	Anatomic Zone of Identified Vessel						No. of Injections
	1	2	3	4	5	0	
Lumbar ILESi	25%	100%	25%	0%	0%	0%	4
Lumbar TFESI	14%	18%	86%	5%	36%	0%	22
Cervical ILESi	0%	100%	50%	0%	50%	0%	4
Cervical TFESI	29%	0%	71%	0%	14%	14%	7

^a Percentages across each injection type may sum to >100% because vessels may be visualized in >1 location simultaneously.

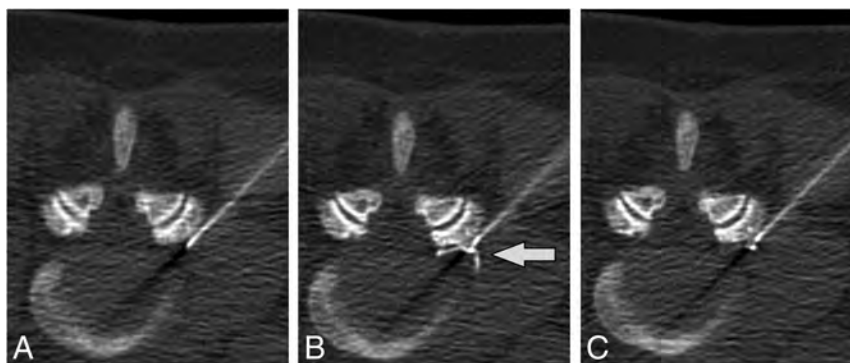


FIG 2. Intravascular injection during lumbar TFESI. Preinjection (A), immediate postinjection (B), and delayed postinjection (C) images demonstrate a vessel in the left foraminal zone (arrow) that washes out on the delayed image.

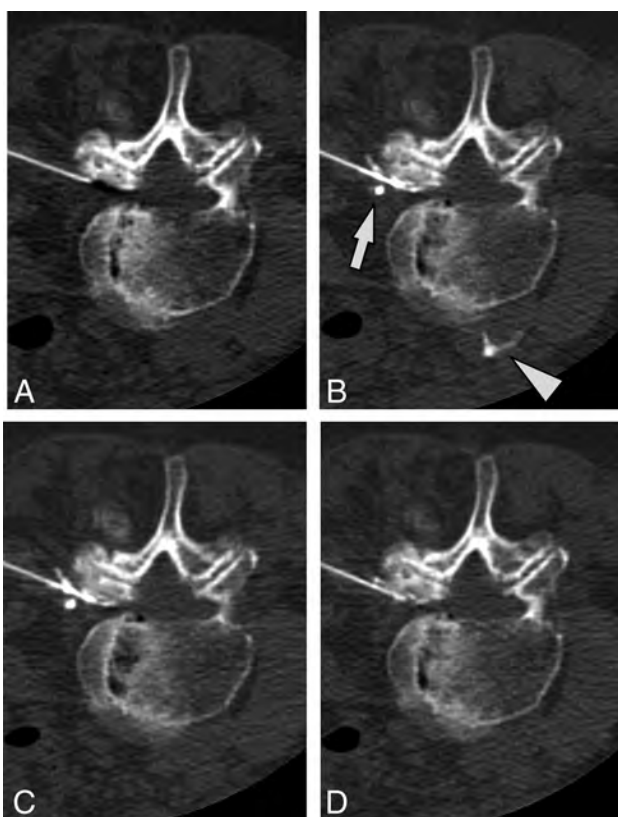


FIG 3. A case of intravascular injection is demonstrated on preinjection (A), immediate postinjection (B), first delayed (C) images, and an additional delayed (D) image. On the immediate postinjection image, contrast is seen in the ascending lumbar vein (arrow) and the inferior vena cava (arrowhead). There is washout of contrast from the inferior vena cava on the first delayed image and from the ascending lumbar vein on the second delayed image.

absence of contrast on the immediate image or there was markedly less contrast than expected given the volume injected. “Delayed washout” was defined as a case of vascular opacification in which dense intravascular contrast was seen on the immediate image but it decreased or disappeared on the delayed postinjection images. Distance from the needle tip to the opacified vessel was assigned to 1 of 4 categories: <1 cm from needle tip to the vessel, >1 cm, both >1 cm and <1 cm, or vessel not seen due to immediate washout. Cases positive for intravascular injection were also classified as showing either vascular opacification alone or simultaneous vascular and epidural contrast.

The readers also attempted to classify the opacified vessel as either venous or arterial and provided a confidence level for this assessment based on criteria set forth in the 5-point scale shown in Table 1. Cases in which the readers disagreed were rereviewed by both readers, and a consensus score was determined. Other patient characteristics, including age and sex, were

also recorded. For data analysis, sacral TFESIs were included with lumbar injections.

Statistical Analysis

Statistical analyses were performed by using commercially available software (GraphPad Prism 6 software, Version 6.0b; GraphPad Software, San Diego, California). The Mann-Whitney *U* test was used to compare differences in age among groups. The Fisher exact test was used to compare differences in sex. *P* values < .05 were considered statistically significant.

RESULTS

Subject Characteristics

A total of 575 consecutive epidural injections were identified during the study period. These included 275 lumbar transforaminal injections, 222 lumbar interlaminar injections, 47 cervical interlaminar injections, 27 cervical transforaminal injections, 3 thoracic transforaminal injections, and 1 thoracic interlaminar injection performed during 390 individual patient encounters. The mean patient age for all injections was 63.5 years (range, 22–92 years). Forty-three percent of injections were performed on male patients, and 57%, on female patients. All injections were technically successful. In all cases in which intravascular injection was identified during the procedure, the needle could be repositioned and the subsequent steroid injection was performed successfully. There were no major complications in any subject.

Incidence of Intravascular Injections

Intravascular injection was observed in 26% of cervical TFESIs (7/27), 9% of cervical interlaminar epidural steroid injections (ILESIs) (4/47), 8% of lumbar TFESIs (22/275), and 2% of lumbar

ILESIs (4/222). No cases of intravascular injection were identified during thoracic epidural injections; however, the study population included only 3 thoracic TFESIs and 1 thoracic ILESI, limiting conclusions regarding incidence, given the small number of cases. The overall rate of intravascular injection for all cases was 6% (37/575). No difference in age ($P = .83$) or sex ($P = .17$) was observed among patients with intravascular injection detected compared with those without.

Characteristics of Observed Intravascular Injections

The locations of vessels identified during intravascular injections are reported in Table 2. The most common location of vessels observed during TFESI was in the foraminal region (zone 3), with 86% and 71% of TFESIs positive for intravascular injections in the lumbar and cervical regions, respectively, showing vascular opacification in this region (Fig 2). For cases positive for intravascular injection during ILESI, the spinal canal (region 2) was the most commonly observed location of vascular opacification, seen in 100% of both cervical and lumbar injections. In 46% of cases (17/37), vessels were seen in >1 region simultaneously. Of note, 30% of cases showed vascular opacification in the anterior paraspinal soft tissues (zone 5) (Fig 3), including 1 case of a lumbar transforaminal injection in which this was the only location where contrast was seen.

Table 3: Characteristics of identified vascular injections

	n	%
Distance from needle tip to vessel		
<1 cm only	11	30%
>1 cm only	2	5%
Both <1 cm and >1 cm	23	62%
Immediate washout (vessel not seen)	1	3%
Combined epidural injection		
Vascular only	25	68%
Epidural + vascular	12	32%
Washout pattern		
None	0	0%
Delayed	32	86%
Immediate	5	14%
Vessel type		
Definite venous (n = 5)	4	11%
Probable venous (n = 4)	27	73%
Indeterminate (n = 3)	4	11%
Probable arterial (n = 2)	2	5%
Definite arterial (n = 1)	0	0%

Data related to the distance from the needle tip, combined epidural and vascular injection, washout pattern, and suspected vessel type are reported in Table 3. Most commonly, vessels were seen simultaneously at both >1 cm and <1 cm from the needle tip (62% of cases) (Fig 4). However, in 2 cases (5%), vessels were only seen >1 cm from the needle tip. In 1 case, immediate washout of contrast resulted in no vessel or epidural contrast being seen despite contrast injection (Fig 5).

Simultaneous epidural and vascular injections were observed in 32% (12/37) with positive results.

Washout of contrast between the initial image and the delayed image was seen in all positive cases. Most commonly, the washout pattern was delayed (86%, 32/37 cases) (Fig 6). However, rapid washout was observed in 14% (5/37) of cases, indicating rapid flow within the vessel.

Most cases were classified as “definitely venous” or “probably venous,” with these 2 categories accounting for 84% of all recognized vascular injections. Four cases (11%) were classified as indeterminate. Two cases (5%) of probable arterial injection were identified, both of which occurred during cervical transforaminal injections.

DISCUSSION

Our investigation demonstrates that intravascular injections can be recognized during CTF-guided epidural injections. We found that intravascular injections were identified most commonly during cervical transforaminal injections, in which they were observed in more than one-quarter of cases. Overall the detection rates for intravascular injections in our study are comparable with or, in some cases, slightly greater than rates previously reported by investigators using conventional fluoroscopy. These findings are important in that they directly contradict claims that the cross-sectional nature of CT imaging precludes detection of intravascular injections.¹⁵⁻¹⁷

Although the incidence of unintended intravascular injections during CTF-guided epidural injections has not been previously reported, to our knowledge, recognition of intravascular injection during fluoroscopically guided procedures by using live fluoroscopy or DSA has received considerable attention in the literature. In a prospective study of 2145 transforaminal injections performed by using live fluoroscopy, Nahm et al⁵ found an incidence of intravascular injection of 20.6% in the cervical region and 6.1%

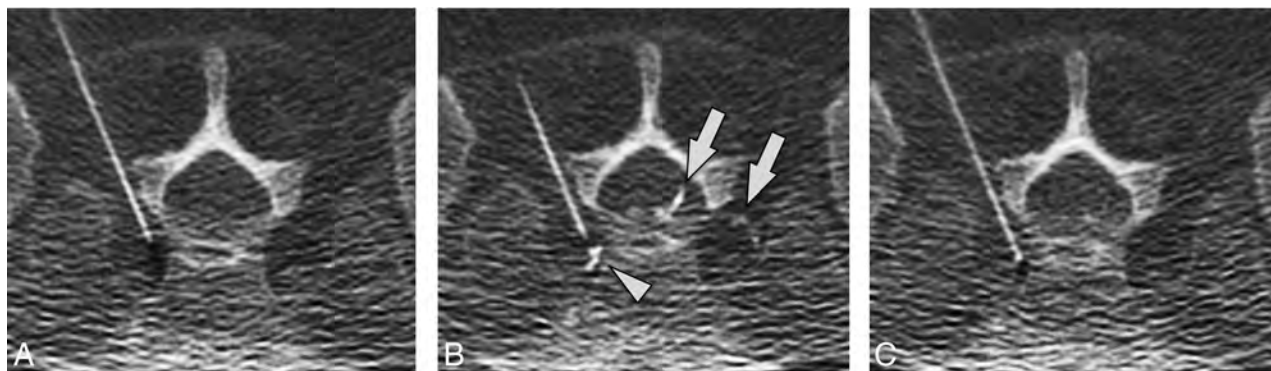


FIG 4. Intravascular contrast seen both close to and more remote from the needle tip. Preinjection (A), immediate postinjection (B), and delayed postinjection (C) images show intravascular contrast at the needle tip (arrowhead) and further away (arrows) in the sacral epidural venous plexus. Note that these vessels are not seen on the delayed washout image. No epidural contrast is seen.

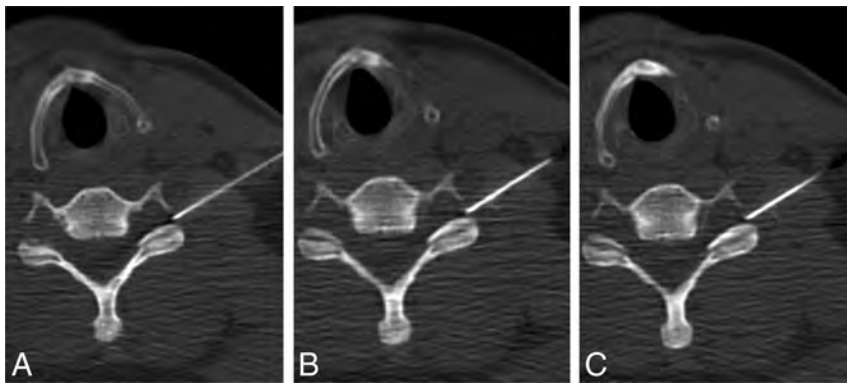


FIG 5. Immediate contrast washout. Preinjection (A), immediate postinjection (B), and delayed postinjection (C) images obtained after injection of 1.0-mL contrast. Neither vascular nor epidural contrast is seen. A preceding injection with 0.2-mL contrast showed similar negative findings, and images obtained cranial and caudal to the needle tip showed no contrast (images not shown).

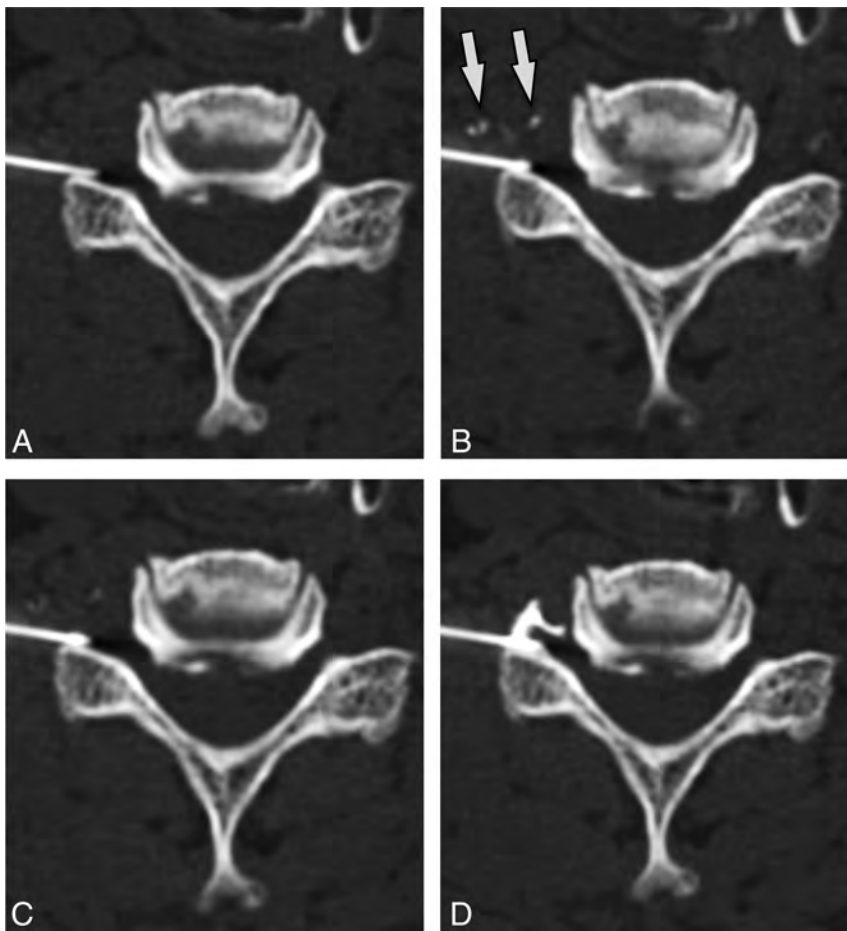


FIG 6. Delayed contrast washout pattern. Preinjection (A), immediate postinjection (B), and delayed postinjection (C) images demonstrate intravascular contrast (arrows) that progressively washes out on delayed images. After needle repositioning (D), re-injection of contrast shows only epidural contrast spread.

in the lumbar region. Furman et al⁶ found a similar rate of 19.4% of intravascular injections in a prospective study of 504 cervical TFESIs. In a separate study of 671 lumbar TFESIs, Furman et al⁷ found a rate of intravascular injection of 11.2%. A recently published prospective investigation by El Abd et al⁹ of 41 cervical and 113 lumbar transforaminal injections found an incidence of intravascular injection of 17% during cervical injections and

15% during lumbar injections when live fluoroscopy was used. Our study found generally higher rates of detection of intravascular injections during cervical TFESIs (26%); our rate of intravascular injections during lumbar TFESIs (8%) was in the middle of the range of rates reported by other authors.

Relatively less attention has been given in the literature to rates of intravascular injection during ILESI. This may reflect the overall lower incidence of vascular events with this approach and a belief that this approach is less likely to result in a neurologic deficit, given the distance from the radiculomedullary arteries that supply the spinal cord. Although rare, catastrophic outcomes presumed to be vascular in nature have been reported following cervical ILESI.²² At minimum, injection into veins during ILESI may decrease the effectiveness of the injection due to decreased epidural deposition of medication.²³ In a retrospective review of complications associated with >10,000 injections, Manchikanti et al²⁴ reported intravascular injections during 4.2% of cervical and 0.5% of lumbar epidural injections. Although our study involved considerably fewer patients, our detection rates of intravascular injection during cervical (9%) and lumbar (2%) ILESI were higher (Fig 7).

DSA has been advocated by some authors as a way to increase detection of intravascular injection into small arteries, leading to criticism of injections performed without DSA, including those performed by using CTF. Data regarding the actual clinical impact of DSA on rates of catastrophic complications, however, is lacking. Nevertheless, several authors have reported cases of intravascular injections identified with DSA that were missed with live fluoroscopy.²⁵⁻²⁷ One prospective investigation found that the use of digital subtraction angiography identified an additional 2.25% of cases of vascular injections that would not have been recognized by

blood flash, aspiration, or live fluoroscopy, though this study did not specify whether the additional injections identified were venous or arterial.⁹ A separate investigation by McLean et al²⁸ reported much higher rates of intravascular injections seen with DSA compared with live fluoroscopy (32.8% versus 17.9%). However, none of the recognized cases in the study, including those seen with both live fluoroscopy and DSA, were judged arte-

rial. Moreover, reliance on DSA does not preclude the possibility of intra-arterial injection and does not guarantee the absence of significant vascular complications.²⁹ Consequently, there is disagreement regarding the role of DSA when performing epidural injections, and this topic is the subject of ongoing, often vigorous debate.^{30,31}

Although most vascular injections are most likely venous, most reported studies either do not or are not able to definitively distinguish venous from arterial injections.⁵ In our study, 2 of the 37 cases with positive results were categorized as probably arterial in nature. Although the temporal and inherent spatial resolutions of CT are inferior to those of DSA, the superior contrast resolution of CT allows the detection of small vessels and lets the operator better judge discordance between the volume of injected contrast and the amount of visualized contrast. In our experience, these factors contribute to the detection of small, rapidly flowing vessels, such as arteries, on CT.

Recognition of simultaneous intravascular and epidural injections is potentially important because proceduralists are more likely to miss a vascular injection if an expected epidural contrast pattern is simultaneously visualized.³² Previous investigations have reported rates of simultaneous epidural and intravascular injection by using live fluoroscopy of between 15% and 19%.^{8,33} In our study, we observed simultaneous epidural and intravascu-

lar injection (Fig 8) at much higher rates (32%) than commonly reported with conventional fluoroscopy.

Despite the successful identification of cases in which vessels were directly visualized at the same time as epidural contrast in our study, we recognize that the cross-sectional nature of CT may impose some limitations as well. For example, purely intravascular injections into vessels that run in the craniocaudal direction (and therefore outside the axial scan plane) would typically be recognized with CTF by the absence of epidural contrast after injection, even if the vessel is not directly seen. However, when simultaneous epidural and intravascular injection occurs involving a vessel oriented in the craniocaudal direction, it is relatively more difficult to recognize, and these injections could potentially be missed in some cases. Nevertheless, our data suggest that the overall rate for detecting intravascular injections, including those that occur concurrently with epidural injections, is not degraded to a major extent by this potential scenario.

Our investigation indicates that attention to several technical aspects of CTF-guided injections can be helpful in facilitating recognition of intravascular injections. First, the use of double-tap intermittent CTF immediately after injection and again 2–3 seconds later to evaluate washout is critical. Washout of vascular contrast was present in all cases, and in most cases, the washout pattern was delayed. If the immediate postinjection image is not

obtained, the vessel may never be identified because it will be absent on more delayed images. Although the double-tap technique may require a few additional CTF images, the overall increase in dose from these images would be negligible in light of the low tube current and narrow collimation associated with CTF imaging, and any minimal dose increase would be outweighed by the potential safety benefits of identifying intravascular injections. Additionally, it is very important for proceduralists to begin by injecting only a relatively small amount of contrast. This helps prevent

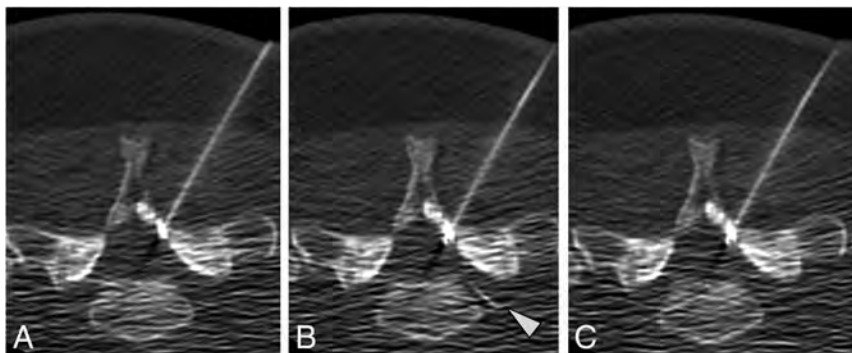


FIG 7. Intravascular injection during cervical ILESI. Preinjection (A), immediate postinjection (B), and delayed postinjection (C) images demonstrate a vessel in the left neural foramen (arrowhead) that washes out on the delayed image.



FIG 8. Simultaneous epidural and intravascular injection. Preinjection (A), immediate postinjection (B), and delayed postinjection (C) images demonstrate a vessel extending into the anterior paraspinal soft tissues (arrowhead) that washes out on the delayed image. Epidural contrast in the neural foramen (arrow) persists on the delayed image. Note that there is contrast in the epidural space of the spinal canal on the preinjection image due to prior injection at an adjacent level.

the vessel from being obscured if there is simultaneous epidural and vascular injection. Proceduralists should also become comfortable with the expected degree of epidural opacification relative to the contrast volume they inject. In some cases, vascular injections will be detected by the absence of expected epidural contrast despite increasing volumes of injected contrast. At the greatest extreme, total or near-total absence of epidural contrast during active injection (assuming intact connector tubing and verification that contrast is actually in the syringe) should indicate that the needle tip is within a high-flow vessel or possibly a vessel running perpendicular to the plane of the image. Finally, the display FOV should be adjusted to include sufficient surrounding soft-tissue structures, including those anterior to the vertebral body, because our data indicate that in some cases, the vessels being opacified with contrast may be remote from the needle tip or even in larger vessels such as the inferior vena cava.

There are several limitations to this investigation. First, and perhaps most important, one can never be sure that all blood vessels, including small-caliber vessels such as radiculomedullary arteries, will be detected when injections are performed under CTF guidance. The ability of CTF to detect some intravascular needle placements, then, should by no means be construed as a guarantee that all intravascular needle placements would be detected. This caveat, however, is also true of injections performed with any imaging technique, including live fluoroscopy and DSA. Additional measures to help mitigate the risk of a vascular event, including the use of nonparticulate steroid and/or an anesthetic test dose, should be considered, particularly for injections with higher risk, such as cervical TFESIs. Second, we compared rates of intravascular injection in our study with previously reported rates with fluoroscopy. Although our data suggest that the rates of detection are generally similar, they do not establish the superiority of one technique versus another, because no direct comparison between modalities was made in this study. The ideal comparison would involve the simultaneous use of CT and fluoroscopy to assess individual injections. Newer technologies such as flat panel CT could potentially facilitate direct comparisons of this type.

Identification of intravascular injection may be related to, but is not the same as, avoidance of significant clinical complications during epidural injections. Because most identified injections are venous and therefore unlikely to result in spinal cord injury or stroke, emphasis should be placed on identifying those techniques that actually reduce complication rates in the clinical setting. Dogmatic assertions or prohibitions regarding the advisability of various injection techniques should be approached cautiously in the absence of such data. Finally, this was a retrospective investigation of a single operator with relatively small numbers of some subtypes of injections. Larger, prospective patient cohorts with multiple proceduralists would be desirable for future investigations.

CONCLUSIONS

Our investigation demonstrates that intravascular injections can be detected with CT fluoroscopy during epidural injections. Rates of detection of intravascular injection in our study were similar to or greater than rates previously reported for injections performed under conventional fluoroscopy. Technical factors such as the double-tap on CTF following contrast injection, assessment for discordance between the volume of injected contrast and the ex-

pected degree of epidural opacification, and maintenance of an appropriate FOV facilitate the detection of such events.

REFERENCES

1. Manchikanti L, Pampati V, Falco FJ, et al. **Assessment of the growth of epidural injections in the Medicare population from 2000 to 2011.** *Pain Physician* 2013;16:E349–64
2. Atluri S, Glaser SE, Shah RV, et al. **Needle position analysis in cases of paralysis from transforaminal epidurals: consider alternative approaches to traditional technique.** *Pain Physician* 2013;16:321–34
3. Abbasi A, Malhotra G, Malanga G, et al. **Complications of interlaminar cervical epidural steroid injections: a review of the literature.** *Spine (Phila Pa 1976)* 2007;32:2144–51
4. Scanlon GC, Moeller-Bertram T, Romanowsky SM, et al. **Cervical transforaminal epidural steroid injections: more dangerous than we think?** *Spine (Phila Pa 1976)* 2007;32:1249–56
5. Nahm FS, Lee CJ, Lee SH, et al. **Risk of intravascular injection in transforaminal epidural injections.** *Anaesthesia* 2010;65:917–21
6. Furman MB, Giovanniello MT, O'Brien EM. **Incidence of intravascular penetration in transforaminal cervical epidural steroid injections.** *Spine (Phila Pa 1976)* 2003;28:21–25
7. Furman MB, O'Brien EM, Zgleszewski TM. **Incidence of intravascular penetration in transforaminal lumbosacral epidural steroid injections.** *Spine (Phila Pa 1976)* 2000;25:2628–32
8. Hong JH, Kim SY, Huh B, et al. **Analysis of inadvertent intradiscal and intravascular injection during lumbar transforaminal epidural steroid injections: a prospective study.** *Reg Anesth Pain Med* 2013;38:520–25
9. El Abd OH, Amadera JE, Pimentel DC, et al. **Intravascular flow detection during transforaminal epidural injections: a prospective assessment.** *Pain Physician* 2014;17:21–27
10. Kennedy DJ, Dreyfuss P, Aprill CN, et al. **Paraplegia following image-guided transforaminal lumbar spine epidural steroid injection: two case reports.** *Pain Med* 2009;10:1389–94
11. Windsor RE, Storm S, Sugar R, et al. **Cervical transforaminal injection: review of the literature, complications, and a suggested technique.** *Pain Physician* 2003;6:457–65
12. Smuck M, Fuller BJ, Chiodo A, et al. **Accuracy of intermittent fluoroscopy to detect intravascular injection during transforaminal epidural injections.** *Spine (Phila Pa 1976)* 2008;33:E205–10
13. Wagner AL. **CT fluoroscopy-guided epidural injections: technique and results.** *AJNR Am J Neuroradiol* 2004;25:1821–23
14. Wolter T, Knoeller S, Berlis A, et al. **CT-guided cervical selective nerve root block with a dorsal approach.** *AJNR Am J Neuroradiol* 2010;31:1831–36
15. DePalma MJ, ed. *iSpine: Evidence-Based Interventional Spine Care.* New York: Demos Medical Publishing; 2011:413
16. North American Spine Society Coverage Committee. **Lumbar Epidural Injections: Defining Appropriate Coverage Positions.** August 13, 2014. <https://www.spine.org/Documents/PolicyPractice/CoverageRecommendations/LumbarEpiduralInjections.pdf>. Accessed August 26, 2014
17. Bogduk N. *International Spine Intervention Society Practice Guideline For Spinal Diagnostic and Treatment Procedures.* San Francisco: International Spine Intervention Society; 2013:409
18. Kranz PG, Abbott M, Abbott D, et al. **Optimal contrast concentration for CT-guided epidural steroid injections.** *AJNR Am J Neuroradiol* 2014;35:191–95
19. Guay J. **The epidural test dose: a review.** *Anesth Analg* 2006;102:921–29
20. Wagner AL. **CT fluoroscopic-guided cervical nerve root blocks.** *AJNR Am J Neuroradiol* 2005;26:43–44
21. Kranz PG, Raduazo PA. **Technique for CT fluoroscopy-guided cervical interlaminar steroid injections.** *AJR Am J Roentgenol* 2012;198:675–77
22. Bose B. **Quadriplegia following cervical epidural steroid injections:**

- case report and review of the literature. *Spine J* 2005;5:558–63
23. Kaplan MS, Cooke J, Collins JG. **Intravascular uptake during fluoroscopically guided cervical interlaminar steroid injection at C6–7: a case report.** *Arch Phys Med Rehabil* 2008;89:553–58
 24. Manchikanti L, Malla Y, Wargo BW, et al. **A prospective evaluation of complications of 10,000 fluoroscopically directed epidural injections.** *Pain Physician* 2012;15:131–40
 25. Yin W, Bogduk N. **Retrograde filling of a thoracic spinal artery during transforaminal injection.** *Pain Med* 2009;10:689–92
 26. Jasper JF. **Role of digital subtraction fluoroscopic imaging in detecting intravascular injections.** *Pain Physician* 2003;6:369–72
 27. Verrills P, Nowesenitz G, Barnard A. **Penetration of a cervical radicular artery during a transforaminal epidural injection.** *Pain Med* 2010;11:229–31
 28. McLean JP, Sigler JD, Plataras CT, et al. **The rate of detection of intravascular injection in cervical transforaminal epidural steroid injections with and without digital subtraction angiography.** *PMR* 2009;1:636–42
 29. Chang Chien GC, Candido KD, Knezevic NN. **Digital subtraction angiography does not reliably prevent paraplegia associated with lumbar transforaminal epidural steroid injection.** *Pain Physician* 2012;15:515–23
 30. Chien GC, Candido KD. **Digital subtraction angiography is not the answer for safe epidural injections.** *Pain Physician* 2014;17:E413–14
 31. El Abd O, Daud Amadera JE, Pimentel DC, et al. **In response to digital subtraction angiography is not the answer for safe epidural injections.** *Pain Physician* 2014;17:E414–15
 32. Smuck M, Fuller BJ, Yoder B, et al. **Incidence of simultaneous epidural and vascular injection during lumbosacral transforaminal epidural injections.** *Spine J* 2007;7:79–82
 33. Smuck M, Tang CT, Fuller BJ. **Incidence of simultaneous epidural and vascular injection during cervical transforaminal epidural injections.** *Spine (Phila Pa 1976)* 2009;34:E751–55

Validation of Multisociety Combined Task Force Definitions of Abnormal Disk Morphology

C.H. Cho, L. Hsu, M.L. Ferrone, D.A. Leonard, M.B. Harris, A.A. Zamani, and C.M. Bono



ABSTRACT

BACKGROUND AND PURPOSE: The multisociety task force descriptively defined abnormal lumbar disk morphology. We aimed to use their definitions to provide a higher level of evidence for the validation of MR imaging in the evaluation of this pathology in patients who have undergone discectomy by retrospectively classifying their preoperative MRI.

MATERIALS AND METHODS: This retrospective, institutional review board–approved study included 54 of 86 consecutive patients (47 men; average age, 44 years) enrolled in an ongoing prospective trial of surgically treated lumbar disk herniation who had preoperative MRI and documented intraoperative classification of the abnormal disk as protrusion, extrusion, or sequestration by the treating surgeon. Preoperative MRI was classified by 2 blinded radiologists; discrepancies were resolved by a third reader. Statistical analysis of interobserver agreement and imaging compared with surgical findings was performed.

RESULTS: The readers disagreed on only 1 of the 54 cases. The third reader resolved the disagreement. Eight protrusions and 46 extrusions were found on imaging, with no sequestrations. At surgery, there were 13 protrusions and 40 extrusions, with 2 of the extrusions also containing sequestrations; the remaining case had only sequestration. There were 16 discrepancies between imaging and surgery, resulting in 70% agreement.

CONCLUSIONS: This study, which was intended to validate the multisociety combined task force definitions of abnormal disk morphology by using MR imaging with a surgical criterion standard, found 70% agreement between imaging diagnosis and surgical findings. Although reasonable, this finding highlights differences that often exist between intraoperative and preoperative imaging findings of lumbar disk herniation.

MR imaging of the lumbar spine with defined specific MR images has gained acceptance as the standard of care for the evaluation of degenerative disk disease.¹ However, the interpretation of these images continues to have much variability. An effort to standardize image reporting brought together multiple national medical societies including the North American Spine Society, American Society of Spine Radiology, and American Society of Neuroradiology. They produced and then updated a consensus document for image descriptions.²

One segment of the consensus document focuses on the mor-

phology of the lumbar disk as it relates to the location of abnormal disk content with respect to the outer annulus.² MR imaging studies evaluating the interobserver and intraobserver reliability of disk morphology by using the definition of the consensus document have been performed.^{3–5} However, these studies lacked analysis of surgical findings for correlation with a criterion standard and, as such, do not provide the highest level of diagnostic evidence.

This study retrospectively classified MR imaging findings in a cohort of consecutive patients with surgically treated disk herniation by using the descriptive definition of abnormal lumbar disk morphology of the multisociety task force, with the aim of providing a high level of evidence for validation of MR imaging by using the combined task force definitions.²

MATERIALS AND METHODS

A retrospective review was performed, with approval from the institutional review board of the study site, of the records of 86 consecutive patients (47 men, 39 women; average age, 44 years) who were enrolled between August 2009 and October 2013 in an ongoing prospective clinical trial evaluating the outcomes of sin-

Received September 8, 2014; accepted after revision October 24.

From the Departments of Radiology (C.H.C., L.H., A.A.Z.) and Orthopedic Surgery (M.L.F., D.A.L., M.B.H., C.M.B.), Brigham and Women's Hospital, Harvard Medical School, Boston, Massachusetts.

Abstract of preliminary work previously presented at: Annual Meeting of the North American Spine Society, November 12–15, 2014; San Francisco, California.

Please address correspondence to Charles H. Cho, MD, MBA, Department of Radiology, Brigham and Women's Hospital, Harvard Medical School, 75 Francis St, Boston, MA 02115; e-mail: ccho81@partners.org

 Indicates article with supplemental on-line appendix.

<http://dx.doi.org/10.3174/ajnr.A4212>

gle-level lumbar discectomy. Inclusion criteria for entry into the prospective study were the presence of a symptomatic single-level lumbar disk herniation, failure of nonoperative treatment, primary radicular pain, and no prior lumbar surgery. Included in prospective data collection was documentation of the intraoperative classification of the herniation as a protrusion, extrusion, or sequestration. For the current study, the intraoperative findings were used as the diagnostic criterion standard because the surgeon is looking directly at the anatomy of the patient. These findings have been used as such in numerous other studies.^{6,7} With continued improvement in imaging, the depiction of a patient's anatomy is becoming clearer and more accurate and is approaching equivalence to looking at it.

Surgical cases were from the clinical practice of 3 attending orthopedic spine surgeons from a single institution. Surgeons recorded operative findings that included classifying the disk herniation as a protrusion, extrusion, or sequestration intraoperatively. In the operative field, the outer margin of the annulus was visually identified. A defect of the annulus with disk material outside the annulus was classified as "extrusion." If there were no defect and no disk material outside the annulus, the classification of "protrusion" was made. "Sequestration" was determined if there was disk material separate from the annular defect with no visible attachment to the parent disk.

Of the 86 patients, 1 patient had no disk herniation noted during surgery, which was presumed to mean the disk had resorbed between imaging and surgery, and 3 patients had incomplete surgical data sheets. These cases were excluded. Of the remaining 82 cases, 54 had presurgical MR images accessible by the PACS of the study institution, so these 54 cases were included in the present study.

In preparation for the current analysis, a summary sheet (Online Appendix 1) was created and reviewed by 3 board-certified neuroradiologists, each with a minimum of 15 years of practice experience and a combined average of >26 years, based on the previously described multisociety task force definitions.² Sample cases from daily practice were used in a face-to-face setting to confirm the understanding of the summary sheet definitions before data collection.

The MR imaging of each subject (mean, 81 ± 75 days before surgery) was reviewed by 2 board-certified radiologists who were blinded to the patient medical history and operative findings. In the evaluation, the disk level with the most substantial abnormality was classified as a protrusion, extrusion, or sequestration by using both axial and sagittal images. Classifications were confined to a single disk. In cases in which >1 disk level had abnormalities, only the more severe level was selected. In 1 case in which there was nearly equivalent severity at 2 disk levels, the surgical level was provided to the readers to create a final, imaging-based classification that could be compared with the surgical classification. Any discrepancy between the 2 readers was resolved by a third blinded reader, and a majority consensus evaluation became the final imaging interpretation. Of note, many of the MR images were from different, outside, referring hospitals. However, all cases included sagittal T1- and sagittal and axial T2-weighted images.

Most important, while the surgeons did have the MR imaging available at the time of surgery, they did not have the findings as

decided by the study radiologists. Additionally, the surgeons were instructed to make their classifications solely on the basis of their intraoperative observations. While having the MR imaging available to surgeons may have been a potential source of bias, surgeons always use MR imaging to plan for their surgery; thus, in practice, surgeons also have that potential source of bias. Research must be applicable to practice, and blinding surgeons to MR imaging would not mimic practice.

All statistical analyses were performed by using STATA/SE 13.1 (StataCorp, College Station, Texas). Agreement between imaging and surgical classifications was calculated by using the Cohen κ , as was agreement between imaging assessments. The weighted κ was not used because disk herniations do not always progress in a standardized manner. A standard 2×2 table was used to determine sensitivity, specificity, and predictive values.

RESULTS

Imaging Findings

Of the 54 cases, the 2 readers disagreed in 3. One case had a final diagnosis discrepancy between protrusion and extrusion based on all images. In the other 2 cases, there was a disagreement on disk description as protrusion or extrusion on the axial plane, but both readers described an extrusion on the sagittal images. Thus, the final diagnosis of extrusion was the same for these 2 cases. All discrepancies were resolved by the third reader. Overall, 53 of 54 cases showed agreement in the final diagnosis between readers. Interobserver agreement between the 2 readers was 98% with a κ of 0.93. There were 8 protrusions, 46 extrusions, and no sequestrations based on imaging findings.

Surgical Findings

Of the 54 surgical cases with MR images, there were 13 protrusions and 40 extrusions, with 2 of the extrusions each occurring in addition to sequestrations. The 1 remaining case had only sequestration and no extrusion.

Imaging and Surgical Agreement

Four cases with an imaging diagnosis of protrusion were found to be extrusions in surgery. Nine cases with imaging diagnoses of extrusion were found to be protrusions in surgery. Whereas imaging data did not reveal any cases of sequestration, in 2 cases with imaging diagnoses of extrusion, surgery showed both extrusion and sequestration; these were considered discrepancies between imaging and surgical findings. In another case, imaging showed extrusion while surgery showed sequestration only. The total number of discrepancies was 16, calculated as an overall agreement of 70% ($\kappa = 0.19$). Table 1 lists all the discrepancy cases and gives descriptions of the imaging findings.

Sensitivity and specificity of detection of a ruptured annulus were 0.90 and 0.31, respectively (Table 2). The positive predictive value was 0.80, while the negative predictive value was 0.50.

DISCUSSION

Prior studies evaluating imaging interpretation of lumbar disk abnormalities have shown moderate interobserver agreement and substantial intraobserver agreement in cohorts of asymptomatic volunteers and symptomatic patients.³ One study included exper-

Table 1: Discrepancy cases between imaging and surgery, with a description of the imaging findings

No.	Disk		Surgical	Description
	Level	Imaging		
1	4/5	Extrusion	Protrusion	On sagittal images, the height of the abnormal disk is slightly greater than the disk height
2	2/3	Extrusion	Extrusion and sequestration	Although imaging suggests a sequestered fragment, there is a thin continuity between the disk fragments visible on MR imaging (Fig 1)
3	4/5	Extrusion	Protrusion	On sagittal images, the height of the abnormal disk is slightly greater and very close in distance to the maximum disk height
4	4/5	Extrusion	Protrusion	On sagittal images, the height of the abnormal disk is very close in distance to the maximum disk height (Fig 2)
5	4/5	Extrusion	Extrusion and sequestration	Sagittal images show a connection between disk fragments
6	4/5	Extrusion	Protrusion	On sagittal images, the abnormal disk appears contained by the outer annulus, but the height of the annulus is slightly greater than the disk height
7	4/5	Extrusion	Protrusion	On sagittal images, the height of the abnormal disk is slightly greater than the disk height
8	5/1	Extrusion	Protrusion	On sagittal images, the height of the abnormal disk is slightly greater than the disk height
9	5/1	Protrusion	Extrusion	On the sagittal view, the low signal of the disk and annulus is very difficult to differentiate (Fig 3)
10	4/5	Extrusion	Protrusion	On sagittal images, the height of the abnormal disk is very similar to the disk height
11	4/5	Protrusion	Extrusion	On the sagittal view, the low signal of the disk and annulus is very difficult to differentiate
12	4/5	Protrusion	Extrusion	On sagittal images, the entire annulus is not clearly defined
13	5/1	Protrusion	Extrusion	On sagittal images, the abnormal disk height is similar to the maximum disk height
14	4/5	Extrusion	Protrusion	On sagittal images, the abnormal disk height is slightly greater than the maximum disk height
15	5/1	Extrusion	Protrusion	On the sagittal view, abnormal disk height is much greater than the normal disk height and the outer annulus appears disrupted; in retrospect, the diagnosis is still extrusion by imaging criteria (Fig 4)
16	4/5	Extrusion	Sequestration	Imaging shows a thin connection between the parent disk and disk the fragment

Table 2: 2 × 2 contingency table for a ruptured-versus-intact annulus as determined surgically and on imaging

Imaging Assessment	Surgical Assessment (Criterion Standard)		Totals
	Annulus Ruptured ^a	Intact Annulus ^b	
Annulus ruptured ^a	37	9	41
Intact annulus ^b	4	4	13
Totals	46	8	54

^a Extrusions and sequestrations.

^b Protrusions only.

rienced readers in a single academic institution; interpretation included descriptions of normal and bulge as well as protrusion and extrusion, with the most common discrepancy occurring between normal and bulge.³ Another study, by using readers from 1 academic center with a prestudy effort to define the review criteria, found near-perfect interreader agreement (summary $\kappa = 0.81$) for normal/bulge, protrusion, and extrusion/sequestration categories.⁴ Other reports replicating conditions close to those of clinical practice by using radiologists from different hospitals with no prior set diagnostic criteria or training showed only moderate interobserver agreement for herniation and fair-to-moderate agreement for disk contour.⁵ Most important, all of the above studies lacked a surgical criterion standard.

In the current study, substantial effort was made to decrease interobserver variability, because the primary goal was to evaluate the correlation with surgical findings. Before data collection, the 3 readers discussed the nomenclature by using daily clinical cases from the previous few months. There was extensive discussion about the definitions of protrusion and extrusion, especially on the sagittal images. In the end, the critical point of interpretation among the readers was the exact location of the outer annulus insertion on the vertebral body, which was crucial in discriminat-

ing protrusion from extrusion. To better understand this anatomy, the readers reviewed studies in the literature, including pathologic and traumatic conditions, in terms of how they affect the outer annulus insertion site and how it is localized above the bony endplate on the sagittal view.⁸⁻¹¹ These studies showed that the insertion of the annulus is beyond the bone edge of the disk; this finding creates discrepancies among readers on the insertion site. With this understanding, we went back to the protrusion definition from the combined task force report² and noted that the insertion site of the annulus cannot be greater than the maximum height of the disk space in the sagittal plane. For uniformity, we therefore decided to use the disk space height to define the difference between protrusion and extrusion. Thus, any disk morphology less than the maximum sagittal disk height was designated as protrusion. This distinction is depicted in On-line Appendix 2.

After this effort to optimize uniform understanding and agreement of the definitions among the radiologists, there was consensus in the final imaging diagnosis of 53 of 54 cases (agreement, 98%; $\kappa = 0.93$). If the 2 other cases of discrepancy in the axial or sagittal description (which did not affect the final diagnosis) are included, the agreement was 51 of 54, or 94%. These values are at least as good as, if not better than, those previously reported.

Initially the surgical level was not provided to the readers because transitional vertebral levels may have directed the attention to an incorrect surgical level by causing the readers to number the vertebrae differently. Thus, the readers were instructed to report the most severe disk level during the imaging analysis. In 1 case, L5-S1 had moderate central protrusion and L4-L5 had a small foraminal protrusion. The latter, despite appearing less severe, was in fact at the symptomatic level of radiculopathy. In this case, the correct level was indicated to the readers at the time of imaging data collection and before the analysis.

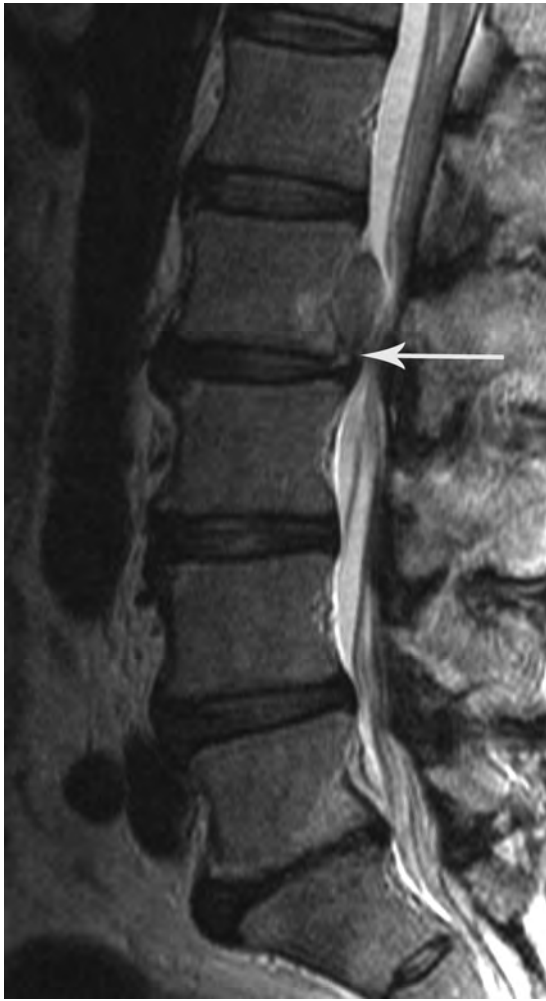


FIG 1. Case 2. Sagittal T2-weighted image shows a thin connection (*arrow*) between the level of abnormal disk and the disk fragment. With imaging, this is classified as extrusion. However, it was classified intraoperatively as extrusion and sequestration.

Overall, our accuracy measurements indicate that imaging is better at determining when the annulus is ruptured than it is at determining that the annulus is intact. Analysis of the discrepancies between imaging and surgery (Table 1) showed the following 3 observations: 1) When the height of the abnormal disk material on the sagittal plane is very close to the maximum height of the normal disk, it becomes difficult to differentiate protrusion from extrusion on imaging (Fig 2). 2) When the disk signal is low on all MR images, differentiation of an abnormal disk from the outer annulus becomes challenging and a small extruded disk cannot be differentiated from a contained (protruded) disk (Fig 3). 3) In differentiating extrusion from sequestration, imaging clearly shows a thin connecting tissue, which, by definition, is considered extrusion (Fig 1). The thin connecting tissue that defines a herniation as an extrusion can be clearly shown on imaging yet not observed in surgery, because the thin sliver of tissue may be very difficult to discern. All discrepancy cases are shown in On-line Appendix 3.

We believe that the effect of variation in imaging parameters on discrepant classifications was minimal in this study. Of the 16 cases with discrepancies, though the magnet strength is not noted



FIG 2. Case 4. Sagittal T2-weighted image shows the height of the abnormal disk herniation (*bold arrows*) compared with the disk height (*thin arrows*). By imaging, this is classified as extrusion. However, it was classified intraoperatively as protrusion.

in all, most appear to have been performed with at least 1.5T. The TR ranged from 3000 to 5760 ms (a single case at 1000 ms); TE, from 90 to 148 ms; section thickness, between 4 and 5 mm (a single case at 3.6 mm); the FOV, from 24 to 30 cm; and the acquisition matrix, between 256 and 512 (a single case, 240 × 175). The overall range of imaging parameters of all these cases is within the standard for achieving high-quality images, which are also in agreement visually as determined by 2 experienced neuroradiologists. With most of the imaging findings being obvious, ultimately we neither think that these discrepancies are due to slight differences in imaging parameters nor believe that variation in imaging parameters compromises the purpose of this study.

Given that at surgery a defect in the posterior annulus differentiates extrusion from protrusion while in imaging it is the relative size of the herniated disk versus the height of base of the annulus that differentiates the 2 categories, it is somewhat surprising that surgery and radiology agree so often. While the approach is different on imaging versus during surgery, the goal in both cases is to determine whether the annulus is ruptured. Because this can be directly observed intraoperatively, surgical standing has been used as the criterion standard, but advancements in imaging can perhaps better define the outer annulus and an-



FIG 3. Case 9. Sagittal T2-weighted image shows decreased signal of the disk material, which makes differentiation of the disk from the annular margin difficult.

nular defects. This change would allow a truer imaging prediction of surgical findings. Imaging needs to be better defined so that it can more accurately and more directly determine the presence or lack of an annular defect instead of relying on morphology to provide clues as to the presence or lack of said defect. As imaging improves and this definition becomes possible, it could enable better correlation of symptoms of a disk herniation to the type of herniation and prediction of surgical-versus-nonoperative outcomes for any given patient on the basis of their MR imaging.

This study has a number of limitations. The time between imaging and surgery was 81 days on the average, so progression or resorption of the disk herniation could have occurred from the time of imaging to surgery. One example of this is case 15 (Fig 4), which, on imaging, was classified as an extrusion but was intraoperatively classified as a protrusion. In addition, the number of cases of sequestration was small, thereby limiting conclusions from analysis of this category. In addition, despite the reasonable (70%) agreement between the imaging diagnosis and surgical findings, the probability of the calculated agreement occurring by chance was high owing to the distribution of classifications, which were mostly extrusions. This is reflected in the low κ of 0.19. Despite this high probability, we think that the study is representative of actual practice, and increasing the sample size would not have significantly altered the pathology distribution. Additionally, agreement on a surgical classification is generally moderate at best.¹² For disk classification, the agreement on the difference between protrusion and extrusion/sequestration would likely be good, but the agreement on the difference between extrusion and sequestration would likely be moderate at best. However, due to the pathology distribution and our resulting focus on the distinction between protrusion and sequestration/extrusion rather than



FIG 4. Case 15. Sagittal T2-weighted image shows disruption of outer annulus (arrow) even on retrospective interpretation; thus, the imaging classification in this case is extrusion. However, it was classified intraoperatively as a protrusion.

the distinction between sequestration and extrusion, the effect of this limitation is unlikely to be substantial.

CONCLUSIONS

In this study, which was intended to validate the multisociety combined task force definitions of abnormal disk morphology by using MR imaging with a surgical criterion standard, there was 70% agreement between the imaging diagnosis and surgical findings. Common trends for the discrepancy are described. Future effort may yield better agreement between surgeons and radiologists as to how they describe disk herniation and abnormalities.

Disclosures: Charles H. Cho—UNRELATED: Board Membership: North American Spine Society (no money). Mitchel B. Harris—UNRELATED: Board Membership: North American Spine Society (no money). Christopher M. Bono—UNRELATED: Board Membership: North American Spine Society (nonmonetary, volunteer); Consultancy: United Healthcare; Expert Testimony: CRICO; Royalties: Wolters Kluwer, for edited books; Other: Journal of the American Academy of Orthopaedic Surgeons. Comments: stipend for being Deputy Editor.

REFERENCES

1. Modic MT, Ross JS. Lumbar degenerative disk disease. *Radiology* 2007;245:43–61
2. Fardon DF, Williams AL, Dohring EJ, et al. Lumbar disc nomenclature: version 2.0, recommendations of the combined task forces of the North American Spine Society, the American Society of Spine Radiology, and the American Society of Neuroradiology. *Spine (Phila Pa 1976)* 2014;39:E1448–65
3. Brant-Zawadzki MN, Jensen MC, Obuchowski N, et al. Interobserver and intraobserver variability in interpretation of lumbar disc abnormalities: a comparison of two nomenclatures. *Spine (Phila Pa 1976)* 1995;20:1257–63; discussion 1264
4. Lurie JD, Tosteson AN, Tosteson TD, et al. Reliability of magnetic

- resonance imaging readings for lumbar disc herniation in the Spine Patient Outcomes Research Trial. *Spine (Phila Pa 1976)* 2008;33:991–98
5. Arana E, Kovacs FM, Royuela A, et al. **Influence of nomenclature in the interpretation of lumbar disk countour on MR imaging: a comparison of the agreement using the combined task force and the Nordic nomenclatures.** *AJNR Am J Neuroradiol* 2011;32:1143–48
 6. Zhuge W, Ben-Galim P, Hipp JA. **Efficacy of MRI for assessment of spinal trauma: correlation with intra-operative findings.** *J Spinal Disord Tech* 2013 Nov 8. [Epub ahead of print]
 7. Hedberg MC, Drayer BP, Flom RA, et al. **Gradient echo (GRASS) MR imaging in cervical radiculopathy.** *AJR Am J Roentgenol* 1988; 150:683–89
 8. Humzah MD, Soames RW. **Human intervertebral disc: structure and function.** *Anat Rec* 1988;220:337–56
 9. Rauschnig W. **Computed tomography and cryomicrotomy of lumbar spine specimens: a new technique for multiplanar anatomic correlation.** *Spine (Phila Pa 1976)* 1983;8:170–80
 10. Tajima N, Kawano K. **Cryomicrotomy of the lumbar spine.** *Spine (Phila Pa 1976)* 1986;11:376–79
 11. Fredrickson BE, Edwards WT, Rauschnig W, et al. **Vertebral burst fractures: an experimental, morphologic, and radiographic study.** *Spine (Phila Pa 1976)* 1992;17:1012–21
 12. Brumback RJ, Jones AL. **Interobserver agreement in the classification of open fractures of the tibia: the results of a survey of two hundred and forty-five orthopaedic surgeons.** *J Bone Joint Surg Am* 1994;76:1162–66

Trevo® XP ProVue Retrievers

See package insert for complete indications, complications, warnings, and instructions for use.

INDICATIONS FOR USE

The Trevo Retriever is intended to restore blood flow in the neurovasculature by removing thrombus in patients experiencing ischemic stroke within 8 hours of symptom onset. Patients who are ineligible for intravenous tissue plasminogen activator (IV t-PA) or who fail IV t-PA therapy are candidates for treatment.

COMPLICATIONS

Procedures requiring percutaneous catheter introduction should not be attempted by physicians unfamiliar with possible complications which may occur during or after the procedure. Possible complications include, but are not limited to, the following: air embolism; hematoma or hemorrhage at puncture site; infection; distal embolization; pain/headache; vessel spasm, thrombosis, dissection, or perforation; emboli; acute occlusion; ischemia; intracranial hemorrhage; false aneurysm formation; neurological deficits including stroke; and death.

COMPATIBILITY

3x20 mm retrievers are compatible with Trevo® Pro 14 Microcatheters (REF 90231) and Trevo® Pro 18 Microcatheters (REF 90238). 4x20 mm retrievers are compatible with Trevo® Pro 18 Microcatheters (REF 90238). Compatibility of the Retriever with other microcatheters has not been established. Performance of the Retriever device may be impacted if a different microcatheter is used. The Merci® Balloon Guide Catheters are recommended for use during thrombus removal procedures. Retrievers are compatible with the Abbott Vascular DOC® Guide Wire Extension (REF 22260)

WARNINGS

- Contents supplied STERILE, using an ethylene oxide (EO) process. Nonpyrogenic.
- To reduce risk of vessel damage, adhere to the following recommendations:
 - Take care to appropriately size Retriever to vessel diameter at intended site of deployment.
 - Do not perform more than six (6) retrieval attempts in same vessel using Retriever devices.
 - Maintain Retriever position in vessel when removing or exchanging Microcatheter.
- To reduce risk of kinking/fracture, adhere to the following recommendations:
 - Immediately after unsheathing Retriever, position Microcatheter tip marker just proximal to shaped section. Maintain Microcatheter tip marker just proximal to shaped section of Retriever during manipulation and withdrawal.
 - Do not rotate or torque Retriever.
 - Use caution when passing Retriever through stented arteries.
- Do not resterilize and reuse. Structural integrity and/or function may be impaired by reuse or cleaning.
- The Retriever is a delicate instrument and should be handled carefully. Before use and when possible during procedure, inspect device carefully for damage. Do not use a device that shows signs of damage. Damage may prevent device from functioning and may cause complications.
- Do not advance or withdraw Retriever against resistance or significant vasospasm. Moving or torquing device against resistance or significant vasospasm may result in damage to vessel or device. Assess cause of resistance using fluoroscopy and if needed resheath the device to withdraw.

- If Retriever is difficult to withdraw from the vessel, do not torque Retriever. Advance Microcatheter distally, gently pull Retriever back into Microcatheter, and remove Retriever and Microcatheter as a unit. If undue resistance is met when withdrawing the Retriever into the Microcatheter, consider extending the Retriever using the Abbott Vascular DOC guidewire extension (REF 22260) so that the Microcatheter can be exchanged for a larger diameter catheter such as a DAC® catheter. Gently withdraw the Retriever into the larger diameter catheter.
- Administer anti-coagulation and anti-platelet medications per standard institutional guidelines.

PRECAUTIONS

- Prescription only – device restricted to use by or on order of a physician.
- Store in cool, dry, dark place.
- Do not use open or damaged packages.
- Use by “Use By” date.
- Exposure to temperatures above 54°C (130°F) may damage device and accessories. Do not autoclave.
- Do not expose Retriever to solvents.
- Use Retriever in conjunction with fluoroscopic visualization and proper anti-coagulation agents.
- To prevent thrombus formation and contrast media crystal formation, maintain a constant infusion of appropriate flush solution between guide catheter and Microcatheter and between Microcatheter and Retriever or guidewire.
- Do not attach a torque device to the shaped proximal end of DOC® Compatible Retriever. Damage may occur, preventing ability to attach DOC® Guide Wire Extension.



Concentric Medical
301 East Evelyn
Mountain View, CA 94041



EMERGO Europe
Molenstraat 15
2513 BH, The Hague
The Netherlands



Stryker Neurovascular
47900 Bayside Parkway
Fremont, CA 94538

stryker.com/neurovascular
stryker.com/emea/neurovascular

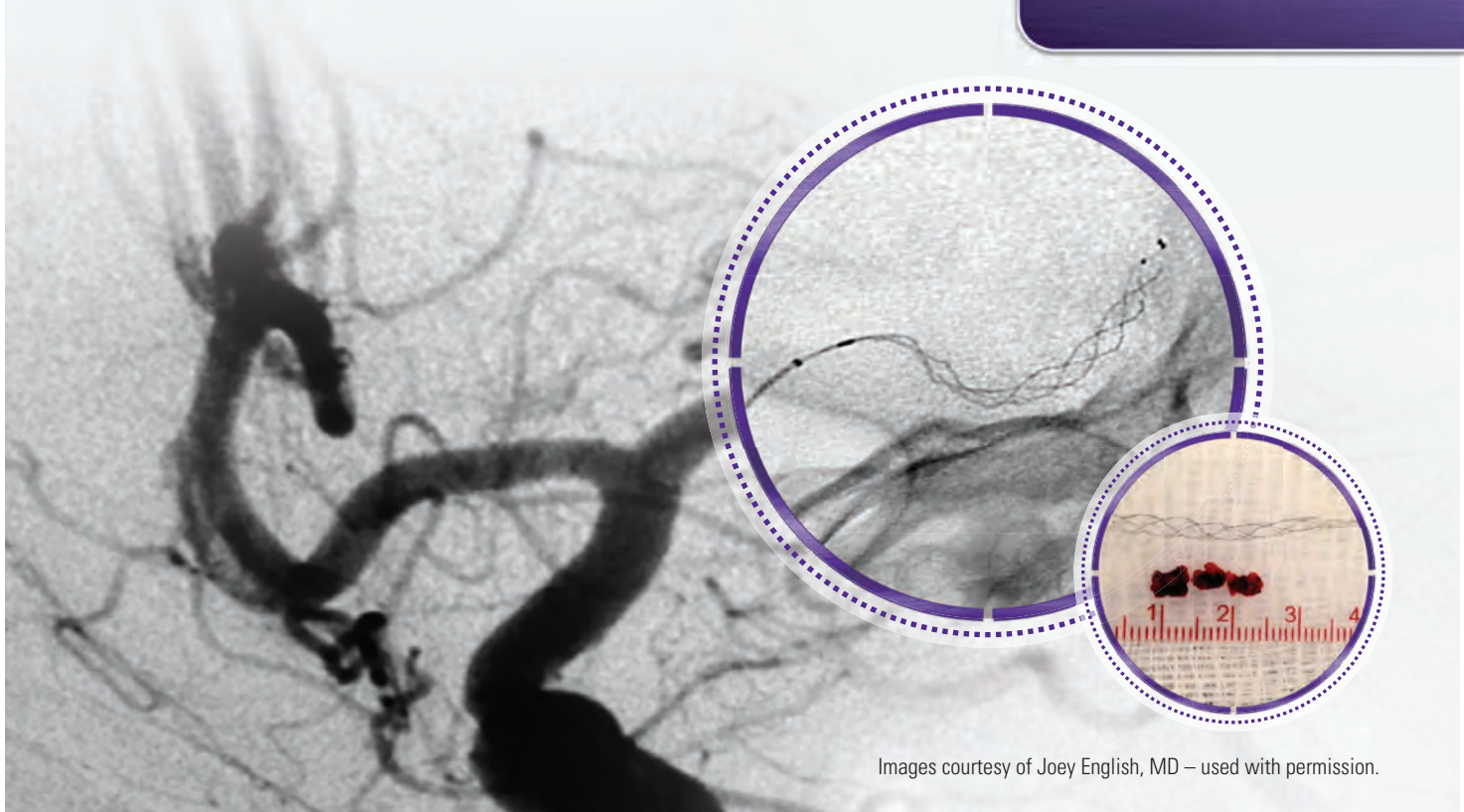
Date of Release: JUN/2014

EX_EN_GL

Stent Retrievers:

The evidence is clear

stryker[®]
Neurovascular



Images courtesy of Joey English, MD – used with permission.

Trial	Number of Patients	Statistically Superior Result for Endovascular Therapy
MR CLEAN ¹	500	
ESCAPE ²	316	
EXTEND-IA ³	70	
SWIFT PRIME ⁴	196	

Stent retrievers ± IV-tPA gave patients up to **3x higher likelihood** of an mRS 0-2 at 90 days than IV-tPA alone^{1,2,3,4}

1. O.A. Berkhemer et al. A Randomized Trial for Intraarterial Treatment for Acute Ischemic Stroke. *N Eng J Med* December 2014.

2. M. Goyal et al. Randomized Assessment of Rapid Endovascular Treatment of Ischemic Stroke. *N Eng J Med* published on February 11, 2015.

3. B.C.V. Campbell et al. Endovascular Therapy for Ischemic Stroke with Perfusion-Imaging Selection. *N Eng J Med* published on February 11, 2015.

4. Results of the SWIFT PRIME Trial were presented by Dr. Jeffrey Saver at the International Stroke Conference in Nashville, TN on Wednesday, February 11, 2015.

Pipeline™ Flex Embolization Device

The Next Advancement in Flow Diversion

CLINICALLY PROVEN BRAID.

0% RECURRENCE

up to 5 years in PUFs¹⁻³

DELIVERY REDEFINED.

Full resheathability and instant braid release for accurate placement without torquing



COVIDIEN

The Pipeline™ Flex embolization device should be used only by physicians trained in percutaneous, intravascular techniques and procedures at medical facilities with the appropriate fluoroscopy equipment. **Indications for Use:** The Pipeline™ Flex embolization device is indicated for the endovascular treatment of adults (22 years of age or older) with large or giant wide-necked intracranial aneurysms (IAs) in the internal carotid artery from the petrous to the superior hypophyseal segments. **CAUTION:** Federal (USA) law restricts this device to sale, distribution and use by or on the order of a physician. Indications, contraindications, warnings and instructions for use can be found in the product labeling supplied with each device. **Contraindications:** The use of the Pipeline™ Flex embolization device is contraindicated for patients with any of the following conditions: 1) Patients with active bacterial infection. 2) Patients in whom dual antiplatelet therapy (aspirin and clopidogrel) is contraindicated. 3) Patients who have not received dual antiplatelet agents prior to the procedure. 4) Patients in whom a pre-existing stent is in place in the parent artery at the target aneurysm location. **Warnings:** 1) Resheathing of the Pipeline™ Flex embolization device more than 2 full cycles may cause damage to the distal or proximal ends of the braid. 2) Persons with known allergy to platinum or cobalt/chromium alloy (including the major elements platinum, cobalt, chromium, nickel, molybdenum or tungsten) may suffer an allergic reaction to the Pipeline™ Flex embolization device implant. 3) Person with known allergy to tin, silver, stainless steel or silicone elastomer may suffer an allergic reaction to the Pipeline™ Flex embolization device delivery system. 4) Do not reprocess or resterilize. Reprocessing and resterilization increase the risk of patient infection and compromised device performance. 5) Delayed rupture may occur with large and giant aneurysms. 6) Placement of multiple Pipeline™ Flex embolization devices may increase the risk of ischemic complications. **REFERENCES** 1. Becske T, Kallmes DF, Saatci I, et al. Pipeline for Uncoilable or Failed Aneurysms: Results from a Multicenter Clinical Trial. *Radiology*. June 2013. 2. IntrePED Presentation by Dr. David Kallmes, SNIS Conference, July 28, 2013. This device should be used only by physicians trained in percutaneous, intravascular techniques and procedures at medical facilities with the appropriate fluoroscopy equipment. The Pipeline™ Flex embolization device should be used by physicians who have received the appropriate training for this device. **Indications for Use:** The Pipeline™ Flex embolization device is intended for endovascular embolization of cerebral aneurysms. 3. Data on file and PUFs 5 year results to be presented at ISC 2015. COVIDIEN, COVIDIEN with logo, and Covidien logo are US and internationally registered trademarks of Covidien AG. Other brands are trademarks of a Covidien company. © 2015 Covidien. MK1372022015A